Magnetotelluric Investigation of the Laguna del Maule Volcanic Field, Central Chile

by

Darcy Raymond Cordell

A thesis submitted in partial fulfillment of the requirements for the degree of

Doctor of Philosophy

in

Geophysics

Department of Physics
University of Alberta

ABSTRACT

This thesis uses the magnetotelluric (MT) method to image the electrical resistivity structure of the Laguna del Maule Volcanic Field (LdMVF) and the regional subduction zone structure of central Chile (36°S) in the vicinity of the 2010 Maule earthquake. The LdMVF surrounds the eponymous Laguna del Maule (LdM) and the area has been experiencing unprecedented and ongoing upward ground deformation greater than 20 cm/year since 2007. This, along with extensive rhyolite eruptions in the last 25 ka, suggests the presence of a restless magmatic system at depth. Broadband MT data were collected at the LdMVF and the data were processed, analyzed and inverted to produce the first three-dimensional image of the electrical resistivity structure of the LdMVF. The shallow subsurface included small low resistivity anomalies directly beneath the lake at 100-300 m depth and at 1 km depth, both interpreted as hydrothermal fluids and alteration. The most significant low resistivity anomaly in the model is located in the mid-crust (10 km depth) and is laterally-offset northwards from vents, lava flows, and the center of deformation. A steeply-dipping conductor is imaged on the western side of the LdMVF in the upper crust (3 km depth) and connects to the mid-crustal conductor. Both the mid- and upper-crustal conductive anomalies are interpreted as zones of partial melt and hydrothermal fluids which suggests that deep source melts may migrate both laterally and vertically as they approach the surface. Detailed sensitivity analyses were performed to elucidate discrepancies between the MT resistivity model and published seismic velocity and density models. These simulations suggest that the MT data are better fit with isolated, steeply-dipping conductors along the mapped Troncoso fault, rather than a single large conductor in the upper crust. This suggests that any large (e.g. 450 km^3) homogeneous mush zone in the upper crust beneath the LdMVF contains relatively little interconnected melt. The MT is imaging a structure-driven magmatic plumbing system which contains batches of eruptible magma and hydrothermal fluids in the upper crust. A relatively small (e.g. 10 km^3) ephemeral magma reservoir in the shallow crust beneath the inflation center could go undetected but larger volumes (e.g. 30 km^3) with

high-melt fraction would have a detectable signature in the MT data. The southeastern LdMVF—on the footwall side of the Troncoso fault—contains no significant geophysical anomalies despite being volcanically active which further suggests that eruptible volumes of magma must be small and ephemeral. The lack of a large electrical resistivity anomaly directly beneath the LdMVF provides an important constraint on the magma plumbing system.

To better understand the regional context in which the LdMVF is situated, broadband and long-period MT data were collected along a 380-km profile from the Pacific Ocean to western Argentina. These data were used to image the deeper subduction zone structure and better understand the role that fluids play in earthquake rupture and magma genesis. The data measured a regional geoelectric strike of N15°W ± 19° with a notable westward shift at sites on the volcanic arc. The data also suggested some three-dimensional geoelectric structure and possible anisotropic features but two-dimensional isotropic inverse modelling was employed as an approximation. The preferred inversion model included several conductors along the plate interface related to fluid release from compaction and metamorphic reactions in the forearc, and higher pressure-temperature metamorphic reactions and flux melting in the backarc. A resistor on the plate interface near the Moho is interpreted as a strong, dry asperity which may affect the co-seismic slip behavior of large megathrust earthquakes at this latitude. This resistor is correlated with the previously identified Cobquecura high velocity anomaly from seismic tomography. Beneath the volcanic arc, two conductors in the upper crust (<10 km depth) were interpreted as partial melt beneath the Tatara-San Pedro Volcano and the LdMVF. A deeper conductor in the lower crust (>25 km depth) underlies both volcanoes and suggests a connected network of melt in a thermally-mature lower crust.

PREFACE

Some of the research conducted for this thesis forms part of an international research collaboration[1] led by Dr. Brad Singer at the University of Wisconsin-Madison. Dr. Martyn Unsworth, my supervisor, is the lead collaborator at the University of Alberta. The majority of Chapter 5 has been previously published as D. Cordell, M.J. Unsworth, D. Díaz, 2018, "Imaging the Laguna del Maule Volcanic Field, central Chile using magnetotellurics: Evidence for crustal melt regions laterally-offset from surface vents and lava flows", *Earth and Planetary Science Letters,* vol. 488, 168-180. The majority of Chapter 7 of this thesis has been previously published as D. Cordell, M.J. Unsworth, D. Díaz, V. Reyes-Wagner, C. Currie, S.P. Hicks, 2019, "Fluid and melt pathways in the central Chilean subduction zone near the 2010 Maule earthquake (35°-36° S) as inferred from magnetotelluric data", *Geochemistry, Geophysics, Geosystems,* vol. 21. The majority of Chapter 6 of this thesis has been prepared for submission to *Journal of Geophysical Research*. For all three papers, I was responsible for magnetotelluric data collection, data analysis and manuscript composition.

[1] http://geoscience.wisc.edu/rhyolitic/

ACKNOWLEDGMENTS

I would first like to thank my supervisor, Dr. Martyn Unsworth, for his invaluable help and guidance in collecting and interpreting data and writing this thesis. I would also like to thank other members from the research group, past and present, for their ideas and conversations throughout my time at the University of Alberta including Sean Bettac, Dr. Matthew Comeau, Theron Finley, Cedar Hanneson, Benjamin Lee, Greg Nieuwenhuis, and Dr. Enci Wang. Furthermore, I would like to thank the members of my committee for our discussions and their comments on my thesis.

This project involved a large amount of field work conducted in central Chile and involved many individuals to help collect the data including: Bárbara Blanco, Daniel Cabrera, Matthew Comeau, Daniel Díaz, Ariel Figueroa, Jorge Gacitua, Maria Jose Hernández, Renzo Mancini, Maximiliano Pavez, Gustavo Pérez Guitiérrez, Valentina Reyes-Wagner, and Nicolás Vera Cortés. Special mention is given to Dr. Daniel Díaz, without whom we would not have accomplished very much in Chile. Many thanks to him for the organization of trucks, instruments, supplies, horses, helicopters, field personnel, etc. Special thanks to Brad Singer, Cliff Thurber, and Basil Tikhoff for their logistical support especially in organizing the helicopter. Thank you to Omar Reyes, Luis Burgos and Familia Rancho Los Reyes for the horse adventures in 2016 and Gabriela and José Luis Valdés for their hospitality in 2017. A special thank you to Don Luis Torres for his invaluable knowledge of Laguna del Maule, his logistical support, and numerous boat rescues in inclement weather. I also thank many of the LdM team for conversations and helpful comments throughout the project notably Ninfa Bennington, Nathan Andersen, Hélène Le Mével, and Craig Miller. Thank you to Cathy Hickson and Carolina Rodriguez for providing 2009 to 2012 MT data collected by Alterra Power Corp. (now Innergex Renewable Energy). Thank you to John Booker and Aurora Burd for helping to locate Argentine MT data. Special thanks to the Centro de Excelencia en Geotermia de Los Andes and the Universidad Católica de Chile for use of their Metronix instruments. Thank you to Naser Meqbel for his support with the ModEM software, Randall Mackie for the use of his 2-D MT inversion algorithm, and Alan Jones and Gary McNeice for providing their tensor decomposition program. WestGrid Canada computer clusters were used for all the 3-D inversions. This research was financially supported by the National Science Foundation (EAR-1411779), an NSF Discovery Grant to Dr. Martyn Unsworth, and NSERC CGS-D and PGS-D scholarships.

Finally, I would like to thank my wife, Marya Cordell, for her encouragement and endless support.

TABLE OF CONTENTS

LIST OF TABLES

LIST OF FIGURES

Tr = Tromen; L = Llaima; VI = Villarrica.

Figure 2.5: Geology map of the Maule Region of central Chile. Blue triangles denote stratovolcanoes; yellow triangles show recent rhyolitic volcanoes; black triangles show back-arc volcanoes. Yellow stars show epicenters of major historical earthquakes. See Figure 2.4 for map location. PP = Planchon Peteroa; C = Calabozos Volcanic Field; P = Puelche Volcanic Field; Bo = Bobadilla Caldera; LdMVF = Laguna del Maule Volcanic Field; Va = Varvarco; PM = Payun Matru; DG = Descabezado Grande; CA = Cerro Azul; TSP = Tatara-San Pedro; NdL = Nevados de Longavi; LB = Lomas Blancas; NdC = Nevados de Chillan.

Figure 2.6: Seismicity cross sections in the Southern Volcanic Zone from 1970 (IRIS, 2018). Each dot on the map shows an earthquake epicenter. Yellow stars denote epicenters from important earthquakes. Each inset corresponds to cross-sections along profiles shown by red lines on the map from north (top) to south (bottom). Each inset shows (1) a cross-section of seismicity where earthquake hypocenters (black dots) approximately follow the top of the down-going Nazca plate; (2) A plot of the topography along each profile and; (3) A histogram of earthquake magnitudes along the cross-section.

Figure 2.7: Map showing profiles from geophysical surveys in the Southern Volcanic Zone discussed in detail in text. Note that all studies shown are 3-D surveys with particular profiles chosen for display purposes except for Brasse et al. (2009) which was a 2-D survey.

Figure 2.8: Cross-sections through the three-dimensional seismic tomography model of Pesicek et al. (2012). Inset map shows location of profiles and location of LdMVF and Maule 2010 earthquake. Color bar shows seismic P-wave velocity anomaly in km/s. Modified from Figure 3 in Pesicek et al. (2012).

Figure 2.9: Cross-section through the three-dimensional seismic tomography model of Hicks et al. (2014). Yellow star denotes hypocenter of the 2010 Maule earthquake and yellow triangle is the Laguna del Maule Volcanic Field.

Figure 2.10: Interpretation of the density model from Maksymowicz et al. (2015) based on satellite gravity data.

Figure 2.11: Two-dimensional resistivity model from MT data in the Southern Volcanic Zone along P-P' modified from Brasse et al. (2009). The location of additional profiles x-x' and y-y' from Brasse and Soyer (2001) are shown in the map inset.

Figure 5.7: Root mean square (r.m.s.) data misfit for each station using D+ inversion solution to assess data quality. Poor data fit is found at several sites from 2009. An r.m.s. value of 1.0 is ideal as it suggests that the D+ model is, on average, neither over-fitting or under-fitting the data within error.

Figure 5.8: The directionality and dimensionality of the data based on tensor decomposition (McNeice and Jones, 2001) and phase tensor analysis (Caldwell et al., 2004). Each row shows data at a different frequency (10 Hz, 1 Hz, 0.1 Hz, and 0.01 Hz) for the MT sites used in the inversion. Tensor decomposition skew and tensor decomposition geoelectric strike are shown in the first and second column, respecitvely. High skew indicates more three-dimensional data. The third and fourth columns show the β-skew and geoelectric strike, respectively, derived from phase tensors. Weakly developed geoelectric strike and relatively high skew values suggest largely 3-D structures over the survey area.

Figure 5.9: Induction vectors shown in map view at four different frequencies using the Wiese convention (i.e. induction vectors point away from conductors).

Figure 5.10: Preferred 3-D inversion model results shown using 4 horizontal slices through the model at depths of (A) 0.2 km below lake surface (b.l.s.), (B) 1.2 km b.l.s., (C) 5 km b.l.s., and (D) 11 km b.l.s. Major interpreted features are labelled C1, C2, C3, C3a, C4, and R1. BC = Baños Campanario; IC = Inflation Center; CC = Cerro Campanario; and the outline of the lake is given for reference. White space is air (above topography). The thin lines on each slice represent the 10 Ωm contour. (E) Graph shows r.m.s. misfit as a function of frequency for all stations (light blue lines) and overall (thick red line). (F) Map shows station locations with circles colored as the r.m.s. misfit value at each station. Blue corresponds to low r.m.s. misfit and red corresponds to high r.m.s. misfit.

Figure 5.11: Preferred 3-D inversion model results shown using a fence diagram using two diagonal slices through the model along PQ and QR as shown in map inset. Black dots in the map inset denote MT sounding locations. Profile PQ cuts across major features C3 and C4. Profile QR cuts directly across the inflation center (IC) and shows the edge of C3, as well as C2 and C1. To show more detail of C1 and C2, a model inset is enlarged. The thin dashed lines through the profiles denote the depth locations of the horizontal slices shown in Figure 5.10. BC = Baños Campanario; CC = Cerro Campanario; White space at top of profile is air cells above topography surface

Figure 5.12: Water content as a function of temperature with contours of melt resistivity used for interpretation of features in text. On all plots, the grey box denotes the temperature and water content

ranges based on petrological estimates from Andersen et al. (2017). (a) Water content vs. temperature relationship with contours of melt resistivity for rhyolite melt (Guo et al., 2016). (b) Water content vs. temperature relationship with contours of melt resistivity for dacite melt (Laumonier et al., 2015). (c) Water content vs. temperature relationship with contours of melt resistivity for andesite melt (Guo et al., 2017).

Figure 5.13: Modified Archie's Law (MAL; Glover et al., 2000) plotted as melt fraction vs. melt resistivity with contours of bulk resistivity for m = 1.5.

Figure 5.14: Sensitivity analysis for a uniform, 0.5 Ωm, 500 m thick layer underlying a large portion of the Laguna del Maule Volcanic Field. The anomaly represents a large, crystal-poor magma chamber with 85% rhyolitic melt. (a) The top panel shows the same diagonal fence diagram from Figure 5.11 along PQR through the inversion model with the M1 anomaly added. (b) The apparent resistivity and phase of the impedance tensor components as a function of frequency for site LDM008. (c) The map shows station locations colored by r.m.s. misfit ratio (station misfit with M1 added divided by original station misfit). No site had r.m.s. misfit ratio less than 0.90 so any decrease in r.m.s. is negligible. The small star denotes site LDM008 which had the highest r.m.s. misfit ratio (4.51) with an increase from 0.73 to 3.29. The approximate location of M1 is shown with a black rectangle. BC = Baños Campanario; CC = Cerro Campanario.

Figure 5.15: Sensitivity analysis for a uniform, 500 m thick anomaly (M1) with variable resistivity values. The anomaly was given different uniform resistivity values of 50 Ωm, 20 Ωm, 10 Ωm, and 0.5. The 3-D response was calculated and Site LDM013 is shown for all 4 cases and compared to the original inversion model. Large discrepancies from the data (r.m.s. > 1.5) occur for the 0.5 Ωm anomaly but do not occur for the anomalies with resistivity >10 Ωm.

Figure 5.16: Sensitivity analysis for a layered, 30 km^3 resistivity anomaly (G1) with a maximum conductance of 1400 S. The anomaly has the same dimensions and location as the preferred gravity model described in Miller et al. (2017b). Layer 1 has resistivity of 0.5 Ωm, Layer 2 has resistivity of 6.0 Ωm. See text for more details. (a) The top panel shows the same diagonal fence diagram from Figure 5.11 along PQR through the inversion model with the G1 anomaly added. (b) The apparent resistivity and phase of the impedance tensor components as a function of frequency for site LDM013. (c) The map shows station locations colored by r.m.s. misfit ratio (station misfit with G1 added divided by original station misfit). No site had r.m.s. misfit ratio less than 0.90 so any decrease in r.m.s. is negligible. The

small star denotes site LDM013 which had the highest r.m.s. misfit ratio (2.29) with an increase from 0.82 to 1.88. The approximate location of G1 is shown with a black rectangle. BC = Baños Campanario; CC = Cerro Campanario.

Figure 5.17: The same diagonal slice fence diagram as Figure 5.11 is shown with the location and depth of the G10 (top), G20 (middle), and G30 (bottom) anomalies which were added to the inversion model in order to conduct forward model tests. The bulk resistivity of each feature was varied over six different values (30 Ωm, 10 Ωm, 3 Ωm, 1 Ωm, 0.5 Ωm and 0.3 Ωm) and the forward response was computed for each case (18 models in total).

Figure 5.18: R.M.S. misfit ratio for each MT site as a function of the bulk resistivity for the anomalies (a) G10 (10 km^3), (b) G20 (20 km^3), and (c) G30 (30 km^3), which were added to the original inversion model. Each plot shows how r.m.s. misfit changed for each station (thin, dashed lines) with site LDM013 highlighted (thick line).

Figure 5.19: Sensitivity analysis for a uniform, 10 km^3 anomaly (G10) with variable resistivity values. The anomaly is a simple block at the same location as the anomaly G1 shown in Figure 5.16 but has uniform resistivity rather than a layered geometry. The anomaly was given different uniform resistivity values of 30 Ωm, 10 Ωm, 3 Ωm, 1 Ωm, 0.5 Ωm and 0.3 Ωm. The 3-D response was calculated and Site LDM013 is shown for all 6 cases and compared to the original inversion model. Large discrepancies from the data (r.m.s. > 1.5) occur when the anomaly has a resistivity less than 0.3 Ωm (i.e. 100% melt fraction).

Figure 5.20: Sensitivity analysis for a uniform, 20 km^3 anomaly (G20) with variable resistivity values. The anomaly is a block at the same location as the anomaly G1 shown in Figure 5.16 but has uniform resistivity rather than a layered geometry. The anomaly was given different uniform resistivity values of 30 Ωm, 10 Ωm, 3 Ωm, 1 Ωm, 0.5 Ωm and 0.3 Ωm. The 3-D response was calculated and Site LDM013 is shown for all six cases and compared to the original inversion model. Large discrepancies from the data (r.m.s. > 1.5) occur when the anomaly has a resistivity less than 3 Ωm (i.e. >25% melt fraction).

Figure 5.21: Sensitivity analysis for a uniform, 30 km^3 anomaly (G30) with variable resistivity values. The anomaly has the same dimensions as the anomaly G1 shown in Figure 5.16 but has uniform resistivity rather than a layered geometry. The anomaly was given different uniform resistivity values of 30 Ωm, 10 Ωm, 3 Ωm, 1 Ωm, 0.5 Ωm and 0.3 Ωm. The 3-D response was calculated and Site LDM013 is shown for all six cases and compared to the original inversion model.

response for the *a priori* inversion MT model, and the inversion response for the constrained inversion MT model.

Figure 6.16: Preferred MT resistivity model shown using a north-south vertical slice along A-A' and two horizontal slices at 5 km (2.7 km b.s.l.) and 12 km (10 km b.s.l.) depth. Major interpreted features are labelled C3, C4 and S1. Black dots on horizontal slices and inverted triangles on vertical slice are MT site locations. IC = Inflation center; BC = Baños Campanario hot springs; CC = Cerro Campanario stratovolcano.

Figure 6.17: A comparison to the previously published MT model from Cordell et al. (2018) (see Chapter 5) and the current preferred resistivity model. The vertical and horizontal slices are at the same locations as in Figure 6.16. The bottom panel shows a 2-D histogram comparing the models by counting the number of cells in each resistivity bin. Black dots on horizontal slices and inverted triangles on vertical slice are MT site locations. IC = Inflation center; BC = Baños Campanario hot springs; CC = Cerro Campanario stratovolcano.

Figure 6.18: The ambient noise tomography (ANT) seismic velocity model from Wespestad et al. (2019) shown using a north-south slice along A-A' and a horizontal slice at 5 km depth. The model has no topography but has a model top at 2450 m.a.s.l. The interpreted low velocity zone is labelled V1. Black dots are seismometer locations. IC = Inflation center; BC = Baños Campanario hot springs; CC = Cerro Campanario stratovolcano.

Figure 6.19: A comparison of the preferred MT resistivity model and the seismic velocity model from Wespestad et al. (2019). The seismic velocity model has been interpolated onto the MT model mesh. The models are shown with three NW-SE slices perpendicular to the Troncoso Fault (B-B', C-C', and D-D'). A horizontal slice is also shown at a depth of 5 km (2.6 km b.s.l.). Black dots on horizontal slices and inverted triangles on vertical slice are MT and seismic site locations. IC = Inflation center; BC = Baños Campanario hot springs; CC = Cerro Campanario stratovolcano.

Figure 6.20: Comparison of the MT and seismic models. The left panel shows a 2-D histogram of logarithmic resistivity versus seismic velocity which counts the number of model cells in each resistivity-velocity bin. The right panel shows the Pearson Correlation Coefficient (PCC) as a function of depth where the PCC was calculated for each model layer. Overall PCC was -0.03.

Figure 6.21: The preferred MT resistivity model with perturbation (P1) added. The model is shown with a horizontal slice at 5 km (2.6 km b.s.l.) and two vertical slices along profiles A-A' and D-D'. The shape and location of P1 is determined by the shape of the 450 km^3 low seismic velocity anomaly from Wespestad et al. (2019). The model cells encompassed by P1 have a value of 1 Ωm. Black dots on horizontal slice and inverted triangles on vertical slices. IC = Inflation center; BC = Baños Campanario hot springs; CC = Cerro Campanario stratovolcano.

Figure 6.22: Cross plots of normalized impedance residuals. The x-axis for each plot shows the normalized residuals from the original (preferred) MT inversion response. The y-axis on each plot shows the normalized residuals from a perturbed MT response. Five perturbations are shown with P1 = 1, 3, 15, 50, and 100 Ωm.

Figure 6.23: MT resistivity models from the *a priori* and constrained inversion cases. The top row shows the starting model used for both the *a priori* and constrained inversion. This model includes P1 = 15 Ωm embedded in a 100 Ωm halfspace. The second row shows the results from the *a priori* inversion using a 100 Ωm halfspace as the prior model. The third row shows the results from the constrained inversion in which the model cells in P1 are fixed. Slices are the same as Figure 6.21.

Figure 6.24: Model norm versus r.m.s. misfit convergence curves for the original (preferred) MT inversion, the *a priori* inversion, and the constrained (fixed) inversion. The stars denote the preferred inversion iterations from each case. Corresponding models from those iterations are shown in Figure 6.23.

Figure 6.25: Three-dimensional conceptual model of the Laguna del Maule Volcanic Field looking southeast. The *a priori* inversion resistivity model is shown using a 5 Ωm isosurface. The density model of Miller et al. (2017b) is shown with a -600 kg/m^3 isosurface. The seismic velocity model of Wespestad et al. (2019) is shown using the isosurface described in the text.

Figure 6.26: A conceptual model of a "trans-crustal magma plumbing system". From Cashman et al., 2017. Reprinted with permission from AAAS.

Figure 7.1: Study area in central Chile and western Argentina. Colored circles denote long-period MT (LMT) and BBMT (BBMT) site locations from different field campaigns. Red triangles show the locations of significant volcanoes in the Cordillera Principal. The red star shows the epicentre location of the 2010

M_w 8.8 Maule earthquake. Important towns are shown as black circles. Important volcanoes mentioned in the text are labelled (San Pedro-Tatara, Laguna del Maule, Payún Matrú). Stations mentioned in text are labelled. Profile C-C' denotes the seismic velocity profile from Hicks et al. (2014)). Malargüe FTB = Malargüe Fold and Thrust Belt.

Figure 7.2: Field photos from the field season in 2017. (a) A picture of the NIMS data logger (photo credit: Benjamin Lee); (b) Installing Site CLP014 on the hottest day with highs of 37°C; (c) Installing BBMT site ARG001 near Cerro Campanario; (d) Installing site CLP017 in a tree farm.

Figure 7.3: A table of run times for long period sites. Sites which had significant overlap (e.g. CLP001b and CLP002c) were used as mutual remote reference for processing. Each site generally had 2 - 3 runs for several days.

Figure 7.4: Dimensionality and directionality analysis for MT data. (a) The geoelectric strike for the full dataset using the tensor decomposition of McNeice and Jones (2001); (b) The geoelectric strike for the full dataset using the phase tensor analysis of Caldwell et al. (2004); (c) The median β-skew angle as a function of period where high skew (>3°) indicates three-dimensional resistivity structure; (d) The mean geoelectric strike from phase tensor analysis (α-β) as a function of period.

Figure 7.5: Dimensionality and directionality analysis for MT data. (a) The strike angle for each station along the profile as determined from tensor decomposition (McNeice and Jones, 2001). The average strike (15°) is plotted as blue dashed line and the one circular standard deviation error bar is shown in the grey box. Yellow dots are LMT sites and green dots are BBMT sites. (b) A phase tensor pseudo-section shows the MT profile as a function of period. Each ellipse on the plot denotes the phase tensor for a single period at a single MT site. Each phase tensor is coloured by its β-skew angle where blue indicates relatively 1D or 2D, undistorted data and red indicates data with 3D distortion. TSP = Tatara-San Pedro. LdMVF = Laguna del Maule Volcanic Field. Note that distances along profiles are not to scale.

Figure 7.6: Magnetotelluric (MT) data and pseudo-sections. The top three panels show apparent resistivity and phase data for four MT sites in the Coastal Cordillera (CLP016), Central Valley (P08, CLP008) and Cordillera Principal (LDM029). TE mode is shown as red triangles while TM mode is shown as blue circles. Inversion model fit is shown as solid lines. Sites CLP016 and CLP008 are both LMT whereas P08 and LDM029 are BBMT. Sites P08 and CLP008 are located less than 5 km apart and are shown on the same plot but were treated as separate sites in the inversion. Below are pseudo-section

plots showing a) TE-mode apparent resistivity, b) TE-mode phase, c) TM-mode apparent resistivity, and d) TM-mode phase for each site along the profile as a function of period. All data have been rotated to x= 15° east of north, y = 105° east of north. TE mode is calculated with x-oriented electric fields and y-oriented magnetic field whereas TM mode is the opposite case.

Figure 7.7: A comparison of induction vectors (IVs) plotted in the Wiese convention and tensor decomposition strike. A) A map of IVs at 50 s period. Large scatter shows no consistent trend in induction vector direction. B) A map of IVs at 2000 s period. Here, IVs consistently point towards the northeast. Red triangle = Laguna del Maule Volcanic Field. Yellow triangle = Tatara-San Pedro Volcano. C) A plot of mean induction vector direction as a function of period. The blue dashed line shows the mean profile direction perpendicular to geoelectric strike (grey box denotes one standard deviation).

Figure 7.8: Comparison between two-dimensional inversion models with (a) no static shifts included (final r.m.s. misfit = 3.39) and (b) static shifts included (final r.m.s. misfit = 1.55). TSP = Tatara-San Pedro; LdMVF = Laguna del Maule Volcanic Field. Inverted triangles show BBMT (green) and LMT (yellow) site locations.

Figure 7.9: Comparison between 2-D inversion models using different starting models of (a) 10 Ωm; (b) 100 Ωm; (c) 1000 Ωm and; (d) 10000 Ωm. TSP = Tatara-San Pedro; LdMVF = Laguna del Maule Volcanic Field. Inverted triangles show BBMT (green) and LMT (yellow) site locations.

Figure 7.10: Synthetic experiment with a known two-dimensional resistivity model. (a) the true model with a resistive (10,000 Ωm) subducting slab in a 100 Ωm halfspace. MT data were computed from this model using the same site and frequency distribution as the field data and then contaminated with 5% Gaussian noise. This computed data was then used as input data for two different inversions. (b) the results of an unconstrained inversion. The model images a resistive region which could be interpreted as the slab. (c) the results of a constrained inversion where a tear was included at the top and bottom of the slab interface. Here the model recovers the true model with significantly greater accuracy. Both inversions achieved an r.m.s. misfit of 0.70 with $\tau = 2$. TSP = Tatara-San Pedro; LdMVF = Laguna del Maule Volcanic Field. Inverted triangles show MT site locations.

Figure 7.11: A comparison between an unconstrained (Model #2) and constrained (Model #6) two-dimensional inversion using the full dataset. TSP = Tatara-San Pedro; LdMVF = Laguna del Maule Volcanic Field. Inverted triangles show BBMT (green) and LMT (yellow) site locations.

Figure 7.12: Regularization L-curve test using various τ parameters (0.1, 0.3, 0.5, 1, 2, 3, 5, 10, 30) using all periods with data rotated 15° east of north. The main graph shows model norm versus data misfit. The insets show different model results for different τ values. The value of τ increases going counter-clockwise with the roughest model at the top and the smoothest model at the bottom right. The preferred value is τ = 2 which is the best trade-off between model smoothness and data fit (model with red box around it).

Figure 7.13: Inversion tests with high skew (β>6°) removed. (a) Shows a pseudo-section plot of impedance values at each site along the profile from west to east. Yellow boxes are frequencies where the impedance data were removed with β>6°. In total, 16% of data was removed for this inversion. (b) The model which resulted from using this smaller sub-set of data which better fit the 2-D approximation. (c) The model which included the full data set. In general the features in this model are similar to features in the interpreted model. TSP = Tatara-San Pedro; LdMVF = Laguna del Maule Volcanic Field. Inverted triangles show BBMT (green) and LMT (yellow) site locations.

Figure 7.14: Model which uses only long period data (>10 s). This model was then used as the starting model for the preferred inversion which included all frequencies. TSP = Tatara-San Pedro; LdMVF = Laguna del Maule Volcanic Field. Inverted triangles show BBMT (green) and LMT (yellow) site locations.

Figure 7.15: The preferred 2-D inversion model along the MT profile (a). BBMT sites are shown as green inverted triangles and LMT sites are shown as yellow inverted triangles on the surface of the model. Conductors are labelled C1 through C8 and resistors are labelled R1 through R3. The shallow surface conductor in the Central Valley is labelled S1 and deeper slab-side conductor is labelled A1. The location of the subducting slab is taken from Hayes et al. (2012) and shown as a thick black dashed line. This is the location of the tear which constrained the inversion to have zero smoothing across the boundary. The Moho discontinuity, shown as a thin black line, is taken from the Crust1.0 model of Laske et al. (2013). The location of the 2010 Maule earthquake is shown as a yellow star. Earthquake epicenters are shown as small white dots. TSP = Tatara-San Pedro. LdMVF = Laguna del Maule Volcanic Field. The lower panel (b) shows r.m.s. misfit for the inversion for each station along profile. It also shows the static shift parameters applied to the constrained inversion.

Figure 7.16: Histogram of earthquake epicenters used when plotting the model profiles. The top panel shows histograms from the IRIS (2018) dataset while the bottom panel shows epicenters from the dataset of Hicks et al. (2014). Earthquakes >50 km depth (right of the red line) are excluded when

plotting the Hicks et al. (2014) dataset while earthquakes <50 km depth (left of the red line) are excluded when plotting the IRIS (2018) dataset.

Figure 7.17: Pseudo-section plots for observed data and inverted data response for TE and TM mode apparent resistivity and phase. Residual pseudo-section plots are also shown.

Figure 7.18: Sensitivity map for the preferred inversion model shown in Figure 7.15. The relative sensitivity is unitless and plotted on a logarithmic scale.

Figure 7.19: The mean (a) and standard deviation (b) of all the 16 models shown in this chapter. Statistical analysis was performed on the logarithm of the resistivity and both plots are shown with a logarithmic colorbar.

Figure 7.20: A sensitivity test to examine the ability for the current MT profile to image conductive slab fluids beneath the volcanic arc. The bottom panel shows the same model as Figure 7.15 but with an added 10 Ωm conductor (A) between 90 and 120 km depth directly beneath the volcanic arc. This conductor is similar in size and resistivity to the shallower C3 feature west of the arc. After computing the forward MT response of this edited model, the root mean square misfit increased from 1.51 in the original inversion to 1.53 in the edited model. Apparent resistivity and phase data are shown for LMT site CLP004 which is located on the modern volcanic arc, directly overlying Conductor A. CLP004 had the maximum increase in r.m.s. misfit from 1.47 in the original inversion to 1.65 when conductor A is added.

Figure 7.21: The P-wave velocity seismic tomography model of Hicks et al. (2014) along profile C-C' approximately 75 km south of the current MT profile (see Figure 7.1). The yellow star denotes the location of the 2010 Maule earthquake. Note that the colorbar is flipped from the original figure such that low velocity is blue and high velocity is red. This is done to allow direct color comparison between the MT and seismic models. CA = Cobquecura anomaly. CM = Continental mantle. The yellow triangle denotes the volcanic arc.

Figure 7.22: A comparison between the 3-D seismic tomography model of Hicks et al. (2014) (see Figure 7.21) and the constrained MT model (see Figure 7.15). Both models have been interpolated onto a common mesh. (a) The MT model showing resistivity along the profile as a function of depth with labels matching the features shown in Figure 7.15. (b) A 2-D slice through the 3-D seismic model of Hicks et al. (2014) along the same profile as the MT model. Red denotes low velocity while blue denotes high

velocity. This is the opposite color scale as shown in Hicks et al. (2014) but it is done to allow direct color comparison between the MT and seismic models. Labels denote CA (Cobquecura Anomaly) and CM (Continental Mantle). (c) The shared model space mapped into 4 categories of velocity and resistivity correlations. (d) A correlation histogram showing the number of model cells which share each velocity-resistivity pair.

Figure 8.1: Three-dimensional conceptual model of the Laguna del Maule Volcanic Field looking southeast. The preferred resistivity model is shown using a 5 Ωm isosurface. The density model of Miller et al. (2017b) is shown with a -600 kg/m^3 isosurface. The seismic velocity model of Wespestad et al. (2019) is shown using the isosurface described in Chapter 6. Question marks indicate unresolved questions or uncertain interpretations.

Figure 8.2: The preferred 2-D inversion model along the regional MT profile of the Andean subduction zone at 36°S. Broadband MT sites are shown as green inverted triangles and long-period MT sites are shown as yellow inverted triangles. Features mentioned in text are labelled as conductors (C1 through C8) and resistors (R1 through R3). The location of the subducting slab is taken from Hayes et al. (2012) and shown as a thick black dashed line. The Moho discontinuity, shown as a thin black line, is taken from the Crust1.0 model of Laske et al. (2013). The location of the 2010 Maule earthquake is shown as a yellow star. Earthquake epicenters are shown as small white dots. TSP = Tatara-San Pedro. LdMVF = Laguna del Maule Volcanic Field.

Figure A1.1: A reference map with station locations and labels. The outline of Laguna del Maule is shown for reference.

Figure A1.2: Apparent resistivity and phase for all four impedance components for LDM001 through LDM008. Off-diagonal impedance is shown as red (xy) and blue (yx) while diagonal impedances are shown as magenta (xx) and black (yx). The inversion data fit is shown as a solid line.

Figure A1.3: Apparent resistivity and phase for all impedance components for LDM009 through LDM017. See Figure A1.2 Caption.

Figure A1.4: Apparent resistivity and phase for all impedance components for LDM018 through LDM026. See Figure A1.2 Caption.

Figure A1.5: Apparent resistivity and phase for all impedance components for LDM028 through LDM041.

See Figure A1.2 Caption.

Figure A1.6: Apparent resistivity and phase for all impedance components for LDM042 through LDM049. See Figure A1.2 Caption.

Figure A1.7: Apparent resistivity and phase for all impedance components for LDM053 through LDM060. See Figure A1.2 Caption.

Figure A1.8: Apparent resistivity and phase for all impedance components for LDM061 through LDM068 and MU-011 and MU-012. See Figure A1.2 Caption.

Figure A1.9: Apparent resistivity and phase for all impedance components for MU-019 through MU-051. See Figure A1.2 Caption.

Figure A1.10: Apparent resistivity and phase for all impedance components for MU-052 through MU-095. See Figure A1.2 Caption.

Figure A2.1: Map with site locations and labels. The location of Laguna del Maule is noted with a red triangle.

Figure A2.2: Apparent resistivity and phase curves for the 20 magnetotelluric (MT) sites on the western side of the profile. The impedance tensor is rotated 15° E of N such that the TE mode (red dots) has electric fields parallel to geoelectric strike. The TM mode (blue dots) is orthogonal to the TE mode. The inversion data fit for the preferred inversion (shown in Figure 7.15 in the main text) is shown as a solid red line (TE mode) and blue line (TM mode).

Figure A2.3: Apparent resistivity and phase curves for the 18 magnetotelluric (MT) sites on the eastern side of the profile. See Figure A2.2 caption for details.

LIST OF COMMON SYMBOLS AND ABBREVIATIONS

1-D	One-dimensional
2-D	Two-dimensional
3-D	Three-dimensional
ANT	Ambient Noise Tomography
$\mathbf{b}$	Magnetic Field Flux Vector (Tesla)
EM	Electromagnetic
$\mathbf{e}$	Electric Field Strength Vector (Volts/meter)
$\mathbf{h}$	Magnetic Field Strength Vector (Amps/meter)
InSAR	Interferometric Synthetic Aperture Radar
ka	Thousands of years ago
LdMVF	Laguna del Maule Volcanic Field
LdM	Laguna del Maule
Ma	Millions of years ago
MASH	Melt, Assimilation, Storage and Homogenization
MGS	Mariposa Geothermal System
MPa	Megapascals
MT	Magnetotellurics
Mw	Moment Magnitude Scale
NLCG	Non-linear Conjugate Gradients
SVZ	Southern Volcanic Zone
TSP	Tatara-San Pedro Volcano
wt%	Weight Percentage
Z or $\mathbf{Z}$	Impedance (Ohms) or Impedance Tensor
ϵ_0	Permittivity of Free Space
μ_0	Permeability of Free Space
ρ or ρ_a	Resistivity or Apparent Resistivity (Ohm-meters)
σ	Conductivity (Siemens/meter)
ϕ	Phase of complex number or Porosity
ω	Angular Frequency
Ωm	Ohm-meters

CHAPTER 1: INTRODUCTION

Volcanoes and earthquakes pose a serious threat to society in a variety of ways including loss of life, the destruction of property, disruption of transportation networks, and changes to the global climate (Robock, 2000; Self, 2006; Small and Naumann, 2001). The majority of the world's continental volcanoes and large earthquakes occur along convergent margins known as subduction zones where one plate subducts beneath another as part of the descending limb of a mantle convection cell (Stern, 2002). This makes subduction zones an important place to study earthquakes and volcano hazards. These margins represent important parts of the rock cycle and carbon cycle as they take continental sediments, oceanic sediments, and continental mantle back into the deep Earth (Currie et al., 2007). As the subducting plate descends into the mantle, it experiences increasing temperatures and pressures which causes compaction, mineralogical changes, and metamorphic transitions of down-going rocks which release fluids (Figure 1.1; van Keken et al., 2011). At shallow depths, this fluid can act to lubricate faults or increase pore pressure and plays an important role in subduction zone seismicity and megathrust earthquakes (Stern, 2002). At greater depths, fluids released from the down-going plate induce metamorphic reactions of the continental mantle wedge and, once the temperature rises past the solidus, flux melting of the overlying mantle and crust occurs (Stern, 2002). This partial melt rises due to buoyancy and leads to volcanic eruptions at the surface. Determining the amount of water, the depth at which it is released, and the zones of accumulation of partial melts or aqueous fluids are critical parameters in understanding volcanism and seismicity at subduction zones.

In many cases, partial melt rising from subduction zone flux melting appears to stall in the over-lying lower crust near the Moho discontinuity (Annen et al., 2006; Chaussard and Amelung, 2014). This may be because the rising mafic melt is driven by buoyancy forces and the silicic crust has relatively low density compared to the ultramafic mantle. In the lower crust, the mafic melts may undergo processes such as crystal fractionation and assimilation of country rocks which produce reservoirs of silicic melt in the upper-to-middle crust (Annen et al., 2006; Hildreth and Moorbath, 1988). What is ultimately erupted at the surface at a volcanic vent may have a range of compositions from mafic-to-felsic depending on the volcano. It is an unresolved question as to why different volcanoes produce different suites of erupted products. Some volcanoes produce only basalt while others produce only rhyolite; others produce a variety of compositions. Various ideas have been put forward to explain the

subsurface structure of these systems and how they develop over time. Early simplistic conceptual models suggested that large volumes of high melt-fraction, eruptible magma exists underground in lake-like reservoirs. However, evidence from petrology and geophysics has led to more sophisticated conceptual models which have magma plumbing systems composed of a mixture of low melt-fraction mush and high melt-fraction magma which are dynamic and complex, both spatially and temporally (e.g. Dufek and Bachmann, 2010; Sparks et al., 2019). The scale of these conceptual models is important to consider: some describe the internal structure of a single magma reservoir (often on the crystal-scale) while others seek to describe the macro-scale architecture of the entire magma plumbing system (often with a spatial scale greater than a kilometer). This distinction is important because the different methods used to probe magmatic systems operate on a wide range of spatial scales (e.g. petrology examines individual crystals on the sub-centimeter scale while geophysical methods measure the bulk rock properties of cubic kilometers of the Earth). One existing macro-scale conceptual model envisions a trans-crustal magma system extending from a lower crustal hot zone to the surface which is partially-molten everywhere and includes discrete regions of high melt-fraction eruptible melt surrounded by larger regions of low melt-fraction mush (Figure 1.2; Annen et al., 2006; Cashman and Giordano, 2014; Karakas et al., 2017; Sparks et al., 2019). This conceptual model does not explain all aspects of these systems, but it is a significant step forward in integrating both petrological and geophysical studies. In this conceptual model basaltic magma enters at the base and more silicic magma is concentrated closer to the surface.

Silicic eruptions in particular are responsible for the largest eruptions on Earth and can erupt hundreds of cubic kilometers of material in a single eruption but paradoxically are the most difficult systems to form based on thermal constraints (Bachmann and Bergantz, 2008a). It is important that we better understand the large-scale magmatic processes as well as local storage conditions which cause these large silicic systems to develop in the mid-to-lower crust and furthermore what makes such a volcano go from a period of relative quiescence to a state of unrest (Pritchard and Gregg, 2016). Furthermore, it is important to understand why some silicic magmatic systems erupt while others solidify into plutons and what the ratio is between intrusive and extrusive igneous rocks (Bachmann et al., 2007). These factors will give insight into the size, timing, and eruptive style that is to be expected from a future eruptive episode at a particular volcano and this will inform volcano hazard mitigation and risk management policy.

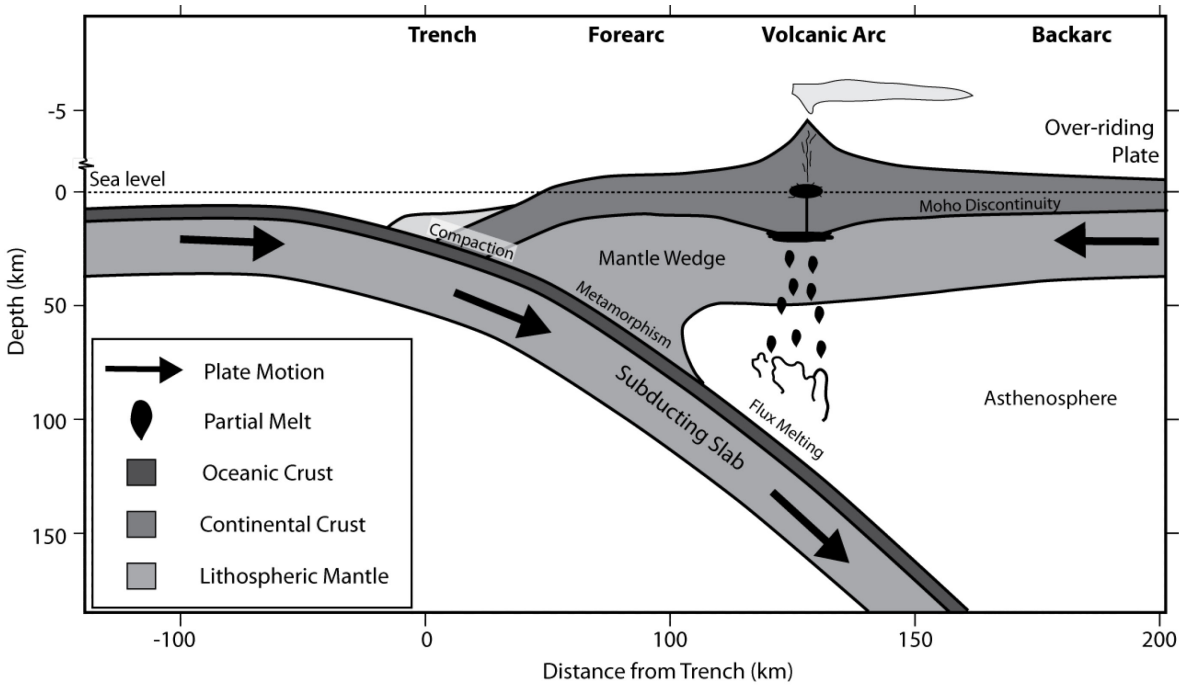

Figure 1.1: A simplified conceptual model of an archetypical subduction zone. Modified from Stern (2002).

Geology and geophysics provide the means to examine how these systems develop to answer the important questions listed above. Geological studies examine eruptive products to infer the conditions under which they formed, the pathways which they took in their evolution, and the conditions under which they erupted. Geophysics uses energy sources measured at the surface to make images of the present subsurface using potential or vector fields. Geological studies can provide detailed insights into the volcanic system in the past and its evolution, but is biased, by necessity, to systems that erupted and/or formed ancient eroded plutons. Geophysical studies make remote measurements of the subsurface and thus require the interpretation of geophysical attributes rather than direct access to rocks. However geophysical studies have the advantage that they can provide an image of the present magmatic system, including both the parts that have not been erupted, and the parts which may never erupt and are destined to become plutons. Compared to geological studies of samples and outcrops, geophysical studies are relatively low-resolution. Models constructed from geophysical data can also be non-unique, which means that it is difficult, if not impossible, to determine relatively small features of the internal structure of a geophysical anomaly. In many cases geophysical data can only determine the homogeneous bulk properties. However, geophysics can place bounds on the size, location and composition of a magmatic system (see Magee et al., 2018 for a review) and by combining multiple geophysical methods, it is possible to provide images of different aspects of a magmatic system e.g.

distinguish small eruptible volumes from larger regions with low-melt fraction. As such, integration of both geological and geophysical data can provide the most comprehensive picture of a given magmatic system. In light of the trans-crustal view of magmatic systems, it is now more necessary than ever to be able to map the location of partially molten rock in the subsurface and make estimates on which parts of a system could contain eruptible magma. Previous studies of silicic systems such as Yellowstone (Farrell et al., 2014; Schmandt et al., 2019; Till et al., 2015), Taupo (Hamling et al., 2016; Hurst et al., 2016), Toba (Koulakov et al., 2016; Stankiewicz et al., 2010), and Long Valley caldera (Hildreth, 2004; Sorey et al., 2003) have highlighted that each system is unique and dynamic. Creating a single conceptual model of these systems may not be possible (Till et al., 2018). Instead, it may be necessary to focus on the reasons why certain systems develop the way they do (Till et al., 2018). The Maule Region of central Chile (35°S - 36°S) is unique along the Andean subduction zone since it contains a large proportion of Pleistocene-to-Quaternary silicic caldera systems in the back-arc, including the Laguna del Maule Volcanic Field (LdMVF). This region is not as well-studied as other large silicic systems but may be the site of the next major silicic eruption.

The LdMVF is a basalt-to-rhyolite system comprised of multiple vents and lava flows distributed over a 200 km^2 area (Figure 1.3). The LdMVF has been active for the last 1.5 Ma and has erupted over 350 km^3 of material including a caldera-forming eruption 950 ka (Hildreth et al., 2010). Over the last 26 ka, there has been a recent flare-up in silicic volcanism and long-term paleo-deformation with the most recent eruptions occurring around 2 ka (Andersen et al., 2017; Singer et al., 2018). The LdMVF has shown signs of significant unrest in the last decade including rapid and prolonged upward ground deformation of greater than 20 cm/yr and several notable seismic swarms (Cardona et al., 2018; Feigl et al., 2014; Le Mével et al., 2015). All this evidence suggests a restless magmatic system at approximately 5 km depth beneath the LdMVF which may be moving towards an eruption.

This thesis is part of a large multi-disciplinary project to better understand the forces and factors which produce and control silicic systems on multiple spatiotemporal scales with the restless LdMVF acting as an ideal natural laboratory of a non-erupting, restless silicic system (Singer et al., 2014). Eruption processes can occur on the scale of minutes or hours while the tectonic forces driving the generation of melt operate on timescales of millions of years (Zellmer and Annen, 2008). Similarly, the eruptive volume which produces the next eruption may be relatively shallow and local to one specific volcanic vent or edifice whereas the plumbing network which facilitated the creation of melt may require a

regional-scale understanding of the full magmatic system extending from the mantle to the surface. As such, this project covers a large range of spatiotemporal scales which includes a regional investigation of the central Chilean subduction zone and associated fluid fluxes from the trench to the backarc, as well as a focused, local investigation of the shallow magma plumbing system beneath the LdMVF.

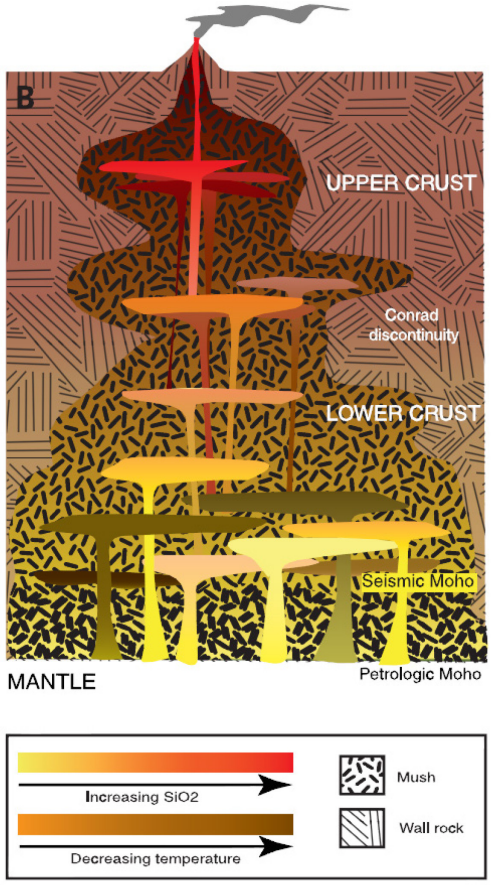

Figure 1.2: A conceptual model of a "trans-crustal" magma system. From Cashman et al., 2017. Reprinted with permission from AAAS.

From a regional perspective, the Maule Region of central Chile (35°S - 36°S) presents an archetypical Andean subduction zone where the incoming oceanic Nazca Plate subducts obliquely beneath the continental South American Plate (Barazangi and Isacks, 1976; Pesicek et al., 2012). This subduction zone has resulted in the construction of the 8000 km Andes mountain range along the western edge of South America (Mpodozis and Ramos, 1989). In the Maule region, the dip of the subducting plate has changed through time resulting in sequences of compression and mountain-building during flat-slab subduction and extension and basin-formation as the slab steepens (Manea et al., 2012; Ramos et al., 2014). During flat-slab subduction, volcanism decreases significantly because the descending slab does not reach high enough temperatures and pressures to induce flux melting and there is no mantle wedge

to bring hot material in contact with the subducting slab via asthenospheric flow. In contrast, a steepening slab causes increased volcanism at a narrow volcanic arc because the slab descends to deeper depths quickly and flux melting occurs (Gutscher et al., 2000). Currently, the Maule region is in a time of slab steepening and has a relatively narrow volcanic arc with a notable string of Quaternary rhyolite calderas (including the LdMVF) and a backarc with an active Quaternary basaltic province indicating extension and lithospheric thinning (Ramos et al., 2014). In 2010, central Chile was struck by a M_w 8.8 Maule megathrust earthquake which caused significant damage and aftershocks. This earthquake appears to have had an influence on the observed deformation rates at the LdMVF and other Chilean volcanoes (Le Mével et al., 2015; Pritchard et al., 2013). This further supports the need to understand both large-scale regional subduction zone processes in conjunction with more focused, local studies.

This thesis uses an electromagnetic (EM) geophysical imaging method known as magnetotellurics (MT) to map the electrical resistivity structure of the regional subduction zone of central Chile and the local magma plumbing system of the LdMVF. The electrical resistivity of a rock is particularly sensitive to fluids such as partial melt, hydrothermal brines, and other aqueous fluids (Pommier, 2014; Unsworth and Rondenay, 2013). As such, understanding the spatial distribution of resistivity can give insight into the location of fluids in subduction zones (e.g. Brasse et al., 2009; Brasse and Eydam, 2008; Hata et al., 2015; Heise et al., 2017; Jödicke et al., 2006; McGary et al., 2014; Pommier and Evans, 2017; Wannamaker et al., 2014; Worzewski et al., 2011) and the geometry of volcanic plumbing systems (e.g. Aizawa et al., 2014; Bertrand et al., 2012; Comeau et al., 2016; Hill et al., 2015; Miensopust et al., 2014; Piña-Varas et al., 2014; Samrock et al., 2018). A range of EM methods could be used to map resistivity. For the type of study considered here, MT is the most suitable because, by using natural signals, it is able to image to both shallow depths (e.g. hundreds of meters) and very deep depths (e.g. tens of kilometers). This allows for a study of the full trans-crustal system including large-scale, deep features at the subducting slab and shallow, local features at specific vents. As a passive geophysical method, MT uses naturally-occurring EM waves from the magnetosphere and ionosphere as a frequency-domain source which induces secondary EM fields in the subsurface (Cagniard, 1953; Chave and Jones, 2012). Strong electric currents will be induced in subsurface conductors, while very little current will be induced in resistors. These induced currents generate magnetic fields that allow the conductors to be detected at the surface. Thus the MT method can map an average (or apparent) resistivity of a 3-D volume beneath a measurement site with frequency as a proxy for depth. The method is frequency-

dependent where lower frequencies sample greater depths and higher frequencies sample shallow depths. Due to a wide bandwidth (e.g. 1000 Hz to 0.0001 Hz), MT is very versatile and able to investigate both shallow, small-scale structures (<500 m) and very deep, large-scale structures (>100 km). MT data can be used to generate 1-D, 2-D, or 3-D models of the electrical resistivity of the Earth.

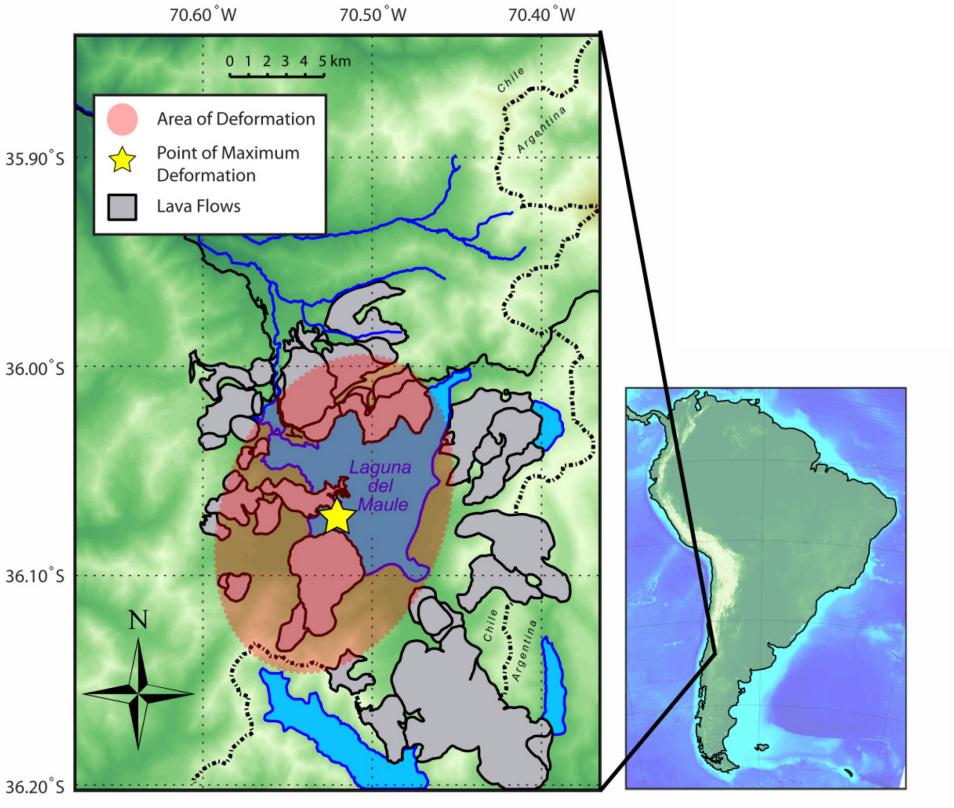

Figure 1.3: Map of the primary study area at the Laguna del Maule Volcanic Field, central Chile. The yellow star denotes the point of maximum observed upward ground deformation and the red oval shows the approximate extent of uplift. Grey polygons are lava flows from Andersen et al. (2017). The black solid line is the main highway.

The focus of this thesis is divided into two parts. The first part describes the data collection, analysis, and inversion of a broadband (1000 Hz to 0.001 Hz) MT array that was installed at the LdMVF between 2015 and 2016 to study the local electrical resistivity structure beneath the volcanic field and the region of ongoing deformation. These MT data and resulting 3-D resistivity model are then interpreted in the context of the other geological and geophysical investigations that took place at the LdMVF, most of which are concurrent with this thesis project and many of which are still on-going. Interpretations are still in flux as the various facets of the project continue to add new information to our understanding of this complex magmatic system. Along with concurrent gravity and seismic tomography studies, this MT study is the first 3-D MT analysis and interpretation of the LdMVF magmatic system. The primary

question to be answered for this project is: “What is the size, distribution, and composition of the magmatic system beneath the LdMVF?” Knowing these parameters will place constraints on the size of future eruptions, the nature of the ongoing unrest, and constrain petrological interpretations. For example, the MT data can be used to produce a 3-D resistivity model that can place bounds on the size and melt fraction of a magma reservoir and determine if a large, high melt-fraction reservoir exists in the shallow crust beneath the LdMVF. This will determine if a large volume of eruptible melt exists at shallow depths in the crust. Alternatively, if only a small, low-melt fraction magma reservoir is identified, then this would suggest that the ongoing deformation is not a sign that the system is moving towards a major eruption. Furthermore, understanding at what depth magma is being stored and differentiated will constrain petrological estimates of residence times and present-day reservoir temperatures.

The second part of this thesis describes the data collection, analysis and inversion of a 350 km-long, trench-perpendicular MT profile stretching from the Pacific Ocean into the backarc of western Argentina. This profile is a mixture of both broadband and long period (1 Hz to 0.0001 Hz) MT data collected between 2015 and 2017 to study the large-scale regional structure of the Chilean subduction zone to place the LdMVF within a regional context. The inversion of these data requires a 2-D assumption and the interpretation integrates previously published seismic tomography results and numerical modelling. The primary questions that this second project seeks to answer are: (1) “Where do the fluids and melts originate which are feeding silicic eruptions and active back-arc volcanism at this latitude of Chile and how does this compare to other latitudes?” and; (2) “What is the relationship between fluids released from the slab and the observed seismicity?” With regard to the first question, knowing the along-arc variations in subduction zone structure can help to explain the anomalous volcanism at this latitude. It can also help inform geodynamic models which seek to better understand the mass balance and the pressure-temperature conditions at subduction zones. With regard to the second question, fluids and subduction zone structure are known to play an important role in seismicity at subduction zones. Thus mapping fluids and structure near the Maule earthquake will give insight into why the earthquake ruptured as it did, and also explain the distribution of zones of stick-slip behaviour versus stable sliding behaviour.

In Chapter 2, a broad overview of the central Chilean subduction zone is presented. This begins with a continental-scale perspective on the tectonic evolution, fluid cycles, and patterns of volcanism in the Andes to place the central Chilean subduction zone within a larger context. This is followed by a more

specific discussion of volcanism and seismicity within the Southern Volcanic Zone (SVZ), and previous regional geophysical work performed in the SVZ.

The spatial scale becomes smaller in Chapter 3, which provides an overview of the LdMVF beginning with the eruptive history of the volcanic field. The geodetic observations, which provided the impetus for the multidisciplinary project, are summarized here. Prior to this project, there was relatively little beyond field mapping and satellite-geodesy and so the remainder of the chapter contains a summary of geological and geophysical studies which have been concurrent and on-going with this thesis work. This work includes updated field mapping, petrochronology, geochemistry, Bouguer gravity density mapping, time-lapse gravity, local seismicity mapping, ambient noise tomography, and surface wave tomography. Here, I also briefly mention a prospective geothermal system to the west of the LdMVF where MT data were collected between 2009 and 2012.

Chapter 4 describes the basic theory of the MT method starting with the motivation for why conductivity (and its inverse, resistivity) is a useful Earth property to investigate different geological targets. Following this, MT theory is developed from basic assumptions of calculating electric and magnetic fields and forward modelling MT data using Maxwell's equations with a 1-D assumption and continues towards forward modelling the fully 3-D Earth. It also outlines the basic MT workflow which includes data collection, time series analysis and spectra estimation, data analysis, and inverse modelling.

Chapter 5 details the data acquisition, time series processing, data analysis, 3-D inversion, and interpretation of the MT data at the LdMVF. This chapter includes detailed information about the field work collected in 2015 and 2016 and also incorporates Bouguer gravity data as an additional constraint on the interpretation. This chapter is an expanded version of Cordell et al. (2018).

Chapter 6 is a continuation of the analysis and interpretation of the 3-D resistivity model at the LdMVF and uses sensitivity tests to develop a more comprehensive joint interpretation of the MT and seismic data. The methodology uses model perturbations, constrained inversions, and analysis of residuals to better understand what features of the 3-D resistivity model are well-resolved and well-constrained relative to other areas. Much of this work is to be published in a manuscript that will be submitted to the *Journal of Geophysical Research: Solid Earth*.

Finally, Chapter 7 describes the regional MT study of the central Chilean subduction zone including data acquisition, time series processing, data analysis, 2-D inversion and interpretation. This incorporates previous regional seismic projects into a joint interpretation and was previously published as Cordell et al. (2019).

Chapter 8 provides a brief summary of the thesis with some final conclusions and a discussion of further work that could be pursued to better understand the LdMVF and the central Chilean subduction zone, as well as silicic systems and subduction zones in general.

CHAPTER 2: THE ANDEAN SUBDUCTION ZONE

2.1 INTRODUCTION

The western edge of South America is dominated by a convergent margin where the Nazca Plate subducts beneath the South American plate. This subduction zone has resulted in uplift, orogenies and volcanism which has created the Andes mountain range which runs along the entire western coast of South America and includes the highest mountains in the Western Hemisphere. The Andean subduction zone can be broadly grouped into three segments based on tectonic history (Figure 2.1a; Gansser, 1973): the Northern Andes of Colombia and Ecuador, the Central Andes of Peru, Bolivia, Chile and Argentina to approximately 46°S latitude, and the Southern Andes of Patagonia. The Andes can also be subdivided into four regions based on modern active volcanism (Figure 2.1b; Ramos, 1999): The Northern Volcanic Zone (NVZ) from 5°N to 2°S, the Central Volcanic Zone (CVZ) from 16°S to 26°S, the Southern Volcanic Zone (SVZ) from 33°S to 46°S, and the Austral Volcanic Zone (AVZ) south of 47°S. Between these volcanic zones are flat slabs, where the subducting slab has a shallower subduction angle for several hundred kilometers before descending steeply. The definitions and terminology based on tectonic history and those based on patterns of volcanism are distinct but similar (see Figure 2.1).

This chapter first provides a broad overview of the tectonic evolution of the Central Andes and subduction processes (Section 2.2), fluid cycles (Section 2.3), and patterns of volcanism (Section 2.4). Section 2.5 provides a review of the volcanism and seismicity in the Southern Volcanic Zone with a specific focus on the Maule region and the 2010 Maule earthquake. The chapter concludes (Section 2.6) with an overview of previous regional geophysical studies in the Southern Volcanic Zone including seismic, gravity, and magnetotelluric (MT) methods.

2.2. TECTONIC EVOLUTION OF THE ANDES

The western edge of South America has been a convergent margin for most of its recent history and has included several pre-Andean orogenies in the Proterozoic and Paleozoic (Mpodozis and Ramos, 1989; Richards, 1995). The Northern and Southern Andes had a generally more complicated evolution due to nearby triple junctions; the Northern Andes in particular included relatively young terrane accretions in

the Cretaceous (Ramos, 1999). Earlier Proterozoic and Paleozoic orogenies of the Central Andes included accretions of the Chilenia and Cuyania terranes to the South American craton (Heredia et al., 2018; Keppie and Ramos, 1999; Martínez et al., 2012; Ramos, 1999). The Andean orogeny began in the early Jurassic and continues to the present and is notable for its lack of accretions throughout that time as the Nazca Plate subducted beneath the South American plate (Mpodozis and Ramos, 1989; Richards, 1995).

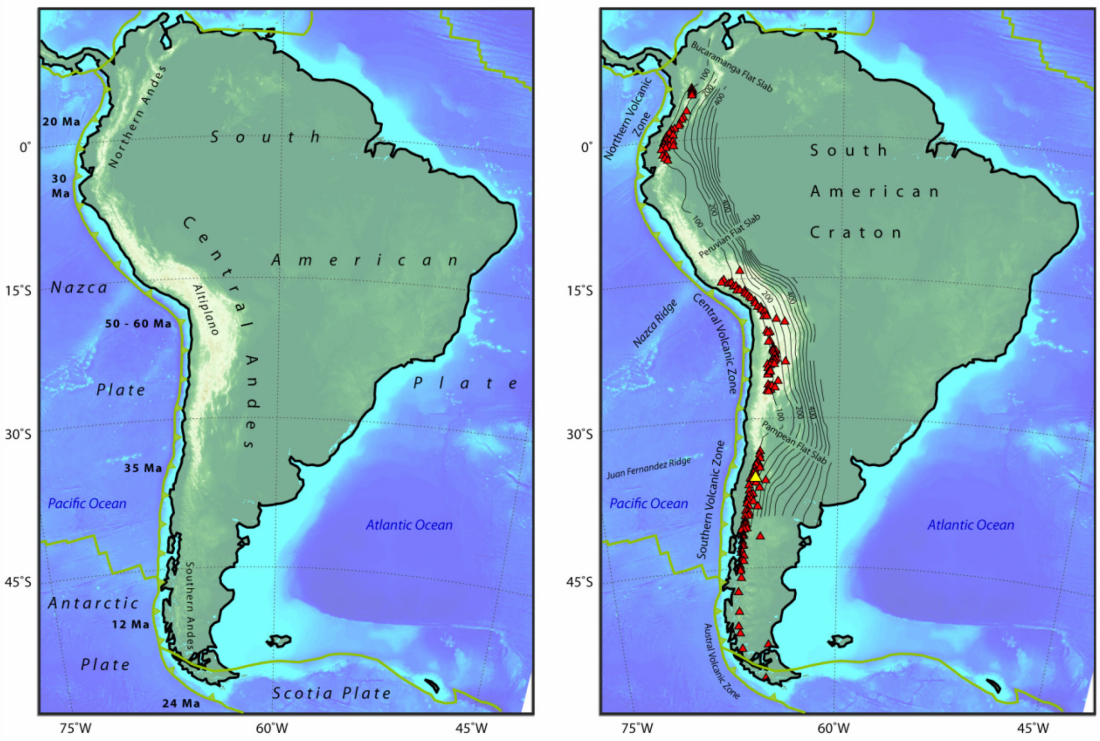

Figure 2.1: Map of South America. The left panel is adapted from Gansser (1973) and defines regions of the Andean margin by tectonic history. Numbers denote the approximate age of the incoming Nazca plate. The right panel is adapted from Ramos (1999) and defines regions of the Andean margin by patterns of modern volcanism. Contours show the depth of the subducting slab. Red triangles denote volcanoes which have erupted in the Pleistocene or Holocene. The yellow triangle is the Laguna del Maule Volcanic Field.

Currently, the Nazca plate subducts beneath the South American plate at rates of 6 - 8 cm/yr (Angermann et al., 1999) although the convergence rate has changed over time (e.g. Charrier et al., 2002; Jordan et al., 2001). Due to the oblique convergence, the Nazca plate is younger to the south and the age of the Nazca plate has been postulated as a reason for the Bolivian orocline (Capitanio et al., 2011). The Bolivian orocline is a concave segment of the Andean margin—an unusual geometry as compared to the convex geometry of most subduction zones worldwide. The orocline also encompasses the forearc region and the Altiplano high plateau (>4000 m) where crustal thickness exceeds 70 km (Figure 2.1a; Capitanio et al., 2011). Throughout the Andean orogeny, the subducting slab angle has

changed along-strike leading to flat slab segments at different points in history along the subduction zone as shown for a portion of the SVZ in Figure 2.2 (Manea et al., 2012; Ramos and Kay, 2006).

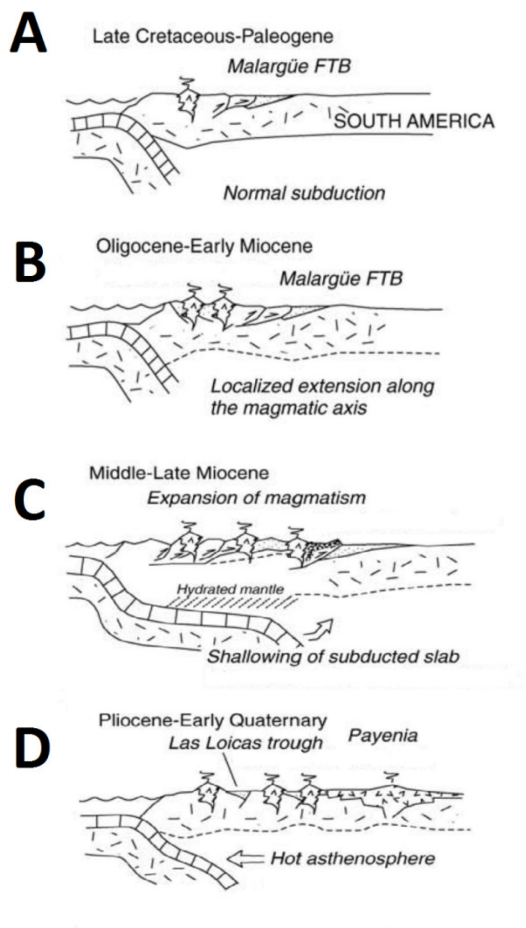

Figure 2.2: Schematic cross-section of the subduction zone in the Southern Volcanic Zone near 36°S and north of the Cortaderas lineament. The slab transitions from "normal" in the late Cretaceous (a - b) to a flat slab by the late Miocene (c) (i.e. the Payenia paleo-flat slab). Currently, the slab is a process of steepening with an injection of hot asthenosphere (d). Modified from Ramos and Kay (2006). The modern LdMVF is located in the Las Loicas trough.

It has been postulated that these transitions are due to changes in plate convergence rate, over-riding plate thickness, trench rollback, or aseismic ridges such as the Juan Fernández Ridge or Nazca Ridge shown in Figure 2.1b (e.g. Gutscher, 2002; Manea et al., 2012). At the current time, there are three notable flat slab segments: the Bucaramanga flat slab north of 5°N, the Peruvian flat slab between 3°S and 12°S, and the Pampean flat slab segment between 27°S and 33°S (Figure 2.1b; Barazangi and Isacks, 1976; Ramos and Folguera, 2009). In these zones, the Nazca plate subducts to approximately 100 km depth before the dip of the plate shallows to approximately 5° and travels almost horizontally eastward for several hundred kilometers before steepening and descending into the asthenosphere. Along the

rest of the subduction zone the subducting plate descends into the asthenosphere at a near constant dip of approximately 30° (Jordan et al., 1983). In the Miocene (13 – 5 Ma), a paleo-flat slab segment called Payenia existed in central Chile and Argentina from 33°S to 38°S as shown in Figure 2.2 (Ramos and Folguera, 2009; Ramos and Kay, 2006). This process of slab steepening and thickening results in changes in deformational history and leads to sequences of compressional mountain-building and extension as well as changes in patterns of volcanism as hot asthenosphere is injected during slab steepening (Figure 2.2; Horton and Fuentes, 2016; Ramos et al., 2014).

Most of the shortening and uplift is accommodated along east-verging detachment faults in the back-arc basin resulting in large fold-and-thrust belts such as the Malargüe fold-and-thrust belt (Figure 2.2; Ramos and Kay, 2006). The deformation history and structural geology of the forearc is not as well understood because of a lack of well-control, intrusive bodies which disrupt lithological continuity, and a lack of stratigraphic markers (Farías et al., 2010). In Central Chile it is notable that the Andean mountain range splits into two ranges (the Coastal Cordillera composed of mostly Paleozoic rocks in the west and Cordillera Principal composed of mostly Mesozoic and young volcanics in the east) with a longitudinal valley (the Central Valley) in the middle (Farías et al., 2010). Much of the uplift of the Andean cordillera may be accommodated by lower crustal thickening due to movement along a major detachment fault (Farías et al., 2010).

2.3 FLUID PROCESSES IN THE ANDEAN SUBDUCTION ZONE

One important aspect of global subduction zones is their ability to transport sediments, oceanic crust, fluids and carbon into the Earth's mantle. Subduction zones are an important part of the rock cycle as they drive plate tectonics via slab pull and they are responsible for building most of the modern continental crust via plutonism and volcanism (Bebout et al., 2018; Stern, 2002). This process ensures that the Earth (including its biosphere) remains a dynamic system. On the outboard side of the trench—and especially near the mid-ocean ridge—the oceanic crust and lithospheric mantle become hydrated with water stored as both pore-fluids and incorporated into hydrous mineral phases (such as serpentinites) due to the temperature and pressure conditions at the sea floor as well as bend-related faulting nearer the trench (Jarrard, 2003; Ranero et al., 2003). As a subducting slab enters a subduction zone and sinks, it undergoes compaction which releases pore-bound fluid. As it descends to greater depths and temperatures, a variety of metamorphic reactions to its crust and lithospheric mantle take place. These transitions follow certain patterns and, at various points, mineral-bound water is released

as shown in the schematic diagram of Figure 2.3 (Peacock, 1990; Poli and Schmidt, 1995; Schmidt and Poli, 1998). The release of water and resulting changes in mineralogy from basalt to eclogite in the descending slab increase its density and cause it to descend faster into the asthenosphere thus driving slab pull.

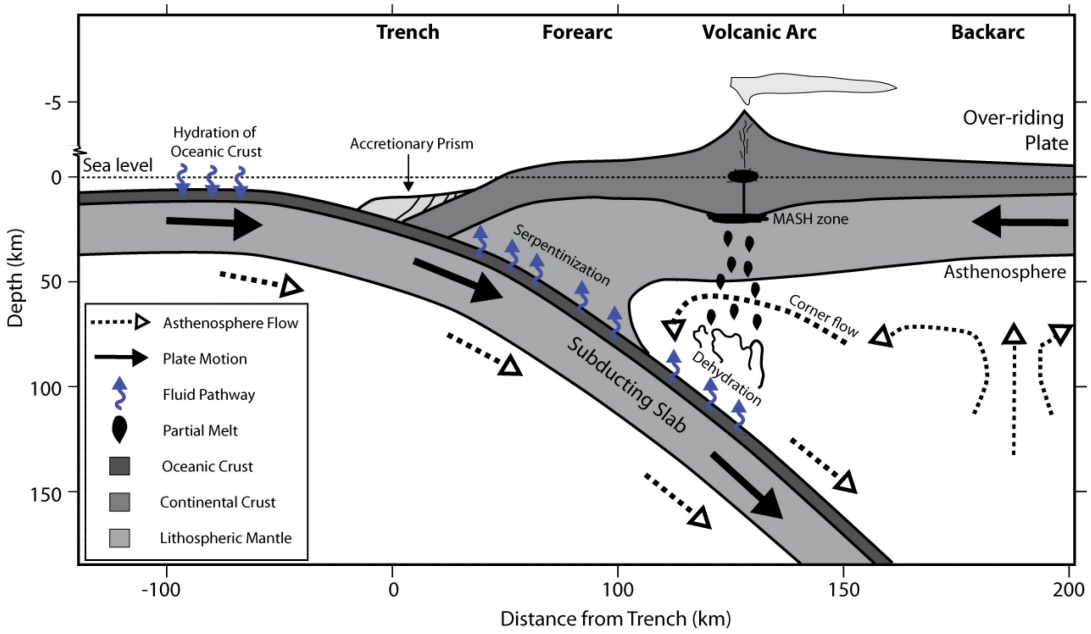

Figure 2.3: Schematic of a typical Andean-style subduction zone. Modified from Stern (2002).

Reviews of global subduction zones show that these fluid fluxes are unique to each subduction zone but are roughly related to the age and temperature of the incoming plate (van Keken et al., 2011). These fluids can then migrate into the crust or mantle of the over-riding plate. Adding water to rocks lowers the solidus temperature and induces partial melting (Grove et al., 2012) – in the same way that adding salt to water lowers the melting point. Melts can then migrate towards the surface and often results in volcanism or plutonism. The fraction of melts which erupt at volcanoes (i.e. extrusive igneous rocks) versus the fraction that solidifies in the upper crust (i.e. intrusive igneous rocks) is known as the intrusive-extrusive ratio (or plutonic-volcanic ratio) and a typical value for most magmatic systems is estimated to be approximately 5:1 (Bachmann et al., 2007).

Fluids which are released from the slab also appear to have an important control on seismicity. The up-dip limit of the seismogenic zone is often attributed to the transition from plastic smectite to more brittle illite, both of which depend on fluid alteration processes (Lauer et al., 2017). The down-dip limit of the seismogenic zone in low-temperature subduction zones is also often related to dehydration of

fluids below the Moho. Olivine in the overlying mantle becomes serpentinized if slab fluids are released into the mantle wedge or lithosphere of the over-riding plate (Stern, 2002). The serpentinized mantle has the ability to allow for more stable-sliding of the plates even though they remain in the brittle temperature regime (Hyndman et al., 1997). In higher-temperature subduction zones, the down-dip limit of the seismogenic zone may simply occur at the brittle-ductile transition. Fluids and dehydration within the seismogenic zone have also been attributed to aseismic creep where dry-rock conditions promote locking within the seismogenic zone (Heise et al., 2017; Saffer, 2017). At greater depths, beyond the brittle-ductile transition, fluids and dehydration have been hypothesized as the cause of intermediate depth earthquakes (>30 km) by raising pore pressures and causing stick-slip behaviour (Dobson et al., 2003; Okazaki and Hirth, 2016) although this is controversial with alternative hypotheses for intermediate depth earthquakes deduced from laboratory experiments and field evidence (e.g Chernak and Hirth, 2010; Scambelluri et al., 2017).

2.3.1 Unresolved Questions About Subduction Zone Fluid Processes

Much has been learned about the effects of the age of the incoming plate, the physical and thermal state of the incoming oceanic lithosphere, structures on the down-going slab (e.g. seamounts), and the importance of subduction erosion, among others (see Bebout et al. (2018) for a review). However, many questions remain about the role of fluids and partial melt in subduction zones including: (1) how fluids are transported within the slab's crust and mantle, and from depth to surface (e.g. Cerpa et al., 2019; Gerya, 2011; Plümper et al., 2017; Wada and Behn, 2015; Wilson et al., 2014) and; (2) how much fluid remains trapped deep within the Earth versus how much is recycled back to exogeneous reservoirs (Cerpa et al., 2019; Plümper et al., 2017; van Keken et al., 2011). Each of these questions will be discussed below.

Regarding (1), pressures in the overlying mantle would be great enough that porosity should be effectively zero and permeability must be created via different means in order for fluids to migrate within the slab and in the overlying mantle wedge (Cerpa et al., 2019). Some possible mechanisms include flow along grain edges, percolation through a viscously-deformable matrix, or water diffusion (Cerpa et al., 2019; Gerya, 2011). However, some argue that these mechanisms would be too slow to effectively drain the subducting plate (Plümper et al., 2017). Other theories suggest a more rapid channelization of fluids induced by pore-fluid pressure which can cause significant, rapid fluid escape from the slab into the overlying mantle (Plümper et al., 2017). Once in the mantle, fluids and melt

pathways may be influenced by different pressure gradients and buoyancy forces. Despite many cartoons showing purely vertical fluid ascent (e.g. Figure 2.3), many numerical modelling efforts and geophysical results seem to indicate that there are significant lateral components as well (Cerpa et al., 2019; Pommier and Evans, 2017; Schilling et al., 2006; Schurr et al., 2003; Soyer and Unsworth, 2006; Wada and Behn, 2015; Wilson et al., 2014). This can be influenced by a variety of factors on a range of spatial scales including large-scale asthenospheric flow and regional temperature regime as well as small-scale grain size characteristics and network connectivity (Wada and Behn, 2015). Finally, it also appears that fluids become "focused" into particular areas (e.g. the forearc or beneath the volcanic arc). Sometimes no geophysical anomaly is imaged beneath the volcanic arc at all, despite this being the location where fluids should accumulate (Pommier and Evans, 2017). Geophysical images which show where fluids are located can help geodynamicists better constrain and update their models and can also give insight into the temperature and pressure regime where metamorphic reactions are occurring.

Regarding (2), accounting for the water and volatiles that enter a subduction zone has important implications for the rock cycle and geological water cycle of the Earth (Plümper et al., 2017; van Keken et al., 2011). In general, there is a significant amount of uncertainty in mass balance estimates of H_2O in subduction zones (Bebout, 1996). Some estimates show a large discrepancy between the amount of water (and other volatiles) entering a subduction zones versus the amount that is returned to the surface. Bebout (1996) and Peacock (1990) both concluded that there is significantly less water coming out of the volcanic arc and thus a significant portion must remain in the overlying forearc crust or mantle, or be recycled deep into the mantle. In contrast, Hilton et al. (2002) found that more water came out of the arc than was subducted suggesting that meteoric sources must be incorporated into erupted products. Additional evidence from numerical modeling suggests that a significant amount of water could remain trapped in the slab, given the right temperature conditions (Abers et al., 2017; van Keken et al., 2011). In all these studies, error bars are large and small changes to the average water content of erupted products can significantly affect the conclusions. Geophysical methods can help to provide some answers to these questions by imaging regions of melt or fluids in subduction zones. Of course, a lack of a geophysical anomaly does not necessarily mean that no fluid is present but it provides important constraints for the Earth's water budget. Finally, the initiation, development and termination of flat slab subduction episodes remain important topics of research.

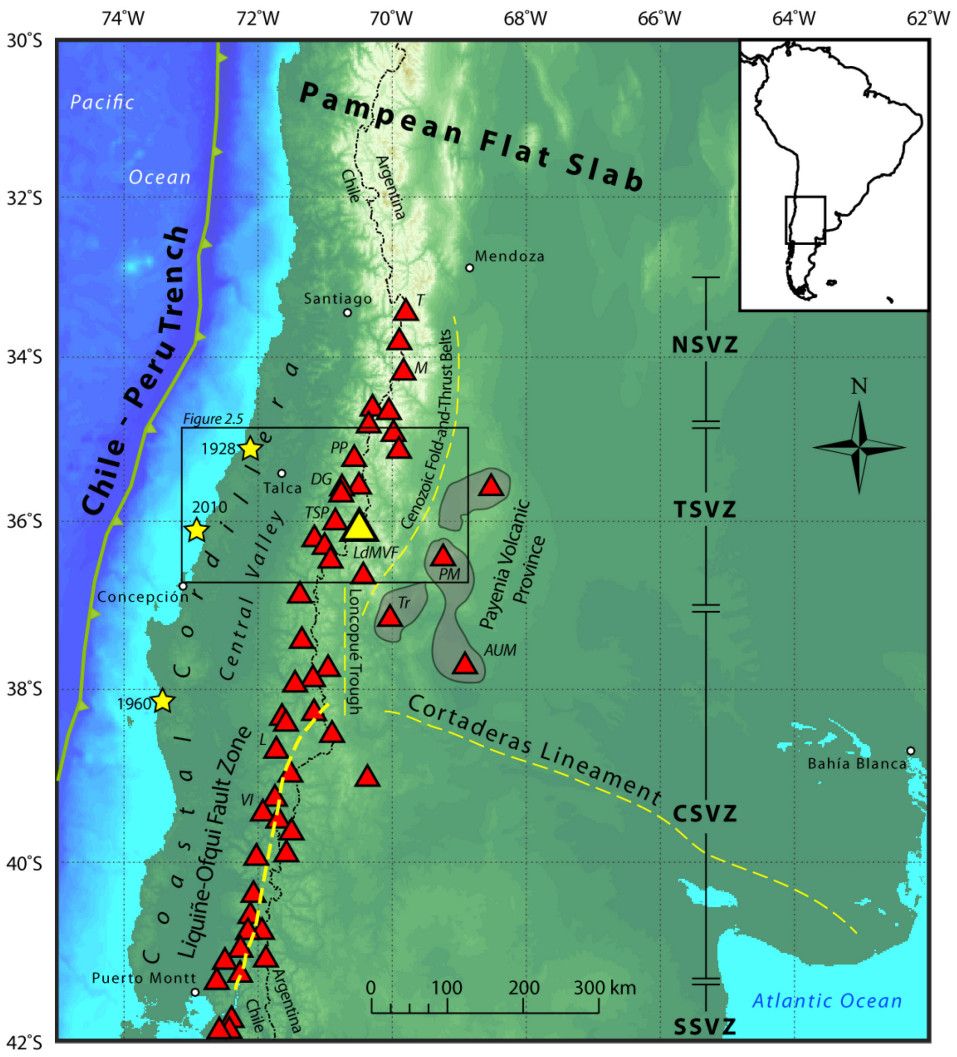

Figure 2.4: Map of the Southern Volcanic Zone. Red triangles are volcanoes which have erupted in the Pleistocene or Holocene. Yellow triangle is the Laguna del Maule Volcanic Field (LdMVF). Yellow stars are epicenters of important historical earthquakes. Black box shows the location of Figure 2.5. NSVZ = Northern Southern Volcanic Zone; TSVZ = Transitional Southern Volcanic Zone; CSVZ = Central Southern Volcanic Zone; SSVZ = Southern Southern Volcanic Zone. PP = Planchon Peteroa; DG = Descabezado Grande; TSP = Tatara-San Pedro, T = Tupungato; M = Maipo; PM = Payun Matru; AUM = Auca Mahuida; Tr = Tromen; L = Llaima; VI = Villarrica.

2.4 PATTERNS OF VOLCANISM IN THE ANDES

As mentioned earlier, modern volcanism in the Andes can be grouped into four zones: the NVZ, CVZ, SVZ, and AVZ (Figure 2.1b; Ramos, 1999). In general the NVZ is composed of basaltic and andesitic volcanoes with primitive products derived from partial melting of the asthenospheric wedge. The CVZ overlies very thick crust leading to more evolved dacitic magmas with a greater degree of crustal

assimilation (Ramos, 1999). The SVZ has more complicated compositions with a general trend to more evolved compositions to the north (i.e. high silica content and greater crustal components; see Section 2.5). The AVZ is relatively under-studied and generally includes poorly-evolved lavas and a complex tectonic history due to the nearby Chile Triple Junction (Ramos, 1999).

In the 1970s, it was noticed that there was a pattern between the locations of the flat-slab segments and related Quaternary arc volcanism (Barazangi and Isacks, 1976; Jordan et al., 1983). As a subducting slab enters the subduction zone, it is relatively cold. If the slab descends with a steep angle, the slab undergoes mineralogical changes with increasing temperature and pressure which release water and induce flux melting of overlying mantle wedge. However, if the slab angle is too shallow (e.g. <10°), then the slab does not reach high enough temperatures or pressures to induce flux melting nor is there any mantle wedge flow to provide hot asthenospheric material to the slab surface. As a result, no volcanism occurs during flat slab subduction (Gutscher et al., 2000). Careful geological mapping, geochronology and geochemistry can show how volcanism changes through time along with changes to the subduction zone geometry (Cembrano and Lara, 2009; Ramos and Folguera, 2009). In general, a normal subduction zone angle will result in a narrow arc of volcanoes; as the subduction angle decreases towards a flat slab, the volcanic arc will widen into the back arc due to slab melting; a mature flat slab will produce a volcanic gap with a cool slab that no longer causes flux melting (Gutscher et al., 2000).

2.5 THE SOUTHERN VOLCANIC ZONE

2.5.1 Overview of Range Crest Volcanism

The SVZ is arguably the most volcanically active region of the Andes in modern times with a full suite of basaltic to rhyolitic lava erupted at the surface (Jacques et al., 2013). There is a general trend to higher silica contents and a larger isotopic crustal signature towards the northern SVZ as the crust gets thicker and the Nazca Plate transitions to the Pampean flat slab (Cembrano and Lara, 2009; Hildreth and Moorbath, 1988; Jacques et al., 2013; Lopez-Escobar et al., 1995). The northern SVZ has crustal thicknesses in excess of 60 km while the southern SVZ has thicknesses between 35 and 42 km (Ramos and Kay, 2006). As shown in Figure 2.4, the SVZ can be further subdivided into the north SVZ (NSVZ; 33°S to 34.5°S), the transitional SVZ (TSVZ; 34.5°S to 37°S), the central SVZ (CSVZ; 37°S to 41.5°S) and the south SVZ (SSVZ; 41.5°S to 46°S) from Lopez-Escobar et al. (1995). The NSVZ is dominated by the eruption of andesites and dacites from volcanoes such as Tupungato and Maipo, which belong to a

north-south oriented volcanic arc. The TSVZ has a wide range of compositions of eruptive products from basalts to rhyolites and includes many rhyolite calderas including the Laguna del Maule Volcanic Field (LdMVF), Planchon-Peteroa as well as more classic stratovolcanoes such as Descabezado Grande and Tatara-San Pedro. The region is also well-known for many hot springs which show both meteoric and magmatic isotopic signatures (Benavente et al., 2016). Volcanic centers in the TSVZ tend to be aligned NW or NNW. The CSVZ has erupted primarily basalts and basaltic andesites with a larger number of stratovolcanoes such as Villarrica and Llaima. Finally, the SSVZ has erupted primarily basalts including volcanoes such as Chaiten and Hudson (not shown in Figure 2.3).

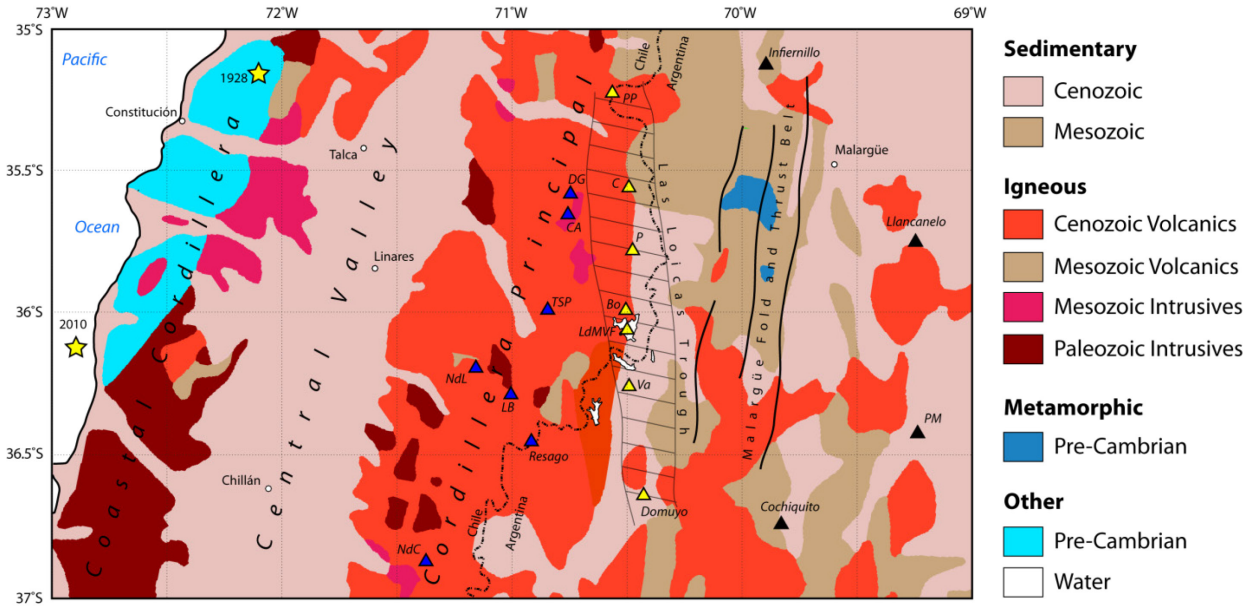

Figure 2.5: Geology map of the Maule Region of central Chile. Blue triangles denote stratovolcanoes; yellow triangles show recent rhyolitic volcanoes; black triangles show back-arc volcanoes. Yellow stars show epicenters of major historical earthquakes. See Figure 2.4 for map location. PP = Planchon Peteroa; C = Calabozos Volcanic Field; P = Puelche Volcanic Field; Bo = Bobadilla Caldera; LdMVF = Laguna del Maule Volcanic Field; Va = Varvarco; PM = Payun Matru; DG = Descabezado Grande; CA = Cerro Azul; TSP = Tatara-San Pedro; NdL = Nevados de Longavi; LB = Lomas Blancas; NdC = Nevados de Chillan.

The SVZ shows significant along-strike variations in volcanism and this is primarily related to tectonics and variations in crustal thickness (Cembrano and Lara, 2009). Both the CSVZ and SSVZ are dominated by the 1000 km Liquiñe-Ofqui Fault Zone (LOFZ), a major intra-arc transpressional strike-slip fault which has impacted the deformational and tectonic history of the region (Figure 2.4; Cembrano and Herv, 1996; Cembrano and Lara, 2009). As shown earlier in Figure 2.2, cycles of compression and extension related to flat-slab subduction have a major impact on volcanism and foreland deformation where compression leads to deformation and crustal thickening and extension leads to a flare-up in volcanism

(Cembrano and Lara, 2009; Ramos et al., 2014; Rojas-Vera et al., 2014a). Today, the CSVZ and TSVZ are located in a unique setting relative to the rest of the Central Andes. The rest of the Central Andes tend to have a concentration of active magmatism along a narrow volcanic arc except in regions of flat-slab subduction where there is little to no volcanism at all. The CSVZ and TSVZ have a much wider magmatic zone which also includes significant back-arc volcanism more than 500 km from the plate boundary (Ramos and Kay, 2006). At this latitude there is also a unique north-northwest extensional trough known as the Las Loicas Trough (Figure 2.5) which contains a large number of quaternary ignimbrites and rhyolite calderas such as Bobadilla, Varvarco, the LdMVF, and Domuyo (Figure 2.5; Folguera et al., 2006). The Las Loicas Trough may be a northward continuation of the LOFZ and a modern analogue of the Loncopué Trough which had similar rhyolitic caldera collapses in the late Pliocene (Figure 2.4 and Figure 2.5; Rojas-Vera et al., 2014b). It has also been suggested that the preponderance of rhyolitic collapse calderas resulted from changes in slab dip during the Pliocene and Quaternary. This caused an injection of hot asthenospheric material north of the Cortaderas lineament which caused crustal melting via basaltic underplating leading to highly-evolved rhyolitic volcanism with strong crustal signatures (Figure 2.2; Ramos and Folguera, 2009; Ramos and Kay, 2006).

2.5.2 Backarc Volcanism

One of the unique aspects of the SVZ (and TSVZ in particular) is the fact that it has had a volcanically-active backarc during the Quaternary. In particular, the Payenia Volcanic Province which includes the Auca Mahuida shield volcano and the Payun Matru shield volcano which have erupted as recently as 1 ka (Figure 2.4; Pallares et al., 2016; Ramos et al., 2014). These are largely composed of Hawaii-style basaltic volcanism with relatively little crustal interaction or silicification of erupted products (Pallares et al., 2016; Ramos and Folguera, 2011). The backarc volcanism had a significant flare-up as the subducting slab went from flat slab subduction to normal subduction over the course of several million years from the Miocene to the Quaternary (Figure 2.2; Ramos and Kay, 2006). The current extensional tectonic setting has favoured increased volcanism in the last 2 Ma (Pallares et al., 2016). While many of the backarc volcanoes have a classic subduction signature associated with hydrous flux melting of the mantle wedge, some do show evidence of an injection of hot asthenosphere during steepening of the slab (Pallares et al., 2016).

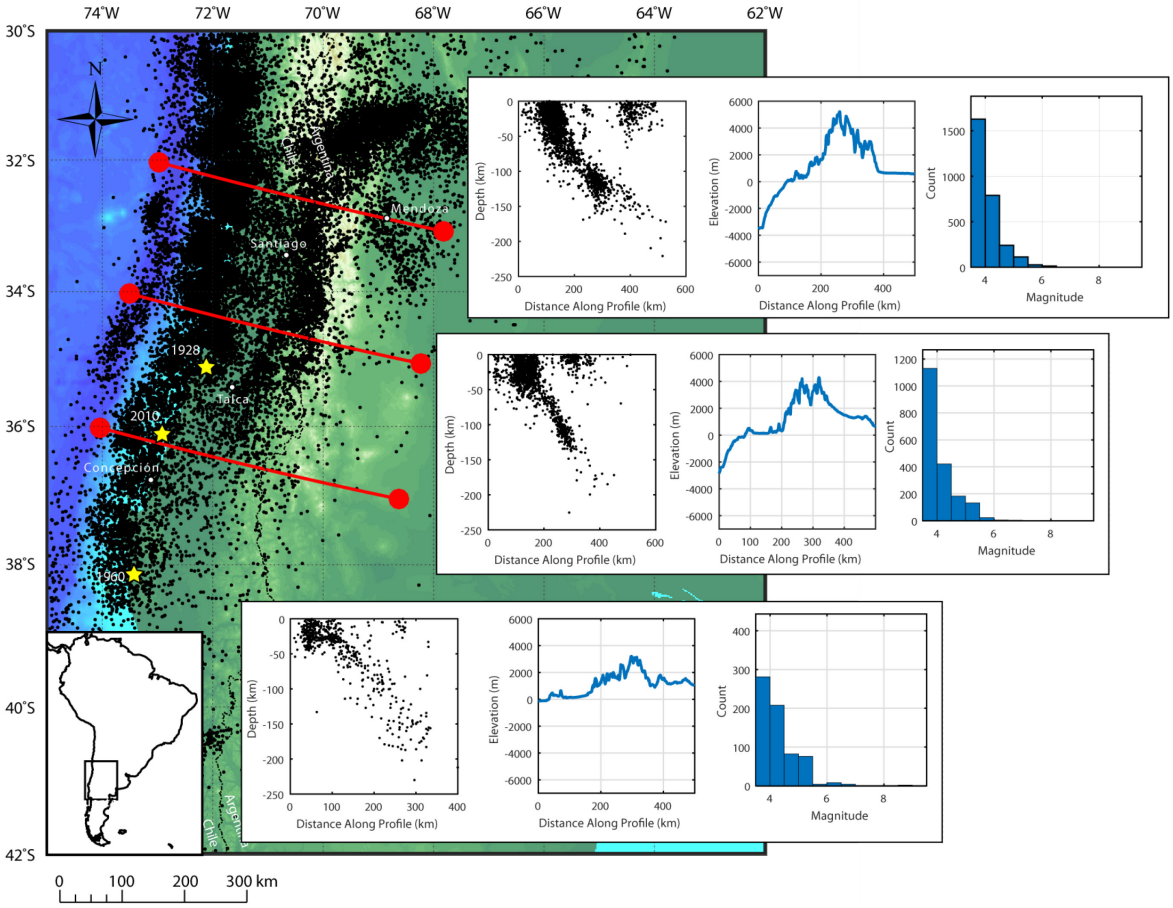

Figure 2.6: Seismicity cross sections in the Southern Volcanic Zone from 1970 (IRIS, 2018). Each dot on the map shows an earthquake epicenter. Yellow stars denote epicenters from important earthquakes. Each inset corresponds to cross-sections along profiles shown by red lines on the map from north (top) to south (bottom). Each inset shows (1) a cross-section of seismicity where earthquake hypocenters (black dots) approximately follow the top of the down-going Nazca plate; (2) A plot of the topography along each profile and; (3) A histogram of earthquake magnitudes along the cross-section.

2.5.3 Seismicity in the Southern Volcanic Zone

As detailed by Ruiz and Madariaga (2018), the Southern Volcanic Zone has seen some of the largest megathrust earthquakes ever recorded, including the 1960 Valdivia earthquake (39.5°S) with a moment magnitude of 9.5 (Cifuentes, 1989), the 2010 Maule earthquake (36.3°S) with moment magnitude of 8.8 (Moreno et al., 2012), and the 1928 Talca earthquake (35.0°S) with a moment magnitude of 8.3 (Figure 2.6; Beck et al., 1998). Over 900 earthquakes with a magnitude greater than 5.0 have been recorded since 1970 (IRIS, 2018). The majority of these earthquakes occur offshore or near the coast with hypocenter depths less than 30 km (Figure 2.6). The fact that such large earthquakes occur here has

been linked to a variety of physical parameters such as subduction angle, trench curvature, and plate velocity (Schellart and Rawlinson, 2013). Ruegg et al. (2009) identified a large seismic gap in the Maule region using GPS to measure strain accumulation. They suggested the potential for a large, worst-case-scenario 8 to 8.5 M_w earthquake in the near future, and their prediction came true a year later when the 2010 Maule earthquake ruptured the subduction zone in a megathrust earthquake in the gap. The largest megathrust earthquakes appear to be primarily controlled by changes in frictional properties at the slab interface perhaps due to fluids released by the down-going slab (Moreno et al., 2018).

There have been links made between the seismicity of the region and volcanic eruptions and/or deformation episodes (Eggert and Walter, 2009). Earthquakes have been shown to sufficiently change the stress field in magma reservoirs which can trigger rapid bubble formation and/or reorganization of melt (Manga and Brodsky, 2006; Marzocchi et al., 2002). Rapid bubble formation or rapid melt segregation can change the buoyancy forces of a magma reservoir and lead to an eruption. This has specifically been investigated with regards to eruptions in the SVZ (Bonali et al., 2013) as well as onset of deformation episodes in the SVZ (Le Mével et al., 2015; Pritchard et al., 2013).

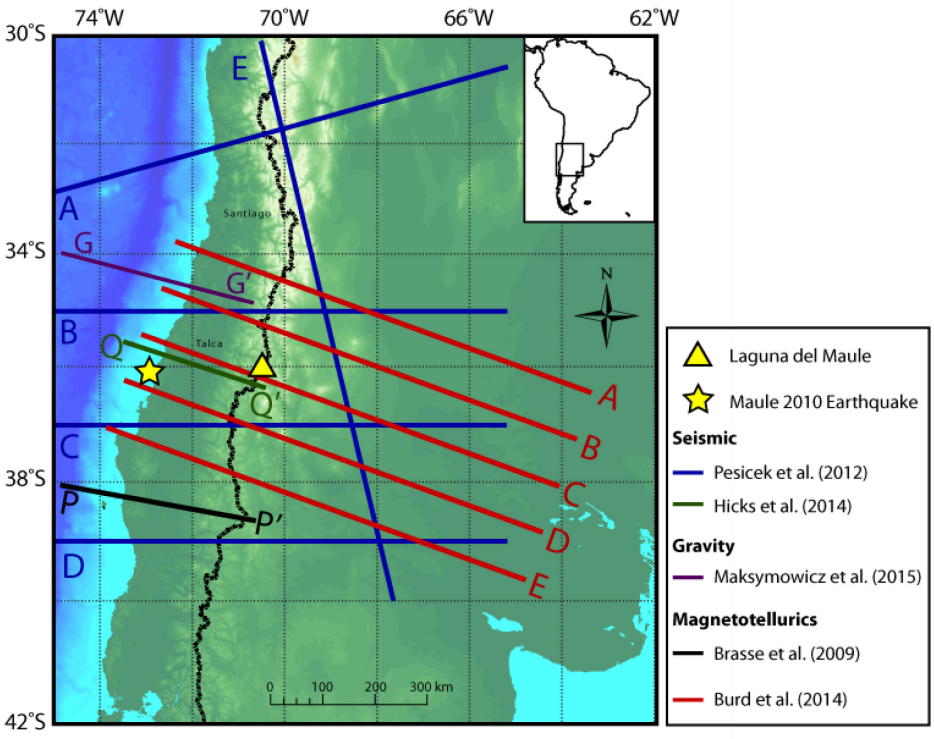

Figure 2.7: Map showing profiles from geophysical surveys in the Southern Volcanic Zone discussed in detail in text. Note that all studies shown are 3-D surveys with particular profiles chosen for display purposes except for Brasse et al. (2009) which was a 2-D survey.

2.6 PREVIOUS REGIONAL GEOPHYSICAL STUDIES IN THE SOUTHERN VOLCANIC ZONE

This section summarizes some of the important geophysical work that has been done in the SVZ. There is a large amount of literature on the subject and so example figures for every study cannot be shown. However, particular seismic studies, gravity studies and previous MT studies which have important implications for the Maule region are highlighted. The profiles for each study discussed in text are shown in Figure 2.7 to show the different scales and areas of interest that each study covers.

2.6.1 Seismic Studies

Early seismic studies in the SVZ often focused on the NSVZ (e.g. Gilbert et al., 2006; Wagner, 2005), the CSVZ (e.g. Bohm et al., 2002; Haberland et al., 2009), and the SSVZ (e.g. Contreras-Reyes et al., 2008a; Lange et al., 2008; Scherwath et al., 2009) with limited work specific to the TSVZ (Heit et al., 2008). The projects in the north were largely driven by the CHARGE network of seismometers to investigate the geometry and along-axis variation of the slab as it transitions from flat-slab to normal subduction (Beck et al., 1998). Based on this imaging it was interpreted that the crustal thickness decreases to the south from 60 - 70 km to 40 km thick (Gilbert et al., 2006; Heit et al., 2008). South of the flat slab, it appears there are higher volumes of melt beneath the volcanic arc whereas beneath the flat slab there is very little evidence of melt or hydrated minerals (Wagner et al., 2005). However, low V_p/V_s ratios suggest that there were previous fluids beneath the flat slab which altered the overlying mantle chemistry and that such fluids may be transient and no longer present (Wagner et al., 2005). Anderson et al. (2004) noted that teleseismic seismic velocity models are anisotropic with an along-axis variation from trench-parallel in the south to trench-perrpendicular in the north. They interpret this as asthenospheric flow in the mantle wedge which is deflected by interactions with the flat slab in the north.

The seismic projects in the CSVZ and SSVZ used different networks (e.g. ISSA 2000, TIPTEQ) to study subduction zone structure in the more volcanically and seismically active parts of the SVZ using both onshore and offshore seismic arrays (Bohm et al., 2002; Haberland et al., 2009). These projects generally focused on the forearc structure in the seismogenic zone since the 1960 Valdivia earthquake occurred in this region. Bohm et al. (2002) identified low velocities in the forearc which may be due to a serpentinized mantle and they located a peak in Benioff zone seismicity at 60 km depth which may be due to dehydration embrittlement. Haberland et al. (2009) use a different seismic array than Bohm et al. (2002) and found no strong evidence for serpentinization in the forearc mantle. Both arrays overlap and

the latter array examined V_p/V_s ratios which is a better marker for serpentinization. Yuan et al. (2006) used teleseismic receiver functions to image deeper structure further in the back-arc in the CSVZ. They identified a thinner crust in the back-arc and a poorly-defined slab interface beneath the volcanic arc which they attributed to eclogitization. Like the NSVZ, Yuan et al. (2006) also suggested partial melting in the lower crust beneath the volcanic arc due to an anomalously high Poisson's ratio. Most studies in the SSVZ focused on the forearc and accretionary wedge and found very little along-axis variation in structure even with changing Nazca plate age (Scherwath et al., 2009). Contreras-Reyes et al. (2008b) showed evidence for extensional bending-related faulting on the outer rise which may help to hydrate the incoming plate in the SSVZ. The intra-arc seismicity of the LOFZ was first analyzed by Lange et al. (2008) which suggests relatively large (e.g. M_w>6.0) earthquakes are possible along the LOFZ. It is worth noting that none of these studies in the SVZ specifically state the thickness of the incoming oceanic lithosphere but a seismic study in northern Chile (20°S - 24°S) estimated it to be approximately 50 km thick which is relatively common for young, oceanic lithosphere (Sodoudi et al., 2011).

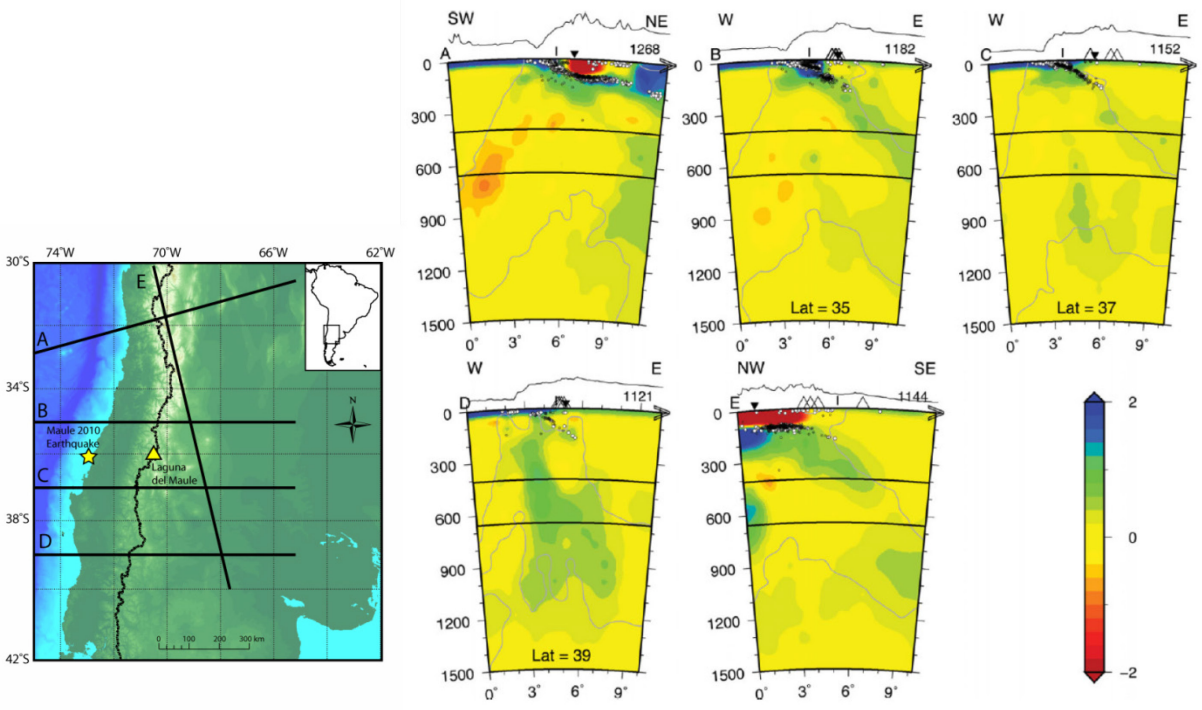

Figure 2.8: Cross-sections through the three-dimensional seismic tomography model of Pesicek et al. (2012). Inset map shows location of profiles and location of LdMVF and Maule 2010 earthquake. Color bar shows seismic P-wave velocity anomaly in km/s. Modified from Figure 3 in Pesicek et al. (2012).

The lack of seismicity in the TSVZ around 36°S made imaging the region difficult (Heit et al., 2008; Wagner et al., 2005). Using the CHARGE network, Heit et al. (2008) concluded that a poorly imaged

Moho beneath the volcanic arc at this latitude (36°S) may be related to melt in the crust or upper mantle. Following the 2010 Maule earthquake, a significant number of studies were conducted to image the region using data from both the earthquake and its aftershocks. This included large-scale tomography of the entire SVZ (e.g. Pesicek et al., 2012; Portner et al., 2017) as well as smaller-scale tomography of the 2010 Maule rupture zone (Contreras-Reyes et al., 2017; Dannowski et al., 2013; Hicks et al., 2014, 2012; Moscoso et al., 2011) and very specific studies on the rupture process itself (e.g. Huang et al., 2017; Lin et al., 2013; Rietbrock et al., 2012).

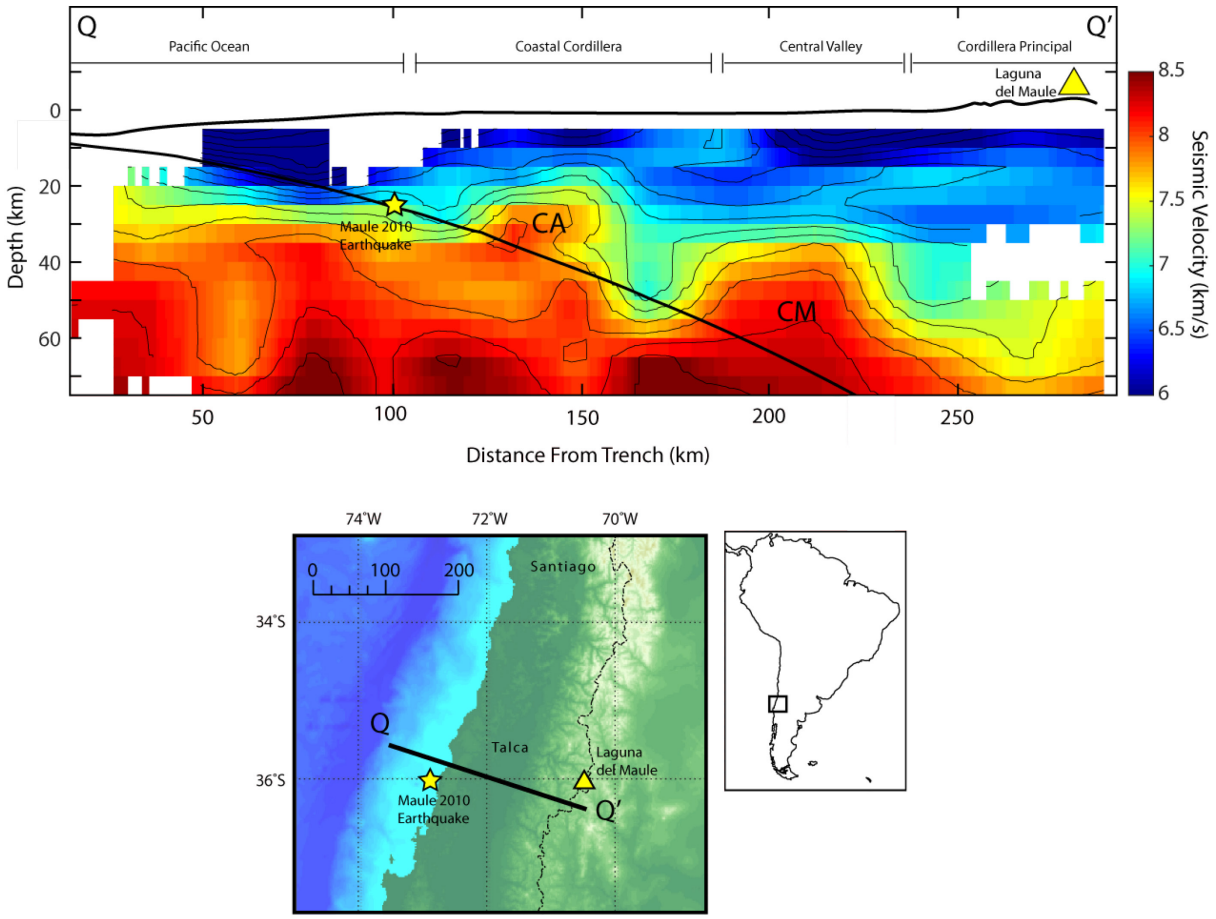

Figure 2.9: Cross-section through the three-dimensional seismic tomography model of Hicks et al. (2014). Yellow star denotes hypocenter of the 2010 Maule earthquake and yellow triangle is the Laguna del Maule Volcanic Field.

A comprehensive, 3-D tomographic model from 30°S to 40°S combined multiple arrays (CHARGE, ISSA) as well as additional aftershock data from the 2010 Maule earthquake to produce a unified view of the deep structure of the region down to the 660 km transition using both teleseismic and local data (Figure 2.8; Pesicek et al., 2012). Increased ray-coverage from the Maule aftershock data allowed better imaging

of the subducting slab structure. They suggested that the transition from flat slab to normal subduction is accommodated by a smooth bend with no evidence of slab tearing. However, a deeper relic slab below 200 km depth dips steeply and appears disconnected from the shallower slab which may indicate tearing and detachment around 38°S (Figure 2.8; Pesicek et al., 2012). A more recent study shows evidence of a sub-slab low velocity anomaly beneath the flat slab related to the relic Juan Fernandez Hot Spot which disappears south of 34°S (Portner et al., 2017).

Dannowski et al. (2013) used receiver functions between 35°S and 36°S latitude to image the subduction zone using both pre- and post-Maule seismicity. Their results suggested that the Moho was located at 38 km depth and a relatively dry mantle wedge. Hicks et al. (2014, 2012) focused on the forearc velocity structure of the Maule region using local earthquake tomography (Figure 2.9). An east-dipping high P-wave velocity anomaly was interpreted as the subducting oceanic crust while a shallow lower velocity anomaly offshore was interpreted as the accretionary complex. As shown in Figure 2.9, they note that there is a significant, high velocity anomaly on the plate interface at approximately 25 km depth which they called the Cobquecura anomaly (CA; Hicks et al., 2014). The up-dip limit of this feature appears to have played a role in stopping the nucleation of the Maule 2010 earthquake rupture. A lack of coseismic slip and aftershock seismicity within or below the anomaly suggests that it is an important structural control on regional seismicity. This feature was initially interpreted as an ancient seamount (Hicks et al., 2012) but further work showed that it was much larger and faster than previously thought (Hicks et al., 2014). One possibility proposed is that the Cobquecura anomaly represents a relic block of ultramafic mantle rocks which were emplaced during the Triassic when the ancient volcanic arc aligned with the present-day Coastal Cordillera (Hicks et al., 2014). This important insight suggests that ancient subduction zone structures can play an important role in modern day tectonics, seismicity and volcanism.

2.6.2 Gravity Studies

Early Bouguer gravity studies in the SVZ focused primarily on large-scale crustal and mantle features using 2-D profiles (e.g. Grow and Bowin, 1975). These generally showed the same patterns of a high Bouguer gravity anomaly near the trench and a negative slope (e.g. decreasing gravity) to the east. Introcaso et al. (1992) used gravity profiles to determine the crustal thickness at 33°S and found an approximate thickness of 33 km at the trench thickening to 70 km beneath the Andean mountain belt. A more comprehensive 3-D gravity survey of the SVZ was conducted by Tassara et al. (2006). They

determined that the crust of the incoming Nazca Plate is, on average, approximately 7 km thick. The lithosphere-asthenosphere boundary (LAB) in the over-riding South American plate was interpreted to be deepest (>100 km) near the Pampean flat slab at approximately 30°S and shallowest to the south. Beneath the Maule region, it is approximately 60 km to the LAB beneath the Cordillera Principal. As mentioned earlier, the incoming oceanic lithosphere has a thickness of approximately 50 km (Sodoudi et al., 2011). Additional work by Tassara et al. (2007) determined the elastic thickness for South America (e.g. the thickness of the rheologically-strong lithosphere). Thickest regions (>100 km) are found over cratons (e.g. the Brazilian craton) while most of central Chile is thin (<20 km thick). It is interesting to note that central Chile (33°S to 37°S) also has an anomalously thin elastic lithosphere offshore in the Nazca plate whereas the majority of the Chilean margin thickens offshore. This also corresponds to anomalously high flexural loading beneath central Chile relative to north Chile (Tassara et al., 2007).

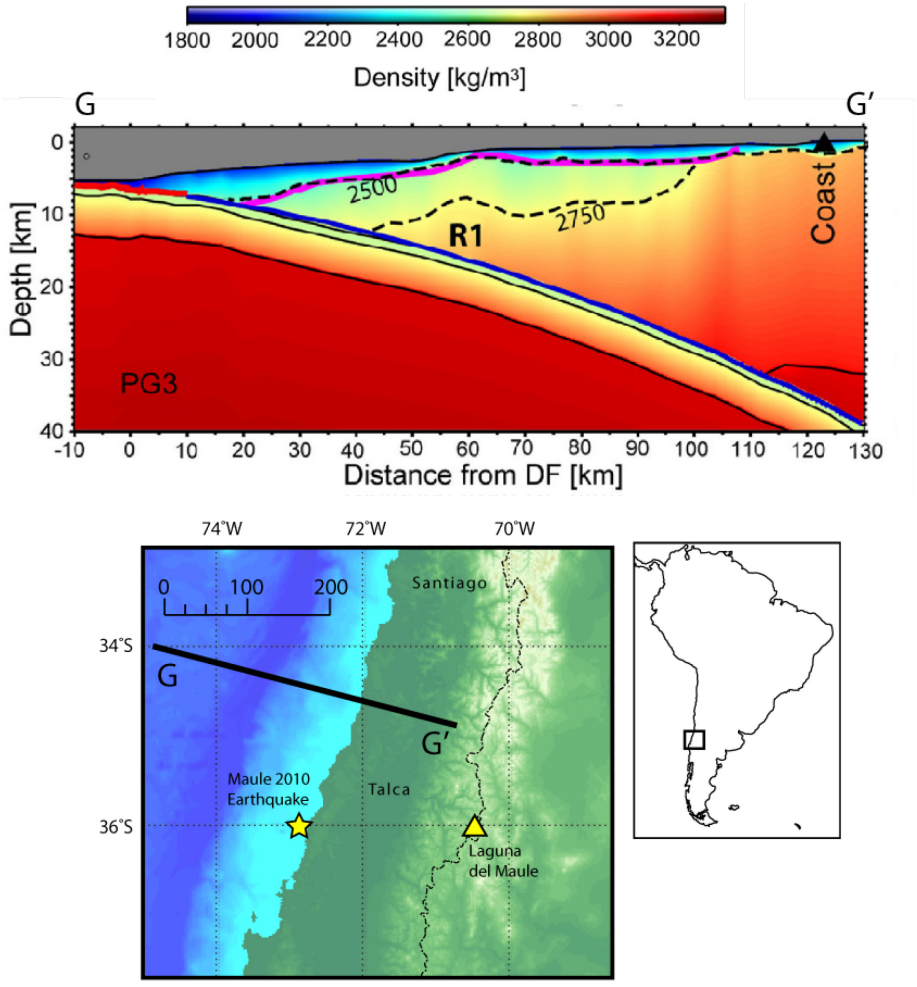

Figure 2.10: Interpretation of the density model from Maksymowicz et al. (2015) based on satellite gravity data.

Following the Maule 2010 earthquake, a more focused and updated model of the Chilean subduction zone between 18°S and 45°S was presented by Tassara and Echaurren (2012) which used additional seismic data to constrain the geometry of the subducting slab and the Moho of the South American plate. They conclude that some large discrepancies (e.g. >40 km) can exist between regional studies and global models such as Slab1.0 (Hayes et al., 2012) or Crust2.0 (Laske et al., 2013) although the differences in the Maule region (e.g. 36°S) are relatively small compared to areas to the north and south. An even more focused Bouguer gravity and magnetic study of the Maule region near the epicenter of the Maule 2010 earthquake was carried out by Maksymowicz et al. (2015) using primarily offshore data. They showed that the region of highest slip during the Maule earthquake occurred where the overlying continental crust was relatively low density with low vertical loading on the down-going slab, and a low effective basal friction coefficient. They also noted that heterogeneities in the lithology of the continental basement along the plate interface may affect the pattern of coseismic slip and aftershocks. These density heterogeneities include a high density anomaly (R1) just offshore which is possibly related to a subducted seamount and may have affected the distribution of aftershocks around this local asperity (Figure 2.10; Maksymowicz et al., 2015). This feature does not directly coincide with the velocity anomaly of Hicks et al. (2014, 2012) because the gravity analysis does not extend far enough east, but both reach the same conclusion that slab asperities influence the rupture processes in the Maule region.

A recent study by Astort et al. (2019) used Bouguer gravity and magnetic data to investigate the subsurface structure of the Payenia Volcanic Province, including the Auca Mahuida volcanic field and Payun Matru in the backarc of Argentina. They imaged a 200 km-wide high density and high susceptibility anomaly beneath the backarc volcanoes which they interpreted as an asthenospheric upwelling consisting of mafic materials intruding into the middle to upper crust and feeding the Payenia Volcanic Province. At greater depth (>100 km), low density values indicate partially molten material within the mantle. Both of these observations suggest the possibility of the Nazca plate tearing at depth. Much of this is in agreement with the previous seismic experiments (e.g. Pesicek et al., 2012) and MT experiments (e.g. Burd et al., 2014; see next section).

2.6.3 Magnetotelluric Studies

There have been relatively few published regional MT studies in the Southern Volcanic Zone investigating the subduction zone structure of the Chilean margin. Here, a review of some of the studies in the CVZ is given followed by a brief review of the limited MT studies in the SVZ.

To the North, in the CVZ, there have been a variety of two-dimensional investigations of the regional structure of the CVZ near the Bolivian orocline and the Altiplano plateau along profiles (e.g. Brasse et al., 2002; Brasse and Eydam, 2008; Schilling et al., 1997; Schwarz and Krüger, 1997). These studies found crustal conductors (10 – 40 km depth) along the volcanic arc which were interpreted as partial melt (Schilling et al., 1997; Schwarz and Krüger, 1997) and a large lower crustal conductor covering much of the southern Altiplano known as the Altiplano Puna Magma Body (APMB) (Brasse et al., 2002; Chmielowski et al., 1999). This large crustal conductor attenuated much of the signal making it difficult to image deeper structures. Brasse and Eydam (2008) collected data in the northern Altiplano and found that the large crustal conductor did not exist there allowing them to image to upper mantle depths. They found a large conductor in the upper mantle interpreted as partial melts and fluids from the subducting Nazca plate; however this conductor was offset from the volcanic arc by approximately 100 km.

A re-analysis of the regional MT data from the CVZ from the 1980s was published by Kühn et al. (2014) using 3-D inversion methodologies. Similar conclusions were made using 3-D inversion: the large crustal conductor (APMB) was the dominant feature and an extremely resistive coastal Cordillera. More detailed 3-D MT work by (Comeau, 2015; Comeau et al., 2016) better delineated the depth and lateral boundaries of the APMB constraining it to approximately 25 km depth. This was interpreted as a wet partial melt – one of the largest volumes of crustal melt in the world (Laumonier et al., 2017).

The first electromagnetic soundings in the SVZ were carried out in the late 1980s around Volcán Villarrica (39°S) using 1-D and 2-D modelling of long-period MT data (Muñoz et al., 1990). These showed a noticeable decrease in resistivity around 35 - 50 km depth interpreted as anomalous heated layer and was not specifically interpreted as partial melt. Two long-period MT profiles were collected by Brasse and Soyer (2001) between Volcán Villarrica and Volcán Llaima (39°S) which extended from the Pacific Ocean to the Argentine border. Both profiles showed similar resistivity structures with a relatively large

moderately-conductive feature in the lower crust (30 km depth) beneath the volcanic arc extending eastwards into Argentina which may be related to fluids or melt in active fault zones such as the Liquiñe-Ofqui Fault Zone (LOFZ). Data were relatively two-dimensional with approximately north-south regional geoelectric strike. The inversions did not recover any image of the slab interface or any upper mantle structures nor did they image any large crustal conductors similar to those found in northern Chile and Bolivia. A third long-period profile was collected between Volcán Llaima and Volcán Lonquimay (38°S) and included offshore data (Brasse et al., 2009). Using isotropic 2-D inversions, they imaged similar conductive structures in the mid-to-lower crust beneath the volcanic arc and extending into the backarc interpreted as partial melt (Figure 2.11). They also image a mid-crustal conductor in the forearc beneath the Central Valley likely related to forearc fluids and a large crustal conductor offshore interpreted as a fluid-rich accretionary wedge. The other important feature they note is that the descending Nazca Plate appears to be imaged as a resistor in their model which correlates with the location of the top of the slab taken from seismic studies.

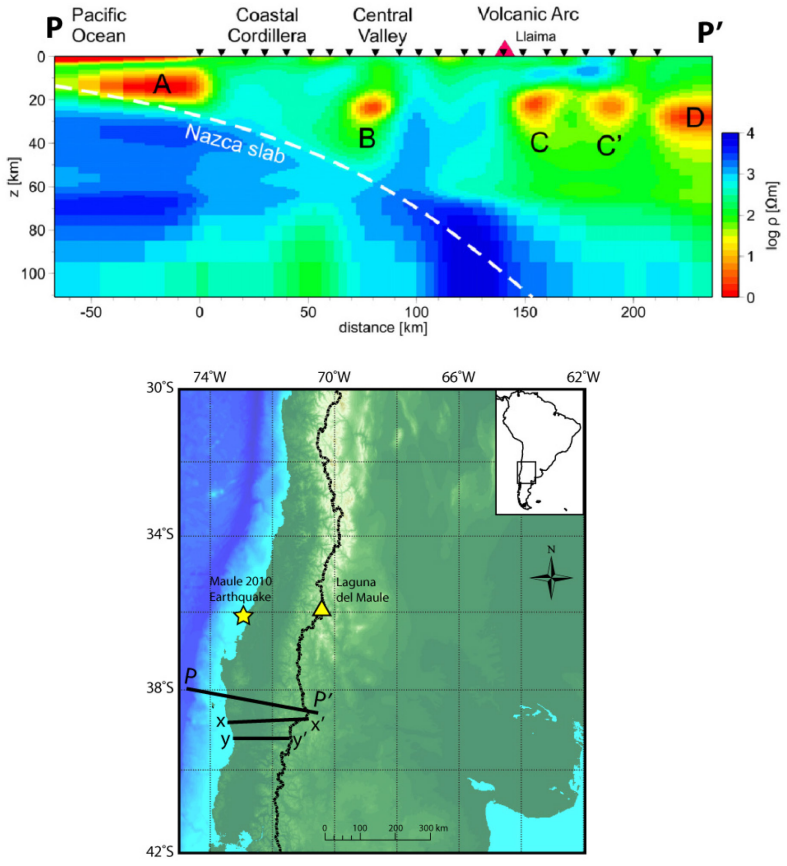

Figure 2.11: Two-dimensional resistivity model from MT data in the Southern Volcanic Zone along P-P' modified from Brasse et al. (2009). The location of additional profiles x-x' and y-y' from Brasse and Soyer (2001) are shown in the map inset.

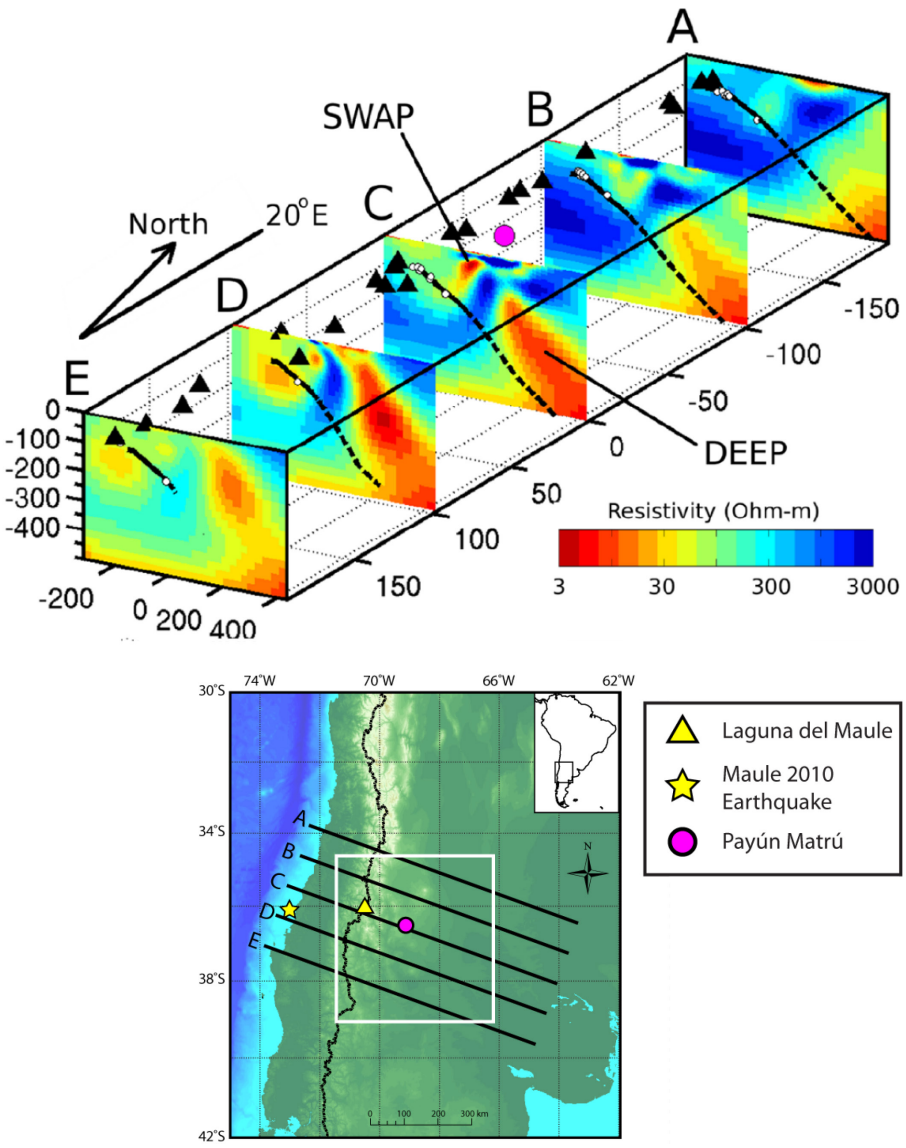

Figure 2.12: Cross-sections through the three-dimensional resistivity model of Burd et al. (2014) obtained from long period MT data in western Argentina. White dots are earthquake hypocenters and the magenta circle is the location of the Payún Matrú volcano. The study region is shown with the white box on the inset map as well as the location of the Laguna del Maule Volcanic Field (yellow triangle) and 2010 Maule earthquake epicenter (yellow star). Modified from Figure 6 in Burd et al. (2014).

Brasse et al. (2009) also noted that lower crustal electrical anisotropy may be an important factor at this latitude of the SVZ. They noted that the MT impedance data were very 2-D with a north-south geoelectric strike but the induction vectors were deflected to the north-east. A truly 2-D scenario would see induction vectors point perpendicular to geoelectric strike. Brasse et al. (2009) used anisotropic

forward modelling to explain the deflected induction vectors by including a lower crustal anisotropic layer between 20 km and 40 km depth with the conductive direction oriented northeast-southwest. This anisotropy is surprising because most surface faults are oriented northwest-southeast. However they note that previous geological work indicates a stress-field oriented northeast-southwest which suggests a fluid-rich and highly fractured lower crust could explain the electrical anisotropy. An isotropic 3D inversion of the SVZ was done by Kapinos et al. (2016) which included a reinterpretation of all the previous MT data collected by Brasse et al. (2009) and Brasse and Soyer (2001). In general, the 3D results broadly confirmed the previous 2D results. Many of the resistivity model features are somewhat poorly constrained because the data is aligned along profiles rather than a true 3D array. More focused 2-D studies of Volcán Villarrica and the LOFZ using broadband MT data have identified conductors associated with the LOFZ down to depths of 10 km where the brittle-ductile transition was expected (Held et al., 2016). Recent 3-D MT work by Díaz et al. (2020) has also shown the importance of the LOFZ in deep-seated magma plumbing systems at Osorno Volcano. In particular, they identified mid- to deep-crustal conductors 10 km offset from the volcano but dipping towards the LOFZ suggesting that the LOFZ is an important fault pathway for melts.

Prior to this thesis work, there was no MT data in the Maule region except for a commercial geothermal exploration project near the LdMVF (see Chapter 3). The nearest study included long-period MT data collected in a 3-D array in the backarc in western Argentina (Burd et al., 2014, 2013). The initial work of Burd et al. (2013) focused on the transition from the Pampean flat slab segment to the normal subduction zone between 31°S - 35°S. The primary feature that they identified and interpreted was a large conductive plume rising from a depth of 410 km to the base of the lithosphere at 100 km depth. There is no evidence of the slab descending deeper than 190 km and they argued that this plume was evidence for a slab window and a torn slab which is in general agreement with the seismic tomography interpretation (Pesicek et al., 2012). Additional long-period MT data were collected further south between 35°S and 38°S to encompass the backarc Payenia Volcanic Province and Payun Matru (Burd et al., 2014). Burd et al. (2014) identified two important conductive features which they called the Shallow Western Asthenospheric Plume (SWAP) and the Deep Eastern Plume (DEEP) (Figure 2.12). The SWAP is a large, west-dipping feature that rises towards the surface from the Nazca slab towards the Payún Matrú caldera (Figure 2.12). It may be connected to the slab but it is not clear from the MT data alone. The DEEP is an east-dipping conductor which rises from 400 km depth towards the surface but lies about 100 km southeast of Payún Matrú. They suggest that the SWAP and DEEP are disconnected and electrically

distinct but that the two features may have been connected in the past prior to the DEEP being decapitated when the paleo-flat slab returned to normal subduction in the late Miocene. Both features are interpreted as a small fraction of partial melt although it may also be due to fluids or brines. The SWAP is identified as the magmatic source of recent Quaternary backarc volcanism in the Payenia Volcanic Province. Despite the increase in seismic and gravity studies following the Maule 2010 earthquake, there have not been any MT studies of the Chilean subduction zone between 30°S and 38°S.

2.7 SUMMARY

The Maule region of central Chile is part of the Andean subduction zone which involves the subducting Nazca Plate and the over-riding South American plate. The region has experienced past flat slab subduction events during the Miocene but currently exhibits normal subduction angle. This history has influenced the spatio-temporal patterns of volcanism and deformation. In its modern configuration, the Maule subduction zone is an archetypical Andean subduction zone. The descending slab releases fluids in a series of metamorphic reactions with increasing temperature and pressure. Under certain pressure and temperature conditions, these fluids lower the melting point of the overlying mantle rocks leading to flux melting and surface volcanism. Both the main volcanic arc and the backarc have been volcanically-active in the Quaternary. This includes typical andesitic stratovolcanoes on the main axis of the Andean cordillera, a northwest-southeast string of rhyolite calderas off-axis to the east, and a large basaltic province in the backarc. The force of the subducting slab creates friction along the plate boundaries which has resulted in significant forearc seismicity including the 2010 Maule megathrust earthquake which ruptured in a large seismic gap.

Previous regional geophysical studies have primarily been focused on the Pampean flat slab to the north or the CSVZ and SSVZ to the south resulting in a lack of geophysical images of the Maule region prior to the 2010 Maule earthquake. These regional geophysical studies have identified major anomalies in the backarc related to the flat slab which shows evidence of asthenospheric upwelling and slab tears as the slab transitions from flat to normal subduction. In the Bolivian orocline in northern Chile, large anomalies in the mid-to-lower crust have been interpreted as regions of significant silicic melt accumulations. Further south in the CSVZ, no such large crustal anomalies are present beneath the volcanic arc. After the 2010 Maule earthquake, there was an increase in seismic and gravity studies in the Maule region. These identified significant anomalies along the plate interface near the area of rupture. The rupture initiation and propagation seems to have been influenced by structures along the

slab interface. There is also evidence of fluids and melt beneath the volcanic arc as well as serpentinization of the forearc mantle. Since the conductivity of a rock is sensitivity to the presence of fluids and melt, there is a clear need for an image of the electrical structure of the Maule region which is one of the primary goals of this thesis.

CHAPTER 3: THE LAGUNA DEL MAULE VOLCANIC FIELD

3.1 INTRODUCTION

Silicic volcanoes are responsible for the largest and most destructive eruptions on Earth and can cause widespread damage to infrastructure, loss of life, and climate change via the emission of ash, aerosols and gases (Self, 2006). Silicic volcanoes occur in various tectonic settings including rift zones (e.g. Krafla, Iceland), hot spots (e.g. Yellowstone, USA), and subduction zones (e.g. Taupo, New Zealand; Chaitén, Chile). There are many important outstanding questions in volcanological studies. For example, it is not well-understood how, why, or how rapidly a volcano goes from a period of relative quiescence to a period of activity (Cashman and Giordano, 2014; Till et al., 2015). Similarly, deformation signals are often interpreted as an indication of activity, but the source of such signals may not be magmatic and may instead be due only to hydrothermal fluids (Biggs and Pritchard, 2017). For silicic systems, there is a thermal problem of how large quantities of eruptive silicic melt can be generated above the solidus temperature, the composition and time-scales of pre-eruptive storage, and why some silicic systems erupt while others solidify as plutons (Annen et al., 2006; Bachmann and Bergantz, 2008a). Determining how much melt solidifies underground as intrusive igneous rocks versus how much melt erupts as lava (i.e. the intrusive-extrusive ratio) is another important question in volcanological studies (Bachmann et al., 2007). Ongoing questions also revolve around the geometry of the volcanic plumbing architecture and its relation to the above questions. It seems clear that there are very few global generalizations that can be made (Chaussard and Amelung, 2014; Zellmer and Annen, 2008). Identifying the location, depth, size and composition of silicic magma reservoirs is important in assessing the size of any future eruptions as well as the current system stability and thermal regime. Finally, geophysical methods which image volcanic systems also have inherent limitations regarding resolution and non-uniqueness and a better understanding of these limitations is vital moving forward (Lees, 2007; Magee et al., 2018; Pritchard and Gregg, 2016). The Laguna del Maule Volcanic Field (LdMVF), central Chile, is an ideal natural laboratory of a restless but non-erupting silicic system to address many of these questions (Singer et al., 2014). The LdMVF has been showing signs of significant deformation since 2007, is host to ongoing shallow seismicity, and has erupted large volumes of silicic melt in the Holocene (Andersen et al., 2017; Cardona et al., 2018; Le Mével et al., 2015). The sudden onset of deformation suggests that LdMVF has very recently moved from a period of quiescence to activity providing a real-time view of a

developing magma-hydrothermal system. Studying both the shallow and deep features of the system will give an integrated view of the volcanic plumbing architecture.

The chapter begins with an overview of silicic volcanism and magma dynamics (Section 3.2) followed by an introduction to the study area (Section 3.3) and the eruptive history from field mapping of the LdMVF (Sections 3.4). Section 3.5 outlines the remarkable geodetic observations which sparked the interdisciplinary project. In Sections 3.6, 3.7 and 3.8, past and ongoing petrological and geophysical studies are summarized and the chapter concludes with a brief overview of the Mariposa Geothermal System (MGS) which is located near the LdMVF on the flanks of the Tatara-San Pedro (TSP) Volcano (Section 3.9).

Table 3.1: Lava categorization based on silica content. Higher silica correlates with greater viscosity and a lower melting point. Definitions from common TAS diagrams. See Frost and Frost (2019).

Basalt	Basaltic Andesite	Andesite	Dacite	Rhyolite	
48 – 52%	52 – 57%	57 – 63%	63 – 68%	>68%	Silica Content
~1300°C	→			700°C – 900°C	Melting Point
Low	→			High	Viscosity

3.2 DYNAMICS OF SILICIC VOLCANISM

Silicic volcanism involves erupted lavas with high silica content (e.g. >63% silica) which includes both dacites and rhyolites (Table 3.1). This is in contrast to lower silica lavas such as andesites (57% - 63% silica), basaltic andesites (52% - 57% silica), and basalts (48% - 52% silica). In general, silica-rich magmas tend to be more viscous and thus result in more explosive eruptions, often creating caldera structures. The largest eruptions on earth (i.e. supervolcanic eruptions) involve large volumes of silicic lava. The questions of how large silica-rich reservoirs form, how melts are transported from mantle to surface, the geometry of the magma plumbing system, how long silicic magmas remains in a molten state prior to eruption, rates of melt production, how much magma remains underground to solidify as a pluton, and what might trigger a large eruption have been persistent problems for many years (Annen et al., 2006; Cashman and Giordano, 2014; Hildreth, 1981; Schöpa and Annen, 2013; Sparks et al., 2019).

Furthermore, as more petrological and geophysical evidence is gathered on these systems, it becomes clear that no two systems are alike and making generalizations is difficult (Zellmer and Annen, 2008). Terminology varies from paper to paper depending on the sub-discipline which makes the subject especially difficult (Sparks et al., 2019). As shown in Figure 3.1, Figure 3.2, and Figure 3.3, a multitude of "cartoons" have been drawn to try to capture the complexity of these systems in simple terms. This is a rapidly evolving field and paradigm shifts appear to be underway (Cashman et al., 2017; Sparks et al., 2019).

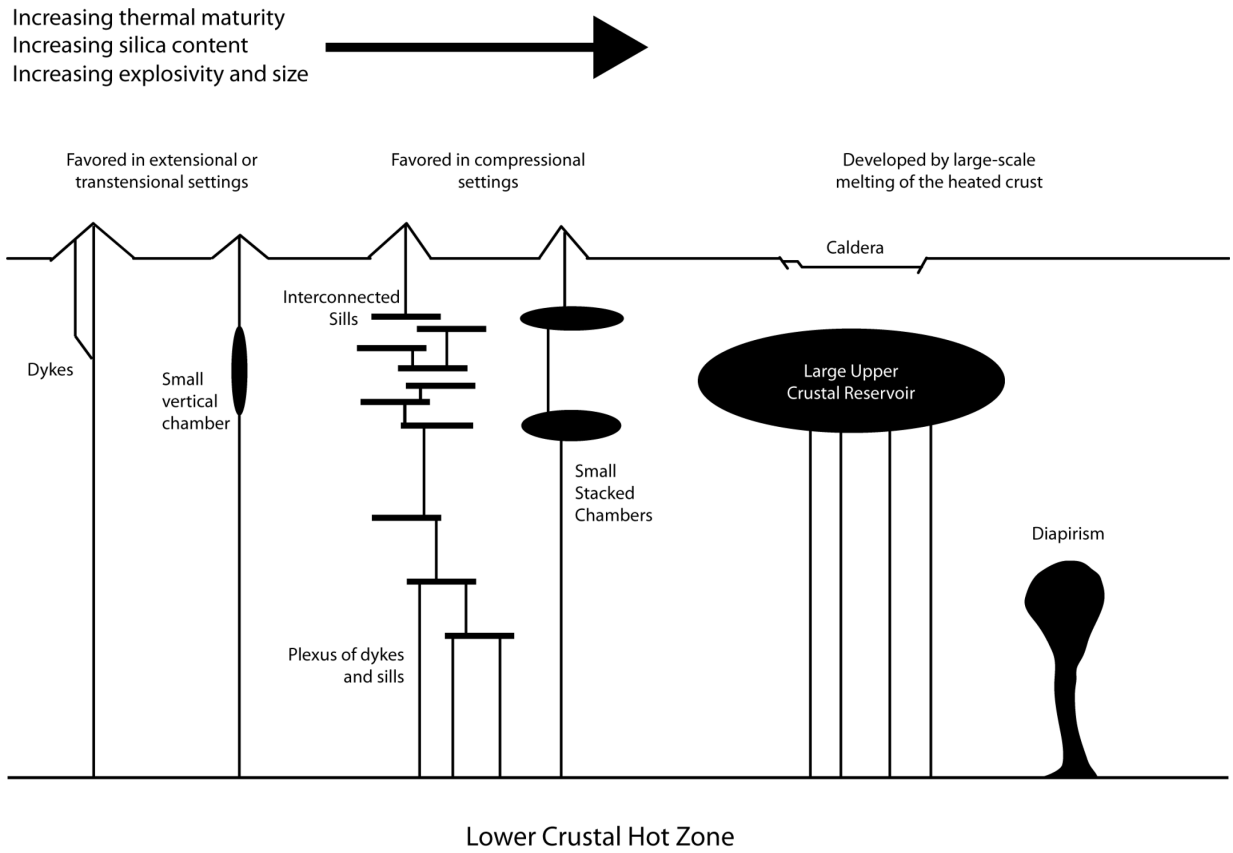

Figure 3.1: Conceptual models of crustal magma systems modified from Zellmer and Annen (2008).

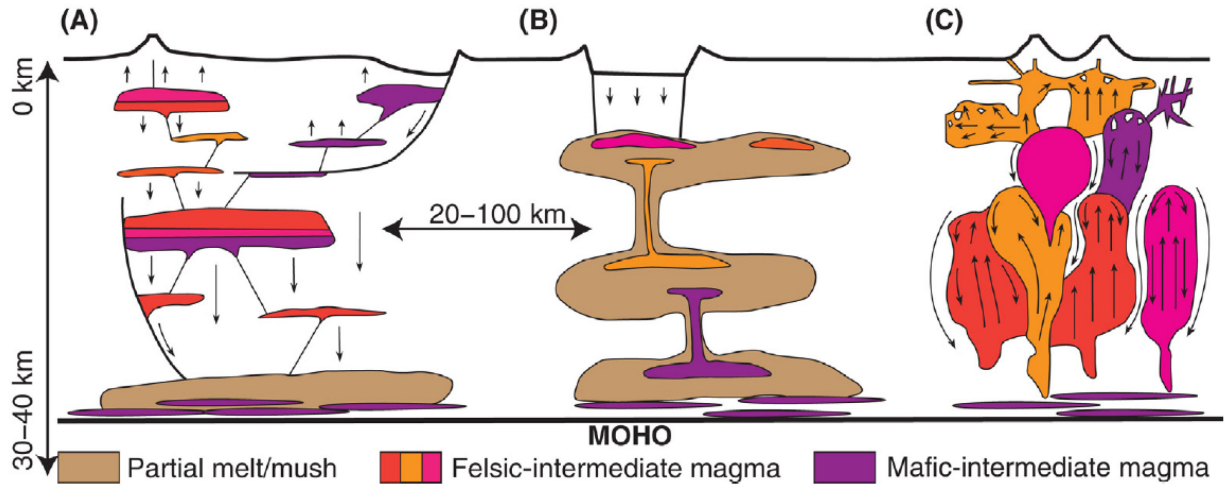

Figure 3.2: Conceptual models of crustal magma systems (from Cruden and Weinberg, 2018).

There are a wide variety of mechanisms that create melt but in general it involves partial melting of the upper mantle under supersolidus pressure and temperature conditions instigated by flux melt or a lower mantle heat source (Cruden and Weinberg, 2018). These low-silica, low viscosity melts then migrate upwards due to buoyancy and undergo a process of silicification in the crust. At what depth this silicfication occurs is debated and may depend on tectonic setting, crustal thermal regime, or may be volcano-specific (Chaussard and Amelung, 2014). Most commonly, it is hypothesized that basaltic melts stall at the density-transition of the crust and mantle forming a "MASH" zone in the lower crust where the magma reservoir undergoes a process of melting, assimilation, storage and homogenization (Hildreth and Moorbath, 1988). This deep crustal hot zone is hypothesized to be long-lived (e.g. $>10^6$ years) and result in low-density, H_2O-rich melts which then ascend into the shallow crust (Annen et al., 2006; Karakas et al., 2017). The geometry by which melts ascend into the crust and to the surface varies depending on the thermal regime of the crust and, perhaps, the tectonic setting (Figure 3.1; Figure 3.2). Similarly, the depth at which silicification occurs may vary and perhaps may occur over a range of depths in a series of different sills, or in a multi-reservoir model, or in a single upper crustal reservoir. Another emerging view is that silicification may occur gradually throughout the lower, middle and upper crust in a large "trans-crustal magma plumbing system" with more felsic magmas at shallower depths (Figure 3.3; Cashman et al., 2017). This has been supported by geophysical and petrological studies (e.g. (Elsworth et al., 2008; Samrock et al., 2018; Schmandt et al., 2019).

Figure 3.3: A conceptual model of a "trans-crustal magma plumbing system". From Cashman et al., 2017. Reprinted with permission from AAAS.

Regardless of the specific depth at which silicification occurs, the process follows three primary (and perhaps simultaneous) mechanisms: 1) melt segregation (i.e. crystal fractionation); 2) crustal assimilation (i.e. anatexis) or; 3) partial melting of the crust (Annen et al., 2015; Bachmann and Bergantz, 2008b; Cruden and Weinberg, 2018). Regarding (1), melt segregation occurs because the melting point of high silica minerals such as quartz (~800°C) is much lower than low silica minerals such as olivine or pyroxene (~1400°C) as first detailed by Bowen (1922). As a melt cools, the low silica minerals reach subsolidus temperatures earlier and crystallize. These crystals often settle out via a process known as crystal fractionation leaving only a silica-rich melt behind (Annen et al., 2015). Regarding (2), anatexis occurs as the incoming basaltic magma melts the surrounding crustal wall rocks. However, this process is very thermally inefficient and poses a variety of problems when creating large volumes of silicic melt and may not be significant (Annen et al., 2015; Bachmann and Bergantz, 2008b). Regarding (3), direct partial melting of the crust is different from anatexis as it does not require any direct injection of basaltic melt. Partial melting of the crust can also occur if the crust is thickened such that the lower crust is at high pressures and temperatures (e.g. from radiogenic heating), or if the crust experiences direct flux melting from incoming hydrous fluids (e.g. Tibet: Nelson et al., 1996; Bolivia: Schilling et al., 2006).

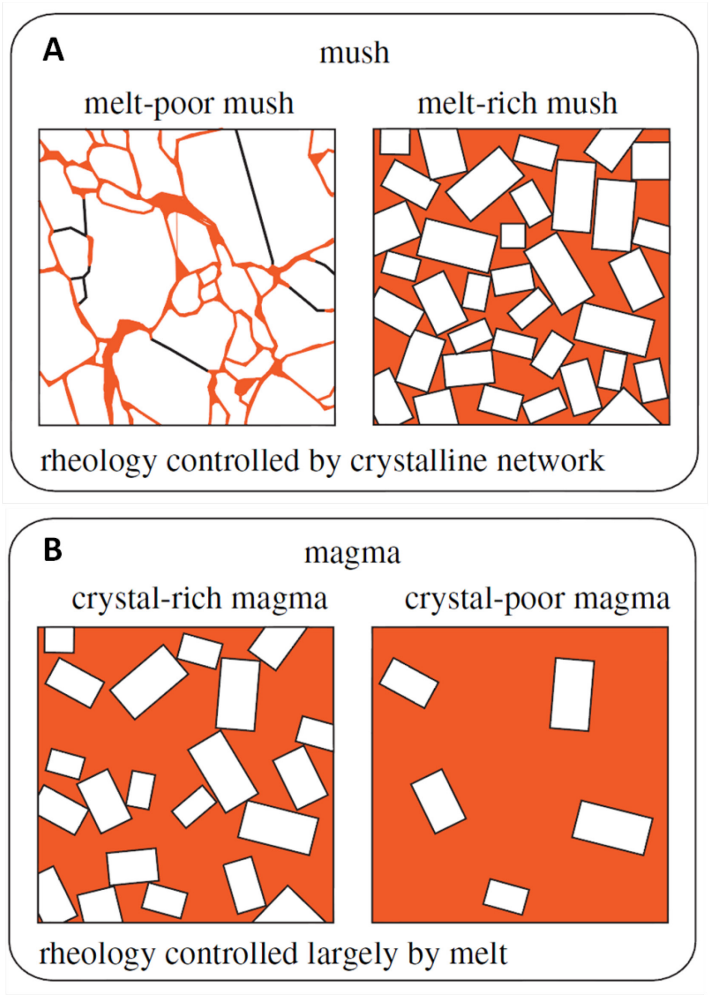

Figure 3.4: Conceptual model of different types of magmas and mushes (from Sparks et al., 2019).

The general formation of silicic melt from basaltic melt is relatively easily explained as detailed above, but an adequate explanation for the formation of large volumes of eruptible silicic melt or large granitoids plutons in the upper crust has not yet been presented (Annen, 2009). Using the definitions of Sparks et al. (2019), a magma reservoir is a part of the magmatic system which includes some volume of melt (±fluid) and is above the solidus temperature. There are thus two types of magma reservoirs with different rheological properties as shown in the conceptual diagram of Figure 3.4. The first is termed a "magma chamber" and is melt-dominated with greater than 30 – 50% melt. The second is termed a "mush" which is crystal-dominated with less than 30% melt. Mush with less than 7% melt is likely to be poorly-connected which will have implications for geophysical imaging (Rosenberg and Handy, 2005). A magma chamber is further divided into a "crystal-poor" magma and a "crystal-rich" magma. Only crystal-poor magma (e.g. >70% melt) is considered to be "eruptible" (i.e. a low enough viscosity to flow). The existence of large, silicic eruptions implies that there must, at some time, be a large volume of

crystal-poor magma in the subsurface. The existence of large granitoids plutons also implies large volumes of silicic melt which never erupt. The problem is that the crust is very cold such that any volume of silicic melt should solidify relatively quickly before a large magma reservoir can develop (Annen, 2009). There are three inter-related ideas that have emerged about how large, crystal-poor silicic magma reservoirs form: 1) incremental intrusion; 2) remobilization and; 3) melt segregation from a mush (Sparks et al., 2019). These processes may operate simultaneously and result in positive feedbacks.

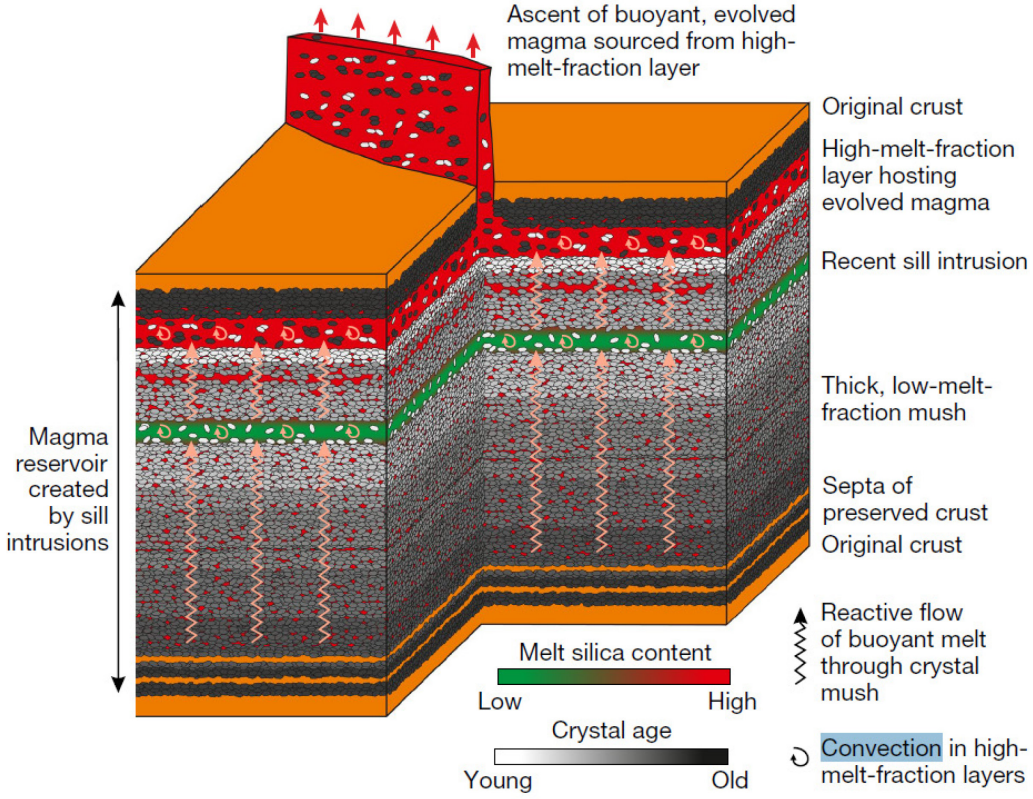

Figure 3.5: Conceptual model of "reactive flow" to rapidly produce large volumes of silicic melt (from Jackson et al., 2018). The scale of this conceptual model may be on the order of tens to hundreds of meters vertically.

Incremental intrusion of thin sheets of magma at the base of a larger reservoir is shown by significant field evidence of granitoids plutons which grow stepwise via a series of pulses of melt from depth (Annen et al., 2015; Hildreth, 1981). If the magma flux rate is high enough or if there is a thermally-mature lower crustal hot zone, these incremental pulses can form a unified, crystal-poor magma reservoir (Annen et al., 2015; Karakas et al., 2017). Remobilization envisions large volumes of the magma stored in a crystal-rich mush volume which is very near (or even below) the solidus temperature (Jackson et al., 2018). Such a mush is more thermally stable than a high melt fraction reservoir and could

remain in a mush-like state for long time periods (Szymanowski et al., 2017). It is relatively thermally efficient to melt significant portions of the base of the mush domain rapidly (i.e. “remobilization”) via a small amount of heat injection or flux melting (Jackson et al., 2018). Finally, melt segregation is similar to remobilization but may not involve any additional heat or volatile flux. In this scenario, a mush is stored at relatively low melt fractions and has some component of crystals and melt. Heavier crystals will tend to undergo compaction and the weight of overlying crystals will squeeze out melt leading to “reactive flow” (Jackson et al., 2018). As such, a “layer-cake” magma reservoir will develop with a high melt fraction magma reservoir at the top which is able to convect (Figure 3.5). The scale of these reservoirs, and the diagram shown in Figure 3.5, is smaller than the large-scale crustal models shown in Figure 3.1, Figure 3.2, and Figure 3.3. Whereas the crustal models operate on scales of kilometers, the magma reservoir model may operate on the scale of tens or hundreds of meters. These processes internal to the magma reservoir would be occurring within single reservoirs, or sills within the larger crustal models. A key component of these three mechanisms is that, without extremely high flux rates, any amount of eruptible magma will likely be relatively ephemeral. In the trans-crustal magma system model, there may be several such reservoirs at different depths from the lower crust to the upper crust and each forms via a similar process.

The final process to consider is the ascent of magma through the crust. The emerging view is that the ascent method depends on the thermal maturity of the crust as shown in Figure 3.1; cool crust has magma ascend via primarily brittle processes (e.g. sills, dykes, existing fractures) while warm crust can have magma ascend via ductile processes (e.g. diapirism) (Sparks et al., 2019; Zellmer and Annen, 2008). In general, diapirism is very difficult to explain under most thermal regimes and dykes dominate (Sparks et al., 2019). However, under the trans-crustal magma system model, much of the crust is within a mush state and thus much of the magma transport occurs through a mush (Cashman et al., 2017). Petrochronological work has suggested that large reservoirs may be extremely short-lived prior to eruption (e.g. months to decades; Druitt et al., 2012; Till et al., 2015)) and this rapid creation of melt can be explained via rapid mush re-organization, channelization of melt, and/or rapid connection of previously disconnected melt lenses (Cashman and Giordano, 2014). These ascent processes are also important when considering eruption triggers (Jellinek and DePaolo, 2003).

These different models of silicic magma body formation and dynamics are derived primarily from petrological work, geological field mapping, and geophysical evidence. But there are many examples of

perplexing petrological results which may not fit with a given model with significant magma mixing or different coeval erupted products (e.g. Cooper et al., 2012; Hildreth, 2004; Stechern et al., 2017) Furthermore geophysical images and deformation signals are sometimes unclear and these systems appear very three-dimensional with lateral and structural components often not incorporated into various models or cartoons (e.g. Biggs et al., 2016; Biggs and Annen, 2019; Kennedy et al., 2018; Klügel et al., 2015). Figure 3.2 shows one example of a cartoon which includes some structural controls on magma plumbing geometry. The ultimate goal is to relate geological and geophysical observations of seismicity or deformation to better forecast eruptions but it is exceedingly difficult and sample sizes are small (Magee et al., 2018; Pritchard and Gregg, 2016).

3.3 THE STUDY AREA: THE LAGUNA DEL MAULE VOLCANIC FIELD

The LdMVF is located close to the Chilean-Argentina border in the Southern Volcanic Zone (SVZ) on the range-crest of the Andes (Figure 3.6; 36°S, 70°W). The nearest major center of population is Talca, Chile (pop: 200,000) which is located approximately 130 km northwest of the LdMVF. The nearest significant town on the Argentine side is San Rafael (pop: 120,000) located more than 250 km northeast of the LdMVF. Smaller centers such as Malargüe, Argentina and Colbún, Chile are located just under 100 km to the northeast and west, respectively. As shown in Figure 3.6, the LdMVF consists of many eruptive vents and lava flows distributed over an area of 500 km^2 surrounding the eponymous high-alpine lake known as Laguna del Maule (LdM; 2165 m a.s.l.). The lake is natural but a man-made dam on the northwest corner of the lake has artificially raised the lake level. The modern lake has a maximum depth of 50 m and an area of approximately 54 km^2. A prominent lava flow forms a peninsula on the western side of the lake which acts as an important landmark (i.e. SW peninsula). Many of the lava flows are recent and relatively un-eroded and can be seen clearly in satellite photos (Figure 3.7). Along the north shore of the lake is Highway 115 which connects Talca to Malargüe. The mid-Pleistocene (150 – 160 ka) Cerro Campanario (3943 m a.s.l.) is a highly-eroded stratovolcano which straddles the international border and is also an important landmark located approximately 20 km northeast of LdM (Figure 3.8; Hildreth et al., 1998).

The LdMVF is part of a northwest-southeast trending string of Quaternary rhyolite calderas located within the Las Loicas Trough (Ramos et al., 2014; see Chapter 2). The nearest other rhyolite calderas are the Puelche Volcanic Field which is located 40 km to the north, and the Varvaco caldera located 35 km to the south. The flows of the LdMVF partially overlap with some of the flows from the Tatara-San Pedro

(TSP) stratovolcano complex located on the main volcanic arc approximately 30 km west of the LdMVF (Singer et al., 1997). The local structural geology is not well-mapped but several important faults have been noted. In particular the Troncoso Fault is mapped to the southwest of LdM running NE-SW along the Troncoso Valley (Figure 3.6; Garibaldi et al., 2020). It is inferred to terminate near the peninsula on the southwest side of the lake. Additional NE-SW trending normal faults have been mapped using reflection seismic and form small extensional grabens beneath the lake (Peterson et al., 2018).

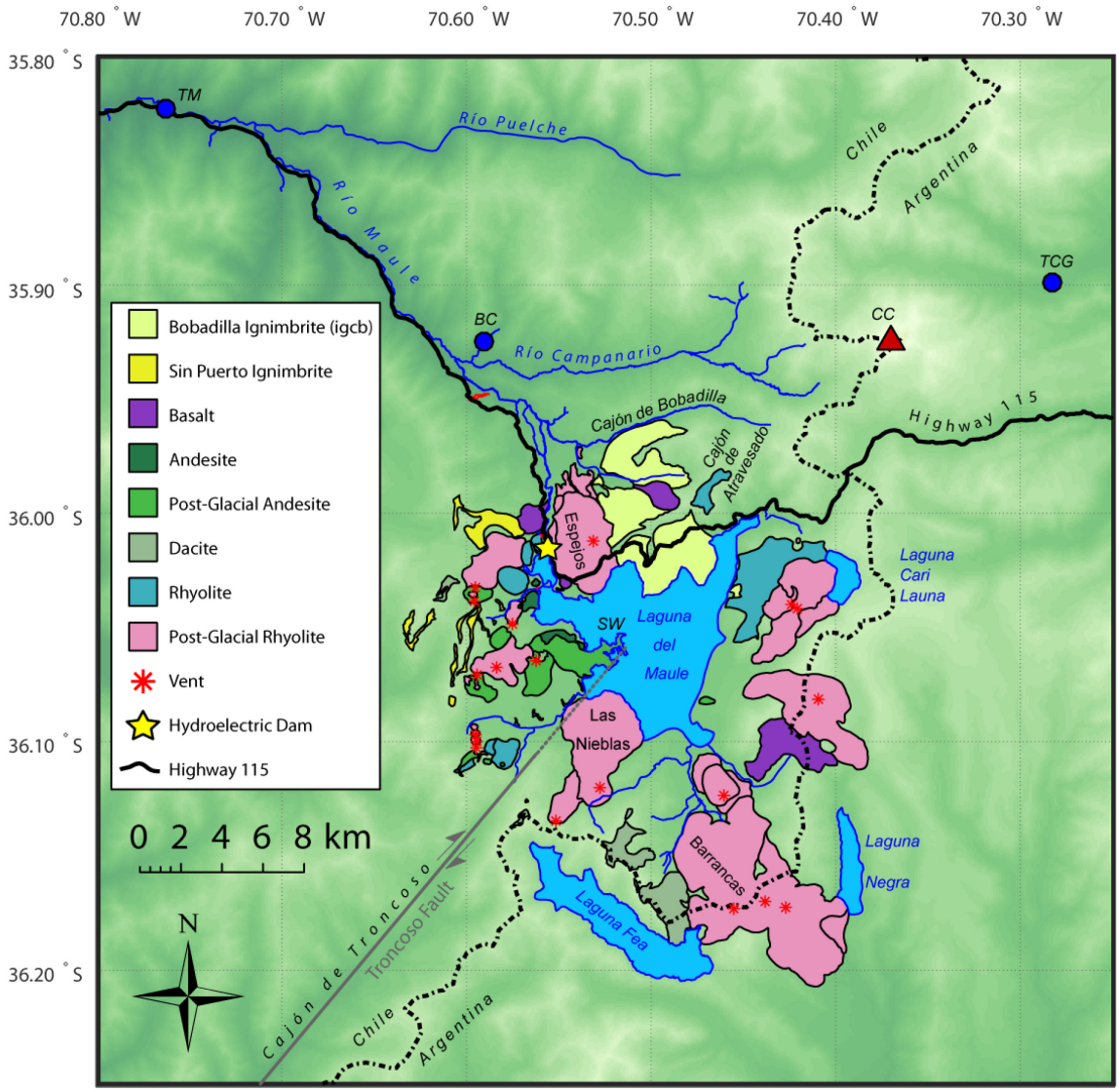

Figure 3.6: Map of the Laguna del Maule Volcanic Field and surrounding area. Mapped lava flows and vent locations are from Andersen et al. (2017). BC = Baños Campanario hot springs; CC = Cerro Campanario stratovolcano; SW = Southwest peninsula andesite; TCG = Termas Cajon Grande hot springs; TM = Terma del Medano hot springs.

Figure 3.7: Satellite picture of the Laguna del Maule Volcanic Field. Stars denote the locations where the photographs were taken in Figure 3.8, Figure 3.9, Figure 3.11, and Figure 3.12. The arrow denotes the direction the photograph is viewing. Number denote important landmarks: 1) Las Nieblas rhyolite; 2) Espejos rhyolite; 3) SW Peninsula andesite; 4) Rhyolite of the NW Coulee; 5) Domo del Maule and; 6) Barrancas rhyolite complex. Photo downloaded from GoogleEarth on April 16, 2019.

The Rio Maule drains from the lake and runs down the Rio Maule valley to the Central Valley and eventually the Pacific Ocean. Significant ongoing hydroelectric projects have altered the valley morphology and changed the course and levels of the river. Immediately to the southeast of LdM are two other lakes: Laguna Fea and Laguna Negra, both in Argentina. Both lakes effectively mark the southeast edge of the LdMVF and both lakes are currently dammed by lava flows from the southeast LdMVF (Figure 3.6). Laguna Cari Launa is another small lava-dammed lake at 2700 m a.s.l., 4 km east of the LdM east shore. There is a notable lack of any mapped hydrothermal activity in the lake basin, but there are some notable hot springs to the north. The Baños Campanario hot spring is located approximately 10 km north of the lake in the Campanario Valley, the Termas El Médano hot springs are located approximately 30 km northwest, and the Termas del Cajon Grande are found 20 km to the northeast in Argentina on the eastern side of Cerro Campanario (Figure 3.6). Benavente et al. (2016)

analyzed the Baños Campanario hot springs and found that it had a notable magmatic signature suggesting that fluids are derived from both meteoric water as well as exsolved magmatic volatiles. This hot spring is also notable for very high levels of total dissolved solids (>20,000 mg/L) relative to the other 49 hot springs sampled in the SVZ with a median of 1248 mg/L (Benavente et al., 2016).

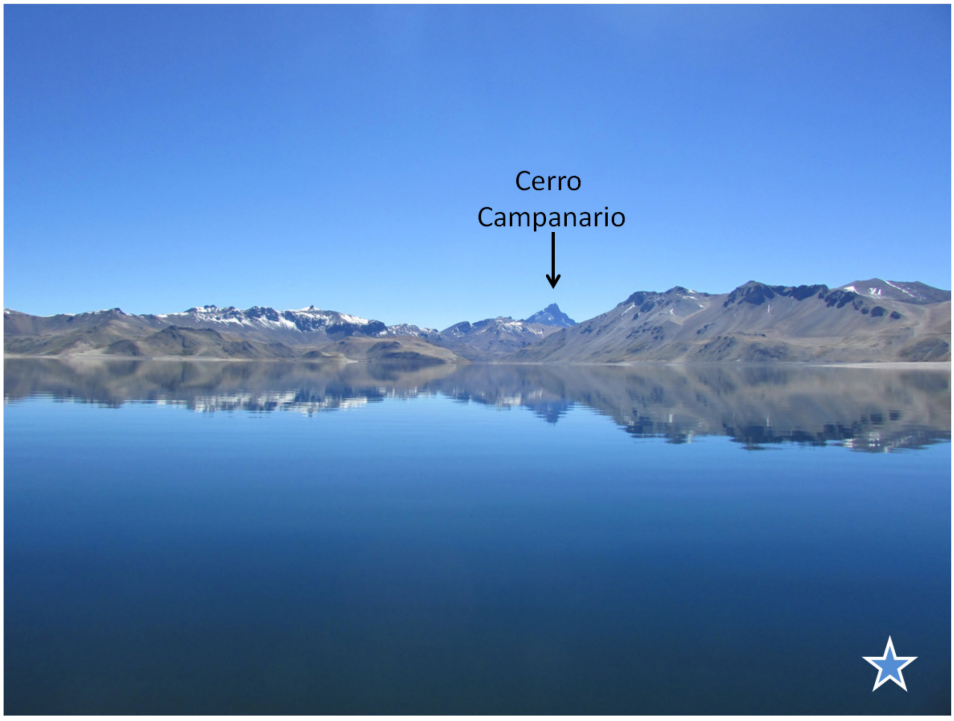

Figure 3.8: Picture of Laguna del Maule looking northeast towards Cerro Campanario from the middle of the lake. Photo taken during field work on March 12, 2017. Blue star matches the location shown on Figure 3.7.

The LdMVF represents the primary topic of this thesis as it is part of a large interdisciplinary project known as Rhyolite Magma Dynamics[1] funded by the National Science Foundation to study this restless rhyolitic system. Prior to this project there was very little in the literature written specifically about the LdMVF. As such, much of this chapter references ongoing work that has been published concurrently as this thesis was being completed.

3.4 ERUPTIVE HISTORY OF THE LAGUNA DEL MAULE VOLCANIC FIELD

The most complete record of the eruptive history of the LdMVF is given by Hildreth et al. (2010) which included extensive field mapping and petrochronological dating over several decades. Earlier work and earlier mapping and eruptive history was completed by Frey et al. (1984) while Drake (1976) studied sub-volcanic sequences and plutons which are exposed to the west in the Rio Maule valley. Most of the

[1] https://geoscience.wisc.edu/rhyolitic/

work by Frey et al. (1984) focused only on flows and units from the last 300 ka and is limited by small sample sizes while Hildreth et al. (2010) considers everything from Pliocene (2.5 – 5 Ma) sub-volcanics, through the Pleistocene (2.5 Ma to 11.7 ka) to the Holocene. Hildreth et al. (2010) identified at least 130 separate vents and over 115 cones, domes and lava flows and estimated that the entire volcanic system has erupted more than 350 km^3 in the last 1.5 Ma. Approximately 40 km^3 (or about 11%) of the estimated erupted products have erupted in the last 26 ka (Andersen et al., 2018). Further work from Fierstein et al. (2013) and Sruoga et al. (2015) suggest that the total volume could be much larger. During this NSF-funded project, Andersen (2017) and Andersen et al. (2019, 2018, 2017) have furthered the understanding of the eruptive history of the LdMVF with a specific focus on the post-glacial (e.g. <25 ka) rhyolites.

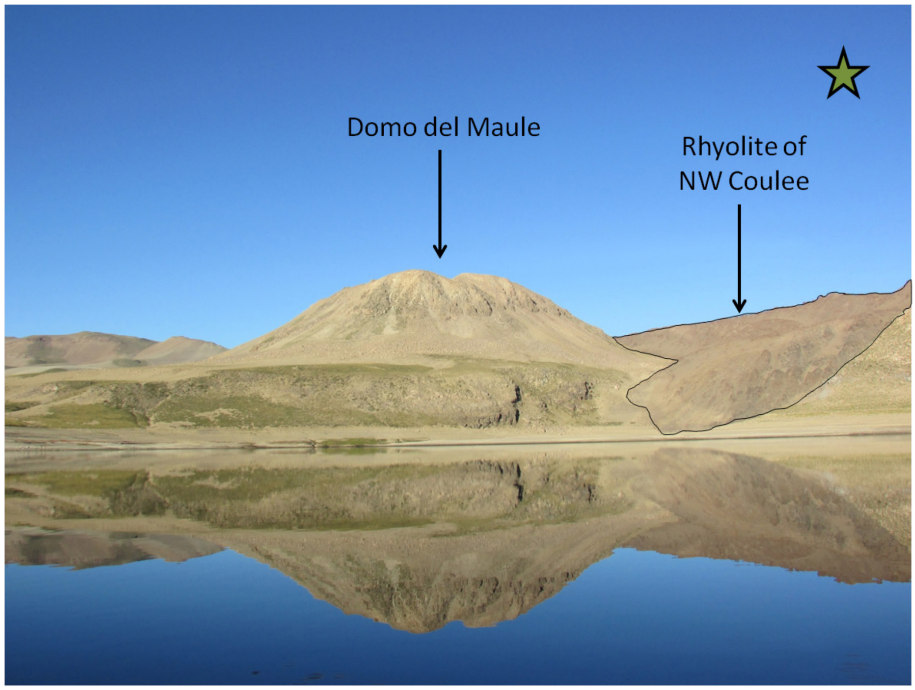

Figure 3.9: Photo of the Domo del Maule and the Rhyolite of the NW Coulee taken during fieldwork on February 19, 2017. Green star matches the location shown in Figure 3.7.

The earliest significant eruption in the LdMVF was the 1.5 Ma Laguna sin Puerto dacite ignimbrite which is heavily eroded but can still be found on some ridges to the north and west of LdM. The vent is assumed to be on the northwest edge of the lake but any such vent structure has been eroded or destroyed by later eruptions. The largest eruption of the LdMVF occurred approximately 950 – 990 ka and is preserved as the large rhyodacite Bobadilla ignimbrite (Figure 3.6; Andersen et al., 2017; Hildreth et al., 2010). This eruption resulted in the collapse of the inferred Bobadilla caldera which is poorly preserved due to high rates of erosion but is estimated to have covered approximately 80 km^2 including

much of the northern lake basin and extending as far north as the Cajon de Bobadilla. Several postcaldera intermediate lava flows are found along the north lake basin and as far as 7 km north of the lake in the Cajón de Bobadilla. These are estimated to have erupted between 700 and 800 ka and, although no central vent has been preserved, Hildreth et al. (2010) suggest that a vent may have existed in the Cajón de Atravesado, 6 km north of the lake (Figure 3.6).

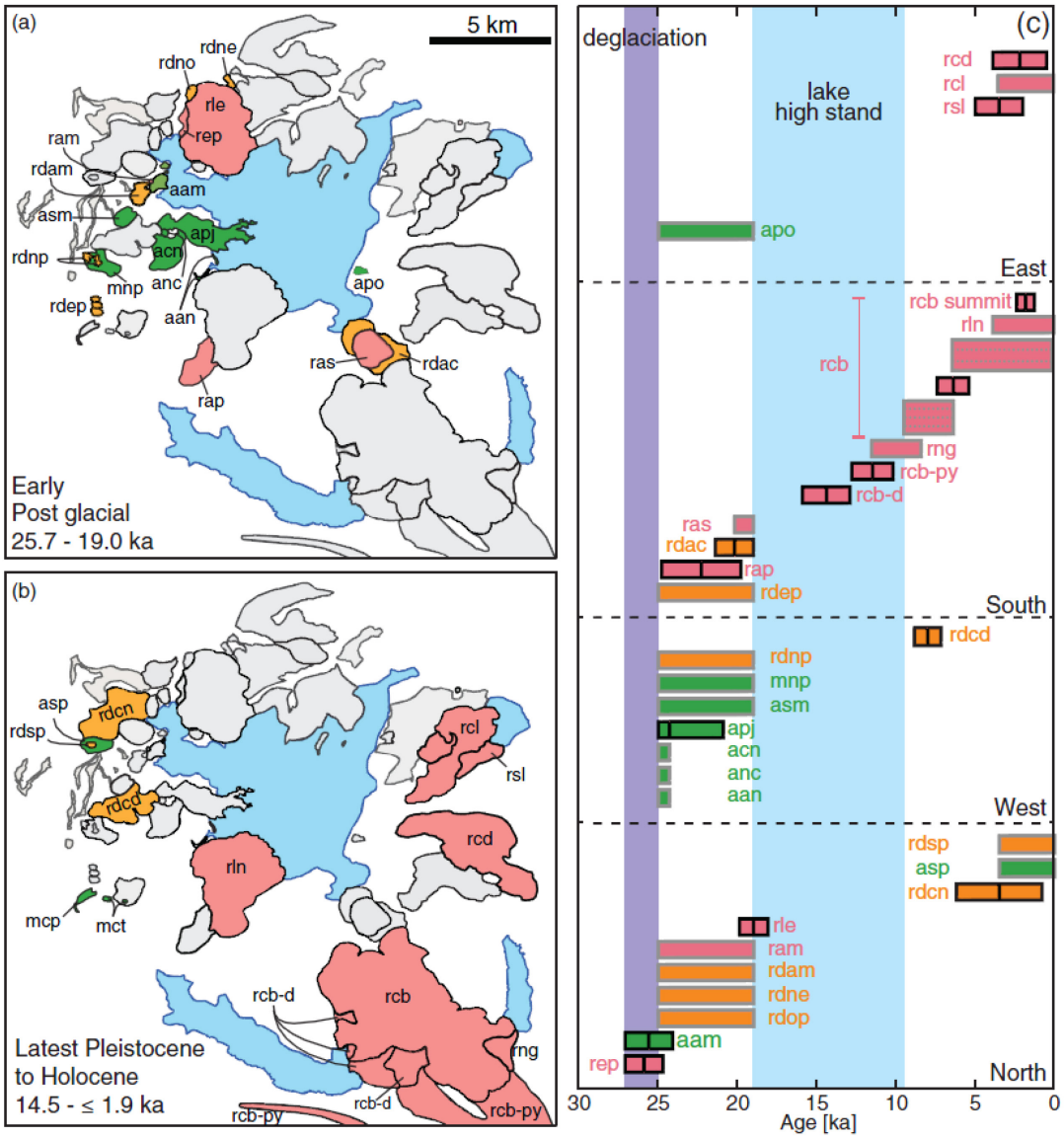

Figure 3.10: Eruptive history of the Late Pleistocene and Holocene. From Andersen et al. (2017).

Throughout the Late Pleistocene, several significant eruptions occurred throughout the lake basin with varying compositions from basalt to rhyolite. This included the Domo del Maule (115 ka) rhyodacite dome, a prominent feature on the west side of the lake which rises to 2520 m.a.s.l. (Figure 3.9; Hildreth

et al., 2010). As the end of the Pleistocene neared, the Maule region experienced early de-glaciation between 23 – 25 ka based on ages of un-glaciated and glaciated lava flows (Singer et al., 2000). This post-glacial period saw a sudden increase in rhyolite volcanism and can be divided into two pulses: the early post glacial (EPG) from 25 ka to 19 ka and the modern pulse (i.e. the latest Pleistocene (14.5 ka) to Holocene (<2 ka)) (Figure 3.10; Andersen et al., 2017). The EPG saw the eruption of the Espejos lava flow at 19 ka which dammed LdM on the northwest corner and raised the lake level by 200 m (Andersen et al., 2017). This paleo-shoreline has been used as a geodetic marker to map paleo-deformation since 19 ka and suggests nearly 70 m of uplift has occurred over the last 20,000 years, effectively raising the southeast side of the lake dramatically (Singer et al., 2018). During the lake high-stand there was a greater concentration of eruptions on the northwest side of the lake basin and included rhyolites (e.g. Rhyolite of the Northwest Coulee; Figure 3.9) as well as several rhyodacites and andesites (e.g. The SW Peninsula Andesite; Figure 3.11) with fewer eruptions to the southeast (Andersen et al., 2017). This time period also included the largest post-glacial eruption: the 20 km^3 Rhyolite of Laguna del Maule whose vent location is unknown but may be beneath the current lake (Fierstein et al., 2016).

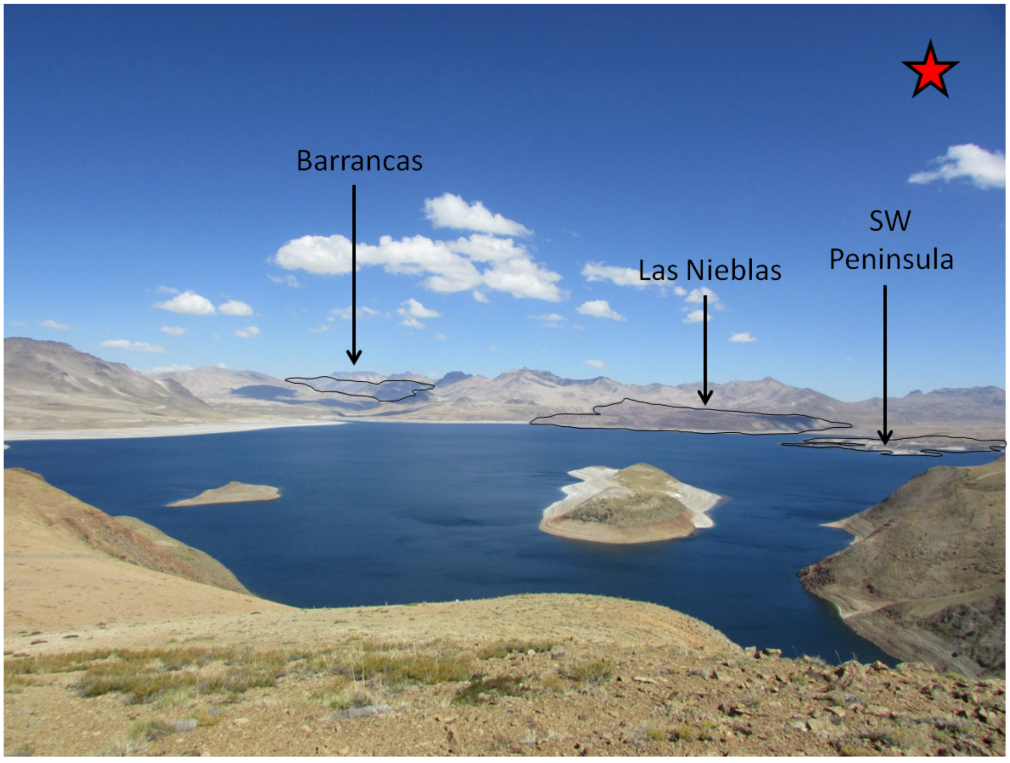

Figure 3.11: Photo of the Laguna del Maule looking south from a bluff on the north shore taken during fieldwork on March 18, 2017. Red star matches the location shown in Figure 3.7.

The second flare-up of volcanism began around 14.5 ka and was almost exclusively rhyolitic with a greater concentration to the southeast at the Barrancas complex and upwards of 50 rhyolitic eruptions (Figure 3.10 and Figure 3.11; Andersen et al., 2018, 2017). The Barrancas complex is a large 13 km by 7 km set of flows and also includes several flows which have travelled many kilometers into Argentina. The LdM experienced a sudden outbreak flood around 9.5 ka which dropped the lake to near its present level after eroding through the Espejos lava flow. After this, between 8 ka and 2 ka, volcanism spread out from Barrancas to include the eastern shore of LdM near Laguna Cari Launa, as well as a return of several eruptions in the northwest. One of the most recent eruptions occurred less than 2 ka from a vent 5 km south of LdM which flowed northwards towards the lake forming the prominent Las Nieblas flow (Andersen et al., 2018). The Las Nieblas can be seen clearly from satellite images (Figure 3.7), and from various vistas around LdM (Figure 3.11). The scale of the flow is remarkable as it is comprised of broken blocks of rhyolite rock over 100 meters tall (Figure 3.12).

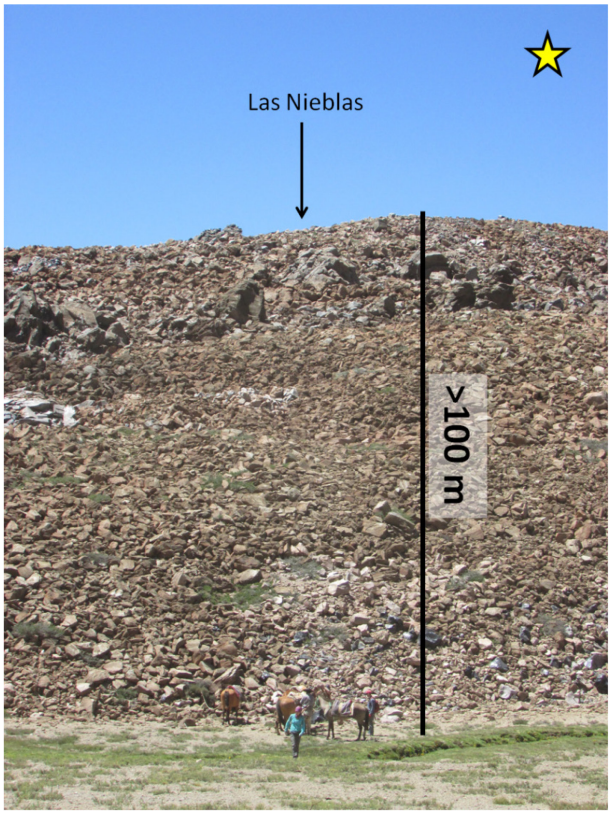

Figure 3.12: Photo of the Las Nieblas rhyolite flow looking east taken during fieldwork on February 26, 2016. Horses and person for scale. Yellow star matches the location shown in Figure 3.7.

In summary, the LdMVF has been active in the last 1.5 Ma with a notable flare-up of rhyolite volcanism in the last 14.5 ka. The volcanic field includes the large Bobadilla caldera eruption at 1.5 Ma which covered the northern portion of the lake and extended up to 6 km north of the lake. The Espejos lava flow dammed the lake around 19 ka and raised the lake level by 200 m before a catastrophic outbreak flood around 9.5 ka dropped the lake to its current level. The most recent eruptions occurred primarily in the south and southeastern portions of the lake basin and included the large Barrancas complex as well as the Las Nieblas rhyolite.

3.5 GEODETIC OBSERVATIONS AT LAGUNA DEL MAULE

Observing ground deformation at volcanoes using satellites and global positioning systems (GPS) has been used for several decades to monitor changes in magma-hydrothermal plumbing systems (Biggs and Pritchard, 2017). Interpreting these signals is difficult as they may be driven by magma injection, hydrothermal fluid movement or some combination of both; not all deforming volcanoes erupt and not all erupting volcanoes deform prior to the eruption (Biggs and Pritchard, 2017). Subsidence is also common at volcanoes and many volcanoes go through repeated periods of inflation and subsidence. The most common satellite-based method is called interferometric synthetic aperture radar (InSAR) and has been used to monitor volcanoes in the SVZ (e.g. Fournier et al., 2010; Pritchard and Simons, 2004).

In a 2010 global survey of InSAR deformation measurements at volcanoes, it was first noticed that the LdMVF was deforming relatively rapidly compared to others at a rate of about 18.5 cm/yr between January 2007 and January 2008 (Fournier et al., 2010). Earlier InSAR surveys of the SVZ between 2003 to 2004 had not detected any deformation signal so it is assumed that the deformation began sometime between 2004 and 2008 (Fournier et al., 2010; Pritchard and Simons, 2004). Fournier et al. (2010) made an initial interpretation of the deformation signal being due to the inflation of a magma reservoir or injection of hydrothermal fluids modelled as a dipping sill at 5 km depth.

A follow-up InSAR survey which comprised data from 2007 to 2012 as well as ground-based GPS measurements from 2012 indicated that the upwards ground deformation had increased to a maximum of 28 cm/yr with the point of maximum inflation centered on the southwestern side of the lake between the SW peninsula and the Las Nieblas rhyolite flow (Figure 3.13; Feigl et al., 2014). This more detailed investigation ruled out many other possible causes, including gravitationally-induced loading and unloading due to changing lake levels. The deformation could be modelled by the inflation of a

rectangular sill at depth of 4.7 to 5.3 km with a length of 6 – 9 km and width of 5 – 6 km with a north-northeast strike and dip to the east which could be due to magma migration or injection, or the result of increased pressure from exsolved volatiles released from a cooling magma reservoir (Feigl et al., 2014). This exciting episode of deformation spurred the funding for the NSF grant which supported the research in this thesis.

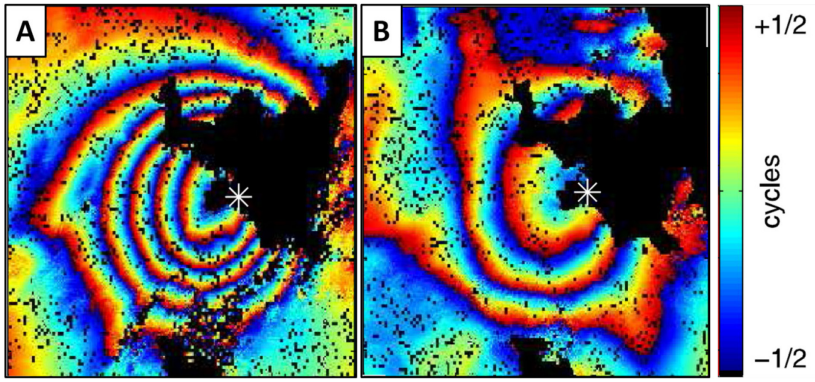

Figure 3.13: InSAR interferograms from Feigl et al. (2014). (A) The interferogram spanning 1058 days from February 2007 to January 2010. One full cycle of phase denotes approximately 118 mm of range change. (B) The second interferogram spanning 77 days from February 2011 to May 2011. One full cycle of phase denotes approximately 15.5 mm of range change.

The current NSF project resulted in a third follow-up investigation of the deformation which included an analysis of all InSAR data from 2003 to 2014 as well as ground-based GPS from 2012 to 2014 (Figure 3.14; Le Mével et al., 2015). The additional data from 2012 to 2014 showed a decrease in the inflation to approximately 19 cm/yr, from the previous high of 28 cm/yr. This is approximated using a double exponential model which includes rapid increases from 2007 to 2010 and then a slow decrease from 2010 to 2014. The deformation includes both vertical and horizontal displacements indicative of a source with radial expansion at depth. It is important to note the coincidence in timing of the change from increasing to decreasing inflation (i.e. the inflection of the double exponential), which occurred in March 2010, with the February 27, 2010 Maule 8.8 Mw megathrust earthquake. Le Mével et al. (2015) hypothesized that the megathrust earthquake may have changed the regional stress state. Changes in deformation rates following the 2010 Maule earthquake have also been noted at other volcanoes in the SVZ such as Tinguiririca, Calabozos, and Nevados de Chillán (Pritchard et al., 2013).

Further work by Le Mével et al. (2016) developed more sophisticated models of magma injection that went beyond simple Mogi sources or sill inflation to include more complex geometries and dynamic

injection of Newtonian fluids. They concluded that the best-fitting source geometry is an ellipsoid with a length of 6.2 km and thickness of 100 m located at 4.5 km depth. A dynamic flow rate of magma injection suggests rates of 0.7 to 1.2 m^3/s, for a total of 0.187 km^3 of magma injected in just over 7 years. When the deformation acceleration is positive, an increase in the magma injection flow rate is implied whereas if the acceleration is negative, a decrease in flow rate is implied. Their modelling included the assumption of laminar magma flow in a vertical conduit as the source. They did not include any structural control in their model or investigate sub-vertical conduits.

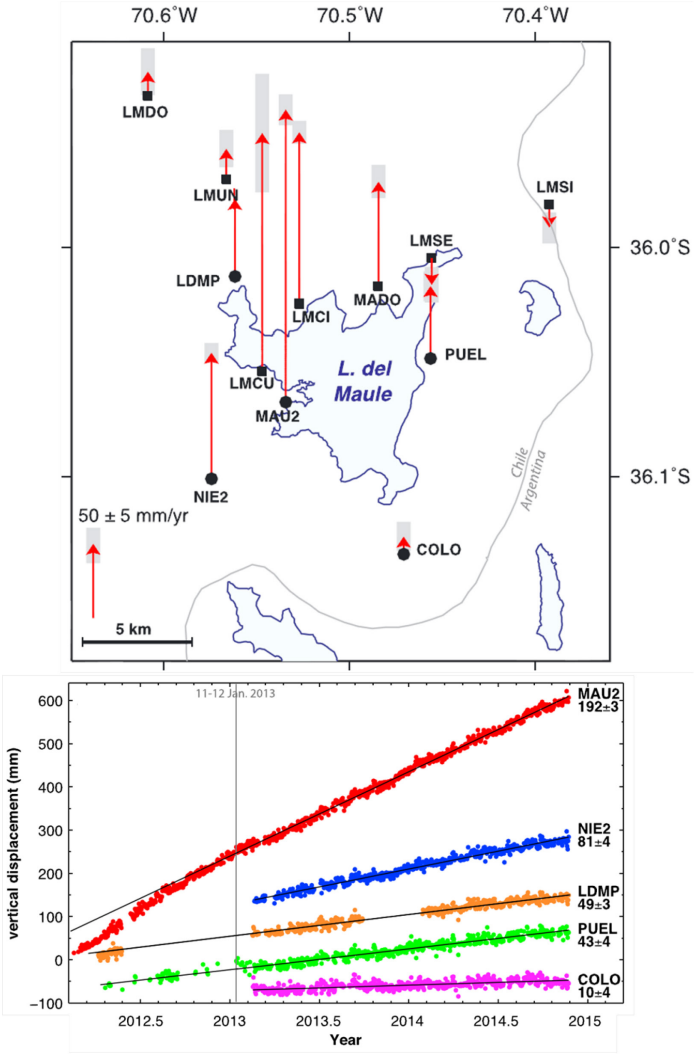

Figure 3.14: Vertical displacement at different GPS stations. From Le Mével et al. (2015).

As shown in Figure 3.15, the rate of deformation and the length of the signal suggest that the LdMVF deformation is the longest prolonged rapid upward ground deformation without an eruption in the world amounting to nearly 3 m of vertical displacement in 12 years. It is an order of magnitude faster than other similar prolonged events at Yellowstone and Three Sisters, and lasted 6 times longer than

similar scale deformation events at Campi Flegrei from 1982 to 1984 (Le Mével et al., 2015). The paleo-shoreline work of Singer et al. (2018) suggests that at least 16 similar style deformation episodes as this would have had to occur to explain the Holocene paleo-shoreline deformation. It is also worth noting that un-published InSAR results suggest that the rate of deformation may once again be increasing and approaching 30 cm/yr between 2014 and 2017 (Le Mével, pers. comm., December 2018). The LdMVF has not erupted in approximately two thousand years, but it is currently showing signs of significant unrest.

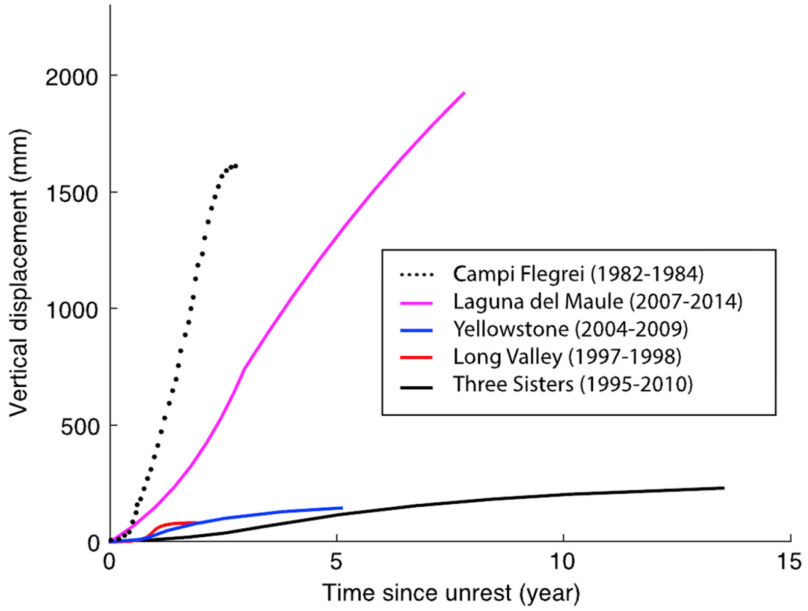

Figure 3.15: Comparison of the deformation at the LdMVF to other rhyolitic systems (from Le Mével et al., 2015).

3.6 GEOCHEMISTRY AND MAGMATIC EVOLUTION AT THE LAGUNA DEL MAULE VOLCANIC FIELD

Understanding how the magma system has evolved both spatially and temporally may help to explain the patterns of eruption as well as the nature of the magma system responsible for the deformation signal today. Frey et al. (1984) noted that the LdMVF lies at a transition between dominantly andesite volcanoes north of 34°S and primarily basalt and basaltic andesite south of 37°S which prompted the definition of the region as the Transitional SVZ (TSVZ; Lopez-Escobar et al., 1995). Early petrology only included lava flows less than 300 ka in age and suggested that there was significant magma mixing and a genetic relationship between the basalts and the rhyolites due to similar isotopic ratios and trace element concentrations (Frey et al., 1984). However, this early study was limited by small sample sizes and was not comprehensive in scope. A similar conclusion regarding compositional similarities was reached by Hildreth et al. (2010) which lead him to conclude that the LdMVF must be fed by a single,

coherent magma system. However, detailed geochemical and petrological analysis of early caldera eruptions (Birsic, 2015) and lavas erupted in the last 26 ka (Andersen et al., 2017) have begun to paint a more complicated picture of the magmatic system.

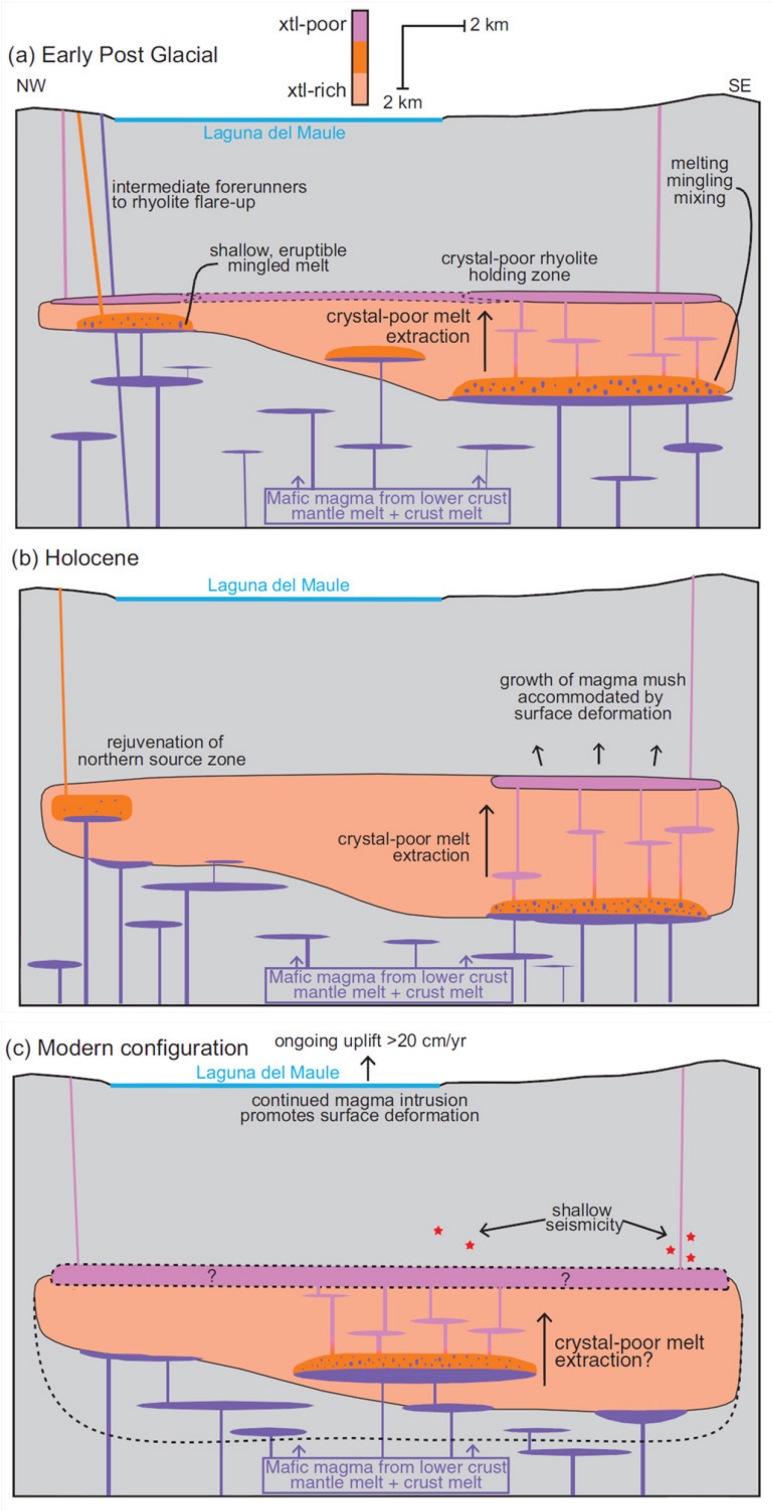

Figure 3.16: Conceptual model of the magmatic evolution of the LdMVF system from Andersen et al. (2017).

Birsic (2015) showed that the 1.5 Ma Laguna Sin Puerto ignimbrite is petrologically distinct from the products of the 950 ka Bobadilla eruption suggesting that the magmas feeding the two eruptions must have evolved under different conditions. Plagioclase zoning of the Laguna Sin Puerto lavas suggests extensive crystal fractionation prior to eruption with mixing between andesitic and rhyodacitic magmas. In contrast, the Bobadilla ignimbrite shows a relatively small degree of magma mixing and a more homogeneous magma supply (Birsic, 2015). The strontium isotope ratios of the two eruptions are quite similar, but the other lines of evidence reject the notion of a co-genetic source (Birsic, 2015). Compositional differences also rule out the idea that the Bobadilla or Laguna Sin Puerto eruptions could act as feeders for later post-glacial rhyolites and are not directly responsible for the modern silicic magma system or at least developed under different circumstances (Andersen et al., 2017; Birsic, 2015).

The post-glacial eruptions at the LdMVF also show a complex spatiotemporal evolution of the magmatic system. Eruptions in the southeast were almost exclusively rhyolitic whereas in the northwest, there was more diversity in composition. Throughout the EPG, Andersen et al. (2017) suggest that the northwest LdMVF saw an expansion of magmatism via lateral growth and shallowing of the magma system (Figure 3.16). Compositional differences in post-glacial rhyolites are not very obvious but suggest an increasing magma reservoir temperature with time between the EPG and the Holocene. Variations in trace element concentrations suggest that eruptions came from small, discrete magma batches within a more compositionally-homogeneous, long-lived upper crustal source (Andersen et al., 2017). Petrochronological data suggests that each magma batch resided in the crust on the order of decades and was relatively ephemeral (Andersen et al., 2018). EPG magmas and Holocene magmas did not co-mingle and had limited interaction (Andersen et al., 2018). The current configuration envisioned by Andersen et al. (2017) is a thick, rhyolite mush underlying the southeastern LdMVF with a thinner mush underlying the northwestern LdMVF which allows for more mafic magmas to penetrate into the shallower crust (Figure 3.16). The lack of petrological evidence of re-heating or mixing of basalt injections (despite increasing reservoir temperatures) suggests that eruptions may have been triggered by an influx of fluids from a deeper mafic source which pressurizes the eruptible magma bodies (Andersen et al., 2018). In this scenario, hydrothermal fluids in the magma-hydrothermal system exist in a separate fluid phase and are not derived from closed system fluid exsolution of the shallow magma body but are rather derived from elsewhere (e.g. a deeper magma body). This scenario implicitly assumes water-saturated magma. Such fluids could rapidly migrate through a magma mush (or via a fault system) but stall below a crystal-poor magma body (Parmigiani et al., 2016). This intriguing

possibility suggests the importance of magma degassing of the modern LdMVF system and the importance of three-phase systems of magma-hydrothermal systems.

3.7 GRAVITY STUDIES

Prior to this NSF project, there was no published geophysical imaging specifically focused on the LdMVF. Earlier gravity studies were regional or continental in scale (see Chapter 2). Concurrent with this thesis project was the deployment of both Bouguer gravity and time-lapse microgravity surveys throughout the LdMVF. Both methods are sensitive to changes in the gravitational field due to density variations in the subsurface. Bouguer gravity measures a static potential field with spatial variations from some background level generally ranging from -50 to 50 mGal after a variety of corrections are made. Higher density anomalies in the subsurface (e.g. dry, crystalline, mafic rocks) are associated with an increase in the strength of the gravity field (i.e. a gravity high) whereas low density anomalies (e.g. sedimentary basins, high porosity zones, partial melt) are associated with a weaker gravitational field. Time-lapse gravity is similar but the measurements are taken successively by returning to the same spot repeatedly and examining any differences after appropriate static corrections are made. Generally, temporal variations to the gravity field are on the order of microgals (μGal).

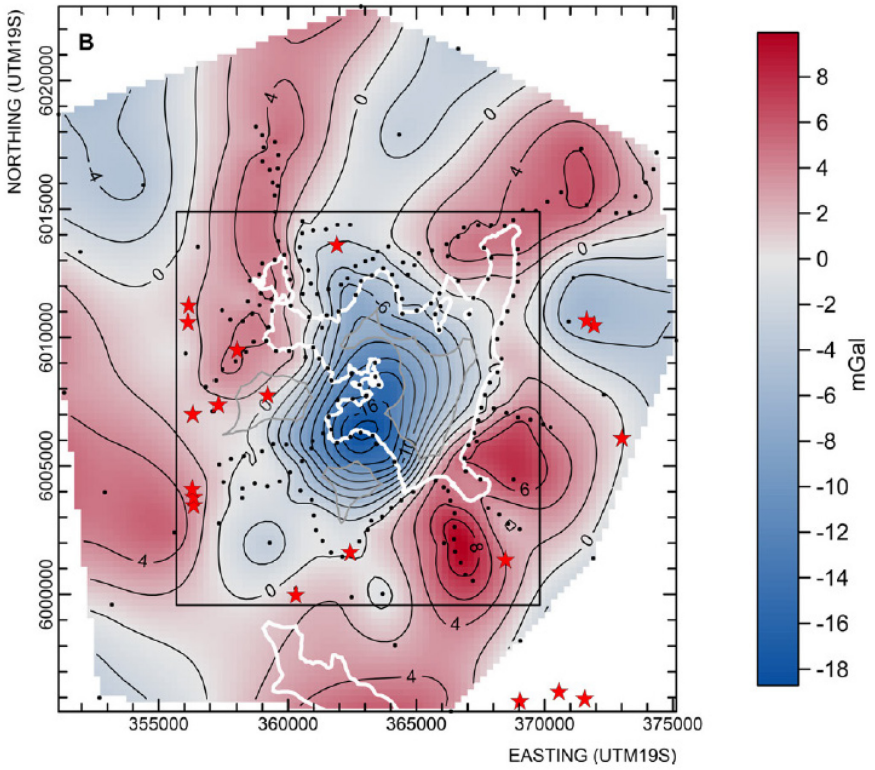

Figure 3.17: Low Bouguer gravity anomaly observed beneath the LdMVF (from Miller et al., 2017b).

3.7.1 Bouguer Gravity

Between 2014 and 2016, a dense array of Bouguer gravity data was collected around LdM with a specific focus on the inflation center (Miller et al., 2017b). The stations ringed the lake and did not extend beyond the lake basin itself except for 16 sites which were not included in the modelled area. These data showed a clear residual Bouguer gravity low centered on the zone of maximum uplift and trending NNE-SSW with a minimum of -19 mGal (Figure 3.17). Some smaller gravity highs were also noted within the array but were not as significant as the primary gravity low. Miller et al. (2017b) inverted these data to produce a suite of 3-D density models on a rectilinear mesh. They use a starting reference density of 2400 kg/m^3 based on previous regional 1-D seismic models. Petrologic arguments and temperature estimates from Andersen et al. (2017) were used to deduce the best-fitting model. The final model is an 1800 kg/m^3 low density anomaly with a volume of 30 km^3 embedded in the shallow crust between 2 km and 5 km depth below lake surface (Figure 3.18; Miller et al., 2017b). The base of this feature aligns approximately with the depth of the inflation source inferred from Feigl et al. (2014) and Le Mével et al. (2016). Surrounding this low density feature is a 115 km^3 halo of 2285 kg/m^3 material which is less dense than the background model of 2400 kg/m^3. Both the background density (2400 kg/m^3), and the low density anomaly (1800 kg/m^3) are quite low relative to global estimates of crustal rock density (e.g. >2700 kg/m^3; see Christensen and Mooney, 1995). It is worth noting that the gravity inversion is highly sensitive to the background density.

Given temperature and pressure constraints, Miller et al. (2017b) interpreted this model as a shallow, 30 km^3, crystal-poor rhyolite melt body with 50% to 85% melt directly beneath the lake surface. This feature is considered eruptible and active but considerations of lithostatic pressure suggest that there is still sufficient crustal loading to compensate for buoyancy forces. They argue buoyancy alone would not trigger an eruption of this feature. To explain the extremely low density of the feature, they suggested that it is important to include the closed system exsolved volatiles (i.e. the vapour phase) in the system. This feature is surrounded by a 115 km^3 relatively crystal-rich mush region with >70% crystal fraction interpreted as likely more andesitic in composition. Given the relatively high melt fractions and relatively large volumes, Andersen et al. (2018) suggested that other volatile sources (rather than closed system volatiles) could help to explain the low density anomaly without such high melt fractions (see Section 3.4).

3.7.2 Time-lapse Microgravity

Between 2013 and 2016, Miller et al. (2017a) collected time-lapse gravity data with an array which covered a similar footprint as the Bouguer gravity survey (although with much coarser station spacing). This was done to investigate whether changes in the magma-hydrothermal system could be detected with changes in the gravity field. They found a significant increase in the gravitational field of just over 120 µGal between April 2013 and January 2014 centered on the region of maximum surface deformation on the southwest side of LdM. Between January 2014 and March 2015 there was relatively modest changes of approximately 50 µGal with a more complex spatial pattern shifted further southwest. A final sequence from March 2015 to February 2016 showed a modest increase in gravity of approximately 70 µGal with a focus once again on the region of maximum deformation. The changes in gravity are best modelled with a thin, vertically-oriented prism with a length of approximately 6 km and vertical width of 110 to 170 m and a variable horizontal thickness between 30 and 150 m depending on the year. The depth of to the top of the prism is between 1.2 and 1.9 km depth with an average of 1.5 km depth below lake surface. The principal orientation of the prism changes depending on the year with more scattered NE to ENE strikes in the first year, a very well-defined NE strike in the second year, and a well-defined ENE strike in the third year.

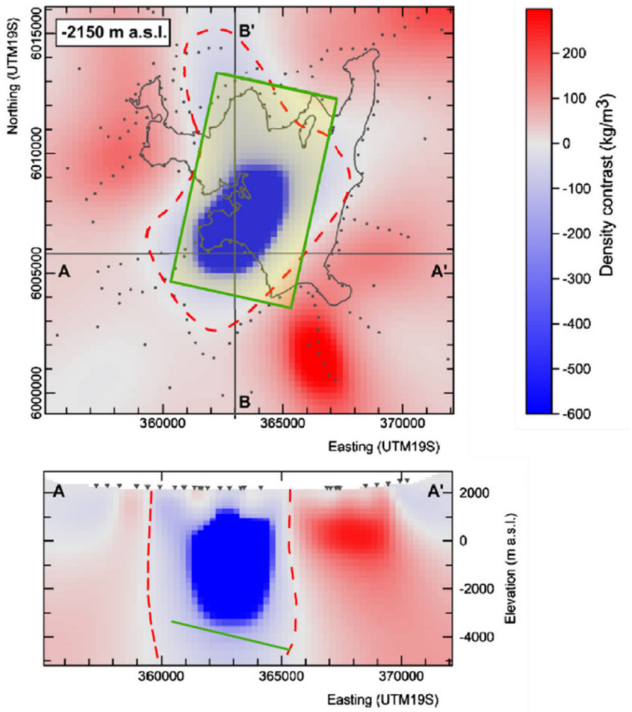

Figure 3.18: Density model for the LdMVF based on inversion of Bouguer gravity data. From Miller et al. (2017b).

Miller et al. (2017a) interpreted these increases in gravity as mass additions due to hydrothermal fluids along the Troncoso fault at approximately 1.5 km depth below LdM rather than magma intrusion or dyking. They show that any mass addition associated with the deeper magma injection at 5 km depth inferred from InSAR deformation modelling would have a very small effect on the gravitational field (<3 μGal) and cannot explain the microgravity results. This suggests that the InSAR deformation and the microgravity mass addition are two separate (but linked) magma-hydrothermal processes. They propose a mechanism whereby the deep inflation causes faults to open, creating additional volume in the system (i.e. secondary porosity) that is subsequently filled with hydrothermal fluids. This interaction between the magma-driven deformation and the fault-driven mass addition suggests that the LdMVF magma-hydrothermal system is complex and various tectono-structural factors should be considered in any geophysical interpretation.

3.8 SEISMIC STUDIES AT THE LAGUNA DEL MAULE VOLCANIC FIELD

A wide range of seismic methodologies can be used to study volcanoes (Lees, 2007; Rawlinson et al., 2010). Prior to this NSF project, there were no published seismic studies focused specifically on the LdMVF although some regional studies were carried out (see Chapter 2). Concurrent with this thesis project was the installation of an array of both permanent and temporary seismometers to map earthquake hypocenters as well as image the subsurface velocity structure using receiver functions, surface wave tomography, ambient noise tomography (ANT) and local earthquake tomography (see Rawlinson et al., 2010 for a review of methodology). All these various methods rely on the idea that seismic waves will travel slower through partial melts and would thus be able to map the volcanic plumbing system although, like all geophysical parameters, multiple geological attributes can influence a geophysical parameter in a non-unique way. Hydrous minerals, elevated sub-solidus temperatures, and lithology can also lead to a decrease in seismic velocity (Lees, 2007).

3.8.1 Local Seismicity

In 2011, the Observatorio Volcanologico de los Andes del Sur (OVDAS) installed 21 broadband seismometers to monitor the LdMVF after the ground deformation was noticed (Cardona et al., 2018; Singer et al., 2014). A set of data for events between 2011 and 2014 was published by Cardona et al. (2018) in which 80% of events were classified as volcano-tectonic in origin. The majority of LdMVF events are clustered on the southwest side of the lake basin and overlie the Troncoso Fault (Figure 3.19). The earthquakes have an average depth of just under 5 km below surface with very few events

below 7 km (Figure 3.19). Another significant cluster of earthquakes was detected to the west near the Tatara-San Pedro Volcano which included the June 2012, Mw 6.2 earthquake and associated swarm.

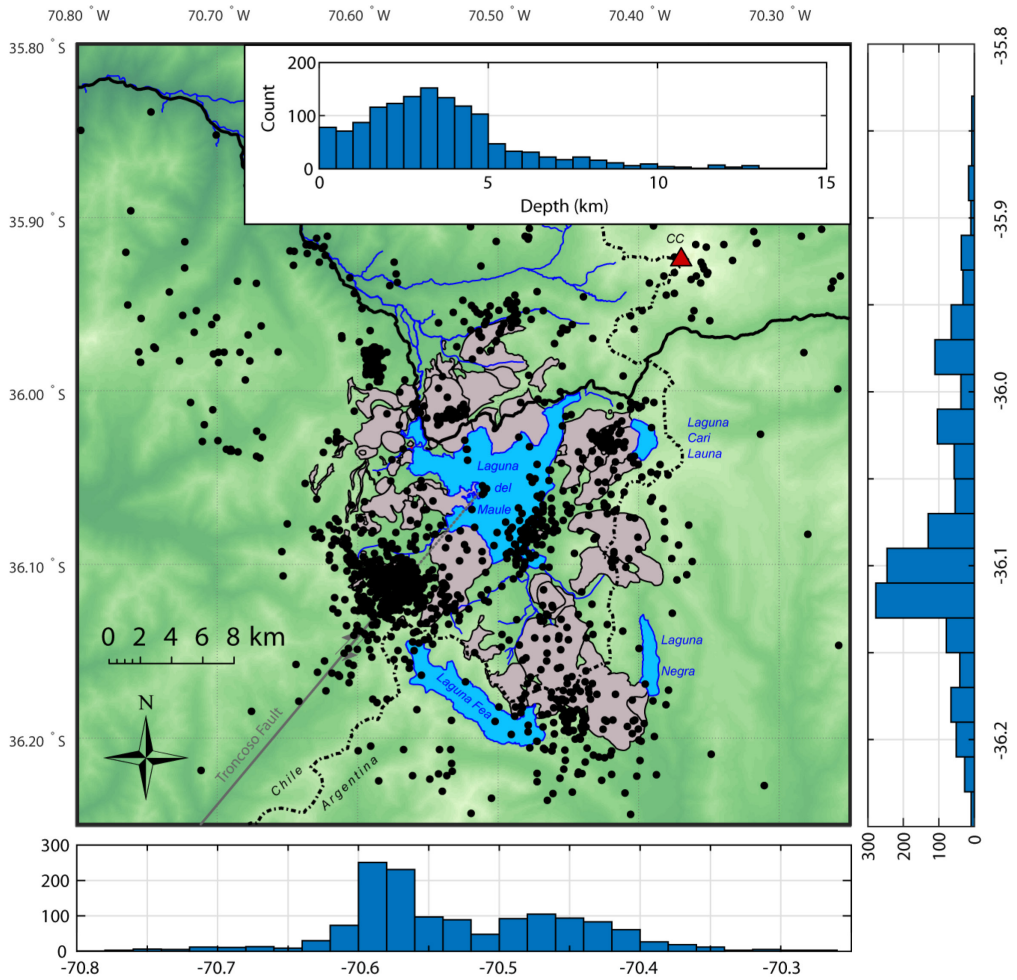

Figure 3.19: Observed seismicity data from 2011 – 2017 using OVDAS events (Cardona et al., 2018).

Temporally, the LdM earthquakes show 14 significant seismic swarms between April 2011 and December 2014 (Cardona et al., 2018). The majority of swarms occurred in 2011 and 2012 with increasing energy but then a significant gap in seismic activity followed through most of 2013. Focal mechanisms indicate dextral strike-slip motion on NE-SW striking nodal planes (i.e. parallel to the Troncoso fault) in a trans-tensional regime. Cardona et al. (2018) argue that the rapid deformation beneath the LdMVF is responsible for increasing stresses on regional faults which triggers cyclic rupturing as measured by seismic swarms. They also suggest that hydrothermal fluid pressurization may also be partially responsible for the increased seismicity as supported by the time-lapse gravity of Miller et al. (2017a). They suggest that the base of the Troncoso fault and the seismicity aligns with the roof of a shallow crystal-rich mush zone beneath the LdMVF.

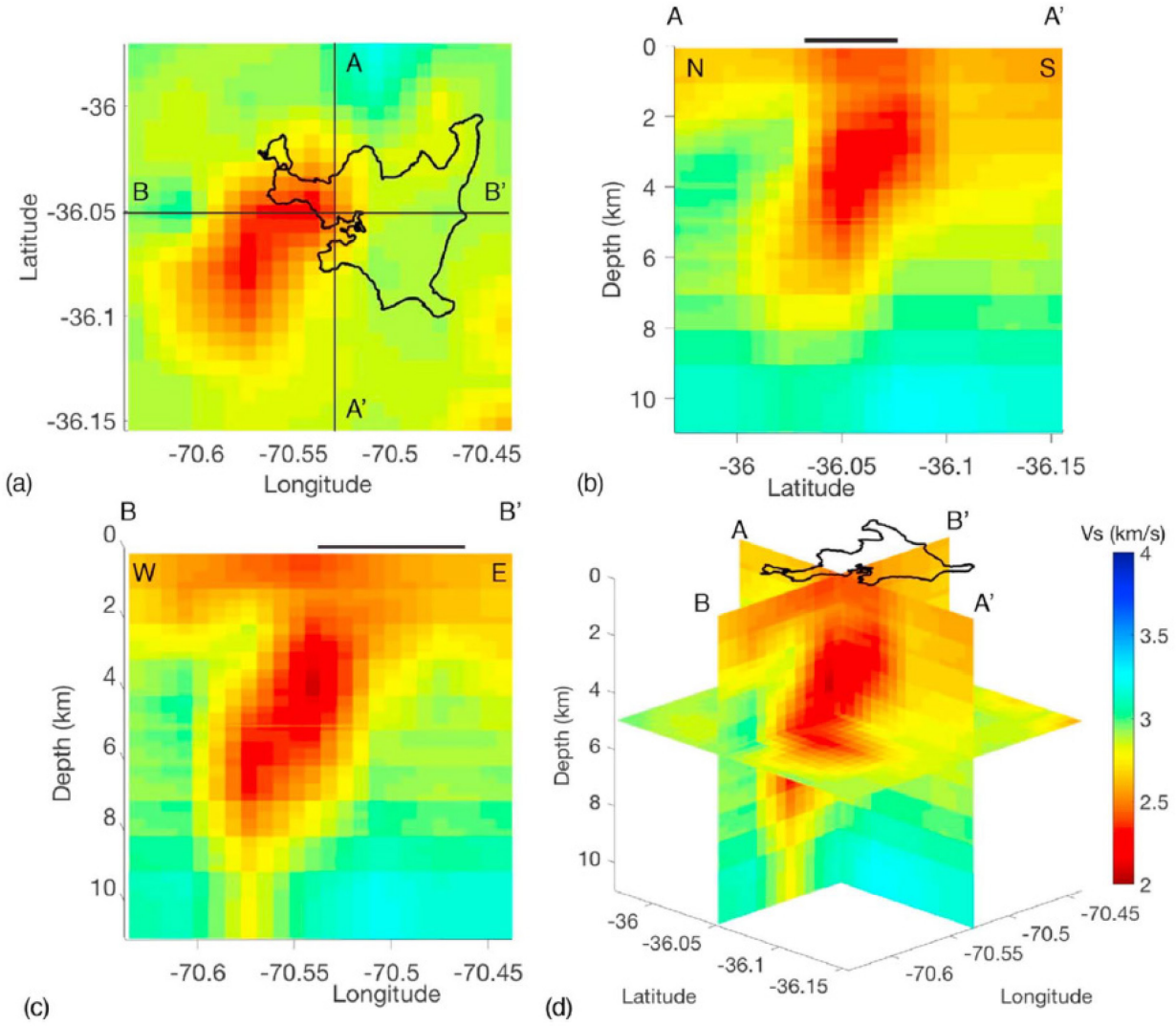

Figure 3.20: Three-dimensional seismic velocity model of the LdMVF derived from ambient noise tomography and surface waves. From Wespestad et al. (2019).

3.8.2 Ambient Noise Tomography and Surface Wave Tomography

An approximately 30 km by 30 km array of 43 seismometers was installed around the LdMVF centered on the point of maximum inflation which measured both ambient noise as well as local earthquakes and surface waves (Wespestad et al., 2019). Station spacing was approximately 3 to 5 km. Wespestad et al. (2019) used novel methods to combine the surface wave and ANT datasets into a single invertible dataset to improve bandwidth and data quality of the resulting dispersion curves. A two-step approach was used to create the 1-D velocity models beneath each node in the velocity map and then all the 1-D models were interpolated into a 3-D volume. The 3-D model included one primary low velocity zone (V1)

on the western side of the lake between 2 and 7 km depth (Figure 3.20). This feature has a south-west strike and dips to the northwest. It is laterally offset from the center of observed deformation by several kilometers. This was interpreted as a 450 km^3 zone of approximately 5 – 6% partial melt.

The low velocity zone is laterally offset from the 30 km^3 very low density anomaly inferred from Bouguer gravity. There is some overlap between V1 and the larger 115 km^3 density anomaly (Wespestad et al., 2019). The V1 anomaly also extends to the southwest of the lake and is roughly aligned with the Troncoso Fault (the dip of the fault is poorly defined but structural mapping suggests it is sub-vertical with perhaps a northwest dip). The V1 anomaly also overlaps with the zone of seismic swarms from Cardona et al. (2018).

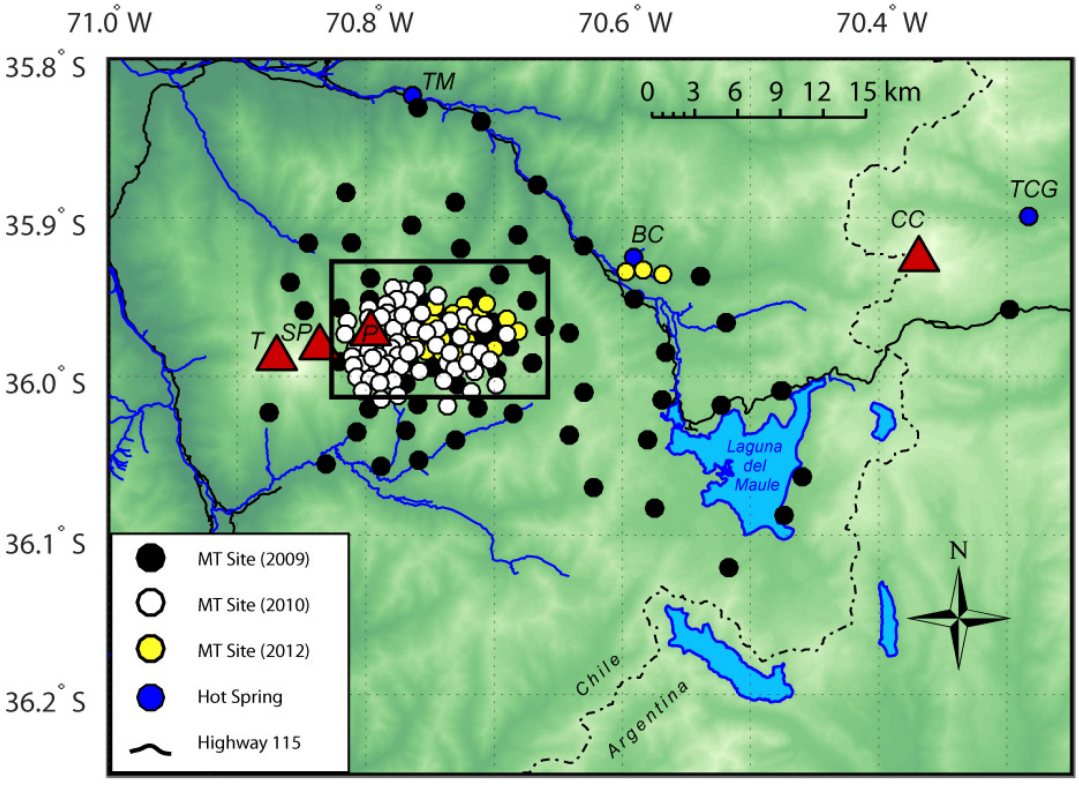

Figure 3.21: Map of magnetotelluric station locations collected between 2009 and 2012 for geothermal exploration (Hickson et al., 2010, 2011). The majority of sites are focused on the Mariposa Geothermal Prospect near the Tatara-San Pedro-Pellado volcano. The region of interest is shown by a black box and is shown in Figure 3.22.

3.9 MAGNETOTELLURICS STUDIES AT THE LAGUNA DEL MAULE VOLCANIC FIELD

The MT method is an electromagnetic geophysical method which maps the subsurface electrical resistivity (see Chapter 4). Prior to this thesis work, there was no MT work published with a specific focus on the LdMVF. There was some commercial MT data collected between 2009 and 2012 with a focus on a geothermal energy prospect near Tatara-San Pedro stratovolcano (Figure 3.21; Hickson et al., 2010, 2011). This section briefly summarizes this work.

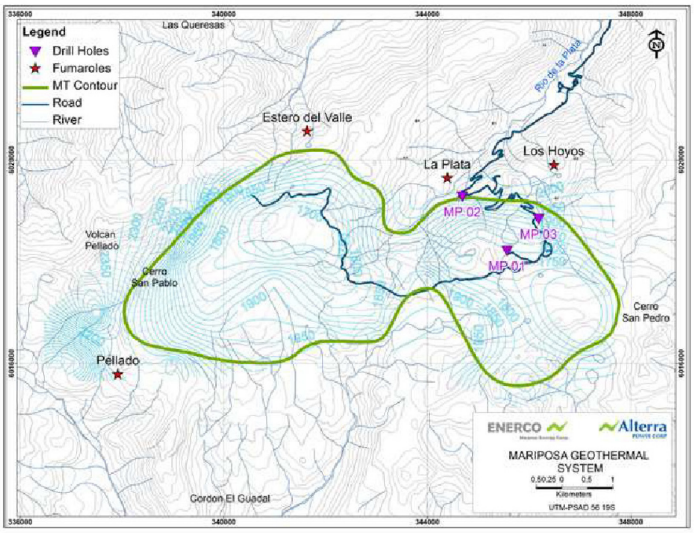

Figure 3.22: The outline of the Mariposa Geothermal Prospect based on a low-resistivity clay cap. Slim hole well locations are shown as blue inverted triangles. From Hickson et al. (2010).

3.9.1 The Mariposa Geothermal System

The Mariposa Geothermal System (MGS) is located on the eastern flanks of the TSP volcano and includes a hydrothermal-fluid hosted reservoir between 700 m and 1000 m depth composed of porous volcaniclastics and capped by an impermeable clay cap (Hickson et al., 2010). Surface expression includes four locations with fumaroles which suggest reservoir temperatures of 200°C to 290°C. Several slim holes were drilled which encountered interlayered smectite-illite between 200 m and 500 m followed by primarily illite past 500 m indicating increased temperature (Hickson et al., 2011). The inferred capacity of the prospect is approximately 320 MWe but has not been further developed (Hickson et al., 2011).

3.9.2 Magnetotellurics at the Mariposa Geothermal System

The MGS was first identified by exploratory MT data acquired in 2009 and 2010 which identified a 27 km^2 butterfly-shaped low resistivity zone interpreted as the clay cap of a geothermal reservoir (Figure 3.22; Hickson et al., 2010). Further data were collected in 2012 to increase data coverage to delineate the edges of the clay cap. In total, over 170 broadband MT stations were collected between 2009 and 2012 with the vast majority (75%) focused on a 200 km^2 area on the flanks of TSP. However, the commercial MT data acquisition did include eight MT sites in the Campanario Valley, Cajon Bobadilla, and the upper Rio Maule Valley, as well as nine MT sites in the LdM basin (Figure 3.21). These MT data were not included in the published models of the MGS but are included in this thesis work (Hickson et al., 2010, 2011; see Chapter 5 and Chapter 6). Because of the commercial focus of the project, no interpretation was made of any resistivity features deeper than the upper 1 to 2 km beneath the MGS although the resistivity model does show a possible upper crustal conductor at approximately 5 km depth beneath the MGS which is inferred to be the magmatic heat source related to the TSP magma plumbing system (Hickson et al., 2011).

Table 3.2: Summary of different geophysical anomalies observed at the LdMVF.

Method	Depth Below Lake Surface	Anomaly Center	Location	Volume	Interpretation
Seismic Tomography	2 - 8 km	(-36.07, -70.58)	West of SW Peninsula	450 km^3	5 - 6% partial melt
Bouguer Gravity	2 - 5 km	(-36.07, -70.52)	Between SW Peninsula and Las Nieblas	30 km^3	50 - 85% partial melt
Time-lapse Gravity	1.5 km	(-36.07, -70.52)	Between SW Peninsula and Las Nieblas	thin vertical crack	Hydrothermal fluids
InSAR Deformation	5 km	(-36.07, -70.52)	Between SW Peninsula and Las Nieblas	thin sill	Partial Melt
Seismicity	3 - 4 km	(-36.12, -70.58)	West of Las Nieblas	N/A	Fluids/Partial Melt

3.10 SUMMARY

The LdMVF has erupted a significant volume of basalt-to-rhyolite lavas in the last 1.5 Ma including a large caldera-forming eruption 950 – 990 ka. In the last 26 ka, there has been a noticeable increase in rhyolite volcanism especially in the southeast of the lava field. Alongside this increase in volcanism has been a notable long-term upward deformation of the southeastern lake basin as evidenced by a tilted paleo-shoreline. There are relatively nuanced and complex spatiotemporal relationships between Holocene rhyolites suggesting that the magma plumbing system is dynamic. Petrological evidence suggests ephemeral eruptive reservoirs with short residence times and laterally-variable reservoir thickness that changes with time between the southeast and northwest. Prolonged and rapid upward surface deformation has been measured in the last 10 years by satellite and GPS data which shows that the LdMVF is currently restless with new magma injection at 5 km depth likely driving the surface uplift.

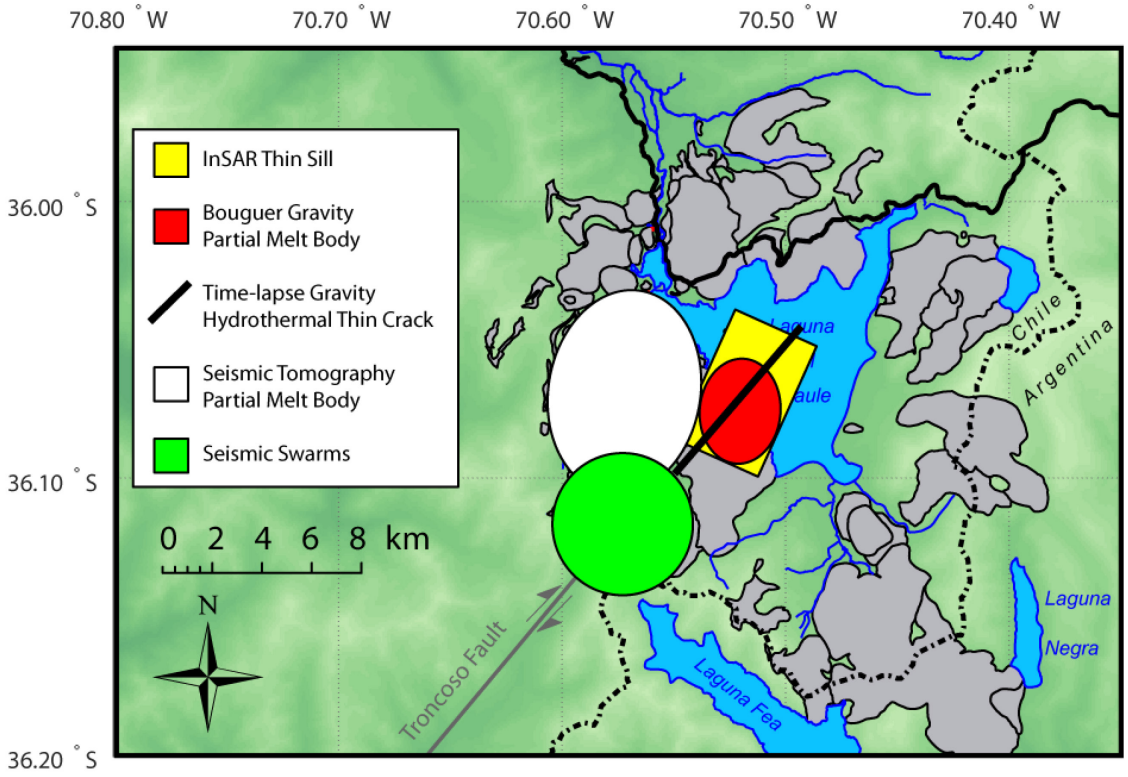

Figure 3.23: Summary map showing the approximate spatial location of geophysical anomalies at the LdMVF.

A wide array of geophysical data has been collected to examine the subsurface structure. Broadly-speaking, most of the area of interest is focused on the southwest side of the lake and lake basin which shows seismic swarms, a low velocity anomaly, a low density Bouguer anomaly, and temporal increases

in gravity suggesting mass addition as summarized in Table 3.2. All of the features do not necessarily align perfectly, but broadly overlap and trend to the northeast-southwest along a similar strike as the Troncoso fault. Figure 3.23 shows a schematic diagram of the locations of the different anomalies.

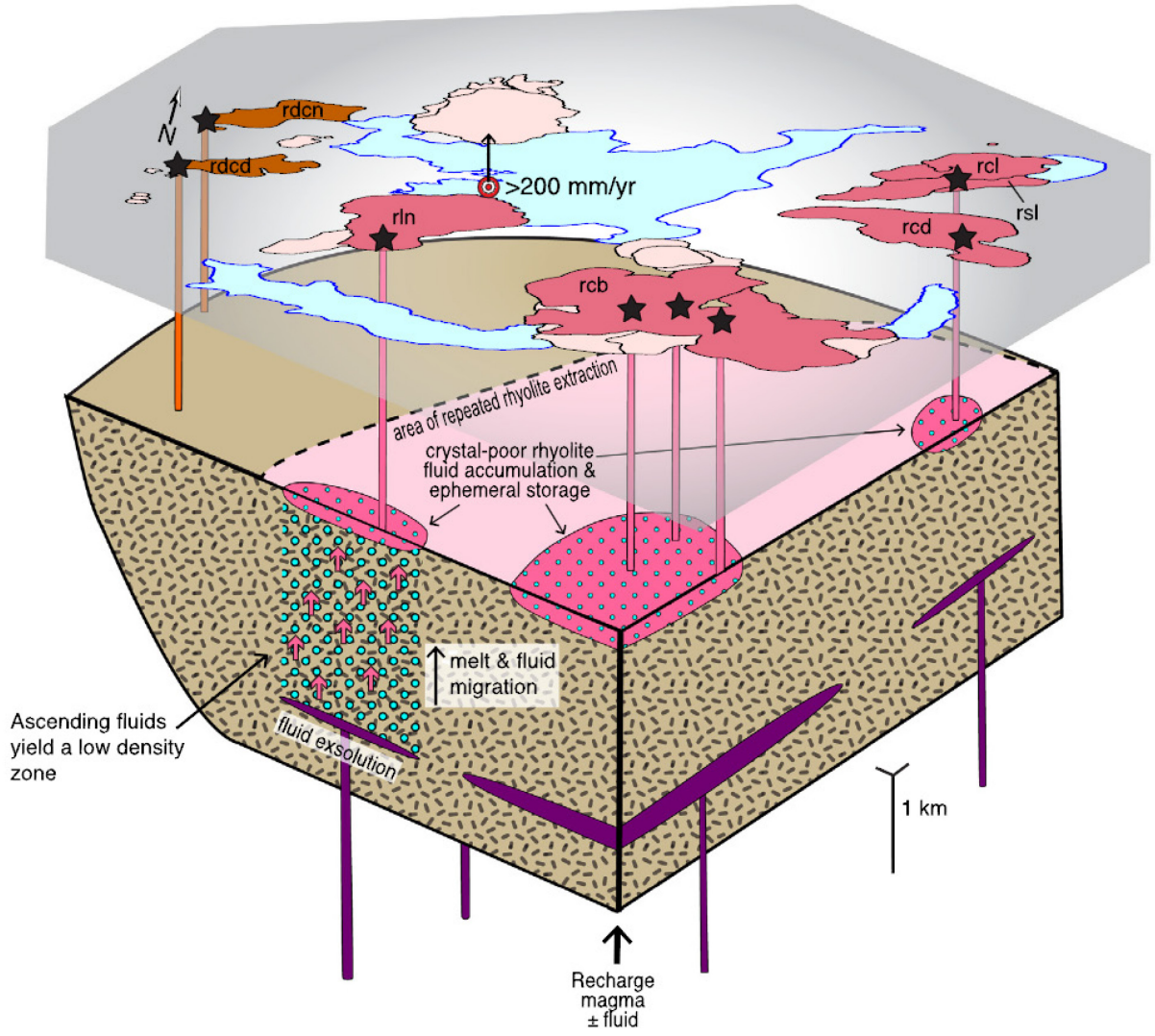

Figure 3.24: Current conceptual model of the LdMVF put forward by Andersen et al. (2018).

The models which have been proposed to explain the eruptive history, deformation patterns, petrological evidence, and geophysical data all suggest a region of crystal-rich melt beneath the LdMVF although the depth, geometry, melt fraction, and precise location of the features do not all agree. In particular, the seismic velocity anomaly is interpreted as 5 – 6% partial melt while the Bouguer gravity density anomaly is interpreted as 50% - 85% melt. The complex magmatic and hydrothermal system at LdMVF gives further evidence that silicic systems are not homogeneous and each system is unique. A conceptual model of the system was proposed by Andersen et al. (2018) and shown in Figure 3.24. Here,

the dark pink regions are small, ephemeral regions of high melt fraction detected by the Bouguer gravity survey whereas the larger beige region would be the more long-lived crystal mush imaged by the seismic tomography. The geometry of this conceptual model does not agree exactly with the geophysical results but it is the current working version for the LdMVF system.

Prior published MT work was limited to a commercial dataset focused on the MGS on the flanks of the TSP stratovolcano, 25 km west of the LdMVF with no interpretation of the magma plumbing system of either the LdMVF or the TSP stratovolcano. This thesis adds a significant amount of MT data to the area in order to better understand the LdMVF magma-hydrothermal system.

CHAPTER 4: MAGNETOTELLURIC THEORY

4.1 INTRODUCTION

The magnetotelluric (MT) method is a passive, frequency-domain, electromagnetic (EM) geophysical method which is sensitive to the conductivity structure of the subsurface. It was recognized early in the 20th century that if a geophysical method could determine the conductivity distribution of the subsurface remotely, such a method would have a wide-range of applications including identifying ore bodies in mining exploration, identifying oil and gas reservoirs or salt dome structures in oil and gas exploration, and groundwater mapping for environmental or engineering uses (Heiland, 1928). The MT method was proposed independently by Cagniard (1953) and Tikhonov (1950). MT uses the measured, naturally-occurring, time-varying electric and magnetic fields of the Earth to estimate the frequency-dependent complex impedance[1] of the subsurface. The complex impedance data are uniquely determined by the conductivity structure of the subsurface, which is unknown. The complex impedance data are then used as the data constraint to solve non-unique 1-D, 2-D, or 3-D inverse problems in an attempt to model the unknown conductivity structure with satisfactory data fit. MT data analysis can be broken into a variety of steps which will be detailed in the following sections in a standard workflow.

The structure of this chapter is as follows. First, the geological factors that control the electrical conductivity of a rock are reviewed. Second, the theoretical basis of how EM waves propagate in the subsurface will be presented with reference to Maxwell's equations of electromagnetism (Maxwell, 1873). Third, it will be explained how EM waves can be modelled and how MT data can be computed for a specificed 1-D, 2-D or 3-D conductivity model of the Earth. Fourth, the sources for the naturally-occurring MT signals are discussed and the processing of measured time-domain signals to the frequency domain is described. Fifth, data analysis methods for collected field data are explained with reference to geoelectric dimensionality and distortion. Finally, geophysical inversion methods are discussed and the methods used to derive a conductivity model from measured data are reviewed.

[1] Here "complex" refers to a number which contains both real and imaginary components of the form $a + bi$ where $i = \sqrt{-1}$. This can also be formulated as a modulus and phase of the form $re^{i\theta}$ where e is the exponential function, $r = \sqrt{a^2 + b^2}$ and $\theta = \tan(b/a)$.

4.2 ELECTRICAL PROPERTIES OF THE EARTH

4.2.1 Electromagnetic Material Properties

When an electromagnetic wave passes through a material, its behaviour is influenced by the electrical and magnetic properties of the material. In particular, the dielectric permittivity (ϵ), magnetic permeability (μ) and electrical conductivity (σ) control how displacement currents, magnetic fields and electric fields propagate in a medium, respectively. Since dielectric permittivity and magnetic permeability generally do not vary significantly in the Earth, the primary EM material property of interest to the MT method is electrical conductivity (or its inverse, resistivity).

Ohm's law states that if a voltage, V (in Volts), is applied across a circuit, it will induce a current, I (in Amps), which is proportional to the resistance, R (in Ohms). The resistance of the circuit is dependent on the material properties of the medium through which the electrical current passes. The resistivity (ρ) is a material property which defines how many charge carriers (e.g. electrons or ions) are available in a material and how easily they are able to move (i.e. how mobile they are). Electrical resistivity is measured in units of Ohm meters (Ωm) where 1 Ω is equal to 1 volt divided by 1 amp. Electrical conductivity is the inverse of resistivity (i.e. $\sigma = 1/\rho$), and is measured in Siemens/m (S/m) where

$$1\ \Omega = 1/\mathrm{S} \tag{4.1}$$

In the remainder of the discussion, the resistance is generally not important and it is the resistivity (i.e. the inherent material property) that is of interest.

4.2.2 Resistivity of Pure Earth Materials and Minerals

The Earth is composed of heterogeneous materials on a variety of spatial scales from microscopic pore-scale heterogeneity to macroscopic crustal-scale heterogeneity. It is useful to first consider the pure materials which make up the Earth broadly categorized as minerals or fluids. Minerals are defined as solid, inorganic, naturally-occurring chemical compounds which often form self-repeating crystal structures. Between minerals or grains (e.g. collections of minerals), there may be fluids such as water, oil, or gas. Given certain temperature and pressure conditions, solid minerals can also melt to form fluids. Different pure materials conduct electricity differently with some acting to impede the flow of electrical current (i.e. resistors with high resistivity). Other pure materials allow electrical current to flow relatively easily (i.e. conductors with low resistivity). Thus, if an electrical current is applied to the Earth,

it will flow more easily through some materials than others. Typical resistivity values for different Earth materials can vary by orders of magnitude from 10^{-7} to 10^{12} Ωm (Figure 4.1; Simpson and Bahr, 2005). In general, naturally-occurring solid minerals at room temperature have a very high resistivity because there is no ability for electrons or ion charge carriers to move through the rigid crystalline lattice. Exceptions include pure metals and metallic sulphides (e.g. copper sulphide mineral deposits) which have excess free electrons, graphite films which are an allotrope of carbon atoms arranged in planar sheets with a free electron in-between (Frost et al., 1989), and clay minerals which are hydrated sheet-silicates with negatively-charged surfaces that attract ions and provide an additional pathway for electrical current (Revil, 2013). These exceptions can be quite conductive and are often important targets in mineral and geothermal exploration (see Meju, 2002; Muñoz, 2014).

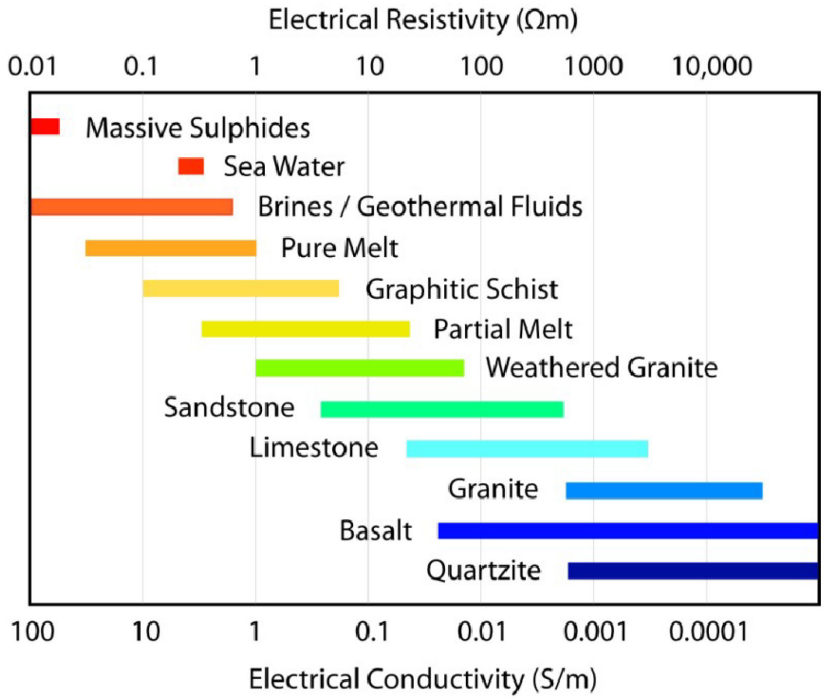

Figure 4.1: The electrical resistivity and electrical conductivity of common Earth materials. From Comeau (2015).

At high pressures in the lower crust and mantle, minerals remain solid but additional conduction mechanisms exist because of the extreme pressures and temperatures. In silicate minerals at high temperature ionic conduction and hopping conduction can occur due to cation vacancies or small impurities in the crystal lattice (Yoshino, 2010). Since hydrogen is the smallest and most mobile ion, it often contributes more to the conductivity via hydrogen diffusion (Yoshino, 2010). If the minerals are hydrated (i.e. they have incorporated a water molecule into their crystal structure), the water molecules can dissociate and hydrogen ions provide an additional pathway for electrical current (Yoshino, 2010). A

small amount of water added to a mineral can increase conductivity by several orders of magnitude. These processes are important in electrical investigations of the Earth's mantle (Pommier, 2014). Thus, for high pressures, the resistivity of minerals is dependent on a variety of factors (e.g. hydrogen content, chemistry, oxygen fugacity, etc.). However, at the low temperatures and pressures of the crust, these factors do not play a major role and most minerals are highly resistive (e.g. $>10^3$ Ωm).

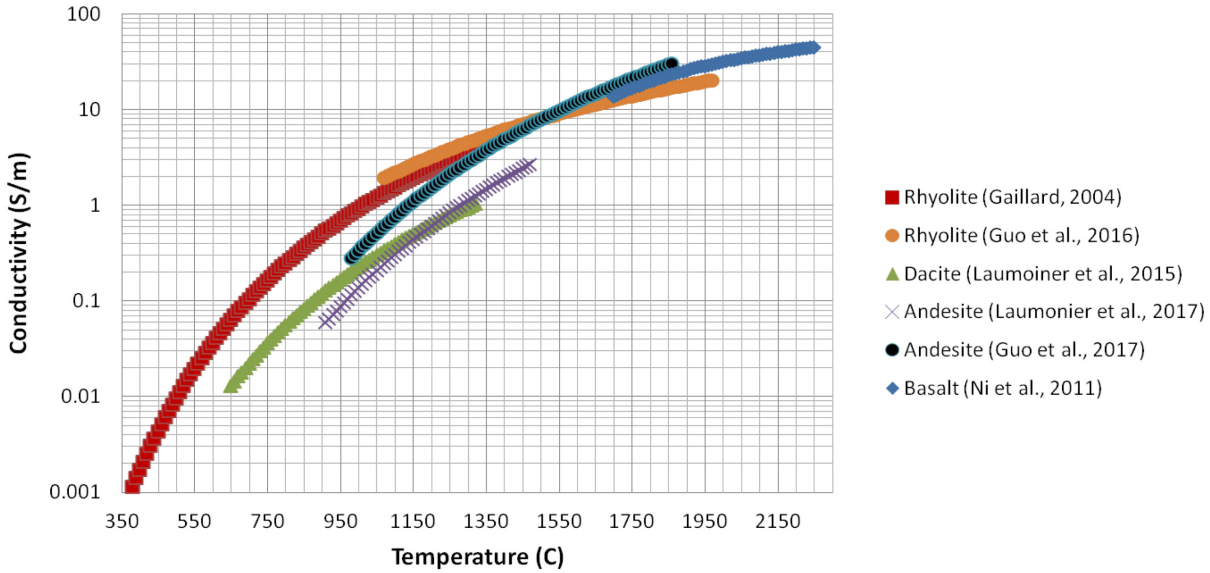

Figure 4.2: A comparison of different melt resistivity relationships at 500 MPa and 2 wt% water content.

4.2.3 Resistivity of Fluids

Fluids are present in large quantities in the Earth in various forms. Water is the most prevalent and exists in pore-spaces and fractures throughout the Earth's crust from shallow soils to sedimentary basins and can have a variety of origins. In all cases, the water contains some amount of dissolved ions which conduct electricity. The more ions that are present (e.g. the more saline), the higher the conductivity of the fluid. For example, drinking water usually has resistivity values between 10 and 200 Ωm while seawater has an average value of around 0.3 Ωm (Walton, 1989). Ultra-pure, de-ionized water is very resistive (>20,000 Ωm) but does not exist in nature. Experimental studies on the resistivity of saline fluids show that they have both a pressure and temperature dependence which are important in geoscience studies (Nesbitt, 1993; Ucok et al., 1980).

When minerals and rocks reach high temperatures, they melt forming a fluid rock phase. These molten minerals no longer have a rigid crystalline structure and ions are free to move. Detecting these melts is

important in volcanological and subduction zone studies (Pommier and Evans, 2017; Pritchard and Gregg, 2016).

The resistivity of a melt depends on a variety of factors including temperature, pressure, water content, composition, and silica content (Pommier, 2014). Different laboratory studies have developed different empirical relations to estimate the resistivity of a particular type of molten igneous rock as summarized in Figure 4.2. For example Gaillard (2004) and Guo et al. (2016) melted rhyolite samples in a laboratory setting and measured the electrical resistivity at a range of temperatures and pressures. Laumonier et al. (2017) and Guo et al. (2017) performed similar experiments on andesitic samples and Ni et al. (2011) examined basalts. Generally these relations follow an Arrhenius equation of the form

$$\ln(\sigma_f) = \ln(\sigma_0) - \frac{E_a + P\Delta V}{RT} \tag{4.2}$$

where σ_f is the melt conductivity, E_a is an empirically-derived activation energy, ΔV is the empirically-derived activation volume, R is the gas constant, σ_0 is some pre-exponential constant, P is the pressure, and T is the temperature. In general, most empirical relations also examine the water content of the magma and find that E_a, σ_0, and ΔV all depend on the water content.

Pommier and Le-Trong (2011) compiled various empirical experiments into a single database known as SIGMELTS where the user could input temperature, pressure, water content, silica content (S in %) and sodium content (N in %), and the melt conductivity could be calculated. However, this 5-D function of melt conductivity, $\sigma_f(T, P, w, S, N)$, was not a smooth function because it stitched different empirical experiments together resulting in discrete jumps and abrupt changes in slope (Figure 4.2). There is currently no smooth 5-D function to calculate the melt resistivity.

Not all fluids are conductors and important exceptions are oil, natural gas, and other gases (Meju, 2002). All of these are resistors. In volcanic settings, accumulations of volcanically-derived gases (e.g. CO_2, SO_2) may be significant (Husen et al., 2004; Julian et al., 1998).

4.2.4 Mixing Models For Multiple Phases

In the Earth, dry, solid minerals generally have a high resistivity (e.g. 10^3 to 10^{12} Ωm). Other materials (e.g. clay minerals, sulphides, brine, melt etc.) have low resistivity / high conductivity. Many Earth

materials consist of a mixture of two phases with different resistivity. Saline fluids occupy pore spaces within a dry rock matrix and magma reservoirs usually exist as a partially molten mush which contains some crystal fraction and some melt fraction. In some cases, multi-phase systems are also present containing minerals, saline fluids and oil for example. To determine the bulk resistivity of a mixed system requires knowledge of the porosity, pore structure, and connectivity of the conductive phase. Various empirical models have been created to determine the bulk resistivity, the most popular (and simple) being Archie's Law (Archie, 1942):

$$\sigma_b = \sigma_f \phi^m \tag{4.3}$$

where σ_b is the bulk conductivity, σ_f is the fluid (or melt) conductivity, ϕ is the porosity (or melt fraction), and m is known as the cementation exponent which usually varies between 1 and 2. The cementation exponent can loosely be described as the level of compaction of the conducting fluid within a non-conducting matrix where larger m corresponds to less connectivity. In other words, m represents the inverse of interconnectivity of the fluid phase. Archie's law is a simple model in that it assumes that (1) the matrix (or host rock) is infinitely resistive and; (2) mineral surface conduction mechanisms are not significant. In particular, clay minerals have significant surface conduction due to a mineral structure which has a negative surface layer which attracts a diffuse layer of positive ions which are able to flow and thus carry electrical current. Archie's law does not include the possibility of clay minerals and thus underestimates the conductivity of a rock which has a significant clay fraction.

A two-phase mixing model which incorporates the resistivity of the host rock was introduced by Glover et al. (2000):

$$\sigma_b = \sigma_h (1 - \phi)^p + \sigma_f \phi^m \tag{4.4}$$

where σ_h is the host rock (or matrix) conductivity and

$$p = \frac{\log(1 - \phi^m)}{\log(1 - \phi)} \tag{4.5}$$

This two-phase mixing model is a better approximation than Archie's law and is still relatively easy to calculate. However, it still does not incorporate clay surface conduction and pore geometry is only parameterized with one variable, m, which may not be able to adequately model the true complexity of the fluid network.

Other more sophisticated models incorporate clay surface conduction (e.g. Waxman and Smits, 1968). An overview of mixing models is given by Glover (2010) and Cai et al. (2017).

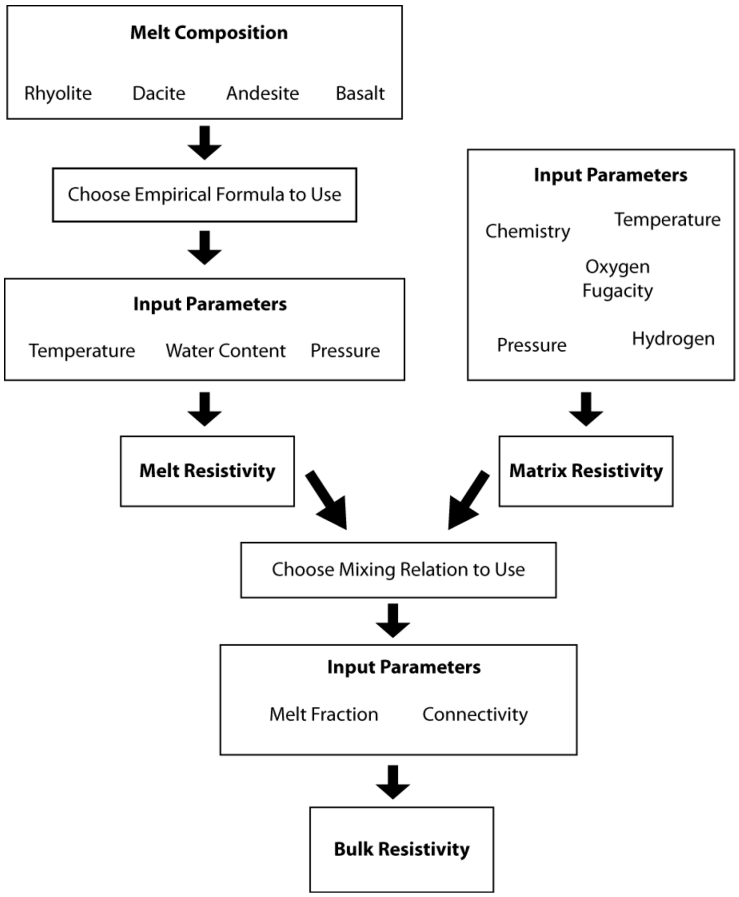

Figure 4.3: Workflow for calculating the bulk resistivity of a partially molten rock. For crustal rocks, the matrix resistivity is generally not calculated as it is assumed to be much larger than the melt resistivity (e.g. $>10^3$ Ωm).

4.2.5 Calculating Bulk Resistivity

The workflow to calculate the bulk resistivity of a rock is shown schematically in Figure 4.3. The melt resistivity and the matrix resistivity must be calculated separately. For the melt resistivity, an empirical formula is chosen based on the composition of the partial melt in question. Known inputs (e.g. temperature, pressure, water content) are used to calculate the melt resistivity. The matrix resistivity can also be calculated based on various parameters (e.g. hydrogen, oxygen fugacity, mineralogy), but this is not so important at the pressures and temperatures of crustal rocks. Then, the melt resistivity and the matrix resistivity are used in a mixing model to compute the bulk resistivity based on assumptions of connectivity. Given all the known parameters that are used as inputs, the bulk resistivity can be uniquely

determined. However, for the inverse problem, this is not true. Given a bulk resistivity it is not possible to determine all the inputs because many different combinations of inputs can yield the same bulk resistivity value.

4.3 THE PHYSICS OF THE MAGNETOTELLURIC METHOD

4.3.1 Maxwell's Equations

The MT method is governed by Maxwell's equations which describe how electric and magnetic fields are related. Maxwell (1873) developed empirical theories of electricity and magnetism from the 19th century into a unified set of four governing equations:

$$\nabla \cdot \mathbf{e} = \frac{\gamma}{\epsilon} \qquad \text{Gauss' Law} \qquad (4.6)$$

$$\nabla \cdot \mathbf{b} = 0 \qquad \text{Gauss' Law for Magnetism} \qquad (4.7)$$

$$\nabla \times \mathbf{e} = -\frac{\partial \mathbf{b}}{\partial t} \qquad \text{Faraday's Law} \qquad (4.8)$$

$$\nabla \times \mathbf{b} = \mu\sigma\mathbf{e} + \mu\epsilon\frac{\partial \mathbf{e}}{\partial t} \qquad \text{Ampere's Law} \qquad (4.9)$$

where $\mathbf{e}$ is the strength of the electric field as a function of position and time, and $\mathbf{b}$ is the magnetic flux density as a function of position and time. Throughout this thesis, bold lower case letters indicate vectors, bold upper-case letters indicate matrices or tensors, and italics denote scalars. The electric charge is given by γ, the conductivity of the medium is given by σ, and the dielectric permittivity and magnetic permeability of the medium are given by ϵ and μ, respectively. The partial derivatives are taken with respect to time, t . The del operator, ∇, is the three-dimensional vector

$$\nabla = \frac{\partial}{\partial x}\hat{\imath} + \frac{\partial}{\partial y}\hat{\jmath} + \frac{\partial}{\partial z}\hat{k} \qquad (4.10)$$

where $\hat{\imath}$, $\hat{\jmath}$, and $\hat{k}$ are unit vectors in the x, y, and z directions, respectively. This definition means that Equations (4.6) and (4.7) describe the divergence of the fields and Equations (4.8) and (4.9) describe the curl of the respective fields. Gauss' Law states that the charge within a given volume is equal to the total electric field flux leaving that volume while Gauss' Law for Magnetism follows from the observation that

magnetic monopoles do not exist. Faraday's Law states that a time-varying magnetic field induces a static electric field. A symmetrical relationship is found in Ampere's Law, which states that a magnetic field is generated by two types of current: conduction current (i.e. a static electric field) and displacement current (i.e. a time-varying electric field). These equations define the properties of EM waves as they propagate through a material with electrical properties σ, ϵ and μ. While Maxwell's equations are most commonly formulated using electric field strength ($\mathbf{e}$) and magnetic flux density ($\mathbf{b}$), it is equally valid to write them using electric current density ($\mathbf{j} = \sigma\mathbf{e}$) and magnetic field strength ($\mathbf{b} = \mu\mathbf{h}$).

4.3.2 Electromagnetic Field Propagation in a Conductive Medium

To understand how the EM field propagates in the Earth, it is first useful to consider a homogeneous, isotropic, conductive medium which has constant dielectric permittivity and magnetic permeability equal to their free space values ($\epsilon = \epsilon_0 = 8.85 \times 10^{-12}$ F/m and $\mu = \mu_0 = 4\pi \times 10^{-7}$ H/m). Taking the curl of both sides of Equation (4.8) and substituting Equation (4.9) results in

$$\nabla(\nabla \cdot \mathbf{e}) - \nabla^2\mathbf{e} = -\mu_0\sigma\frac{\partial \mathbf{e}}{\partial t} - \mu_0\epsilon_0\frac{\partial^2\mathbf{e}}{\partial t^2} \tag{4.11}$$

where $\nabla \cdot \mathbf{e} = 0$ because it is assumed that there are no free charges within the Earth. Free charges would be ions or electrons which build up in one location (e.g. on interfaces between regions of different conductivity) such that there is a time-varying charge density. This assumption is not always justified when the distribution of conductivity underground is not 1-D and leads to static shifts and galvanic distortion (see Section 4.3.5 and Section 4.6).

Equation (4.11) can be simplified further by transforming it to the frequency domain. This is done by assuming a sinusoidal time variation of the electric fields which separates the time dependence from the spatial dependence:

$$\mathbf{e}(x, y, z, t) = \mathbf{e_0}(x, y, z)\mathrm{e}^{-\mathrm{i}\omega\mathrm{t}} \tag{4.12}$$

where ω is the angular frequency and $\mathbf{e_0} = E_x\,\hat{\imath} + E_y\,\hat{\jmath} + E_z\,\hat{k}$, in component form. Throughout this chapter, it is assumed that both the electric and magnetic fields are functions of frequency. Since the MT problem rarely deals with frequencies larger than 10000 Hz and the conductivity of the subsurface is

rarely less than 0.1 Ωm, it can be seen that the second term on the right-hand side of Equation (4.11) (i.e. the displacement current term) is negligible and can be ignored. Therefore

$$\nabla^2 \mathbf{e_0} = -i\omega\mu_0\sigma\mathbf{e_0}\,. \tag{4.13}$$

This is a diffusion equation meaning that EM fields propagate diffusively within the Earth rather than as waves. Since the MT source signal is assumed to be remote and incident from the atmosphere, the angle of refraction at the air-Earth interface will be so small that it can be safely assumed that the direction of propagation is vertically downward (i.e. in the positive *z*-direction). Furthermore, if it can be assumed that the wave is plane-polarized in the *x*-direction which simplifies the diffusion equation into an ordinary differential equation:

$$\frac{\partial^2 E_x}{\partial z^2} + i\omega\mu_0\sigma E_x = 0 \tag{4.14}$$

where E_x is the *x*-component of the plane-polarized electric field. It can be shown that this ordinary differential equation has the solution of the form

$$E_x(z,\omega) = E_x^S e^{-z\sqrt{-i\omega\mu_0\sigma}} \tag{4.15}$$

where E_x^S is the electric field measured at the surface at $z = 0$. This solution shows how the electric field behaves in a homogenous halfspace medium and it can be seen that the magnitude of the electric field decays exponentially with depth. The rate of exponential decay also depends on the frequency of the signal and the conductivity of the halfspace. The skin depth, δ, is defined as the depth at which the magnitude of the surface signal, E_x^S, has decayed by a factor $1/e$. Substitution into Equation (4.15) results in the skin depth equation

$$\delta = \sqrt{\frac{2}{\omega\mu_0\sigma}} \tag{4.16}$$

which is an important and useful estimate of the depth a given signal is sensitive to. Depending on the depth target of interest in an MT survey, this has implications for the frequency range needed to detect the target. It also has implications in numerical modeling and inversion problems because boundary effects must be avoided. Electric fields are often forced to decay to zero at the boundaries of numerical models which is non-physical, thus model mesh boundaries must be far enough away (as per Equation (4.16)) such that the area of interest to be modelled is not affected by this non-physical electric field.

The behaviour of the magnetic field is similar under the above assumptions where the magnetic field at the surface is defined as $\mathbf{h_0} = H_x\,\hat{\imath} + H_y\,\hat{\jmath} + H_z\,\hat{k}$. This results in a similar solution to the electric field:

$$H_y(z,\omega) = -\frac{1}{i\mu_0\omega} E_x^S e^{-\sqrt{-i\omega\mu_0\sigma}z} \tag{4.17}$$

Based on the fact that

$$H_y = \frac{1}{i\mu_0\omega}\frac{\partial E_x}{\partial z} \tag{4.18}$$

4.3.3 Complex Impedance

Equations (4.15) and (4.17) show that the magnetic field is scaled and phase-shifted from the electric field. The magnetotelluric method relies on the ratio of the measured electric and magnetic field strengths at the surface of the Earth known as the complex impedance, $Z(\omega)$ with units of Ω. Taking the ratio of the field strengths has an advantage over individual measurements of electric or magnetic components because it removes the need to know the source term (Cagniard, 1953) and allows for quantitative estimates of the resistivity of the subsurface (Yungul et al., 1973). In the case of a halfspace, division of Equation (4.15) by Equation (4.17) results in a quantitative value for the conductivity (or resistivity) of the subsurface:

$$\frac{1}{\mu_0\omega}\left|\frac{E_x(\omega)}{H_y(\omega)}\right|^2 = \frac{1}{\mu_0\omega}|Z_{xy}(\omega)|^2 = \frac{1}{\sigma_0} = \rho_0 \tag{4.19}$$

where ρ_0 is the unique resistivity of a given halfspace in Ωm and Z_{xy} is the complex impedance with subscripts denoting that the electric and magnetic fields are taken in the x- and y-directions, respectively.

4.3.4 Apparent Resistivity and Phase

The impedance is a complex quantity with both real and imaginary components which are frequency dependent. Another way of considering a complex quantity is to plot it in polar coordinates with both modulus and phase components. In MT, a polar representation of the complex impedance is often used for ease of interpretation. In this way, the impedance is written as

$$Z_{xy}(\omega) = \left|Z_{xy}(\omega)\right| e^{i\phi(\omega)} \tag{4.20}$$

where $|Z_{xy}|$ is the modulus and ϕ is the impedance phase. Following from Equation (4.19), the modulus can be squared and scaled to give units of Ωm. In this way, the apparent resistivity is defined as

$$\rho_a(\omega) = \frac{1}{\mu_0 \omega} \left| Z_{xy}(\omega) \right|^2 \tag{4.21}$$

For a uniform halfspace, the apparent resistivity equals the true resistivity. However, for a heterogeneous media, the apparent resistivity can be viewed as the volumetric average of the true resistivities over a hemisphere beneath the measurement point. It is dependent on the frequency which determines the maximum depth that the hemisphere is sensitive to in accordance with the skin depth equation of Equation (4.16). Since $\rho_a < 0$ is non-physical, there is no ambiguity when converting from complex impedance to apparent resistivity and phase[2].

The apparent resistivity and phase are inter-related and dependent and have a variety of useful analytical and interpretational properties (Weidelt, 1972). When plotted as a function of period (or its inverse, frequency), the apparent resistivity will be decreasing when it is sensitive to a conductor and increasing when it is sensitive to a resistor with period (or frequency) acting as proxy for depth. The phase for a uniform halfspace will equal exactly 45°. When apparent resistivity is increasing, the phase will be less than 45°, whereas if apparent resistivity is decreasing, the phase will be greater than 45°.

4.3.5 Electromagnetic Field Propagation in a 2-D or 3-D Earth

The above discussion has thus far assumed a 1-D conductivity model consisting of either a simple halfspace, or a series of layers infinite in horizontal extent (e.g. left panel of Figure 4.4). Such models simplify the mathematical analysis but real Earth models are more accurately described as 2-D or 3-D (middle and right panels of Figure 4.4). In these cases, the diffusion equations for electric and magnetic fields do not simplify to ordinary differential equations with simple solutions. It also means that a downward propagating electric or magnetic wave induce secondary fields with components in all three orthogonal directions of a given coordinate frame. This results in six component quantities: E_x, E_y, E_z, H_x, H_y, and H_z. For the MT method, it is assumed that $E_z \approx 0$ at the surface because of the high resistivity contrast at the air-Earth interface. It is also logistically difficult to measure the vertical electric field since it would require a large vertical dipole.

[2] If there was no physical restriction on ρ_a, then $\left| Z_{xy} \right| = \pm\sqrt{\mu_0 \omega \rho_a}$. But because $\rho_a > 0$, we can neglect the negative solution and thus the modulus of the complex impedance is always positive.

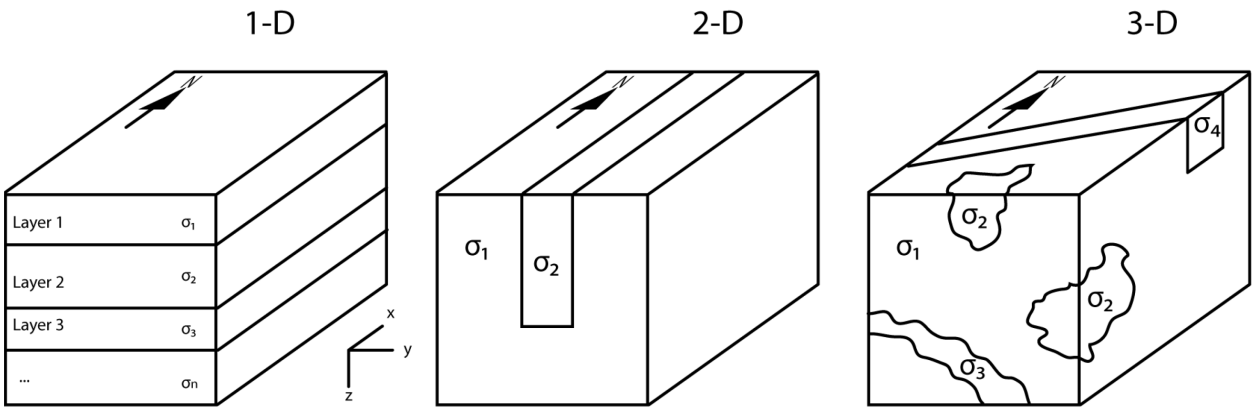

Figure 4.4: Schematic diagrams of one-dimensional (left), two-dimensional (middle), and three-dimensional (right) conductivity distributions in the Earth.

In the ideal 2-D case shown in the middle panel of Figure 4.4, there is no variation in conductivity in the *x*-direction (i.e. the geoelectric strike is in the *x*-direction) and thus all derivatives with respect to *x* go to zero. This results in a de-coupling of Maxwell's Equations (4.8) and (4.9) into two modes. The first mode contains the components E_x, H_y, and H_z and is known as the transverse electric (TE) mode because the electric field component is parallel to strike:

$$\frac{\partial H_z}{\partial y} - \frac{\partial H_y}{\partial z} = \sigma E_x \tag{4.22}$$

$$\frac{\partial E_x}{\partial z} = -i\omega\mu_0 H_y \tag{4.23}$$

$$\frac{\partial E_x}{\partial y} = i\omega\mu_0 H_z. \tag{4.24}$$

The second mode contains the components H_x, E_y, and E_z and is known as the transverse magnetic (TM) mode:

$$\frac{\partial E_z}{\partial y} - \frac{\partial E_y}{\partial z} = -i\omega\mu_0 H_x \tag{4.25}$$

$$\frac{\partial H_x}{\partial z} = \sigma H_y \tag{4.26}$$

$$\frac{\partial H_x}{\partial y} = -\sigma H_z. \tag{4.27}$$

The two modes will propagate differently because in the TE mode the electric currents do not cross boundaries between regions with different conductivity. In contrast the TM mode includes electric field components that cross conductivity boundaries in $\sigma(y, z)$. This results in the build up of electric charges on boundary surfaces and also requires the partial differential equation solution to incorporate spatial derivatives in conductivity in the y and z directions.

Unlike 1-D MT problems, both 2-D and 3-D problems result in all six field components including vertical components of the electric and magnetic fields. However, in MT, only the horizontal field components are measured. The tipper electromagnetic method utilizes vertical field components as is discussed in Section 4.3.7. In three-dimensional MT problems, no simplification of Maxwell's Equations can be made and all field components are coupled. This results in relationships between source fields and induced fields that are often unintuitive and difficult to visualize.

4.3.6 The Impedance Tensor

When discussing 1-D conductivity structures, the apparent resistivity and phase do not depend on the the choice of coordinate system. Because of this, the impedance can be calculated using either the E_x and H_y components of Equation (4.19) or the E_y and H_x components and the answer will be identical. In other words

$$Z(\omega) = Z_{xy}(\omega) = -Z_{yx}(\omega). \tag{4.28}$$

The negative sign comes about from the definition of the cross-product in Maxwell's equations and implies that the magnitude—and the resulting apparent resistivity—are identical but the phase is shifted. In another way, this can be written as a tensor:

$$\begin{bmatrix} E_x(\omega) \\ E_y(\omega) \end{bmatrix} = \begin{bmatrix} 0 & Z(\omega) \\ -Z(\omega) & 0 \end{bmatrix} \begin{bmatrix} H_x(\omega) \\ H_y(\omega) \end{bmatrix} \tag{4.29}$$

In 2-D conductivity structures, the choice of measurement coordinates relative to the model structure is important. The TE mode is thus defined as the direction with electric current parallel to strike and the TM mode is the direction with magnetic fields parallel to strike. Even though most examples, derivations, and MT data collection assume a coordinate system with x to the north, the TE mode does not generally point north unless the geological structure has a north-south geoelectric strike. When the data are in the coordinate system such that *x* is parallel to the geoelectric strike, the impedance tensor

diagonal components equal to zero and $|Z_{xy}| \neq |Z_{yx}|$. The impedance tensor for 2-D conductivity structures can be written as:

$$\begin{bmatrix} E_x(\omega) \\ E_y(\omega) \end{bmatrix} = \begin{bmatrix} 0 & Z_{xy}(\omega) \\ Z_{yx}(\omega) & 0 \end{bmatrix} \begin{bmatrix} H_x(\omega) \\ H_y(\omega) \end{bmatrix}. \tag{4.30}$$

In 3-D conductivity structures, there is a coupling between all components of Maxwell's equations and as such the tensor is a full matrix, $\mathbf{Z}$, with the form:

$$\begin{bmatrix} E_x(\omega) \\ E_y(\omega) \end{bmatrix} = \begin{bmatrix} Z_{xx}(\omega) & Z_{xy}(\omega) \\ Z_{yx}(\omega) & Z_{yy}(\omega) \end{bmatrix} \begin{bmatrix} H_x(\omega) \\ H_y(\omega) \end{bmatrix}. \tag{4.31}$$

This can be written compactly as

$$\mathbf{e} = \mathbf{Zh} \tag{4.32}$$

In real field data, all components of the impedance tensor are calculated (as discussed in Section 4.5) and if large diagonal components are observed, this could indicate 3-D geologic structure but also depends on the coordinate system which the data are collected in relative to the regional geoelectric strike direction (see Section 4.6).

4.3.7 Vertical Geomagnetic Transfer Functions

As mentioned earlier, 2-D and 3-D resistivity structure also generally result in vertical electric and magnetic fields. Because the resistivity of the air is very high (e.g. 10^9 Ωm), no electric currents can cross the air-Earth interface and thus $E_z \rightarrow 0$ at the surface (Chave and Jones, 2012). However, this is not the case for the vertical magnetic fields and as a result a transfer function, $\mathbf{T}$, can be constructed using magnetic fields commonly called the tipper:

$$H_z(\omega) = \begin{bmatrix} T_x(\omega) & T_y(\omega) \end{bmatrix} \begin{bmatrix} H_x(\omega) \\ H_y(\omega) \end{bmatrix}. \tag{4.33}$$

Like the impedance tensor ($\mathbf{Z}$), the tipper transfer function ($\mathbf{T}$) contains frequency-dependent information about the Earth. Because these are complex quantities, it is often more common to plot the vector of the real components in map view (Gregori and Lanzerotti, 1980). These vectors are known as induction vectors and they will align parallel to conductivity gradients. In other words, if there is a large conductor oriented north-south in the subsurface, an induction vector will point east-west. The direction of the head or tail of the vector is arbitrary. The Parkinson convention has induction vectors

pointing towards conductors while the Wiese convention has induction vectors pointing away (Simpson and Bahr, 2005).

While tipper data is independent from MT impedance tensor data, they can both be derived from the same physical assumptions in Maxwell's equations. As we will see in the next section, when modelling EM waves, it is natural and necessary to solve for both vertical and horizontal components. Thus, once all field components are measured, it is straightforward to compute both $\mathbf{Z}$ and $\mathbf{T}$. As a result, tipper data is often collected alongside MT data to provide an additional constraint on the subsurface resistivity structure.

4.4 FORWARD MODELLING OF MAGNETOTELLURIC DATA

4.4.1 One-Dimensional Conductivity Models

For 1-D, layered media like that shown on the left panel of Figure 4.4, the horizontal electric and magnetic field components will propagate diffusively in each layer and be continuous at layer boundaries. A linear transfer function which recursively relates the observed admittance, $C(\omega)$, measured at the surface, to the layered subsurface conductivity was first derived analytically by Wait (1954). The admittance is related to the complex impedance by

$$Z_{xy}(\omega) = i\omega C(\omega) \tag{4.34}$$

Since an analytical solution exists for the 1-D forward problem, it is not necessary to proceed with a numerical solution. A 1-D conductivity model will produce a unique set of admittance data. However, a given set of admittance data can be arrived at via an infinite number of layered Earth models. This is an important result which means that the MT inverse problem is inherently non-unique. However, for 1-D conductivity models, the product of conductivity and thickness (known as the conductance) can be uniquely determined. If conductivity increases while thickness decreases such that the product remains the same, the apparent resistivity and phase curves will remain nearly identical.

4.4.2 The Special Case of One-Dimensional D+ Solutions

The 1-D conductivity model described above is a layered model where each layer is assigned a particular thickness and conductivity value. The greater the number of layers and the thinner the layers, the better the true Earth conductivity can be approximated.

However, there are sometimes reasons to proceed with non-physical solutions which have unique physical properties. In particular, the D+ model exploits the fact that MT measures the conductance of a layer, rather than determining the conductivity and thickness separately. The D+ model assumes that the Earth is composed of infinitely thin and infinitely conductive layers which have finite conductance embedded in an infinitely resistive halfspace (Parker, 1980; Parker and Whaler, 1981). In other words, the resistivity structure can be approximated as a series of delta functions:

$$\sigma_n = \int_{z_n-\epsilon}^{z_n+\epsilon} \tau_n \delta(z - z_n)\ dz\,. \tag{4.35}$$

Each n^{th} layer at a depth of z_n has an infinite conductivity but a finite integrated conductivity (i.e. conductance) equal to τ_n. By transforming the 1-D Maxwell's equations from conductivity to conductance (Parker, 1980), an alternative expression for the complex admittance can be derived which takes Wait's algorithm to the limit as the thickness of each conductive layer goes to zero and the conductivity goes to infinity. In this model, the admittance can be calculated using a similar recursion relation which takes the form of a continued fraction where $C_1(\omega)$ is the admittance measured at the surface:

$$C_n(\omega) = z_{n-1} - z_n + \frac{1}{i\omega\mu_0\tau_n + \dfrac{1}{C_{n+1}(\omega)}}. \tag{4.36}$$

This solution has some unique properties. First of all, the final expression of the admittance measured at the surface, $C(\omega)$ can be converted to a partial fraction known as the spectral function of the complex admittance:

$$C(\omega) = a_0 + \sum_{n=1}^{N} \frac{a_n}{\lambda_n + i\omega} \qquad a_0 \geq 0,\ \ a_n > 0 \tag{4.37}$$

The spectral function (Weidelt, 2005, 1972) has poles (or zeros) at λ_n where λ_n from $n = 1 \ldots N$ represents a set of resonant frequencies of the infinitely-conductive sheets. Given a set of MT data, the best fitting a and λ parameters can be found via inversion to examine how well a set of MT data can be fit to the D+ model. The D+ model is special because it was shown by Parker (1980) that any 1-D resistivity model can be fit to a D+ model exactly and uniquely. When noise is present, the D+ model fits 1-D admittance data with minimum misfit (Parker and Whaler, 1981). This was further expanded to show that all TM mode response and most (but not all) TE mode responses in a 2-D model can also be fit by a D+ model (Parker, 2010; Weidelt and Kaikkonen, 1994). If TE and TM MT data can be fit to a D+

model with low misfit, this implies that those data are phase-consistent, reliable, and of relatively high quality (i.e. low noise). If TE and TM MT data cannot be fit to a D+ model, it implies that they are either very noisy, an error occurred in processing, or there are very unique 2-D or 3-D distortions present.

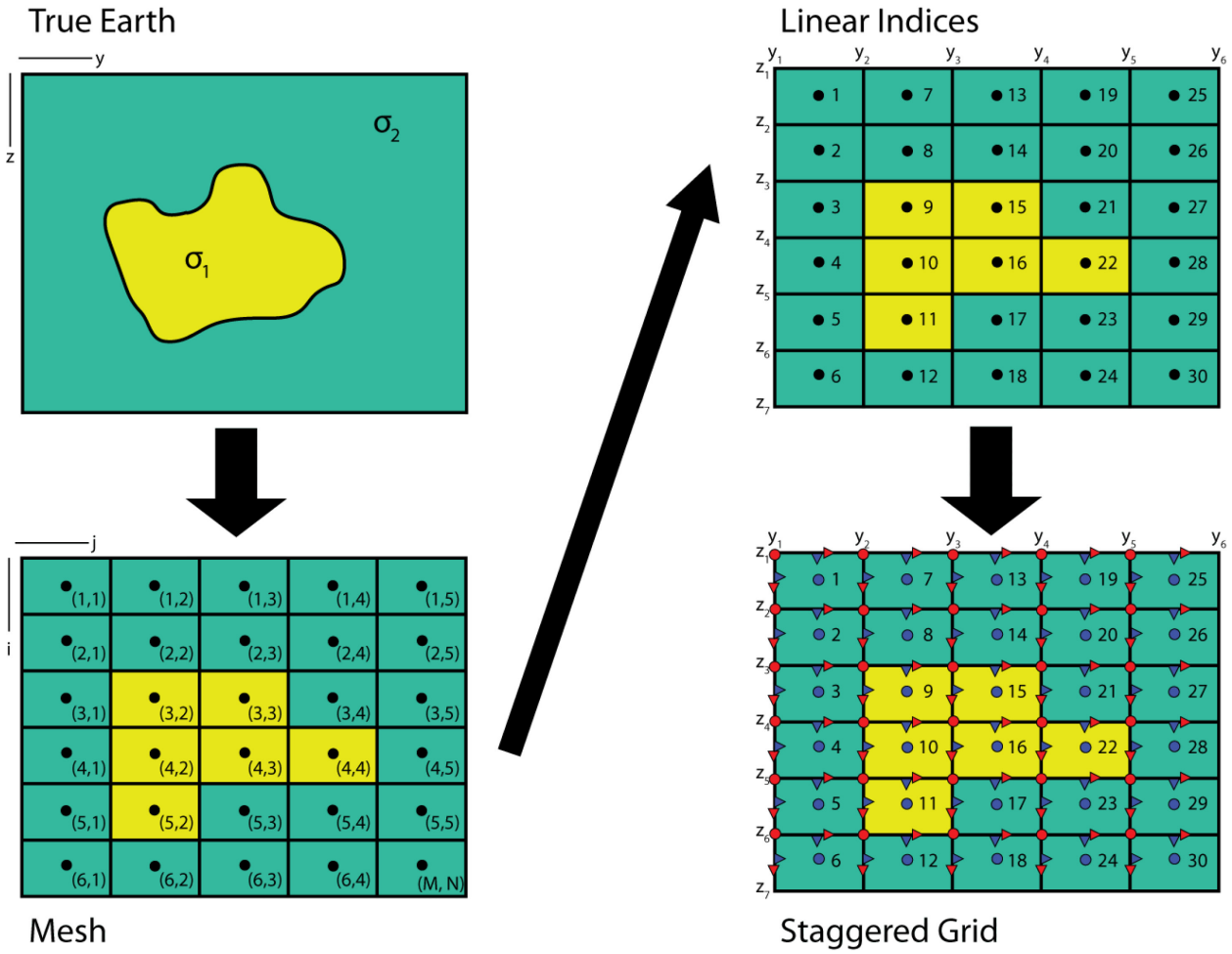

Figure 4.5: Schematic diagram of a staggered grid for solution of Maxwell's equations using finite differences. Top left panel: The true Earth conductivity structure consisting of one anomaly with a conductivity $\boldsymbol{\sigma_1}$ embedded in a halfspace with conductivity $\boldsymbol{\sigma_2}$. Bottom left panel: The true conductivity structure is discretized onto a grid mesh consisting of 30 model cells with indices (i,j). Top right panel: The 2-D grid can be restructured into a linear vector of indices labelled 1 through 30. Bottom right panel: The electric fields (red circles and triangles) are defined on cell edges and nodes with the x-component coming out of the page (red circles). The magnetic field (blue circles and triangles) are defined at cell faces and cell centers with the x-component coming out of the page (blue circles).

4.4.3 Two-Dimensional Conductivity Models

The two independent TE and TM modes in 2-D MT problem are defined by Equations (4.22) through (4.27). In general, these equations do not have analytic solutions. Some exceptions include the quarter space model of D'Erceville and Kunetz (1962) that can be solved with a power series and the TE mode thin-sheet model of Parker (2011). The thin-sheet model of consists of a vertical thin conductor with variable horizontally-integrated conductivity placed in the center of some model space. The solution for the TE mode is closed-form but no TM mode solution has been derived as yet. As a result, for arbitrary 2-D conductivity models, the two modes must be solved independently using finite difference or finite element methods. This is best done using matrix operators to describe a model space on a staggered grid[3] (Haber, 2015; Yee, 1966). A schematic diagram of the mesh for a finite difference staggered grid is shown in Figure 4.5 for a 2-D mesh where the electric fields are defined at cell nodes (or edges) while the magnetic fields are defined at cell centers (or faces).

Assuming a model space contains *M* model cells in the y direction and *N* model cells in the z direction, an *MN* x *MN* linear system of equations can be constructed to solve for the field components E_x (for the TE mode) and H_x (for the TM mode). In the example in Figure 4.5, there are 5 model cells in the y-direction and 6 model cells in the z-direction for a total of 30 model parameters requiring the solution of a 30 x 30 linear system. For the TE mode, the linear system to be solved simplifies to

$$\mathbf{e_x} = \left[\mathbf{D_y^B D_y^F} + \mathbf{D_z^B D_z^F} - i\omega\mu_0 \mathrm{diag}(\boldsymbol{\sigma})\right]^{-1} \mathbf{s_e} \tag{4.38}$$

where $\mathbf{e_x}$ is an (*MN* x 1) vector of electric field values for each model cell subscripted linearly (Figure 4.5), $\mathbf{D_y}$ and $\mathbf{D_z}$ are (*MN* x *MN*) penta-diagonal derivative operators constructed using Kronecker products of tri-diagonal 1-D operators in y and z. The **B** and **F** superscripts denote backwards or forward differences. The diag() operator creates an (*MN* x *MN*) matrix with the conductivity values associated with each model cell along the diagonals of the matrix. The $\mathbf{s_e}$ term is a vector describing the sources. In general, Dirichlet boundary conditions are imposed at the edges of the model mesh. At the air-Earth interface, a constant source is imposed (e.g. a plane-wave source) while at the other edges, the electric field is forced to decay to zero (e.g. an infinitely conductive edge). Padding cells are included in the mesh to ensure that edge effects of the infinite conductor do not influence the modelled data.

[3] A good resource is the free online videos at https://empossible.net/academics/emp5337/

The solution for the TM mode is similar to that for the TE mode. The solution solves for H_x and the derivative operators must be modified to take into account spatial derivatives in resistivity in the y and z directions (Smith, 1996):

$$\mathbf{h_x} = \left[\mathbf{D_y^F}\text{diag}(\boldsymbol{\sigma})\mathbf{D_y^B} + \mathbf{D_z^F}\text{diag}(\boldsymbol{\sigma})\mathbf{D_z^B} - i\omega\mu_0\mathbf{I}\right]^{-1}\mathbf{s_b} \tag{4.39}$$

where $\mathbf{I}$ is an (*MN* x *MN*) identity matrix. Notice that the forward and backward difference operators in the derivatives are in the reverse order for the magnetic field solution. This is because the electric fields are defined on cell edges while magnetic fields are defined at cell centers (Figure 4.5). Once a solution for the field components in the x-direction has been obtained, derivative operators are used to solve for the remaining field components, including the z-components.

4.4.4 Three-Dimensional Conductivity Models

The 3-D finite difference problem is more complicated because the 6 equations from the cross-products in Maxwell's equations do not de-couple into independent sets. As a result, the entire system must be solved as a single linear system (e.g. Haber, 2014):

$$\begin{bmatrix} \mathbf{C} & i\omega\mathbf{I} \\ -\text{diag}(\boldsymbol{\sigma}) & \mathbf{C^T}\text{diag}(\mu_0) \end{bmatrix}\begin{bmatrix}\mathbf{e}\\ \mathbf{b}\end{bmatrix} = \begin{bmatrix}\mathbf{0}\\ \mathbf{s}\end{bmatrix} \tag{4.40}$$

where $\mathbf{e}$ and $\mathbf{b}$ are now linearized vectors of all three components on the entire *M* x *N* x *P* 3-D model. These represent vectors with size (3*MNP* x 1). Similarly, the $\boldsymbol{\sigma}$ and $\mathbf{s}$ are both (*MNP* x 1) vectors of the linearized conductivity model and source terms, respectively. $\mathbf{I}$ is an (*MNP* x *MNP*) identity matrix and $\mathbf{C}$ is a staggered-grid cross product operator of the same size. The entire matrix operator for the linear system is (12*MNP* x 12*MNP*). Even a small 10 x 10 x 10 model space would result in a 12000 x 12000 linear system. Clearly, such large linear systems significantly increase the computational costs of solving the 3-D forward problem (Siripunvaraporn, 2012). This has resulted in a large variety of different algorithms and methods for efficiently solving the MT forward problem in 3-D (e.g. Mackie et al., 1994; Madden and Mackie, 1989; Newman and Alumbaugh, 1997) and only in the last ten years has it become computational feasible to solve model spaces with sizes of geologic interest (e.g. Egbert and Kelbert, 2012; Siripunvaraporn, 2012). While most common forward modelling algorithms use finite difference methods, there are also finite-element methods (e.g. Grayver, 2015; Wannamaker et al., 1986), integral methods, (e.g. Avdeev, 2005) and more complicated mesh structures (e.g. octree meshes; Heagy et al.,

2017). These other methods are often more difficult to implement and/or more computationally expensive and so they have not gained as much widespread use (Miensopust et al., 2013).

4.5 ESTIMATING THE MAGNETOTELLURIC IMPEDANCE TENSOR FROM FIELD DATA

4.5.1 Electromagnetic Source Signals

To create an image of the subsurface resistivity structure using an EM geophysical method, an EM source must be present which propagates into the Earth and induces secondary EM fields in the Earth. In any geophysical application, the source can be either active or passive. Active means that the source is created during the experiment and is well-characterized in time, space and mathematical description. This type of source is used in most EM geophysical methods (e.g. time-domain EM, controlled-source EM, loop-loop EM; see Telford et al., 1990). A passive method means that the source is naturally-occurring and often poorly known or difficult to describe mathematically. MT is relatively unique in that it is one of the few EM geophysical methods that rely on a passive EM source.

In MT, the source fields arise from two phenomena: (1) interactions of the solar wind with the Earth's magnetic field and (2) global lightning activity. The incoming solar wind consists of high-velocity charged particles. When these particles hit the Earth's magnetosphere they are deflected and result in complex currents of ionized plasma located in the Earth's ionosphere with greater complexity near the equator and near the poles. These high-velocity charged particles create EM waves which propagate downwards and into the Earth. Variations in solar activity results in different classes of perturbations some of which are daily signals (e.g. *Sq*), caused by solar storms (e.g. *Dst*), and caused by magnetospheric pulsations (e.g. *Pc3*, *Pc5* etc.) (see Viljanen, 2012 for a review). All of these sources generally result in perturbations which fluctuate with frequencies <1 Hz. Higher frequency signals >1 Hz used in broadband MT come from global lightning activity and resulting Schumann resonance in the atmospheric waveguide between the Earth and the ionosphere (Viljanen, 2012). A lightning strike is analogous to a massive antenna that radiates EM energy into the waveguide and the EM energy is amplified in the waveguide due to the resonance effect. Principal Schumann resonances occur between 7 Hz and 30 Hz (Sentman, 1996).

The solar wind disturbances and global lightning strikes are fundamentally random and their location, amplitude, and wavelet shape are unknown. As shown in Section 4.3, the MT method circumvents these unknowns by assuming that a) the source is far enough away that it can be approximated as a plane

wave at the surface (Madden and Nelson, 1964; Price, 1962), and b) the angle of refraction at the air-Earth interface is so great that the incident wave can be approximated as propagating vertically into the Earth. The assumption of a uniform, planar source is most valid at mid-latitudes where complex polar and equatorial electrojets are not present. MT modelling and field data which includes source effects has shown that discrepancies can be significant (e.g. Lezaeta et al., 2007; Viljanen et al., 1999).

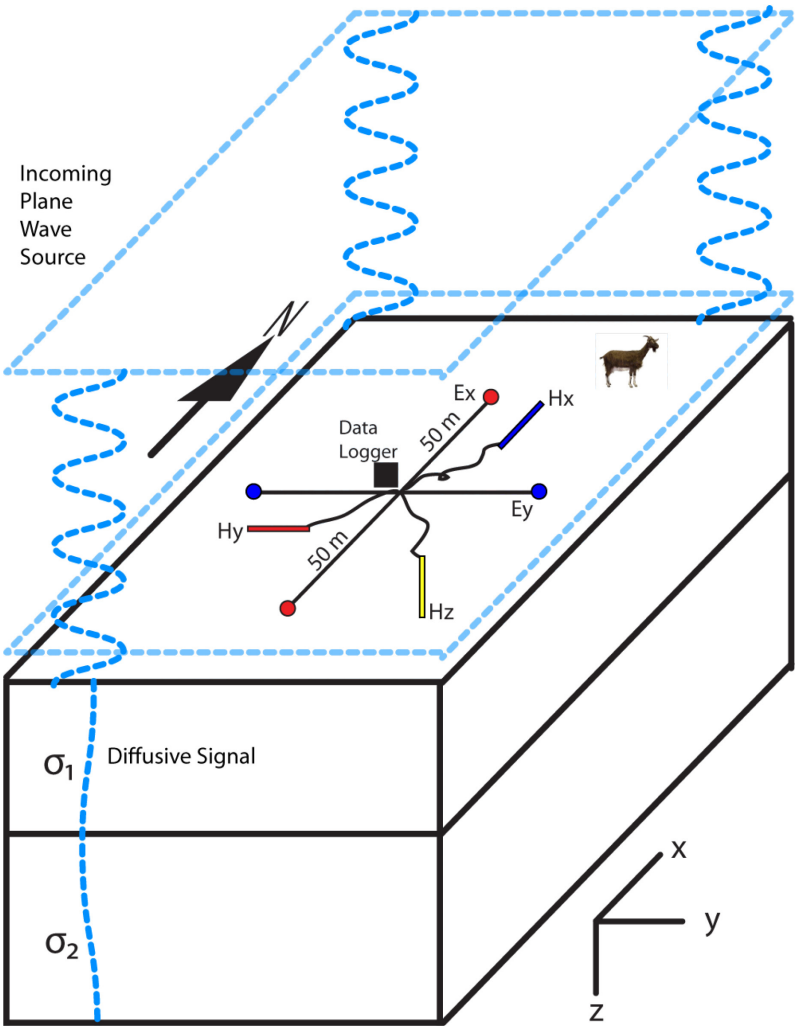

Figure 4.6: Schematic diagram of an MT site with TE mode (red) electric dipoles and induction coils and TM mode (blue) electric dipoles and induction coils. The vertical induction coil (yellow) measures the z-component of the magnetic field. Dipoles are generally 100 m in length with a data logger in the center. The incoming source wave is assumed to be a plane wave everywhere parallel to the Earth.

4.5.2 Magnetotelluric Instrumentation

In order to collect MT data, it is necessary to measure the natural time-varying electric and magnetic fields at the surface of the Earth. These measurements are the vector sum of both the primary source fields and the secondary fields induced in the Earth. Both the electric and magnetic fields are vector fields so multiple components are measured. An idealized site layout is shown in Figure 4.6. Usually the north-south and east-west electric and magnetic field components are measured simultaneously as well as the vertical magnetic field. This gives a total of 5 components. The site set-up may be rotated to make installation easier, as long as the electric and magnetic fields remain orthogonal. The fields can be mathematically rotated to the geographic co-ordinate system used for subsequent analysis. A given electric field component (e.g. the north-south component) is calculated by measuring the voltage between two buried, non-polarizing electrodes separated by a known distance (e.g. 100 m) and forming a dipole (e.g. in the north-south direction). The electric field value is measured in volts per metre and voltages are usually on the order of millivolts. Electrodes are composed of an electrolyte mixture with a chemical composition that ensures stability over long time intervals with limited electrochemical interactions with the ground. Common electrode mixtures consist of lead-lead chloride ($Pb\text{-}PbCl_2$) or silver-silver chloride (Ag-AgCl) (Petiau, 2000). Electrodes need good ground contact with low contact resistance to enable low-noise measurements. The vertical electric field is not measured in the MT method partly because there is an assumption that the vertical field approaches zero at the surface and also because it is impractical to construct a 50 or 100 m dipole vertically.

The magnetic field can be measured using two different sensors: an induction coil or a fluxgate magnetometer. Induction coils consist of many thousands of turns of copper wire wrapped around a core with a high magnetic permeability (e.g. iron). The more turns of copper wire, the higher the sensitivity of the coil to the rate of change (i.e. time derivative) of the magnetic field (Stanley and Tinkler, 1983). As a trade-off, the more turns of copper wire, the heavier the coil. Because of this, practical induction coils are usually limited to periods <1000 s and are used primarily in broadband MT. An induction coil only measures one magnetic field component, so three orthogonal induction coils are needed to measure the north-south, east-west and vertical magnetic field components. In contrast, fluxgate magnetometers are much more sensitive to long-period magnetic field variations (e.g. >1000 s) and usually measure all three field components simultaneously. A fluxgate magnetometer works by driving an alternating current through one coil of wire which is wrapped around a ring core of

magnetically permeable material which undergoes magnetic saturation on each current cycle. On the opposite side of the ring is a second coil of wire which measures an induced current. If there is no external magnetic field, then both the input and output current will cancel. But if the magnetometer is in an external field then the currents will not cancel and the difference can be related to the strength of the external field (Primdahl, 1979). This effect is primarily sensitive to the amplitude of the external field rather than its derivative so the fluxgate is useful in measuring long-period signals which also generally have the largest amplitude (e.g. diurnal *Sq*). However, fluxgates cannot reliably measure periods <1 s because the amplitudes of natural signals are usually quite small at high frequency and thus the noise from the instrument degrades the signal quality (i.e. a poor signal-to-noise ratio). For both induction coil and fluxgate magnetometer, the magnetic field strength is measured in nanotesla (nT).

Both the magnetic field and electric field data are recorded in a data acquisition system which includes an analog-to-digital converter. Usually these converters sample the signal at variable rates depending on the frequency of interest, Nyquist aliasing considerations, and data storage. Common sample rates range from 1 Hz to 4096 Hz.

4.5.3 Auto- and Cross-Spectra

Given noise-free data, the solution to Equation (4.32) for the impedance tensor is given by

$$\mathbf{Z} = \left(\mathbf{e}\,\mathbf{b}^{\mathbf{H}}\right)\left(\mathbf{b}\,\mathbf{b}^{\mathbf{H}}\right)^{-1} \tag{4.41}$$

where $\mathbf{e} = [E_x(\omega) \quad E_y(\omega)]^T$ and similarly for $\mathbf{b}$. The **H** subscript denotes complex conjugate Hermitian, and the terms in parentheses are the cross- and auto-spectra, respectively (Chave and Thomson, 1989). Thus, in order to solve for the impedance tensor given collected time series data, we must convert these time series data to the frequency domain and compute auto- and cross-spectra.

A simplistic approach to convert the measured time series to the frequency domain would be to take the discrete Fourier transform (or fast Fourier transform) of a given component over the entire recording period with N time samples such that

$$E_x(\omega_m) = \sum_{n=0}^{N-1} E_x(t_n) e^{-i2\pi mn\Delta t/N} \qquad m = 0,1,\ldots N-1 \tag{4.42}$$

where $\omega_m = 2\pi/(N\Delta t)$, $E_x(\omega_m)$ is the complex Fourier coefficient for the m^{th} sample, ω_m, and $E_x(t_n)$ is the time series value at the n^{th} time sample, t_n. In Equation (4.42), E_x can be swapped for any of the 5 measured components and this equation maps the spacing in the time domain to the frequency domain.

However, a "brute force" Fourier transform such as this will give poor results because the MT source amplitudes are random in a wide-sense stationary time series (Cantwell, 1960). A random time-stationary series will result in similarly random Fourier coefficients (Blackman and Tukey, 1958). Therefore applying a simple fast Fourier transform to an entire $E(t)$ or $H(t)$ time series will not result in useful data and will instead be overwhelmed by random noise. The way to extract useful information from low-frequency EM induction data is to use spectral analysis to compute the power spectral density (e.g. auto-spectra) of the signal (Madden, 1964). This can be accomplished in a variety of ways but generally involves four steps: windowing, transforming, averaging (or smoothing), and stacking.

First, the time series for each field component is split into windows containing *L* data points. Each window is de-trended and tapered at the edges using e.g. a Hanning window or Slepian taper (Chave and Jones, 2012). Next, the Fourier transform is computed for each window independently to yield *L* complex Fourier coefficients for each window with a maximum frequency related to Nyquist at $1/(2\Delta t)$ and a minimum frequency of $1/(2L\Delta t)$. This generally results in a large number of linearly-spaced frequencies (e.g. 256). Because MT varies in logarithmic space and is dispersive with decreasing resolution with depth, it is only necessary to have 6 – 10 evaluation frequencies per logarithmic decade (Simpson and Bahr, 2005; Weidelt, 1972). An averaging procedure is performed in the frequency domain for each window to evaluate the frequency spectrum at only a few logarithmically-spaced frequencies. This is commonly done using kernel density estimation or the Parzen window method (Jones et al., 1989). Once the Fourier coefficients for each evaluation frequency are known for each window and each field component, all windows can be stacked together resulting in an auto-spectra at a given evaluation frequency. This can also be done to compute cross-spectra.

In order to get higher evaluation frequencies, shorter window lengths are used (i.e. smaller L). This results in more windows and more stacking which leads to more consistent and reliable spectra estimates. For lower frequencies (i.e. longer periods), much longer window lengths are required often coupled with cascade decimation whereby the number of data points in each window remains the same (e.g. 256) but data points are excluded (e.g. use every 2$^{\text{nd}}$, 4$^{\text{th}}$, 8$^{\text{th}}$, etc. data point) to make the window

length longer (Jones et al., 1989). The longest possible period that can be obtained is to use one window over the whole time series (i.e. let $L = N$). However, in this case, since only one window is used, no summation or stacking can take place and the estimate is very unreliable. In general, it is necessary to have at least 20 to 100 windows in order to obtain reliable estimates.

4.5.4 Least Squares vs. Robust Estimation Methods

The solution for the impedance tensor shown in Equation (4.41) is only true for exact, noise-free data (Chave and Jones, 2012). In real data, an unknown noise term is included which must be minimized. Sims et al. (1971) showed that a least-squares method for estimating the impedance tensor components results in six independent ways to estimate each tensor component using auto- and cross-spectra combinations. Two of the six equations are unstable, two are biased downwards by auto-spectra in the magnetic fields (which amplify noise) and two are biased upwards by auto-spectra in the electric fields.

The least-squares method works well and is the simplest method; however it has a series of assumptions which are often violated in MT. The primary assumption is that the error in the components is independent and Gaussian (Chave et al., 1987; Chave and Thomson, 1989). This may not be true given that cultural noise sources or source field effects may be present for a short duration and affect all the components leading to co-related errors. The second is that spikes in the data may lead to extreme outliers in the least-squares regression which are non-Gaussian in nature. This led to the development of "robust" methods using M-estimates or bounded influence estimators (Chave, 2017; Chave et al., 1987; Chave and Thomson, 2004; Egbert and Booker, 1986). These are automated schemes that decrease the influence of outliers by repeatedly calculating the residuals $\mathbf{r} = \mathbf{e} - \mathbf{b} \cdot \mathbf{Z}$ and updating $\mathbf{Z}$ by removing window estimates which do not pass some criterion. These more statistically-robust methods also have the advantage of producing more accurate estimates of error terms using the covariance matrix whereas least-squares give only general Gaussian noise estimates (Chave, 2017; Jones et al., 1989). Further updates include coherence sorting (an additional criterion as to when to exclude data; Egbert and Livelybrooks, 1996), additional smoothing constraints (Larsen et al., 1996). Chave (2017) provides a recent review of many of the methods.

4.5.5 Remote Reference Techniques

An additional way to minimize noise and biasing when computing tensor data using least-squares and or robust methods is to include magnetic field data from a remote site which was recording simultaneously

as the site currently being processed. This is known as the remote reference technique (Gamble et al., 1979) which was originally developed to remove upward and downward biases in least-squares estimates. This method works by removing auto-spectra from least-squares estimates and including magnetic field data from a remote site instead. This method only works when noise at the local station is uncorrelated from the noise at the remote station which can be surprisingly close for high frequencies (e.g. 200 m; Goubau et al., 1984). However, it must not be so far away that the planar source field is significantly different which can also be quite far (e.g. 215 km; Shalivahan and Bhattacharya, 2002).

4.5.6 Source Field Effects and Cultural Noise

An important assumption of MT is that the source is far away, random and planar. Robust processing measures are usually able to remove most source field effects but certain aspects may remain and lead to poor impedance estimates with significant scatter especially at long periods which have fewer time windows to stack. This is also significant when cultural noise sources (e.g. electric generating stations, DC train lines, etc.) are present which may be non-random and relatively close to the MT measurement location (Szarka, 1987). Assessing the level of noise present in an MT sounding and removing outliers is an important process to ensure high data quality.

4.6 ANALYZING MAGNETOTELLURIC IMPEDANCE AND TIPPER DATA

After field impedance tensor data are estimated using time-series analysis, it is typical to have 20 to 100 frequencies per site over a range of frequencies from 0.0001 to 1000 Hz depending on the instrumentation, length of recording, and quality or strength of source. A typical field campaign can range from 10 MT sites located along a profile to more than 300 MT sites located in a large array. Analysis of MT data is primarily focused on two questions regarding the dimensionality of the Earth structure. The first is whether the MT data are distorted in some way which violates any of the physical assumptions described in Section 4.3. The second is whether the dimensionality of an individual MT site (or an entire dataset) can be approximated, interpreted and modeled as 1-D, 2-D or 3-D. For example, if an MT sounding (or entire survey) can be approximated as 1-D, then it may not be necessary to undergo time-consuming 3-D inverse modelling. Distortion and dimensionality are related because distortion is often caused by 3-D features which are neglected in a 1-D or 2-D interpretation.

4.6.1 Causes of Distortion and Error

There are a range of sources of distortion and error in MT data. The MT method is built upon a variety of important assumptions (as discussed in Section 4.3). Often these assumptions hold within error and distortion effects can be ignored. An important assumption is that no free charges are present in the Earth and, if this assumption is violated, then galvanic distortion occurs. Often, one indication of distortion (or highly three-dimensional structure) is out of quadrant phases. One- and two-dimensional isotropic models with well-behaved source fields should result in phases between 0° and 90° for the xy mode and -90° to -180° for the yx mode. If one of the following distorting factors occurs, it may result in out of quadrant phases.

Local inhomogeneities: If an MT site is located in or near a small region of anomalously low or high conductivity which is beyond the ability for the highest sampled frequency to detect, this will lead to galvanic distortions in the observed data (Groom and Bailey, 1991; Wannamaker et al., 1984). This is the primary cause of most distortion because a small feature will create 3-D galvanic effects which are frequency-independent and can distort the larger-scale electric fields.

Point-source Measurement: The MT method assumes that the electric and magnetic field are being measured at a point when, in reality, an electric dipole often spans 100 m or more. As a result, different electrodes may be located in different geology. This results in distortion and bias in tensor estimates (Jones, 1988).

Topography: Similar to the above two factors, local topography can also influence the observed resistivity values. If an MT site is located on a hill or in a valley, electric currents may be weaker or stronger. These effects were investigated by Jiracek (1990) and Wannamaker (1986). Topography can also have an influence on a much larger regional scale as well. For example, valleys or coastlines can lead to a phenomenon known as current channelling, which distort the regional electric fields to preferentially flow in a particular direction (Jones, 1983).

Anisotropy: The vast majority of MT analysis and modelling implicitly assumes that the Earth is isotropic wherein conductivity measurement is a scalar independent of direction. In reality, experiments have shown that many rocks and common geological environments can be anisotropic (Guo et al., 2011;

Nover, 2005; Pommier, 2014). This means that a more accurate representation of the resistivity structure involves a 9-component tensor

$$\mathbf{P}(x,y,z) = \begin{bmatrix} \rho_{xx} & \rho_{xy} & \rho_{xz} \\ \rho_{yx} & \rho_{yy} & \rho_{yz} \\ \rho_{zx} & \rho_{zy} & \rho_{zz} \end{bmatrix} \tag{4.43}$$

with three principal components (ρ_x, ρ_y, ρ_z) that can be found by rotation of the tensor to the principal axes (Heise et al., 2006). If an anisotropic Earth is assumed to be isotropic, it can lead to incorrect interpretations of false conducting layers. For example, a uniform, anisotropic halfspace underlying a isotropic layer could see phase splits on xy and yx impedance components which are due to anisotropy but appear to indicate 2-D structure (Heise et al., 2006). Anisotropy can also lead to a deflection of induction vectors away from 2-D geoelectric strike (Heise et al., 2006). Anisotropic inversions for MT data do exist (e.g. Cao et al., 2018) but they are relatively new and not widely used.

In a perfect world, all these distortion effects could be accounted for by fully 3-D forward modelling which had a mesh on the centimeter-scale that could solve for local inhomogeneities, model the MT site as a non-point source, include high-resolution topography and solve for anisotropic resistivity models. However, current memory and computational restrictions necessitate a coarser mesh with interpolated topography, a point-source measurement and isotropic resistivity. As a result, MT field work, data analysis and inverse modeling must be carried out with the knowledge that the effects of distortion can be minimized but not removed completely.

4.6.2 D+ Methods

The D+ model discussed in Section 4.4.2 can be used as a useful interpretational tool to examine whether a dataset is consistent and reliable (Beamish and Travassos, 1992; Parker and Booker, 1996; Weidelt and Kaikkonen, 1994). If an MT sounding curve cannot be fit to a D+ model, this implies that something strange is happening at that site and more careful analysis is necessary. Data which do not fit a D+ model with low misfit should be checked to ensure that processing of the channels was carried out properly or if there were errors in field procedures. It is also a useful way to find outlier data points which do not conform to the smooth dispersive physics of MT (Weidelt, 1972). It is also possible that the poor fit is due to unique local or regional geology (e.g. significant 3-D effects, galvanic distortion, electrical anisotropy, etc.). Thus, the D+ model has been used as a useful interpretation and data quality tool in analyzing field MT data (Parker and Booker, 1996; Weidelt and Kaikkonen, 1994). It is often used

as a “first-pass” technique in assessing data quality and removing outliers and bad data points and finding processing or field procedural errors. Generally the D+ model is applied with a particular error level and if a particular MT data point lies outside the D+ response solution, it is an indication that this point may be an outlier.

4.6.3 Tensor Rotation

The MT impedance tensor defined in Equation (4.31) is a rank-2 tensor which can be rotated mathematically to any coordinate system. Any rank-2 tensor can undergo such a rotation by multiplying the tensor by a rotation matrix:

$$\mathbf{R} = \begin{bmatrix} \cos(\theta) & \sin(\theta) \\ -\sin(\theta) & \cos(\theta) \end{bmatrix} \tag{4.44}$$

where θ is the angle to rotate points clockwise in the xy plane. The rotated impedance tensor is given by

$$\mathbf{Z_R} = \mathbf{RZR^T}. \tag{4.45}$$

Often it is desirable to rotate the impedance tensor to a coordinate system different from the coordinate system in which the data was collected. Most often, data are collected and processed with the *x*-direction pointing to geomagnetic north and the *y*-direction pointing to geomagnetic east. However, if the geoelectric strike is determined to be at some angle east of north, then it may be desirable to rotate the impedance tensor to that coordinate frame to make a 2-D approximation more valid (e.g. minimize the diagonal components of the impedance tensor). This rotation will also make interpretation of data more intuitive since, in this coordinate frame, the approximation of the 2-D TE mode corresponds to the xy impedance component and the TM mode corresponds to the yx impedance component. A rotation of 90° has the effect of swapping the off-diagonal components. If 2-D modelling and interpretation is done, then it is necessary to rotate the impedance to the correct direction to avoid mixing modes.

4.6.4 Rotational Invariants

The impedance tensor components are dependent on the coordinate system they were collected in and often the geoelectric strike is not known with certainty beforehand. As a result, collected impedance data are ambiguous as to which component is the TE or TM mode, or if there is a mixing of modes. In the late 1980s and 1990s, there was a concerted effort to develop parameters of the impedance tensor which were independent of rotation (e.g. Berdichevsky and Dmitriev, 1976; Ranganayaki, 1984; Szarka

and Menvielle, 1997). These rotational invariants contained information about the impedance tensor that went beyond the apparent resistivity and phase, both of which are dependent on rotation. These invariants also opened up the door to analyzing the impedance tensor to find geoelectric strike direction, distortion parameters and dimensionality measures. It was shown conclusively by Szarka and Menvielle (1997) that the MT impedance tensor has 7 independent rotational invariants which can be summarized in a variety of ways such as the trace of the tensor, the sum of squares of the tensor and the determinant of the tensor.

Rotational invariants lead to an ability to assess the dimensionality of a given tensor because 1-D, 2-D or 3-D resistivity structure will have specific classes. For example, the Swift skew, κ, is a rotational invariant which can be used to determine if the resistivity structure has significant 3-D components:

$$\kappa = \frac{|Z_{xx} + Z_{yy}|}{|Z_{xy} - Z_{yx}|} \tag{4.46}$$

Convention states that if $\kappa > 0.3$ then there are 3-D induction effects present. Swift skew may not be able to assess the presence of small-scale distortions due to local inhomogeneities and may only be able to identify large-scale induction effects (Swift, 1967).

4.6.5 Tensor Decomposition

A more complete and rigorous mathematical description of distortion was described by Groom and Bailey (1989) and Groom and Bailey (1991) known as tensor decomposition. In this case, Groom-Bailey decomposition identified that any impedance tensor will have some amount of distortion present and they showed that the measured tensor can be decomposed into a "distortion tensor" and an "un-distorted tensor" along with a rotation matrix:

$$\mathbf{Z}_{obs}(\theta_r) = \mathbf{R}(\theta_r)\,\mathbf{C}\,\mathbf{Z_t}\,\mathbf{R^T}(\theta_r) \tag{4.47}$$

where $\mathbf{C}$ is the distortion tensor, $\mathbf{Z_t}$ is the undistorted impedance and θ_r is the regional geoelectric strike angle. This formulation recognizes that a 2-D regional inductive structure that was rotated to minimize the diagonal components would not recover the true geoelectric regional strike because additional galvanic distortions are "warping" the regional electric fields (Groom and Bailey, 1989). Their goal was to decompose the distortion tensor into determinable and indeterminable parts and this was accomplished by defining

$$\mathbf{C} = g\,\mathbf{T}\,\mathbf{S}\,\mathbf{A} = g\begin{bmatrix} 1 & -\tan(\theta_t) \\ \tan(\theta_t) & 1 \end{bmatrix}\begin{bmatrix} 1 & \tan(\theta_s) \\ \tan(\theta_s) & 1 \end{bmatrix}\begin{bmatrix} 1+a & 0 \\ 0 & 1-a \end{bmatrix} \quad (4.48)$$

Where θ_t is the twist angle (i.e. the local strike of a distorting inhomogeneity which is different from the regional strike), θ_s is the shear angle (i.e. the distortion of fields away from orthogonality), g is a multiplicative gain (i.e. a shift parameter) and a is an anisotropy factor (i.e. the ellipticity of the local inhomogeneity).

It was shown by Groom and Bailey (1989) that g is indeterminable while all other components are determinable and thus the undistorted impedance tensor can be recovered with an unknown multiplicative constant applied. When doing further analysis and modelling (especially 1-D or 2-D modelling), it is desirable to invert using the undistorted tensor estimate which excludes small-scale 3-D galvanic effects. The tensor decomposition discussed here results in a twist, shear, regional strike and anisotropy parameter for each frequency at each MT site. McNeice and Jones (2001) further developed tensor decomposition by introducing statistical methods to fit a more general twist, shear, strike and anisotropy for a range of periods and multiple sites. In this way, an overall average estimate of geoelectric strike can be found for all periods over an entire survey area. Groom-Bailey decomposition assumes that all the distortion is due to the electric currents with no distortion to the magnetic field. This assumption breaks down under certain conditions (Chave and Smith, 1994).

4.6.6 Static Shifts

This unknown gain parameter is known as a static shift and is a common effect produced by local inhomogeneities, topography and point-source measurements. Static shifts are caused by any multi-dimensional structure which has depths and dimensions which are less than the penetration depths of the source field. These result in multiplicative "shifts" to the entire apparent resistivity curve up or down independent of frequency because of excessive electrical current density near the inhomogeneity (Jones, 1988). This is because small inhomogeneities result in charges building up on surfaces and this violates the assumption that no free charges exist in the Earth (see Section 4.3.2 and Equation (4.11)). This can have significant implications and result in incorrect estimates of skin depth, sensitivity and true resistivity as shown by examples (e.g. Berdichevsky et al., 1998; Jones, 1988). Since tensor decomposition cannot determine the gain correction, there have been a variety of other methods proposed to remove static shifts such as regional averaging (Jones, 1988), using transient

electromagnetic soundings (TEM; Sternberg et al., 1988), or fitting for static shifts during inversion (e.g. DeGroot-Hedlin, 1991).

4.6.7 Phase Tensors

The decomposition of the distortion tensor as shown in Equation (4.48) is not the only way to perform a tensor decomposition and many possibilities exist (e.g. Bahr, 1988; Yee and Paulson, 1988). A particularly useful type of tensor decomposition is known as the phase tensor and was introduced by Caldwell et al. (2004):

$$\mathbf{\Phi} = \mathbf{X}^{-1}\mathbf{Y} \tag{4.49}$$

where $\mathbf{X} = \mathrm{real}(\mathbf{Z})$ and $\mathbf{Y} = \mathrm{imag}(\mathbf{Z})$.

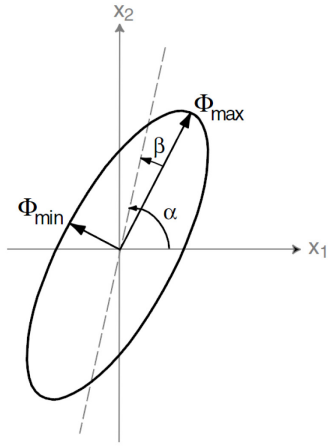

Figure 4.7: Schematic diagram of a phase tensor ellipse and the relation between minimum and maximum phase tensor singular values and the strike angle ($\boldsymbol{\alpha} - \boldsymbol{\beta}$). From Figure 1 in Caldwell et al. (2004).

The phase tensor has the useful property that it is unaffected by local distortions to the regional electric field. The phase tensor is a useful interpretational tool because it can be decomposed into a geoelectric strike angle, α, a skew angle, β, which measures the tensor asymmetry, and a maximum and minimum phase tensor values:

$$\mathbf{\Phi} = \mathbf{R}^{\mathbf{T}}(\alpha - \beta)\begin{bmatrix}\Phi_{\max} & 0 \\ 0 & \Phi_{\min}\end{bmatrix}\mathbf{R}(\alpha + \beta) \tag{4.50}$$

As shown in Figure 4.7, The maximum and minimum phase tensor components can be plotted as the maximum and minimum axes of an ellipse and plotted in map view with the entire ellipse rotated to the geoelectric strike ($\alpha - \beta$). The skew angle is a measure of dimensionality. If the phase tensor plot is a circle with $\beta = 0°$, this indicates 1-D structure while a phase tensor plotted as an ellipse with $\beta = 0°$

indicates 2-D structure. If $\beta \neq 0°$, this is an indication of quasi-2-D or 3-D structure. In general, if $\beta > 3°$, it can be assumed that 3-D inductive effects dominate (Booker, 2014).

4.7 INVERSION OF MAGNETOTELLURIC DATA

4.7.1 Basics of Geophysical Inversion

The dimensionality analysis described in Section 4.6 provides some useful information about the geoelectric structure of the Earth beneath the survey area. However, all the above data analysis and data interpretation involve impedances as a function of frequency (e.g. $Z(\omega)$) and not as a function of depth within the Earth.

The primary goal of most MT investigations is to map the subsurface structure in terms of electrical resistivity as a function of position (e.g. $\rho(x, y, z)$). The impedance data at a particular frequency are sensitive to a volumetric average of the true resistivity structure within a hemisphere beneath the measurement point with a radius of the skin depth for that particular frequency. As discussed in Section 4.4, given a known model of the Earth, predicted MT data can be calculated by passing the model through a forward modelling operation:

$$\mathbf{d_p} = F[\mathbf{m}] \tag{4.51}$$

where $\mathbf{d_p}$ is a vector of predicted data (e.g. real and imaginary impedance values), $\mathbf{m}$ is a vector of model parameters (e.g. resistivity values defined at cell centers on a 3-D mesh), and F is the forward operator (e.g. some finite difference algorithm). This process takes a known model in $\rho(x, y, z)$ and computes a unique set of impedance values, $Z_{ij}(\omega)$, for that model.

The opposite process which takes observed data, $\mathbf{d}$, and solves for an unknown model, $\mathbf{m}$ is known as a geophysical inverse problem:

$$\mathbf{m} = F^{-1}[\mathbf{d}] \tag{4.52}$$

In the MT case, the solution takes $\mathbf{d} = [Z_1, Z_2, \dots Z_N]$ and solves for $\mathbf{m} = [\rho_1, \rho_2 \dots \rho_M]$. In this notation, there are $2N$ independent data parameters (real and imaginary impedances) and M model parameters equal to the number of cell centers in a finite difference (or finite element) mesh.

In many geophysical applications, including MT, the inverse problem is non-unique and non-linear (Parker, 1994). Non-uniqueness means that for a given dataset there is an infinite set of models that can fit the data

$$F^{-1}[\mathbf{d}] = \{\mathbf{m}_1, \mathbf{m}_2, \mathbf{m}_3 \dots\} \tag{4.53}$$

This is because of three reasons: 1) The physics of the MT problem implies an inherent non-uniqueness between conductivity and thickness (or volume); 2) Most realistic MT inverse problems have $M > N$ such that there are more unknown model parameters than known data values and; 3) All real field data contains an error term such that $\mathbf{m} = F^{-1}[\mathbf{d} + \mathbf{e}]$ (Parker, 1977). The non-uniqueness of the inverse problem means that any model is only an approximation of the true Earth structure and care must be taken in finding an inverse model which best represents the Earth.

The non-linearity of the problem implies that there is no linear operator matrix that can be formed which multiplies the model vector to find the data vector (e.g. there is no $\mathbf{G}$ operator which satisfies $\mathbf{d} = \mathbf{G}\mathbf{m}$). Non-linear problems are, in general, much more difficult to solve than linear problems and most methods seek to linearize the problem prior to finding a solution.

4.7.2 Tikhonov Regularization

There are a range of different inversion methodologies employed in setting up the MT inverse problem. A particular modelling philosophy which has guided MT inverse methodology is to use minimum-structure models which seek to minimize data misfit and model smoothness balanced by a user-defined regularization parameter (Egbert and Kelbert, 2012; Heagy et al., 2017; Siripunvaraporn, 2012):

$$U(\mathbf{m}, \tau) = (\mathbf{d} - F[\mathbf{m}])^T \mathbf{C}_\mathbf{d}^{-1} (\mathbf{d} - F[\mathbf{m}]) + \tau (\mathbf{m} - \mathbf{m_0})^T \mathbf{C}_\mathbf{m}^{-1} (\mathbf{m} - \mathbf{m_0}) \tag{4.54}$$

where U is the function to be minimized, $\mathbf{m_0}$ is some initial reference model, τ is the regularization parameter[4], and $\| \quad \|_2 = (\ )^T(\ )$ denotes the L2, Euclidean norm. Here, $\mathbf{C_d}$ is the data covariance matrix (i.e. diagonal matrix containing data errors) and $\mathbf{C_m}$ is the model covariance (i.e. a matrix that enforces smoothness via derivatives or weights). This methodology is known as Tikhonov regularization or damped least-squares (Heagy et al., 2017). There are a variety of ways to define the model

[4] The regularization parameter often goes by a variety of names including τ, λ, or ν among others (Kelbert et al., 2014; Parker, 1994; Robertson et al., 2020; Rodi and Mackie, 2001).

smoothness term (i.e. the second term in Equation (4.54)) and some authors have used a second-difference approach rather than a more general model covariance matrix (e.g. Rodi and Mackie, 2001).

This method avoids solutions which are arbitrarily rough and contain artefacts while still fitting the data. The D+ model discussed in Section 4.4.2 is the opposite extreme scenario of a maximum-roughness model with sharp spikes in conductivity. In reality, the Earth is neither smoothly varying, nor is it composed of sharp spikes but the minimum-structure philosophy of inverse modelling and Tikhonov regularization has formed the basis of nearly all MT inversion algorithms. This is partly because the diffusive physics of MT implies that sharp boundaries cannot be resolved anyway, so it is better to interpret smooth models (Constable et al., 1987).

4.7.3 A Review of Inversion Algorithm Methodologies

There are two general steps that need to be carried out in order to solve the inverse problem. The first is deciding which algorithm should be used to minimize Equation (4.54) and the second is how to efficiently compute the relevant derivatives (e.g. gradient, Jacobian, Hessian) for the chosen algorithm. There are two primary classes of algorithms used to minimize Equation (4.54): Gauss-Newton (GN), and Non-linear Conjugate Gradients (NLCG) (Siripunvaraporn, 2012). In its simplest expression, the GN method involve taking the derivative of $U(\mathbf{m}, \tau)$ with respect to $\mathbf{m}$ and setting the derivative to zero then re-arranging algebraically into a linear form which can be solved iteratively from some initial guess, $\mathbf{m_0}$ (Egbert and Kelbert, 2012):

$$\mathbf{\Delta m}_k = \left(\mathbf{J^T J} + \tau \mathbf{I}\right)^{-1} (\mathbf{J^T r} - \tau \mathbf{m}_k) \tag{4.55}$$

where $\mathbf{r} = \mathbf{d} - F[\mathbf{m}]$ is the residual and $\mathbf{J}$ is the Jacobian defined as

$$\mathbf{J}_{ij} = \frac{\partial (F[\mathbf{m}])_i}{\partial m_j} \tag{4.56}$$

The Occam's inversion method of Constable et al. (1987) uses a modified form of GN which solves the system in one step given an initial model and initial misfit rather than iteratively solving the system (Siripunvaraporn, 2012). GN methods and variants are also used by Haber et al. (2000) and Siripunvaraporn and Egbert (2009) among others. GN methods are susceptible to local minima and must explicitly define and store the Jacobian matrix in memory, making this method difficult to implement for larger, 3-D problems.

The NLCG method is more commonly used because of its speed and computational efficiency (e.g. Kelbert et al., 2014; Newman and Alumbaugh, 2000; Rodi and Mackie, 2001). Like GN, NLCG works by finding the derivative of Equation (4.54) with respect to $\mathbf{m}$. This gradient, $\mathbf{u}_k$, is then used to calculate a new search direction to more rapidly converge to the solution

$$\mathbf{m}_{k+1} = \mathbf{m}_k + \alpha_k \mathbf{u}_k \tag{4.57}$$

by finding some step length, α_k, which minimizes the right-hand side (Siripunvaraporn, 2012). This method saves memory by never explicitly storing the Jacobian in memory but is no faster than GN. A schematic of this solution-finding approach is shown in Figure 4.8.

Other less commonly used methods include the Quasi-Newton method (e.g. Haber, 2005), q-q plotting (e.g. Matsuno et al., 2014), and Bayesian methods (e.g. Chen et al., 2012) but none of these have yet gained widespread use and many have primarily been applied only to 1-D or 2-D inverse problems. In this thesis, the NLCG is used for both 2-D and 3-D inversion modeling.

4.7.4 Joint Inversion Methods

A joint inversion is a method of combining multiple datasets into a single interpretable model. This can be done in a variety of ways. The most direct approach is to combine the two datasets into a single inversion algorithm while a less direct approach uses the result of one inversion model from one dataset to constrain the model of a different dataset (Moorkamp, 2017).

In MT, it is common and relatively easy to combine other EM methods in a direct joint inversion. It is common to include vertical magnetic transfer functions in a joint inversion (e.g. Siripunvaraporn and Egbert, 2009). It is also possible to include other EM methods such as airborne EM surveys (e.g. Lee et al., 2018) or controlled source EM (e.g. Key, 2016). Combining non-EM data (e.g. gravity or seismic data) generally requires a less direct approach because the geophysical attributes being measured (e.g. density or seismic velocity) obey different physics and respond to different geological parameters. A common approach is to use cross-gradients between models to find similar model structure in two datasets (e.g. Gallardo and Meju, 2011, 2003; Gao and Zhang, 2018) or genetic algorithms to find solutions which match both datasets (e.g. Moorkamp et al., 2010).

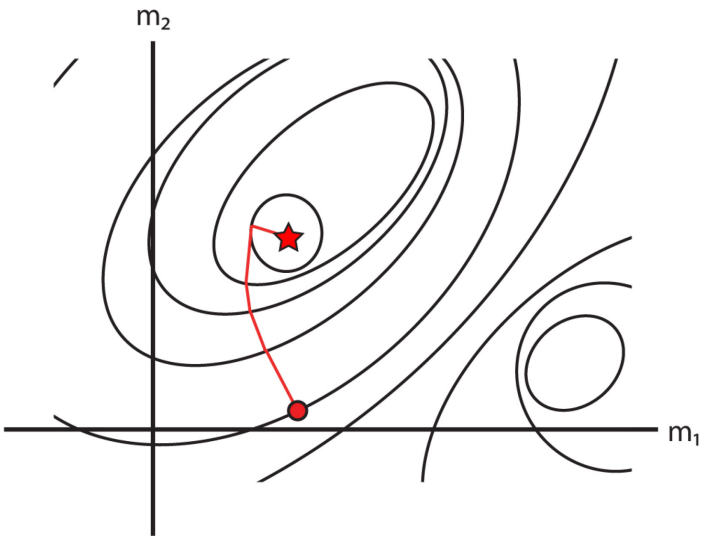

Figure 4.8: A schematic diagram of the solution-finding approach for the gradient-based NLCG algorithm. A simple two-parameter model space is shown where black ovals show contours of the cost function to be minimized. A global minimum is shown by the red star. A starting guess is given at the red circle. The algorithm computes the steepest descent direction (e.g. the perpendicular to the tangent) and then steps forward. This is repeated until the solution is found within some threshold.

4.8 SUMMARY

This chapter has provided an overview of the MT method beginning with the geological motivation to learn about the conductivity structure of the Earth. Different Earth materials have differing conductivity values by several orders of magnitude which makes it desirable to map and image specific targets (e.g. conductive sulphides for mineral exploration or partial melt in volcanological applications). The theoretical basis of MT method uses time-domain electric and magnetic fields collected at the surface of the Earth to infer subsurface conductivity structure. This is done by transforming orthogonal, horizontal electric and magnetic field components to the frequency domain and computing the Earth impedance tensor. The impedance tensor provides frequency-dependent information about the Earth which can be examined using data analysis techniques to assess the dimensionality and distortion present in the MT data. The final product of an MT data workflow, is a model of the Earth's conductivity structure as a function of depth and position. This is found using geophysical inversion techniques which generally seek spatially-smooth conductivity models which adequately fit the impedance tensor data within some threshold. The inversion model can then be interpreted geologically to make decisions regarding exploration targets, infer past geological processes, or assess seismic or volcanological hazards.

CHAPTER 5: MAGNETOTELLURIC STUDY OF THE LAGUNA DEL MAULE VOLCANIC FIELD, CENTRAL CHILE

5.1 INTRODUCTION

The Laguna del Maule Volcanic Field (LdMVF), central Chile is the primary target of study in this thesis. This chapter details that study and most of the material in this chapter is taken from Cordell et al. (2018) published in *Earth and Planetary Science Letters*. The Laguna del Maule volcanic field (36° S, 70.5° W) is located on the Andean range crest in the Southern Volcanic Zone in central Chile. It includes a high concentration of basaltic-to-rhyolitic lava surrounding Laguna del Maule (LdM) near the Chile-Argentina border (Figure 5.1; Andersen et al., 2017). A 200 km^2 area of LdMVF has been experiencing rapid upward ground deformation since at least 2007 as indicated by satellite obervations with InSAR and ground-based geodetic observations that include GPS (Feigl et al., 2014). InSAR deformation modelling suggests that an inflation source is located at a depth of approximately 5 km below lake surface which has been interpreted as the addition of material into the upper crust (Le Mével et al., 2016). Bouguer gravity data also show a large gravity low beneath the lake which has been modelled as a low density body at a depth of 2 to 5 km (Miller et al., 2017b) and surface wave and ambient noise tomography showed a low velocity zone at 2 to 8 km depth on the west side of the lake (Wespestad et al., 2019). Seismicity has been detected around LdM with prominent swarms to the southwest near the Troncoso fault at an average depth of approximately 2 km below sea level (Cardona et al., 2018). The distribution of lava flows, previous caldera eruptions, ground deformation, and gravity anomalies suggests that the LdMVF sits above a restless magmatic system which has the potential for large, explosive eruptions. This magmatic system is hypothesized to be a large, laterally-extensive crystal-rich mush zone with the observed inflation caused by mass addition from a deeper crystal-poor basaltic source (Andersen et al., 2018, 2017; Singer et al., 2014). Chapter 3 describes more background about the study area, geological setting, eruptive history, and ongoing geophysical and petrological studies being conducted at the LdMVF.

In this study, the focus is on the use of a passive electromagnetic geophysical method known as magnetotellurics (see Chapter 4) which was used to image the electrical structure of the LdMVF and

surrounding area. The magnetotelluric (MT) method has been previously applied at other volcanoes to identify magma bodies in the shallow crust, investigate deformation sources, and study shallow hydrothermal systems (e.g. Aizawa et al., 2014; Comeau et al., 2016; Heise et al., 2010; Muñoz, 2014). MT is suited to studying the LdMVF because it is able to locate zones of hydrothermal fluid and/or partial melt and place limits on the size and composition of inferred magma bodies.

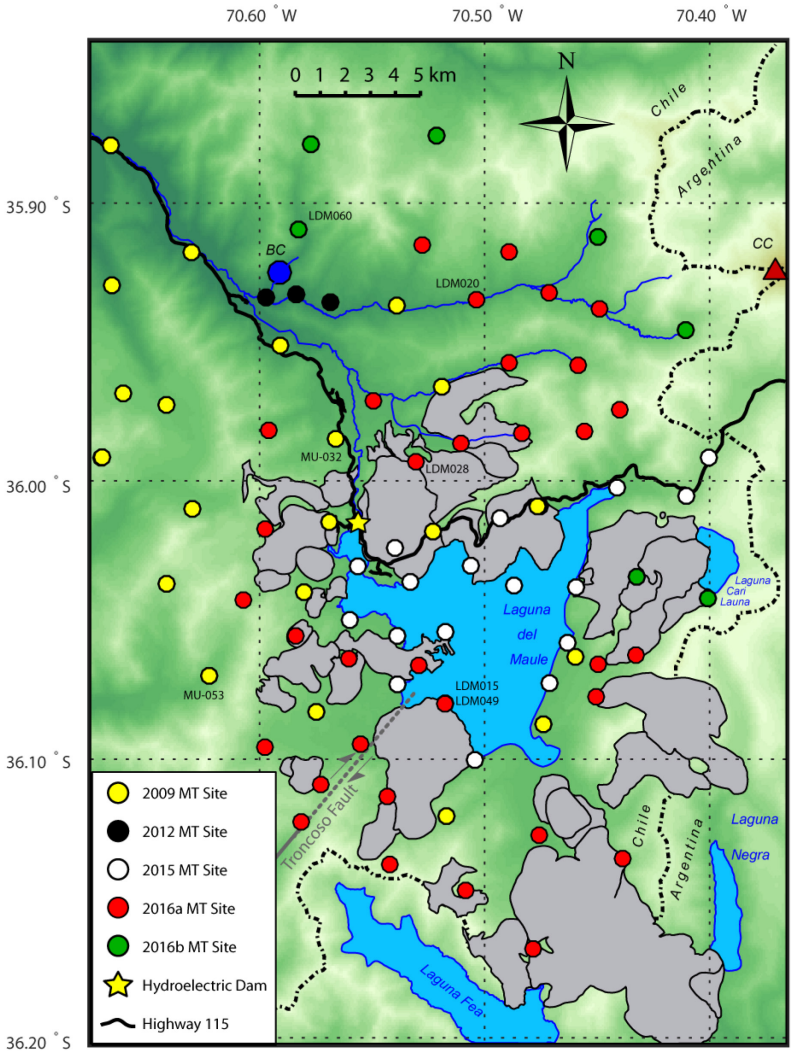

Figure 5.1: Map of the MT sites collected in the Laguna del Maule Volcanic Field study area between 2009 and 2016 shown as colored circles. Grey polygons are Pleistocene-Holocene lava flows (Andersen et al., 2017). The Troncoso Fault is a grey line with the inferred portion being dashed (Garibaldi et al., 2020). Sites which are mentioned in text are labelled. BC = Baños Campanario; CC = Cerro Campanario.

5.2 FIELD CAMPAIGNS

5.2.1 Previous Data

Prior to the project described in this thesis, Alterra Power Corporation purchased a geothermal exploration lease around the LdMVF and the Tatara-San Pedro (TSP) volcano. The lease and MT data are now held by Innergex Renewable Energy[1]. As part of their geothermal exploration program, Alterra Power Corporation collected 173 broadband MT sites (Site names: MU-XXX) between 2009 and 2012 focused primarily on the TSP geothermal prospect (Hickson et al., 2010; see Chapter 3, Section 3.9). However, 20 MT sites from the survey 2009 and 2010 surveys were located within the LdMVF study area (e.g. east of 70.67°W; Figure 5.1). These 20 sites were collected using five-component (E_x, E_y, H_x, H_y, H_z), GPS-synchronized Phoenix MTU-5A instruments, 100 m telluric dipoles, and Pb-$PbCl_2$ electrodes. A fixed remove reference station continuously recorded near Cerro Campanario (CC). Data were recorded for approximately 24 hours at each site and time series were processed using robust, remote referencing techniques with additional smoothing constraints (Larsen et al., 1996). Usable impedances spanned a bandwidth of 0.003 to 300 Hz. The impedance data for all MT sites were generously provided for this thesis project, but time series were not available. As such, it was not possible to re-process the time series data.

5.2.2 Field Season In 2015

During the austral autumn of 2015, field work was conducted by the University of Alberta and the Universidad de Chile. This field season lasted three weeks and was primarily focused on acquiring a small number of stations around the inflation center within the LdM basin to improve coverage beyond the 20 sites previously collected by Alterra. The LdMVF is relatively remote and mountainous with only one road along the north shore of the lake making logistics difficult. Cabins located on the western side of the lake near the dam provided a base for all field work operations. To avoid the costs of shipping University of Alberta instruments to Chile, two Metronix ADU-07 MT instruments were borrowed from the Universidad de Chile along with MFS-07 induction coils (Figure 5.2a,b), EFP-06 Pb-PbCl electrodes (Figure 5.2c), and 80 - 90 m telluric dipoles (Figure 5.2d). Twelve 5-component MT sites were collected by boat along the shore of LdM as well as five sites accessed by truck along the road from the dam to the Argentine border (Figure 5.1). Average grid spacing was planned to be between 2 and 3 km and

[1] And previously held by Energy Development Corporation (EDC)

most MT sites were installed on sandy beaches or wind-eroded volcaniclastics deposits. Data were recorded for between 18 and 36 hours with mutual remote reference. In total, 17 broadband MT sites were collected in three weeks.

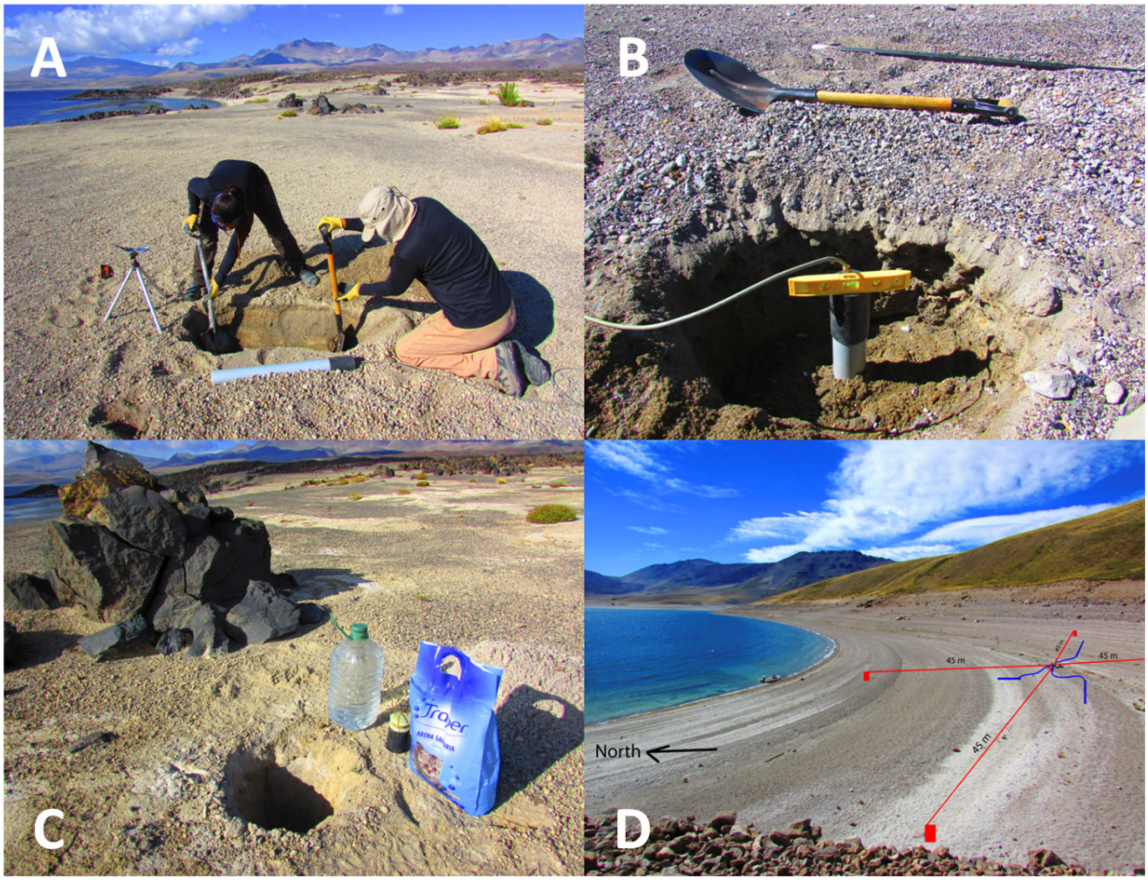

Figure 5.2: Field photos from the field season in 2015. (a) Digging the horizontal H_x induction coil at site LDM013; (b) The vertical H_z induction coil at site LDM013; (c) A hole for the electrode (black cylinder) with water and kitty litter to retain moisture at site LDM013; (d) Site layout on a beach with 90 m dipoles at site LDM006. The inflatable boat is parked on the beach for scale.

5.2.3 Field Season In 2016

After collecting the 2015 data, a second field season was planned to expand the grid to cover the entire LdM basin to the Argentine border and expand to the north and southwest. The 2016 field season lasted a cumulative 9 weeks between January and March. The first deployment lasted one week and used helicopter to access six remote locations on the southeast of the lake basin as well as two sites accessed by boat and hiking on the eastern side of the lake basin (2016a in Figure 5.1). The same equipment was used as in 2015. The second deployment lasted 6 weeks in February 2016. This deployment used horses

loaded with camping gear and MT equipment to access MT sites in the southwest LdM basin, Cajón de Bobadilla, and the Campanario Valley (2016a; Figure 5.1). For this deployment, the same instruments were used as before along with two additional Metronix ADU-07e instruments borrowed from the Pontificia Universidad Católica de Chile.

Figure 5.3: Field photos from 2016. (a) The mule (el burro) loaded with an MT site near Espejos; (b) MT site LDM043 accessed by helicopter in the SE lake basin; (c) Horses loaded with MT equipment in the Campanario Valley; (d) Horse adventures.

The use of horses was very challenging (e.g. Figure 5.3) and much slower than expected and some significant instrumentation issues and failures required several sites to be repeated. Furthermore, a damaged magnetometer made it difficult to measure the H_z component at several sites, limiting the

total number of measured vertical magnetic transfer functions. In general, 100 m dipoles were used, although some narrow valleys required shorter lengths which decreased data quality. Most sites were installed in valleys in sandy volcaniclastic sediments. Originally, the plan had been to install a total of 37 sites including sites in the Cajón de Troncoso. In total, only 22 sites were collected and these sites in the southwest were never reached. Two more sites were collected by boat between horse-trips.

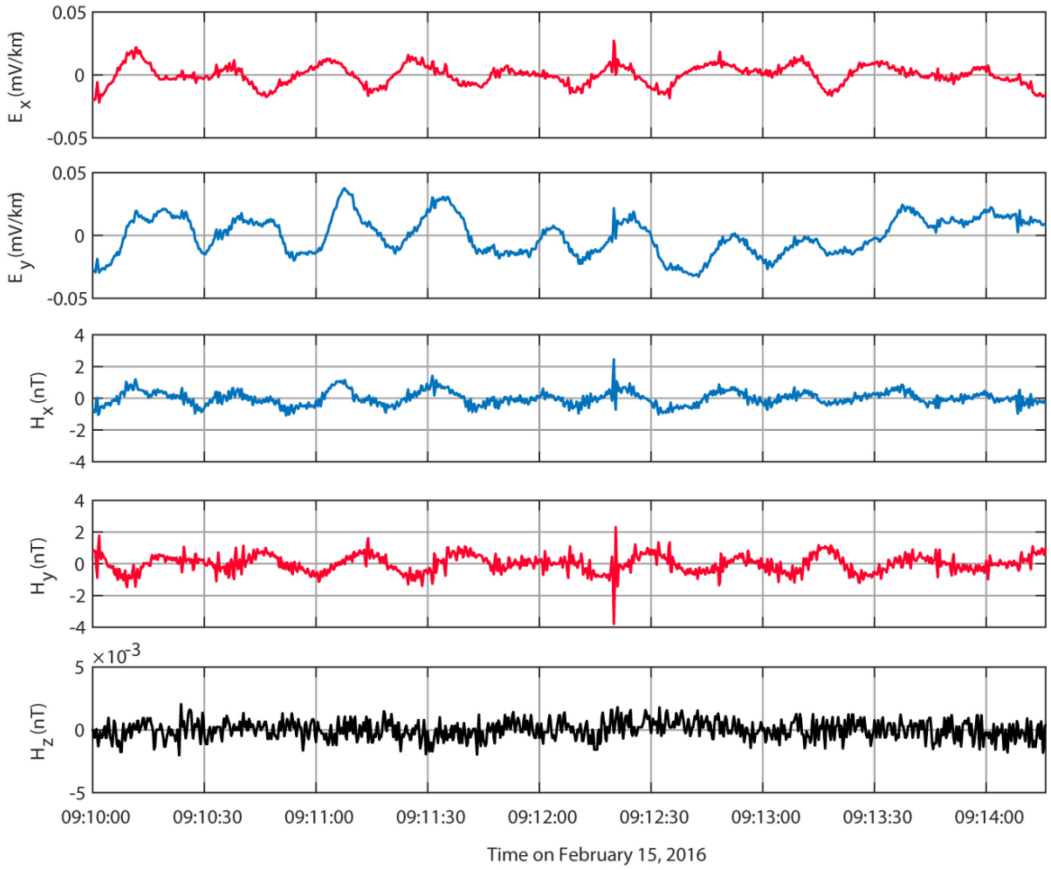

Figure 5.4: An example of time series data collected at Site LDM028 near the Espejos lava flow. The figure shows a 5 minute window from 9:10 AM to 9:15 AM on February 15, 2016. The red curves are fields associated with the xy mode and the blue curves are fields associated with the yx mode where x denotes north and y denotes east.

The final two-week deployment was carried out in March 2016 by collaborators at the Universidad de Chile using helicopter to access five remote sites north of the Campanario Valley and two sites near Laguna Cari Launa (2016b; Figure 5.1). In total, 39 broadband MT sites were collected in 2016. Between 2015 and 2016, a total of 56 MT sites were collected in 12 weeks (Site names: LDMXXX). Of the 56 sites, 46 sites included all five components (impedance plus tipper) while 10 sites collected impedance-only data. The difficult conditions and instrument issues meant that, on average, less than one MT site was collected per day. The full dataset (2009 through 2016) included 76 sites.

5.3 TIME SERIES PROCESSING

Raw MT time series data include 4 channels measuring the horizontal components of the electric and magnetic fields. A fifth channel to measure the vertical component of the magnetic field is optional and is used to produce vertical magnetic field transfer functions. An example time series from site LDM028 is shown in Figure 5.4 for a 5 minute recording window on February 15, 2016. This example shows field oscillations that have a period of approximately 15 to 30 seconds related to magnetospheric disturbances. There is also a high frequency spike in all field components around 9:12:15 am which is likely related to distant lightning activity. In general the magnitude of the vertical magnetic component is an order of magnitude smaller than the horizontal components meaning that the vertical component is much noisier. Each site's time series was converted to frequency-dependent impedance tensors using the Fourier transform and time series analysis (see Chapter 4). All 58 MT sites were processed using the robust method of Egbert and Booker (1986) with remote reference methods applied when possible. Much of the initial data analysis and inversions were done using these processed curves. In 2017, the data were re-processed using the robust method with smoothing constraints of Larsen et al. (1996) and remote reference methods were applied when possible. The re-processing was done to provide smoother, less noisy curves as well as to ensure that all the data (from 2009 to 2016) was processed using the same algorithm. Re-processing was carried out by CGG. Resulting impedance data covered a broad range of frequencies from 2600 Hz to 0.0003 Hz. After time series processing, 75 MT site impedances were available for use in the LdM project along with an additional 156 MT sites near TSP.

5.4 DATA ANALYSIS

5.4.1 Apparent Resistivity and Phase

Pseudo-section frequency slices of the determinant of the impedance tensor are shown in Figure 5.5 plotted as determinant average apparent resistivity and phase (Ranganayaki, 1984). The apparent resistivity is quite low (<10 Ωm) in both components at all frequencies in the area around the inflation center indicating relatively low resistivity at both shallow and deep depths. High phases at higher frequencies (10 Hz) around the inflation center indicate decreasing resistivity at shallow depth but lower phases at low frequencies indicate increasing resistivity at deeper depths. Low apparent resistivities and very high phases at low frequencies (<0.1 Hz) to the north of LdM suggest a strong conductor at depth to the north.

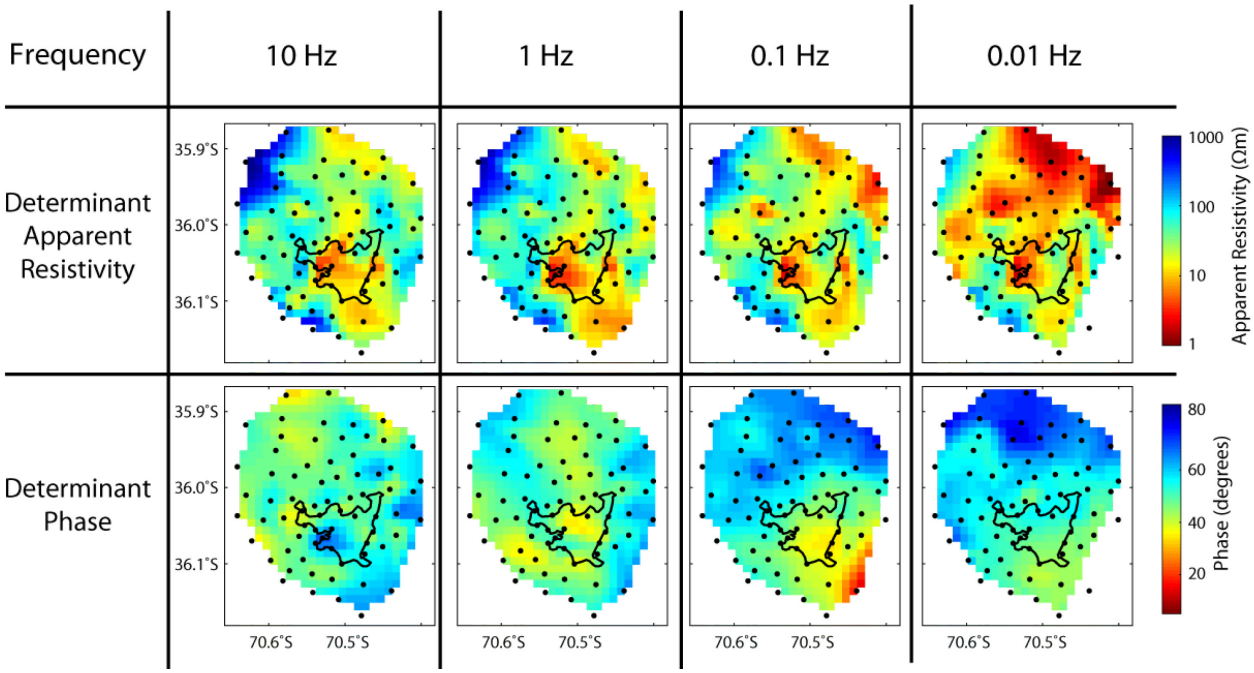

Figure 5.5: Each column shows data at a different frequency (10 Hz, 1 Hz, 0.1 Hz, and 0.01 Hz) for the MT sites used in the inversion. The two rows show the interpolated apparent resistivity (row 1) and phase (row 2) data for the determinant average of the complex impedance with red indicating areas of low apparent resistivity and low phase, respectively. Black dots indicate MT site locations. The outline of Laguna del Maule is given for reference.

Specific representative sites are chosen near the inflation center (LDM049), in the Campanario Valley (LDM020), and the Rio Maule valley (LDM028) shown in Figure 5.6. It is worth noting that the dataset is very heterogeneous with very few significant spatial trends between sites. Sites near the inflation center tend to have apparent resistivity curves which are decreasing from 100 Ωm down to near 1 Ωm around a frequency of 1 Hz. Below 1 Hz, the curves are flatter with some showing an increase and decrease. This suggests two conductors at depth, the first detected around 1 Hz and the second at deeper depths detected at less than 0.01 Hz. This is more pronounced in the phases as shown at site LDM049 (Figure 5.6). The sites near the lake are also very 1-D until approximately 1 Hz before becoming more 2-D or 3-D with off-diagonal phase splits and larger diagonal components.

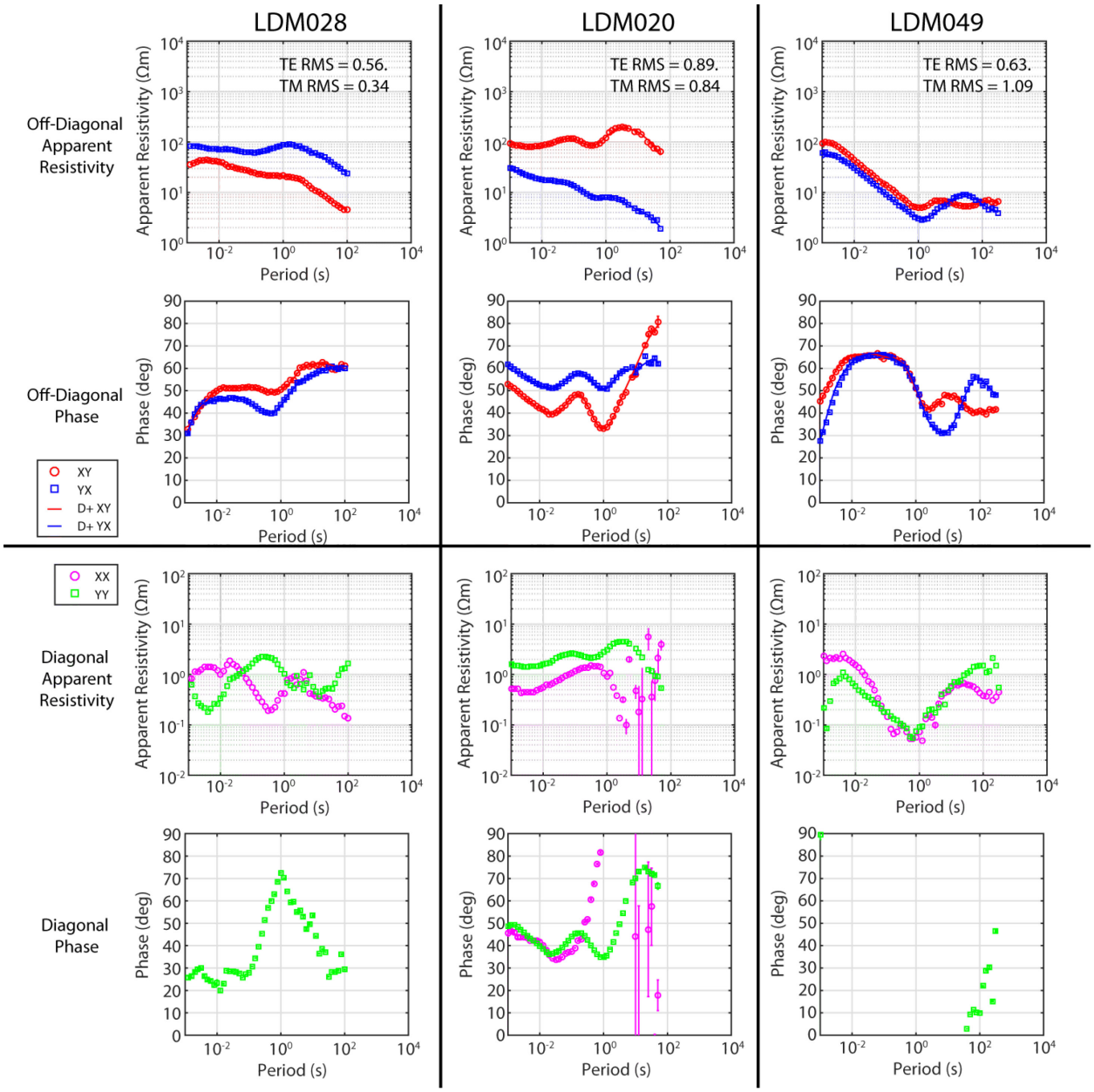

Figure 5.6: Representative apparent resistivity and phase curves for sites in the Rio Maule valley (LDM028), the Campanario Valley (LDM020) and the lake basin near the inflation center (LDM049). All site locations are shown in Figure 5.1.

Sites in the Campanario Valley tend to have apparent resistivity curves which decrease with decreasing frequency beginning around 100 Ωm and decrease to near 1 Ωm by 0.01 Hz. The effect is generally more pronounced in the yx impedance component as shown in LDM020. This suggests a conductor oriented primarily in the east-west direction. LDM028 is located in the Rio Maule valley near the Espejos lava flow. Similar to LDM020, both modes decrease from approximately 100 Ωm at high frequencies down

towards 10 Ωm at 0.01 Hz. However, here the decrease in apparent resistivity is more evident in the xy component suggesting that conductors are oriented in the north-south direction. Other sites in the Rio Maule valley have different characteristics and there is no clear trend for these sites.

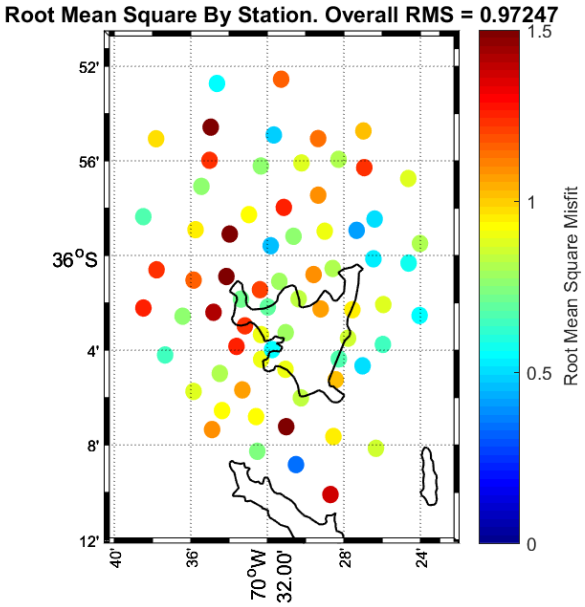

Figure 5.7: Root mean square (r.m.s.) data misfit for each station using D+ inversion solution to assess data quality. Poor data fit is found at several sites from 2009. An r.m.s. value of 1.0 is ideal as it suggests that the D+ model is, on average, neither over-fitting or under-fitting the data within error.

5.4.2 D+ Modelling

To assess data quality, D+ modelling was used to fit 1-D curves to each of the off-diagonal impedances at each site with representative sites D+ data fits shown in Figure 5.6. Because the D+ model is a minimum misfit model (Parker, 1980), it can be used to select an error floor which achieves a desirable misfit (e.g. an r.m.s. misfit of 1.0). The D+ model is unable to fit out-of-quadrant phases (i.e. when the phase lag between the electric and magnetic is greater than 90° or less than 0°). Out-of-quadrant phases can often occur in complex geologic environments which include anisotropy or current channelling (see Chapter 4). In assessing the apparent resistivity curves, it is clear that the LdM dataset has relatively few out-of-quadrant phases (see Appendix 1). Each site and each off-diagonal impedance component is fit individually, but the overall misfit can be computed for the entire vector of impedance data. Overall, data quality is good with low root-mean-square (r.m.s.) misfit near 1.0 when using a 2% error floor for the off-diagonal impedances for the entire dataset (Figure 5.7). Larger D+ misfit (e.g. r.m.s. > 1.5) is found at 3 stations (LDM060, MU-055, and MU-032) and it is worth noting that most of the higher r.m.s.

sites are from the earlier 2009-2012 data. Low D+ misfit values with small error floors are often, but not always, an indication of relatively smooth, low-noise impedance data (Parker, 2010). Special exceptions exist which violate D+ assumptions even when phases are in-quadrant but such examples have thus far been geologically unrealistic (Parker, 2010).

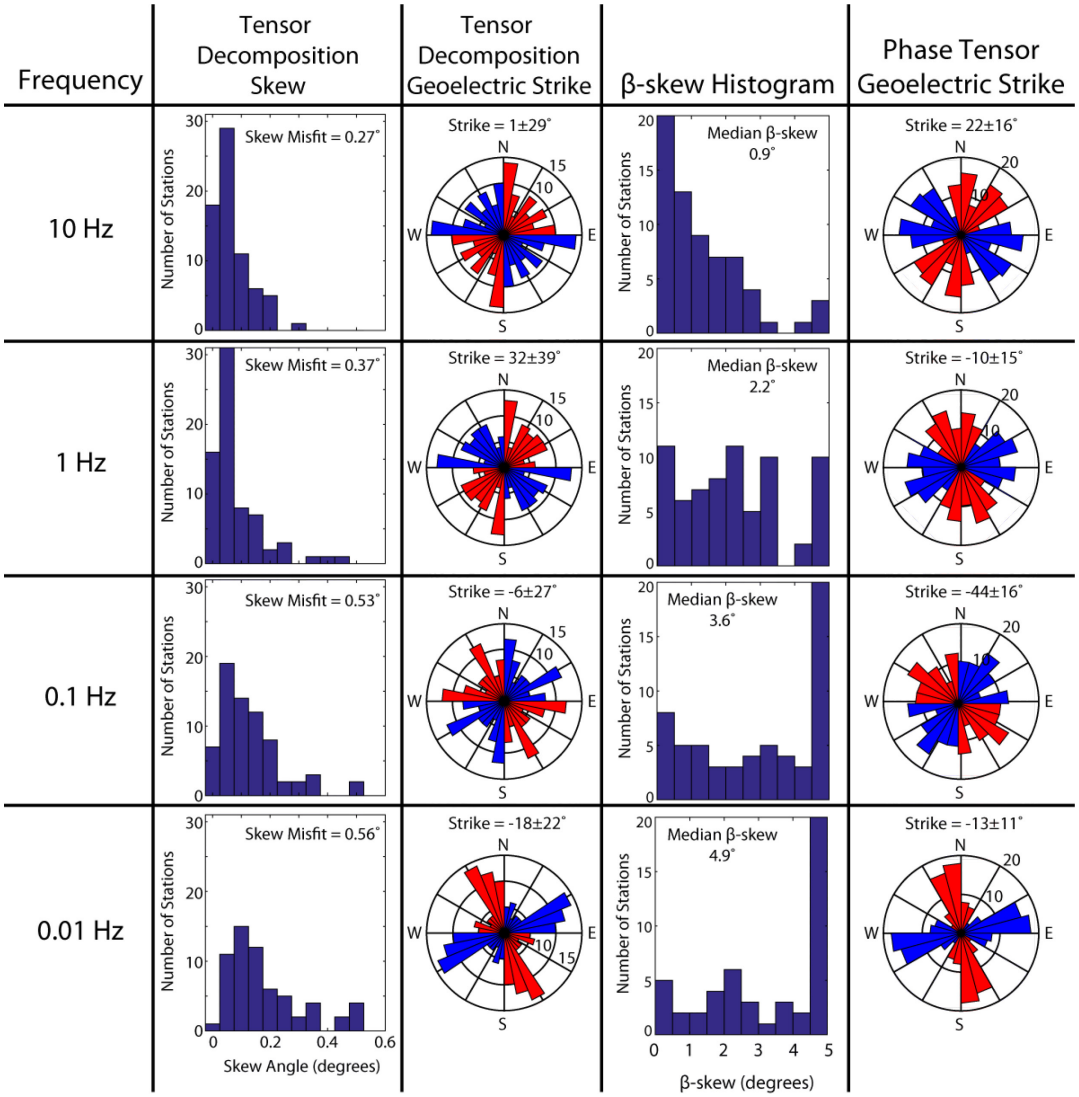

Figure 5.8: The directionality and dimensionality of the data based on tensor decomposition (McNeice and Jones, 2001) and phase tensor analysis (Caldwell et al., 2004). Each row shows data at a different frequency (10 Hz, 1 Hz, 0.1 Hz, and 0.01 Hz) for the MT sites used in the inversion. Tensor decomposition skew and tensor decomposition geoelectric strike are shown in the first and second column, respecitvely. High skew indicates more three-dimensional data. The third and fourth columns show the β-skew and geoelectric strike, respectively, derived from phase tensors. Weakly developed geoelectric strike and relatively high skew values suggest largely 3-D structures over the survey area.

5.4.3 Tensor Decomposition

The directionality of the MT data was investigated using the multi-site, multi-frequency tensor decomposition of McNeice and Jones (2001) and shown in Figure 5.8. This tensor decomposition provides a significant amount of information regarding the amount of distortion present in the data as well as the overall geoelectric strike. For the entire period range from 0.001 s to 1000 s, the overall strike is 15°±24° W of N. For the entire MT dataset, this suggests that the data are not overall 2-D because of the large error bar on the strike angle estimate. However, the Las Loicas trough is an extensional feature which trends approximately N15° W (Ramos et al., 2014) and perhaps this is the regional feature that the LdM MT data are sensitive to. In general the tensor decomposition skew is relatively low (e.g. <0.1°) suggesting that the MT impedance data are, on average, relatively undistorted by 3-D galvanic effects. However, looking at only longer period data, it is clear that 3-D effects are present at longer periods.

5.4.4 Phase Tensors

The dimensionality of the MT data was further investigated using phase tensor analysis of Caldwell et al. (2004) as shown in Figure 5.8. High beta-skew angles (>3°) at long periods (>10 s) suggest complex, three-dimensional (3-D) geoelectric structure at depth and necessitate a 3-D modelling approach (Booker, 2014). At very long periods (100 s), phase tensors indicate a weakly-developed strike of N13°W as shown in rose diagrams. This is similar to the geoelectric strike arrived at via tensor decomposition. In general both the phase tensor analysis and the tensor decomposition provide complimentary pictures of the dimensionality and directionality of the MT data. It is worth noting that the geoelectric strike of this dataset is in contrast to the N5°E regional geoelectric strike described by the 2-D MT study of Reyes-Wagner et al. (2017) at this latitude, which included data collection in the Central Valley and Cordillera Principal. This may be a further indication of a change in structural setting between the Cordillera Principal and the Las Loicas extensional trough in which the LdMVF is located (see Chapter 7; Ramos et al., 2014). At higher frequencies, there is no clear geoelectric strike direction in the data.

5.4.5 Induction Vectors

Induction vectors can be plotted to show gradients in conductivity where induction vector arrows point away from conductors in map view using the Wiese convention (Gregori and Lanzerotti, 1980; Figure 5.9). These arrows are generally quite small (~0.1) and scattered at short periods (e.g. <1 s) as there is a

very heterogeneous near surface structure depending on the site location. At approximately 3 s period, it is interesting to note that nearly all induction vectors around the lake point away from the center of the lake (i.e. the center of deformation). This suggests a conductive anomaly beneath the lake. Between 25 s and 80 s, the induction vectors almost uniformly point to the southwest which suggests a conductive anomaly at depth to the northeast. Between periods of 80 s and 200 s, the induction vectors turn to the north-northwest suggesting a conductive anomaly to the south-southeast. These complicated induction vectors show multiple different local and regional structures which varies greatly with increasing period. This further confirms that the data are very three-dimensional and lack a consistent geoelectric strike. Multiple regional and local conductive features at different locations must lead to this pattern of induction vectors.

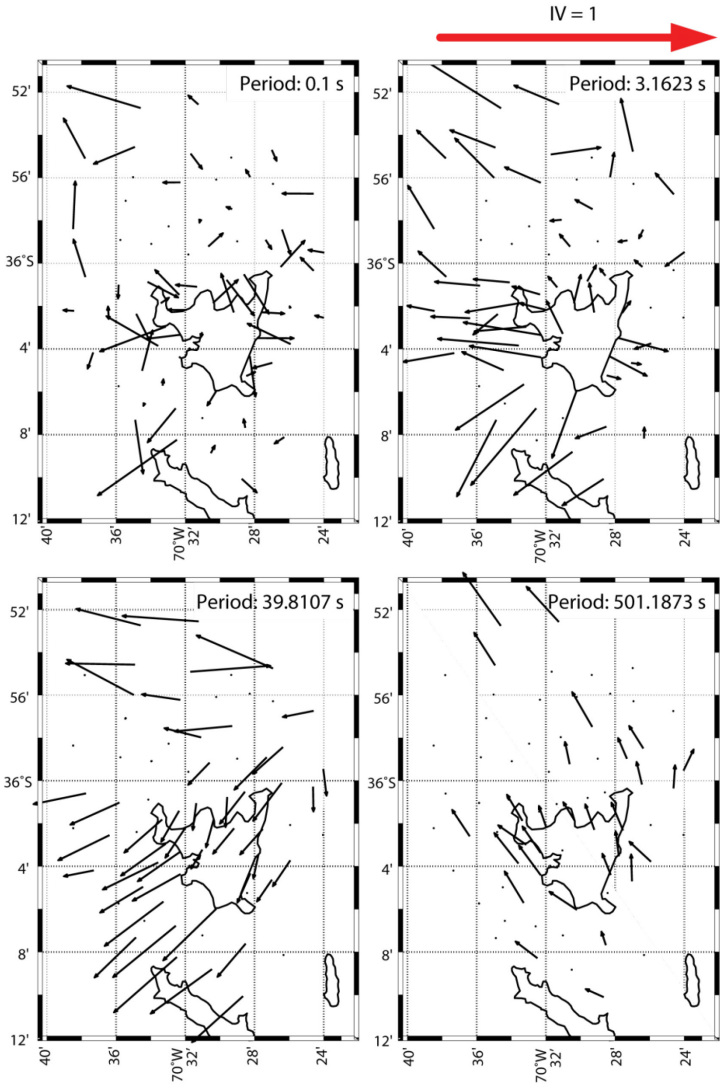

Figure 5.9: Induction vectors shown in map view at four different frequencies using the Wiese convention (i.e. induction vectors point away from conductors).

5.5 THREE-DIMENSIONAL MAGNETOTELLURIC INVERSION

5.5.1 Data Selection

As discussed below, several MT sites in the LdM basin from the earlier geothermal exploration were excluded. In the Campanario Valley, MU-094 and MU-096 were excluded because they are less than 2 km from MU-095, which was included. On the east side of LdM, MU-062 was a poor quality site from 2009 and in 2015, site LDM010 was collected to replace it. LDM038 and LDM027 were excluded due to poor data quality. In total, 71 sites were used for the three-dimensional MT inversion of the area of observed upward deformation including the lake basin and valleys to the north. Data were edited and quality controlled using visual examination of the apparent resistivity and phase curves to remove outliers with the aid of D+ models. After editing noisy data points, the longest period in the dataset was 2000 s. The shortest period used in the inversion is 0.001 s.

5.5.2 Inversion Parameters

The ModEM 3-D inversion algorithm of Kelbert et al. (2014) was used for all 3-D inversions at the LdMVF. The forward modelling uses finite difference methods to calculate the MT response of a 3-D resistivity model, and the inversion uses a non-linear conjugate gradient method to find a model that fits the measured MT data (Kelbert et al., 2014). Both diagonal and off-diagonal impedance components were inverted. Various parameters were investigated and the primary resistivity features of the model were largely independent of chosen parameters. Chapter 6 describes the inversion parameters and their effect on the inverse model solutions in more detail. The mesh shown has 500 m horizontal cells in the central region (35 km x 25 km) with 12 padding cells in each direction increasing geometrically to cover a 425 km x 425 km model space. Since the LdMVF is located more than 200 km from the ocean, and the longest period used was 2000 s, the ocean was not included in the model (see Reyes-Wagner et al., 2017 and Chapter 7 for a discussion of the ocean effect on regional data). Topography was included using cells with vertical thickness of 50 m. The model included over 2700 m of topographic relief in the central mesh with a maximum elevation of 3875 m a.s.l. and minimum elevation of 1175 m a.s.l. The vertical cells increased gradually in thickness to a maximum depth of 700 km. The entire model volume was 98 x 74 x 124 cells and the inversion was begun with an initial 100 Ωm halfspace starting model and a default model covariance length scale of γ = 0.3.

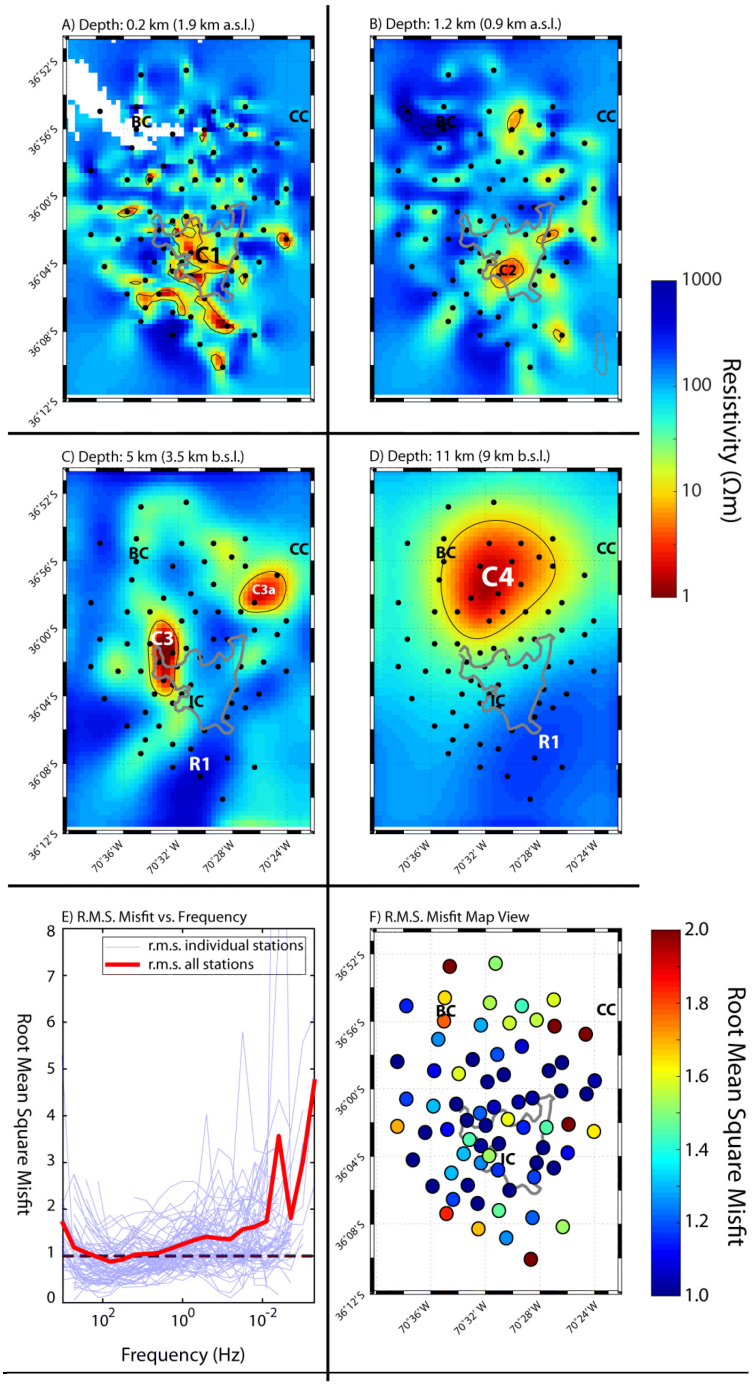

Figure 5.10: Preferred 3-D inversion model results shown using 4 horizontal slices through the model at depths of (A) 0.2 km below lake surface (b.l.s.), (B) 1.2 km b.l.s., (C) 5 km b.l.s., and (D) 11 km b.l.s. Major interpreted features are labelled C1, C2, C3, C3a, C4, and R1. BC = Baños Campanario; IC = Inflation Center; CC = Cerro Campanario; and the outline of the lake is given for reference. White space is air (above topography). The thin lines on each slice represent the 10 Ωm contour. (E) Graph shows r.m.s. misfit as a function of frequency for all stations (light blue lines) and overall (thick red line). (F) Map shows station locations with circles colored as the r.m.s. misfit value at each station. Blue corresponds to low r.m.s. misfit and red corresponds to high r.m.s. misfit.

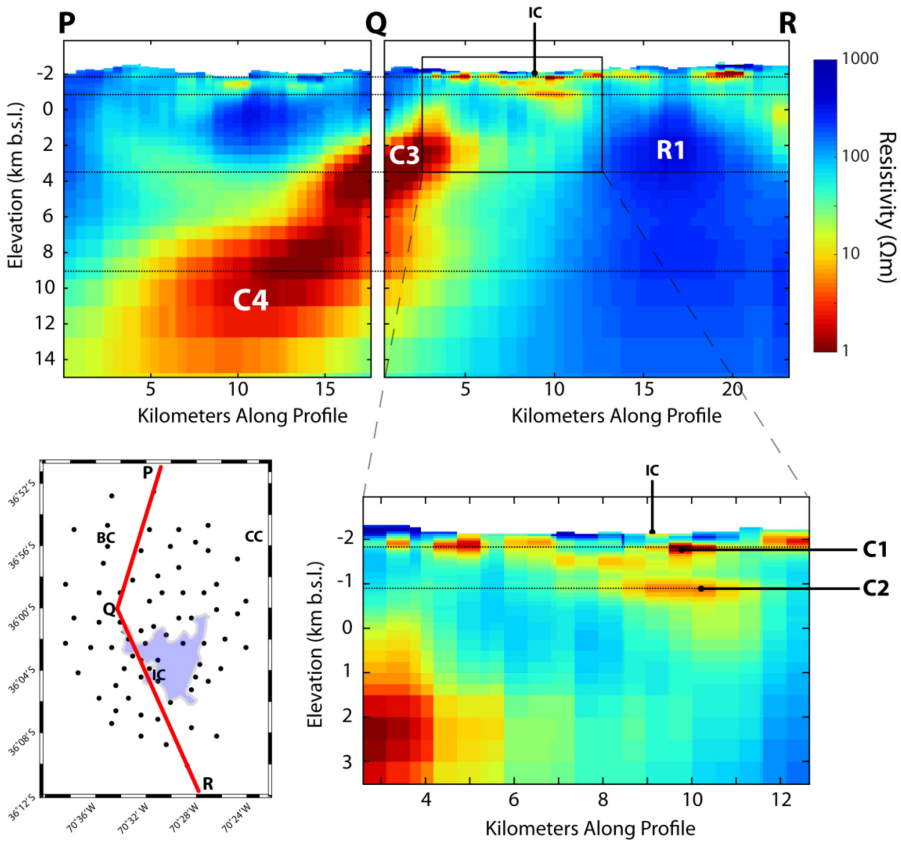

Figure 5.11: Preferred 3-D inversion model results shown using a fence diagram using two diagonal slices through the model along PQ and QR as shown in map inset. Black dots in the map inset denote MT sounding locations. Profile PQ cuts across major features C3 and C4. Profile QR cuts directly across the inflation center (IC) and shows the edge of C3, as well as C2 and C1. To show more detail of C1 and C2, a model inset is enlarged. The thin dashed lines through the profiles denote the depth locations of the horizontal slices shown in Figure 5.10. BC = Baños Campanario; CC = Cerro Campanario; White space at top of profile is air cells above topography surface

5.5.3 Preferred Inverse Model

The preferred 3-D resistivity model obtained from inversion of the full-impedance MT data is shown in Figure 5.10 and Figure 5.11. A satisfactory total r.m.s. misfit value of 1.46 was reached after 89 iterations using a 6% error floor (ϵ = 0.06) on all impedance components. The r.m.s. misfit is shown as a function of frequency and for each station in map view in Figure 5.10e and Figure 5.10f, respectively. All data curves with model fit are shown in Appendix 1. Higher r.m.s. misfit is generally found at stations on the edge of the array and at lower frequencies.

The resistivity model contains four primary anomalies with resistivity less than 10 Ωm. Depths to anomalies are cited as depth below lake surface of LdM (2165 m a.s.l.). Because of the diffuse nature of the MT signal, the depth to a given feature is best determined by the inflection point of a depth-resistivity curve rather than the point of minimum resistivity as shown in synthetic studies (Comeau et al., 2016). Other weaker conductive features (between 10 Ωm and 100 Ωm) are also present but these were often small, poorly constrained on the edge of the array, or weakly conductive and are not interpreted in the present work. The entire surficial geoelectric structure is inhomogeneous and influenced by topography and local geology immediately adjacent to the MT site locations (Figure 5.10a). The roughness of the surface layer may also be related to the inversion model generating structure to fit static shifts and related galvanic effects.

At shallow depths, the largest and most continuous feature is C1: a thin, near-surface, low-resistivity anomaly (<1 Ωm) at approximately 100 m depth (2.0 km a.s.l.). C1 is centered on the point of maximum observed inflation with additional zones of low resistivity to the southeast. C2 is a shallow, low-resistivity anomaly at approximately 1.0 km depth (1.1 km a.s.l.) which is also spatially coincident with the zone of maximum inflation (Figure 5.10b). It has dimensions of 4 km by 3 km and a minimum resistivity of 1 Ωm. C2 does not appear in all inversion tests and does not appear to be required in order to adequately fit the MT impedance data and thus may be an artefact.

To the north and northwest of the inflation center are two conductors (C3 and C4). C4 is the deepest low-resistivity feature in the model with a depth of 8 – 9 km (6 – 7 km b.s.l.) located beneath the Río Campanario Valley and Bobadilla Canyons (Figure 5.10d). The minimum resistivity of C4 is approximately 1.5 Ωm. From C4, two conductive lobes extend towards the surface. The first lobe (Espejos Conductor; C3), extends upward at 45° from the southwestern edge of C4, trending north-south beneath the Río Maule Valley (Figure 5.11). It terminates at a depth of approximately 3 km (1 km b.s.l.) beneath the western side of the lake. This feature has a strong conductive signature (<0.3 Ωm) and was previously identified using preliminary Alterra MT data (Singer et al., 2014). The second lobe (C3a) extends from the eastern edge of C4 and trends southeast, terminating at 3 km depth near the 160 ka Cerro Campanario stratovolcano (Hildreth et al., 1998). Unfortunately, C3a is on the edge of the array and is less conductive than C3, so it is difficult to interpret. The apparent connection between C4 and shallower features (C3 and C3a) may be partly due to diffusive smoothing of the inversion algorithm as resolution decreases with depth, but may be indicative of a geological connection. A regional two-

dimensional MT study of the electrical structure of central Chile at this latitude identified conductors at approximately the same location and depth as both C3 and C4 (Reyes-Wagner et al., 2017).

5.6 INTERPRETATION

5.6.1 Interpretation of Shallow Conductors

There are two main features (C1 and C2) directly beneath LdM and the region of rapid surface uplift. Since C1 is relatively shallow and spatially coincident with the lake bed, it is important to confirm that C1 is not due to free ions in the lake water. The electrical resistivity of the lake water was measured at four surface locations in 2017 and the measurements had an average value of 53±5 Ωm. This suggests the water is relatively fresh and fed primarily by snow melt, since most natural freshwater lakes have a range of resistivities from 10 - 50 Ωm where higher resistivity indicates low total dissolved solids (USGS, 2017). Therefore, considering the resistivity of the water is quite high, the lake itself cannot be the source of the conductive anomaly (C1). It is likely that this conductor is the result of conductive hydrothermal fluids and/or clay-bearing sediments similar to that found at other volcano-hydrothermal systems (Muñoz, 2014 and references therein). The resistivity is quite low suggesting either: 1) a high-salinity hydrothermal fluid; or 2) an altered smectite clay with high cation exchange capacity or some combination (Muñoz, 2014). If LdM were underlain by a shallow high-salinity reservoir, it would be expected that the lake water would be more saline due to fluid pathways between lake and shallow reservoir. As such, clay must play some role in the resistivity of the hydrothermal system and MT may be imaging the clay cap of the system. Smectite clay is indicative of the temperature of the hydrothermal fluid, with the smectite-illite transition occurring around 150°C. Illite is more resistive than smectite, so the low bulk resistivity of C1 suggests a reservoir temperature <150˚C (Muñoz, 2014). Heat and fluid may be supplied from the deeper conductive features C3 and C4 (see Section 5.6.2). The presence of hydrothermal fluids at depths of 1.5 km has also been confirmed by time-lapse gravity studies (Miller et al., 2017a). While it is unlikely that MT would be able to detect a thin opening related to the time-lapse gravity, the MT data may be detecting a more long-lived, shallow hydrothermal zone beneath the lake.

The MT model shows a relatively weak conductor (C2) at 1 km depth directly below the center of inflation but the feature does not appear in all inversion models. In general, MT requires that the conductance (i.e. product of thickness and conductivity) of an underlying layer is greater than the overlying layer in order to be detected with confidence (Jones, 1999). The maximum conductance of C1 is approximately 400 S. The maximum conductance of C2 is also 400 S and is therefore on the limit of

detection and, without further constraints, could be considered an artefact. Removing C2 has very little effect on data fit and is primarily constrained by only one station (LDM049). The anomalies C3 and C4 both have maximum conductance values >5000 S and neither underlie C1, so C1 has no effect on the imaging of these features.

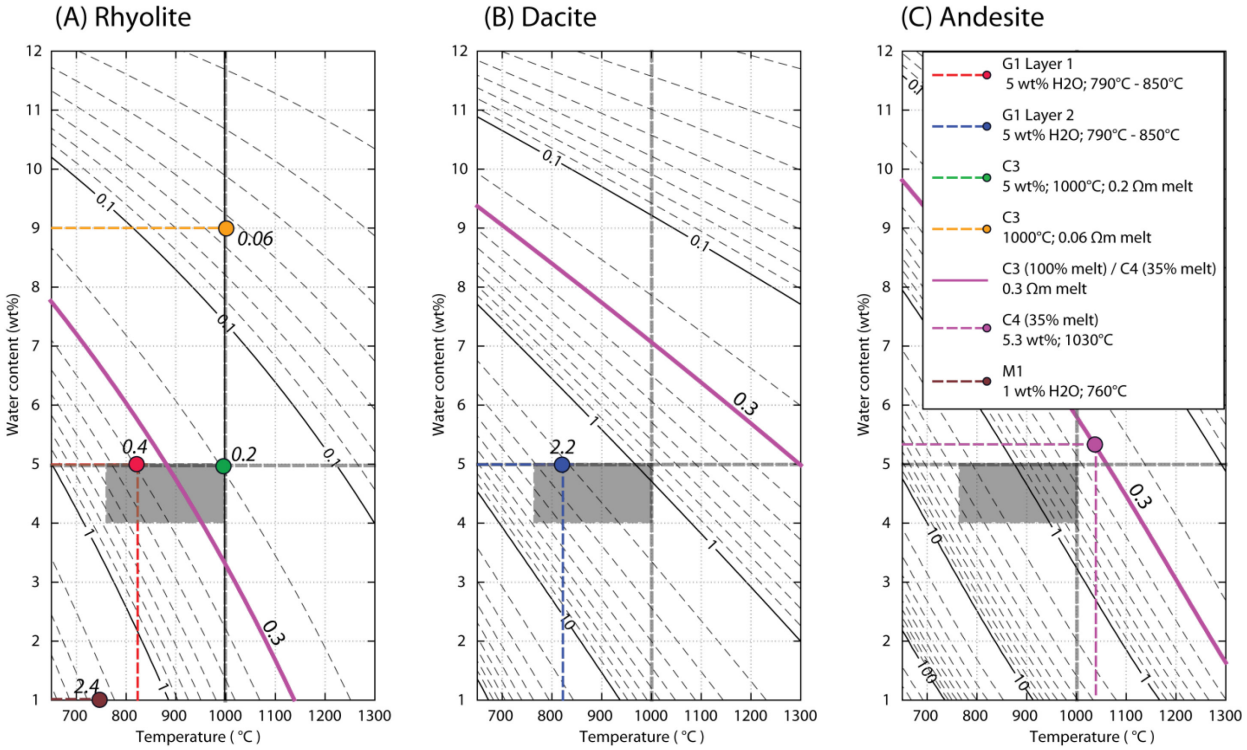

Figure 5.12: Water content as a function of temperature with contours of melt resistivity used for interpretation of features in text. On all plots, the grey box denotes the temperature and water content ranges based on petrological estimates from Andersen et al. (2017). (a) Water content vs. temperature relationship with contours of melt resistivity for rhyolite melt (Guo et al., 2016). (b) Water content vs. temperature relationship with contours of melt resistivity for dacite melt (Laumonier et al., 2015). (c) Water content vs. temperature relationship with contours of melt resistivity for andesite melt (Guo et al., 2017).

5.6.2 Interpretation of Deeper Conductors

The Espejos Conductor (C3) is the most robust feature in the MT model and was detected in prior, less detailed 2-D and 3-D MT studies (Reyes-Wagner et al., 2017; Singer et al., 2014). Given the proximity to both the recent basaltic-to-rhyolitic vents in the northwest, the 950 ka Bobadilla caldera, and the saline Baños Campanario hot springs, it is possible that C3 and/or C4 could be a region containing partial melt, hydrothermal fluids, hydrothermal alteration, or some combination. The depth of C4 at approximately 9

km below surface (7 km b.s.l.) supports a magmatic interpretation since this is a common depth at which partial melt accumulates at the upper-to-middle crust boundary (Chaussard and Amelung, 2014; Cruden and Weinberg, 2018). The distribution of seismicity can also constrain the depth of the brittle-ductile transition (Ogawa et al., 2014). While there is significant seismicity to the southwest of LdM along the Troncoso fault at 3 to 5 km depth (see Chapter 3), there is a notable lack of seismicity to the north of LdM (i.e. near C3 or C4) which may suggest a hotter, more ductile zone. C3 could be interpreted as a hydrothermal system of exsolved fluids related to C4 (Newman et al., 1985). However, given the inferred melt present at shallower depths inferred from gravity studies (Miller et al., 2017b; see Section 5.6.4) and the lack of seismicity, it seems likely that C3 contains some amount of partial melt.

There is no clear Bouguer gravity signature associated with C3 or C4 (Miller et al., 2017b). For C4, this can be explained by the lack of gravity stations north of the lake. The lack of gravity signature associated with C3 can be used as an additional constraint on the composition suggesting that C3 is a higher density anomaly nearer to the 2400 kg/m^3 background density used by Miller et al. (2017b).

The minimum bulk resistivity of C3 is low (0.3 Ωm) which is difficult to explain without including large amounts of dissolved water in the melt to increase the conductivity (Laumonier et al., 2017). Andersen et al. (2017) give petrological estimates for the temperature range of 760°C to 1000°C and water contents of 4-5 wt% for erupted lavas at the LdMVF. Using the empirical relation for rhyolite from Guo et al. (2016), it can be seen that the estimated melt resistivity would be between 0.2 Ωm and 0.8 Ωm (grey box in Figure 5.12a). Given the modelled bulk resistivity of C3 (0.3 Ωm), these melt resistivity values correspond to melt fractions greater than 75% based on Modified Archie's Law (MAL) from Glover et al. (2000) (Figure 5.13). The empirical relations for dacite (Figure 5.12b; Laumonier et al., 2015) or andesite (Figure 5.12c; Guo et al., 2017) cannot explain the modelled bulk resistivity for C3 even with 100% melt, unless water content or temperature are significantly higher. A rhyolite melt fraction of 75% is quite high for such a large, shallow anomaly and in order to arrive at a lower melt fraction estimate, either temperature or water content (or both) must be higher. An increase in either parameter is not supported by petrological data but, by their nature, such data can only sample previously erupted material and may not be indicative of magma storage conditions today, especially if eruptible reservoirs are ephemeral. Furthermore, aqueous fluids in subduction zones have been widely studied and should not be ruled out as an explanation (e.g. Laumonier et al., 2017; Wannamaker et al., 2014). The presence of nearby hot springs with strong magmatic signature is further evidence that water is present in the

upper crust (Benavente et al., 2016). It is possible that C3 is a magma-hydrothermal system composed of both hydrous partial melt and free-water hydrothermal fluids. For example, if the magma-hydrothermal system included 9 wt% water, then the melt fraction could be less than 35% (Figure 5.12a and Figure 5.13).

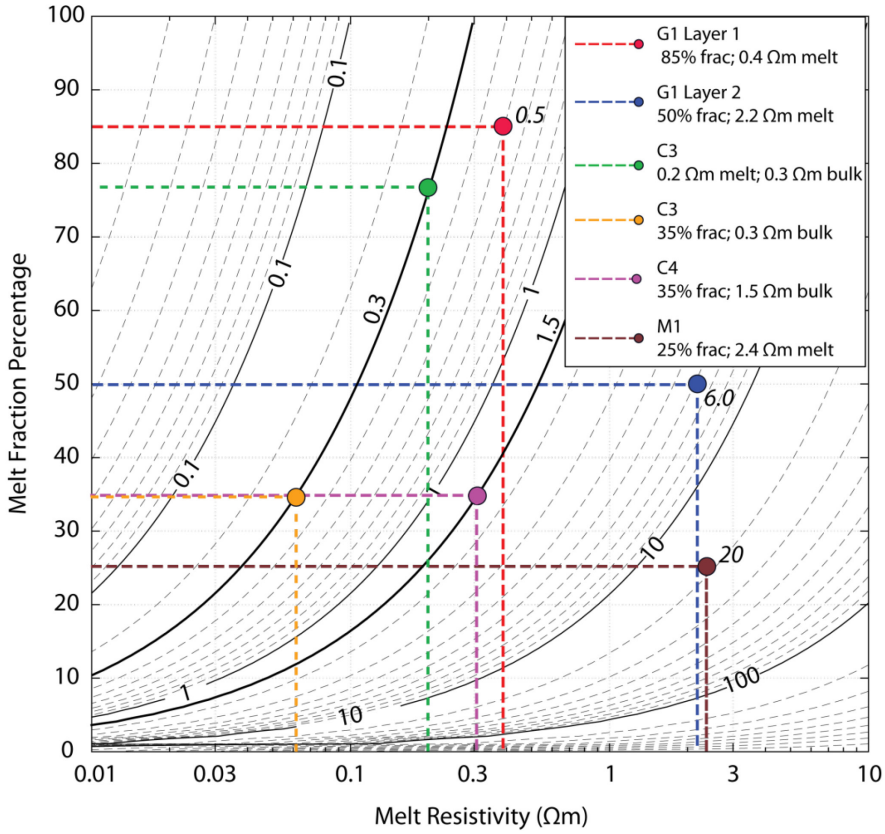

Figure 5.13: Modified Archie's Law (MAL; Glover et al., 2000) plotted as melt fraction vs. melt resistivity with contours of bulk resistivity for m = 1.5.

For C4, a similar analysis was undertaken where the minimum modelled bulk resistivity of 1.5 Ωm is greater than for C3. Thus C4 can be explained with a relatively low melt fraction without invoking high water contents. In terms of volcanic hazards, an important question to ask is whether C4 could be considered a large eruptible volume of relatively crystal-poor magma. In order to be considered an eruptible volume, the melt fraction should be greater than 35% at which point the viscosity of the reservoir becomes low enough to allow it to flow (Bachmann and Bergantz, 2008a). For this to be the case for C4, using MAL, the melt resistivity would need to be greater than 0.3 Ωm (Figure 5.13). The 0.3 Ωm melt resistivity contour is highlighted in Figure 5.12 for the empirical relations for rhyolite (Guo et al., 2016), dacite (Laumonier et al., 2015), and andesite (Guo et al., 2017). As can be seen in Figure 5.12a, this melt resistivity contour passes through the range of petrological estimates from Andersen et

al. (2017) and suggests that C4 could be explained as a relatively low melt fraction crystal-rich rhyolite mush which is not currently eruptible. However, both dacite and andesite melts would require melt fractions greater than 35% to explain the modelled bulk resistivity under the assumption that the petrological estimates are valid for C4 (Figure 5.12b and Figure 5.12c).

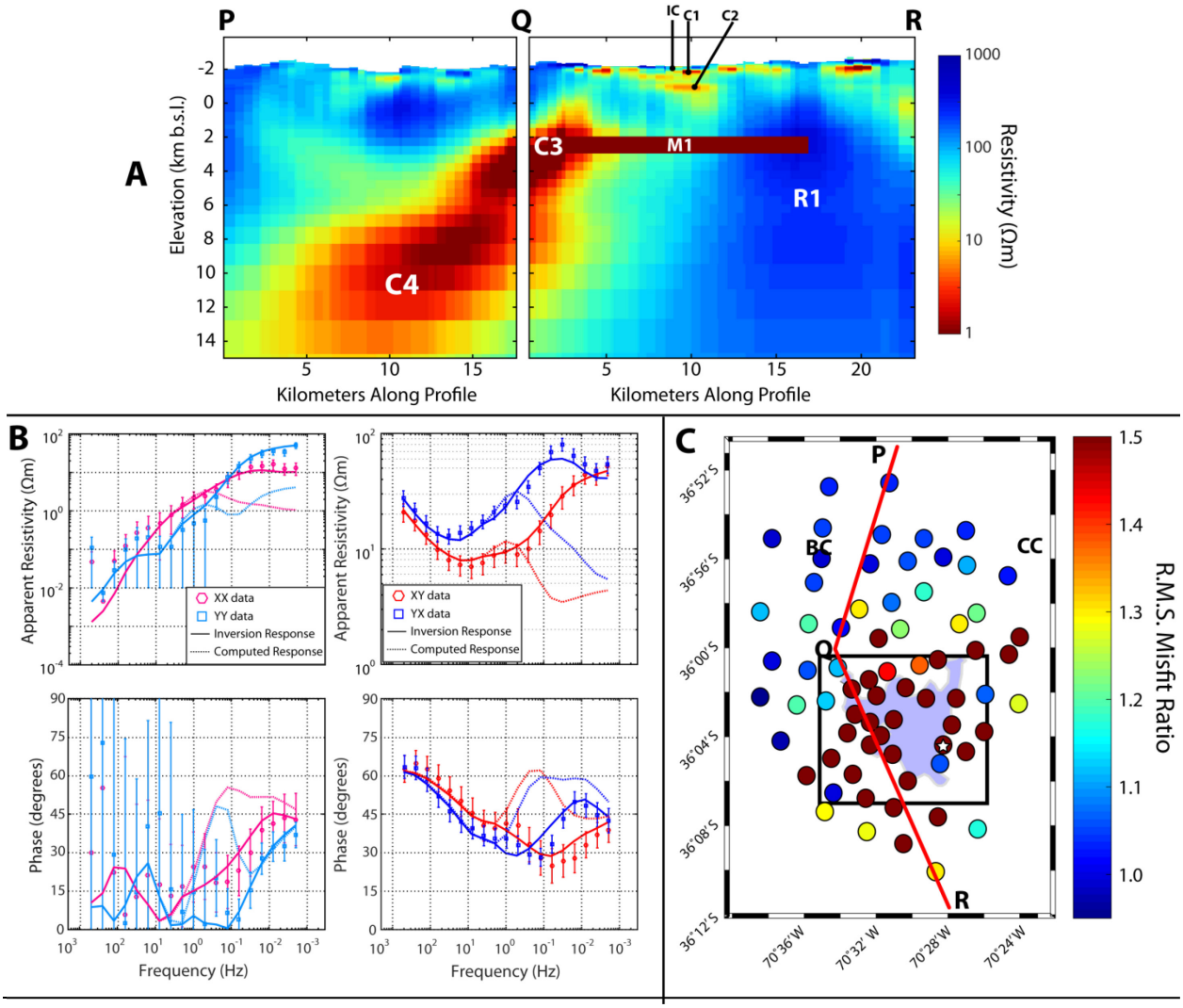

Figure 5.14: Sensitivity analysis for a uniform, 0.5 Ωm, 500 m thick layer underlying a large portion of the Laguna del Maule Volcanic Field. The anomaly represents a large, crystal-poor magma chamber with 85% rhyolitic melt. (a) The top panel shows the same diagonal fence diagram from Figure 5.11 along PQR through the inversion model with the M1 anomaly added. (b) The apparent resistivity and phase of the impedance tensor components as a function of frequency for site LDM008. (c) The map shows station locations colored by r.m.s. misfit ratio (station misfit with M1 added divided by original station misfit). No site had r.m.s. misfit ratio less than 0.90 so any decrease in r.m.s. is negligible. The small star denotes site LDM008 which had the highest r.m.s. misfit ratio (4.51) with an increase from 0.73 to 3.29. The approximate location of M1 is shown with a black rectangle. BC = Baños Campanario; CC = Cerro Campanario.

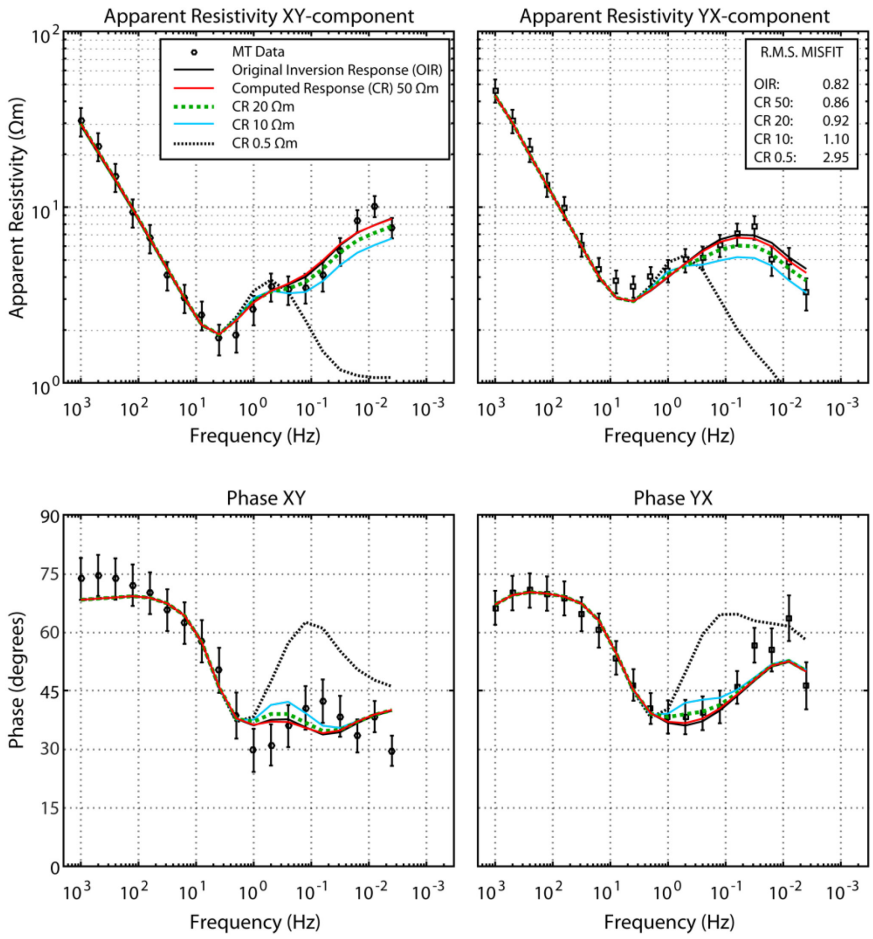

Figure 5.15: Sensitivity analysis for a uniform, 500 m thick anomaly (M1) with variable resistivity values. The anomaly was given different uniform resistivity values of 50 Ωm, 20 Ωm, 10 Ωm, and 0.5. The 3-D response was calculated and Site LDM013 is shown for all 4 cases and compared to the original inversion model. Large discrepancies from the data (r.m.s. > 1.5) occur for the 0.5 Ωm anomaly but do not occur for the anomalies with resistivity >10 Ωm.

5.6.3 Interpretation of the Southern LdMVF Resistivity Structure

There are no major conductive features imaged to the south of LdM and much of the southeast LdM basin is resistive at depth (R1; see Figure 5.10 and Figure 5.11). This is surprising given the large volume of post-glacial erupted material to the southeast of LdM.

The lack of conductors to the south and east makes it unlikely that the entire LdMVF is underlain by a large crystal-poor reservoir. To test this hypothesis, a continuous, 0.5 Ωm conductive layer was added to the original inversion model at a depth of 4 km and with a spatial extent matching the extent of LdMVF (Figure 5.14a). The layer (M1) has a thickness of 500 m and represents a continuous, crystal-poor (85%)

rhyolite reservoir at a temperature of 800°C and 5 wt% H_2O (Figure 5.13). The shape of the added anomaly was chosen to encompass most of the vents around LdMVF. Large changes to r.m.s. misfit are seen at sites around much of LdM with maximum discrepancies at sites in the southeast (Figure 5.14c). At site LDM008, the r.m.s. misfit increased from 0.73 in the original inversion, to 3.29 in the edited model and large discrepancies were seen in all impedance components (Figure 5.14b). Total r.m.s. misfit increased to 2.24 for all data points and most of this increase occurred at periods greater than 1 s.

A shallow (<5 km), crystal-rich, rhyolite mush underlying the entire LdMVF is consistent with the MT data provided that the melt is relatively anhydrous, has relatively low melt fraction, and is at the lower end of temperature estimates from petrological data. For example, a 25% melt fraction mush with 1 wt% H_2O at 760˚C results in a bulk resistivity of approximately 20 Ωm (Figure 5.12a, Figure 5.13). And a similar melt containing only 10% melt fraction would have a bulk resistivity >50 Ωm. Given the overlying conductor (C1) which attenuates signal, it would be unlikely that MT could detect such a mush zone, even if it were 500 m thick and MT data was collected directly above the anomaly at site LDM013 (see Figure 5.15). The lack of large conductors beneath LdMVF provides an important petrological constraint and this interpretation is consistent with the inferred 115 km^3 mush zone imaged by Bouguer gravity data which Miller et al. (2017b) suggested was anhydrous (1 wt% H_2O) and relatively low melt fraction (30%).

5.6.4 Integrating MT Data With the Density Model Derived From Bouguer Gravity Data

Miller et al. (2017b) showed that a 30 km^3, 3 km-thick, crystallinity-zoned magma reservoir with 50 - 85% rhyolitic melt from 2 – 5 km depth located directly beneath the lake is consistent with the Bouguer gravity data. This additional constraint suggests that C2 may be a poorly-resolved portion of a larger anomaly or an additional hydrothermal system overlying the anomaly imaged by Miller et al. (2017b). However, it is surprising that MT does not image a large conductor in the same spatial location as the anomaly of Miller et al. (2017b) since both MT and gravity methods should be sensitive to high melt fraction partial melt. As such, a sensitivity analysis is necessary to assess whether such a magma body as described by Miller et al. (2017b) could go undetected with MT. By adding a conductive anomaly which matches the size, location, and composition of the magma body inferred from the Bouguer gravity data, forward modelling tests can be used to compare the computed MT response of the edited model to the original data and inversion model response.

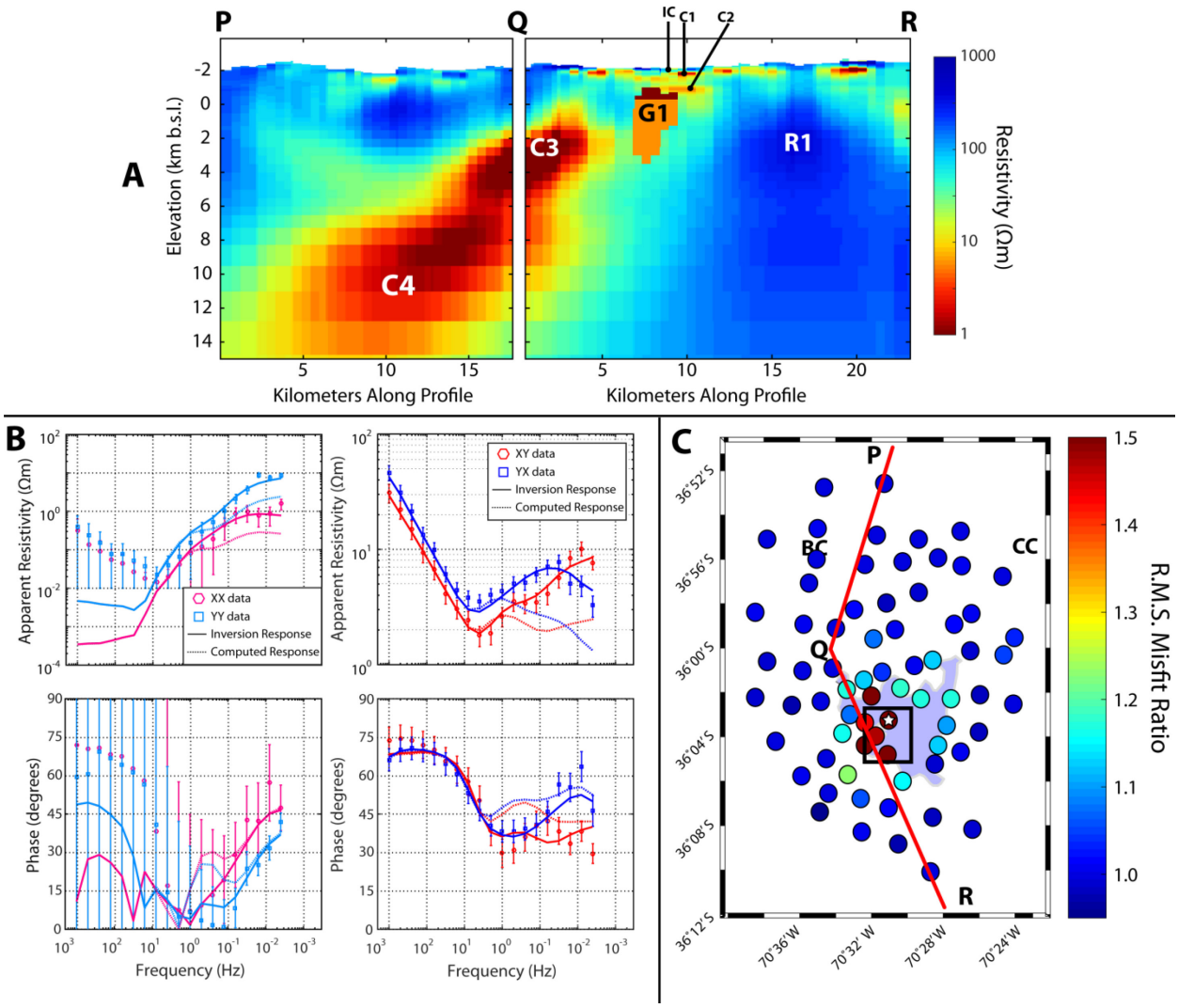

Figure 5.16: Sensitivity analysis for a layered, 30 km^3 resistivity anomaly (G1) with a maximum conductance of 1400 S. The anomaly has the same dimensions and location as the preferred gravity model described in Miller et al. (2017b). Layer 1 has resistivity of 0.5 Ωm, Layer 2 has resistivity of 6.0 Ωm. See text for more details. (a) The top panel shows the same diagonal fence diagram from Figure 5.11 along PQR through the inversion model with the G1 anomaly added. (b) The apparent resistivity and phase of the impedance tensor components as a function of frequency for site LDM013. (c) The map shows station locations colored by r.m.s. misfit ratio (station misfit with G1 added divided by original station misfit). No site had r.m.s. misfit ratio less than 0.90 so any decrease in r.m.s. is negligible. The small star denotes site LDM013 which had the highest r.m.s. misfit ratio (2.29) with an increase from 0.82 to 1.88. The approximate location of G1 is shown with a black rectangle. BC = Baños Campanario; CC = Cerro Campanario.

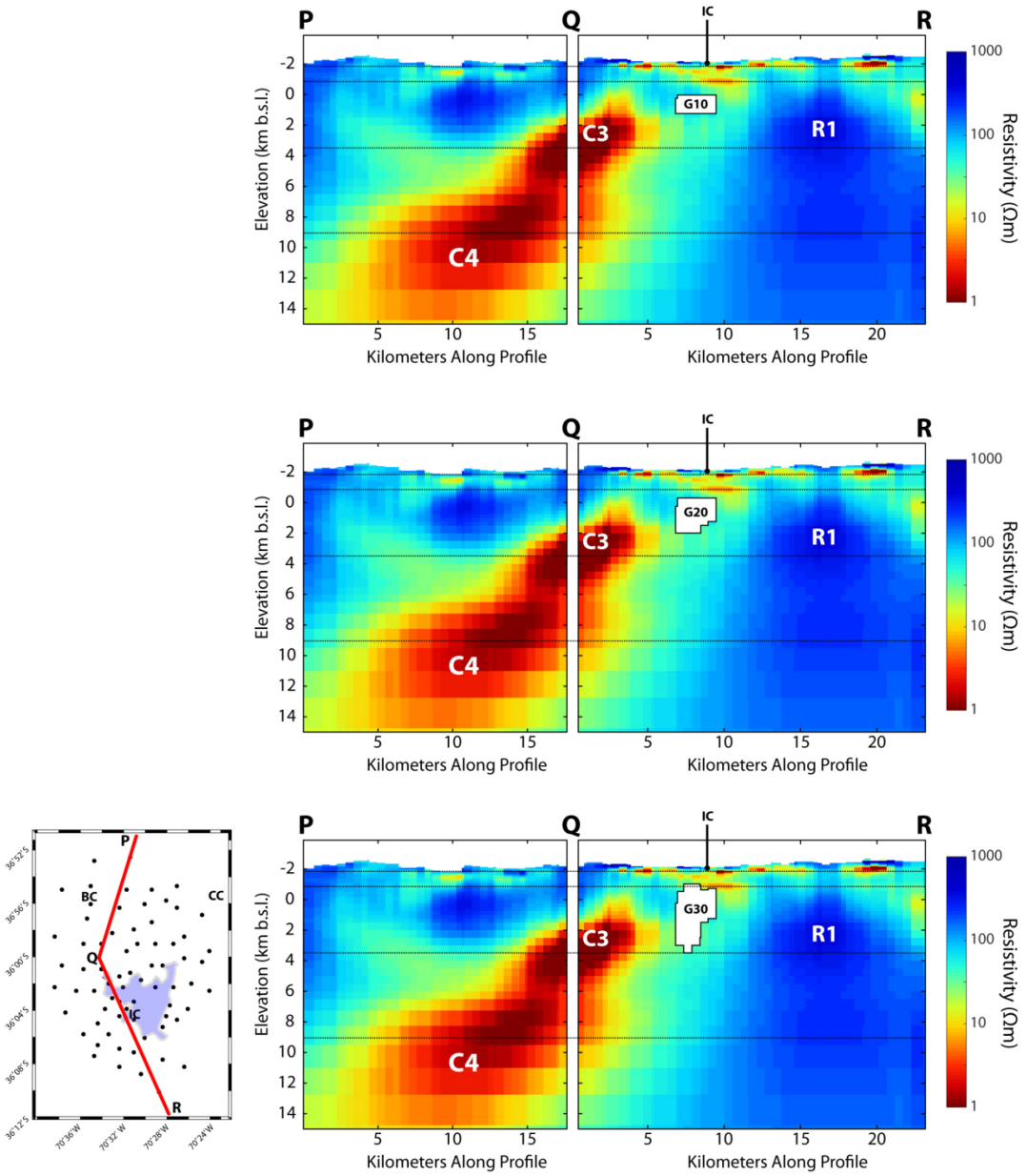

Figure 5.17: The same diagonal slice fence diagram as Figure 5.11 is shown with the location and depth of the G10 (top), G20 (middle), and G30 (bottom) anomalies which were added to the inversion model in order to conduct forward model tests. The bulk resistivity of each feature was varied over six different values (30 Ωm, 10 Ωm, 3 Ωm, 1 Ωm, 0.5 Ωm and 0.3 Ωm) and the forward response was computed for each case (18 models in total).

To do this, the resistivity of the modelled density anomaly must be estimated based on the water content, silica content and temperature of the melt. Pressure also plays a role but, for the pressures under consideration (50 - 200 MPa), any effect of pressure is negligible (Unsworth and Rondenay, 2013). Since the magma chamber is likely to be crystallinity-zoned, a simplified two-layer magma chamber is

assumed (Andersen et al., 2017; Miller et al., 2017b). The top layer is a 500 m-thick, 85% rhyolitic melt between 790°C and 850°C with 5 wt% H_2O. The lower layer is a 2.5 km-thick, 5 wt% H_2O, 50% dacitic melt between 790°C and 850°C. The temperature and water content ranges are taken from Miller et al. (2017b) to allow for direct comparison. The silica content and thickness of each layer is somewhat arbitrary based on the assumption that fractionation is occurring with silica-rich, high-melt fraction components collecting near the top of the reservoir. Using the empirical relation for rhyolite from Guo et al. (2016), the average pure melt resistivity of Layer 1 is estimated to be approximately 0.4 Ωm (Figure 5.12a). The empirical relationship for dacitic melt from Laumonier et al. (2015) is used for Layer 2 resulting in an average pure melt resistivity of approximately 2.2 Ωm (Figure 5.12b). The final step is to calculate the bulk resistivity of each layer. Using MAL, the estimated bulk resistivity of Layer 1 is approximately 0.5 Ωm while for Layer 2 the average value is 6 Ωm (Figure 5.13).

To test whether such an anomaly could be detected, a layered resistivity anomaly (G1) was added to the MT inversion model with the same dimensions and location as the -600 kg/m^3 Bouguer density isosurface from Miller et al. (2017b) (Figure 5.16). The exact volume of G1 is 28 km^3 after interpolation. The maximum conductance of the anomaly was 1400 S. The depth to the anomaly is less than the width and the conductance is quite large so on initial inspection it seems that the anomaly should have an MT response based on previous studies of magma bodies (Newman et al., 1985). The MT impedance response was computed for the edited model and compared to the inversion response of the original model and MT data.

Figure 5.16 shows the results of this forward modelling experiment and highlights site LDM013, located on the southwestern peninsula, which showed the greatest increase in r.m.s. misfit between the inversion response and the computed response of the edited model. At this site, the r.m.s. misfit ratio (i.e. the ratio between the misfit from the edited model divided by the misfit from the original model) was 2.29 indicating the misfit more than doubled (from 0.82 in the original model to 1.88 in the edited model). This suggests a much poorer fit when the gravity anomaly is added. As can be seen in Figure 5.16, the high frequencies are still fit well for the off-diagonal impedance components but at periods greater than 1 s, the computed response no longer fits the measured data. The diagonal components are generally much noisier than the off-diagonal components at all sites (see Appendix 1) and this is true of LDM013 as well. The inversion fails to fit the diagonal components at short periods (<0.1 s) whether G1 is added or not. Importantly, when G1 is added, the fit to the diagonal components also becomes

worse at long periods (> 10 s). In Figure 5.16, the difference in r.m.s. misfit ratio for each station is shown in map view. This highlights the spatial sensitivity of the added gravity anomaly. This modelling test shows large increases in r.m.s. misfit when the G1 anomaly is added suggesting that a 30 km^3, 50 to 85% melt fraction anomaly is not consistent with the MT data.

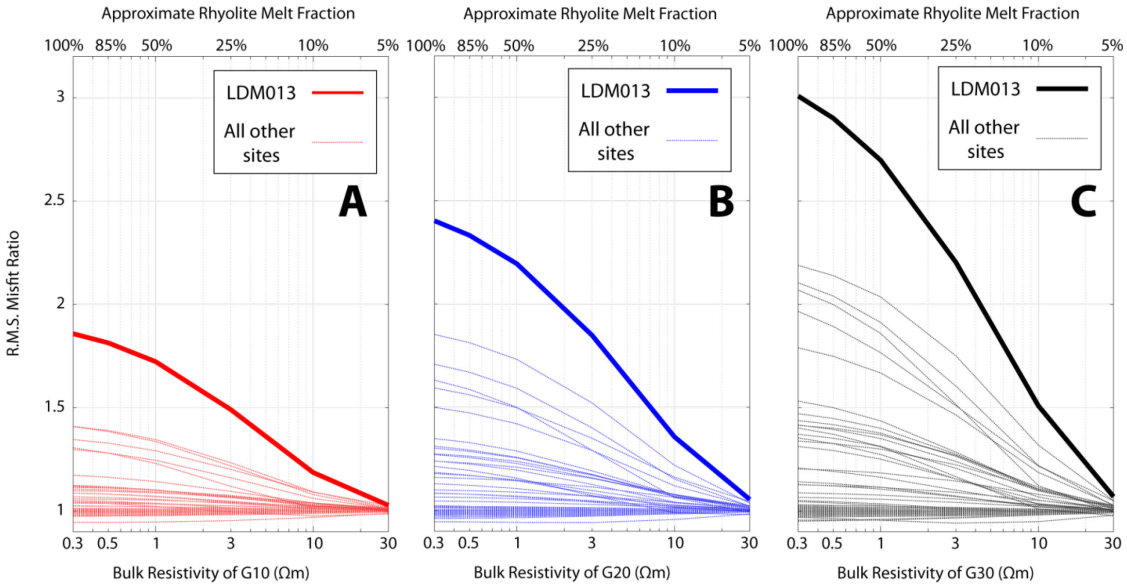

Figure 5.18: R.M.S. misfit ratio for each MT site as a function of the bulk resistivity for the anomalies (a) G10 (10 km^3), (b) G20 (20 km^3), and (c) G30 (30 km^3), which were added to the original inversion model. Each plot shows how r.m.s. misfit changed for each station (thin, dashed lines) with site LDM013 highlighted (thick line).

Since the Bouguer gravity data show a clear data anomaly, it is useful to ask how small or how resistive an anomaly would need to be to go undetected by the MT data. To test this, three different sized anomalies at 2 km depth were investigated with different bulk resistivity values. A 30 km^3 anomaly (G30) was set to have bulk resistivity values of 0.3, 0.5, 1, 3, 10, and 30 Ωm. These bulk resistivities correspond to rhyolite melt fractions of roughly 100%, 85%, 50%, 25%, 10%, and 5%, respectively assuming a 0.4 Ωm melt resistivity (see Figure 5.13). The same bulk resistivity values were applied to two smaller features: a 20 km^3 anomaly (G20), and a 10 km^3 anomaly (G10) (Figure 5.17).

Figure 5.18 shows the r.m.s. misfit ratio for each MT station as a function of bulk resistivity for the anomaly. As can be seen in Figure 5.18, most stations have an r.m.s. misfit ratio near 1 regardless of the composition or size of the anomaly. This is due to the fact that most stations are far from the anomaly and cannot detect it. However, there is a general upward trend in the r.m.s. misfit ratio as the bulk

resistivity of a given anomaly is decreased and as the size is increased. Figure 5.18 highlights LDM013, which had the greatest increases in r.m.s misfit. In order to keep the r.m.s. misfit ratio at LDM013 relatively low (e.g. <2), G30 needs to have a bulk resistivity greater than approximately 5 Ωm. This corresponds to a rhyolitic magma body with a melt fraction less than 25%. In contrast, a small, 10 km^3 anomaly (G10) is outside the resolution limits of the current MT array and sees almost no change in r.m.s. misfit, even at relatively high melt fraction (e.g. >50% melt). The maximum conductance of G10 is greater than the conductance of C1 for resistivity values of 0.3, 0.5, and 1 Ωm. A 20 km^3 anomaly could also go undetected but would need lower melt fraction (e.g. <50% melt). This exercise provides a range of possible models which are consistent with the MT results while excluding certain models as inconsistent. More complete data curves for LDM013 for each of the three cases are shown in Figure 5.19, Figure 5.20, and Figure 5.21.

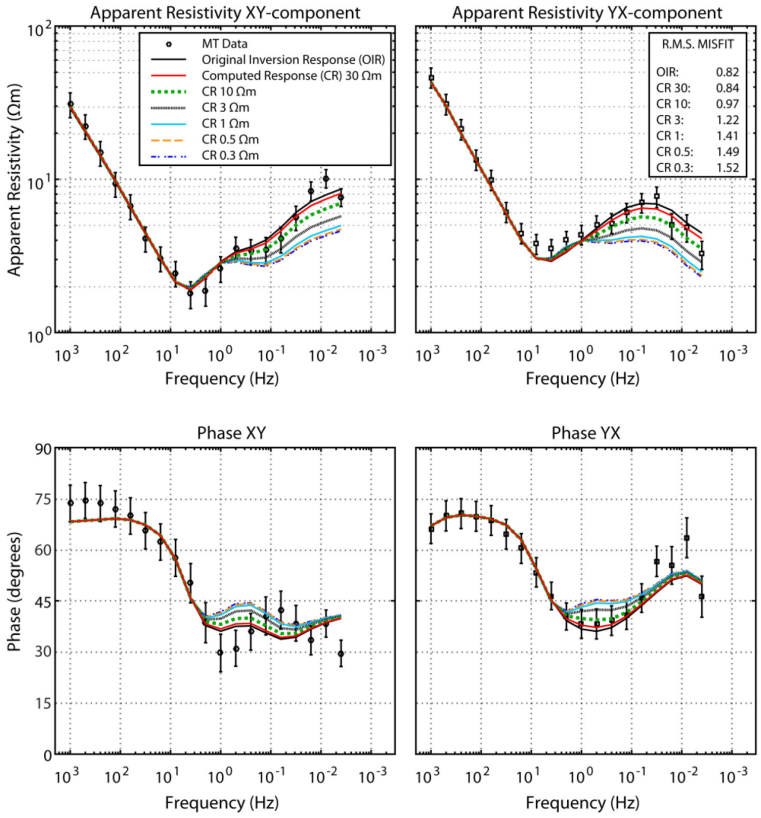

Figure 5.19: Sensitivity analysis for a uniform, 10 km^3 anomaly (G10) with variable resistivity values. The anomaly is a simple block at the same location as the anomaly G1 shown in Figure 5.16 but has uniform resistivity rather than a layered geometry. The anomaly was given different uniform resistivity values of 30 Ωm, 10 Ωm, 3 Ωm, 1 Ωm, 0.5 Ωm and 0.3 Ωm. The 3-D response was calculated and Site LDM013 is shown for all 6 cases and compared to the original inversion model. Large discrepancies from the data (r.m.s. > 1.5) occur when the anomaly has a resistivity less than 0.3 Ωm (i.e. 100% melt fraction).

A final possibility to consider is that the temperature of the melt has a very strong effect on both the density and resistivity of the magma body. Recent petrological estimates from Andersen et al. (2017) suggest melt temperatures could be as low as 760°C and these are based on erupted products. If the magma storage temperature is low, it could result in increased bulk resistivity and decreased bulk density which would make gravity data more sensitive to the anomaly while making electrical data less sensitive to the anomaly. The lack of a strong electrical signature in the MT data provides an important constraint on the available geological interpretations of the LdMVF magma system.

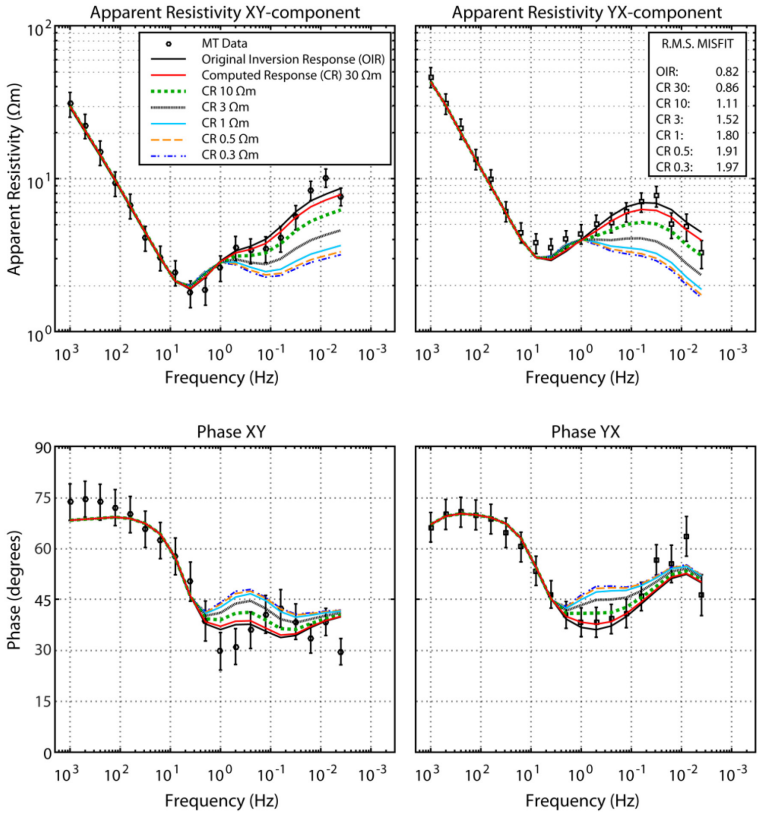

Figure 5.20: Sensitivity analysis for a uniform, 20 km^3 anomaly (G20) with variable resistivity values. The anomaly is a block at the same location as the anomaly G1 shown in Figure 5.16 but has uniform resistivity rather than a layered geometry. The anomaly was given different uniform resistivity values of 30 Ωm, 10 Ωm, 3 Ωm, 1 Ωm, 0.5 Ωm and 0.3 Ωm. The 3-D response was calculated and Site LDM013 is shown for all six cases and compared to the original inversion model. Large discrepancies from the data (r.m.s. > 1.5) occur when the anomaly has a resistivity less than 3 Ωm (i.e. >25% melt fraction).

5.6.5 Integrating Deformation Model

The MT inversion does not image any conductor with the same location or depth as the inflation source modelled by Feigl et al. (2014) or Le Mével et al. (2016). The inflation source is modelled as either a 9 km by 5 km basaltic sill oriented north-northeast at 5 km depth or a penny-shaped crack with radius of 6.2 km and depth of 4.5 km. Over the course of 7 years of observation, an estimated 0.19 km^3 of material has been injected (Le Mével et al., 2016). Simple geometric estimates suggest an opening of between 1 to 4 meters. Using the empirical relation of Ni et al. (2011), a resistivity of 0.1 Ωm for a pure basaltic melt injection is a reasonable approximation. However, even with a highly-conductive, pure melt injection, a 4 m thick sill could not be imaged by the MT data. Taking into account the potential attenuation by C1, the limiting thickness for resolving such a feature at 5 km depth is >20 m given a simplistic, ideal 1-D assumption (Figure 5.22).

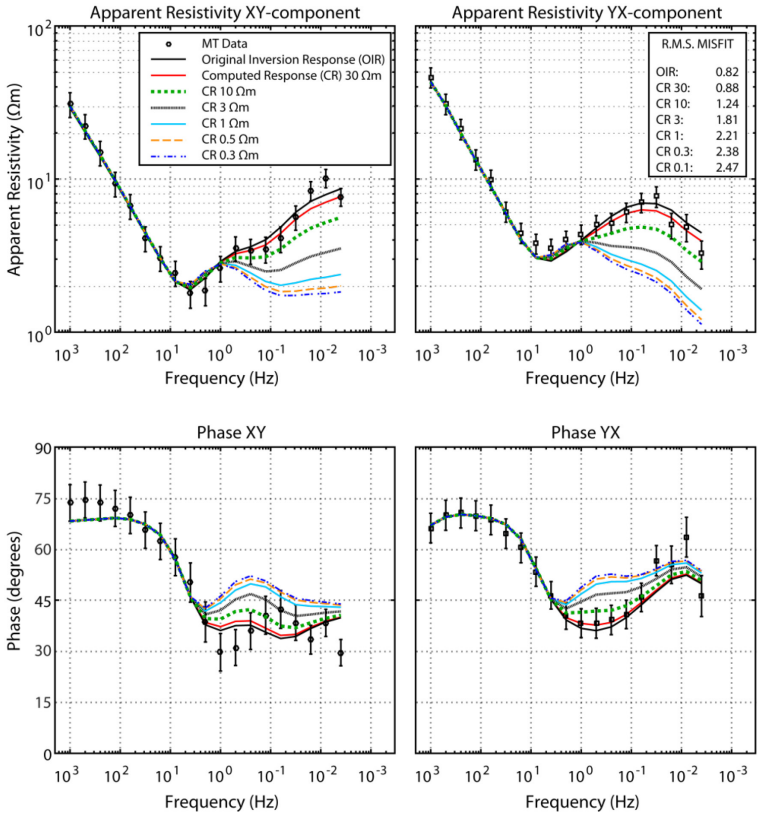

Figure 5.21: Sensitivity analysis for a uniform, 30 km^3 anomaly (G30) with variable resistivity values. The anomaly has the same dimensions as the anomaly G1 shown in Figure 5.16 but has uniform resistivity rather than a layered geometry. The anomaly was given different uniform resistivity values of 30 Ωm, 10 Ωm, 3 Ωm, 1 Ωm, 0.5 Ωm and 0.3 Ωm. The 3-D response was calculated and Site LDM013 is shown for all six cases and compared to the original inversion model.

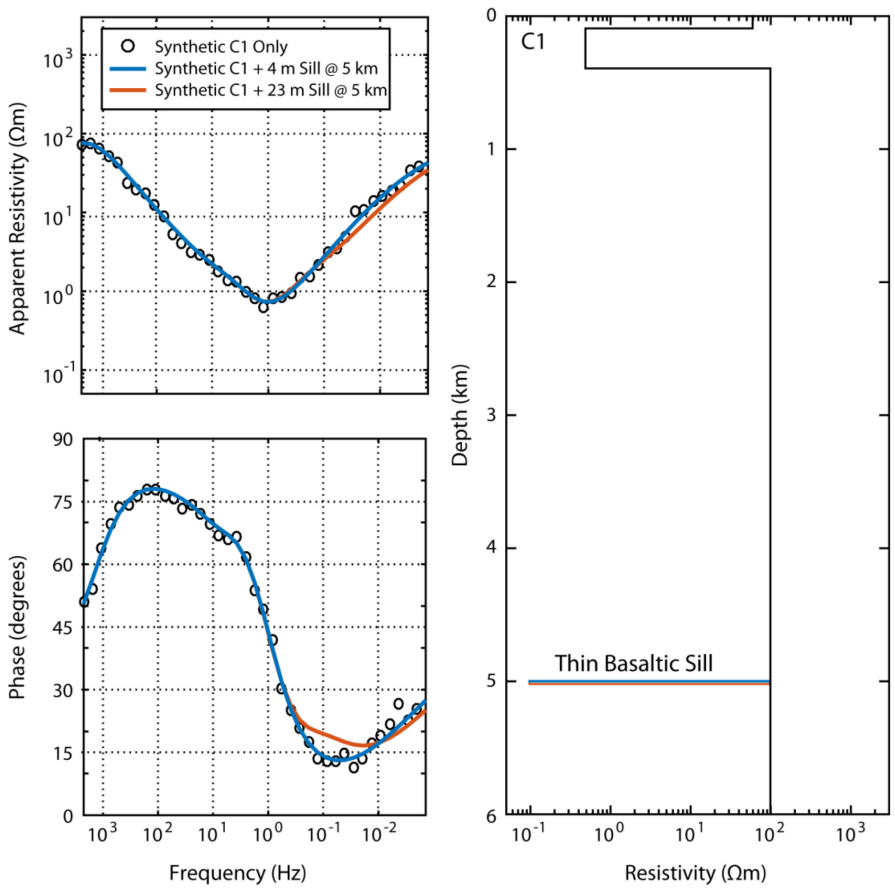

Figure 5.22: Simple, ideal one-dimensional (1-D) resolution test for thin basalt sill injection at 5 km depth with a resistivity of 0.1 Ωm. The two panels on the left are apparent resistivity and phase for the 1-D MT response of the models shown on the right. The black dots are the 1-D synthetic MT data with 6% error calculated from the background model which includes a simplified 1-D anomaly representing overlying C1 at a depth of 100 m with a conductance of 400 S (0.5 Ωm, 200 m thick). The blue line shows synthetic data when a 4 m thick sill is added (0.40 r.m.s. misfit relative to the background data). The blue line shows synthetic data when a 23 m thick sill is added (2.01 r.m.s. misfit relative to the background data).

5.7 SUMMARY

The MT model suggests that the LdMVF is fed from a multi-chamber magmatic column with a large, deep (> 8 km), melt region to the north (C4) providing heat and melt to shallower (<5 km depth), zones beneath the LdMVF. This heat and melt injection allows for the formation of melt and hydrothermal fluids in the northwest LdMVF (C3). An even shallower anomaly (<3 km depth) identified with Bouguer gravity data is located directly beneath LdM. MT forward modelling tests show that this anomaly (G1) is unlikely to be a large (30 km^3), high melt fraction (>50%) anomaly. However, a smaller (e.g. 10 - 20 km^3)

or lower melt fraction magma body would not be detectable with MT. This shallow feature (G1) may be part of a larger crystal mush zone as suggested by Andersen et al. (2017) which is reactivated by heat and melt from C4. However, such a shallow mush would need to have very low water content (e.g. 1%) and low temperature (e.g. 760˚C) in order to go undetected by MT.

The fact that C4 underlies the inferred outline of the 950 ka Bobadilla caldera from Hildreth et al. (2010) suggests that C4 may be a large, long-lived magma reservoir in the mid-crust which is responsible for providing material for the largest observed eruptions in the LdMVF. Mafic recharge from the lower crust is required to maintain a large zone of partial melt at 9 km depth for 1 Ma. However, intrusion rates do not need to be high and could be as low as 10^{-4} km^3/yr assuming the lower crust (>25 km depth) is considered thermally mature (Karakas et al., 2017).

Crucially, the deepest conductive region (C4) lies outside the zone of deformation and beyond the edge of any post-glacial vents or lava flows. No major conductive features are imaged to the south or southeast of the LdM basin and, in fact, much of this region is resistive at depth. This implies that source melts for the northwestern vents in the LdMVF travel both vertically and laterally (5 – 10 km) as they migrate to the surface. The progression from C4 to C3 to G1 shows a potential pathway from a deeper, northern reservoir to a shallow reservoir directly beneath the LdMVF (Figure 5.11). This interpretation is not conventional in terms of conceptual magma plumbing models which generally assume purely vertical ascent; however such distances are not unreasonable and have been seen at other volcanoes and calderas (e.g. Aizawa et al., 2014; Bato et al., 2018; Díaz et al., 2020; Hill et al., 2009; Hübert et al., 2018; Klügel et al., 2015). In particular, at El Hierro in the Canary Islands, Klügel et al. (2015) found lateral movement of approximately 15-20 km from a long-term lower-crustal reservoir which provided material for more ephemeral, shallow reservoirs. Past studies using seismic reflection commonly show lateral transport of magma along pre-existing structural boundaries as reviewed by Magee et al. (2018) and Magee et al. (2016). This has implications for magma transport mechanisms, local structural stress regimes, and the source material for the observed inflation at the LdMVF. The presence of the Troncoso fault could potentially provide a structural barrier to magma ascent and act as a conduit for magma flow; such structural control on magma plumbing systems has been observed elsewhere (e.g. Magee et al., 2016 and references therein). Structural evidence from the LdMVF suggests that the hanging wall of the Troncoso fault is more heavily faulted meaning that there may be easier pathways for less evolved magmas to reach the surface (Garibaldi et al., 2020; Keranen et al., 2016).

The MT model and interpretation presented here suggests that there is a difference between the southeast and northwest LdMVF in terms of melt generation and fluid transport since the northwest contains significant conductive anomalies (C3 and C4) while the southeast is largely resistive (R1). However, the southeast also contains large volumes of post-glacial rhyolite so it is important to ask where the magma and heat that drives these eruptions is coming from. Two possible explanations can be offered. The first is that the large volume of melt to the north (C4) is providing heat and melt to both the northwest and southeast LdMVF. This would require relatively long lateral distances (e.g. >20 km from C4 to Barrancas vents) and there is little geological evidence to support this interpretation. The second possibility is that the erupted lavas in the northwest and southeast have two different source regions with the southeast source region being too deep to be resolved with the current MT array or beyond the edges of the current MT array. Petrological evidence from Andersen et al. (2017) showed that there is a compositional distinction between the post-glacial lavas in the northwest and southeast LdMVF, although differences are relatively subtle. The MT model and interpretation, along with these other lines of evidence, support the possibility that the source regions of melt for the southeast and northwest vents are different. More geophysical and geological evidence is necessary to better understand the source regions for the southeast vents of the LdMVF including further exploration in Argentina and more detailed study of the Barrancas complex.

CHAPTER 6: ASSESSING NON-UNIQUENESS AND MODEL SENSITIVITY TO AID THE INTERPRETATION OF MAGNETOTELLURIC INVERSE MODELS

6.1 INTRODUCTION

Using geophysical data to determine the composition and structure of the Earth is limited by non-uniqueness. This non-uniqueness arises in two distinct parts of the data analysis. The first arises in solving a geophysical inverse problem to determine a geophysical parameter (e.g. electrical conductivity, density, or seismic velocity) which fit a set of geophysical data (e.g. magnetotellurics, gravity, or seismic data) within some threshold or tolerance. Most realistic geophysical inverse problems are inherently non-unique meaning that many different Earth models can be found that fit the observed data equally well. This non-uniqueness arises because: (a) real data are noisy; (b) the problem is under-determined (i.e. there are more model parameters than data points) and; (c) there are often limitations of the inherent physics of the geophysical method (Parker, 1994). A second type of non-uniqueness arises in the geological interpretation of a geophysical model. This is because a particular geophysical parameter can be explained by many combinations of rock composition, temperature, pressure, porosity, etc. (e.g. Lees, 2007; Murphy and Egbert, 2019; Unsworth and Rondenay, 2013). In light of this non-uniqueness, it is necessary to determine the most reliable interpretations and inferences about the geology by exploring the solution space and the data sensitivity.

These two aspects of non-uniqueness are especially important when geophysical methods are applied in volcanology to investigate the size, location, and composition of crustal magma reservoirs. Determining these parameters of the volcanic plumbing system has important implications about the size, frequency and stability of a given volcano (Pritchard and Gregg, 2016). Geophysical studies of volcanos were first reviewed by Iyer (1984) and in the intervening years many studies have been made using a variety of methods (e.g. Araña et al., 2000; Comeau et al., 2016; Delph et al., 2017; Didana et al., 2014; Koulakov et al., 2016; Ogawa et al., 2014; Pous et al., 2002; Samrock et al., 2018; Sherburn et al., 2003; Stankiewicz et al., 2010). The geological environment of a volcano is often structurally complex and heterogeneous and it is difficult to make global generalizations about the structure of these systems.

For magnetotelluric (MT) studies at volcanos in particular, these two types of non-uniqueness are relevant because partial melt is not always conductive, especially when the melt has high silica content and low melt fraction. Furthermore, many volcanic systems are coupled to hydrothermal systems which consist of thin lenses or reservoirs of conductive saline fluids (Afanasyev et al., 2018). Thus it can be difficult to decide if a conductor is a large volume of melt with a low melt fraction, or a smaller volume of well-connected brine. In reality, it is most likely that both of these two phases—partial melt and hydrothermal fluids—co-exist in the subsurface (e.g. Laumonier et al., 2017). The presence of shallow hydrothermal reservoirs overlying deeper partial melt presents an additional resolution problem and further complicates the interpretation of features. The structure of volcanic plumbing systems may also consist of thin, high melt fraction dykes and sills or larger, more homogeneous low melt fraction reservoirs, and it is unclear that MT would be able to distinguish between these two end members.

To address non-uniqueness, and reduce the uncertainty in interpretation, a powerful approach is to combine information from multiple geophysical methods. Recently, several volcanoes have been investigated with multiple different geophysical methods such as magnetotellurics (MT), seismic tomography, and gravity measurements (e.g. Árnason et al., 2007; Chaussard and Amelung, 2014; García-Yeguas et al., 2017; Magee et al., 2018; Pritchard et al., 2018). These methods are sensitive to electrical conductivity, acoustic seismic velocity, and density, respectively. In general, partial melt will have a high conductivity, low velocity and low density so it is expected that geophysical inverse models of each parameter will include features which correlate spatially and that interpretations would be congruous (Unsworth and Rondenay, 2013). In some cases, the anomalies imaged by the various methods agree relatively well in terms of location, size and interpreted composition (e.g. Comeau et al., 2016; Heise et al., 2016; Ogawa et al., 2014). However, in many cases there is a discrepancy between the spatial location of anomalies determined by the different methods and/or the interpretations from different methods (e.g. Jiracek et al., 1983; Piña-Varas et al., 2018; Samrock et al., 2015; Stanley and Blakely, 1995).

The discrepancies may be due to some combination of differences in resolution between methods and/or differences in how a geophysical attribute maps to rock properties (e.g. electrical resistivity depends primarily on connected conductive networks whereas seismic velocity depends on bulk properties). In this way, a discrepancy between different methods does not necessarily imply a failure of any (or all) methods but instead may provide important additional constraints on interpretations and

thus reduce non-uniqueness (e.g. Cook and Jones, 1995). But it is important to assess whether discrepancies between methods are allowable within data error or not. For example, if the depths to two features are offset, it may be due to some fundamental difference in the geology (e.g. a layered magma reservoir), or it may simply be that the depth is poorly constrained and has large error bars (Comeau, 2015). Thus there are two types of discrepancies:

a) A real discrepancy is one where different geophysical methods are sensitive to real differences in subsurface geology within the errors of the measurements. In this case the discrepancy between the different models is real and provides additional information about the subsurface structure.
b) An apparent discrepancy is one where the differences are due solely to inversion non-uniqueness within error and a congruous model is possible and preferred as the simpler explanation.

The goal is to try to distinguish between real and apparent discrepancies.

There are a variety of ways to investigate model non-uniqueness and data sensitivity in inversion modelling. These can broadly be grouped into two categories: sensitivity analysis and hypothesis testing. Sensitivity analysis deals with describing the overall sensitivity of the model space in a general way by using e.g. the Jacobian (Kalscheuer et al., 2010; Kalscheuer and Pedersen, 2007), Monte Carlo or boot-strapping methods (Rosas-Carbajal et al., 2014; Schnaidt and Heinson, 2015), or extremal bounds analysis (Meju, 2009). These methods, while useful, are often computational expensive and difficult to implement. They also provide only a general sensitivity rather than testing whether specific model features are interpretable or whether specific geological features could go undetected. In contrast, hypothesis testing uses forward modelling and constrained inversions to test the sensitivity of specific model features (e.g. Bedrosian, 2007). This is often done by adding a specific feature to a model (i.e. perturbing an existing model) and either computing the data response of the perturbed model, or running an inversion with the perturbation as an additional *a priori* constraint. If discrepancies between geophysical methods exist, then hypothesis testing can be used to test whether discrepancies are real or apparent.

It is important to mention that different data sets can be combined via joint inversion. These methods do not explicitly test sensitivity or non-uniqueness but provide a way to examine the model (or set of

models) which best fit both data sets. Joint inversion methods are often computationally expensive, difficult to implement, and have a variety of additional complexities beyond the scope of this chapter (e.g. Gabas and Marcuello, 2003; Moorkamp, 2017). One of the cautions of these methods is that they implicitly assume that features in models are correlated (Moorkamp, 2017). However, this is not necessarily true since different methods have different resolution and are sensitive to different geological properties as mentioned above. Some cross-gradient methods have been developed to try to avoid the correlative effects of joint inversion (e.g. Gallardo and Meju, 2011; Gao and Zhang, 2018). These cross-gradient methods still assume structural coupling but enable the model to have no coupling if the data warrants it. Joint inversion methods can be very useful but are not considered here.

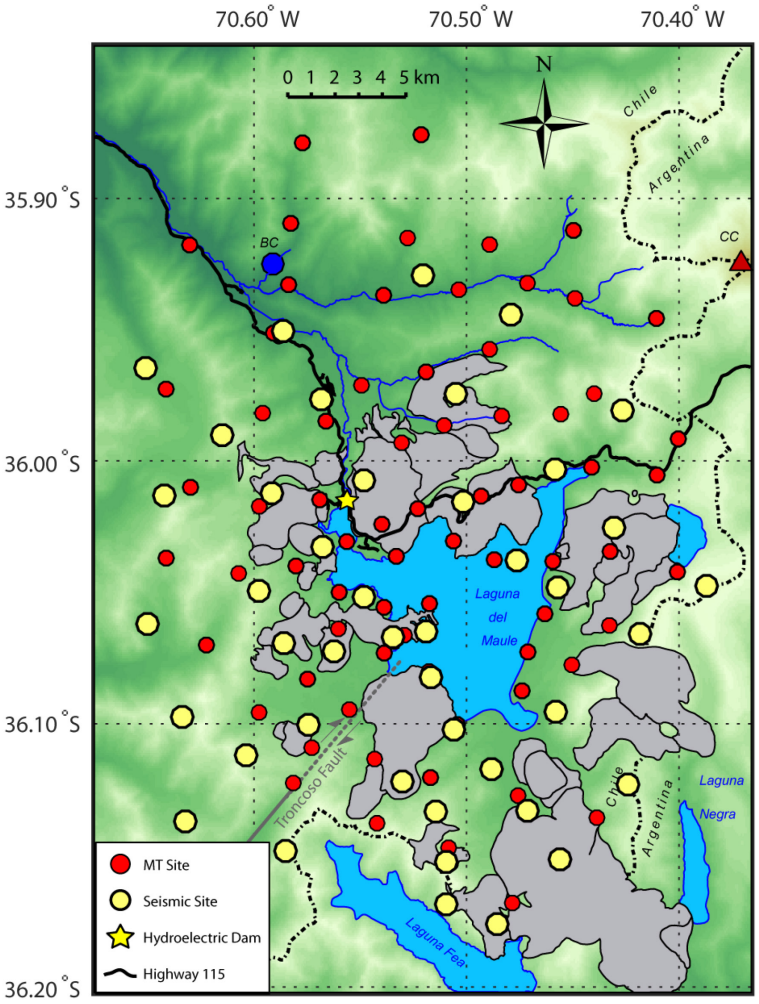

Figure 6.1: Map of Laguna del Maule Volcanic Field. Grey polygons are mapped lava flows from Andersen et al. (2017). Magnetotelluric site locations are red dots from Cordell et al. (2018) (see Chapter 5). Seismic sites are yellow dots from Wespestad et al. (2019). BC = Baños Campanario hot springs; CC = Cerro Campanario.

In this chapter, the non-uniqueness and data sensitivity of three-dimensional MT inverse models is examined by using seismic constraints and performing a variety of hypothesis tests. This is done using the statistical analysis of perturbed data residuals (e.g. Lee et al., 2020) and constrained inversions (see Bedrosian, 2007 for a review). The Laguna del Maule Volcanic Field (LdMVF) in central Chile (Figure 6.1) is used as a case study because it is a unique volcanic setting where MT and seismic data have been collected concurrently (Cordell et al., 2018; Wespestad et al., 2019). The LdMVF has been showing signs of significant unrest in the last ten years including upward ground deformation and seismic swarms (Cardona et al., 2018; Le Mével et al., 2015). The LdMVF is an exceptional natural laboratory with a high concentration of recent rhyolite eruptions which indicates the presence of a dynamic silicic system at depth (Andersen et al., 2019, 2018, 2017). A better understanding of the plumbing of the magmatic system is necessary to make inferences about the size of future eruptions as well as the overall composition and stability of the present day magmatic system. MT data, surface wave seismic data and ambient noise tomography (ANT) seismic data were collected at the LdMVF between 2015 and 2018 and resistivity and seismic velocity models were previously published by Cordell et al. (2018) (see Chapter 5) and Wespestad et al. (2019), respectively. Both models show a significant anomaly at depths between 2 to 7 km below surface and both were interpreted as indicating the presence of partial melt beneath the LdMVF. However, the spatial location of the anomalies is offset by several kilometers and the geometry, size and interpreted composition of the proposed magma reservoir is somewhat inconsistent between the two methods. The aim of this study is to re-analyze the MT modelling results in light of the seismic results to determine whether these incongruities and discrepancies are due to inversion non-uniqueness or due to actual subsurface structure. In other words, the question is whether a reasonable, spatially smooth resistivity model with adequate fit to the measured MT data can be found that is consistent with the seismic velocity anomaly. If not, then it is more likely—though not proven—that the differences between the models are due to real geology.

Section 6.2 of this chapter presents the theory and methodology used in the chapter as well as some synthetic examples to illustrate the methodology. Section 6.3 is a parenthetical section which examines various model parameters to determine the preferred resistivity model at the LdMVF without any seismic constraint. Section 6.4 adds in the seismic constraints using hypothesis testing with perturbed models and constrained inversions. Finally, Section 6.5 provides a discussion of the results and conclusions including a conceptual model of the LdMVF magmatic system.

6.2 METHODOLOGY

6.2.1 Magnetotelluric Inversion Methodology

Magnetotelluric data are collected by measuring the orthogonal, horizontal electric and magnetic field components in the time domain. After taking the Fourier transform, these components can be related using a 2 × 2 matrix of electrical impedances in the frequency domain (Chave and Jones, 2012):

$$\begin{bmatrix} E_x \\ E_y \end{bmatrix} = \begin{bmatrix} Z_{xx} & Z_{xy} \\ Z_{yx} & Z_{yy} \end{bmatrix} \begin{bmatrix} H_x \\ H_y \end{bmatrix} \tag{6.1}$$

where the subscripts x and y denote fields in the north and east directions, respectively, and all variables are functions of angular frequency, ω.

The MT inverse problem takes the frequency-domain electrical impedance data, $Z_{ij}(\omega)$, and uses these as a data constraint to solve for a resistivity model of the Earth's subsurface. In most realistic MT surveys, the number of cells in the resistivity model is much larger than the number of data points to be used as a constraint and no unique solution exists. Thus, the inverse problem is ill-posed and requires an additional constraint or regularization (Parker, 1994). The underlying philosophy used in many approaches to MT inversion is that the resistivity model should be smooth with minimum structure (e.g. Constable et al., 1987; Egbert and Kelbert, 2012) and thus we seek to minimize the following objective function:

$$U(\lambda) = \phi_d + \lambda \phi_m \tag{6.2}$$

where ϕ_d is the data misfit penalty, ϕ_m is the model smoothness penalty, and λ is the regularization (or trade-off) parameter[1] which weights the relative importance of each term. A large regularization parameter will give greater weight to minimizing the model smoothness at the expense of poor data fit. In contrast, a small regularization parameter will give greater weight to minimizing the data misfit with a rougher model. An L2-norm is used to define data misfit penalty and the model smoothness penalty such that the objective function becomes

$$U(\mathbf{d}, \mathbf{m}, \lambda) = (\mathbf{d} - F[\mathbf{m}])^T \mathbf{C_d}^{-1} (\mathbf{d} - F[\mathbf{m}]) + \lambda (\mathbf{m} - \mathbf{m_0})^T \mathbf{C_m}^{-1} (\mathbf{m} - \mathbf{m_0}) \tag{6.3}$$

[1] The regularization parameter often goes by a variety of names including τ, λ, or ν among others (Kelbert et al., 2014; Parker, 1994; Robertson et al., 2020; Rodi and Mackie, 2001).

where $\mathbf{d}$ is a $N \times 1$ vector containing real and imaginary MT impedance data for all sites, frequencies and tensor components, $\mathbf{m}$ is the 3-D resistivity model re-arranged into an $M \times 1$ column vector, $\mathbf{m_0}$ is a reference conductivity model (usually a halfspace) of the same size as $\mathbf{m}$, and $F[\mathbf{m}]$ is the forward operator which computes predicted data from $\mathbf{m}$. The data covariance matrix, $\mathbf{C_d}$, is an $N \times N$ matrix containing data errors for each data point along the diagonal. The impedance data errors are often scaled with a relative error floor, $\epsilon > 0$, as some fraction of the off-diagonal impedance magnitudes because statistical data errors calculated during time series processing are too small and do not capture frequency-to-frequency noise (see Miensopust, 2017). The model covariance matrix, $\mathbf{C_m}$, is an $M \times M$ matrix which includes smoothing parameters with length scale, $0 < \gamma < 1$; the covariance matrix can be made very versatile to include different model domains, fixed model cells, and/or different smoothing length scale directions[2] (Egbert and Kelbert, 2012; Kelbert et al., 2014).

The first term of Equation (6.3) pertains to the data misfit penalty, ϕ_d. This is often reported as a scaled χ^2 statistic such as r.m.s. $= \sqrt{(1/N)\phi_d}$. Data misfit and model norm can be manually scaled by changing ϵ (which changes $\mathbf{C_d}$) and γ (which changes $\mathbf{C_m}$), respectively. Since the underlying modeling philosophy seeks minimum structure smooth solutions with adequate data fit, ϵ and γ must be chosen such that the inverse solution has a white r.m.s. misfit close to unity (or $\chi^2 = N$), a model norm close to zero, and geologically-realistic resistivity values. A white r.m.s. misfit of unity implies that data are being neither under-fit nor over-fit within error on average and that there are no spatial- or frequency-dependent trends in misfit. A model norm of zero would imply that the difference between the inverse model and the reference halfspace model is zero (e.g. the model is identical to the halfspace and has no structure). In practice, larger model norm also implies greater spread in the maximum and minimum resistivity values. Models with high model norm can sometimes include very unrealistic resistivity bounds (e.g. 10^{-3} Ωm to 10^{6} Ωm). There are a variety of different methods that have been suggested for finding optimal error floors and smoothing length scales (Miensopust, 2017; Robertson et al., 2020; Slezak et al., 2018). The choice of these parameters is somewhat arbitrary but it is important to keep these parameters constant when comparing different inversion solutions.

[2] The model covariance length scale can be given a different value for each orthogonal direction (x, y, or z). This allows for different levels of smoothing in different directions. Similarly, the smoothing can also be turned on or off for any model cell, essentially giving a different value of γ for every model cell. Here, γ is taken to be a single number applied to every model cell with equal weighting in all orthogonal directions.

Most algorithms used to minimize $U(\mathbf{d}, \mathbf{m})$ work by linearizing the objective function and then iteratively stepping towards some solution $\mathbf{m}_{k+1}$ given some prior model $\mathbf{m}_k$ (e.g. Kelbert et al., 2014; Siripunvaraporn, 2012). This iterative scheme requires an initial starting model, $\mathbf{m_s}$, as a first guess to begin the iterative process. Note that $\mathbf{m_s}$ and $\mathbf{m_0}$ are different. The reference model, $\mathbf{m_0}$, is used to define "smoothness" such that the final model, $\mathbf{m}$, is smooth relative to $\mathbf{m_0}$. If $\mathbf{m_0}$ is rough, then the inverse solution will be rough. For this reason, $\mathbf{m_0}$ is usually chosen as a halfspace. The starting model can be anything and can also be used to include *a priori* information (e.g. Bedrosian, 2007). It is also worth noting that a trivial solution exists if ϵ is scaled such that the r.m.s. is unity for $\mathbf{m_s}$.

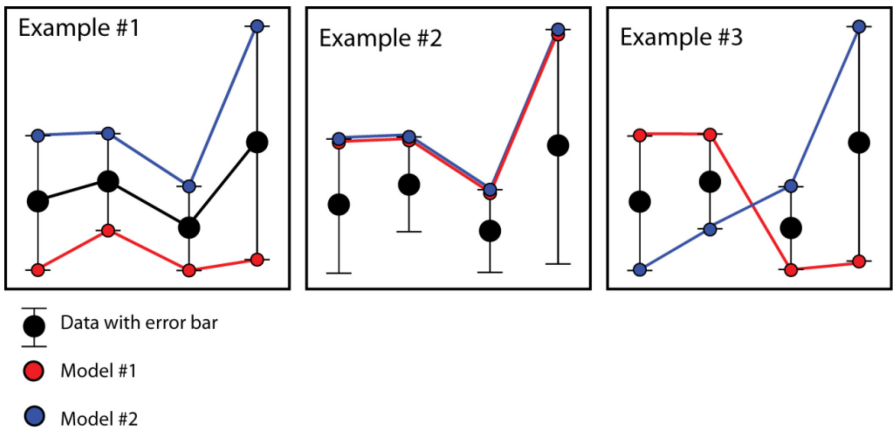

Figure 6.2: Example of a single data set with three different model comparisons. All the models have a normalized r.m.s. misfit of 1 implying good data fit.

6.2.2 Statistical Analysis of Residuals from Inverse Model Perturbations

Hypothesis testing is carried out by taking a model and perturbing or manipulating it in some way by adding, removing or replacing certain features of the model with a new resistivity value to explore the inverse solution space (Bedrosian, 2007). The most common method of hypothesis testing involves perturbing the preferred inversion model, $\mathbf{m_f}$, and then computing the MT forward response (i.e. the perturbed response) and comparing it to the original inversion response (e.g. Baba et al., 2006; Becken et al., 2008; Burd et al., 2014; Thiel and Heinson, 2010). This method is relatively fast and only requires one forward computation of the perturbed model. In assessing whether the perturbed response is different from the original response, most MT practitioners have used either visual examination of the MT apparent resistivity and phase curves and/or the relative change in data misfit. Visually assessing the difference in the curves is subjective and the relative change in data misfit says nothing of whether the

change is statistically significant or not. A notable exception is Baba et al. (2006) who used a two-sided F-test to test whether two model responses (e.g. an isotropic model response and an anisotropic model response) were statistically different within some confidence level. They used the ratio of the variances of the residuals (i.e. the ratio of the squared r.m.s. misfit values) as their test statistic. Their method was more statistically rigorous in using the F-test which is a parametric analysis of variance (ANOVA) test which assumes both distributions of residuals are Gaussian.

One drawback of using changes in a summary statistic such as r.m.s. misfit or variance is that these summary statistics use the absolute distance between data points and modelled points. This means that changes in r.m.s. misfit and/or variance fail to measure up- or down-biasing. It is possible to construct scenarios where one model response is biased up and the other is biased down but both have identical misfit. For example, Figure 6.2 shows three examples using an identical dataset. In the first example, Model #1 is biased downwards while Model #2 is biased upwards from the true data. Since each predicted data point touches the error bar, the residual, r, is equal to the error, Δd, and thus the squared normalized residual is 1 for all data points:

$$r^2 = \left(\frac{d_{obs} - d_{pred}}{\Delta d}\right)^2 = \left(\frac{\Delta d}{\Delta d}\right)^2 = 1 \tag{6.4}$$

Taking the sum of the squares results in an r.m.s. misfit of 1:

$$r.m.s. = \sqrt{\frac{1}{N}\phi_d} = \sqrt{\frac{1}{N}\sum_{k=1}^{N}\left(\frac{d_{obs}^k - d_{pred}^k}{\Delta d^k}\right)^2} = 1 \tag{6.5}$$

The same is true in both Examples #2 and #3 in Figure 6.2. In each case, the predicted data points touch the error bars and so the overall r.m.s. misfit for all cases is 1. However, visually examining Figure 6.2 clearly shows that Example #2 has nearly identical models whereas Example #3 has very different models (i.e. one trends up while the other trends down). Example #1 has very similar models but they are simply shifted vertically from one another. The r.m.s. misfit summary statistic does not capture any of this variation in the models.

In an effort to improve upon the assessment of the data fit of a perturbed model, statistical tests can be used to determine whether the sets of normalized residuals from the original inversion model and the normalized residuals from a perturbed model are drawn from the same underlying distribution. One of

the most basic variant of this test is the two-sample Kolmogorov-Smirnov (KS) test and has been applied to MT data by Lee et al. (2020). The null hypothesis of the KS test is that the two sets are drawn from the same distribution. This hypothesis is rejected if the distributions are different, based on a defined significance level. If the original inversion model and the perturbed model have the same MT response, then the distributions of residuals will be identical and result in the null hypothesis being confirmed with an asymptotic p-value near unity. However, if there is a difference between the two responses, then the residuals will not be the same and the KS test will result in p-values less than unity. Small p-values suggest larger differences between the distributions. It is common to use a significance threshold of $\alpha = 0.05$ to show that a result is statistically significant if $p < \alpha$. However, this is simply a convention and, in reality, it is often necessary to choose a lower significance level (e.g. 10^{-3}). This test can be performed on any two sets of residuals and is very quick to compute. As such, it is useful to show the KS test for the entire set (e.g. all residuals) but the KS test can also be shown for each MT site or each frequency to determine where significant changes are occurring in the residual distribution in both location and frequency. The test is sensitive to the number of data points, so comparing different data groupings (e.g. by site, by frequency, etc.) may result in statistical significance for some groupings but not others.

The test works by finding the maximum difference between the two empirical distribution functions for each set of residuals. This maximum difference is called the D-statistic and can be compared to a critical value of

$$D_{crit} = \sqrt{-\frac{1}{2}\ln(\alpha)}\sqrt{\frac{n+m}{nm}} \tag{6.6}$$

where n and m are the number of residuals in each of the two sets of residuals and α is the significance level. If the D-statistic is greater than D_{crit} then the null hypothesis is rejected. This can also be converted to an asymptotic p-value.

The KS test has several benefits over other statistical tests: 1) It is easy to compute and relatively simple to conceptualize; 2) it tests for difference in mean, median, and variance in the distributions simultaneously; 3) it is non-parametric and makes no assumption about the underlying distribution of the two data sets (i.e. if the residuals are non-Gaussian, the test still works) and; 4) it is sensitive to upwards and downwards biasing whereas other more common measures of goodness-of-fit (e.g. chi-square statistic, r.m.s. misfit or L2-norm) only measure absolute distance. If the distributions are

different within some significance level, then it implies that it is not random chance that has resulted in these differences but rather it is due to the perturbation. As with any statistical test, it is a tool that has benefits and drawbacks. One limitation of the KS test is that it is relatively insensitive to large outliers (unlike r.m.s.). As a result, a model perturbation that causes a large outlier on a very small number of data residuals may cause a statistically significant increase to the r.m.s. (e.g. by using the F-test) while not indicating statistical significance using the KS test. It is important to be cognizant of the limitations while using the KS test. For more details on the KS test, see Miller and Kahn (1962), or DeGroot and Schervish (2012).

A useful way to visualize the differences between the two datasets is to make a cross-plot of the two sets of normalized residuals (i.e. the perturbed residuals versus the original residuals). The y-axis is the observed data minus the predicted data with the model perturbation *(*$y = d_{obs} - d_{perturbed}$) and the x-axis is the observed data minus the original predicted data ($x = d_{obs} - d_{pred}$). Points which are unchanged lie along the diagonal $y = x$. Points above that line are down-biased (e.g. the impedance became more negative) while the points below the line are up-biased (e.g. the impedance became more positive). Points in the upper and lower triangular quadrants bounded by the lines $y = |x|$ and $y = -|x|$ represent modeled impedance values which became worse after the model was perturbed (e.g. the residual increased at those points when the perturbation was added) while points in the left and right quadrants improved (e.g. the residual decreased when the perturbation was added). This is a useful way of looking at a large dataset quickly to assess the number of data points which showed large perturbations and how many data points had misfit improve versus how many had misfit worsen.

6.2.3 One-Dimensional Synthetic Examples

To illustrate the benefits of the KS test and cross-plots, a synthetic example is shown in Figure 6.3 using a simple, one-dimensional, three-layer conductivity model. The synthetic "observed" data were computed analytically using a 100 Ωm halfspace with a 500 m thick, 1 Ωm layer located at a depth of 2 km (black line in Figure 6.3a). The data were contaminated with 5% Gaussian noise, with errors assigned as 5% relative error in both the real and imaginary components of the impedance. Apparent resistivity and phase data are shown in Figure 6.3b. It is assumed that the true model is unknown and there are two different, competing models which need to be evaluated. The first model is a 0.5 Ωm layer in a 100 Ωm halfspace (i.e. the "inversion model") while the other is a 1.7 Ωm layer in a 100 Ωm halfspace (i.e. the "perturbed model") (Figure 6.3a). MT data responses are calculated for both these models (blue and

red lines in Figure 6.3b). In this example, the r.m.s. misfit from the inversion response is 3.32 while the r.m.s. misfit for the perturbed response is 3.31. These are very similar and so, looking at this summary statistic alone is not a good indication that the inversion model and perturbed model are different. Similarly, the F-test of Baba et al. (2006) would result in the conclusion that the two models are equivalent since the ratio of the variances (i.e. the ratio of the squared r.m.s. misfit) is close to one. This fact—that two different models can have essentially the same misfit within data error—is a key component in the non-uniqueness of geophysical inversion. The KS test and cross-plots highlight the discrepancy very well in this example. The empirical distribution function (ECDF) for each set of normalized real and imaginary impedance residuals is shown in Figure 6.3c. Because the one set has a large number of negative residuals while the other has a large number of positive residuals, there is a large gap between the two ECDFs. The maximum difference between the two ECDFs (0.58) is larger than the critical value (D_{crit} = 0.14). The resulting p-value for the KS test is on the order 10^{-24} indicating a high statistical significance that the two sets of residuals are drawn from different distributions.

The cross plot of two identical models would fall along the 1:1 diagonal line in Figure 6.3d, however in this synthetic case, there is a group of points in the bottom right quadrant with an approximately equal number of impedance residuals having better and worse data fits after the perturbation is added (hence the identical r.m.s. for the original inversion and the perturbed model). The cross plots also show that most of the impedance values were biased up (e.g. the residuals became more positive) after the perturbation was added because most of the points lie below the 1:1 line.

Another slightly more complicated 1-D example is shown in Figure 6.4 and considers a real 1-D smooth inversion. The true data comes from an unknown synthetic model with 80 frequencies contaminated with 2% noise (Figure 6.4b). A 1-D Occam inversion (Constable et al., 1987) solved for a smooth model consisting of 137 layers with a data misfit of 0.995. Suppose that external information (e.g. borehole data) showed that the surface layer was 200 Ωm and from 2 to 5 km was a sequence of resistive 2000 Ωm rocks followed by a conductive unit at 5.5 km depth. Using these parameters, the Occam inversion model was edited to include additional structure (Figure 6.4a). The resulting r.m.s. misfit of the perturbed model is 0.997, nearly identical to the original inversion and the visual fit of the curves is also similar (Figure 6.4b). But the models are clearly different: one is smooth with no significant resistor while the other contains a 3 km thick, 2000 Ωm resistor. The reason for this is that when the original inversion is biased down from the true data, the perturbed model is biased up and vice versa (Figure 6.4b). No

comparison of r.m.s. misfit (including the F-test) would suggest a difference between the models. The KS test, ECDFs, and cross-plots are able to clearly show this distinction in the data in Figure 6.4c and d. The maximum difference in the two ECDFs is 0.325 which is larger than the critical value (D_{crit}= 0.14). The KS test results in a p-value on the order of 10^{-8} which strongly suggests that the two sets of residuals are drawn from different distributions (despite having identical misfit). The cross-plot of residuals in Figure 6.4d also clearly shows that the residuals are not the same with many points plotting in different quadrants. Some residuals became better after adding the perturbation while an approximately equal number became worse.

These simple examples highlight some of the limitation of using only r.m.s. to compare different model results and some of the benefits of including additional statistical tests, such as the KS test, when comparing model responses. In a 1-D case with only one MT station, it is easy to look at the curves and the model to see the difference, but a similar phenomenon can occur with 2-D or 3-D data with hundreds of sites and complicated model structures where two sets of MT responses (e.g. inversion response and perturbed response) have similar summary misfit statistics (relative to some observed data) but a different distribution of residuals.

6.2.4 Constrained Inversions

When using three-dimensional inversions, the above method of hypothesis testing is desirable because it is relatively quick requiring only a single forward computation of the perturbed model. However, it is limited by the fact that it makes an implicit assumption that the original inversion model is the best-fitting model for the solution space and all perturbations are evaluated with this inversion model as a benchmark. It may be possible for the data to be better fit—or equally well fit—with the perturbation added if the inversion is allowed to change within this *a priori* constraint. The methodology of using constrained inversions is similar to that of Bedrosian (2007) where the perturbed model cells are included in the starting model halfspace, $\mathbf{m_s}$, and then this perturbed inversion is run to convergence to a new solution. There are two permutations to this methodology. In one variation, the perturbed cells are fixed and not allowed to change from their given resistivity value (i.e. a modification of both $\mathbf{m_s}$ and $\mathbf{C_m}$). In a second variation, the perturbed cells are included in the starting model but allowed to change as the inversion progresses (i.e. a modification of $\mathbf{m_s}$ only). When comparing inversions, changing $\mathbf{C_m}$ will change the topology of the objective function and so comparing the convergence of inversions with different model covariance matrices should be done with caution.

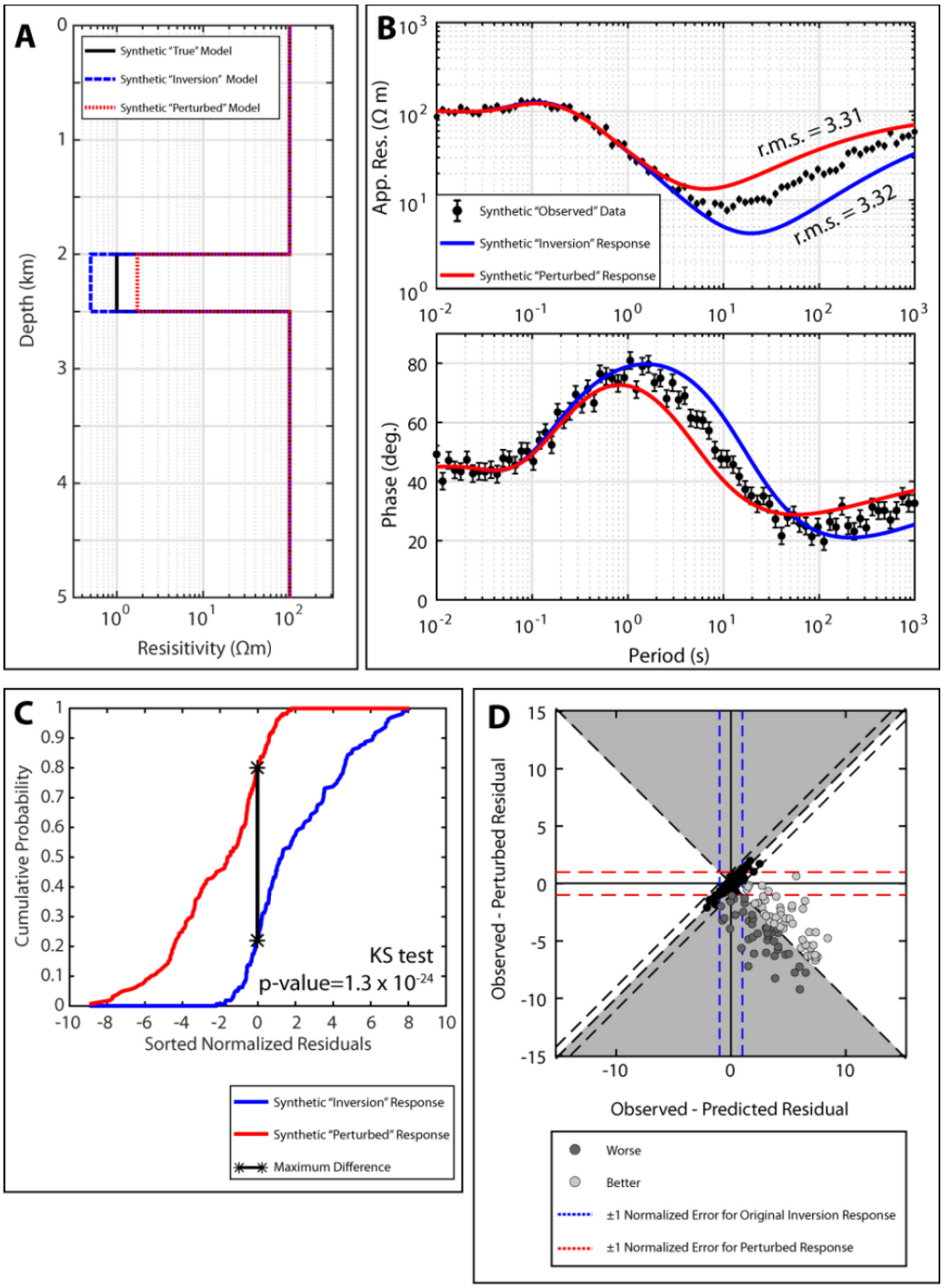

Figure 6.3: Synthetic example to illustrate the benefit of the KS test. (a) The one-dimensional models used for the test. The "true" model is the black line. (b) The apparent resistivity and phase synthetic data (black dots) computed from the true model and model responses computed from the two test models. (c) The empirical distribution functions for the normalized residuals of the two test models. (d) Cross plots of the two sets of normalized residuals. Light grey triangular regions denote areas where residuals became larger after adding the perturbation; white triangular regions show areas where residuals became smaller.

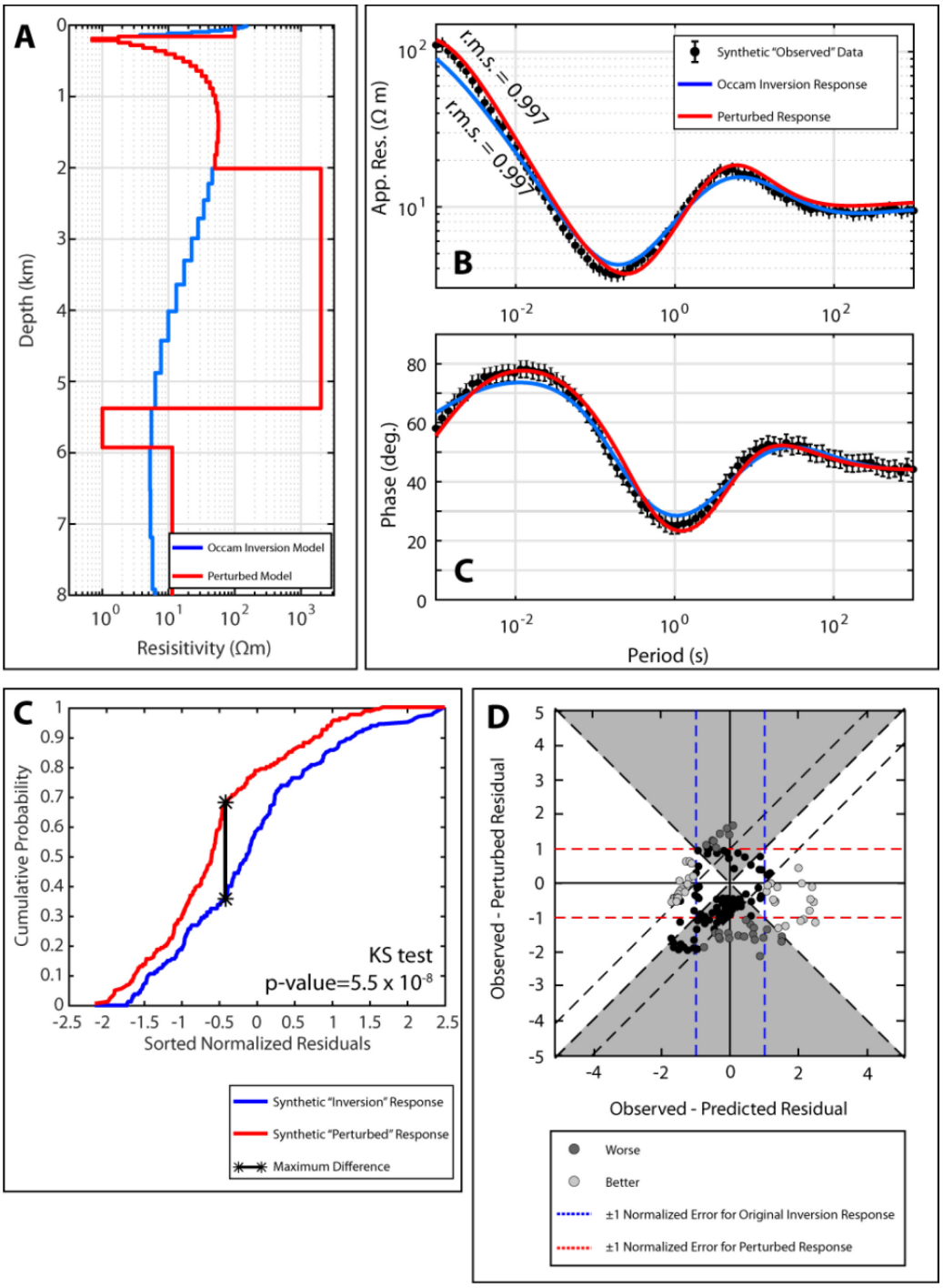

Figure 6.4: Second synthetic example to illustrate the benefit of the KS test. (a) The 1-D Occam inversion model and perturbed model. (b) The apparent resistivity and phase synthetic data (black dots) computed from the unknown true model, and model responses computed from the inversion model and perturbed model. (c) The empirical distribution functions for the normalized residuals. (d) Cross plots of the two sets of normalized residuals. Light grey triangular regions denote areas where residuals became larger after adding the perturbation; white triangular regions show areas where residuals became smaller.

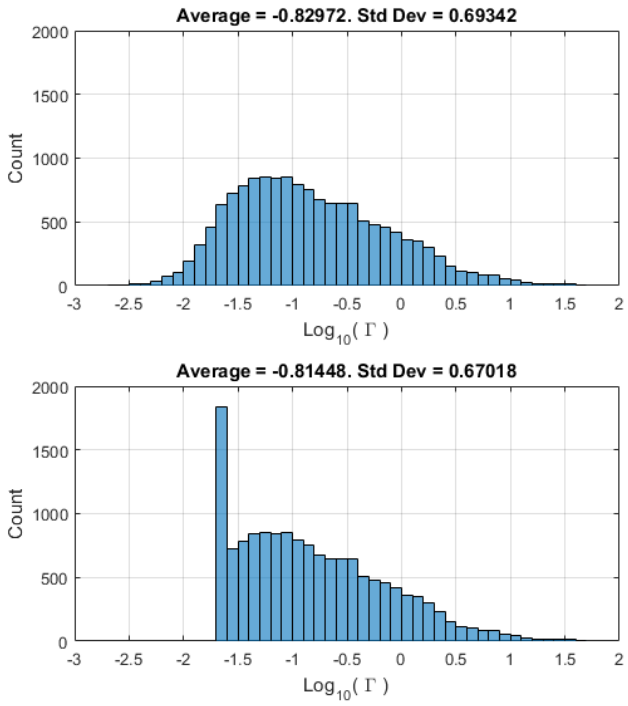

Figure 6.5: Histogram of the relative error for the inversion data set on a logarithmic scale for (a) the original dataset and (b) after applying a 2% error floor.

The new inversion solution may have a similar or lower r.m.s. misfit to the original inversion which would imply that the data can be adequately fit with or without the perturbation. However, the model may be significantly rougher (i.e. a larger model norm) and may include new artefacts, complicated structures, and/or geologically-unrealistic features. As mentioned earlier, the underlying philosophy of MT inversion is that models should contain minimum structure. So even if the new inverse model has a similar data fit, the model norm may be much larger suggesting a poorer model. It is preferable to examine both model norm and data misfit to see which inversion best balances the two terms in Equation (6.3). It is also possible to compare different inversion methodologies using the KS test and cross plots. Rather than simply comparing the r.m.s. misfit between two inversions, the KS test can be used to examine whether the two inversions have the same distribution of residuals. If they do, then there is a stronger case to be made that these two models are equally valid and can be interpreted as such. If the distribution of residuals is different, then it is more likely that the model responses are distinct within data error.

6.3 LAGUNA DEL MAULE MAGNETOTELLURIC DATA SELECTION AND INVERSION PARAMETERS

As described above, much of the hypothesis testing workflow uses an existing "preferred" inversion model as a benchmark to compare to other perturbed models. As such, it is important to do a thorough examination of the model space before deciding on a preferred inversion to interpret. When performing 3-D inversions, it is important to consider the inputs and how they will influence the output. This section examines a variety of factors which influence the inversion solution. In general, there are too many variables to thoroughly investigate the solution space including data selection, mesh design, inversion parameters, and inversion algorithm (Miensopust, 2017; Robertson et al., 2020). For this reason, any investigation of inverse models must necessarily make certain choices as to which variables will remain constant throughout the investigation.

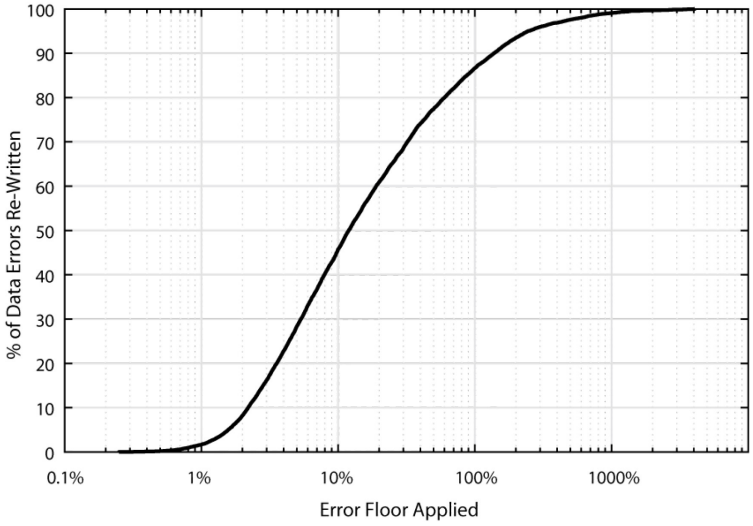

Figure 6.6: Percentage of Data Errors Changed versus the Error Floor.

For all modelling in this chapter, the ModEM inversion algorithm is used (Kelbert et al., 2014). This analysis uses the same MT dataset described in Chapter 5 from the LdMVF (Cordell et al., 2018). The dataset includes 71 stations with all four impedance components and 22 frequencies logarithmically spaced between 0.005 Hz to 1000 Hz. The total number of data points is $N = 9{,}776$. The model mesh was kept constant and used interpolated SRTM topography which is nearly identical to the model mesh used in Chapter 5. The model mesh has 98 x 74 x 120 cells ($M = 870{,}240$) including 12 padding cells in the north-south and east-west directions which grow geometrically by a factor of 1.5 out to 200 km to avoid boundary effects. The core of the mesh includes 500 m x 500 m cells. In the z-direction, there are 51 topography cells with a thickness of 50 m beginning at 3.8 km a.s.l., and 69 Earth cells which grow

approximately geometrically to a depth of 700 km. It would be interesting to explore the effects of cell size, station distribution, inversion algorithm and frequency distribution, among other factors, but the 3-D inverse problem remains computationally intensive so it was not possible to do so. See Miensopust (2017) for a review of some of these variables which effect inversion solutions. Here, we examine the effect of error floor (Section 6.3.1), starting model (6.3.2), and covariance smoothing (6.3.3). After these various tests and explorations of the solution space, the preferred inverse model is presented in Section 6.3.4.

6.3.1 Error Floor

To examine the effect of changing the error floor (ϵ), an investigation of the relative data error is necessary. Relative error is defined as

$$\Gamma = \frac{\Delta Z_{ij}}{\sqrt{|Z_{xy}||Z_{yx}|}} \tag{6.7}$$

Where ΔZ_{ij} is the real-valued error of each impedance tensor component for a given station and frequency as determined by the statistical time series processing. A histogram of the relative error of the inversion dataset is shown in Figure 6.5a. The relative error follows a roughly Gaussian distribution in logarithmic space with a mean relative error of 14.8%. Figure 6.5b shows the same dataset with a 2% error floor applied. Here, all relative errors less than 2% (-1.7 in logarithmic space) are replaced with 2% relative error.

Another way to consider error floors is to look at the percentage of data errors which are re-written as a function of error floor. In other words, the empirical cumulative distribution function of the relative errors. This is shown in Figure 6.6. From the graph, it can be seen that an error floor of 12% will result in 50% of the errors being re-written. There is no rule regarding how many errors should be changed for the inversion, but some logical choices would be to begin by setting the error floor to the mean relative error (ϵ =14.8%), or to set it so that 50% of the data errors are changed (in this case ϵ =12%). If an inversion is being run with a very large percentage (e.g. 90%) or very small percentage (e.g. 0.5%) of errors being re-written, it is likely that this error floor is not suitable for the dataset.

Eight different inversions were run with different error floor values (2.5%, 5%, 6%, 8%, 10%, 12%, 14.8%, and 20%) to examine the effect on the inversion solution and the results are summarized in Table 6.1. Each inversion used a 100 Ωm halfspace starting model and model covariance length scale of γ=0.3.

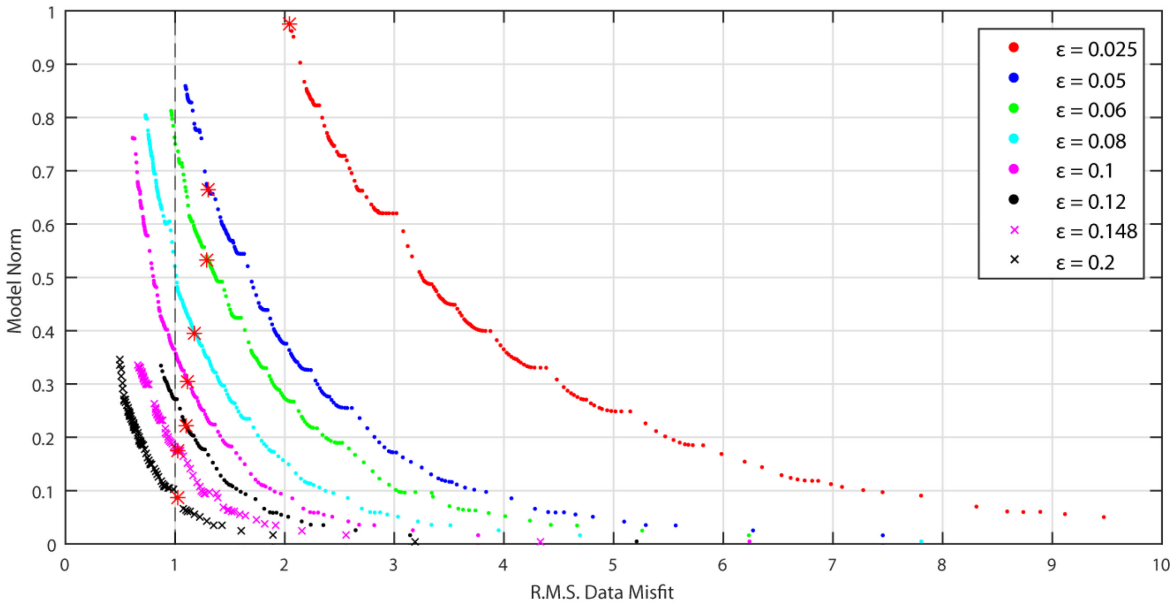

Figure 6.7: Model norm versus data misfit convergence curves for inversions with varying error floor. The red asterisk on each convergence curve shows the optimal inversion iteration.

When comparing inversion solutions, it is useful to compare the convergence curves, as shown in Figure 6.7, which plot data misfit versus model norm as a function of iteration (i.e. the two competing terms in Equation (6.2)). All the inversions begin with a halfspace and thus start on the right of the plot with high misfit and zero model norm. The inversions progress to the left and decrease the misfit at the expense of a higher model norm (i.e. a rougher model). As can be seen in Figure 6.7, using an error floor of 2.5% results in both high model norm and high misfit for both the initial and final iteration whereas larger error floors (e.g. 20%) results in both low model norm and low misfit. Thus, error floor effectively scales r.m.s. misfit. An r.m.s. misfit of unity is desirable for noisy data, but there is no statistical or theoretical rule on what the optimal model norm should be. As a result, there are six different error floors which result in an r.m.s. of unity (Table 6.1). However, equivalent r.m.s. misfit does not mean identical models since the errors are different and thus the resulting model norm is different. In general, for equivalent r.m.s. misfit, the model norm is higher for inversions which used a lower error floor. The two smallest error floors (5% and 2.5%) could not achieve an r.m.s. of unity after running for 300 iterations with final $\lambda = 10^{-8}$. This suggests that error floors less than 5% are not suitable for this dataset.

Figure 6.8 shows N-S slices through the model from the iteration which achieved an r.m.s. of unity for each inversion solution. As can be seen, higher error floor results in a smoother model with less structure even though all the shown models have the same r.m.s. The inversions using 2.5% and 5% error floor are not shown because they did not converge to an r.m.s. of unity.

Table 6.1: Inversion results when varying error floor[3]

Error Floor, ϵ	Initial r.m.s	Final r.m.s.	# of Iterations	Iteration # with r.m.s. = 1	Optimal Iteration #	Optimal r.m.s	Runtime (days)	Final λ
2.5%	40.88	2.04	300	N/A	300	N/A[4]	6.9	10^{-8}
5%	20.56	1.09	300	N/A	203	1.31	7	10^{-8}
6%	17.15	0.96	300	292	151	1.30	5.2	10^{-4}
8%	12.89	0.76	300	163	95	1.18	N/A[5]	10^{-5}
10%	10.32	0.61	264	90	67	1.11	6.1	10^{-8}
12%[6]	8.61	0.73	123	53	46	1.10	8.3	1
14.8%	6.99	0.50	202	33	30	1.03	4.3	10^{-1}
20%	5.17	0.50	123	14	13	1.02	3.1	10^{-1}

The model from the final iteration for each inversion is shown in Figure 6.9. For most error floors, the final models are nearly identical for most chosen error floors. Like in Figure 6.8, the inversions which use a larger error floor have smoother models (and this is also evident from the convergence curves). However, the differences between the 5%, 6%, 8% and even 10% models are very subtle and it is only at much higher error floors (e.g. >12%) that the smoothness of the final solution becomes apparent visually. This suggests that re-weighting less than 50% of the data errors does not cause a visual change to the smoothness of the model solution. Using a 6% error floor results in an inversion which most-closely converges to an r.m.s. of unity. This suggests that using a 6% error floor is ideal for the noise-level in this dataset. An error floor of 6% results in 30% of data errors being re-weighted (Figure 6.6).

[3] Inversions stopped running due to one of the following criteria: minimum r.m.s. of 0.5, maximum number of iterations of 300, maximum runtime of 7 days, or minimum λ of 10^{-8}.
[4] Since the "optimal iteration" for the 2.5% error floor was the final iteration, it would be necessary to run more iterations to confirm which is the optimal iteration.
[5] The total runtime for this inversion was never recorded.
[6] This inversion would not converge as normal for unknown reasons due to problems with node failures on the WestGrid computing cluster.

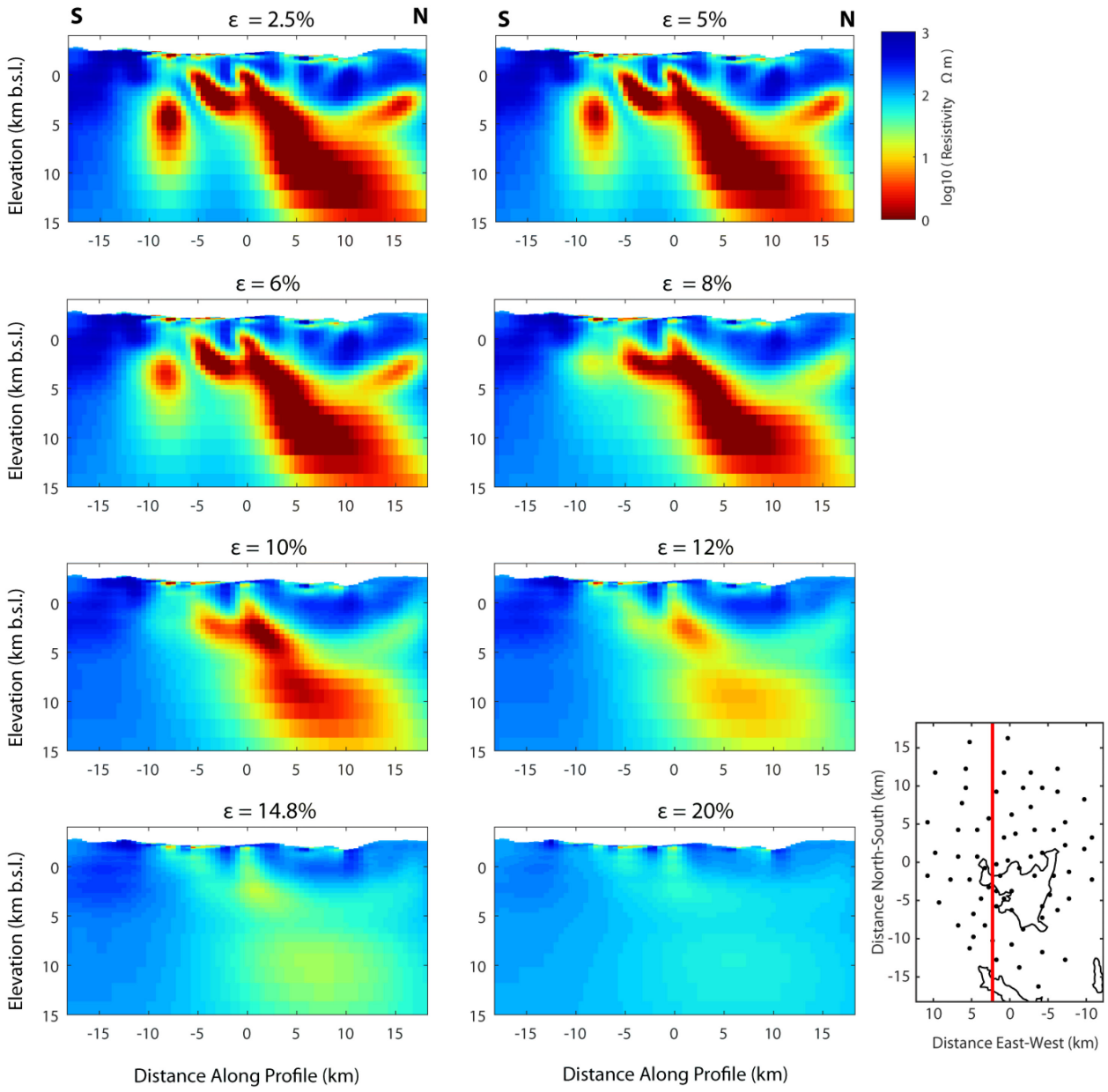

Figure 6.8: North-south model slices for inversions using varying error floors. The iteration shown is the one which achieved an r.m.s. of unity. The location of the vertical slice is shown on the inset map at bottom right.

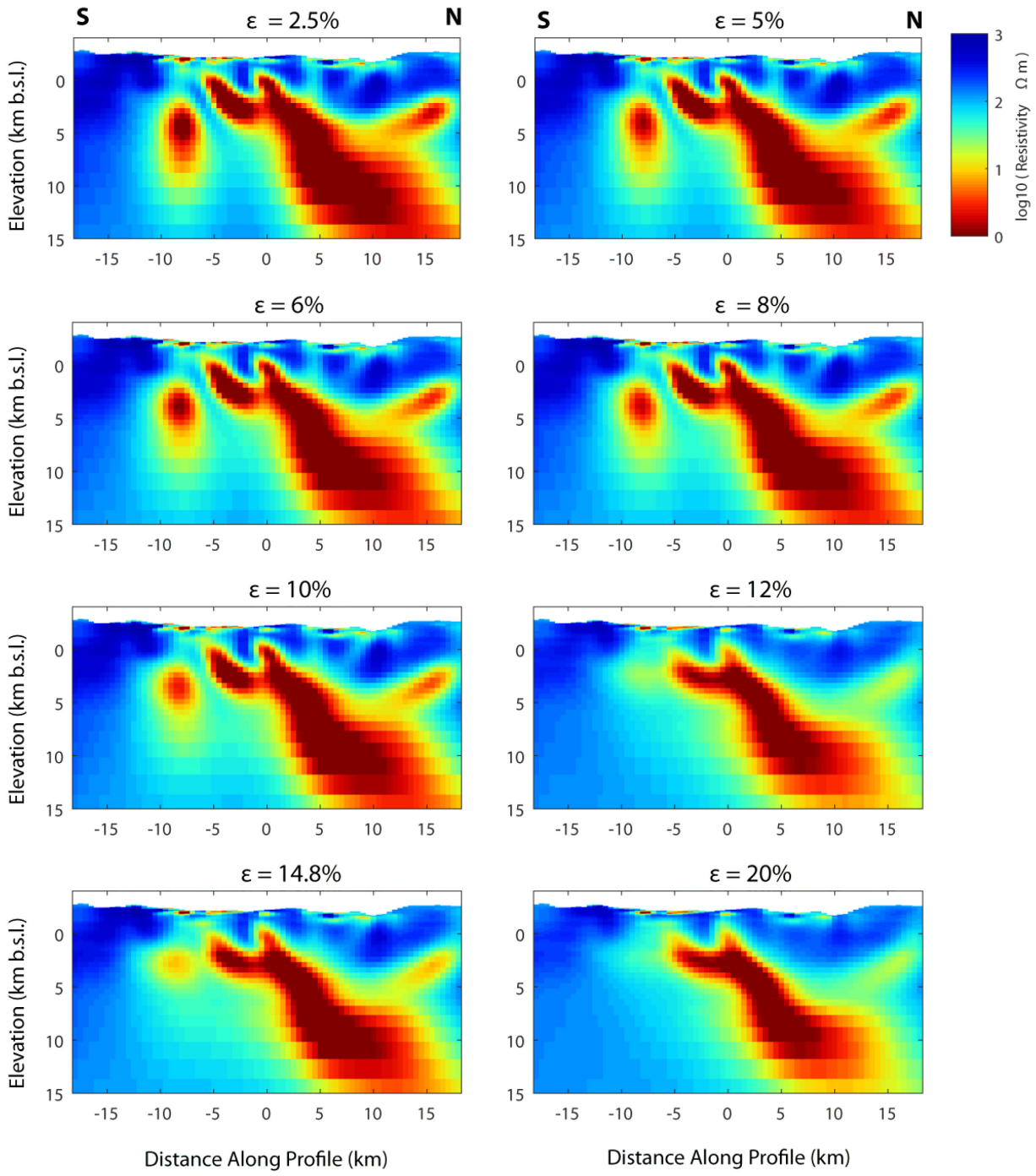

Figure 6.9: North-south model slices for the final iteration of inversion models using varying error floors. The location of the north-south slice is the same as shown in Figure 6.8.

ModEM seeks to minimize both terms in Equation (6.3) to zero. However, as the inversion progresses the regularization parameter (λ) decreases which gives less weight to the model norm. This means that at later iterations, ModEM seeks to minimize only the data misfit regardless of how rough the model solution becomes. In practice, this tends to cause later iterations to have unrealistically rough models with unrealistic, extreme resistivity values and geologically-unlikely artefacts. This is clear in Figure 6.9 where large volumes of the models have resistivities less than 0.1 Ωm. Instead of choosing the final model iteration, it may be better to choose the model which minimizes the model norm and minimizes the distance between the r.m.s. misfit and a misfit of unity. The optimal inversion iteration for each error floor is listed in Table 6.1.

Table 6.2: Inversion results when varying starting and prior model[7]

Starting Model, $\mathbf{m_s}$	Initial r.m.s.	Final r.m.s	# of Iterations	Iteration # with r.m.s.=1	Optimal Iteration #	Optimal r.m.s	Runtime (days)	Final λ
10 Ωm	5.38	1.07	229	N/A	76	1.32	8.8	10^{-8}
100 Ωm	16.65	1.11	256	N/A	141	1.33	8.3	10^{-8}
1000 Ωm	61.26	1.53	300	N/A	248	1.62	8.9	10^{-5}

6.3.2 Starting Model and Reference Model

The choice of starting model, $\mathbf{m_s}$ and reference model, $\mathbf{m_0}$ is also an important factor in influencing the overall inversion (Robertson et al., 2020). In general, if we change $\mathbf{m_s}$ without changing $\mathbf{m_0}$, then the topology of the objective function remains unchanged and the inversion should ideally have the same minimum but only start at a different location. However, changing $\mathbf{m_0}$ influences the topology of the objective function and thus changes the minimum location of the inversion solution. In general, it is preferable to keep the starting model and the reference model the same so that the inversion seeks smooth variations from the starting model itself. To investigate the effect of the starting model, three different inversions were run with 10, 100, and 1000 Ωm starting model (and reference model). Error floor and model covariance length scale were kept constant at ϵ = 0.08 and γ = 0.3. It is worth noting that the mean apparent resistivity for the survey area is approximately 90 Ωm for the off-diagonal components, so it is anticipated that a starting model of 100 Ωm will be preferable.

[7] Inversions stopped running due to one of the following criteria: minimum r.m.s. of 0.5, maximum number of iterations of 300, maximum runtime of 10 days, or minimum λ of 10^{-8}. Note that these inversions were run earlier using a more preliminary dataset than the other tests.

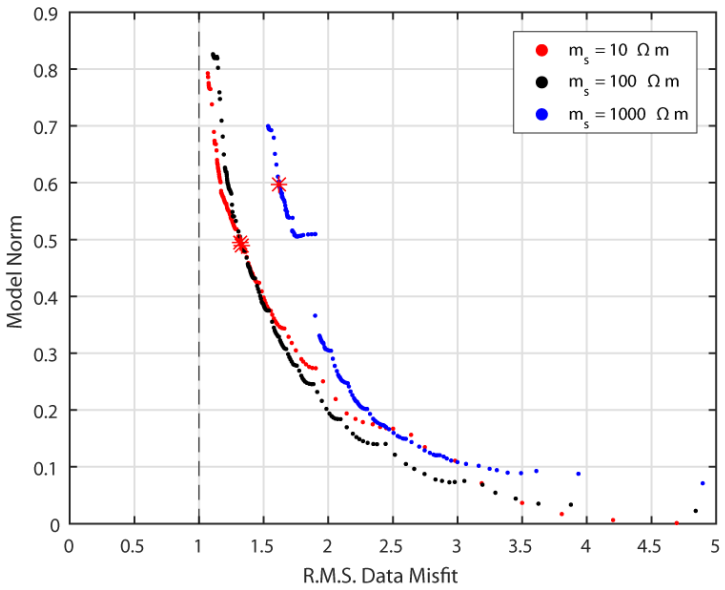

Figure 6.10: Model norm versus data misfit convergence curves for inversions with varying starting model. The red asterisk on each convergence curve shows the optimal inversion iteration.

The results from this test are summarized in Table 6.2. The inversion convergence curves and north-south model slices for the final iteration are shown in Figure 6.10 and Figure 6.11, respectively. The inversion which used a starting model of 10 Ωm began with the lowest r.m.s. whereas the 1000 Ωm starting model began with a very high r.m.s. misfit of 61.26. Both the 10 and 100 Ωm starting models converged to similar misfit and model norm whereas the 1000 Ωm starting model converged to a higher misfit (and higher norm) solution. The optimal models for the 10 and 100 Ωm starting model also have almost identical r.m.s. misfit (1.33 or 1.32) and model norm (approximately 0.5). This suggests that both starting models perform similarly in the inversion. The top row of model slices shown in Figure 6.11 highlight the fact that the choice of starting model has a significant impact on the model features and resistivities. Even when the color bar is scaled to the respective inversions halfspace value (as shown in the bottom row of Figure 6.11), the geometry and depth of the features is still considerably different. In general, a higher initial halfspace resistivity leads to the inversion placing features at greater depth due to the skin depth equation (see Equation (4.16) in Chapter 4).

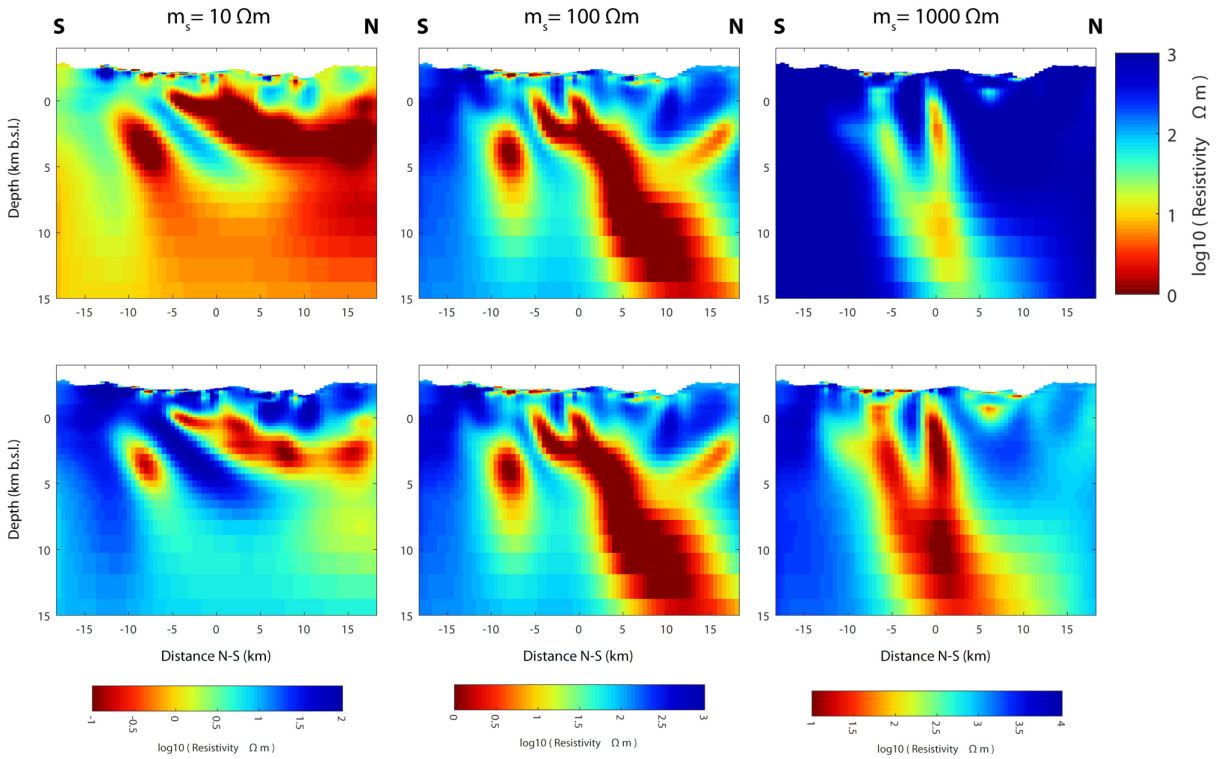

Figure 6.11: North-south model slices for the final iteration of inversion models using difference starting models. The top row shows the models plotted with identical color scales. The bottom row shows the same models plotted with different color scales normalized to the starting model halfspace value (i.e. the starting model halfspace value is the same color on each plot). The location of the north-south slice is the same as shown in Figure 6.8.

The similarity in the summary statistics (i.e. model norm and r.m.s. misfit) between the 10 and 100 Ωm starting model inversions given the visual difference in the models is striking. This provides a cautionary tale that summary statistics can be misleading especially when the topology of the objective function is altered by changing $\mathbf{m_0}$. In general, the 100 Ωm starting model provides less extreme resistivity values which are more geologically realistic whereas the 10 Ωm starting model has large volumes of the model below 1 Ωm. As mentioned earlier, the average apparent resistivity of the off-diagonal impedance components is approximately 90 Ωm. Thus, all future models use a 100 Ωm halfspace starting model and prior model.

6.3.3 Model Covariance

The final parameter which is investigated which influences the objective function is the model covariance length scale, γ, as applied to the model covariance matrix, $\mathbf{C_m}$. It is generally stated that a smaller covariance length scale will result in a rougher inverse model and a larger covariance length

scale will result in a smoother model (Robertson et al., 2020). However, there is a somewhat complicated relationship between γ, the model norm, the inversion convergence, and the visual smoothness of the model. To investigate this, the covariance length scale was given different values of 0.1, 0.3, and 0.5. A 6% error floor was applied for all the inversions and the inversion was started from a 100 Ωm halfspace. The convergence curves for these three inversions are shown in Figure 6.12 and Table 6.3 summarizes the results.

Table 6.3: Inversion results when varying model covariance length scale[8]

Covariance γ	Initial r.m.s.	Final r.m.s	# of Iterations	Iteration # with r.m.s.=1	Optimal Iteration #	Optimal r.m.s	Runtime (days)	Final λ
0.1	17.15	1.26	376	N/A	373	1.26	11.0	10^{-8}
0.3	17.15	0.96	300	292	151	1.30	5.2	10^{-4}
0.5	17.15	0.85	281	191	42	1.60	11.0	10^{-8}

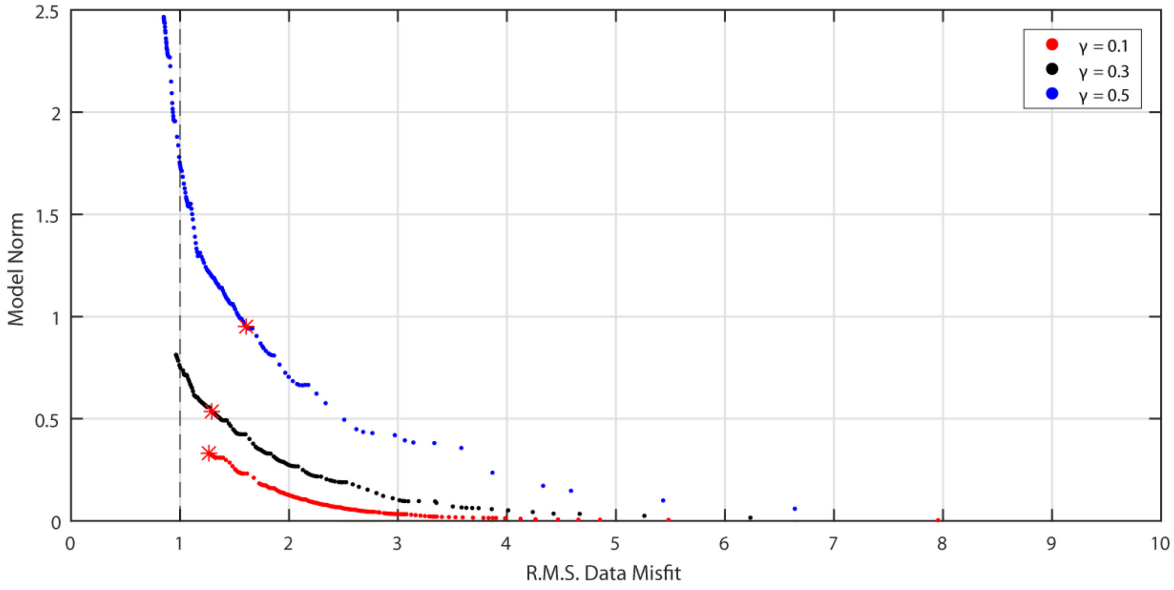

Figure 6.12: Model norm versus data misfit convergence curves for inversions with varying covariance length scales. The red asterisk on each convergence curve shows the optimal inversion iteration.

[8] Inversions stopped running due to one of the following criteria: minimum r.m.s. of 0.5, maximum number of iterations of 300, maximum runtime of 15 days, or minimum λ of 10^{-8}.

From the convergence curves, it is clear that using a covariance length scale of γ = 0.1 does not allow the inversion to converge. It gets stuck in a local minimum with an r.m.s. of 1.26 and stops converging due to small step length. Using a value of γ = 0.5 allows the model to converge fully but results in a very high model norm (e.g. a rough model). Figure 6.13 shows N-S slices through model from the final iteration for the three inversions using different covariance length scales. The top row of Figure 6.13 shows the models plotted as a function of depth. Based on visual examination, it appears that the model using γ=0.1 results in a smoother model than γ=0.5 with both less structure and less extreme resistivity values. These results are counterintuitive to the way that the covariance parameter is usually explained where higher values should result in smoother models.

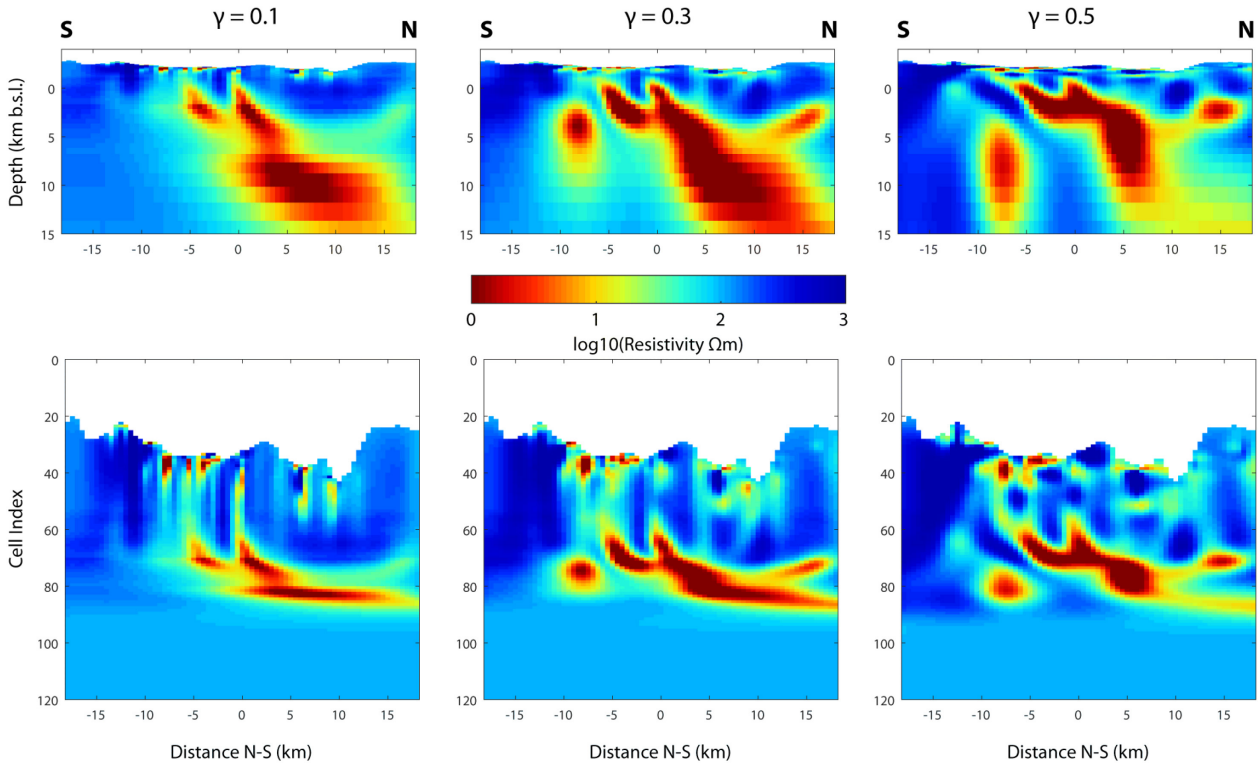

Figure 6.13: North-south model slices for the final iteration of inversion models using difference covariance length scales. The top row shows the models plotted as a function of depth as per normal model visualization. The bottom row shows the same models plotted as a function of z-cell index. The location of the north-south slice is the same as shown in Figure 6.8.

The counterintuitive results are due to the fact that the explanation of the covariance parameter is an over-simplification. There are three complications to the covariance parameters.

(1) The choice of γ influences the inversion algorithm convergence. If one inversion can converge further than another inversion, it will likely result in higher model norm. If an inversion becomes stuck in a local minimum then the model norm will likely be lower. It is difficult to predict which covariance parameters will result in inversions becoming stuck in a local minimum.

(2) The application of the model covariance length scale is independent of cell size. MT models generally have very thin cells at the surface (e.g. 50 m thick) and very thick cells at the base (e.g. 50 km thick). But the model covariance smoothing applies across cells rather than across distances. As a result, the model may be rough, but all the roughness is contained within the upper 500 m. This effect is shown in the second row of Figure 6.13. Instead of plotting the models as a function of depth, the models are plotted as a function of cell index. This view of the model clearly shows that using γ=0.1 results in a rougher model than γ=0.5. But the roughness (or smoothness) in the models is most evident in the top 60 cells which is equivalent to the top 1.5 km. This confirms that a smaller γ does indeed result in a rougher model on a cell-by-cell basis. However, this still does not explain why the model norm is lower for the model with γ=0.1 compared to the model with γ=0.5.

(3) The final counterintuitive aspect of the model covariance length scale is that it influences cell-to-cell variations (e.g. resistivity gradients) whereas model norm compares variations from the prior model, $\mathbf{m_0}$. As a result, a model may be "rough" when comparing adjacent cells while the absolute differences in resistivity from the prior model are relatively small. For example, based on visual examination of the second row of Figure 6.13, the cell-to-cell variations in the γ=0.1 case are larger than the cell-to-cell variations in the γ=0.5 case. However, the overall differences from the prior model are greater in the γ=0.5 case which includes more extreme resistivity values (e.g. <1 Ωm and >1000 Ωm), hence the higher model norm in Figure 6.12.

The interplay of these three factors which influence the resulting inversion models makes it very difficult to predict how a given dataset and model mesh will respond to a given covariance value. A conservative method is to use the default value of γ=0.3 which has been shown to give reasonable results. (e.g. Robertson et al., 2020).

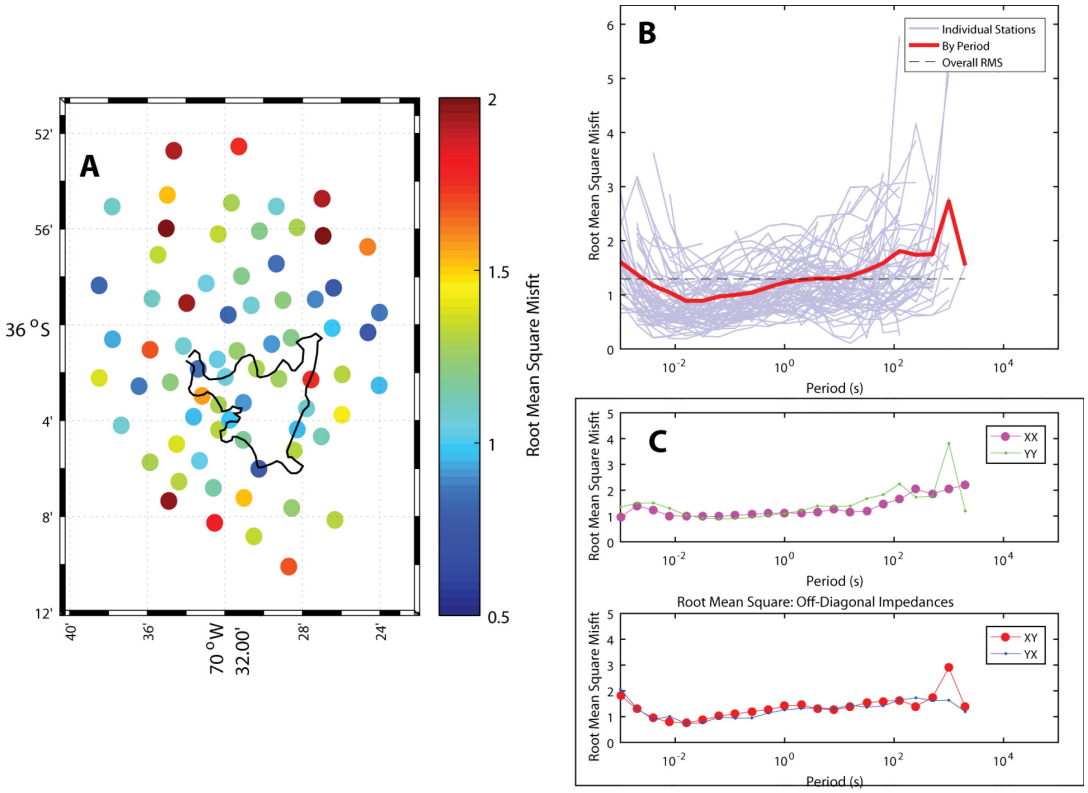

Figure 6.14: Data r.m.s. misfit for the preferred inversion model. (a) shows the r.m.s. misfit as a function of MT station. (b) shows the r.m.s. misfit as a function of period for each station (blue lines) and all stations (red line). (c) shows the r.m.s. misfit as a function of period for each component of the impedance tensor. Overall r.m.s. misfit was 1.30.

6.3.4 Current Magnetotelluric Inversion Model

Based on the above tests, the preferred inversion uses a relative error floor of $\epsilon = 0.06$ such that the inversion converged to approximately an r.m.s. of unity after 291 iterations (Figure 6.7). A model covariance smoothing parameter of $\gamma = 0.3$ was used and a 100 Ωm halfspace was used for $\mathbf{m_0}$ and $\mathbf{m_s}$. The optimal iteration model was found at iteration 151 (r.m.s. misfit of 1.30, model norm of 0.53; Table 6.1). The data misfit between the observed data and the inversion response is shown in Figure 6.14 in map view for each station and as a function of period and impedance component. In general, the r.m.s. misfit is relatively uniform both spatially and as a function of frequency with only some small outliers at long periods (>100 s). The misfit is similar for both diagonal and off-diagonal components and stations with higher misfit tend to be located on the edges of the array as expected. Representative data fit at sites LDM002, LDM013 and LDM039 are shown in Figure 6.15. The resistivity model is shown in Figure 6.16 using horizontal and diagonal slices. In general, the primary conductive features in this model are similar

to those presented by Cordell et al. (2018) as shown in Figure 6.17. The model of Cordell et al. (2018) had an r.m.s. misfit of 1.47 and a model norm of 0.41 meaning that the model was smoother at the expense of higher misfit compared to the updated model presented here. The updated model provides a better trade-off between model norm and misfit by minimizing the distance to an r.m.s. of unity and a model norm of zero.

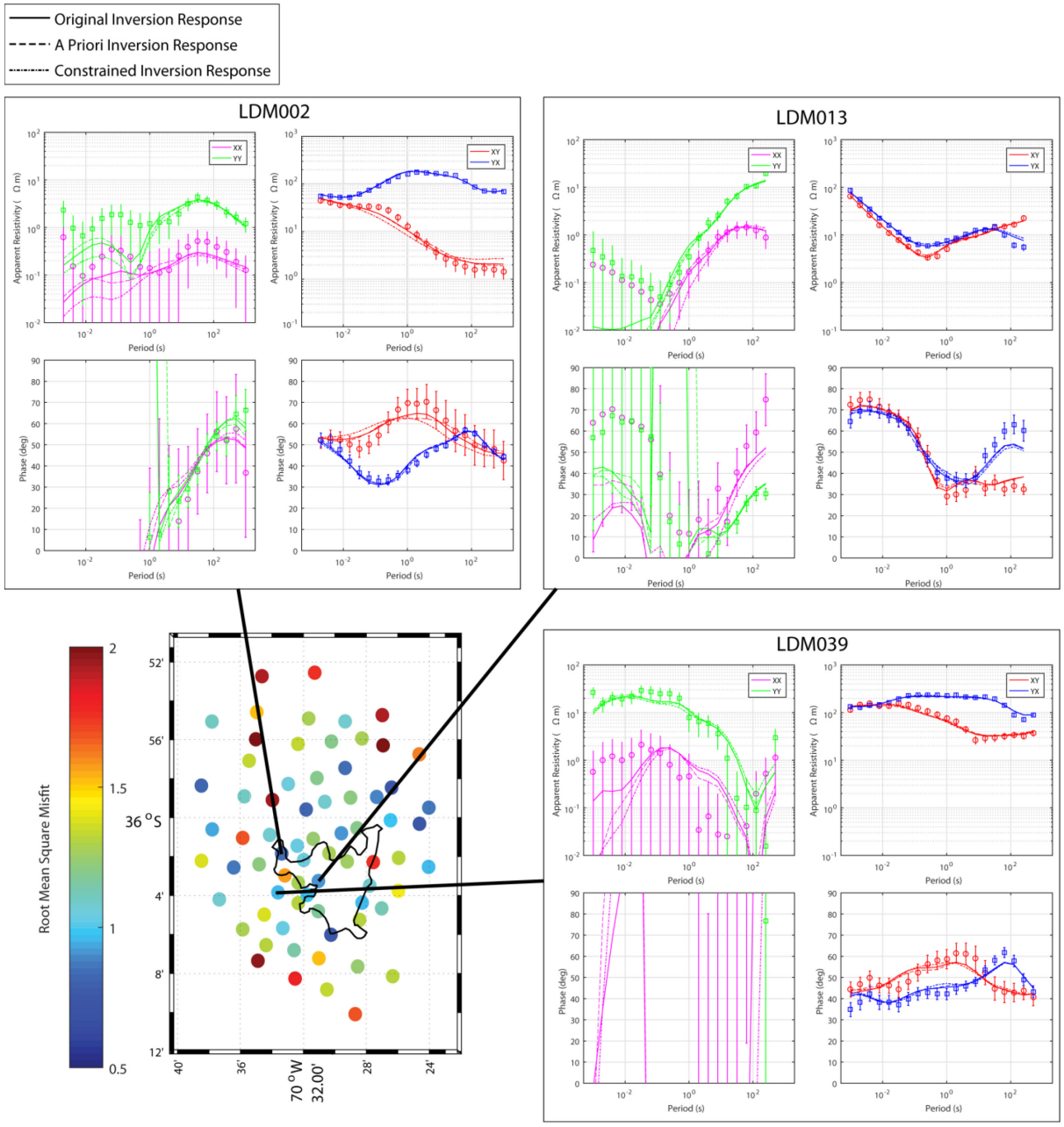

Figure 6.15: MT data curves for selected sites. The map shows r.m.s. misfit as a function of station. Each station shows the observed MT data, the inversion response for the preferred MT model, the inversion response for the *a priori* inversion MT model, and the inversion response for the constrained inversion MT model.

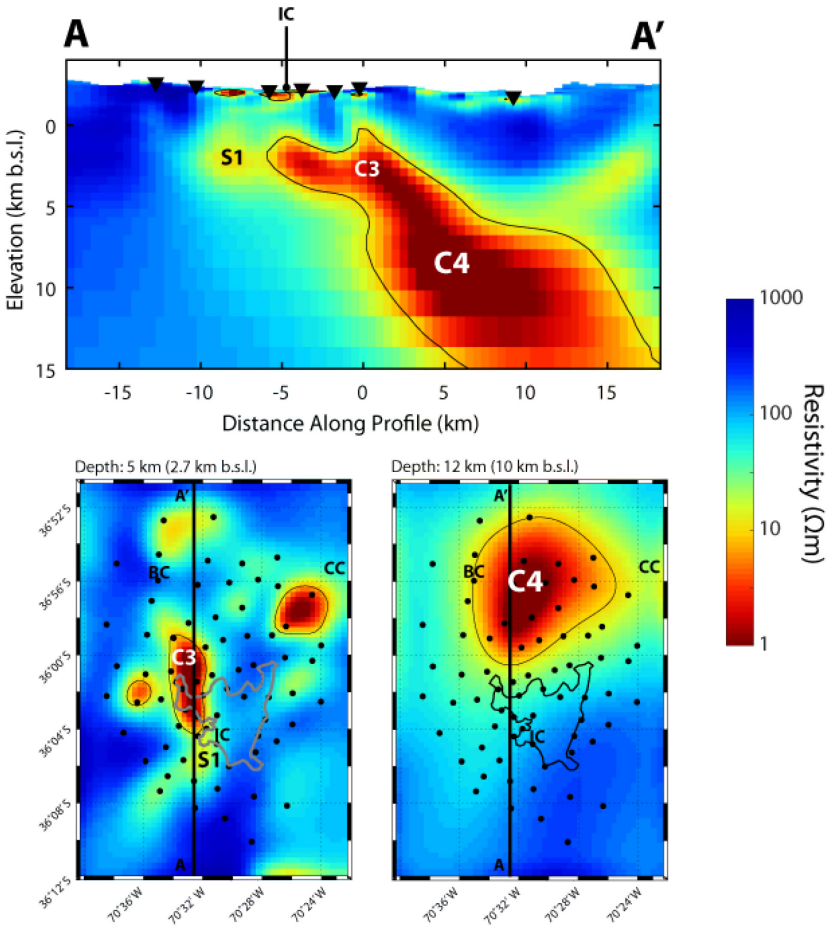

Figure 6.16: Preferred MT resistivity model shown using a north-south vertical slice along A-A' and two horizontal slices at 5 km (2.7 km b.s.l.) and 12 km (10 km b.s.l.) depth. Major interpreted features are labelled C3, C4 and S1. Black dots on horizontal slices and inverted triangles on vertical slice are MT site locations. IC = Inflation center; BC = Baños Campanario hot springs; CC = Cerro Campanario stratovolcano.

The resulting model shown in Figure 6.16 includes the upper crustal Espejos conductor (C3) with a very low bulk resistivity (minimum resistivity of 0.3 Ωm) at a depth of 3 km beneath the western side of the lake and the Espejos lava flow. This conductor dips to the north-northwest and was interpreted by Cordell et al. (2018) as partial melt with a significant hydrothermal fluid component. Another primary conductive feature in the mid-crust is the Campanario conductor (C4) at a depth of 9 – 10 km located to the north of the lake. The Campanario conductor was interpreted as a zone of partial melt with less than 35% melt (Cordell et al., 2018). It is important to note that the Espejos conductor (C3) is a conductive lobe connected to the Campanario conductor (C4) coming up towards the western side of the lake near the area of observed deformation. It was suggested by Cordell et al. (2018) that this model showed evidence for both vertical and lateral transport of magma from the deeper feature (C4) along a dipping

conduit (C3) towards the observed center of deformation and an active hydrothermal zone. It is also possible that the Espejos conductor is a conduit containing hydrothermal fluids and/or alteration products and does not currently contain any partial melt. The fact that the Campanario conductor lies to the north, outside the zone of current deformation, raises the possibility that mid-to-lower crustal zones where the melt originates may not lie directly beneath the surface vents and lava flows. It also points the possibility that melt transport at the LdMVF has significant structural controls in addition to the normal assumptions of buoyant ascent. The model also shows a somewhat conductive feature (S1; 20 Ωm) further south but it is relatively weak and may be an inversion artefact and is not interpreted.

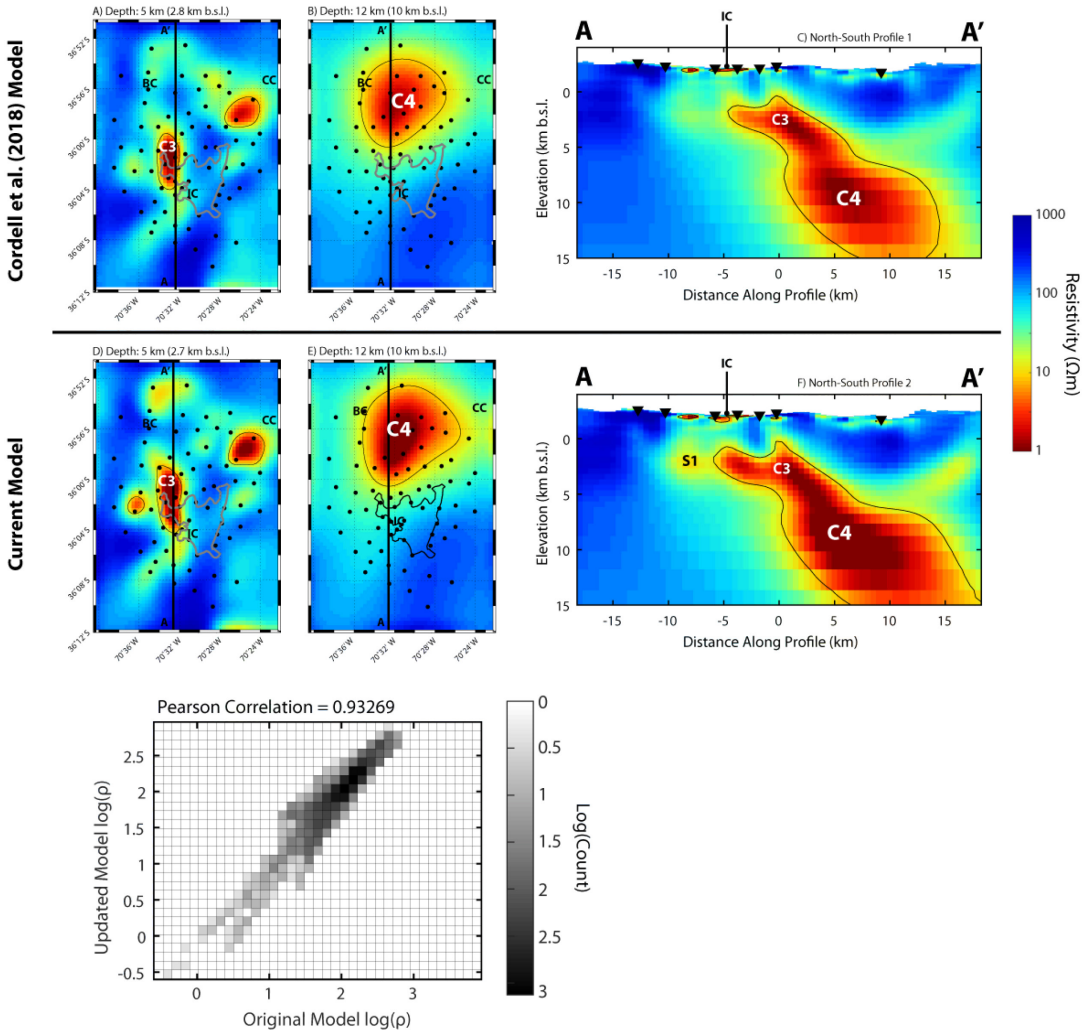

Figure 6.17: A comparison to the previously published MT model from Cordell et al. (2018) (see Chapter 5) and the current preferred resistivity model. The vertical and horizontal slices are at the same locations as in Figure 6.16. The bottom panel shows a 2-D histogram comparing the models by counting the number of cells in each resistivity bin. Black dots on horizontal slices and inverted triangles on vertical slice are MT site locations. IC = Inflation center; BC = Baños Campanario hot springs; CC = Cerro Campanario stratovolcano.

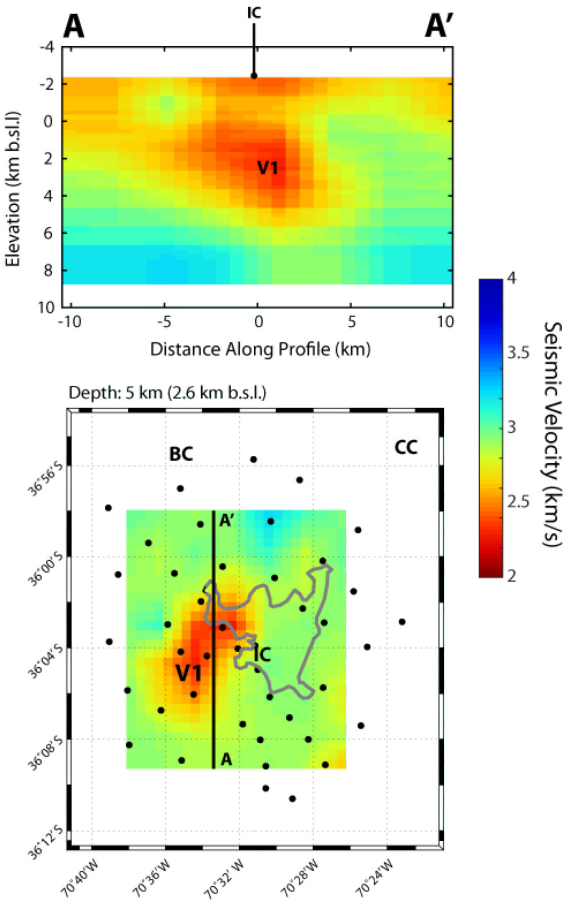

Figure 6.18: The ambient noise tomography (ANT) seismic velocity model from Wespestad et al. (2019) shown using a north-south slice along A-A' and a horizontal slice at 5 km depth. The model has no topography but has a model top at 2450 m.a.s.l. The interpreted low velocity zone is labelled V1. Black dots are seismometer locations. IC = Inflation center; BC = Baños Campanario hot springs; CC = Cerro Campanario stratovolcano.

6.4 INCORPORATING SEISMIC CONSTRAINTS AT LAGUNA DEL MAULE

6.4.1 Initial Comparison Between Preferred Resistivity Model and Seismic Velocity Model

A seismic velocity model was produced using ambient noise tomography (ANT) and surface wave data previously published by Wespestad et al. (2019). The seismic data included 43 seismic instruments collected on a 26 km by 22 km array with 3 – 5 km station spacing (Wespestad et al., 2019). The array covered a similar footprint as the MT array (Figure 6.1). Wespestad et al. (2019) used novel methods to combine the surface wave and ANT datasets into a single invertible dataset to improve bandwidth and data quality of the resulting dispersion curves. A two-step approach was used to create the 1-D velocity models beneath each node in the velocity map and then the 1-D models were interpolated onto a 3-D

volume with 29, 25, and 41 model cells in the north-south, east-west, and vertical directions, respectively. Horizontal and vertical cells had a width of 750 m and 250 m, respectively. The vertical cells also included two padding cells with thicknesses of 800 m and 1300 m so the maximum depth of the model was approximately 9.5 km below sea level. See Wespestad et al. (2019) for more details on the inversion methodology. The 3-D model is shown in Figure 6.18 and included one primary low velocity zone (V1) on the western side of the lake between 2 and 8 km depth. This feature had a south-west strike and dipped to the northwest. It was laterally offset from the center of observed deformation by several kilometers. This was interpreted as a 450 km^3 zone of approximately 5 – 6% partial melt. It is worth noting that there was also a recently published teleseismic tomography model from Bai et al. (in review) which shows a similar upper crustal low velocity zone and also includes images to depths of 50 km. The teleseismic model has model cells that are 4 km x 4 km x 4 km which is significantly larger than both the MT model cells and the ANT seismic model cells. Direct comparison of structures in the upper crust (e.g. <10 km) using the teleseismic model is difficult as the entire area of interest is only captured by 2 model cells in the z-direction. As such, the teleseismic model is not compared directly to the MT, although both Bai et al. (in review) and Wespestad et al. (2019) show a low velocity zone in a similar location in the upper crust so it is likely that a comparison of the MT resistivity model to Bai et al. (in review) would yield similar results as a comparison to Wespestad et al. (2019).

There are some similarities between the MT and seismic models but also some significant differences. V1 and C3 overlap on the western side of the lake but, while C3 dips to the north and is aligned north-south, V1 dips to the north-west and trends southwest-northeast. V1 extends further to the southwest and parallels the inferred location of the Troncoso fault (Figure 6.1; Singer et al., 2018). This region is moderately conductive in the resistivity model (S1) but nearly an order of magnitude less conductive than C3. The inferred volume of V1 is also significantly larger than C3 and the melt fraction is interpreted to be very low (e.g. 5%) compared to the inferred melt fractions for C3 (e.g. >35% plus hydrothermal fluids). The fact that the seismic data does not image the deeper feature to the north (C4) is likely due to poor station coverage, a lack of ray-paths, and a lack of low frequencies. The seismic model space only images reliably to a depth of 8 km. As a result, the primary features of interest in comparing the seismic and MT models are V1 and C3. Both features should be well-constrained by good 3-D data coverage and adequate bandwidth. The question remains whether the differences in C3 and V1 are due to resolution and non-uniqueness of the methods or whether these differences provide important additional information about the geology, geometry and composition of this magmatic-hydrothermal system.

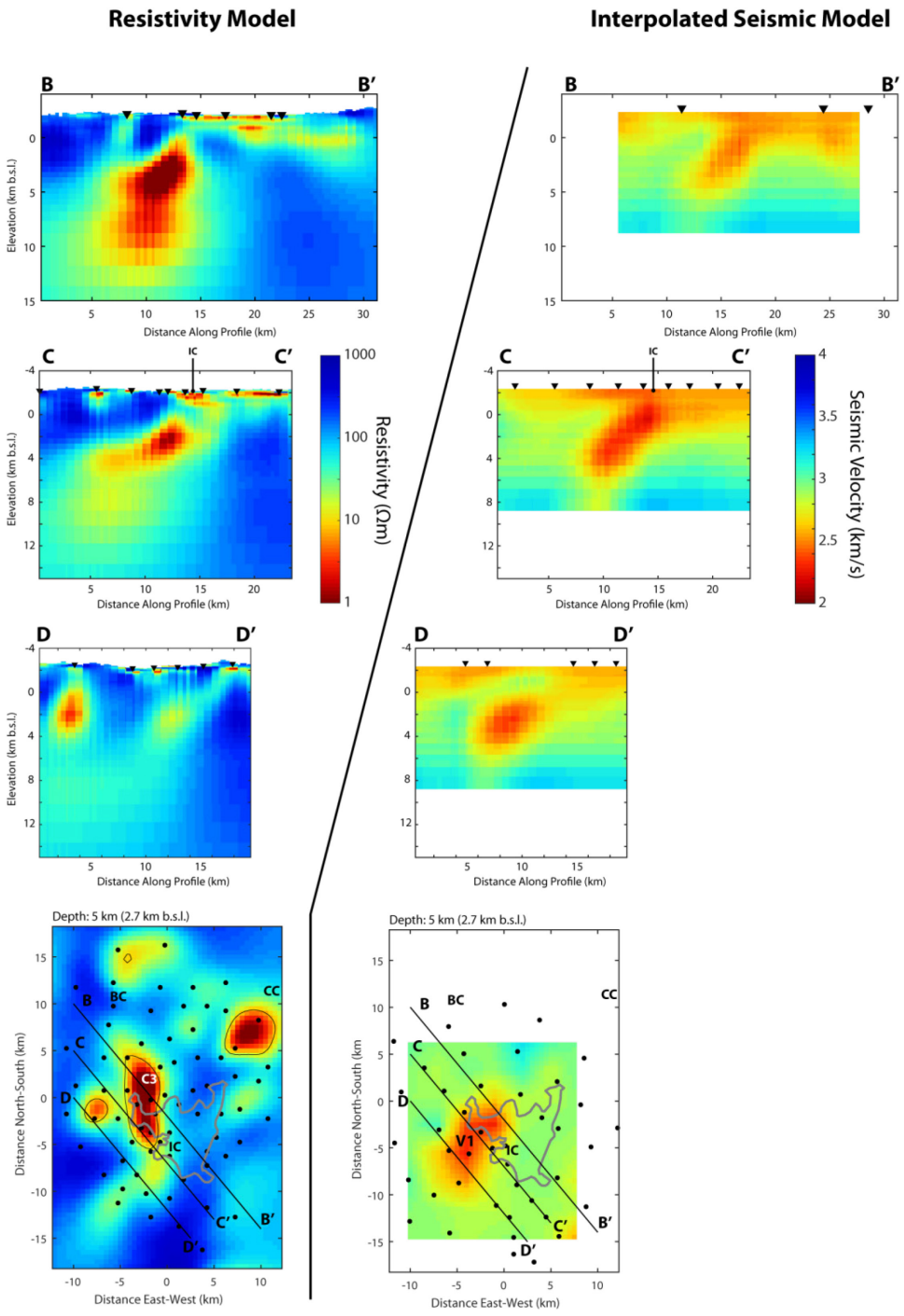

Figure 6.19: A comparison of the preferred MT resistivity model and the seismic velocity model from Wespestad et al. (2019). The seismic velocity model has been interpolated onto the MT model mesh. The models are shown with three NW-SE slices perpendicular to the Troncoso Fault (B-B', C-C', and D-D'). A horizontal slice is also shown at a depth of 5 km (2.6 km b.s.l.). Black dots on horizontal slices and inverted triangles on vertical slice are MT and seismic site locations. IC = Inflation center; BC = Baños Campanario hot springs; CC = Cerro Campanario stratovolcano.

It is also important to note that Bouguer gravity and time-lapse gravity data have also been collected at the LdMVF (Miller et al., 2017b, 2017a). Both show some interesting correlations and discrepancies between the seismic and MT models (see Cordell et al., 2018 and Wespestad et al. 2019). Further work could be done to elucidate the differences between the MT and gravity (or the seismic and gravity) but it is beyond the scope of this thesis.

6.4.2 Statistical Analysis of Residuals from Model Perturbations

The fact that the seismic velocity anomaly and the MT resistivity anomaly are offset from one another requires an explanation. As mentioned earlier, the discrepancy could be a real discrepancy (i.e. due to real geology) or an apparent discrepancy (i.e. due to inversion non-uniqueness). To examine the MT sensitivity to this velocity anomaly, the seismic model was first interpolated onto the MT model mesh (Figure 6.19). The statistical correlation between the two model spaces is useful to investigate since it would be expected low velocity should correlate with low resistivity. This is because partial melt or fluids have both low resistivity and low velocity. To assess the correlation, the Pearson correlation coefficient (PCC) is used which measures the linear correlation between two variables for each model cell. The PCC varies between -1 and +1 with 0 indicating no correlation, -1 indicating a perfectly negative linear correlation (i.e. high velocity correlates with low resistivity), and +1 indicating perfectly positive linear correlation. The shared model space has an overall Pearson correlation coefficient of -0.03 indicating neither negative nor positive correlation between the two models (Figure 6.20a). The correlation coefficient as a function of depth is shown in Figure 6.20b with a maximum correlation between the models occurring around 0 km b.s.l. and 6 km b.s.l. with positive correlation coefficients of 0.34 and 0.37, respectively. The minimum between these is found at 2.2 km b.s.l. (Pearson correlation of 0.14) which is where the Espejos conductor (C3) and V1 begin to be imaged.

There is no agreed upon definition of a velocity anomaly volume (Lees, 2007). In this study, the volume occupied by the velocity anomaly was defined by finding model cells in each layer which were more than one standard deviation below the mean velocity in that layer. The top 5 km of the model space was excluded (i.e. everything above 1 km b.s.l.) because the seismic model did not include topography and does not have high enough frequency content to reliably image the near surface structure. The total volume of the velocity anomaly was 442 km^3, similar to the volume of 450 km^3 given by Wespestad et al. (2019). In the resistivity model, the model cells within the volume of the velocity anomaly were changed to 12 different resistivity values between 1 and 100 Ωm. These represented a set of perturbed models

with the 1 Ωm case shown in Figure 6.21. The resistivity of the anomaly is a proxy for the melt fraction, water content, temperature and pressure with the melt fraction being the primary determinant (Glover et al., 2000). Each different resistivity value represents an approximate melt fraction for a shallow rhyolite melt with a melt resistivity of 0.4 Ωm (following the method of Cordell et al., 2018; Guo et al., 2016). A forward calculation was performed for each perturbed model.

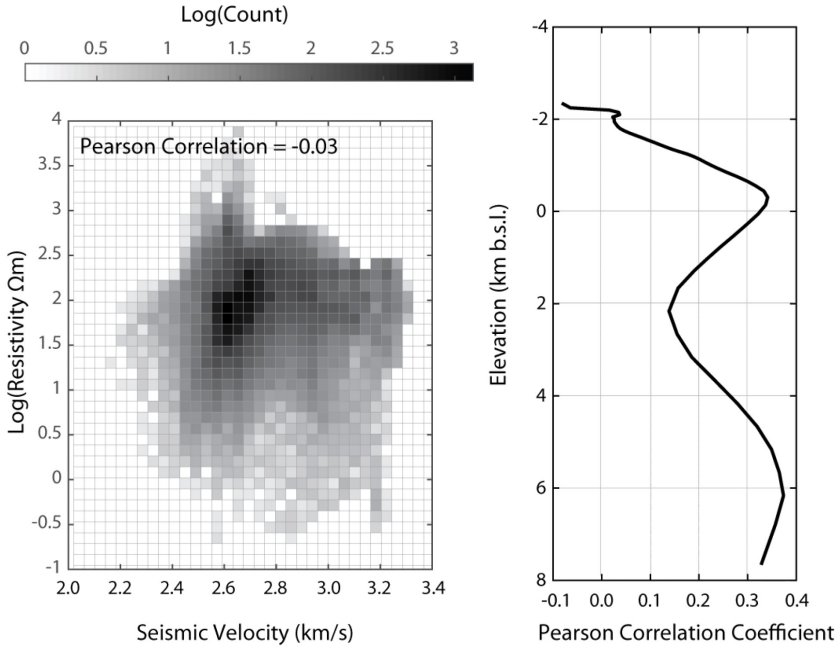

Figure 6.20: Comparison of the MT and seismic models. The left panel shows a 2-D histogram of logarithmic resistivity versus seismic velocity which counts the number of model cells in each resistivity-velocity bin. The right panel shows the Pearson Correlation Coefficient (PCC) as a function of depth where the PCC was calculated for each model layer. Overall PCC was -0.03.

The normalized residuals of the original inversion response were then compared to the normalized residuals of the perturbed response using the KS test, F-test, and cross plots. A summary of these perturbed models and statistical tests is shown in Table 6.4. For the KS test, a p-value less than $\alpha < 0.05$ is considered statistically significant by convention but it is worth noting that this choice is somewhat arbitrary. As can be seen in Table 6.4, all the models resulted in a statistically significant difference in the distributions. This implies that all the perturbed model responses are different from the original model response with a high degree of confidence. This further implies that the seismic anomaly's size and location is incompatible with the present MT model, assuming that the seismic anomaly represents a homogenous magma reservoir with some spatially-uniform melt fraction. This incompatibility makes sense because the seismic anomaly straddles both resistive and conductive regions of the resistivity

model space. Adding a resistive seismic anomaly (e.g. P1 with 100 Ωm) makes sites near the conductor (C3) have poor fit while adding a conductive seismic anomaly (e.g. P1 with 1 Ωm) makes sites near the resistors have poor fit. Thus there is no way to adequately fit the data with this homogeneous anomaly added. Table 6.4 also shows the difference in r.m.s. misfit and the ratio of the squared r.m.s. misfits (i.e. the ratio of the variance; Baba et al., 2006). Recall that the original inversion had a misfit of 1.30. As can be seen, the difference in r.m.s. misfit is quite small for many of the models which may lead to the conclusion that the perturbed model response is statistically the same as the original model response. However, according to the F-test with 9776 degrees of freedom, if the ratio of the squared r.m.s. misfit values lies outside the bounds (0.9673,1.034) then the null hypothesis should be rejected with 95% confidence (i.e. α=0.05). All the ratios in Table 6.4 lie outside those bounds, suggesting that the perturbation has a statistically significant impact on the r.m.s.

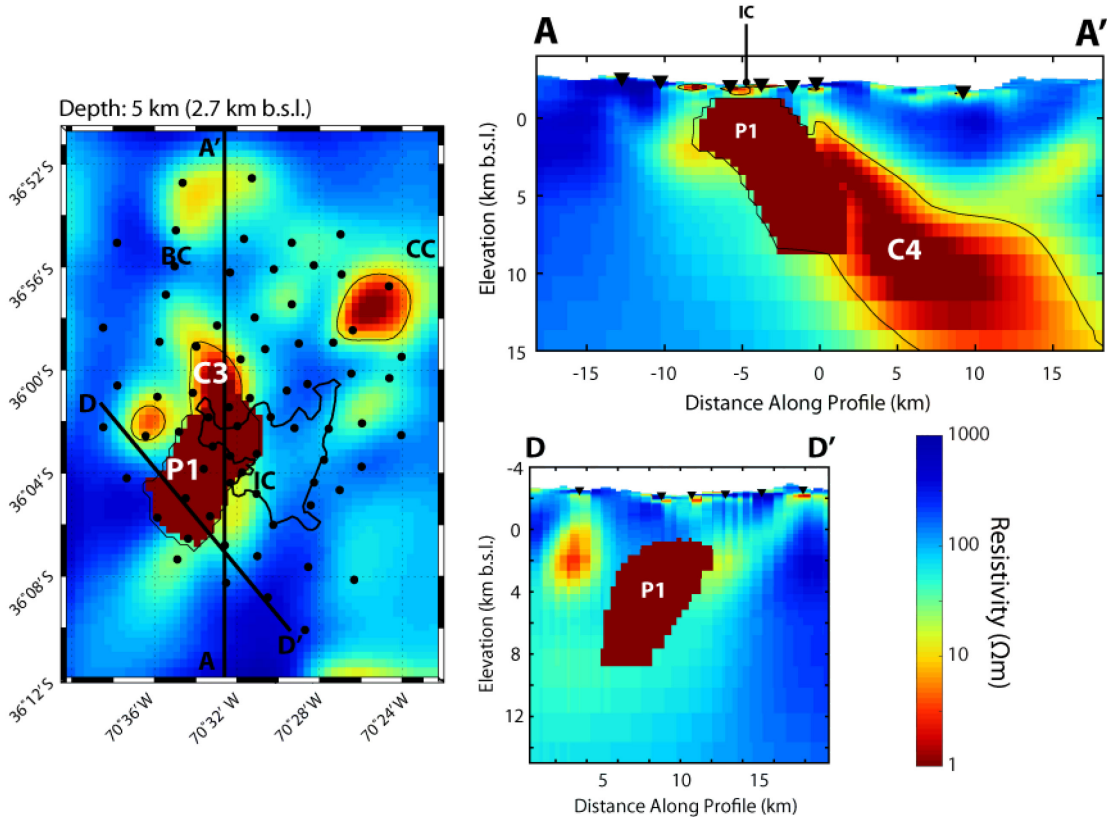

Figure 6.21: The preferred MT resistivity model with perturbation (P1) added. The model is shown with a horizontal slice at 5 km (2.6 km b.s.l.) and two vertical slices along profiles A-A' and D-D'. The shape and location of P1 is determined by the shape of the 450 km^3 low seismic velocity anomaly from Wespestad et al. (2019). The model cells encompassed by P1 have a value of 1 Ωm. Black dots on horizontal slice and inverted triangles on vertical slices. IC = Inflation center; BC = Baños Campanario hot springs; CC = Cerro Campanario stratovolcano.

Despite a relatively small change in r.m.s., the distributions of residuals are statistically distinct, as indicated by both the KS test and the F-test. Figure 6.22 illustrates these differences visually by showing cross plots of the residuals for the forward response with the 1, 3, 15, 50, and 100 Ωm anomalies added. The x-axis shows the normalized residuals from the original inversion while the y-axis shows the normalized perturbed residuals. Blue points show residuals which became worse (i.e. farther from the true data point; larger misfit) after adding the anomaly while red points show residuals which became better (i.e. nearer to the true data point; smaller misfit). As can be seen, in all cases, there are some red points where misfit improved. Furthermore, all cross plots have some points which are near the line $y = -x$ which implies that the absolute value of these points is identical and they contribute equally to the r.m.s. misfit despite being a reflection about the true data point. The 1 Ωm and 3 Ωm responses have similar cross plots whereas the 100 Ωm has residuals which are biased to the lower half of the plot. This implies that impedances were, on average, becoming more positive after the perturbation was added (e.g. apparent resistivity is biased up). The 15 Ωm and 50 Ωm cross plots also look similar although, in general, the 50 Ωm cross plot has more scatter and a slightly lower p-value.

Table 6.4: Statistical analysis of responses from the MT resistivity model which includes the seismic anomaly (P1) as a perturbation with various bulk resistivity values.

Resistivity of Seismic Anomaly (P1)	Approximate Melt Fraction	Overall KS Test p-value (α=0.05)	Difference in r.m.s. mifit	Ratio of Squared r.m.s. misfit
1 Ωm	50%	1×10^{-24}	1.38	4.25
3 Ωm	25%	2×10^{-15}	0.90	2.86
10 Ωm	10%	3×10^{-4}	0.26	1.44
15 Ωm	8%	0.017	0.13	1.21
20 Ωm	7%	0.0096	0.09	1.14
25 Ωm	6%	0.0060	0.09	1.14
30 Ωm	5.5%	0.0069	0.11	1.18
35 Ωm	5%	0.004	0.15	1.24
40 Ωm	4.5%	0.0046	0.18	1.30
50 Ωm	4%	0.0014	0.25	1.42
80 Ωm	3%	5×10^{-5}	0.41	1.73
100 Ωm	2%	1×10^{-5}	0.48	1.87

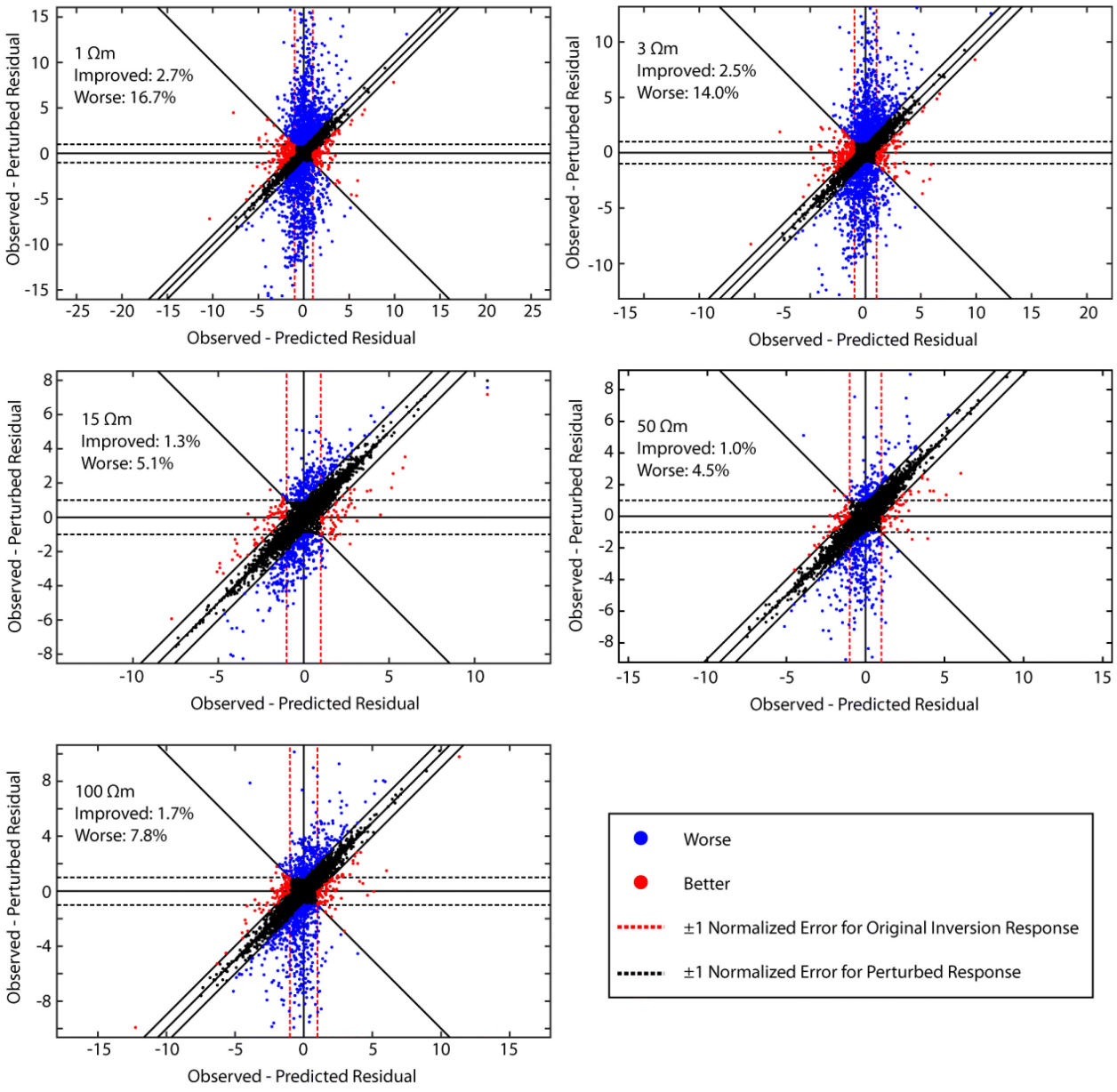

Figure 6.22: Cross plots of normalized impedance residuals. The x-axis for each plot shows the normalized residuals from the original (preferred) MT inversion response. The y-axis on each plot shows the normalized residuals from a perturbed MT response. Five perturbations are shown with P1 = 1, 3, 15, 50, and 100 Ωm.

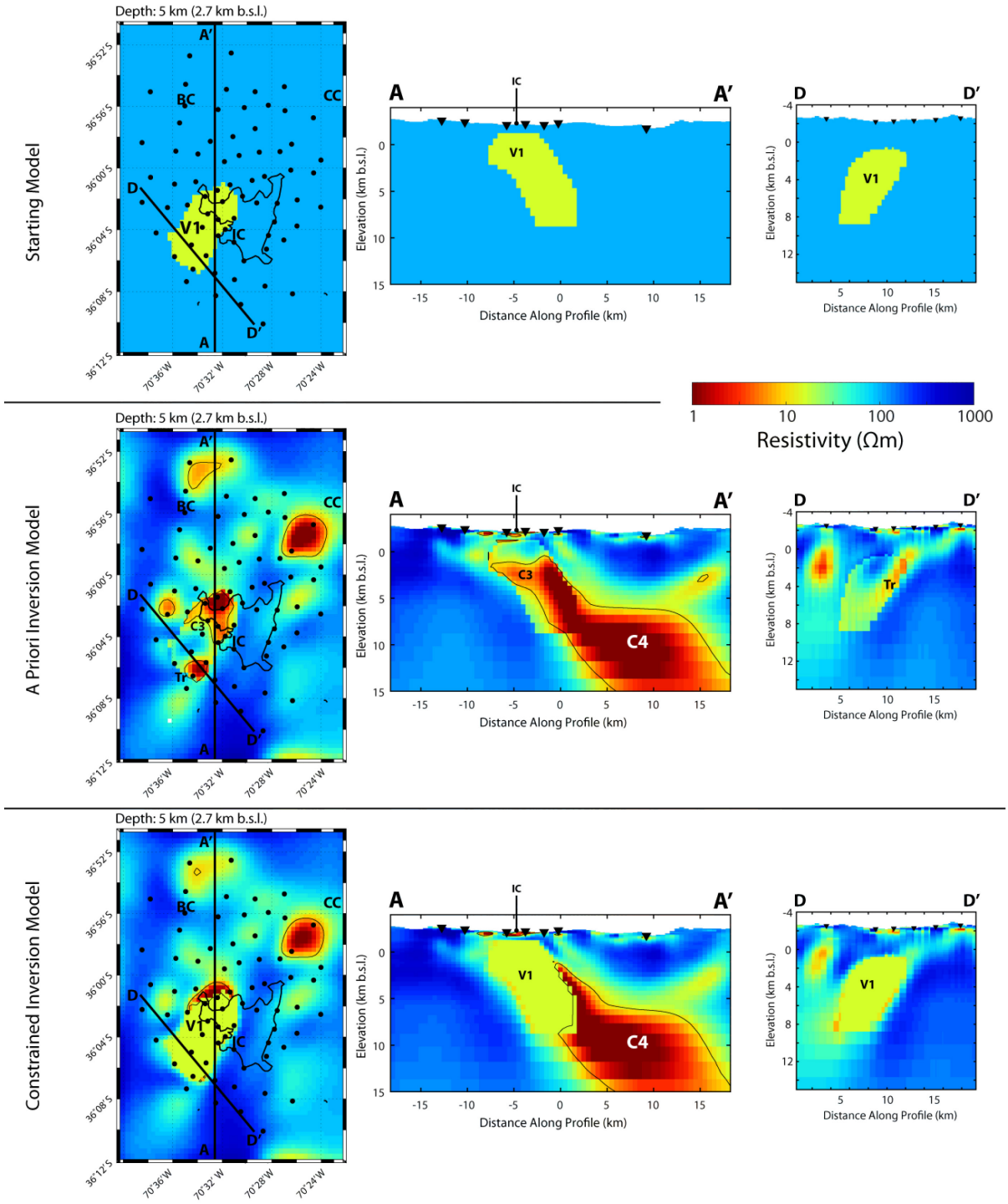

Figure 6.23: MT resistivity models from the *a priori* and constrained inversion cases. The top row shows the starting model used for both the *a priori* and constrained inversion. This model includes P1 = 15 Ωm embedded in a 100 Ωm halfspace. The second row shows the results from the *a priori* inversion using a 100 Ωm halfspace as the prior model. The third row shows the results from the constrained inversion in which the model cells in P1 are fixed. Slices are the same as Figure 6.21.

Despite all the residuals showing significant differences upon adding the anomaly perturbation, there is still a maximum in the KS test p-value around 15 Ωm (p = 0.017). This also corresponds with a minimum in the ratio of the variances around 20 Ωm. This implies that, while the distributions are statistically different, they are relatively less different than the other perturbed models. This implies that the best fitting model has a melt fraction of 7 to 8%. The estimates from Wespestad et al. (2019) suggest a bulk melt fraction of approximately 5% for the velocity anomaly. These low bulk melt fraction estimates from seismic also suggest that the melt would be poorly-connected (Rosenberg and Handy, 2005) which would likely make them more difficult to detect with MT. Given the assumptions present in melt fraction estimates, this is a relatively good agreement but it may be the case that the MT is resolving smaller scale features (e.g. C3) within a larger body of low melt fraction mush.

6.4.3 Constrained Inversions with A Priori Starting Model

The above method uses the original MT inversion model as the basis for evaluating perturbations. However, it is possible that the data could be fit better or achieve a more reasonable model if given additional information to begin the inversion. In this case, the 15 Ωm anomaly (V1) was added to the 100 Ωm halfspace as a starting model ($\mathbf{m_s}$) as shown in the top panel of Figure 6.23. The reference model, $\mathbf{m_0}$, remained unchanged as a 100 Ωm halfspace and all model cells were allowed to change as the inversion progressed. In other words, all that is changing between this inversion and the original inversion is the starting guess includes *a priori* information. This inversion converged to an r.m.s. of unity after 299 iterations (Figure 6.24). Iteration 212 optimized both model norm and data misfit with an r.m.s. of 1.23 and normalized model norm of 0.68. The misfit is somewhat better than the original model misfit (r.m.s. = 1.30) but the model norm is higher. As mentioned earlier, the KS test can be used to examine the differences between any two sets of residuals. Here, the original inversion residuals and the constrained inversion residuals are compared using the KS test and result in a p-value of 0.03. The combination of lower r.m.s. and a statistically significant difference in residuals suggests that the *a priori* assumption results in a distinct model within data error with better data fit. This better data fit is achieved by making the model rougher with higher model norm.

The optimal model is shown in Figure 6.23b using the same horizontal, vertical and diagonal slices as Figure 6.21. The Campanario conductor (C4) to the north remains relatively unchanged upon adding V1 to the starting model when compared to the original inversion (Figure 6.16). But the geometry of the Espejos conductor (C3) changes in some notable ways. The depth to C3 is somewhat deeper (e.g. 4 km

below surface) and the top of C3 is flatter which better agrees with the interpretation of the top of C3 as a sill around 4 km depth. The connection between C3 and C4 is also steeper which suggests that the dip of C3 is not well constrained in the original model and a steeper conductor is possible. It is more realistic to interpret a steeply dipping conductor as a conduit for partial melt from C4 to the inflation center rather than a shallow dipping conduit. Most magma movement is driven by buoyant ascent and so lateral movement of magma over large distances is relatively rare. However, even here there is a significant (i.e. several kilometers) lateral offset from C4 to the surface. Geological evidence from exposed ancient volcanic systems sometimes show long lateral distances of magma emplacement (e.g. Healy et al., 2018).

There is a more pronounced conductor to the southwest (Tr) near the Troncoso Fault which dips steeply to the northwest. This Troncoso conductor may be related to fluids or partial melt in the fault system and has a similar strike and dip to mapped structural features (Garibaldi et al., 2020). This conductor is at a similar location as the previously identified feature S1 but this inversion makes the feature much more pronounced and suggests that S1 is not an artefact and should be interpreted. It is also important to note that some parts of V1 become more resistive. The western part of the seismic velocity anomaly returns to approximately the halfspace value (e.g. near 100 Ωm) and the shallowest portions of the seismic anomaly (e.g. <1 km b.s.l.) become similarly resistive. Like the model perturbations in Section 6.4.2, this further suggests that the MT has the ability to resolve discrete features (e.g. a separation between C3 and Tr) while the seismic data may not be able to resolve them.

6.4.4 Constrained Inversions with Fixed Model Cells

The final variation to consider is similar to the above method but, in this case, the model shown in Figure 6.23a is used as both the reference model, $\mathbf{m_0}$ and the starting model, $\mathbf{m_s}$ with the model cells of V1 fixed at 15 Ωm for all iterations by changing the model covariance $\mathbf{C_m}$. This helps explicitly test whether a 15 Ωm melt reservoir can fit the MT data as equally well as the unconstrained original inversion with similar model norm. This constrained inversion converged to an r.m.s. of approximately unity after 255 iterations and the optimal model was found at Iteration #156 with an r.m.s. of 1.34 and normalized model norm of 0.56 (Figure 6.24). This resistivity model has higher data misfit and higher model norm than the original inversion, suggesting both poorer data fit and a greater deviation from the minimum-structure ideal of smooth MT inverse solutions. However, the KS test between the two sets of residuals results in a p-value of 0.54 which is above the threshold of significance. This suggests that the

distributions of residuals are not distinct within the data error. This is interesting in that it shows that the model can fit the feature with neither better nor worse fit from the original inversion, if it is allowed to also change the surrounding cells.

The resistivity model is shown in Figure 6.23c. Similar to the *a priori* model (Figure 6.23b), the constrained model has no noticeable change to the geometry or location of the Campanario conductor (C4). The Espejos conductor (C3) is mostly subsumed by the fixed 15 Ωm V1 anomaly. This suggests that the V1 anomaly can be adequately fit by the MT data using a 15 Ωm resistivity value if the model is allowed to change around those fixed model cells. This suggests that a 7 – 8% melt fraction mush reservoir would be compatible with the MT data.

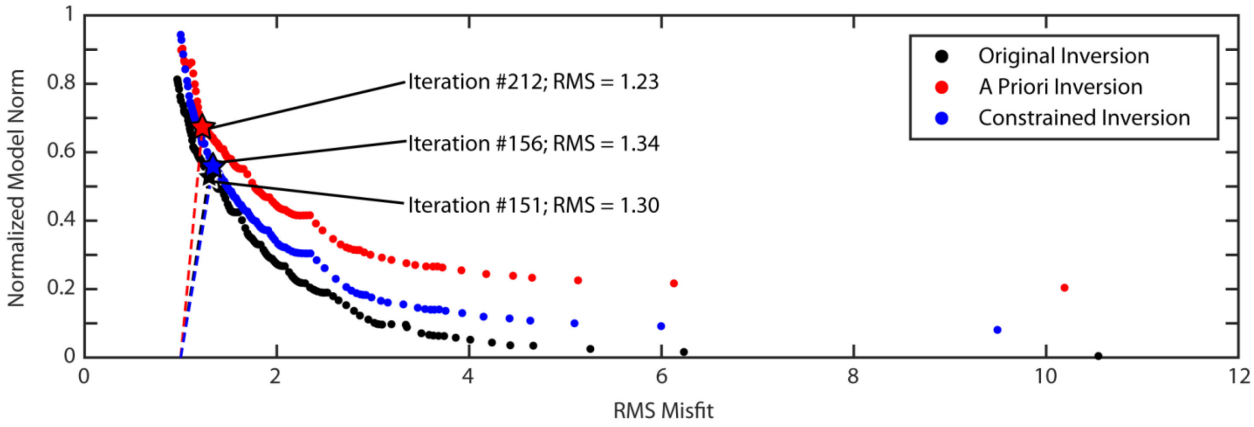

Figure 6.24: Model norm versus r.m.s. misfit convergence curves for the original (preferred) MT inversion, the *a priori* inversion, and the constrained (fixed) inversion. The stars denote the preferred inversion iterations from each case. Corresponding models from those iterations are shown in Figure 6.23.

6.5 SUMMARY

This study aimed to elucidate differences between the MT resistivity model and a previously-published seismic velocity model to better understand the magma plumbing system beneath the LdMVF. This resulted in three different resistivity models of the sub-surface: (1) the preferred (original) inversion, (2) the unconstrained *a priori* inversion, and (3) the constrained fixed inversion. A set of perturbed resistivity models were created by including an anomaly in the preferred inversion model at the same location as the seismic velocity anomaly with different bulk resistivity values. The added anomaly represented a homogenous magma reservoir with varying melt fractions. It was found using the

statistical analysis of residuals that none of the perturbed resistivity models resulted in a better data fit than the original inversion and that all the perturbed resistivity models had distributions of residuals that were different from the original inversion residuals with a high degree of confidence. This suggests that the seismic velocity model and the MT resistivity model and their interpretations are incompatible within the error levels of the MT data. An anomaly with a bulk resistivity of 15 Ωm at the same location as the seismic anomaly caused the smallest change to the data fit and would represent a 7 – 8% rhyolite melt fraction which is similar to the 5% estimate from the interpretation of the seismic velocity anomaly (Wespestad et al., 2019).

The above analysis did not allow the inversion algorithm to seek a new solution but instead assumed that the original MT inversion model was the proper benchmark from which to assess data fit. To further the analysis, additional inversions were run using the 15 Ωm resistivity anomaly at the same location as the seismic anomaly as an *a priori* constraint. Inversions were able to converge to adequate solutions with the feature added as both an *a priori* "first guess" and as a fixed feature. In the *a priori* case, the solution looks very similar to the original inversion with much of the seismic anomaly being returned to the halfspace resistivity value (or greater). However, in this case, the Espejos conductor (C3) dips more steeply to the northwest, in better agreement with the dip and strike of the seismic anomaly. This suggests that the dip of C3 is not well constrained and may be steeper. Also, a more prominent conductor (Tr) is imaged in the MT inversion to the southwest near the Troncoso fault, perhaps related to fluids or melt within the fault system. This inversion was able to achieve a lower r.m.s. misfit with a different distribution of residuals compared to the original inversion based on the KS test. However, the better fit also resulted in a higher model norm (i.e. rougher) resistivity model. The inversion which includes a fixed resistive anomaly in the same location as the seismic anomaly also achieves an adequate data fit although the distribution of residuals is not statistically distinct from the original inversion. The MT solution is non-unique, as expected, and a wide range of possibilities exist. However, based on this analysis, it seems that the MT data are best fit when the seismic anomaly is separated into discrete features (C3 and Tr) rather than combined into a homogeneous conductive (or resistive anomaly). This is borne out by three lines of evidences:

1) The KS test gave significant results (p-value < 0.05) when comparing the distribution of residuals for all perturbations. No homogeneous perturbation was able to fit the data as well as that of the original inversion.

2) The *a priori* inversion splits the low resistivity seismic anomaly into discrete conductors separated by a resistor and results in a solution with better fit and a set of residuals which is statistically distinct from the original inversion.

3) The inversion with fixed cells has a higher data misfit than the *a priori* inversion and has a distribution of residuals which is not statistically distinct from the original inversion.

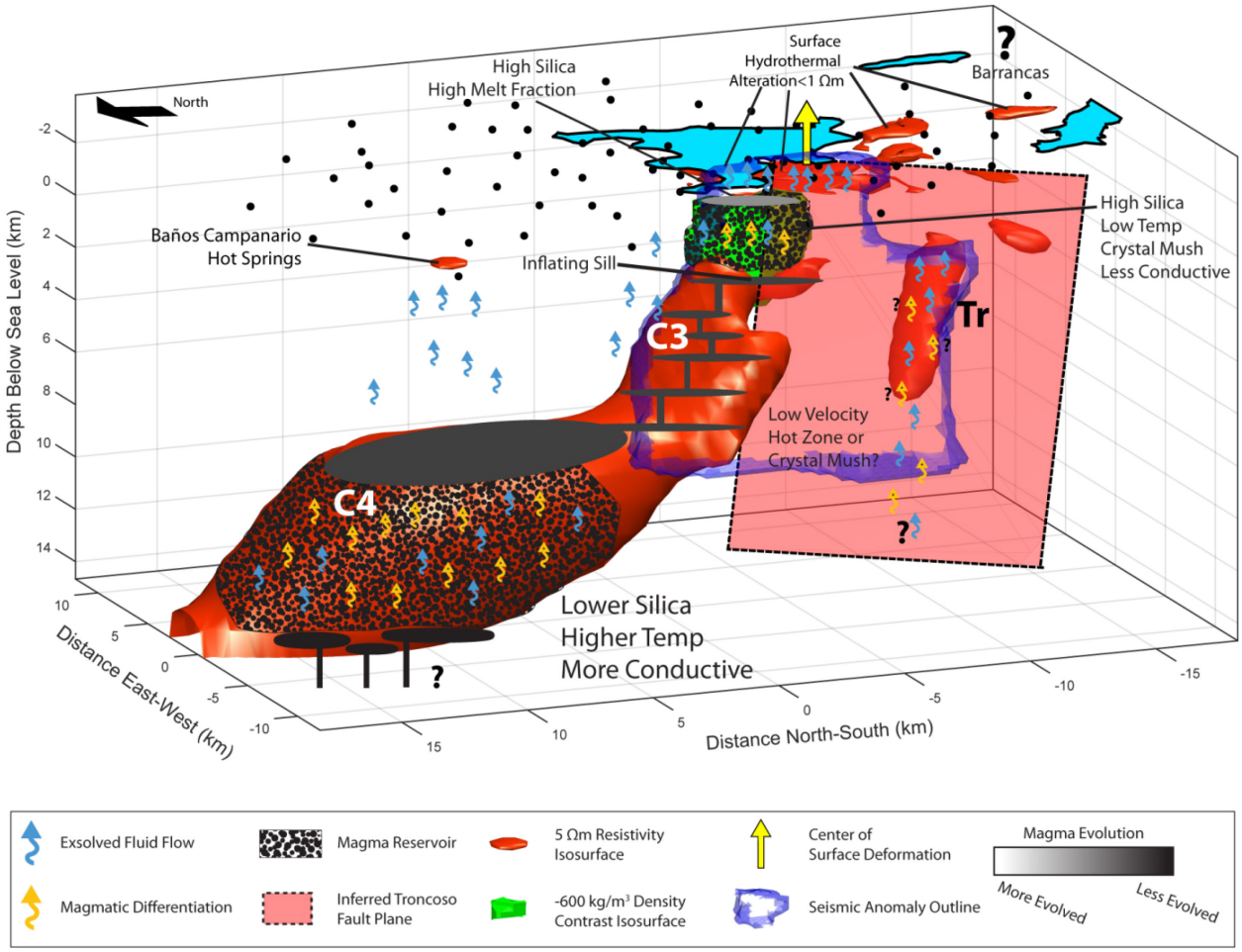

Figure 6.25: Three-dimensional conceptual model of the Laguna del Maule Volcanic Field looking southeast. The *a priori* inversion resistivity model is shown using a 5 Ωm isosurface. The density model of Miller et al. (2017b) is shown with a -600 kg/m^3 isosurface. The seismic velocity model of Wespestad et al. (2019) is shown using the isosurface described in the text.

The *a priori* model which has discrete, smaller conductors (e.g. C3, Tr) has better data fit than models which combine those conductors into a homogeneous conductor. This is the final preferred model which best incorporates the seismic model into the MT model and interpretation. The inclusion of the seismic velocity anomaly in the *a priori* model helps to better define the geometry of the Espejos conductor (C3) as a more steeply dipping feature which makes the interpretation of the conductor as a magmatic conduit (or dyke) from C4 to the surface more plausible. Furthermore, the *a priori* model also makes the Troncoso conductor (Tr) more well-defined which may indicate fluids or partial melt in the fault system to the southwest. This also coincides with the location with significant seismicity (Cardona et al., 2018). Finally, it is important to note that none of the perturbations or inversion tests influenced the depth or geometry of the Campanario conductor (C4) to the north. It would appear that this conductor is too far to the north and too deep to be strongly influenced by the shallow features near the inflation center.

Figure 6.26: A conceptual model of a "trans-crustal magma plumbing system". From Cashman et al., 2017. Reprinted with permission from AAAS.

This analysis suggests that differences between the seismic model and original MT resistivity model are giving additional information about the subsurface geology. The seismic is likely imaging a relatively resistive, low melt-fraction mush (or sub-solidus hot zone; Lees, 2007) in the upper crust beneath LdMVF while the MT is imaging more conductive, discrete features within the system which may

represent more ephemeral zones of high melt fraction and/or exsolved hydrothermal fluids. A more thorough analysis of the resolution of the seismic model would be required to further prove this hypothesis by testing whether the seismic could resolve the discrete features (C3 and Tr). Greater MT data coverage to the southwest would help to image the Troncoso conductor more clearly, and more seismic data to the north would be required to examine the Campanario conductor (C4).

A three-dimensional conceptual model of the LdMVF trans-crustal magmatic-hydrothermal system is shown in Figure 6.25 using the *a priori* inversion model as a guide. At a depth of 10 km in the mid-crust, there is as partially molten mush imaged as C4 to the north of the LdMVF. Crystal-poor basalt melts originating deeper in the lower crust and mantle likely supply heat, and prevent the system from solidifying over geological time scales. Within the mid-crustal magma mush, there is likely some differentiation, with more crystal-poor silicic melts concentrated near the top. These crystal-poor melts are able to flow and migrate both laterally (southwards) and vertically (upwards) along a pre-existing structural boundary (i.e. the Troncoso fault). This conduit is imaged as C3 and may be a series of sills and dykes (as shown in Figure 6.25) or as inclined sheets. At 4 km depth below surface, C3 becomes horizontal and is at a similar depth as the inferred inflating sill from geodetic methods (Feigl et al., 2014; Le Mével et al., 2015). A small, shallow, low-temperature, upper crustal magma reservoir directly beneath the observed inflation center is imaged by Bouguer gravity (green in Figure 6.25). This upper-crustal reservoir is likely too small to be imaged by MT or seismic surface wave tomography data. At the top of the upper crustal reservoir is a lens of higher melt fractions and/or hydrothermal fluids which is likely imaged by gravity measurements and MT (see Chapter 5). Along with partial melt, there is also likely a significant hydrothermal component to the system with exsolved fluids derived from partial melts reaching the surface at hot springs such as Baños Campanario and significant hydrothermal alteration at shallow depths beneath the LdMVF, both of which are imaged as conductors. To the southwest, along the Troncoso fault is another conductor (Tr) likely related to fluids and partial melt and also linked to observed seismicity. The source of fluids to Tr is unclear, whether from a deeper feature directly below Tr or laterally sourced from C3 along the Troncoso Fault. The presence of a large slow velocity seismic anomaly which encompasses both C3 and Tr, suggests that much of the subsurface between the two conductive features is hot and perhaps partially molten. Seismic is sensitive to bulk properties while MT is sensitive to connected phases and, as such, the seismic data may be sensing a larger homogeneous mush region with poorly-connected, low melt fraction (e.g. 5%) partial melt which is relatively resistive. The MT is sensing discrete regions of well-connected higher melt fraction partial

melt and/or hydrothermal fluids within the shallow magmatic system. These smaller, discrete features may not be resolvable with the seismic array. The discrepancies between the MT, gravity and seismic provide important information about the geology.

This conceptual model is similar to the trans-crustal magma system model proposed by Cashman et al. (2017) and shown in Figure 6.26. This model has smaller regions of ephemeral, well-connected, high melt fraction partial melt embedded within larger regions of more long-lived, homogeneous mush. A key difference between the two models is that, in the conceptual model at LdMVF, there is a notable dip to the features to the north-northwest. Most conceptual models show purely vertical ascent. However, magma will travel along the path of least resistance and, if there is a fault or structural boundary in the crust, magma will preferentially travel along that boundary (Magee et al., 2018). There are other examples of lateral movement of magma and/or fluids at other volcanoes such as the Canary Islands (Klügel et al., 2015), Yellowstone (Kelbert et al., 2012), Iceland (Bato et al., 2018), and Japan (Brothelande et al., 2018). At Osorno Volcano in southern Chile, Díaz et al. (2020) found evidence for lateral movement of magma and specifically linked it to fault systems. The current study of the LdMVF suggests that the LdMVF magmatic system is structurally complex and suggests that it is necessary to look outside the boundaries of surface vents and lava flows when exploring volcanic plumbing systems.

CHAPTER 7: REGIONAL MAGNETOTELLURIC STUDY OF THE CENTRAL CHILEAN SUBDUCTION ZONE

7.1 INTRODUCTION

The regional subduction zone structure of central Chile was the second focus of this thesis. The goal of this second study was to put the detailed study of the Laguna del Maule Volcanic Field (LdMVF) into a regional context. This chapter details this regional investigation and most of the material is taken from Cordell et al. (2019) which was published in *Geochemistry, Geophysics, Geosystems*.

Subduction zone margins account for the majority of global volcanic hazards and include many of the world's most earthquake-prone areas. It has been recognized that water and hydrated minerals play a vital role in magma generation and seismicity at subduction zones (Stern, 2002). Various numerical simulations and laboratory studies suggest that phase transitions of these hydrated minerals are responsible for the upward migration of water-rich melt into the over-riding crust (e.g. Grove et al., 2012; Hacker, 2008; Petrelli et al., 2018). These fluids then lower the solidus temperature of the overlying mantle rocks, generating hydrous mafic melts. Determining the amount of water, the depth at which it is released, and the location of zones of accumulation where aqueous fluids and partial melt are concentrated are all critical parameters in examining magma flux and magma genesis (Petrelli et al., 2018; Völker and Stipp, 2015). Furthermore, it has been widely suggested that fluids control the distribution of seismic and aseismic zones within a subduction zone and thus understanding the relationship between seismicity and fluid distribution is important (Saffer, 2017).

The magnetotelluric (MT) method has been used to image a number of subduction zones including Cascadia (McGary et al., 2014; Wannamaker et al., 2014), Costa Rica (Worzewski et al., 2011), southern Mexico (Jödicke et al., 2006), Japan (Hata et al., 2015), New Zealand (Heise et al., 2017; Wannamaker et al., 2009), and the Central Andes (Brasse and Eydam, 2008; Unsworth et al., 2018). This geophysical method is useful in these studies of subduction zone processes because the presence of interconnected aqueous fluids and/or partial melts increases the conductivity of both crustal and mantle rocks (see Chapter 4). The MT studies of subduction zones have highlighted that there is great variability in

electrical structure, both as a function of depth and also along strike. In terms of variations in structure as a function of depth as a plate subducts, the following features have been reported from MT studies:

- shallow (<15 km) conductors interpreted to be associated with expulsion of fluid from pore spaces
- mantle wedge conductors (~50 km) that have been interpreted as the addition of fluids derived from the metamorphic transition of the down-going slab from basalt to eclogite (Pommier and Evans, 2017)
- deeper conductors within the mantle wedge (>60 km) have sometimes been observed and have been interpreted as water released by the breakdown of serpentinite and partial melt in the mantle wedge due to flux melting (e.g. McGary et al., 2014).

This suggests significant along-strike variations related to the incoming plate properties (e.g. fractures, serpentinization, temperature) that may be related to structures such as seamounts and plate age as well as the structure of the upper plate mantle wedge (Pommier and Evans, 2017).

The Maule region of central Chile has experienced some significant earthquakes and volcanic eruptions in the last century, in addition to the current unrest at the LdMVF and an unusually active Quaternary basalt province in the backarc. Chapter 2 describes more details of the regional geology of this region. The unique volcanism and seismicity of the Maule Region shows that this is an active part of the Andean subduction system which requires further study in order to determine the relationship between subduction zone structure and fluid fluxes. Previous passive seismic studies have shown low velocity regions coinciding with regions of fluids, as well as anomalously high velocity regions on the plate interface which may be asperities (i.e. unevenness or roughness of the slab surface) which encourage plate locking, affecting the slip distribution of megathrust earthquakes (Hicks et al., 2014, 2012). Asperities and pore fluid pressures have also been linked to the recurrence intervals for large megathrust earthquakes in Chile (Moreno et al., 2018) as well as other subduction zones (Schellart and Rawlinson, 2013). Therefore, understanding fluid flux and asperities in this region is important.

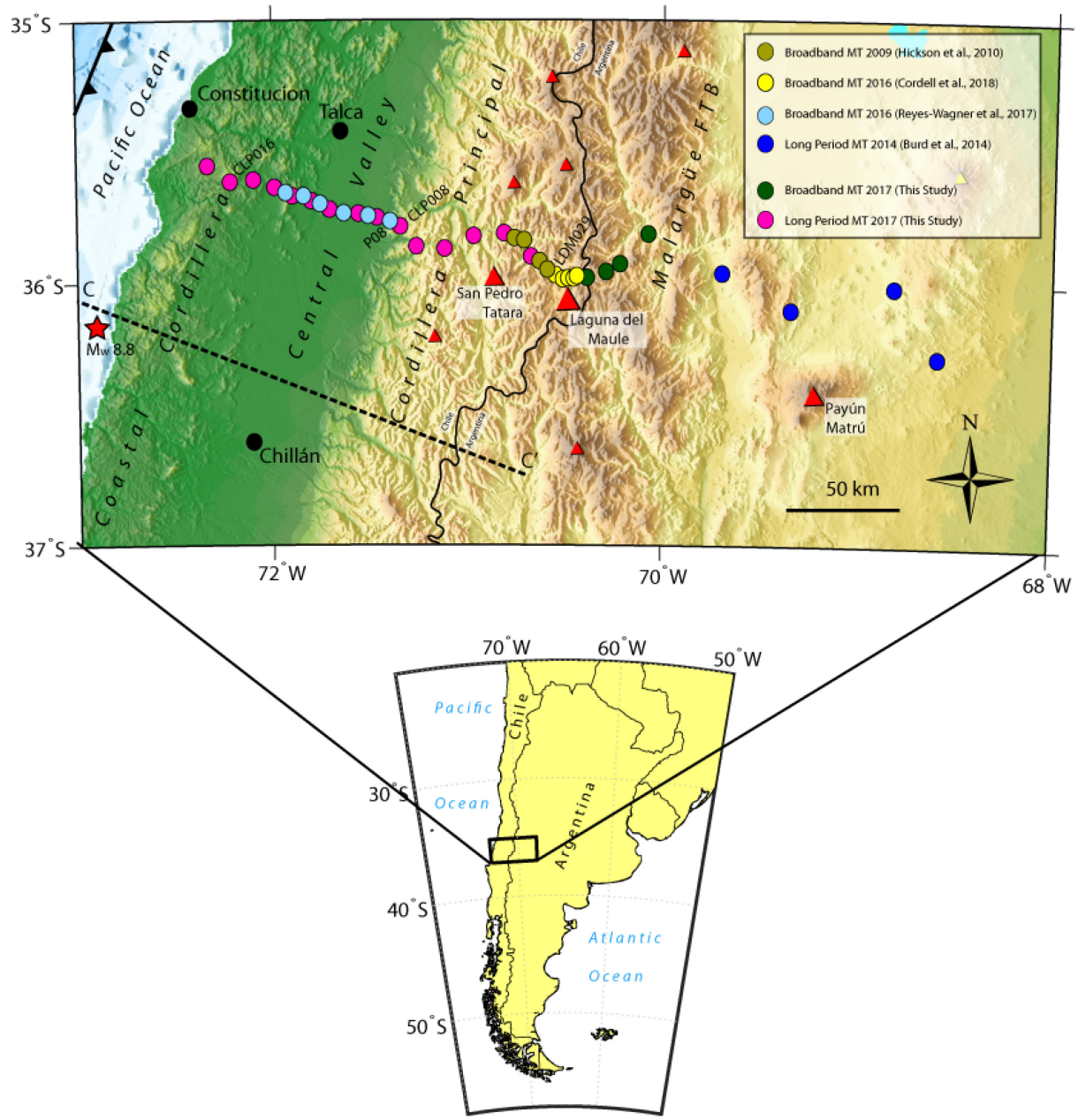

Figure 7.1: Study area in central Chile and western Argentina. Colored circles denote long-period MT (LMT) and BBMT (BBMT) site locations from different field campaigns. Red triangles show the locations of significant volcanoes in the Cordillera Principal. The red star shows the epicentre location of the 2010 M_w 8.8 Maule earthquake. Important towns are shown as black circles. Important volcanoes mentioned in the text are labelled (San Pedro-Tatara, Laguna del Maule, Payún Matrú). Stations mentioned in text are labelled. Profile C-C' denotes the seismic velocity profile from Hicks et al. (2014)). Malargüe FTB = Malargüe Fold and Thrust Belt.

The South American plate at this latitude can be divided into four broad geological units from west to east (Figure 7.1). Along the Pacific Ocean, the Coastal Cordillera consists primarily of outcrops of Paleozoic metamorphic rocks from ancient accretionary wedge complexes (Hervé et al., 2013). To the east, the Central Valley is a 70 km-wide depression filled with up to 500 m of Quaternary sediments and ignimbritic cover (Farías et al., 2008). The Cordillera Principal is a 60 km-wide mountain range which consists of Mesozoic-to-Cenozoic volcanic sequences and exposed plutons as well as modern Quaternary volcanic edifices such as Tatara-San Pedro (TSP) and Cerro Azul (Hildreth and Moorbath, 1988; Singer et al., 1997). Finally, to the east in the backarc region is the Malargüe fold and thrust (FT) belt which includes deformed Mesozoic units and the front ranges of the eastern Andes (Ramos et al., 2014). Between the Malargüe FT belt and the Principal Cordillera is the northwest-trending Las Loicas trough which includes numerous calderas and volcanic fields such as Calabozos, Puelche and the LdMVF (Ramos et al., 2014). The current geometry is one of normal subduction as shown by regional teleseismic studies (Pesicek et al., 2012). However a flat slab was present at this location from 5 – 3 Ma and steepened around 2 Ma (Ramos et al., 2014). As the slab flattened between 14 – 10 Ma, the arc migrated eastward into the foreland and broadened before arc magmatism stopped almost entirely for two million years (Ramos et al., 2014). The most recent steepening cycle has led to increased volcanism including many Quaternary rhyolite calderas and flood basalts. It is suggested that the process of steepening may still be ongoing (Ramos et al., 2014).

In this study, MT data collected in 2017 were used to investigate the distribution of fluids and partial melt from the Chilean coast to western Argentina along a two-dimensional (2-D) profile perpendicular to the trench. In addition to the collected data, data from previous authors and field seasons were also included along the profile (see Section 7.2.1). Two-dimensional isotropic inversions were employed and additional information from previous seismic studies was incorporated into an integrated interpretation. In general, the Earth's conductivity structure is three-dimensional and the MT impedance tensor has complex values and is a full 2 x 2 matrix (see Chapter 4). However, if the Earth has a 2-D structure, where the conductivity does not vary significantly in the geoelectric strike direction, the diagonal components of the tensor are small (i.e. close to zero) when the co-ordinate system is parallel to the strike direction. In this case, Maxwell's equations decouple into two independent modes, the transverse magnetic (TM) mode and the transverse electric (TE) mode. In many applications, a 2-D assumption can be valid if the impedance tensor data are rotated so that the diagonal components are minimized.

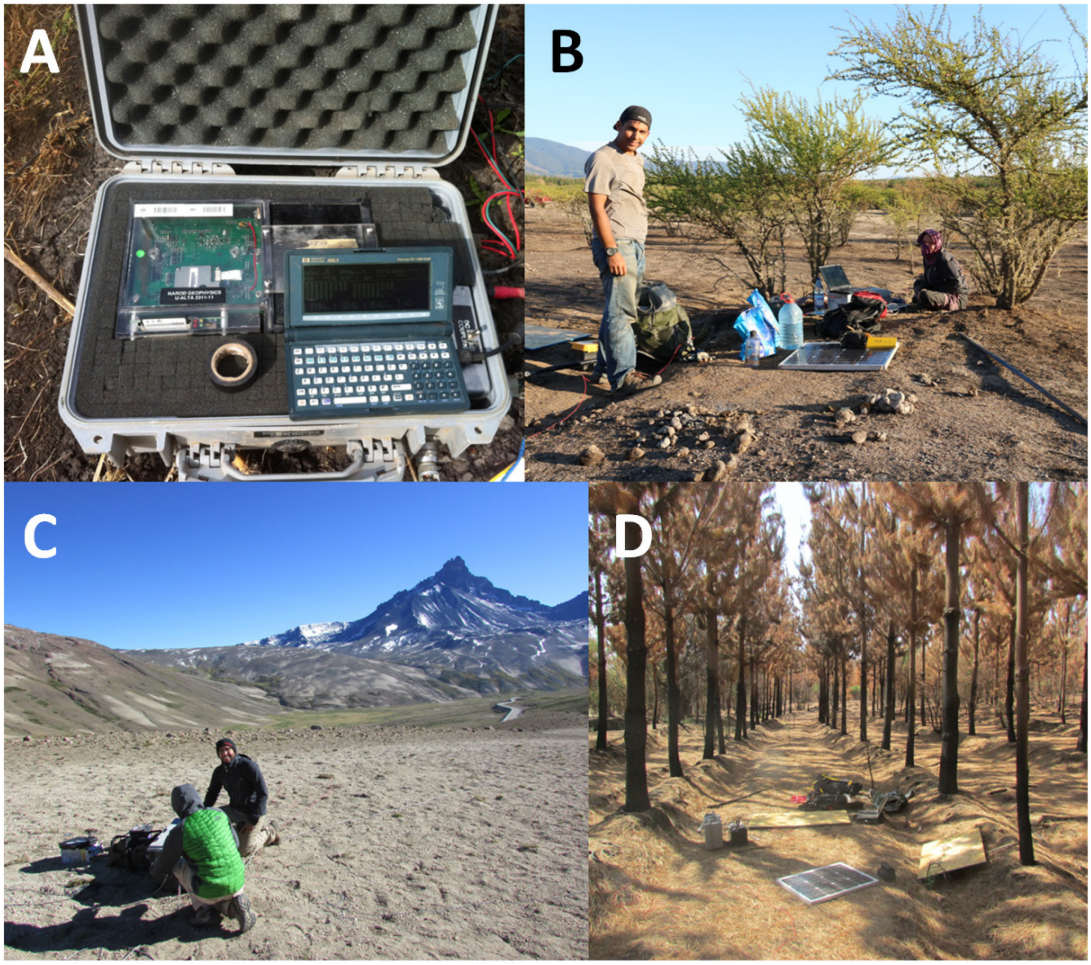

Figure 7.2: Field photos from the field season in 2017. (a) A picture of the NIMS data logger (photo credit: Benjamin Lee); (b) Installing Site CLP014 on the hottest day with highs of 37°C; (c) Installing BBMT site ARG001 near Cerro Campanario; (d) Installing site CLP017 in a tree farm.

7.2 FIELD CAMPAIGNS

7.2.1 Previously Collected Data

In 2016, broadband MT (BBMT) data were collected at 11 stations in the Central Valley on a profile extending from the Coastal Cordillera to the edge of the Cordillera Principal (Figure 7.1; Reyes-Wagner et al., 2017). These data were collected using Metronix ADU-07e MT instruments and gave data in the frequency band 0.001 – 1000 Hz. Reyes-Wagner et al. (2017) used these BBMT data to create a two-dimensional inversion model of the subduction zone at this latitude. However, the profile only measured

BBMT data and was only able to reliably image the upper 30 km of the crust. For the current study, 6 of these BBMT sites were included in the profile.

Burd et al. (2014) collected a grid of long-period MT (LMT) sites in western Argentina for a study of the Payenia volcanic province. These data were made available for use in the current thesis as impedance data. Four of these sites, which were located on the 2-D profile line, were used in this study (Figure 7.1).

Previous BBMT data described in Chapter 5 near Tatara-San Pedro and the LdMVF were also used for the regional profile. Sites were chosen based on data quality as well as how far they were from the profile line. As shown in Figure 7.1, four sites from the commercial geothermal exploration (Hickson et al., 2010) were used and five sites from the 2015-2016 LdMVF field seasons were used (see Chapter 5; Cordell et al., 2018).

7.2.2 2017 Field Season

As mentioned above, the profile of Reyes-Wagner et al. (2017) used only BBMT data with limited sensitivity at depth based on the skin depth equation (Equation (4.16) in Chapter 4). In order to measure the longer periods needed to image the deeper parts of the subduction zone in the lower crust, mantle, and subducting slab, LMT data were required. In February and March of 2017, 17 LMT stations were collected using the Narod Intelligent Magnetotelluric Systems (NIMS) data logger, Pb-$PbCl_2$ electrodes, fluxgate magnetometers, and approximately 90 m dipoles (Figure 7.2). These data were collected from the Pacific Ocean to the Chile-Argentina border (Figure 7.1). Due to difficulties of exporting the Canadian LMT equipment to Argentina, it was not possible to collect LMT data in Argentina during this field campaign. However, 4 additional BBMT stations were installed for between 12 and 48 hours in western Argentina (Figure 7.1) using the Metronix ADU-07 data logger from the Universidad de Chile to extend the profile eastward into the backarc and connect the profile to the previously collected LMT sites from Burd et al. (2014) (Figure 7.2). LMT sites were installed for 5 to 23 days with multiple runs. The overlap between runs is shown in Figure 7.3. Several logistical difficulties were encountered including several days spent in Argentina when the highway to return to Chile was closed due to snow. Temperatures of greater than 37°C in the Central Valley also slowed the progress. Digging conditions were variable depending on location with sites in the Central Valley and Coastal Cordillera being installed in dry, brick-like clay, and most other sites in the east being in sandy volcaniclastics. In total, 21 sites were collected in 2017 over a >200 km-long profile. Including the previous data, a total of 19 LMT sites were included

and 19 BBMT sites for a total of 38 sites along a 400 km-long, trench-perpendicular profile trending N105°E from the Pacific Ocean to western Argentina (Figure 7.1).

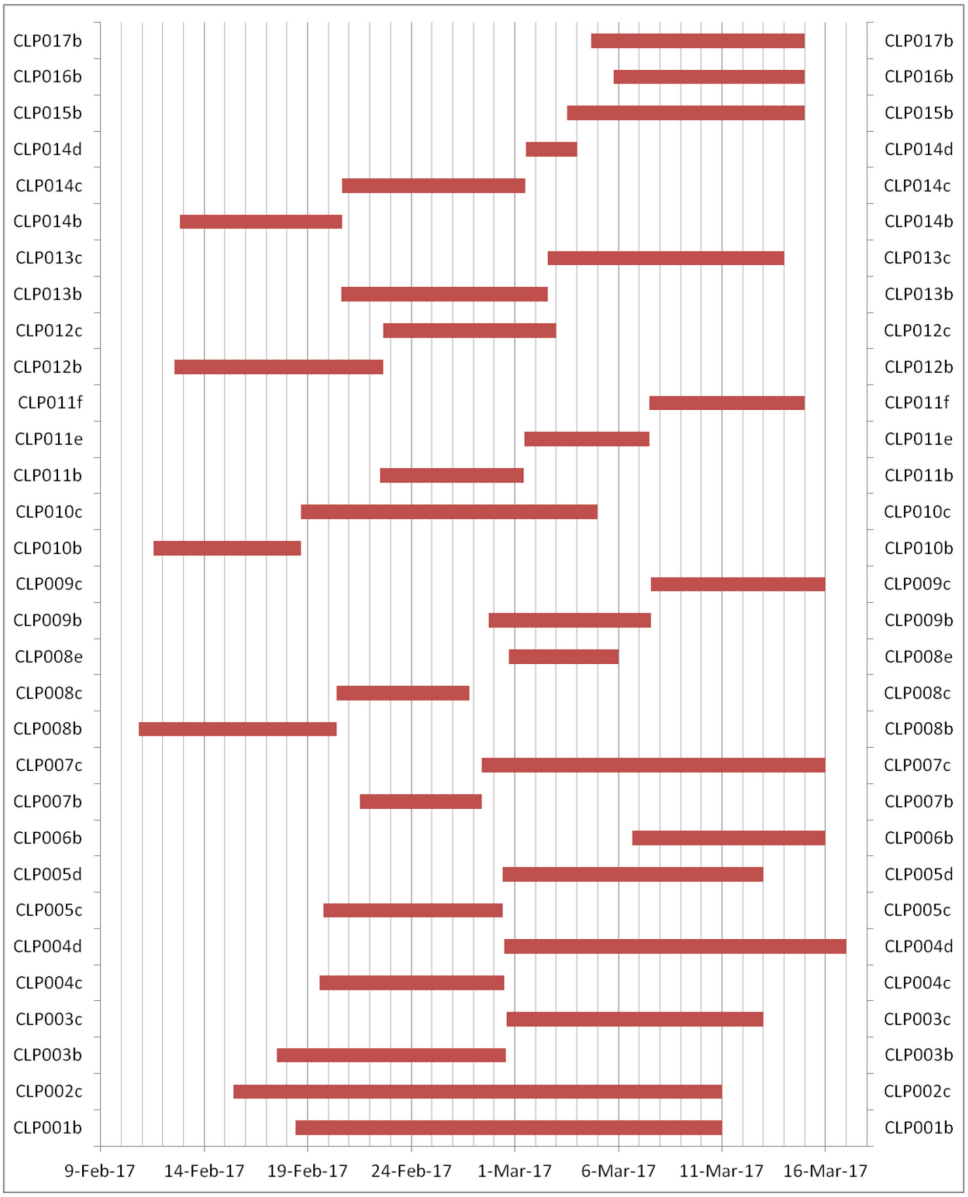

Figure 7.3: A table of run times for long period sites. Sites which had significant overlap (e.g. CLP001b and CLP002c) were used as mutual remote reference for processing. Each site generally had 2 - 3 runs for several days.

7.3 TIME SERIES PROCESSING

The MT time series collected in 2017 included 15 LMT sites in Chile and 4 BBMT sites in western Argentina. Time series data include 4 channels measuring the horizontal components of the electric and magnetic field as well as a fifth channel to measure the vertical magnetic field. The long period data

recorded time series data for between 5 and 23 days and the robust data processing methods of Egbert and Booker (1986) were applied using remote reference techniques where synchronous data were available as shown by the overlaps in Figure 7.3. LMT data measured periods from 6 s to 25,000 s although data beyond 10,000 s was generally quite noisy. The BBMT data were measured for between 12 and 48 hours and time series were processed using the robust methods with the smoothing constraints of Larsen et al. (1996). Resulting BBMT impedance data covered a range of frequencies from 2600 Hz to 0.0003 Hz although only data up to 1000 Hz was included in the analysis and inversions.

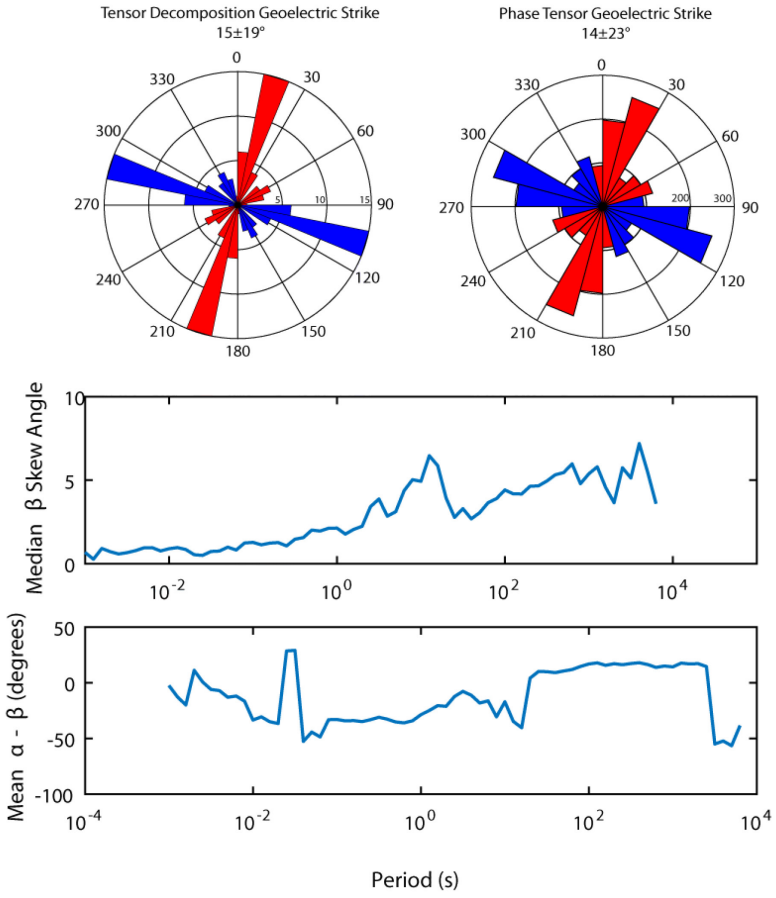

Figure 7.4: Dimensionality and directionality analysis for MT data. (a) The geoelectric strike for the full dataset using the tensor decomposition of McNeice and Jones (2001); (b) The geoelectric strike for the full dataset using the phase tensor analysis of Caldwell et al. (2004); (c) The median β-skew angle as a function of period where high skew (>3°) indicates three-dimensional resistivity structure; (d) The mean geoelectric strike from phase tensor analysis (α-β) as a function of period.

7.4 DATA ANALYSIS

7.4.1 Directionality and Dimensionality

An analysis of the directionality and dimensionality of the impedance tensor data was carried out to determine if a 2D assumption was valid for modelling the subsurface conductivity on this profile. This was done using the tensor decomposition methods of McNeice and Jones (2001) as well as an analysis of the phase tensors (Caldwell et al., 2004).

Multi-site, multi-frequency tensor decomposition shows a regional strike of N15°E ± 19° for periods greater than 1 s (Figure 7.4). Geoelectric strike estimates from phase tensor analysis gave a similar value of N14°E ± 23° for periods >1 s. Both of these are within the uncertainty of the N5°E regional strike obtained using only BBMT although the longer periods provide more consistent regional strike (Reyes-Wagner et al., 2017). Mean strike and one-standard deviation uncertainty was estimated using directional statistics (Mardia, 1972) where one standard deviation in radians equals

$$\sigma = \frac{1}{4}\sqrt{-2\ln(\bar{r})} \tag{7.1}$$

where $\bar{r}$ is the mean resultant (i.e. the length of the vector of mean sine and mean cosine of the strike). The factor of 1/4 is necessary because the quadrant of the geoelectric strike is inherently ambiguous and requires further interpretation from geology. In this case, because the Andes run approximately north-south, the regional geoelectric strike was taken to be approximately north-south, rather than east-west.

There is a clear along-profile change in the geoelectric structure across the Cordillera Principal (Figure 7.5). On the west side of the profile, tensor decomposition results in a well-defined strike of N15°E ± 4° while on the east side of the profile, the strike is much more poorly-defined and oriented N27°W ± 26° with several stations in the Cordillera Principal having a strike direction near N60°E (or N30°W). This may be due to the effect of the extremely conductive ocean (e.g. average resistivity of 0.3 Ωm) on the western side of the profile and more complicated geology (e.g. the north-west trending Las Loicas trough) affecting the regional picture on the eastern side of the profile (Ramos et al., 2014). It could also be a result of more short period data being available on the eastern side of the profile which samples smaller, local structures.

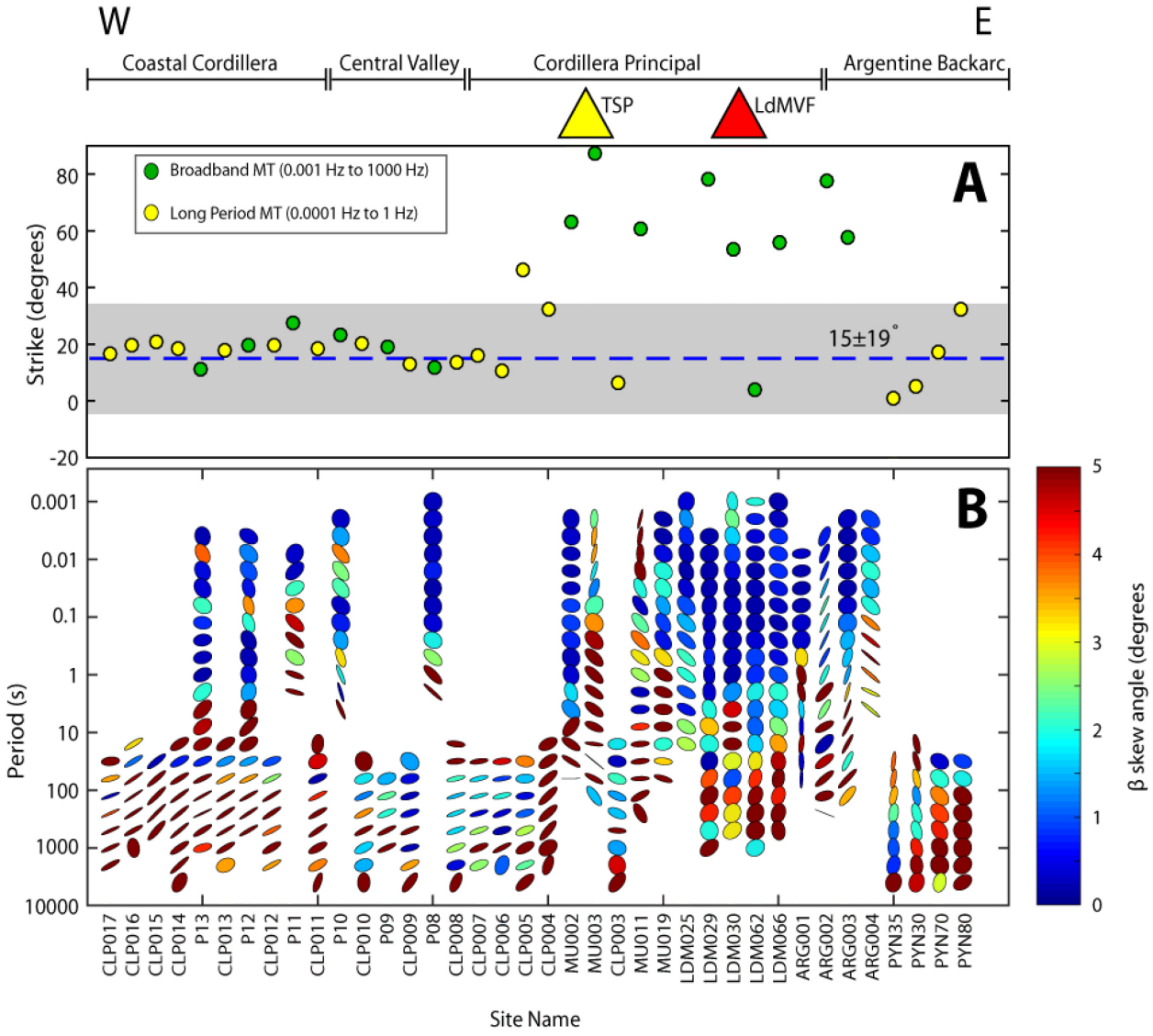

Figure 7.5: Dimensionality and directionality analysis for MT data. (a) The strike angle for each station along the profile as determined from tensor decomposition (McNeice and Jones, 2001). The average strike (15°) is plotted as blue dashed line and the one circular standard deviation error bar is shown in the grey box. Yellow dots are LMT sites and green dots are BBMT sites. (b) A phase tensor pseudo-section shows the MT profile as a function of period. Each ellipse on the plot denotes the phase tensor for a single period at a single MT site. Each phase tensor is coloured by its β-skew angle where blue indicates relatively 1D or 2D, undistorted data and red indicates data with 3D distortion. TSP = Tatara-San Pedro. LdMVF = Laguna del Maule Volcanic Field. Note that distances along profiles are not to scale.

High skew values (β > 3°) obtained from phase tensor analysis were observed at nearly all periods greater than 10 s, suggesting some significant 3D induction effects at depth especially on the east side of the profile (Figure 7.5; Booker, 2014). In general, skew increases with period meaning that there are more 3-D effects at longer periods (Figure 7.4). It is worth noting that inconsistent strike direction is not an indication of 3-D structure since most sites with inconsistent strike have low skew values and are located in the northwest-trending Las Loicas trough.

7.4.2 Apparent Resistivity and Phase Curves

All apparent resistivity and phase curves for the Transverse Electric (TE) and Transverse Magnetic (TM) modes are shown in Appendix 2 where the tensor impedance data are rotated to the regional strike of N15°E. The TE mode data are data collected in the coordinate system which has electric fields parallel to strike, whereas the TM mode data are collected in the coordinate system which has magnetic fields parallel to strike (see Chapter 4, Section 4.4.3). The geoelectric strike for this region is approximately N15°E, but impedance data were collected in the field using geographic coordinates such that electric and magnetic fields were collected north-south and east-west. If the impedance tensor is rotated N15°E, then the tensor is aligned the geoelectric strike and the off-diagonal components of the tensor become the TE and TM modes. Pseudo-section plots of the apparent resistivity and phase for rotated off-diagonal components of the impedance tensor are shown in Figure 7.6. The main geological units can be seen in pseudo-section: 1) The highly resistive metamorphic block of the Coastal Cordillera is seen in the apparent resistivity for both TE and TM modes; 2) the low resistivity volcaniclastic and sedimentary fill of the Central Valley; and 3) a generally low resistivity volcanic arc and backarc. The phase split is also apparent on the western side of the profile which indicates an ocean effect as the TM mode tends to have very low phases (<10°) at long periods (>100 s) while the TE mode has moderate to high phases (>75°) at long periods. At very long periods (>2000 s), some out of quadrant phases were observed which may suggest anisotropic structure, coastal effects, and/or complicated 3-D geometry (Heise and Pous, 2003; Selway et al., 2012). The fact that the profile is a mixture of both BBMT and LMT is apparent in the pseudo-section. There is an irregular sampling of different frequency bands with more long period data on the western side of the profile (i.e. west of the Cordillera Principal), a bias towards higher frequencies in the middle of the profile (i.e. in the Cordillera Principal), and a return to longer period sites on the eastern side of the profile (i.e. east of the Cordillera Principal). This has an impact on the inversions and necessitates a two-step procedure as detailed below.

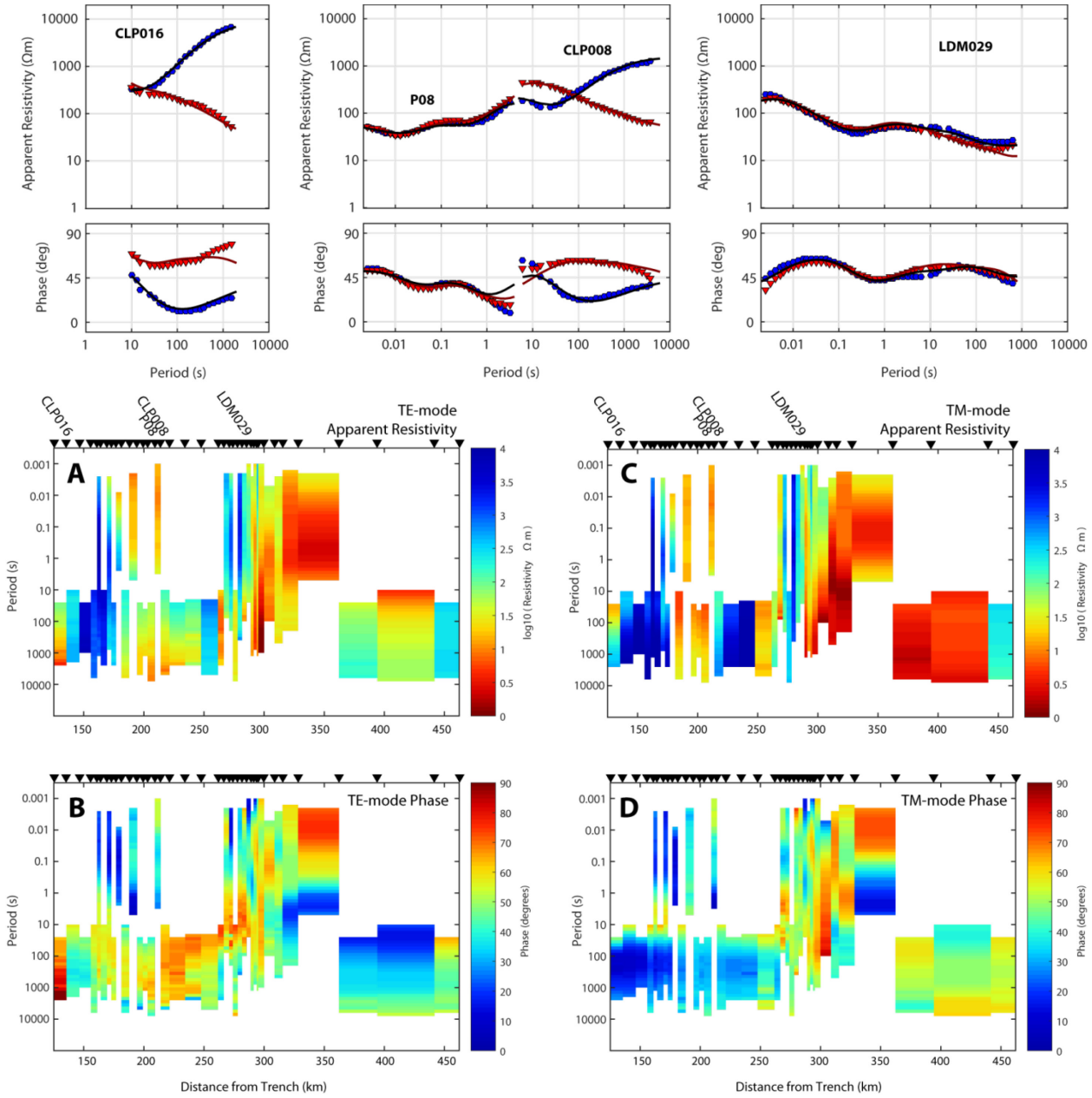

Figure 7.6: Magnetotelluric (MT) data and pseudo-sections. The top three panels show apparent resistivity and phase data for four MT sites in the Coastal Cordillera (CLP016), Central Valley (P08, CLP008) and Cordillera Principal (LDM029). TE mode is shown as red triangles while TM mode is shown as blue circles. Inversion model fit is shown as solid lines. Sites CLP016 and CLP008 are both LMT whereas P08 and LDM029 are BBMT. Sites P08 and CLP008 are located less than 5 km apart and are shown on the same plot but were treated as separate sites in the inversion. Below are pseudo-section plots showing a) TE-mode apparent resistivity, b) TE-mode phase, c) TM-mode apparent resistivity, and d) TM-mode phase for each site along the profile as a function of period. All data have been rotated to x= 15° east of north, y = 105° east of north. TE mode is calculated with x-oriented electric fields and y-oriented magnetic field whereas TM mode is the opposite case.

The apparent resistivity and phase data are shown for four sites, CLP016, P08, CLP008 and LDM029 in Figure 7.6. CLP016 is a long period site located in the Coastal Cordillera and shows steeply decreasing TE-mode apparent resistivity and steeply increasing TM-mode apparent resistivity which is a typical of the coast effect. Further east, P08 is a BBMT site and CLP008 is a LMT site. These sites are only 5 km apart and are combined to show how the BBMT and LMT compare but were inverted as separate sites in the inversion. The match is quite good for the apparent resistivity although there is a mismatch in the phases between the bands which may be due to poor data quality at shorter frequencies for the long period data or different near-surface structure. It is worth noting that CLP008 lies in a valley while P08 is on a flat section of the Central Valley. Finally, LDM029 is shown as a representative BBMT site in the Cordillera Principal near the LdMVF and shows two-distinct minima in the apparent resistivity curve indicating the presence of shallower and deeper conductors.

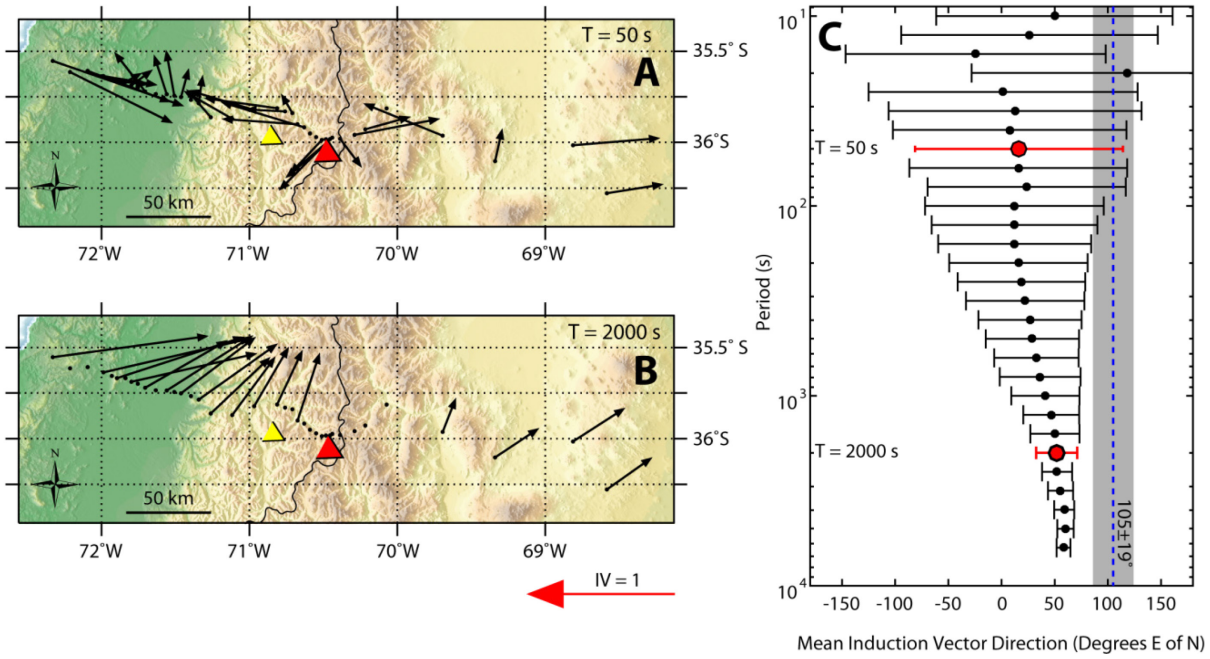

Figure 7.7: A comparison of induction vectors (IVs) plotted in the Wiese convention and tensor decomposition strike. A) A map of IVs at 50 s period. Large scatter shows no consistent trend in induction vector direction. B) A map of IVs at 2000 s period. Here, IVs consistently point towards the northeast. Red triangle = Laguna del Maule Volcanic Field. Yellow triangle = Tatara-San Pedro Volcano. C) A plot of mean induction vector direction as a function of period. The blue dashed line shows the mean profile direction perpendicular to geoelectric strike (grey box denotes one standard deviation).

7.4.3 Induction Vectors and Anisotropy

Vertical magnetic field data were collected at all sites along the profile except for two BBMT sites. This additional field component allowed for the computation of vertical magnetic transfer functions (i.e. the ratio of the vertical component to the horizontal component). Induction vectors (IVs) represent both components of the vertical magnetic field transfer function. IVs have both real and imaginary components. In map view, the real component of the vectors can be plotted as arrows which point away from conductors where the length of the arrow indicates the magnitude of the sum as shown in Figure 7.7 at periods of 50 s and 2000 s, respectively.

Sites in the Coastal Cordillera show large IVs (i.e. long arrows) at short period (Figure 7.7a) which point away from the Pacific Ocean likely indicating the large ocean effect at short periods. However, at sites in the Central Valley and the Cordillera Principal, the IVs are very scattered at short periods. All the IVs surrounding the LdMVF point away from one another, suggesting a conductor at depth beneath the LdMVF. At relatively greater depths (i.e. longer periods; Figure 7.7b), the IVs are very consistent in pointing towards the northeast at all sites along the profile which have long period data. This suggests a regional structure at depth. However, under a 2D isotropic assumption, it is expected that IVs will be perpendicular to the geoelectric strike since all conductors will be aligned orthogonal to the geoelectric strike. Figure 7.7c shows that this is not the case. Using directional statistics, the mean and standard deviation of the induction vector direction was calculated at each period and is plotted as a function of period. It can be seen that the scatter in the IVs is very large at short periods but at longer periods, the error bars are much smaller indicating a much more consistent direction. More importantly, the direction of the IVs is approximately N50°E which is not perpendicular to the geoelectric strike as a determined by tensor decomposition. In an ideal 2D scenario, it would be expected that the induction vectors would all point at N105°E ± 19° (the grey box in Figure 7.7c). This further suggests that the ideal 2D, isotropic assumption is being violated. Brasse et al. (2009) found a similar phenomenon in the southern Andes (38° - 41° S) where induction vectors also pointed uniformly to the northeast at periods greater than 3000 s. They showed that this discrepancy could be accounted for with an anisotropic layer in the over-riding South American plate which they attributed to a fractured and fluid-rich lower crust though they do not differentiate between partial melt fluids or hydrothermal fluids.

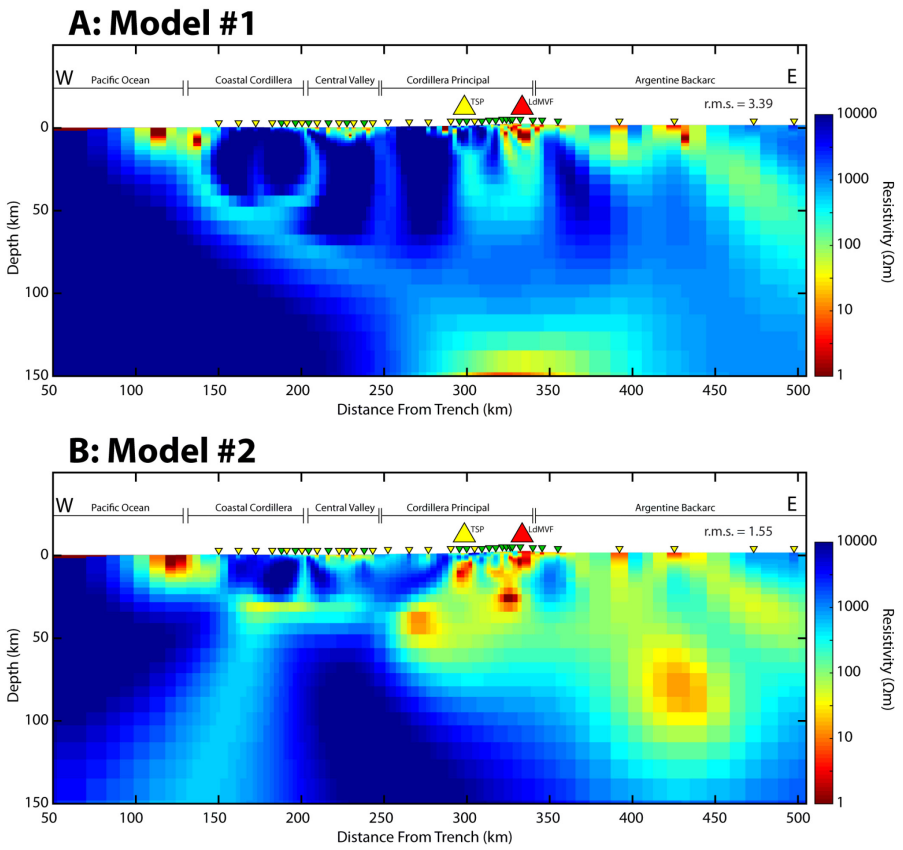

Figure 7.8: Comparison between two-dimensional inversion models with (a) no static shifts included (final r.m.s. misfit = 3.39) and (b) static shifts included (final r.m.s. misfit = 1.55). TSP = Tatara-San Pedro; LdMVF = Laguna del Maule Volcanic Field. Inverted triangles show BBMT (green) and LMT (yellow) site locations.

7.5 TWO-DIMENSIONAL MAGNETOTELLURIC DATA INVERSION

7.5.1 Data Selection and Model Parameters

The above data analysis shows that the data contain some interesting 3-D induction effects, some inconsistent strike values above the Cordillera Principal, and evidence of electrical anisotropy in the lower crust. With these considerations in mind, a 2D isotropic inversion was carried out with the understanding that resulting inversion model may be more robust on the west side of the profile where the strike is better defined. The impedance data were rotated to N15°E, representing the best-fitting regional strike, and impedance data were inverted to find the best-fitting model using the non-linear conjugate gradient (NLCG) method of Rodi and Mackie (2001). The ocean was included with a fixed resistivity of 0.3 Ωm using local bathymetry.

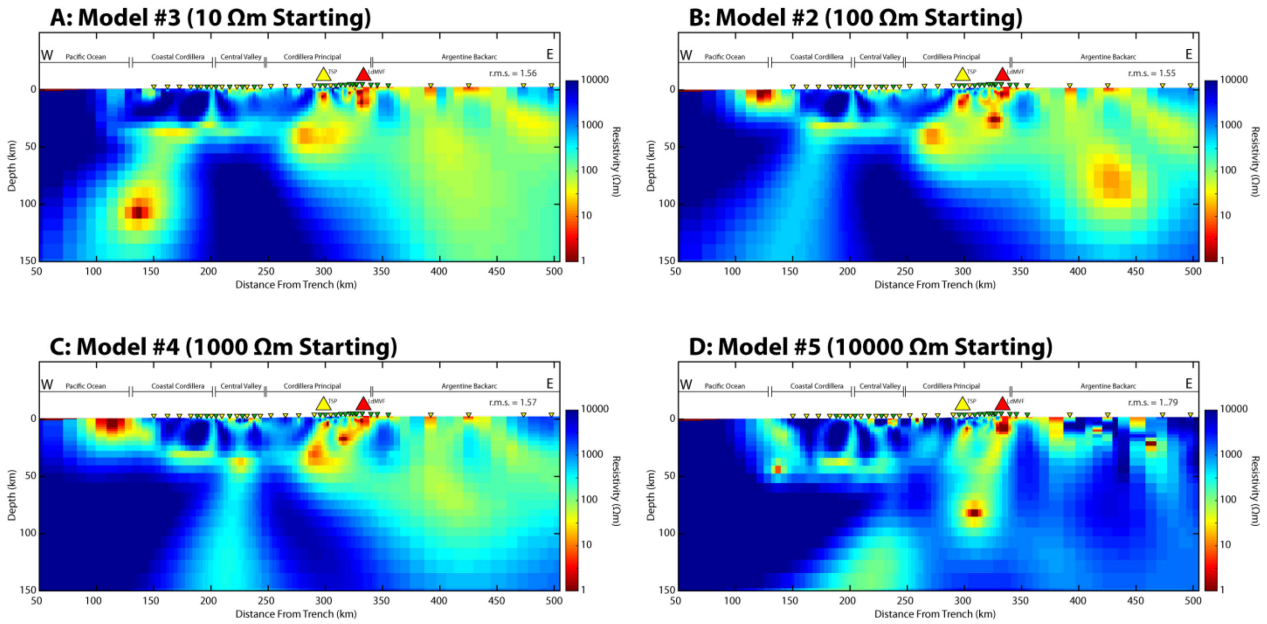

Figure 7.9: Comparison between 2-D inversion models using different starting models of (a) 10 Ωm; (b) 100 Ωm; (c) 1000 Ωm and; (d) 10000 Ωm. TSP = Tatara-San Pedro; LdMVF = Laguna del Maule Volcanic Field. Inverted triangles show BBMT (green) and LMT (yellow) site locations.

The data set used in the inversion included 19 LMT sites (10 s to 10,000 s) sites and 19 BBMT sites (0.001 s to 1000 s) with a total of 2590 complex impedance data points. Sites were projected onto a N105°E profile with interpolated topography. The TE mode was consistently noisier than the TM mode, so an error floor of 10% was applied to the TE mode and 5% to the TM mode. This choice of error floor effectively down-weights the importance of the TE mode data in the inversion. The starting model had 97 vertical cells beginning with 50 m-thick topography cells and growing geometrically to a maximum thickness of 73.9 km at a depth of 450 km. The model included 86 horizontal cells with variable width with a mean value of 3.5 km. The model also included 12 horizontal padding cells in each direction growing geometrically to 750 km from the center with maximum cell width of 217 km. The inversion algorithm of Rodi and Mackie (2001) allows for a variety of different inversion parameters including incorporating a static shift parameter, choosing a starting model, applying *a priori* constraints, and varying the regularization parameter. Additional tests could also be applied to test for e.g. the effect of error floor, data selection, mesh design etc., but it is impossible to explore all permutations of the model space. For all inversions, the ocean was fixed at 0.3 Ωm with bathymetry data from the ETOPO1 NOAA dataset[1]. A no-smoothing boundary was imposed at the ocean floor.

[1] https://maps.ngdc.noaa.gov/viewers/wcs-client/

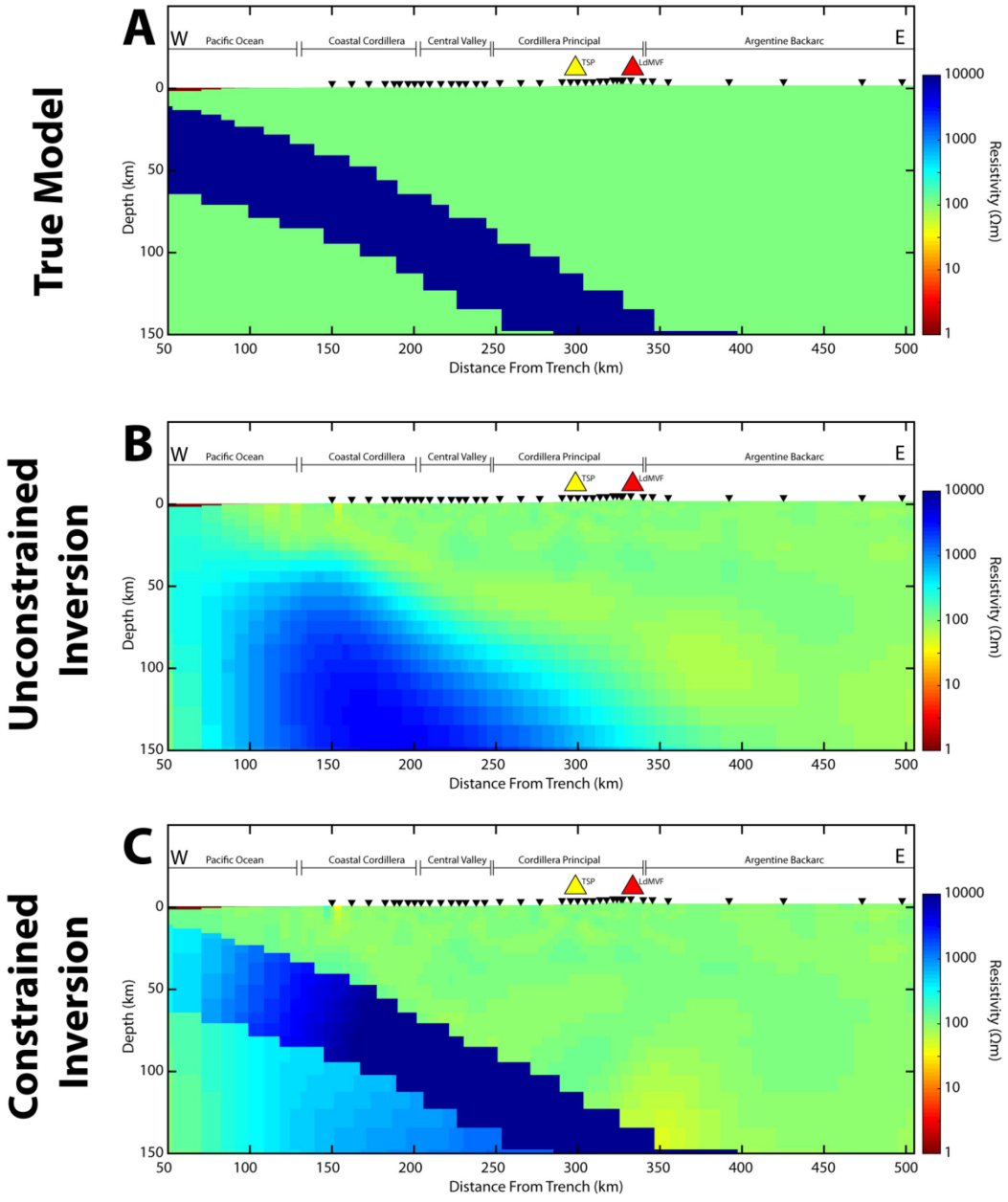

Figure 7.10: Synthetic experiment with a known two-dimensional resistivity model. (a) the true model with a resistive (10,000 Ωm) subducting slab in a 100 Ωm halfspace. MT data were computed from this model using the same site and frequency distribution as the field data and then contaminated with 5% Gaussian noise. This computed data was then used as input data for two different inversions. (b) the results of an unconstrained inversion. The model images a resistive region which could be interpreted as the slab. (c) the results of a constrained inversion where a tear was included at the top and bottom of the slab interface. Here the model recovers the true model with significantly greater accuracy. Both inversions achieved an r.m.s. misfit of 0.70 with $\tau = 2$. TSP = Tatara-San Pedro; LdMVF = Laguna del Maule Volcanic Field. Inverted triangles show MT site locations.

Here, static shifts, starting model, *a priori* constraints, regularization parameter, and data selection are all explored in Sections 7.5.2 through 7.5.7. After this analysis, the final preferred inversion model is presented in Section 7.5.8. For each case, the initial test uses the simplest assumptions and complexity is increased with each step. First, an inversion was run with no static shift parameters allowed, using a 100 Ωm halfspace with no *a priori* constraints and a regularization parameter of $\tau = 2$, and all frequencies for data selection. For reference, the resulting model from this inversion is called Model #1. This simple inversion resulted in an r.m.s. misfit of 3.39 after 200 iterations. The model is shown in Figure 7.8a.

7.5.2 Static Shifts

The inversion algorithm allows static shift factors to be inverted in order to better fit the data. Static shift factors are applied to the data as direct multipliers of the apparent resistivity for each mode independently (i.e. scaling the magnitude of the impedance tensor component without changing the phase). This is done with an additional damping parameter which forces the inversion to fit the data using only static shift factors first before proceeding to fit the data using changes to the model resistivity at later iterations. The data shows some evidence of significant static shifts. When data are inverted with static shift corrections included, the data misfit decreases considerably to an r.m.s. of 1.55 and the model changes considerably (Figure 7.8b; Model #2). The benefit of including the static shift factors is apparent by the vast reduction in r.m.s. misfit. As such, all future inversions include inverting for static shifts.

7.5.3 Varying Starting Model

The choice of starting model can have a major effect on an inversion. Several different inversions were run with different starting model halfspace values of 10 Ωm (Model #3), 100 Ωm (Model #2), 1000 Ωm (Model #4) and 10000 Ωm (Model #5). This allowed for an investigation of which starting model achieved the best data fit and gave the most geologically reasonable models. The resulting inversion models from using different starting models are shown in Figure 7.9. The 100 Ωm starting model resulting in an inversion model with the lowest r.m.s. misfit (1.55) although both the 10 Ωm starting model and 1000 Ωm starting model also achieved good r.m.s. misfit of 1.56 and 1.57, respectively. The 10000 Ωm starting model had higher r.m.s. misfit of 1.79. The 100 Ωm and 1000 Ωm models also look quite similar whereas the 10 Ωm and 10000 Ωm models contain several different features and are generally rougher at depth.

A suitable choice can be made by inspection of the measured MT data. The mean apparent resistivity for the off-diagonals at the highest frequencies was approximately 100 Ωm while the entire frequency band had a mean apparent resistivity of 1200 Ωm. This suggests that both the 100 Ωm starting model or the 1000 Ωm starting model would be reasonable. Both converged to a similar solution whereas the other cases contained suspect features at depths where there is likely less data sensitivity. The 100 Ωm starting model resulted in lower misfit so all further inversions were started from a 100 Ωm halfspace.

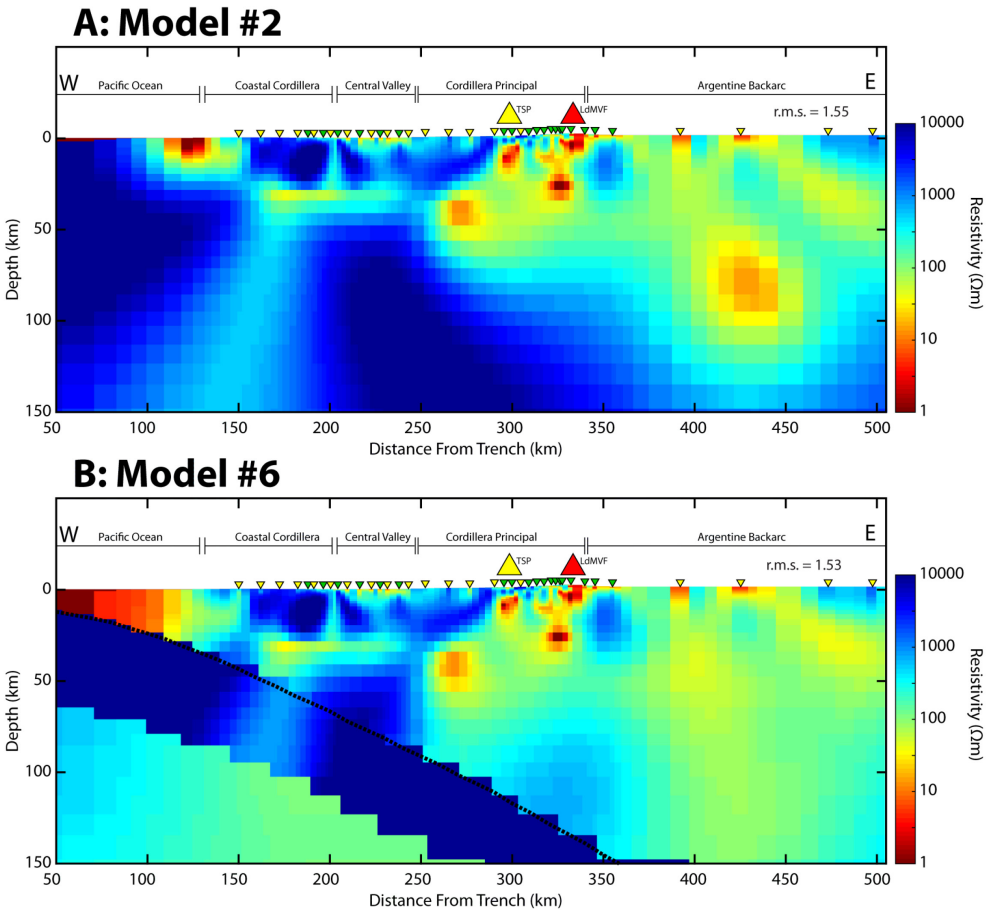

Figure 7.11: A comparison between an unconstrained (Model #2) and constrained (Model #6) two-dimensional inversion using the full dataset. TSP = Tatara-San Pedro; LdMVF = Laguna del Maule Volcanic Field. Inverted triangles show BBMT (green) and LMT (yellow) site locations.

7.5.4 Constraining Subducting Slab Position

A variety of possible *a priori* model constraints and options can be investigated in an effort to create the most plausible resistivity model. In one variation, a smoothing constraint was placed on the model at the top and bottom of the Nazca plate using the Slab 1.0 model of Hayes et al. (2012) and an estimated plate thickness of 50 km (Sodoudi et al., 2011). Because MT inversions are non-unique, it is preferable to include the *a priori* information of the slab interface to the model which will result in more geologically consistent models with fewer unknowns (Pommier and Evans, 2017). This is illustrated using a synthetic experiment whereby an unconstrained and constrained model are compared to a known "true" model using the same frequency and station distribution as the real data (Figure 7.10). In the constrained case, the true geometry of the known slab is recovered very accurately compared to the very smooth, unconstrained case.

For this particular profile, it seems that whether the slab constraint is imposed (Model #6) or not has little effect on the shallow conductive features because most features are the same in both models in Figure 7.11. However, at depth, the imposition of the slab boundary constraint tends to smooth down features towards the slab interface. The addition of the *a priori* knowledge as a constraint is preferable and likely results in a more accurate model. As such, the additional constraint will be used throughout the remainder of this chapter.

7.5.5 Varying Regularization Parameter

The MT inverse problem is non-unique due to a combination of being an under-determined problem as well as the inherent physics of the MT method. The problem is generally under-determined because there are more model parameters than data parameters. The physics of the MT method is primarily sensitive to conductance (the product of thickness and conductivity) whereas the inverse problems solves for conductivity. As a result, there are a variety of different resistivity models that can fit a set of data equally well. In general, MT inversion algorithms use a Tikhonov regularization which imposes smoothness on the inverse solution by defining the objective function to be minimized as

$$U(\tau) = \Phi_d + \tau\Phi_m \tag{7.2}$$

where Φ_d is the data misfit constraint (usually defined as an L2-norm) and Φ_m is the model smoothness constraint. Smoothness can be defined in a variety of ways. The algorithm being used for this investigation uses a second-difference matrix operator to smooth the model. The regularization

parameter[2] (τ) in Equation (7.2) is used to weight the model norm versus the data misfit in the inversion cost function. Higher values of τ result in smoother models with poorer data fit while lower values of τ results in rougher models (i.e. more structure) with better data fit. The choice of τ is somewhat arbitrary but a guiding principle is to set it such that the trade-off between model smoothness and data misfit is optimized.

The regularization parameter was varied from τ = 0.1 to τ = 30 using 9 different values to produce an L-curve which plots model norm versus data misfit as shown in Figure 7.12. The optimal smoothing parameter is found by selecting the model which is nearest the origin. For this dataset, the optimal value was found to be τ = 2 when using a 100 Ωm starting model. All further inversions use this value for τ.

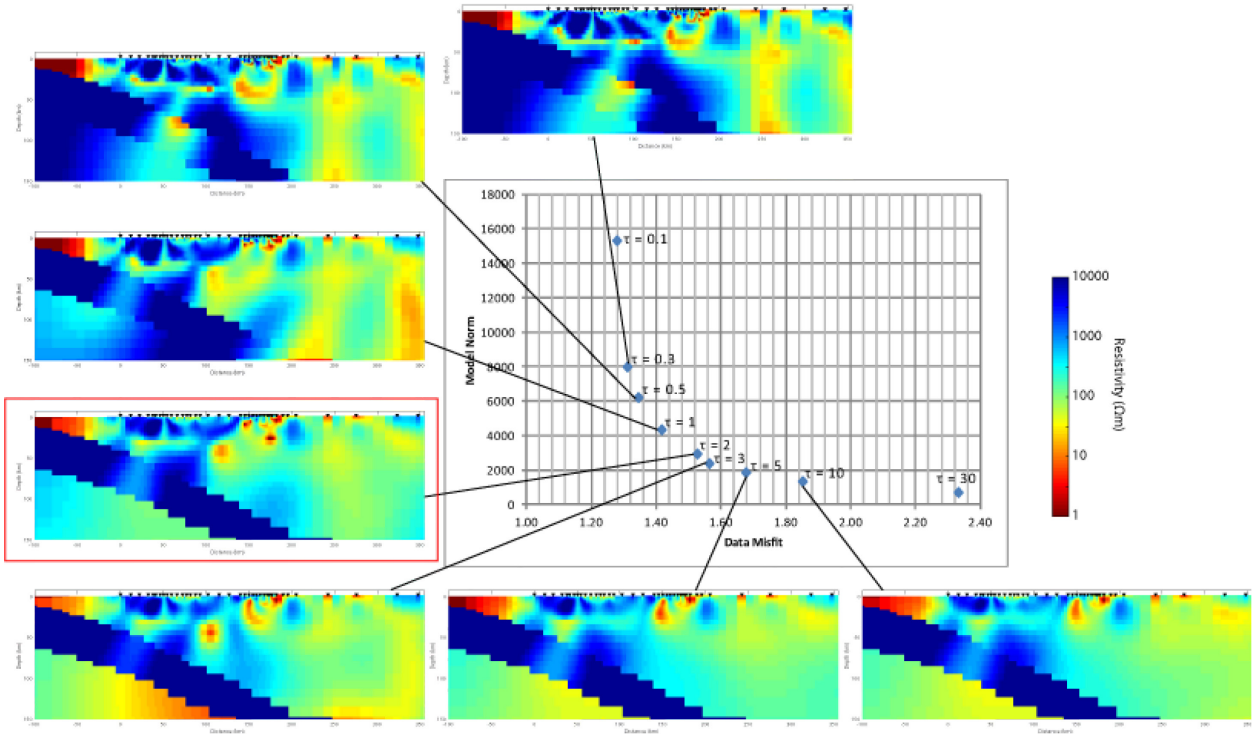

Figure 7.12: Regularization L-curve test using various $\boldsymbol{\tau}$ parameters (0.1, 0.3, 0.5, 1, 2, 3, 5, 10, 30) using all periods with data rotated 15° east of north. The main graph shows model norm versus data misfit. The insets show different model results for different $\boldsymbol{\tau}$ values. The value of $\boldsymbol{\tau}$ increases going counter-clockwise with the roughest model at the top and the smoothest model at the bottom right. The preferred value is $\boldsymbol{\tau}$ = 2 which is the best trade-off between model smoothness and data fit (model with red box around it).

[2] The regularization parameter often goes by a variety of names including τ, λ, or ν among others (Kelbert et al., 2014; Parker, 1994; Robertson et al., 2020; Rodi and Mackie, 2001).

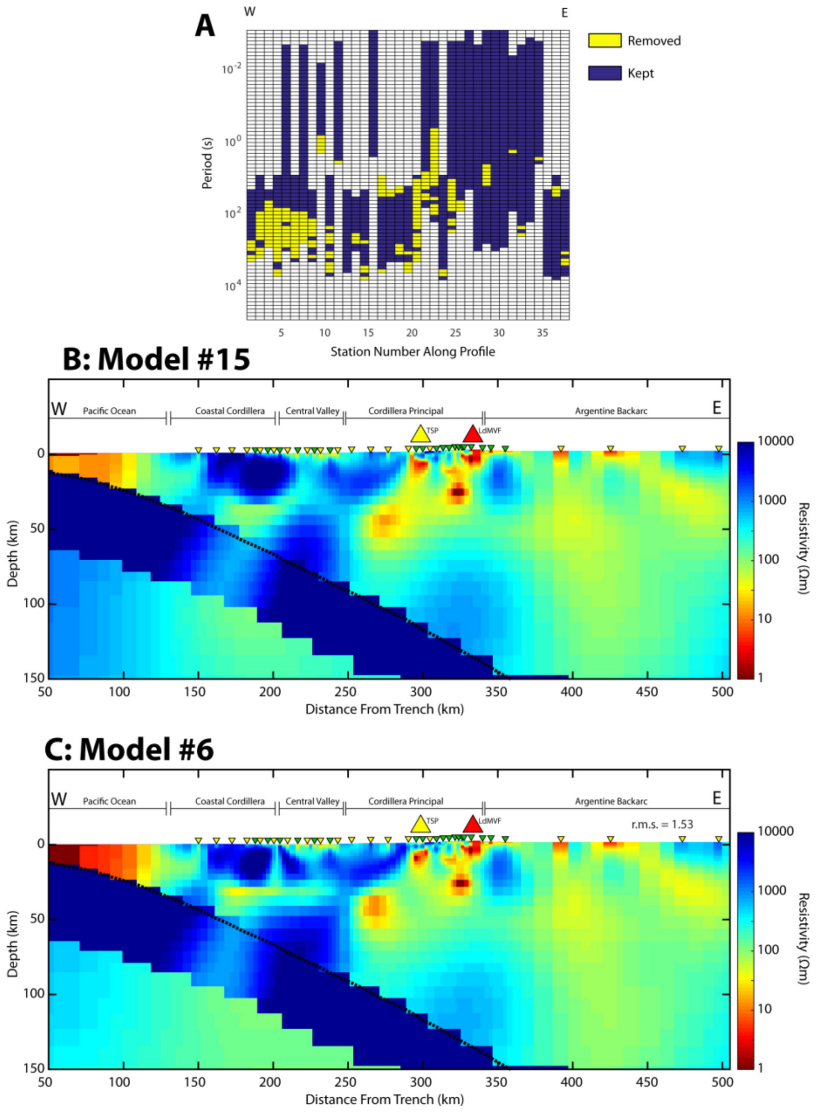

Figure 7.13: Inversion tests with high skew (β>6°) removed. (a) Shows a pseudo-section plot of impedance values at each site along the profile from west to east. Yellow boxes are frequencies where the impedance data were removed with β>6°. In total, 16% of data was removed for this inversion. (b) The model which resulted from using this smaller sub-set of data which better fit the 2-D approximation. (c) The model which included the full data set. In general the features in this model are similar to features in the interpreted model. TSP = Tatara-San Pedro; LdMVF = Laguna del Maule Volcanic Field. Inverted triangles show BBMT (green) and LMT (yellow) site locations.

7.5.6 Removing High-Skew Data

Since impedances with high β skew angles suggest the presence of 3-D resistivity structures (Booker, 2014), it may be reasonable to remove these data from the inversion and only invert the low-skew impedance values. This would result in data with more 3-D data excluded. To investigate this, very high

skew impedance data (β > 6°) were removed and only the low skew data was inverted (Model #15). This decreased the amount of data available, especially at long periods, as shown in Figure 7.13a and thus decreased resolution overall. This limited data set was inverted and the model is shown in Figure 7.13b which achieved an r.m.s. of 1.55 after 200 iterations. In general, the model features are relatively un-changed by removing the high beta-skew data points as compared to the inversion using the full dataset shown in Figure 7.13c. Model #15 may be a more accurate 2-D approximation with high skew data removed, but because 16% of the data were removed, it was viewed as a poor trade-off. All further inversions used the full data set and included both low- and high-skew data.

7.5.7 Two-Step Inversion Approach

A final methodology which was ultimately used as the preferred inversion model involved inverting only the long periods (>10 s) and using the resulting inversion model as the starting model for a second run with all periods. This two-step methodology proved an effective means of giving greater weight to the long period data while still resolving shallow structure.

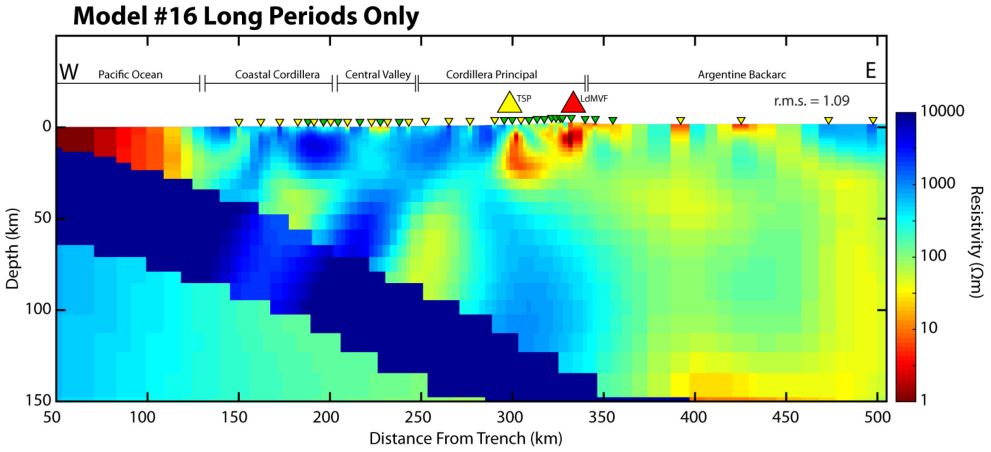

Figure 7.14: Model which uses only long period data (>10 s). This model was then used as the starting model for the preferred inversion which included all frequencies. TSP = Tatara-San Pedro; LdMVF = Laguna del Maule Volcanic Field. Inverted triangles show BBMT (green) and LMT (yellow) site locations.

The long period data is more of interest here because we are interested in resolving deeper subduction zone structures. Longer period data also tend to have better defined strike angles (although equally-so have more 3-D inductive effects as indicated by higher skew angles). The LMT only inversion model

(Model #16) is shown in Figure 7.14 for the constrained case. This inversion model was then used as the starting model for the inversion with the full frequency set (Model #17; Figure 7.15).

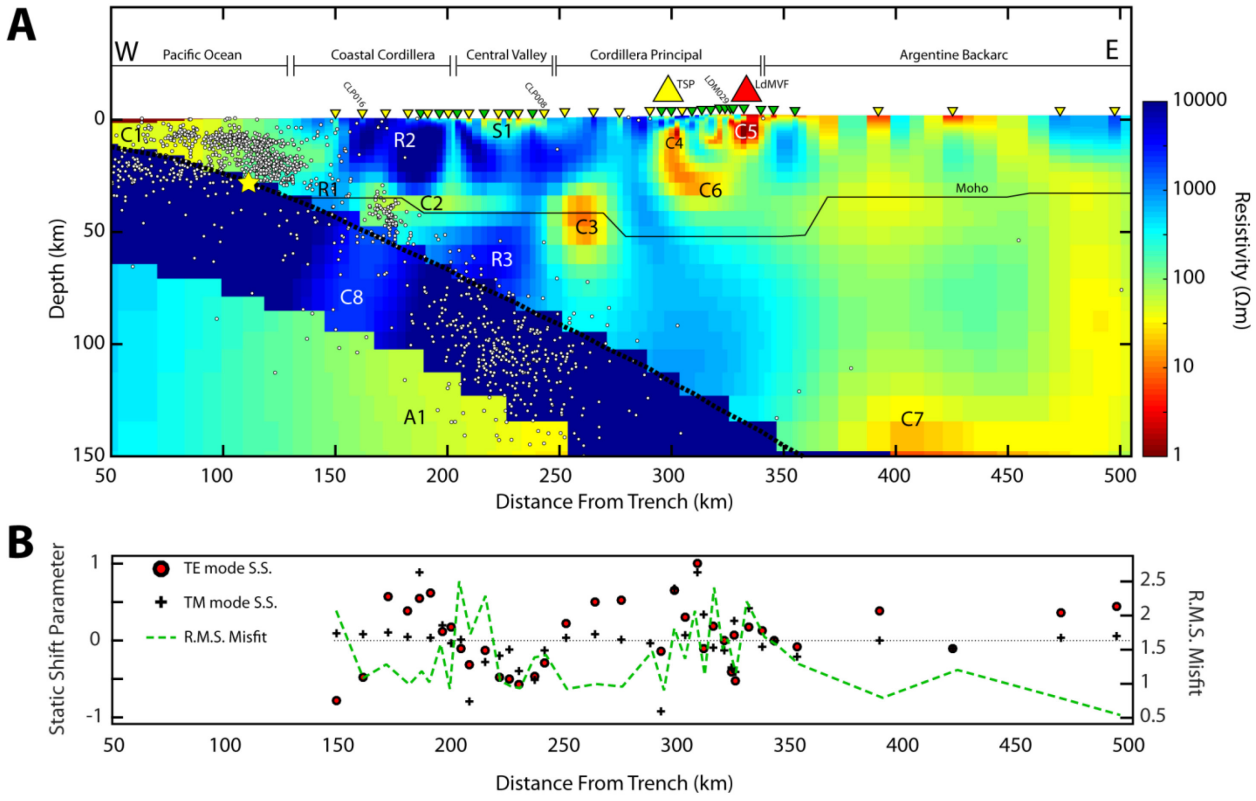

Figure 7.15: The preferred 2-D inversion model along the MT profile (a). BBMT sites are shown as green inverted triangles and LMT sites are shown as yellow inverted triangles on the surface of the model. Conductors are labelled C1 through C8 and resistors are labelled R1 through R3. The shallow surface conductor in the Central Valley is labelled S1 and deeper slab-side conductor is labelled A1. The location of the subducting slab is taken from Hayes et al. (2012) and shown as a thick black dashed line. This is the location of the tear which constrained the inversion to have zero smoothing across the boundary. The Moho discontinuity, shown as a thin black line, is taken from the Crust1.0 model of Laske et al. (2013). The location of the 2010 Maule earthquake is shown as a yellow star. Earthquake epicenters are shown as small white dots. TSP = Tatara-San Pedro. LdMVF = Laguna del Maule Volcanic Field. The lower panel (b) shows r.m.s. misfit for the inversion for each station along profile. It also shows the static shift parameters applied to the constrained inversion.

7.5.8 Preferred Two-Dimensional Model

The final, preferred inversion model (Figure 7.15; Model #17) used a 100 Ωm starting model and a regularization parameter of τ = 2. Static shifts were inverted for and a no-smoothing constraint was imposed at the top and bottom of the slab. The final inversion used both TE and TM modes with the two-step methodology whereby the low frequencies were inverted first followed by the full frequency set. Vertical magnetic transfer function data were not included because they have significant deviations from the two-dimensional assumptions (see Section 7.4.3). It is worth noting that, in general, the primary conductive and resistive features were robust and independent of modelling methodology. The preferred two-dimensional model was chosen based on data fit, a desire to image deeper structures, an understanding that including more information in the starting model via slab constraint is preferable, and whether the resulting model was geological reasonable in both form and resistivity values. The model shown in Figure 7.15 also includes the location of the slab from Hayes et al. (2012), and the location of the Moho from Laske et al. (2013). Deep earthquake epicenters (>50 km) are from IRIS (2018) while shallow earthquake epicenters (<50 km) are taken from an improved database from Hicks et al. (2014) using earthquake aftershocks from the 2010 Maule earthquake (Figure 7.16). Earthquakes within 50 km of the profile are projected onto the profile.

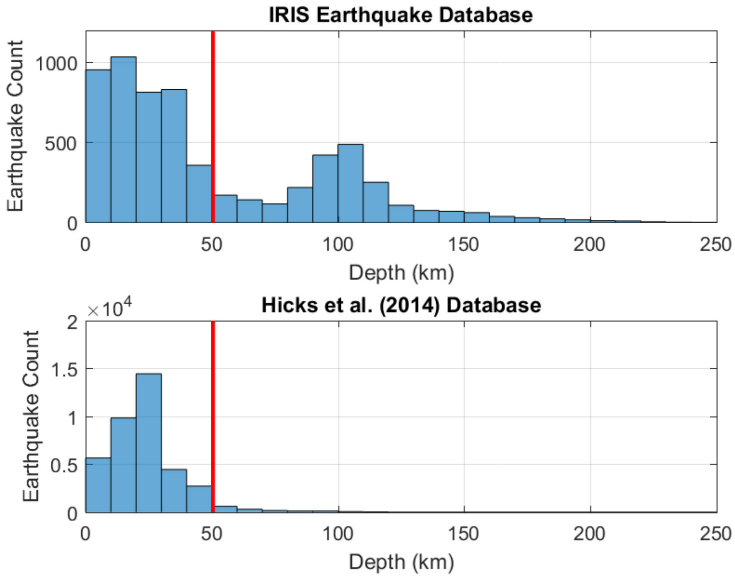

Figure 7.16: Histogram of earthquake epicenters used when plotting the model profiles. The top panel shows histograms from the IRIS (2018) dataset while the bottom panel shows epicenters from the dataset of Hicks et al. (2014). Earthquakes >50 km depth (right of the red line) are excluded when plotting the Hicks et al. (2014) dataset while earthquakes <50 km depth (left of the red line) are excluded when plotting the IRIS (2018) dataset.

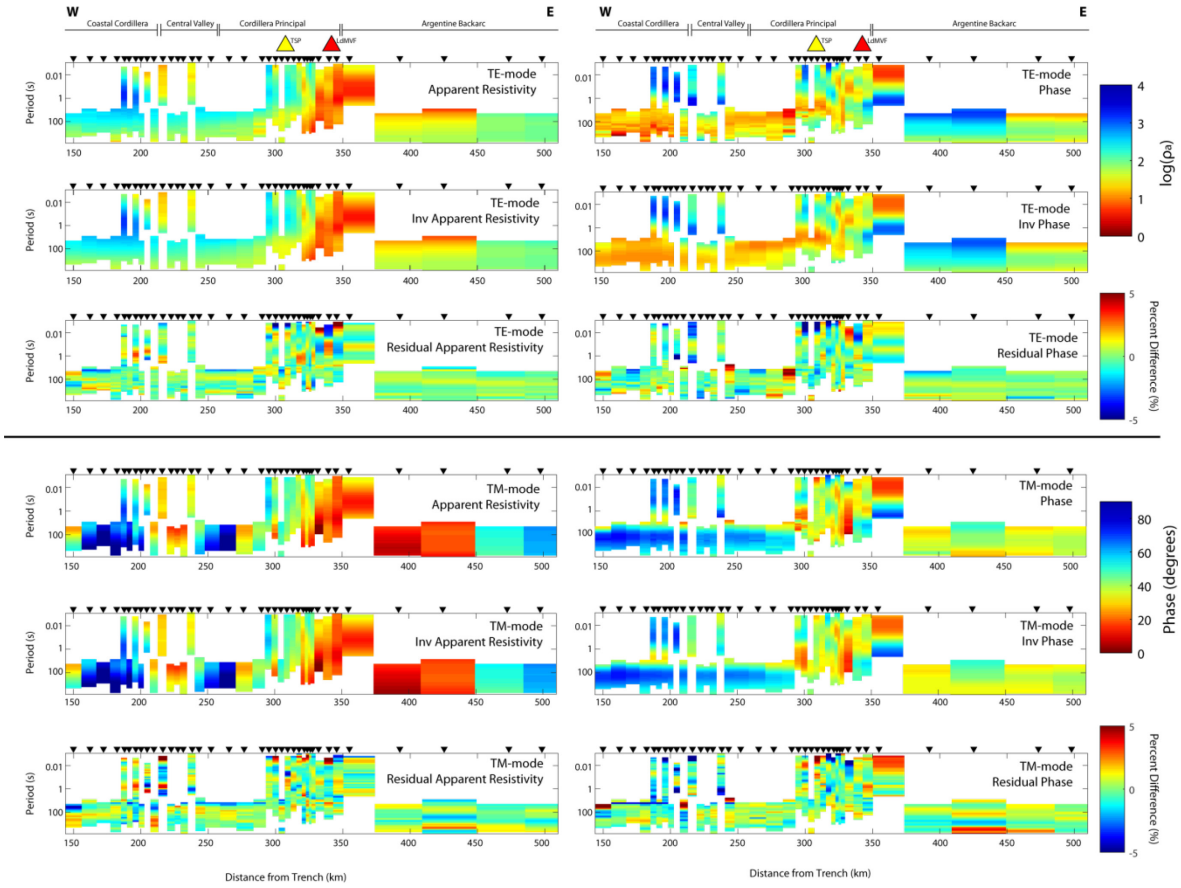

Figure 7.17: Pseudo-section plots for observed data and inverted data response for TE and TM mode apparent resistivity and phase. Residual pseudo-section plots are also shown.

The constrained inversion has root mean square data misfit value after 200 iterations of 1.51. Figure 7.15b shows the r.m.s. misfit for each station as well as the static shift parameters for the constrained case. The r.m.s. misfit plot indicates higher misfit near the volcanic arc as expected due to scattered geoelectric strike directions observed in that area. Pseudo-sections of the data, the inversion response, and the percent difference between the two are shown in Figure 7.17 and the inversion data fit is shown for sites CLP016, P08, CLP008, and LDM029 in Figure 7.6. Because the inversion uses an irregular combination of both LMT and BBMT sites, it is important to be aware of the relative sensitivity of the model. A relative sensitivity map is shown in Figure 7.18. The sensitivity can be defined as the diagonal of the matrix

$$\mathbf{S} = \mathbf{J}^{\mathrm{H}}\mathbf{C}_{\mathbf{d}}^{-1}\mathbf{J} \tag{7.3}$$

where $\mathbf{J}$ is the Jacobian, $\mathbf{C_d}$ is the data covariance and the subscript H denotes the Hermitian transpose (Mackie and Madden, 1993; Rodi and Mackie, 2001). The diagonal can then be reshaped into the same size matrix as the model giving a relative sensitivity value for each model cell. This sensitivity matrix gives an indication of which features may be relatively more robust and which features may be poorly resolved. In general, resolution is good above 100 km although, due to the lack of long period sites near the volcanic arc and overlying conductors, resolution is poorer at depth beneath the volcanic arc. Finally, all the models from Section 7.5 are averaged in Figure 7.19 and both the mean resistivity and standard deviation of each model cell is shown in logarithmic space. This gives a sense of the overall ensemble model resistivity and areas with high standard deviation represent areas with less sensitivity or confidence in those features. A summary of all the models is given in Table 7.1.

7.6 INTERPRETATION OF THE PREFERRED RESISTIVITY MODEL

There are 10 primary conductive features present in the preferred inversion model and three significant resistive features, all of which were investigated using sensitivity tests. The features are labelled on Figure 7.15 as follows: S1, C1, C2, C3, C4, C5, C6, C7, C8, R1, R2, R3 and A1. Each feature will be interpreted below and grouped based on the geology.

7.6.1 Interpretation of Near-Surface Features West of the Cordillera Principal

At the surface, a conductor (S1) coincides with the volcaniclastic sedimentary fill of the Central Valley west of the Cordillera Principal (Reyes-Wagner et al., 2017). Further west, adjacent to the Central Valley, is R2, which is a very strong resistor (>10,000 Ωm) likely related to the Paleozoic accretionary metamorphic complexes of the Coastal Cordillera (Hervé et al., 2013). R2 likely has few fluid pathways to conduct current and instead consists of dry, unfractured rock. To the west of R2 is C1, which is a surface conductor (<10 Ωm) located at shallow depth (<15 km) beneath the trench and ocean. This conductor is poorly resolved with the current MT dataset and would require offshore MT data to improve the resolution of this feature (Evans et al., 2002). The difference in shape and resistivity of this feature in the constrained and unconstrained inversions highlights this insensitivity. However, a strong conductor in the accretionary wedge is expected and would likely be due to early dehydration as pore-bound fluids are expelled from the down-going slab at shallow depths via compaction and lithification (Hyndman et al., 1997). Additionally, conductivity could be enhanced by a preponderance of clay-rich minerals (e.g. smectite) which provide additional pathways for electrical current to flow along the surface of mineral grains (Hyndman et al., 1997; Pommier and Evans, 2017).

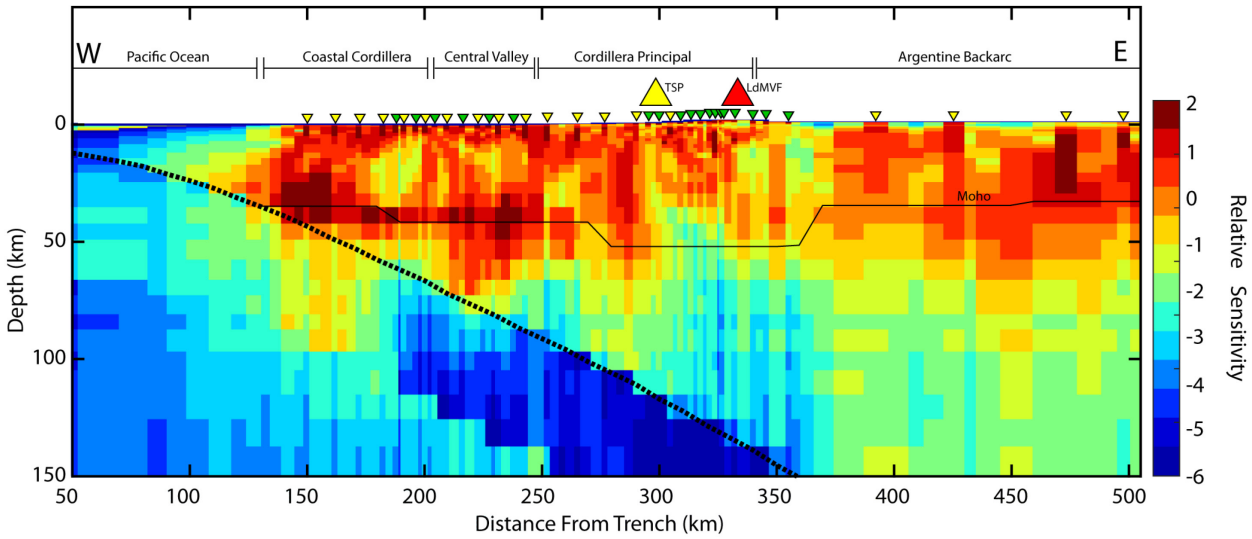

Figure 7.18: Sensitivity map for the preferred inversion model shown in Figure 7.15. The relative sensitivity is unitless and plotted on a logarithmic scale.

7.6.2 Interpretation of the Forearc Slab Surface Structure

On the edge of the MT profile at 150 km east of the trench a resistor (R1) is located at 25 km depth. East of R1, between 150 km and 200 km east of the trench, a weaker conductor (C2; 30 to 50 Ωm) is located at 25 to 30 km depth beneath the highly resistive Coastal Cordillera (R2). The depth to C2 is consistent in both the constrained and unconstrained inversion and is notably more than 15 km above the slab interface and is in a similar location as anomalies found in MT studies in southern Chile (Brasse et al., 2009). C2 also spreads out laterally eastward, extending parallel to the Moho. This conductor is likely the result of fluids released from prograde metamorphism of clay-rich oceanic upper crustal sediments as they transition to the blueschist facies (Hensen et al., 2004; Peacock, 1990; Völker and Stipp, 2015). The fact that this conductor is located approximately 10 kilometers above the slab interface may suggest that this region is more permeable and/or faulted which allows dehydrating fluids to migrate upwards into the over-riding crust before being trapped beneath the less permeable Paleozoic block (R2). It also important to note that the slab itself is approximately an order of magnitude more conductive (C8) directly beneath C2 and C8 correlates with the transition from inter-plate to intra-slab seismicity. This feature is also more pronounced in the unconstrained inversion (Figure 7.11) and becomes even more prominent at low τ values (Figure 7.12).

Table 7.1: A summary of the different models tested and shown in this chapter. These models were used to construct the mean and standard deviation model shown in Figure 7.19.

Model	Static Shifts	Starting Model	Slab Constraint	τ	Data Set	r.m.s. Misfit
1	No	100 Ωm	No	2	Full	3.39
2	Yes	100 Ωm	No	2	Full	1.55
3	Yes	10 Ωm	No	2	Full	1.58
4	Yes	1000 Ωm	No	2	Full	1.57
5	Yes	10000 Ωm	No	2	Full	1.79
6	Yes	100 Ωm	Yes	2	Full	1.53
7	Yes	100 Ωm	Yes	0.1	Full	1.28
8	Yes	100 Ωm	Yes	0.3	Full	1.31
9	Yes	100 Ωm	Yes	0.5	Full	1.34
10	Yes	100 Ωm	Yes	1	Full	1.42
11	Yes	100 Ωm	Yes	3	Full	1.56
12	Yes	100 Ωm	Yes	5	Full	1.68
13	Yes	100 Ωm	Yes	10	Full	1.85
14	Yes	100 Ωm	Yes	30	Full	2.33
15	Yes	100 Ωm	Yes	2	Low Skew Only	1.55
16	Yes	100 Ωm	Yes	2	Long Periods Only	1.09
17	Yes	Model 16	Yes	2	Full	1.51

7.6.3 Interpretation of Mantle Wedge Structure

Continuing down the slab interface, east of C2 is the beginning of the mantle wedge. A resistive block (R3, >1000 Ωm) at approximately 60 km depth and 225 km from the trench represents part of the mantle wedge with a low fluid content and suggests that there are minimal dehydration reactions occurring along the slab at this location. At 250 km from the trench and at 40 km depth, is a prominent conductor (C3, <10 Ωm) which straddles the continental Moho. This conductor is located approximately 30 to 40 km west of the modern volcanic arc. When the slab constraint is imposed (Figure 7.15), the area at the slab interface beneath C3 is an order of magnitude more conductive than R3. When the slab

constraint is not included (Figure 7.11), C3 is weaker and smoothed eastward and appears connected to other conductors beneath the volcanic arc. The two inversions neither confirm nor refute the idea that there is a geological connection and a denser data array is needed in this area to provide greater constraint on the model. This conductor likely signifies an important dehydration event at a depth of approximately 80 to 90 km along the slab interface related to the breakdown of amphibole and the transition to the eclogite facies which releases fluids into the overlying mantle (Hacker, 2008; Poli and Schmidt, 1995; van Keken et al., 2011). This assumes vertical fluid transport although, depending on the properties of the mantle, it is possible that C3 is a result of fluid focussing from fluids derived from a wide range of depths (Wada and Behn, 2015; Wilson et al., 2014).

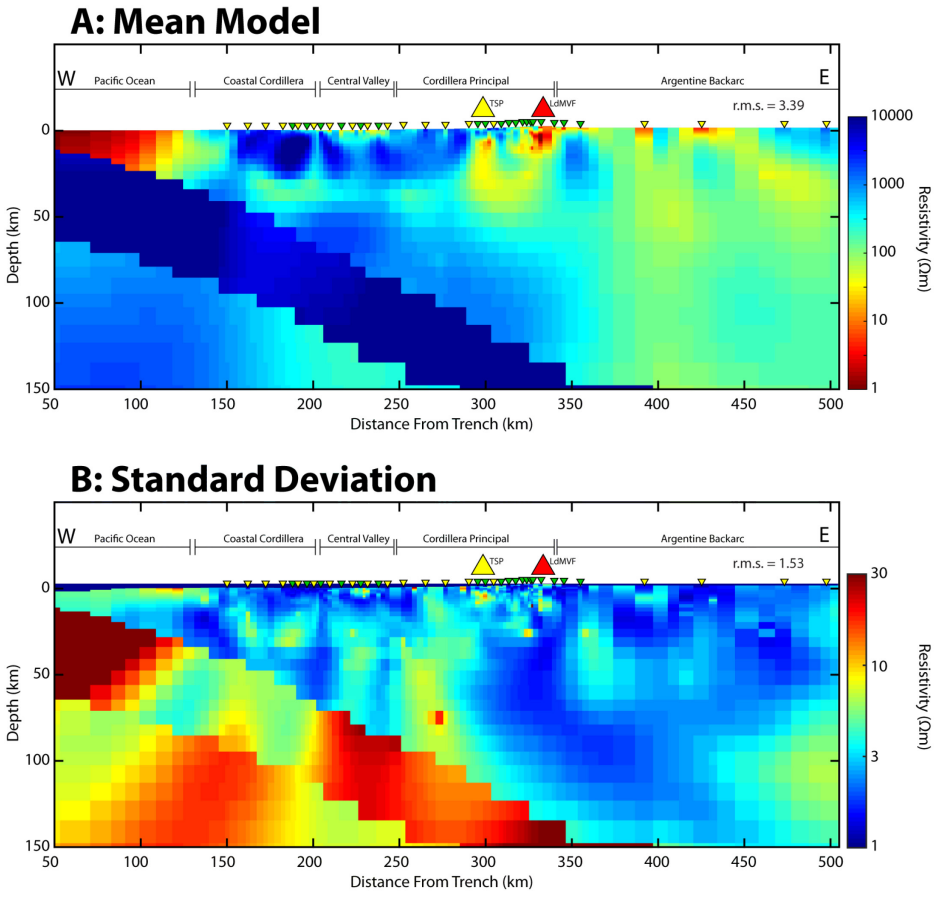

Figure 7.19: The mean (a) and standard deviation (b) of all the 16 models shown in this chapter. Statistical analysis was performed on the logarithm of the resistivity and both plots are shown with a logarithmic colorbar.

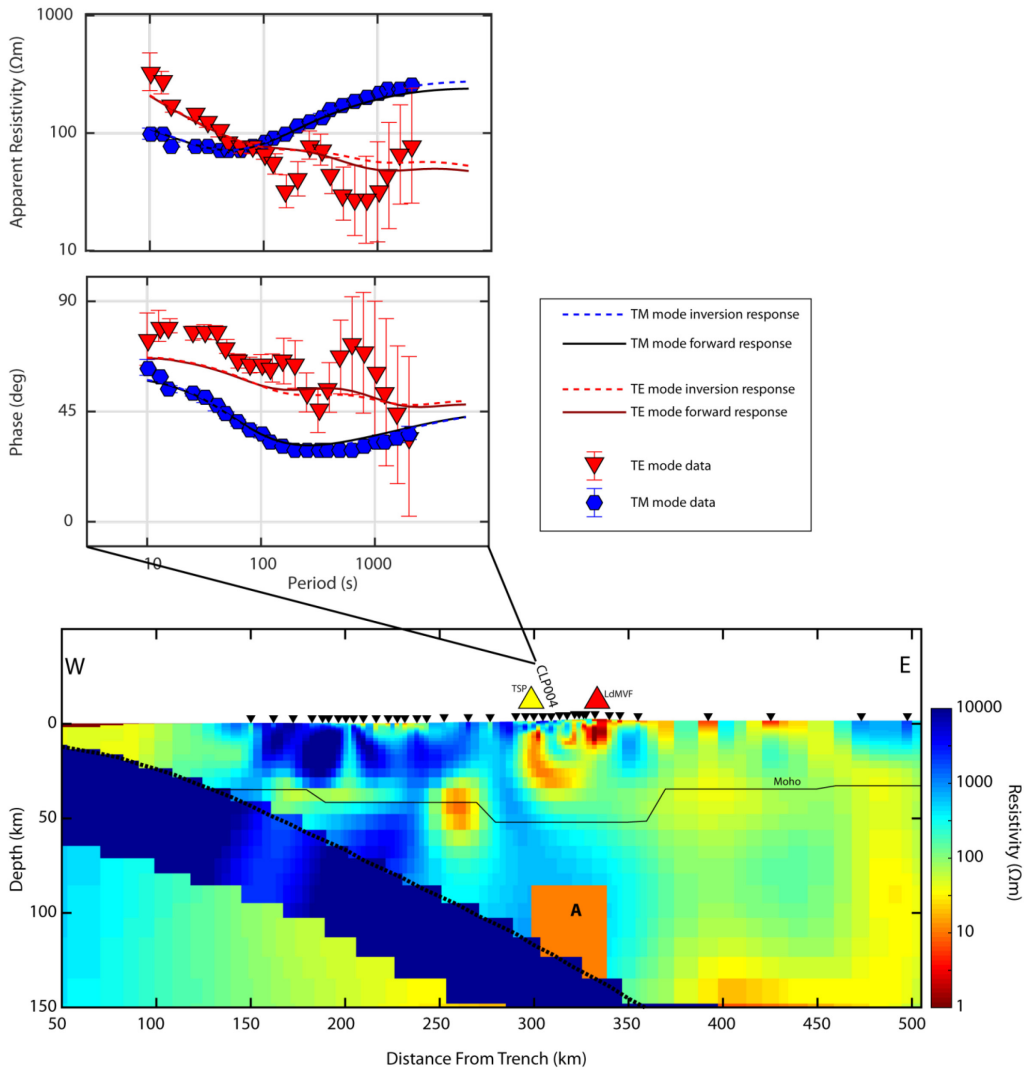

Figure 7.20: A sensitivity test to examine the ability for the current MT profile to image conductive slab fluids beneath the volcanic arc. The bottom panel shows the same model as Figure 7.15 but with an added 10 Ωm conductor (A) between 90 and 120 km depth directly beneath the volcanic arc. This conductor is similar in size and resistivity to the shallower C3 feature west of the arc. After computing the forward MT response of this edited model, the root mean square misfit increased from 1.51 in the original inversion to 1.53 in the edited model. Apparent resistivity and phase data are shown for LMT site CLP004 which is located on the modern volcanic arc, directly overlying Conductor A. CLP004 had the maximum increase in r.m.s. misfit from 1.47 in the original inversion to 1.65 when conductor A is added.

A mantle wedge conductor similar to C3 has been imaged at similar depths in subduction zones around the world (see Worzewski et al., 2011 and references therein). However, in the sample of models from Worzewski et al. (2011), the anomaly in south Chile from Brasse et al. (2009) is a notable outlier, being >60 km west of the volcanic arc. As seen in Figure 7.15, C3 is only 40 km west of the volcanic arc which is

more in line with the global average. This suggests some significant along strike variation in mantle wedge structure between south Chile and central Chile which may be linked to the thermal structure of the down-going slab. The Nazca plate in south Chile is younger and hotter which may lead to basalt-eclogite dehydration at shallower depths than central Chile. This is supported by numerical modelling by Völker and Stipp (2015) who showed that a significant dehydration event occurs approximately 50 km west of the volcanic arc for the Maule region but occurs further west when the Nazca plate is younger (i.e. in south Chile). This is also supported by earlier numerical work showing that intermediate temperature slabs release more water earlier (i.e. shallower) than low temperature slabs (e.g. Kerrick and Connolly, 2001). Forearc fluids trapped in the lower crust and upper mantle (C2 and C3) may account for some of the missing fluids which are not accounted for when calculating volcanic H_2O output and deep slab water sequestration (Worzewski et al., 2011).

7.6.4 Interpretation of the Volcanic Arc Structure

Directly beneath the volcanic arc, there are three crustal conductors present. A large conductor (C4) directly beneath TSP at shallow depth (<10 km) likely represents a zone of partial melt associated with this recently active system and responsible for heat and hydrothermal fluids as identified by recent geothermal exploration projects (Hickson et al., 2011). To the east, beneath the back-arc LdMVF, a large conductor (C5) stretches over a large region 325 km to 350 km east of the trench at shallow depth (<10 km). This likely represents a poorly-resolved portion of the highly three-dimensional LdMVF magmatic system as detailed by Cordell et al. (2018). Below both TSP and the LdMVF, there is a large conductor (C6) at intermediate depths of 25 to 40 km. This is likely a lower-crustal MASH zone (Hildreth and Moorbath, 1988) where mafic melts rising due to buoyancy from the subducting slab stall at the crust-mantle density boundary. Here, melts differentiate and assimilate crustal components and become more felsic before rising further into the crust as more andesitic-to-silicic melts (Ducea et al., 2015). The location of C6 appears to be above the Moho which may be due to limited resolution in the lower crust beneath C4 and C5 in the MT model (see Figure 7.18), or the coarse resolution of the global model of the Moho boundary. However it could have a geological explanation if the lower crust is unusually dense (e.g. granulite facies). It appears that C6 could be a lower crustal zone which feeds melts to both TSP and the LdMVF from a common source. Petrological analyses at both complexes show similar isotopic compositions and both suggest lower crustal assimilation (Andersen et al., 2017; Davidson et al., 1987). Deep connections between volcanoes have also been seen elsewhere (e.g. Bato et al., 2018; Biggs et al., 2016; Brothelande et al., 2018; McGary et al., 2014). In the unconstrained inversion (Figure 7.11),

another conductor (C9) is also present to the east of LdMVF at shallow depth (<15 km), however this feature is rarely present in other inversions and seems to be an artefact of the LMT inversion which struggles to resolve shallow structure.

7.6.5 Interpretation of the Back-Arc and Asthenosphere

The final deep features in the model are the conductive backarc, specifically a deep conductor at >130 km depth (C7), and the conductive sub-slab asthenosphere (A1). Due to the sparse MT station spacing in Argentina, any conductive anomalies in the backarc are poorly resolved and on the edge of the profile. However, it is clear that the entire backarc is quite conductive which is in agreement with the three-dimensional MT analysis of the Payún Matrú complex and surrounding area made by Burd et al. (2014) in which they identified the Shallow Western Asthenospheric Plume (SWAP) approximately 100 km east of the LdMVF. C7 may be a poorly-resolved 2D version of the 3D SWAP feature and may be due to fluid and partial melting related to de-serpentinization of the slab and high temperatures at depth (Völker and Stipp, 2015). Numerical modelling by Völker and Stipp (2015) suggest that a large amount of down-going fluids (e.g. >80%) remains in the subducting slab into the backarc in the Maule region. This value is greater than in southern Chile and significantly greater than in other younger subduction zones such as Cascadia (van Keken et al., 2011). This could explain why the backarc conductor, C7, is so much larger than the forearc conductors and farther east than similar conductors in Cascadia (e.g. Wannamaker et al., 2014). The Nazca sub-slab asthenosphere (A1) is only present when the slab is imposed but, with a value between 10 and 100 Ωm, can be explained by a small amount of partial melt and/or hydrated mantle (Worzewski et al., 2011).

7.6.6 Summary of Interpretation

An important conclusion from the inversion model is that the slab interface beneath the MT profile is not characterized by a continuous conductive zone along the interface, but instead shows a sequence of resistive and conductive features as the slab descends from the surface to a depth of 150 km (Figure 7.15a) (C1, R1, C2, R3, C3, C7). This sequence of conductors suggests discrete locations and depths where fluids are released in large quantities and are able to accumulate in the overlying crust and mantle. This stepwise continuous dehydration has been supported by numerical studies (e.g. Schmidt and Poli, 1998; van Keken et al., 2011) and is in contrast to single phase dehydration models in which dehydration occurs at a single depth. This segmentation of conductors has also been reported in other

MT images of subduction zones (e.g. Jödicke et al., 2006; Soyer and Unsworth, 2006; Wannamaker et al., 2014).

It is also interesting to note that no deep conductive features are imaged on the slab interface or in the mantle wedge directly beneath the volcanic arc. This may partly be due to model resolution as (a) only a few long period MT stations were collected near the LdMVF and (b) the overlying conductors (C4, C5, and C6) will attenuate EM signals and limit model resolution at depth. For example, a conductor of similar size and resistivity as C3 could exist at the slab interface beneath the volcanic arc and would not be detected with the current MT profile (Figure 7.20). However, fluid release prior to the amphibole stability (i.e. <75 km) is generally much greater in volume than at pressures higher than amphibole stability (e.g. >75 km) and thus high conductivity fluids may be less prevalent at the slab interface 300 km east of the trench (Schmidt and Poli, 1998; van Keken et al., 2011). Furthermore, the conductive backarc (C7) as shown in Figure 7.15 and by Burd et al. (2014) suggests the possibility that partial melting and de-serpentinization occurs deeper and further east than younger subduction to the south.

7.7 INCORPORATING SEISMIC TOMOGRAPHY AND SEISMICITY

7.7.1 Correlations with Previous Seismic Tomography Studies

In previous 3-D seismic tomography studies, Hicks et al. (2014, 2012) imaged an undulating high velocity structure along the plate interface at distances between 100 km and 200 km east of the trench (Features CA and CM in Figure 7.21). This structure is similar to the sequence of conductors and resistors imaged in the forearc of the constrained MT model (Figure 7.15). A comparison between the MT model and seismic model is shown in Figure 7.22. Following the joint interpretation methods of Bedrosian et al. (2007), a slice was taken through the seismic velocity tomography model of Hicks et al. (2014) at the same location as the 2-D MT profile. Both the MT model and seismic model were interpolated onto the coarser seismic tomography grid with 10 km by 2.5 km cells to allow for direct comparison (Figure 7.22a, b). Note that the seismic model does not extend as far east and as deep as the MT model, so some of the structures near the LdMVF and the Argentine backarc were excluded from this analysis. The comparison also excludes the upper 5 km because the MT model included topography while the seismic model did not and because the BBMT model samples relatively small, heterogeneous structures in the near surface while the seismic velocity model is poorly constrained in the near-surface due to a lack of very shallow sources. A correlation histogram is shown for the shared model space (Figure 7.22d). The

shared model space has a positive Pearson correlation coefficient of 0.32 indicating a weak linear correlation where higher velocities correlate with higher resistivities. This is expected since cold, dry rocks have high velocities and high resistivities while warm, fluid-rich rocks have low velocities and low resistivities.

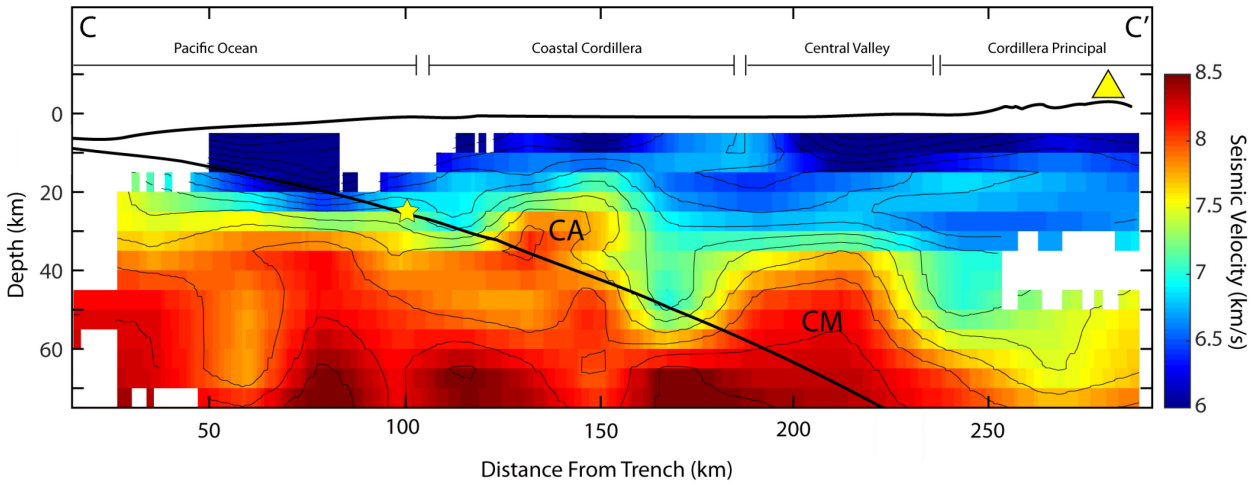

Figure 7.21: The P-wave velocity seismic tomography model of Hicks et al. (2014) along profile C-C′ approximately 75 km south of the current MT profile (see Figure 7.1). The yellow star denotes the location of the 2010 Maule earthquake. Note that the colorbar is flipped from the original figure such that low velocity is blue and high velocity is red. This is done to allow direct color comparison between the MT and seismic models. CA = Cobquecura anomaly. CM = Continental mantle. The yellow triangle denotes the volcanic arc.

The correlations are broadly grouped into four zones: (1) low velocity and low resistivity, (2) high velocity and high resistivity, (3) low velocity and high resistivity, and; (4) high velocity and low resistivity (Figure 7.22c). A high resistivity is defined as any model cell greater than 100 Ωm (i.e. resistive deviations from the starting halfspace) and similarly low resistivity was assigned to any model cell less than 100 Ωm (i.e. conductive deviations from the starting halfspace). A low velocity is defined as any model cell with less than 7 km/s and high velocity is any model cell with greater than 7 km/s using the terminology of Hicks et al. (2014). The conductors C1 and C2 both are in Zone 1 indicating both low seismic velocity and resistivity, which can be interpreted as a region of fluids. A low V_p (<5.5 km/s) and high V_p/V_s ratio (>1.8) has been identified in the same area as C1 giving additional evidence for a high fluid content due to over-pressured sediments at shallow depth near the trench (Hicks et al., 2014). Despite the fact that C1 is on the edge of the MT profile, the good correlation between the seismic and MT models at this location suggests that it may be a real structure linked to expulsion of fluids from pore

spaces. The conductor C2 also correlates with a low-velocity zone from Hicks et al. (2014). They did not specifically interpret this low-velocity zone but, with the addition of MT, it seems that this low V_p and high V_p/V_s ratio zone may correspond to dehydration-related fluids and/or a serpentinized mantle. This zone is also associated with high afterslip following the Maule 2010 earthquake as evidenced by a cluster of aftershocks (Rietbrock et al., 2012), and large aseismic afterslip (Lin et al., 2013) which also indicates fluid-driven processes. Farther east, towards the edge of the seismic model, Zone 1 also correlates with the top of the C3 conductor just west of the volcanic arc. Unfortunately, the seismic model does not extend east to the LdMVF or backarc to provide additional constraints to the structures along the volcanic arc. C4 is on the edge of the tomography model and does lie in Zone 1 but it is not necessarily evidence of a seismic anomaly related to the LdMVF volcanic system. More recent work using ambient noise tomography indicates there is a low V_s anomaly beneath the LdMVF between 3 and 8 km depth (Wespestad et al., 2019; see Chapter 6).

The resistive down-going slab correlates with Zone 2 indicating relatively dry, cold and impermeable mafics and ultramafics. The shallow structure (i.e. <20 km depth) east of the Pacific Ocean is within Zone 3 and is broadly low velocity and simultaneously higher resistivity (e.g. R2). This may be due to smearing in the tomography model as the frequency bandwidth for tomography studies does not allow for detailed study of near-surface structures. The resistor R1 coincides with the high velocity Cobquecura anomaly (*CA*) which was initially interpreted as an ancient seamount on the subducting slab (Hicks et al., 2012) and was also noted as a density high in the gravity survey of Maksymowicz et al. (2015). Further geological interpretation and additional seismic data suggests that it is more likely to be a dense block of peridotite above the modern slab which fed Triassic intrusions into the Coastal Cordillera when it was an ancient volcanic arc (Hicks et al., 2014). The interpretation of this feature as a cold block of unaltered and relatively impermeable peridotite is supported by the MT model which shows a resistor (R1) in that location. The center of the Cobquecura anomaly in the 3-D seismic tomography model is approximately 75 km south of the MT profile and thus the resistivity model may only be imaging the northern edge of this resistive block. The resistor R3 aligns with feature *CM* in Hicks et al. (2014) and is likely the eastward limit of the non-convecting mantle wedge.

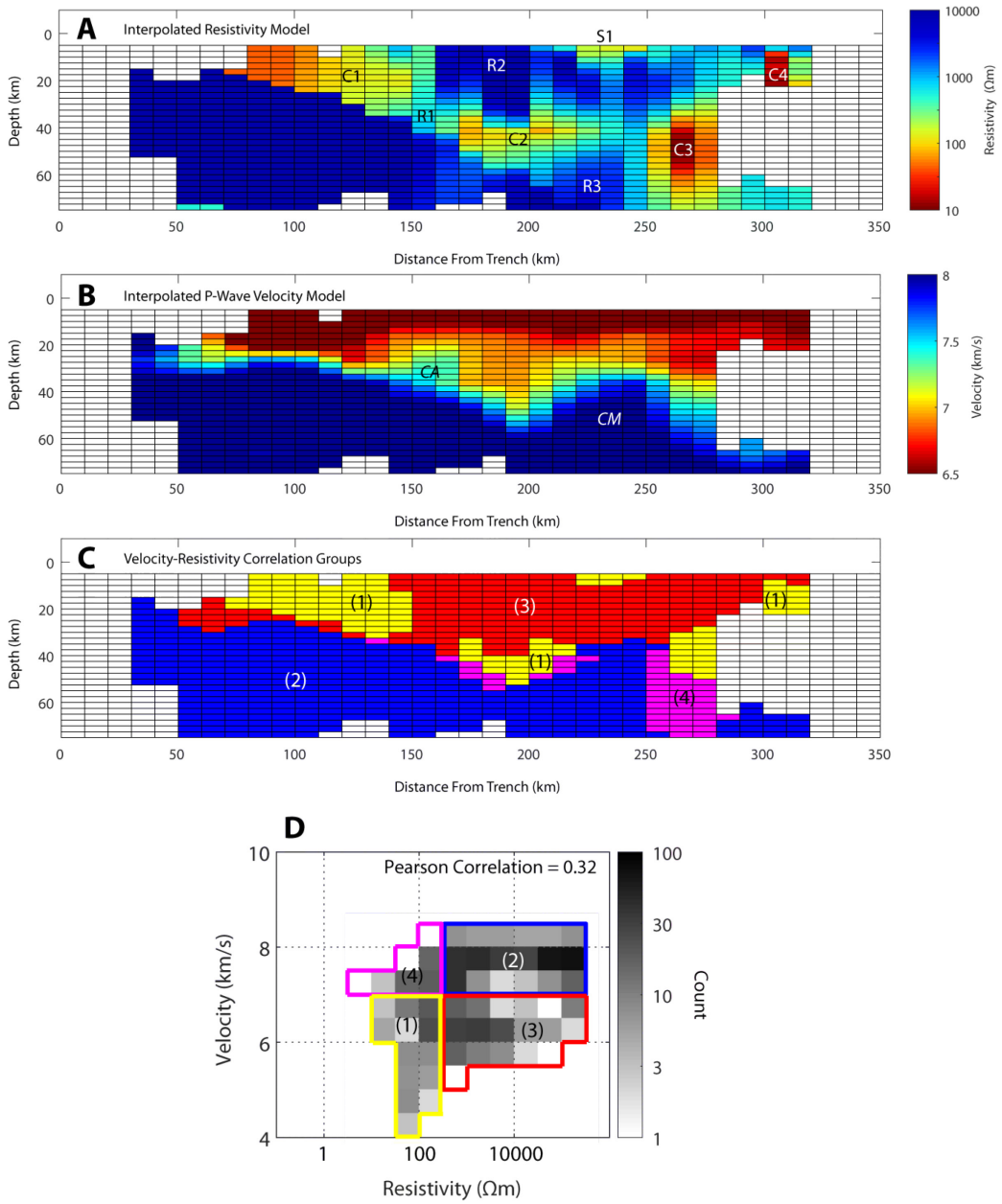

Figure 7.22: A comparison between the 3-D seismic tomography model of Hicks et al. (2014) (see Figure 7.21) and the constrained MT model (see Figure 7.15). Both models have been interpolated onto a common mesh. (a) The MT model showing resistivity along the profile as a function of depth with labels matching the features shown in Figure 7.15. (b) A 2-D slice through the 3-D seismic model of Hicks et al. (2014) along the same profile as the MT model. Red denotes low velocity while blue denotes high velocity. This is the opposite color scale as shown in Hicks et al. (2014) but it is done to allow direct color comparison between the MT and seismic models. Labels denote CA (Cobquecura Anomaly) and CM (Continental Mantle). (c) The shared model space mapped into 4 categories of velocity and resistivity correlations. (d) A correlation histogram showing the number of model cells which share each velocity-resistivity pair.

Zone 4 shows high velocities and low resistivities and correlates with the base of conductor C3. This is somewhat surprising since the depth aligns with the expected release of large volumes of fluid as down-going rocks transition to the eclogite facies and as such one would expect a low velocity structure. This anomalous correlation is most likely explained by the fact that it is on the edge of the seismic tomography model where there is limited resolution to the east at depth. However, a geological explanation is also possible since the basalt-eclogite transition is accompanied by an increase in velocity in the down-going slab due to an increase in density (Pommier and Evans, 2017).

7.7.2 Correlations with Observed Seismicity

The seismicity of the region can be grouped broadly into two primary clusters. The first cluster is a group of shallow focus earthquakes at depths less than 25 km and west of the Chilean coast (Figure 7.15). This seismogenic zone is prone to brittle fracture and stress accumulation which leads to large megathrust earthquakes such as the 2010 Maule earthquake (Hicks et al., 2012; Moscoso et al., 2011). This cluster overlaps with C1 which is interpreted as early fluid release. Moreno et al. (2014) showed that regions of high fluid content are associated with higher pore pressure which leads to aseismic slip behavior. A more complete 3-D MT survey with offshore sites would be needed to see if there is any 3-D heterogeneity to the structure of C1 as was found in New Zealand (Heise et al., 2017).

The second cluster of earthquakes is at intermediate depths of 75 km to 100 km depth approximately 200 to 250 km east of the trench (Figure 7.15). This second cluster is located almost entirely within the resistive down-going slab and underlies both R3 and C3. These intraslab earthquakes are likely driven by dehydration embrittlement as fluids are released (Hacker et al., 2003). The fact that no conductor is imaged at the same location as these intra-slab earthquakes suggests that the fluids in the slab occupy relatively small, disconnected pore spaces that go undetected by the MT data. Fluid focusing effects may play a role in collecting these fluids into a connected zone which is imaged as the forearc mantle wedge conductor (C3).

Between these two clusters of earthquakes are some additional correlations. The resistor R1 has almost no seismicity associated with it. This further suggests that R1 is an anomalous hard, strong asperity on the plate interface which defines the down-dip limit of rupture of large earthquakes (Hicks et al., 2014). There is a small cluster of earthquakes associated with C2 directly above C8 (Figure 7.15). The seismicity in this cluster occurred following the 2010 Maule earthquake (i.e. post-seismic rather than co-seismic)

and, prior to that, there was relatively little seismicity here in the interseismic period (Lin et al., 2013). This suggests that most stress is accommodated via aseismic slip. Fluids released from the slab (C2 and C8) may lead to serpentinization of the forearc mantle which is associated with stable-sliding and often defines the down-dip limit of the seismogenic zone (Hyndman et al., 1997). This is further supported by a relatively high V_p/V_s ratio in this region (Hicks et al., 2014). The fact that some earthquakes did occur in C2 following the 2010 Maule earthquake suggests that fluid-driven diffusion stress processes may be important here and that this region may be a transitional zone of conditional stability that becomes unstable during transient high strain events (Lay et al., 2012). Dehydration at C2 and C8 may also induce small earthquakes (<2.5 magnitude) which are not detected in the earthquake databsase of Hicks et al. (2014). The MT results suggest that fluid release and serpentinization of the forearc mantle may be an important control on aseismic zones, whereas relatively fluid-poor regions (e.g. R1) result in increased frictional plate-locking and more stick-slip behavior.

7.8 SUMMARY

The resistivity model presented in this paper allows us to investigate a range of subduction processes operating at different locations and at different spatial scales in the central Chilean subduction zone. The MT model is interpreted as revealing a comprehensive fluid and dehydration cycle from the forearc to the backarc including significant pore-fluid expulsion (C1), blueschist facies dehydration and basalt-eclogite dehydration (C2 and C3), and de-serpentinization at depth (C7). This suggests that fluid release does not necessarily occur at one step but occurs in a punctuated step-wise continuous fashion at different depths during important mineral transitions as suggested by the numerical modelling of subduction zones (Schmidt and Poli, 1998; van Keken et al., 2011; Völker and Stipp, 2015). The position of the wedge conductor (C3) is similar to that found by other MT studies of subduction zones worldwide but is deeper and nearer to the volcanic arc than the conductor identified in south Chile by Brasse et al. (2009). This highlights the effect of along strike variations in the thermal regime, fluid release, slab structure and permeability as the Nazca plate is younger and hotter further south which means the transition to eclogite may occur at a shallower depth (Völker and Stipp, 2015).

The volcanic arc beneath central Chile contains several important upper crustal (C4 and C5) and lower crustal (C6) conductors, likely representing local regions of melt accumulation. The conductor geometry raises the possibility that the arc volcanoes (e.g. TSP) and the back-arc LdMVF share a common lower crustal zone of melt accumulation (C6) which may explain their similar isotopic signatures. As shown by

Cordell et al. (2018), the electrical structure around the LdMVF is highly 3D and, as such, conductor C5 is likely a 2D approximation of the complex 3D structure which is not well imaged due to the coarser mesh used in this regional study.

As seen in other MT studies (see Pommier and Evans, 2017) the addition of the slab constraint in the MT model helps to image important structures on the plate interface and results in a resistivity model which better aligns with previous seismic tomography studies and numerical studies. The resistive anomaly R1 coincides with a velocity high which supports the interpretation of Hicks et al. (2014) that this region of the subduction zone has significant strong asperities of dense peridotite or ancient seamounts. These asperities may encourage plate locking and may help explain why large megathrust earthquakes, such as the 2010 Maule earthquake, initiate at this latitude as stresses concentrate at a strong structural contrast. The relatively aseismic zone between 40 km and 60 km depth is likely related to slab dehydration (C2, C8) and serpentinization of the forearc mantle which leads to stable-sliding and may be conditionally stable. Intermediate-depth earthquakes down-dip of the aseismic zone do not appear to be correlated with any conductor which suggests that fluids associated with dehydration embrittlement are relatively isolated and cannot be imaged with MT. However, fluids released at depth migrate upwards and become focused into a connected zone in the forearc mantle (C3).

Induction vectors suggest a potentially anisotropic lower crust, similar to observations in southern Chile (Brasse et al., 2009). This highlights the need for future anisotropic inversions of this region as they would further elucidate the effects of anisotropy in this region of Chile. The generally three-dimensional data also highlights the need for a more comprehensive, 3D MT array in this area of central Chile. An extension of the array to the south would be able to better image the Cobquecura anomaly while extension to the north would image the transition to the Pampean flat slab. Such an array would likely give even greater insight into along-arc variation in Chilean subduction zone structure.

CHAPTER 8: CONCLUSION

8.1 SUMMARY OF THESIS

This thesis describes two investigations of the subsurface electrical resistivity structure of central Chile. The primary target of interest—and the motivating factor for this thesis—was the Laguna del Maule Volcanic Field (LdMVF) which has been showing signs of significant unrest since 2007. The first investigation dealt explicitly with the LdMVF by using a local grid of broadband MT measurements that were inverted to produce a 3-D electrical resistivity model of the subsurface from the surface to a depth of 15 km. This 3-D model gave significant insights into the magmatic and hydrothermal plumbing system beneath this volcano. The second investigation sought to place the LdMVF within its regional context by imaging the electrical resistivity structure of the subduction zone from the surface to the asthenosphere along an east-west profile in central Chile from the Pacific Ocean to the backarc of western Argentina. This not only mapped important fluid and melt pathways in the mantle wedge and lower crust, but also gave important insights into the interplay of fluids and seismicity in the seismogenic zone in the vicinity of the 2010 Maule earthquake. Each of the two investigations is summarized in the following two sections.

8.1.1 Magnetotelluric Study at the Laguna del Maule Volcanic Field

The Laguna del Maule Volcanic Field in central Chile has been experiencing upward ground deformation of approximately 20 cm/year over a 400 km^2 area since 2007, and notable seismic swarms have occurred along the Troncoso fault to the southwest of the LdMVF since at least 2011 (Cardona et al., 2018; Feigl et al., 2014; Le Mével et al., 2016, 2015). The LdMVF has a record of voluminous rhyolite eruptions over the last 25 ka (Andersen et al., 2019, 2018, 2017) and significant deformation as evidenced by paleo-shoreline tilt data (Singer et al., 2018). The most recent eruption was 2 ka and the region has been active since a large caldera-forming eruption occurred at 950 ka. The combination of current unrest and past eruptions suggest that the LdMVF may be moving toward another eruptive phase with active magma intrusion. This provides a rare example of being able to study an active, but non-erupting, rhyolitic system.

The majority of knowledge about the LdMVF prior to 2014 was summarized by Hildreth et al. (2010) and included field mapping and dating of mapped lava flows. Inflation was first noticed by Fournier et al. (2010) and later investigated more thoroughly by Feigl et al. (2014). After 2014, the observed ground deformation necessitated a more detailed study of the LdMVF using the latest geological, petrological, and geophysical methods. The NSF-funded Rhyolite Magma Dynamics project (Singer et al., 2014) lead to a large number of publications on the LdMVF including further mapping and dating (Andersen et al., 2017; Birsic, 2015; Fierstein et al., 2016, 2013; Sruoga et al., 2015), detailed petrochronological analysis and modelling (Andersen et al., 2019, 2018), deformation modelling and mapping (Le Mével et al., 2016, 2015; Pritchard et al., 2013; Singer et al., 2018), structural mapping and modelling (Garibaldi et al., 2020; Zhan et al., 2019), crustal seismicity observations (Cardona et al., 2018), magnetotellurics data collection (Cordell et al., 2019, 2018; Reyes-Wagner et al., 2017), Bouguer gravity data collection (Miller et al., 2017b), time-lapse microgravity data collection (Miller et al., 2017a), seismic tomography modelling (Wespestad et al., 2019), reflection seismic data collection (Peterson et al., 2018), and media attention (e.g. De la Jara and O'Brien, 2016; Hall, 2018).

The MT method is an electromagnetic geophysical technique which measures horizontal electric and magnetic fields at the surface to determine the complex impedance tensor at the surface of the Earth. The impedance tensor is dependent on the inductive effects of electrically conductive and resistive structures within the Earth. The depth at which the impedance tensor is sensitive depends on the frequency of the source signal. The MT method operates over a wide range of frequencies (e.g. 0.0001 Hz to 1000 Hz) and can therefore image both shallow (<100 m) and deep (>100 km) geological structures. Molten rock, clay alteration, hydrothermal fluids and brines are generally more conductive than the surrounding host rock and thus the MT method is well-suited to studying magma-hydrothermal plumbing systems.

The local MT study at the LdMVF used broadband MT data collected at 71 sites between 2009 and 2016 to produce a 3-D electrical resistivity model of the subsurface from the surface to approximately 15 km depth. Preliminary data analysis using phase tensors, tensor decomposition and visual examination of apparent resistivity and phase curves indicated that the subsurface had complex 3-D geoelectric structures with a conductor to the north. Using the MT data as a constraint, the ModEM inversion algorithm was used to obtain a 3-D resistivity model and a variety of inversion control parameters were investigated including error floor, starting model, and model covariance length scale. The preferred

resistivity model contains four important conductive features and a conceptual model is shown in Figure 8.1. In the near-surface, there is a conductive anomaly (C1) at approximately 100-300 m depth that is spatially coincident with the lakebed and which is interpreted as surficial hydrothermal fluids and/or hydrothermal clay alteration. At a depth of 1 km below the surface, a conductive anomaly (C2) is located directly beneath the inflation center. C2 is likely related to a shallow NE-SW trending fault-hosted hydrothermal system that was also detected using time-lapse microgravity (Miller et al., 2017a). On the western side of the LdMVF, a north-dipping conductor (C3) is located with its top at a depth of 2.5 km. This dipping conductor is connected to the largest conductor in the model (C4) at a depth of 10 km to the north of the LdMVF. Both C3 and C4 were interpreted as partial melt with a significant hydrothermal fluid component either dissolved in the melt or as a separate phase. Another important feature in the inversion resistivity model was a resistive block (R1) that encompassed much of the southeastern portion of the resistivity model from a depth of 2 km to a depth of 15 km, including the Barrancas complex of the southeastern LdMVF. In general, the conductive features in the model were all concentrated in the northwestern portion of the model while the southeastern portion of the model was largely resistive at depths greater than 2 km. This broad pattern aligned with the trend of the Troncoso Fault with conductive features located on the hanging-wall side of the fault and the footwall encompassing R1 (Garibaldi et al., 2020).

A 3-D density model derived from Bouguer gravity data and a 3-D seismic velocity model derived from ANT and surface wave data have been published at the LdMVF and are shown in Figure 8.1 (Miller et al., 2017b; Wespestad et al., 2019). The density model showed a single, 30 km^3, low-density anomaly directly beneath the inflation center between depths of 2 and 5 km. This was interpreted as being due to a region containing 50 – 85% partial melt (Miller et al., 2017b). The seismic velocity model showed a single, large 450 km^3, low-velocity anomaly on the west and southwestern side of the lake from a depth of 2 km to a depth of 8 km. This feature was interpreted as being due to a region of 5-6% homogeneous partial melt (Wespestad et al., 2019). It is worth noting that both the gravity and seismic methods did not image any small-scale near-surface structures (e.g. <1 km depth), nor were they able to resolve deeper mid-crustal structures (e.g. >8 km depth) due to survey design, limited bandwidth, and/or limitations of the underlying physics. The MT model provided the greatest depth range for the magmatic plumbing system from surface to 15 km depth. For this reason, features C1, C2 and C4 were not constrained by Bouguer gravity or seismic data. C3 was the only feature which overlapped with the Bouguer gravity and seismic tomography resolution limits. Thus, comparison between the MT and the

other two geophysical imaging methods was focused primarily on comparisons with C3. None of the three geophysical methods (Bouguer gravity, seismic, or MT) imaged an anomaly in the same location although there was a substantial overlap between the MT anomaly (C3) and the seismic velocity anomaly (V1), as well as overlap between the velocity anomaly and the density anomaly. Explaining why there was a discrepancy between the images (and the interpretation of those images) is a key component of this thesis.

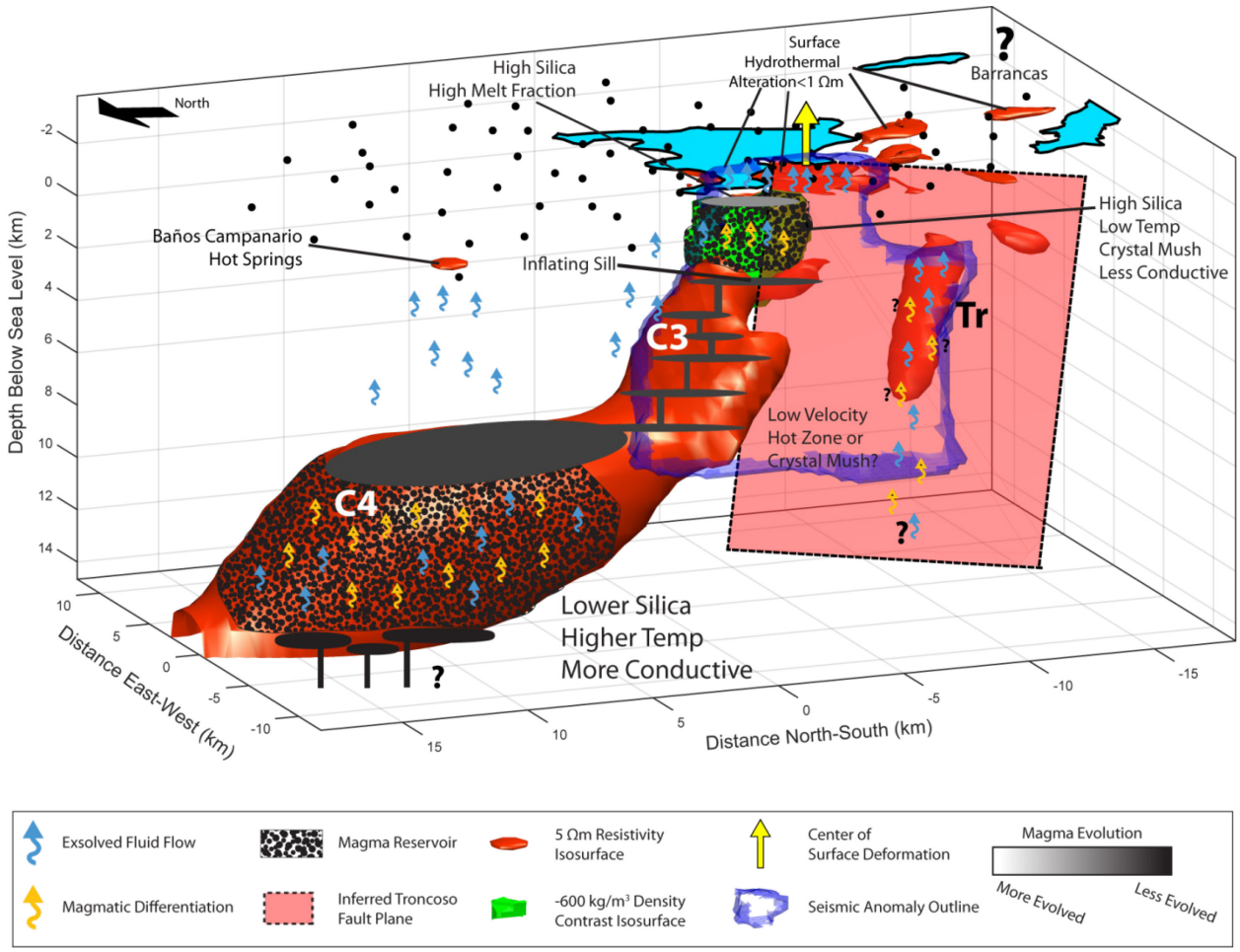

Figure 8.1: Three-dimensional conceptual model of the Laguna del Maule Volcanic Field looking southeast. The preferred resistivity model is shown using a 5 Ωm isosurface. The density model of Miller et al. (2017b) is shown with a -600 kg/m^3 isosurface. The seismic velocity model of Wespestad et al. (2019) is shown using the isosurface described in Chapter 6. Question marks indicate unresolved questions or uncertain interpretations.

To investigate the discrepancies between the density and resistivity models, detailed sensitivity analyses and hypothesis testing was carried out on the resistivity model and MT data using the density anomaly as a constraint. The primary conclusion of this investigation was that it was unlikely that a large volume

(30 km^3) of high melt fraction (50-85%) partial melt could exist at such shallow depth (<3 km) beneath the inflation center without having a substantial response in the MT data. However, a magma body with a smaller volume (e.g. 10 – 20 km^3) and lower melt fraction (e.g. 5-25%) could go undetected. Given the assumptions made in the gravity modelling, it is possible that a magma body with a smaller volume and lower melt fraction could also fit the Bouguer gravity data (Miller et al., 2017b). The possibility of a small amount of exsolved gas would also lead to a larger gravity signature and a smaller resistivity signature since gas is low density and high resistivity.

To investigate the discrepancies between the seismic velocity model and the resistivity model, similar sensitivity analyses and hypothesis testing were carried out using the velocity anomaly as a constraint. This was done using both forward modelling and constrained inversions. The forward modelling methodology showed that a homogeneous anomaly with a range of bulk resistivity values in the same location as the seismic anomaly could not be fit to the MT data with statistical significance using the preferred inversion model although a 15 Ωm anomaly had the smallest impact on the data fit. Additional MT inversions used a 15 Ωm resistivity anomaly, in the same location as the seismic velocity anomaly, as an additional constraint. In one case, the anomaly was added to the starting model as an *a priori* guess. In the other case, the resistivity of the anomaly was fixed (i.e. constrained) and not allowed to change as the inversion progressed. In both cases, the inversion converged well and gave a relatively good fit to the measured data. This suggests that the MT data are relatively insensitive to this feature. However the *a priori* inversion achieved a better data fit by splitting the *a priori* 15 Ωm anomaly into two separate conductors. The first conductor closely resembled C3 from the original inversion with a steeper dip, a slightly deeper top at 4 km depth, and a trend more to the northwest rather than north. The second conductor (Tr) was located to the southwest along the inferred location of the Troncoso Fault and also aligned with the location of observed seismic swarms (Cardona et al., 2018). Both features (C3 and Tr) dipped steeply to the northwest, in the same direction as the Troncoso fault. It is worth noting that the addition of the seismic constraints to the inversion had no appreciable impact on any of the previously interpreted conductive features C1, C2, and C4. The only feature that was impacted was C3. Considering the resolution limitations of ANT, it is possible that the seismic velocity model is unable to resolve the discrete features C3 and Tr and tends to smooth them into a single feature. An additional possibility is that the seismic data is sensing fluid phases (e.g. crystal-poor partial melt and hydrothermal fluids) as well as some combination of crystal-rich mush and elevated sub-solidus temperatures. A crystal-rich mush would be relatively resistive and difficult to image with MT. It is generally difficult to use

geophysical imaging methods to image the internal structure of a magma body since geophysical methods sample large volumes and thus interpret anomalies as relatively homogeneous bulk properties. However, despite these challenges, combining the MT, seismic and gravity results suggests that each method may be imaging important aspects of the same system; the seismic is able to image a large region of low melt fraction partial melt while the MT images smaller, more discrete features which are likely higher melt-fraction (or more fluid-rich) and thus represent the more mobile, eruptible components of the trans-crustal system. The Bouguer gravity images a low density anomaly in the shallow crust which is likely beyond the resolution limits of either the MT or the seismic but the very low density may be indicative of a vapour phase in the shallow magmatic plumbing system.

8.1.2 Magnetotelluric Study of the Central Chilean Subduction Zone

To place the LdMVF within its regional context, an MT study of the subduction zone in central Chile was carried out. The subduction zone of central Chile is part of the larger Andean subduction zone where the oceanic Nazca Plate subducts beneath the continental South American plate. This plate boundary follows the entire length of western South America and is primarily responsible for the formation of the Andean mountain range, the Bolivian Altiplano, and much of the present day volcanism and seismicity in South America. The subduction zone in central Chile around 36°S is notable for several reasons. Firstly, it is located near the transitional zone from the Pampean flat slab in the north with no volcanism and the region of normal subduction of the Southern Volcanic Zone to the south with primarily andesitic stratovolcanoes. At 36°S latitude, there is a preponderance of rhyolitic calderas—including the LdMVF—which are generally uncommon in the rest of the Southern Volcanic Zone. There are also large basalt lava flows erupted from shield volcanoes in the backarc of western Argentina which is unique to the modern Andes. Finally, this latitude is also the location of several major earthquakes, most notably the 2010 M_w 8.8 Maule earthquake. Understanding the role of deep subduction fluids in magma genesis at the LdMVF and volcanic arc was an important goal of this study as well as mapping fluids along the subduction zone interface and their relation to observed seismicity.

The regional study of the subduction zone in central Chile used both broadband and long-period MT data collected at 28 sites between 2009 and 2017 along a 380 km profile from the Pacific Ocean to western Argentina. Preliminary data analysis using tensor decomposition indicated a regional geoelectric strike of approximately N15°E ± 19° for frequencies less than 1 Hz. The strike was the most well-defined on the western and eastern ends of the profile with sites over the volcanic arc showing a

slightly different and more scattered strike of N27°W ± 26°. Phase tensor skew angles were relatively large (>6°) at most sites for frequencies less than 0.1 Hz suggesting significant 3-D or quasi-2-D geoelectric structure. At low frequencies (<0.1 Hz), induction vectors pointed N50°E which was not perpendicular to the geoelectric strike as expected in an ideal 2-D scenario. This suggests potentially more complex geology and could perhaps be explained by an anisotropic layer in the lower crust.

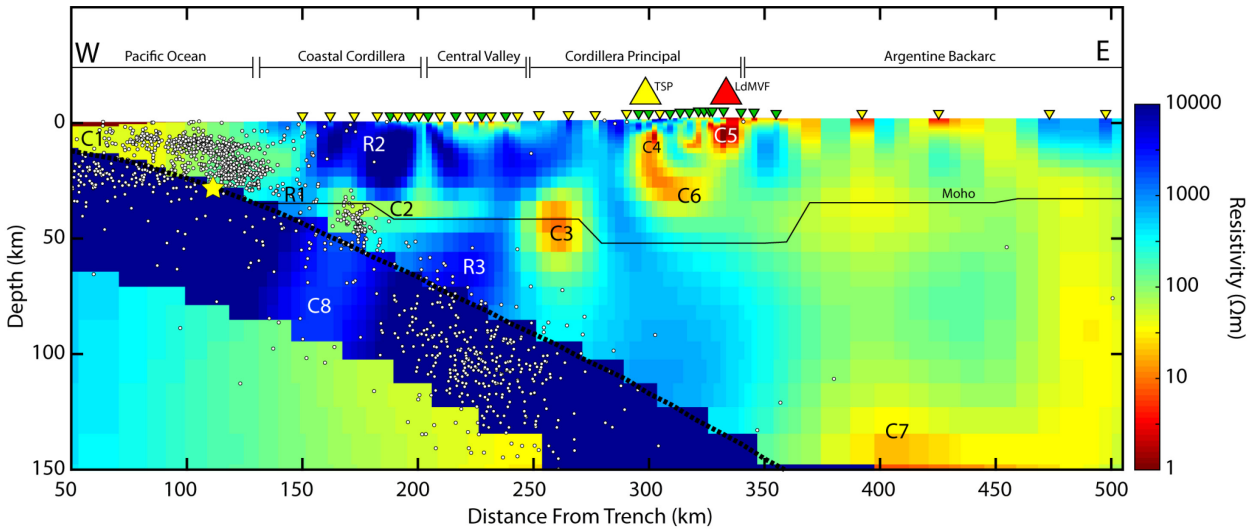

Figure 8.2: The preferred 2-D inversion model along the regional MT profile of the Andean subduction zone at 36°S. Broadband MT sites are shown as green inverted triangles and long-period MT sites are shown as yellow inverted triangles. Features mentioned in text are labelled as conductors (C1 through C8) and resistors (R1 through R3). The location of the subducting slab is taken from Hayes et al. (2012) and shown as a thick black dashed line. The Moho discontinuity, shown as a thin black line, is taken from the Crust1.0 model of Laske et al. (2013). The location of the 2010 Maule earthquake is shown as a yellow star. Earthquake epicenters are shown as small white dots. TSP = Tatara-San Pedro. LdMVF = Laguna del Maule Volcanic Field.

Using both the broadband and long-period MT data as a constraint, the isotropic 2-D inversion algorithm of Rodi and Mackie (2001) was used to solve for a 2-D resistivity model along the profile. This was done with the knowledge that some of the 2-D isotropic assumptions were being violated. A variety of inversion parameters were investigated including static shifts, starting model, regularization parameter, data selection, and *a priori* subducting slab location. The preferred model shown in Figure 8.2 contained many interpretable conductive and resistive features. The slab interface included a sequence of alternating conductors and resistors from the surface to the asthenosphere (C1, R1, C2, R3, C3, C7). The conductors were interpreted as important regions of fluid release and fluid accumulation due to compaction (C1), metamorphic reactions (C2, C3), and metamorphic reactions and flux melting (C7). The

resistors were interpreted to be regions with relatively little fluid accumulation suggesting dry, impermeable, cold rock. The Cobquecura Anomaly (R1), at a depth of approximately 30 km along the slab interface, coincided with a notable aseismic gap between two clusters of seismicity. This feature also correlated with a high-velocity seismic anomaly and is interpreted as a dense, dry, impermeable asperity on the plate interface which affects co-seismic slip behaviour of large megathrust earthquakes. This helps explain why the subduction zone at this latitude tends to experience very large earthquakes and why the 2010 Maule earthquake did not rupture far inland. The down-dip limit of the seismogenic zone is correlated with a conductor (C2) that is related to fluid release which may serpentinize the forearc mantle and lead to stable-sliding rather than stick-slip behaviour. The timing of seismicity in this region pre- and post-Maule earthquake suggests that fluid-driven diffusion stresses result in a conditionally-stable transitional zone that only ruptures following transient high-strain events. Intermediate-depth earthquakes down-dip of the aseismic zone are not directly associated with any conductor, so if dehydration embrittlement is initiating these earthquakes, the associated fluids must be relatively isolated and are not imaged with MT. These fluids are focused into a large region of fluid accumulation in the cold-nose of the mantle wedge (C3).

Beneath the volcanic arc there are three additional conductors (C4, C5, and C6). C4 and C5 are both located in the upper crust (<10 km depth). These are likely due to the presence of fluids and partial melt associated with the (a) Tatara-San Pedro (TSP) volcano on the modern volcanic arc (C4) and; (b) the LdMVF in the backarc (C5). The conductor beneath the LdMVF is likely a poorly-resolved, 2-D approximation of the crustal conductors imaged in 3-D using the local array described above. The lower crust underlying both the volcanic arc at TSP and the back-arc LdMVF is conductive (C6). This suggests that the lower crust is thermally-mature and may contain a significant amount of partial melt which was the source of magma erupted at both TSP and LdMVF. It is also notable that there is no significant conductor located at the slab interface beneath the volcanic arc. This suggests that melt accumulations are relatively small beneath the volcanic arc and perhaps melt and fluids are focused upwards from the backarc (C7) via the velocity field related to mantle wedge flow (e.g. Wada and Behn, 2015; Wilson et al., 2014). This suggests that conceptual models (e.g. Stern, 2002) which show vertical ascent of material from the slab directly beneath the volcanic arc may not be valid in all circumstances and fluids may be originate from greater depths in the back-arc. This idea has also been supported by an MT study in the Bolivian Andes which showed no significant conductors were present at the slab surface directly beneath the volcanic arc, while large conductors were located in the backarc (Brasse and Eydam, 2008).

This geometry of mantle wedge conductor is not common. Studies in Cascadia, Japan and Costa Rica have all shown conductors extending from the slab to the surface beneath the volcanic arc (Hata et al., 2015; Wannamaker et al., 2014; Worzewski et al., 2014). It is interesting that the only other anomalous resistivity model was also found in the Andes. This suggests that there may be unique geodynamic circumstances in the Andes which produce greater interactions of slab generated melts with the horizontal velocity field in the mantle wedge (e.g. low permeability and/or high fluid viscosity; Wilson et al., 2014). This additional constraint can help better inform geodynamic models developed for the Andes. However, given that this anomalous electrical resistivity structure has only been identified in two MT profiles, additional long-period MT profiles and 3-D arrays are required to confirm that the anomalous electrical resistivity structure beneath the volcanic arc and back-arc is present throughout the Andes.

8.2 IMPORTANT FINDINGS

Prior to this work, there were no published 3-D models of the resistivity structure beneath the LdMVF, nor any regional study of the resistivity structure of the Andean subduction zone at this latitude. The nearest regional MT studies of the Andean subduction zone were 500 km to the south, more than 1000 km north, or focused on the backarc of Argentina (e.g. Brasse et al., 2009; Brasse and Eydam, 2008; Burd et al., 2014, 2013). The only local MT study was focused on near-surface geothermal exploration to the west of the LdMVF (Hickson et al., 2010). Much about the subsurface structure in this area was unknown and this thesis project had some surprising findings. Below are the nine most important results.

1) There is no large, homogeneous conductor directly beneath the LdMVF (Figure 8.1). The primary hypothesis driving this project was that the LdMVF was underlain by a large, shallow, homogeneous magma reservoir. The lack of a conductor suggests that any mush volume beneath the LdMVF must be some combination (or all) of the following: low melt fraction, small volume, low water content, and/or poorly-connected. Upper crustal, eruptible volumes of high melt fraction, well-connected partial melt must be relatively small and/or ephemeral which broadly agrees with petrological results (Andersen et al., 2019; 2018).
2) There is a large conductor in the mid-crust at a depth of 10 km to the north of the LdMVF, laterally-offset from surface vents and lava flows, and the observed deformation. This conductor is located at a depth where partial melt often accumulates in the crust (Cruden and Weinberg, 2018). A N-S

trending lobe from this conductor slopes upwards towards the inflation center and the western side of the LdMVF, terminating at a depth of 3-4 km (Figure 8.1). This is a conductive pathway from the mid-crust (in the north) to the upper crust (beneath the LdMVF). This suggests that partial melt and hydrothermal fluids migrate both laterally and vertically as they approach the surface as has been observed at a number of other volcanoes (e.g. Klügel et al., 2015; Magee et al., 2018).

3) The southeastern portion of the LdMVF is largely resistive and also shows no significant anomalies in both the density and seismic velocity models. The southeastern LdMVF includes the Barrancas complex (Figure 8.1) which has produced the majority of rhyolite eruptions in the Holocene and is the high-point of paleo-shoreline deformation, so the lack of geophysical anomalies beneath this recently-active area is surprising. This further suggests that upper crustal volumes of eruptible melt are relatively small and ephemeral, although geophysical data in the southeastern LdMVF are sparser so interpretations are less certain.
4) The large-scale pattern of electrical resistivity anomalies shows conductors primarily on the hanging-wall side of the NE-SW trending Troncoso fault—a normal fault which dips to the northwest. No significant conductors were imaged on the footwall below a depth of 2 km. This suggests that this fault is an important structural boundary in the magma-hydrothermal system and that fluid movement may be structure-driven. This further suggests that conceptual models which neglect structural geology may not be sufficient to adequately describe the complexity of some volcanic systems.
5) The lower crust at depths of approximately 30 km beneath the volcanic arc is conductive (1 Ωm; Figure 8.2) suggesting that it is thermally mature with high heat flow which explains how mid-crustal magma reservoirs can persist at the LdMVF. This lower crustal hot zone appears to be laterally extensive suggesting a connection between the back-arc LdMVF and volcanoes on the modern volcanic arc (e.g. TSP). Deep crustal connections between systems have been seen at other volcanoes (e.g. Bato et al., 2018) and the LdMVF and TSP show similar petrological characteristics (Hildreth et al., 2010).
6) The above results all suggest that the magma-hydrothermal system at the LdMVF is complex, trans-crustal, and three-dimensional. It is not consistent with simple conceptual models involving a single crustal magma reservoir and magma movement driven by only vertical buoyant ascent. Instead the results point to a dynamic system with small ephemeral magma batches in the upper crust and magma movement controlled by structural boundaries. A multi-scale, trans-crustal geophysical approach is necessary to gain a complete understanding of volcanic systems. Geophysical surveys of

volcanic systems should be designed with the understanding that large parts of the magmatic plumbing system may be offset from the surface expression of the volcano.

7) The subduction slab interface is not characterized by a single conductor but rather multiple conductors separated by resistors suggesting distinct regions of fluid accumulation in the crust and mantle wedge (Figure 8.2). A significant mantle wedge conductor is imaged in the forearc, similar to other subduction zone studies in Chile and elsewhere, but no conductor is imaged directly beneath the volcanic arc. This suggests that the pathway taken by partial melt may be controlled by pressure gradients in the velocity field caused by mantle wedge flow (e.g. Wilson et al., 2014). This suggests that fluid focusing may be important at this latitude in the Andes and simplistic conceptual models of subduction zones which show partial melt rising vertically from the slab to the volcanic arc may not always correct. This observation can be used to improve geodynamic models and determine the actual depths where melt is produced in subduction zones.
8) The down-dip limit of the seismogenic zone correlates with a conductor which suggests that the down-dip limit is controlled by slab fluids which alter the forearc mantle and lead to stable-sliding rather than stick-slip behaviour. However, this region may be conditionally-stable due to fluid-driven diffusion stress processes and may rupture during high strain events such as it did immediately following the 2010 Maule earthquake.
9) The Cobquecura Anomaly, a large, dry, resistive asperity on the plate interface, affects the coseismic slip behaviour of megathrust earthquakes at this latitude. This asperity helps to explain why the 2010 Maule earthquake did not rupture further inland, and may also explain why large magnitude earthquakes tend to occur here. This feature also correlates well with a high velocity anomaly.

8.3 FUTURE WORK

Despite significant gains in understanding the LdMVF magmatic plumbing system and the Chilean subduction zone throughout this project, there are still many unresolved questions which could be answered to develop a complete understanding of this region. There are three primary areas that could still be explored regarding local data acquisition, modelling methodology and regional data acquisition to further improve our understanding and help answer unresolved questions.

1) The lack of geophysical anomalies in the volcanically-active southeastern LdMVF should be explored further. MT data coverage is sparse in the southeast because of the logistical complexities in crossing the international border and the extremely remote and mountainous terrain with no road access. As

such, the recently-active Barrancas complex is on the edge of the MT array. It would be very useful to acquire additional broadband MT data (and other geophysical data) around the Barrancas complex in the southeastern LdMVF in both Chile and Argentina. Further work here would help answer questions about the size and location of the magma reservoirs that caused the Barrancas eruptions. The possibility that the mid-crustal conductor to the north of the LdMVF provides heat and material to the Barrancas complex seems unlikely—though not impossible—given the 20 km lateral distance separating the two (Magee et al., 2018). As such, a mid- or lower-crustal conductor closer to the Barrancas complex is hypothesized.

2) It is necessary to carry out full joint inversion of MT, seismic and gravity datasets. This thesis only presents constrained inversions of MT data using *a priori* constraints from the seismic and gravity data. A full joint inversion would invert multiple datasets (e.g. MT-gravity, MT-seismic, seismic-gravity, or all three) to minimize an objective function which contains both datasets and solves for multiple model spaces simultaneously. Some of this work is ongoing using a modified version of the cross-gradient approach of Gao and Zhang (2018). This would further the goal of integrating the three datasets and may help to further explain the discrepancies and differences between the three models in terms of either real geology or resolution issues of the methods and/or datasets.
3) The regional MT data shows some significant 3-D effects and potential anisotropy as well. These effects on the modelled features could be explored using 2-D anisotropic inversions or 3-D isotropic inversions of the profile data. Recently-developed 3-D anisotropic inversions (e.g. Cao et al., 2018) could also be tested on this dataset relative to the 2-D anisotropic inversion.
4) Given that the MT data measured on the regional profile showed some significant 3-D effects, a fully 3-D MT array is necessary to reliably image the complexity of the Andean subduction zone at 36°S latitude. The existing regional MT data could be broadened into a 3-D array with both onshore and offshore MT data in a study analogous to a study of the Hikurangi subduction zone in New Zealand (Heise et al., 2017). This would be a significant undertaking but would give a much more detailed picture of the subducting slab interface and the areas of fluid release. It would also give greater insight into the spatial relationship between zones of fluid release and observed seismicity. In particular, it would be useful to map the along-strike extent of the Cobquecura resistivity anomaly and determine if it correlates with the 3-D seismic velocity model further south, where it becomes an even faster velocity anomaly in the vicinity of the 2010 Maule earthquake. Offshore MT data would allow for a more detailed analysis and interpretation of the up-dip limit of the seismogenic zone which was too far offshore to be constrained with the current onshore MT dataset.

REFERENCES

Abers, G.A., Keken, P.E. Van, Hacker, B.R., 2017. The cold and relatively dry nature of mantle forearcs in subduction zones. Nat. Geosci. 10, 333–337. doi:10.1038/ngeo2922

Afanasyev, A., Blundy, J., Melnik, O., Sparks, S., 2018. Formation of magmatic brine lenses via focussed fluid-flow beneath volcanoes. Earth Planet. Sci. Lett. 486, 119–128. doi:10.1016/j.epsl.2018.01.013

Aizawa, K., Koyama, T., Hase, H., Uyeshima, M., Kanda, W., Utsugi, M., Yoshimura, R., Yamaya, Y., Hashimoto, T., Yamazaki, K., Komatsu, S., Watanabe, A., Miyakawa, A., Ogawa, Y., 2014. Three-dimensional resistivity structure and magma plumbing system of the Kirishima Volcanoes as inferred from broadband magnetotelluric data. J. Geophys. Res. Solid Earth 119, 198–215. doi:10.1002/2013JB010682.Received

Andersen, N.L., 2017. Perspectives on protracted and punctuated rhyolite magma dynamics from integrated geochemistry and geochronology. PhD Thesis. University of Wisconsin-Madison.

Andersen, N.L., Singer, B.S., Coble, M.A., 2019. Repeated Rhyolite Eruption From Heterogeneous Hot Zones Embedded Within a Cool , Shallow Magma Reservoir. J. Geophys. Res. Solid Earth 124, 1–19. doi:10.1029/2018JB016418

Andersen, N.L., Singer, B.S., Costa, F., Fournelle, J., Herrin, J.S., Fabbro, G.N., 2018. Petrochronologic perspective on rhyolite volcano unrest at Laguna del Maule, Chile. Earth Planet. Sci. Lett. 493, 57–70. doi:10.1016/j.epsl.2018.03.043

Andersen, N.L., Singer, B.S., Jicha, B.R., Beard, B.L., Johnson, C.M., Licciardi, J.M., 2017. Pleistocene to Holocene Growth of a Large Upper Crustal Rhyolitic Magma Reservoir beneath the Active Laguna del Maule Volcanic Field, Central Chile. J. Petrol. 58, 85–114. doi:10.1093/petrology/egx006

Anderson, M.L., Zandt, G., Triep, E., Fouch, M., Beck, S., 2004. Anisotropy and mantle flow in the Chile-Argentina subduction zone from shear wave splitting analysis. Geophys. Res. Lett. 31, 2–5. doi:10.1029/2004GL020906

Angermann, D., Klotz, J., Reigber, C., 1999. Space-geodetic estimation of the Nazca-South America Euler vector. Earth Planet. Sci. Lett. 171, 329–334.

Annen, C., 2009. From plutons to magma chambers: Thermal constraints on the accumulation of eruptible silicic magma in the upper crust. Earth Planet. Sci. Lett. 284, 409–416. doi:10.1016/j.epsl.2009.05.006

Annen, C., Blundy, J.D., Leuthold, J., Sparks, R.S.J., 2015. Construction and evolution of igneous bodies: Towards an integrated perspective of crustal magmatism. Lithos 230, 206–221. doi:10.1016/j.lithos.2015.05.008

Annen, C., Blundy, J.D., Sparks, R.S.J., 2006. The genesis of intermediate and silicic magmas in deep crustal hot zones. J. Petrol. 47, 505–539. doi:10.1093/petrology/egi084

Araña, V., Camacho, A.G., Garcia, A., Montesinos, F.G., Blanco, I., Vieira, R., Felpeto, A., 2000. Internal structure of Tenerife (Canary Islands) based on gravity, aeromagnetic and volcanological data. J. Volcanol. Geotherm. Res. 103, 43–64. doi:10.1016/S0377-0273(00)00215-8

Archie, G.E., 1942. The Electrical Resistivity Log as an Aid in Determining Some Reservoir Characteristics. Trans. AIME 146, 54–62.

Árnason, K., Vilhjálmsson, A.M., Bjornsdottir, T., 2007. A study of the Krafla Volcano using gravity, micro earthquake and MT data, in: Short Course II on Surface Exploration for Geothermal Resources. Lake Naivasha, Kenya, pp. 1–14.

Astort, A., Colavitto, B., Sagripanti, L., García, H., Echaurren, A., Soler, S., Ruíz, F., 2019. Crustal and mantle structure beneath the southern Payenia Volcanic Province using gravity and magnetic data. Tectonics 38, 144–158. doi:10.1029/2017TC004806

Avdeev, D.B., 2005. Three-dimensional electromagnetic modelling and inversion from theory to application. Surv. Geophys. 26, 767–799. doi:10.1007/s10712-005-1836-2

Baba, K., Chave, A.D., Evans, R.L., Hirth, G., Mackie, R.L., 2006. Mantle dynamics beneath the East Pacific Rise at 17°S : Insights from the Mantle Electromagnetic and Tomography (MELT) experiment. J. Geophys. Res. 111, 1–18. doi:10.1029/2004JB003598

Bachmann, O., Bergantz, G.W., 2008a. The magma reservoirs that feed supereruptions. Elements 4, 17–21. doi:10.2113/GSELEMENTS.4.1.17

Bachmann, O., Bergantz, G.W., 2008b. Rhyolites and their source mushes across tectonic settings. J. Petrol. 49, 2277–2285. doi:10.1093/petrology/egn068

Bachmann, O., Miller, C.F., de Silva, S.L., 2007. The volcanic-plutonic connection as a stage for understanding crustal magmatism. J. Volcanol. Geotherm. Res. 167, 1–23. doi:10.1016/j.jvolgeores.2007.08.002

Bahr, K., 1988. Interpretation of the magnetotelluric impedance tensor: Regional induction and local telluric distortion. J. Geophys. 62, 119–127.

Bai, T., Thurber, C., Lanza, F., Singer, B.S., Cardona, C., in review. Teleseismic tomography of the Laguna del Maule Volcanic Field in Chile. J. Geophys. Res. Solid Earth xxx, 1–21.

Barazangi, M., Isacks, B.L., 1976. Spatial distribution of earthquakes and subduction of the Nazca plate beneath South America. Geology 4, 686–692.

Bato, M.G., Pinel, V., Yan, Y., Jouanne, F., Vandemeulebrouck, J., 2018. Possible deep connection between volcanic systems evidenced by sequential assimilation of geodetic data. Sci. Rep. 8, 1–13. doi:10.1038/s41598-018-29811-x

Beamish, D., Travassos, J.M., 1992. The use of the D+ solution in magnetotelluric interpretation. J. Appl. Geophys. 29, 1–19.

Bebout, G.E., 1996. Volatile Transfer and Recycling at Convergent Margins : Mass-Balance and Insights from High-P/T Metamorphic Rocks. Geophys. Monogr. Ser. 96, 179–193. doi:10.1029/GM096p0179

Bebout, G.E., Scholl, D.W., Stern, R.J., Wallace, L.M., Agard, P., 2018. Twenty Years of Subduction Zone Science: Subduction Top to Bottom 2 (ST2B-2). GSA Today 28, 4–10. doi:10.1130/GSATG354A.1.

Beck, S., Barrientos, S., Kausel, E., Reyes, M., 1998. Source characteristics of historic earthquakes along

the central Chile subduction zone. J. South Am. Earth Sci. 11, 115–129. doi:10.1016/S0895-9811(98)00005-4

Becken, M., Ritter, O., Burkhardt, H., 2008. Mode separation of magnetotelluric responses in three-dimensional environments. Geophys. J. Int. 172, 67–86. doi:10.1111/j.1365-246X.2007.03612.x

Bedrosian, P.A., 2007. MT+, Integrating Magnetotellurics to Determine Earth Structure, Physical State, and Processes. Surv. Geophys. 28, 121–167. doi:10.1007/s10712-007-9019-6

Bedrosian, P.A., Maercklin, N., Weckmann, U., Bartov, Y., Ryberg, T., Ritter, O., 2007. Lithology-derived structure classification from the joint interpretation of magnetotelluric and seismic models. Geophys. J. Int. 170, 737–748. doi:10.1111/j.1365-246X.2007.03440.x

Benavente, O., Tassi, F., Reich, M., Aguilera, F., Capecchiacci, F., Gutiérrez, F., Vaselli, O., Rizzo, A., 2016. Chemical and isotopic features of cold and thermal fluids discharged in the Southern Volcanic Zone between 32.5°S and 36°S: Insights into the physical and chemical processes controlling fluid geochemistry in geothermal systems of Central Chile. Chem. Geol. 420, 97–113. doi:10.1016/j.chemgeo.2015.11.010

Berdichevsky, M.N., Dmitriev, V.I., 1976. Distortion of magnetic and electric fields by near-surface lateral inhomogeneities. Acta Geod. Geophy. Mont. Acad. Sci. Hungary 11, 447–483.

Berdichevsky, M.N., Dmitriev, V.I., Pozdnjakova, E.E., 1998. On two-dimensional interpretation of magnetotelluric soundings. Geophys. J. Int. 133, 585–606. doi:10.1046/j.1365-246X.1998.01333.x

Bertrand, E.A., Caldwell, T.G., Hill, G.J., Wallin, E.L., Bennie, S.L., Cozens, N., Onacha, S.A., Ryan, G.A., Walter, C., Zaino, A., Wameyo, P., 2012. Magnetotelluric imaging of upper-crustal convection plumes beneath the Taupo Volcanic Zone, New Zealand. Geophys. Res. Lett. 39, 1–6. doi:10.1029/2011GL050177

Biggs, J., Annen, C., 2019. The lateral growth and coalesence of magma systems. Philos. Trans. R. Soc. A 377.

Biggs, J., Pritchard, M.E., 2017. Global volcano monitoring: What does it mean when volcanoes deform? Elements 13, 17–22. doi:10.2113/gselements.13.1.17

Biggs, J., Robertson, E., Cashman, K., 2016. The lateral extent of volcanic interactions during unrest and eruption. Nat. Geosci. 9, 308–311. doi:10.1038/ngeo2658

Birsic, E.M., 2015. Petrology and 40Ar/39Ar Chronology of the Laguna Sin Puerto and Bobadilla ignimbrites, Laguna del Maule Volcanic Field, Chile. MSc Thesis. University of Wisconsin-Madison.

Blackman, R.B., Tukey, J.W., 1958. The measurement of power spectra from the point of view of communications engineering. Bell Syst. Tech. J. 485–569.

Bohm, M., Lüth, S., Echtler, H.P., Asch, G., Bataille, K., Bruhn, C., Rietbrock, A., Wigger, P., 2002. The Southern Andes between 36 S and 40 S latitude: seismicity and average seismic velocities. Tectonophysics 356, 275–289.

Bonali, F.L., Tibaldi, A., Corazzato, C., Tormey, D.R., Lara, L.E., 2013. Quantifying the effect of large earthquakes in promoting eruptions due to stress changes on magma pathway: The Chile case.

Tectonophysics 583, 54–67. doi:10.1016/j.tecto.2012.10.025

Booker, J.R., 2014. The Magnetotelluric Phase Tensor: A Critical Review. Surv. Geophys. 35, 7–40. doi:10.1007/s10712-013-9234-2

Bowen, N.L., 1922. The reaction principle in petrogenesis. J. Geol. 30, 177–182.

Brasse, H., Eydam, D., 2008. Electrical conductivity beneath the Bolivian Orocline and its relation to subduction processes at the South American continental margin. J. Geophys. Res. 113, 1–14. doi:10.1029/2007JB005142

Brasse, H., Kapinos, G., Li, Y., Mütschard, L., Soyer, W., Eydam, D., 2009. Structural electrical anisotropy in the crust at the South-Central Chilean continental margin as inferred from geomagnetic transfer functions. Phys. Earth Planet. Inter. 173, 7–16. doi:10.1016/j.pepi.2008.10.017

Brasse, H., Lezaeta, P., Rath, V., Schwalenberg, K., Soyer, W., Haak, V., 2002. The Bolivian Altiplano conductivity anomaly. J. Geophys. Res. 107. doi:10.1029/2001JB000391

Brasse, H., Soyer, W., 2001. A magnetotelluric study in the Southern Chilean Andes. Geophys. Res. Lett. 28, 3757–3760. doi:10.1029/2001GL013224

Brothelande, E., Amelung, F., Yunjun, Z., Wdowinski, S., 2018. Geodetic evidence for interconnectivity between Aira and Kirishima magmatic systems, Japan. Sci. Rep. 8, 1–10. doi:10.1038/s41598-018-28026-4

Burd, A.I., Booker, J.R., Mackie, R., Favetto, A., Pomposiello, M.C., 2014. Three-dimensional electrical conductivity in the mantle beneath the Payún Matrú Volcanic Field in the Andean backarc of Argentina near 36.5 S: Evidence for decapitation of a mantle plume by resurgent upper mantle shear during slab steepening. Geophys. J. Int. 198, 812–827. doi:10.1093/gji/ggu145

Burd, A.I., Booker, J.R., Mackie, R., Pomposiello, C., Favetto, A., 2013. Electrical conductivity of the Pampean shallow subduction region of Argentina near 33 S: Evidence for a slab window. Geochemistry, Geophys. Geosystems 14, 3192–3209. doi:10.1002/ggge.20213

Cagniard, L., 1953. Basic theory of the magneto-telluric method of geophysical prospecting. Geophysics 18, 605–635. doi:10.1190/1.1437915

Cai, J., Wei, W., Hu, X., Wood, D.A., 2017. Electrical conductivity models in saturated porous media: A review. Earth-Science Rev. 171, 419–433. doi:10.1016/j.earscirev.2017.06.013

Caldwell, T.G., Bibby, H.M., Brown, C., 2004. The magnetotelluric phase tensor. Geophys. J. Int. 158, 457–469. doi:10.1111/j.1365-246X.2004.02281.x

Cantwell, T., 1960. Detection and analysis of low frequency magnetotelluric signals. Massachusetts Institute of Technology. doi:10.1017/CBO9781107415324.004

Cao, H., Wang, K., Wang, T., Hua, B., 2018. Three-dimensional magnetotelluric axial anisotropic forward modeling and inversion. J. Appl. Geophys. 153, 75–89. doi:10.1016/j.jappgeo.2018.04.015

Capitanio, F.A., Faccenna, C., Zlotnik, S., Stegman, D.R., 2011. Subduction dynamics and the origin of Andean orogeny and the Bolivian orocline. Nature 480, 83–86. doi:10.1038/nature10596

Cardona, C., Tassara, A., Gil-cruz, F., Lara, L., Morales, S., Kohler, P., Franco, L., 2018. Crustal seismicity associated to rapid surface uplift at Laguna del Maule Volcanic Complex , Southern Volcanic Zone of the Andes. J. Volcanol. Geotherm. Res. doi:10.1016/j.jvolgeores.2018.01.009

Cashman, K. V., Giordano, G., 2014. Calderas and magma reservoirs. J. Volcanol. Geotherm. Res. 288, 28–45. doi:10.1016/j.jvolgeores.2014.09.007

Cashman, K. V., Sparks, R.S.J., Blundy, J.D., 2017. Vertically extensive and unstable magmatic systems: A unified view of igneous processes. Science (80-.). 355, eaag3055. doi:10.1126/science.aag3055

Cembrano, J., Herv, F., 1996. The Liquifie Ofqui fault zone: a long-lived intra-arc fault system in southern Chile. Tectonophysics 259, 55–66.

Cembrano, J., Lara, L., 2009. The link between volcanism and tectonics in the southern volcanic zone of the Chilean Andes: A review. Tectonophysics 471, 96–113. doi:10.1016/j.tecto.2009.02.038

Cerpa, N.G., Wada, I., Wilson, C.R., 2019. Effects of fluid influx, fluid viscosity, and fluid density on fluid migration in the mantle wedge and their implications for hydrous melting. Geosphere 15, 1–23.

Charrier, R., Baeza, O., Elgueta, S., Flynn, J.J., Gans, P., Kay, S.M., Muñoz, N., Wyss, a. R., Zurita, E., 2002. Evidence for Cenozoic extensional basin development and tectonic inversion south of the flat-slab segment, southern Central Andes, Chile (33°-36°S.L.). J. South Am. Earth Sci. 15, 117–139.

Chaussard, E., Amelung, F., 2014. Regional controls on magma ascent and storage in volcanic arcs. Geochemistry, Geophys. Geosystems 15, 1407–1418. doi:10.1002/2015GC005918.Received

Chave, A.D., 2017. Estimation of the Magnetotelluric Response Function: The Path from Robust Estimation to a Stable MLE. Surv. Geophys. 38, 837–867.

Chave, A.D., Jones, A.G., 2012. The Magnetotelluric Method - Theory and Practice. Cambridge Unviersity Press, Cambridge, UK.

Chave, A.D., Smith, J., 1994. On electric and magnetic galvanic distortion tensor decompositions. J. Geophys. Res. Solid … 99, 4669–4682.

Chave, A.D., Thomson, D.J., 2004. Bounded influence magnetotelluric response function estimation. Geophys. J. Int. 157, 988–1006. doi:10.1111/j.1365-246X.2004.02203.x

Chave, A.D., Thomson, D.J., 1989. Some comments on magnetotelluric response function estimation. J. Geophys. Res. Solid Earth 94, 14215–14225. doi:10.1029/JB094iB10p14215

Chave, A.D., Thomson, D.J., Ander, M.E., 1987. On the Robust Estimation of Power Spectra, Coherences, and Transfer Functions. J. Geophys. Res. 92, 633–648.

Chen, J., Hoversten, G.M., Key, K., Nordquist, G., Cumming, W., 2012. Stochastic inversion of magnetotelluric data using a sharp boundary parameterization and application to a geothermal site. Geophysics 77, E265–E279. doi:10.1190/geo2011-0430.1

Chernak, L.J., Hirth, G., 2010. Deformation of antigorite serpentinite at high temperature and pressure. Earth Planet. Sci. Lett. 296, 23–33. doi:10.1016/j.epsl.2010.04.035

Chmielowski, J., Zandt, G., Haberland, C.A., 1999. The Central Andean Altiplano-Puna Magma Body.

Geophys. Res. Lett. 26, 783–786.

Christensen, N.I., Mooney, W.D., 1995. Seismic velocity structure and composition of the continental crust: A global view. J. Geophys. Res. 100, 9761–9788.

Cifuentes, I.L., 1989. The 1960 Chilean Earthquakes. J. Geophys. Res. 94, 665–680.

Comeau, M.J., 2015. Electric Structure of the Altiplano-Puna Magma Body and Volcan Uturuncu from Magnetotelluric Data. PhD Thesis. University of Alberta.

Comeau, M.J., Unsworth, M.J., Cordell, D., 2016. New constraints on the magma distribution and composition beneath Volcán Uturuncu and the southern Bolivian Altiplano from magnetotelluric data. Geosphere 12, 1391–1421. doi:10.1130/GES01277.1

Constable, S., Parker, R.L., Constable, C., 1987. Occam's inversion: A practical algorithm for generating smooth models from electromagnetic sounding data. Geophysics 52, 289–300.

Contreras-Reyes, E., Grevemeyer, I., Flueh, E.R., Reichert, C., 2008a. Upper lithospheric structure of the subduction zone offshore of southern Arauco peninsula, Chile, at ~38 ° S. J. Geophys. Res. 113, 1–19. doi:10.1029/2007JB005569

Contreras-Reyes, E., Grevemeyer, I., Flueh, E.R., Scherwath, M., Bialas, J., 2008b. Effect of trench-outer rise bending-related faulting on seismic Poisson's ratio and mantle anisotropy: a case study offshore of Southern Central Chile. Geophys. J. Int. 173, 142–156. doi:10.1111/j.1365-246X.2008.03716.x

Contreras-Reyes, E., Maksymowicz, A., Lange, D., Grevemeyer, I., Muñoz-Linford, P., Moscoso, E., 2017. On the relationship between structure, morphology and large coseismic slip: A case study of the Mw 8.8 Maule, Chile 2010 earthquake. Earth Planet. Sci. Lett. 478, 27–39. doi:10.1016/j.epsl.2017.08.028

Cook, F.A., Jones, A.G., 1995. Seismic reflections and electrical conductivity : A case of Holmes's curious dog? Geology 23, 141–144.

Cooper, G.F., Wilson, C.J.N., Millet, M.A., Baker, J.A., Smith, E.G.C., 2012. Systematic tapping of independent magma chambers during the 1Ma Kidnappers supereruption. Earth Planet. Sci. Lett. 313–314, 23–33. doi:10.1016/j.epsl.2011.11.006

Cordell, D., Unsworth, M.J., Díaz, D., 2018. Imaging the Laguna del Maule Volcanic Field, central Chile using magnetotellurics: Evidence for crustal melt regions laterally-offset from surface vents and lava flows. Earth Planet. Sci. Lett. 488, 168–180. doi:10.1016/j.epsl.2018.01.007

Cordell, D., Unsworth, M.J., Diaz, D., Reyes-Wagner, V., 2019. Fluid and Melt Pathways in the Central Chilean Subduction Zone Near the 2010 Maule Earthquake (35–36°S) as Inferred From Magnetotelluric Data. Geochemistry, Geophys. Geosystems 20, 1–18. doi:10.1029/2018GC008167

Cruden, A.R., Weinberg, R.F., 2018. Mechanisms of Magma Transport and Storage in the Lower and Middle Crust—Magma Segregation , Ascent and Emplacement, in: Volcanic and Igneous Plumbing Systems. Elsevier Inc., pp. 13–53. doi:10.1016/B978-0-12-809749-6/00002-9

Currie, C.A., Beaumont, C., Huismans, R.S., 2007. The fate of subducted sediments: A case for backarc

intrusion and underplating. Geology 35, 1111–1114. doi:10.1130/G24098A.1

D'Erceville, I., Kunetz, G., 1962. The effect of a fault on the Earth's natural electromagnetic field. Geophysics 27, 651–665.

Dannowski, A., Grevemeyer, I., Kraft, H., Arroyo, I., Thorwart, M., 2013. Crustal thickness and mantle wedge structure from receiver functions in the Chilean Maule region at 35°S. Tectonophysics 592, 159–164. doi:10.1016/j.tecto.2013.02.015

Davidson, J.P., Dungan, M. a., Ferguson, K.M., Colucci, M.T., 1987. Crust-magma interactions and the evolution of arc magma: the San Pedro-Pellado volcanic complex, southern Chilean Andes. Geology 15, 443–446.

De la Jara, A., O'Brien, R., 2016. Unusual Chile volcano activity sparks interest, worries. Reuters. https://www.reuters.com/article/us-chile-volcano-idUSKBN1421HP (accessed 27.3.20).

DeGroot-Hedlin, C., 1991. Removal of static shift in two dimensions by regularized inversion. Geophysics 56, 2102–2106.

DeGroot, M.H., Schervish, M.J., 2012. Probability and Statistics, 4th ed. Pearson Education, Boston, MA.

Delph, J.R., Ward, K.M., Zandt, G., Ducea, M.N., Beck, S.L., 2017. Imaging a magma plumbing system from MASH zone to magma reservoir. Earth Planet. Sci. Lett. 457, 313–324. doi:10.1016/j.epsl.2016.10.008

Díaz, D., Zuñiga, F., Castruccio, A., 2020. The interaction between active crustal faults and volcanism: A case study of the Liquiñe-Ofqui Fault Zone and Osorno volcano, southern Andes, using magnetotellurics. J. Volcanol. Geotherm. Res. 393, 106806. doi:10.1016/j.jvolgeores.2020.106806

Didana, Y., Thiel, S., Heinson, G., 2014. Magnetotelluric imaging of upper crustal partial melt at Tendaho graben in Afar, Ethiopia. Geophys. Res. Lett. doi:10.1002/2014GL060000.1.

Dobson, P.F., Kneafsey, T.J., Hulen, J., Simmons, A., 2003. Porosity, permeability, and fluid flow in the Yellowstone geothermal system, Wyoming. J. Volcanol. Geotherm. Res. 123, 313–324. doi:10.1016/S0377-0273(03)00039-8

Drake, R., 1976. Chronology of Cenozoic igneous and tectonic events in the central Chilean Andes—latitudes 35 30' to 36 S. J. Volcanol. Geotherm. Res. 1.

Druitt, T.H., Costa, F., Deloule, E., Dungan, M., Scaillet, B., 2012. Decadal to monthly timescales of magma transfer and reservoir growth at a caldera volcano. Nature 482, 77–80. doi:10.1038/nature10706

Ducea, M.N., Saleeby, J.B., Bergantz, G.W., 2015. The architecture, chemistry, and evolution of continental magmatic arcs. Annu. Rev. Earth Planet. Sci. 43, 299–331. doi:10.1146/annurev-earth-060614-105049

Dufek, J., Bachmann, O., 2010. Quantum magmatism: Magmatic compositional gaps generated by melt-crystal dynamics. Geoogy 38, 687–690. doi:10.1130/G30831.1

Egbert, G.D., Booker, J.R., 1986. Robust estimation of geomagnetic transfer-functions. Geophys. J. R. Astr. Soc. 87, 173–194.

Egbert, G.D., Kelbert, A., 2012. Computational recipes for electromagnetic inverse problems. Geophys. J. Int. 189, 251–267. doi:10.1111/j.1365-246X.2011.05347.x

Egbert, G.D., Livelybrooks, D.W., 1996. Single station magnetotelluric impedance estimation: Coherence weighting and the regression M-estimate. Geophysics 61, 964–970. doi:10.1190/1.1444045

Eggert, S., Walter, T.R., 2009. Volcanic activity before and after large tectonic earthquakes: Observations and statistical significance. Tectonophysics 471, 14–26. doi:10.1016/j.tecto.2008.10.003

Elsworth, D., Mattioli, G., Taron, J., Voight, B., Herd, R., 2008. Implications of Magma Transfer Between Multiple Reservoirs on Eruption Cycling. Science (80-.). 322, 246–248. doi:10.1126/science.1161297

Evans, R.L., Chave, A.D., Booker, J.R., 2002. On the importance of offshore data for magnetotelluric studies of ocean-continent subduction systems. Geophys. Res. Lett. 29, 1–4.

Farías, M., Charrier, R., Carretier, S., Martinod, J., Fock, A., Campbell, D., Cáceres, J., Comte, D., 2008. Late Miocene high and rapid surface uplift and its erosional response in the Andes of central Chile (33° – 35° S). Tectonics 27, 1–22. doi:10.1029/2006TC002046

Farías, M., Comte, D., Charrier, R., Martinod, J., David, C., Tassara, A., Tapia, F., Fock, A., 2010. Crustal-scale structural architecture in central Chile based on seismicity and surface geology: Implications for Andean mountain building. Tectonics 29, 1–22. doi:10.1029/2009TC002480

Farrell, J., Smith, R.B., Husen, S., Diehl, T., 2014. Tomography from 26years of seismicity revealing that the spatial extent of the Yellowstone crustal magma reservoir extends well beyond the Yellowstone caldera. Geophys. Res. Lett. 41, 3068–3073. doi:10.1002/2014GL059588.Received

Feigl, K.L., Le Mével, H., Tabrez Ali, S., Cordova, L., Andersen, N.L., DeMets, C., Singer, B.S., 2014. Rapid uplift in Laguna del Maule volcanic field of the Andean Southern Volcanic zone (Chile) 2007-2012. Geophys. J. Int. 196, 885–901. doi:10.1093/gji/ggt438

Fierstein, J., Sruoga, P., Amigo, A., Elissondo, M., 2016. Post-glacial Laguna del Maule: Multi-stage rhyolitic edifices built by >50 eruptive events over 14 kyr, in: Cities on Volcanoes 9. Puerto Varas, Chile.

Fierstein, J., Sruoga, P., Amigo, Á., Elissondo, M., Rosas, M., 2013. Tephra in Argentina establishes postglacial eruptive history of Laguna del Maule volcanic field in Chile, in: IAVCEI 2013 Scientific Assemblyt. Kagoshima, Japan, p. V31F–03.

Folguera, A., Zapata, T., Ramos, V.A., 2006. Late Cenozoic extension and the evolution of the Neuquén Andes, in: Kay, S.M., Ramos, V.A. (Eds.), Evolution of an Andean Margin: A Tectonic and Magmatic View from the Andes to the Neuquén Basin (35-39 S Lat). Geological Society of America, pp. 267–285. doi:10.1130/2006.2407(12).

Fournier, T.J., Pritchard, M.E., Riddick, S.N., 2010. Duration, magnitude, and frequency of subaerial volcano deformation events: New results from Latin America using InSAR and a global synthesis. Geochemistry, Geophys. Geosystems 11, n/a-n/a. doi:10.1029/2009GC002558

Frey, F., Gerlach, D., Hickey, R., Lopez-Escobar, L., Munizaga-Villavicencio, F., 1984. Petrogenesis of the Laguna del Maule volcanic complex, Chile (36 S). Contrib. to Mineral. Petrol. 88, 133–149.

Frost, B.R., Frost, C.D., 2019. Essentials of Igneous and Metamorphic Petrology, 2nd ed. Cambridge Unviersity Press, Cambridge, UK. doi:10.1017/9781108685047

Frost, B.R., Fyfe, W.S., Tazaki, K., Chan, T., 1989. Grain-boundary graphite in rocks and implications for high electrical conductivity in the lower crust. Nature 340, 134–136.

Gabas, A., Marcuello, A., 2003. The relative influence of different types of magnetotelluric data on joint inversions. Earth Planets Sp. 55, 243–248.

Gaillard, F., 2004. Laboratory measurements of electrical conductivity of hydrous and dry silicic melts under pressure. Earth Planet. Sci. Lett. 218, 215–228. doi:10.1016/S0012-821X(03)00639-3

Gallardo, L.A., Meju, M.A., 2011. Structure-coupled Multiphysics Imaging in Geophysical Science. Rev. Geophys. 49, 1–19. doi:10.1029/2010RG000330.1.INTRODUCTION

Gallardo, L.A., Meju, M.A., 2003. Characterization of heterogeneous near-surface materials by joint 2D inversion of dc resistivity and seismic data. Geophys. Res. Lett. 30, 2–5. doi:10.1029/2003GL017370

Gamble, T.D., Goubau, W.M., Clarke, J., 1979. Magnetotellurics with a remote magnetic reference. Geophysics 44, 53–68. doi:10.1190/1.1440923

Gansser, A., 1973. Facts and theories on the Andes. Geol. Soc. London 129, 93–131.

Gao, J., Zhang, H., 2018. An efficient sequential strategy for realizing cross-gradient joint inversion: Method and its application to two-dimensional cross borehole seismic travel time and DC resistivity tomography. Geophys. J. Int. 1–37. doi:10.1093/gji/ggy026/4828334

García-Yeguas, A., Ledo, J., Piña-Varas, P., Prudencio, J., Queralt, P., Marcuello, A., Ibañez, J.M., Benjumea, B., Sánchez-Alzola, A., Pérez, N., 2017. A 3D joint interpretation of magnetotelluric and seismic tomographic models: The case of the volcanic island of Tenerife. Comput. Geosci. 109, 95–105. doi:10.1016/j.cageo.2017.08.003

Garibaldi, N., Tikoff, B., Peterson, D., Davis, J.R., Keranen, K., 2020. Statistical separation of tectonic and inflation-driven components of deformation on silicic reservoirs, Laguna del Maule volcanic field, Chile. J. Volcanol. Geotherm. Res. 389, 106744. doi:10.1016/j.jvolgeores.2019.106744

Gerya, T., 2011. Future directions in subduction modeling. J. Geodyn. 52, 344–378. doi:10.1016/j.jog.2011.06.005

Gilbert, H., Beck, S., Zandt, G., 2006. Lithospheric and upper mantle structure of central Chile and Argentina. Geophys. J. Int. 165, 383–398. doi:10.1111/j.1365-246X.2006.02867.x

Glover, P.W.J., 2010. A generalized Archie's law for n phases. Geophysics 75, 247–265.

Glover, P.W.J., Hole, M.J., Pous, J., 2000. A modified Archie's law for two conducting phases. Earth Planet. Sci. Lett. 180, 369–383. doi:10.1016/S0012-821X(00)00168-0

Goubau, W.M., Maxton, P.M., Koch, R.H., Clarke, J., 1984. Noise correlation lengths in remote reference magnetotellurics. Geophysics 49, 433–438.

Grayver, A. V, 2015. Parallel three-dimensional magnetotelluric inversion using adaptive finite-element

method. Part I: theory and synthetic study. Geophys. J. Int. 202, 584–603. doi:10.1093/gji/ggv165

Gregori, G.P., Lanzerotti, L.J., 1980. Geomagnetic Depth Sounding by Induction Arrow Representation: A Review. Rev. Geophys. Sp. Phys. 18, 203–209.

Groom, R.W., Bailey, R., 1991. Analytic investigations of the effects of near-surface three-dimensional galvanic scatterers on MT tensor decompositions. Geophysics 56, 496–518.

Groom, R.W., Bailey, R.C., 1989. Decomposition of magnetotelluric impedance tensors in the presence of local three-dimensional galvanic distortion. J. Geophys. Res. 94, 1913–1925. doi:10.1029/JB094iB02p01913

Grove, T.L., Till, C.B., Krawczynski, M.J., 2012. The Role of H2O in Subduction Zone Magmatism. Annu. Rev. Earth Planet. Sci. 40, 413–439. doi:10.1146/annurev-earth-042711-105310

Grow, J.A., Bowin, C.O., 1975. Evidence for high-density crust and mantle beneath the Chile Trench due to the descending lithosphere. J. Geophys. Res. 80, 1449–1458.

Guo, X., Li, B., Ni, H., Mao, Z., 2017. Electrical conductivity of hydrous andesitic melts pertinent to subduction zones. J. Geophys. Res. Solid Earth 122, 1777–1788. doi:10.1002/2016JB013524

Guo, X., Yoshino, T., Katayama, I., 2011. Electrical conductivity anisotropy of deformed talc rocks and serpentinites at 3 GPa. Phys. Earth Planet. Inter. 188, 69–81. doi:10.1016/j.pepi.2011.06.012

Guo, X., Zhang, L., Behrens, H., Ni, H., 2016. Probing the status of felsic magma reservoirs: Constraints from the P-T-H2O dependences of electrical conductivity of rhyolitic melt. Earth Planet. Sci. Lett. 433, 54–62. doi:10.1016/j.epsl.2015.10.036

Gutscher, M.-A., 2002. Andean subduction styles and their effect on thermal structure and interplate coupling. J. South Am. Earth Sci. 15, 3–10.

Gutscher, M.-A., Maury, R., Eissen, J.-P., Bourdon, E., 2000. Can slab melting be caused by flat subduction? Geology 28, 535–538.

Haber, E., 2015. Computational Methods in Geophysical Electromagnetics. Society for Industrial and Applied Mathematics, Philadelphia, USA.

Haber, E., 2005. Quasi-Newton methods for large-scale electromagnetic inverse problems. Inverse Probl. 21, 305–323. doi:10.1088/0266-5611/21/1/019

Haber, E., Ascher, U.M., Aruliah, D.A., Oldenburg, D.W., 2000. Fast Simulation of 3D Electromagnetic Problems Using Potentials. J. Comput. Phys. 163, 150–171. doi:10.1006/jcph.2000.6545

Haberland, C., Rietbrock, A., Lange, D., Bataille, K., Dahm, T., 2009. Structure of the seismogenic zone of the southcentral Chilean margin revealed by local earthquake traveltime tomography. J. Geophys. Res. 114, 1–17. doi:10.1029/2008JB005802

Hacker, B.R., 2008. H2O subduction beyond arcs. Geochemistry, Geophys. Geosystems 9, 1–24. doi:10.1029/2007GC001707

Hacker, B.R., Peacock, S.M., Abers, G.A., Holloway, S.D., 2003. Subduction factory 2 . Are intermediate-depth earthquakes in subducting slabs linked to metamorphic dehydration reactions? J. Geophys.

Res. 108, 11-1-11–8. doi:10.1029/2001JB001129

Hall, S., 2018. A Supervolcano with a Cold Heart May Be Brewing in Chile. Sci. Am. 1–17. https://www.scientificamerican.com/article/a-supervolcano-with-a-cold-heart-may-be-brewing-in-chile/ (accessed 27.3.20).

Hamling, I.J., Hreinsdóttir, S., Bannister, S., Palmer, N., 2016. Off-axis magmatism along a subaerial back-arc rift: Observations from the Taupo Volcanic Zone, New Zealand. Sci. Adv. 2, e1600288. doi:10.1126/sciadv.1600288

Hata, M., Oshiman, N., Yoshimura, R., Tanaka, Y., Uyeshima, M., 2015. Three-dimensional electromagnetic imaging of upwelling fluids in the Kyushu subduction zone, Japan. J. Geophys. Res. Solid Earth 120, 1–17. doi:10.1002/2014JB011336.Received

Hayes, G.P., Wald, D.J., Johnson, R.L., 2012. Slab1.0: A three-dimensional model of global subduction zone geometries. J. Geophys. Res. 117, 1–15. doi:10.1029/2011JB008524

Heagy, L.J., Cockett, R., Kang, S., Rosenkjaer, G.K., Oldenburg, D.W., 2017. A framework for simulation and inversion in electromagnetics. Comput. Geosci. 107, 1–19. doi:10.1016/j.cageo.2017.06.018

Healy, D., Rizzo, R.E., Du, M., Farrell, N.J.C., Hole, M.J., Muirhead, D., 2018. Field evidence for the lateral emplacement of igneous dykes: Implications for 3D mechanical models and the plumbing beneath fissure eruptions. Volcanica 1, 85–105.

Heiland, C.A., 1928. Geophysical methods of prospecting with special reference to magnetic, radioactive, and electric methods. J. Geophys. Res. 33, 1–17.

Heise, W., Caldwell, T.G., Bertrand, E.A., Hill, G.J., Bennie, S.L., Palmer, N.G., 2016. Imaging the deep source of the Rotorua and Waimangu geothermal fields, Taupo Volcanic Zone, New Zealand. J. Volcanol. Geotherm. Res. 314, 39–48. doi:10.1016/j.jvolgeores.2015.10.017

Heise, W., Caldwell, T.G., Bibby, H.M., Bennie, S.L., 2010. Three-dimensional electrical resistivity image of magma beneath an active continental rift, Taupo Volcanic Zone, New Zealand. Geophys. Res. Lett. 37, 2–6. doi:10.1029/2010GL043110

Heise, W., Caldwell, T.G., Bibby, H.M., Brown, C., 2006. Anisotropy and phase splits in magnetotellurics. Phys. Earth Planet. Inter. 158, 107–121. doi:10.1016/j.pepi.2006.03.021

Heise, W., Grant Caldwell, T., Bannister, S., Bertrand, E.A., Ogawa, Y., Bennie, S.L., Ichihara, H., 2017. Mapping subduction interface coupling using magnetotellurics: Hikurangi margin, New Zealand. Geophys. Res. Lett. 44, 9261–9266. doi:10.1002/2017GL074641

Heise, W., Pous, J., 2003. Anomalous phases exceeding 90 degrees in magnetotellurics: Anisotropic model studies and a field example. Geophys. J. Int. 155, 308–318. doi:10.1046/j.1365-246X.2003.02050.x

Heit, B., Yuan, X., Bianchi, M., Sodoudi, F., Kind, R., 2008. Crustal thickness estimation beneath the southern central Andes at 30°S and 36°S from S wave receiver function analysis. Geophys. J. Int. 174, 249–254. doi:10.1111/j.1365-246X.2008.03780.x

Held, S., Schill, E., Pavez, M., Díaz, D., Muñoz, G., Morata, D., Kohl, T., 2016. Resistivity distribution from

mid-crustal conductor to near-surface across the 1200 km long Liquiñe-Ofqui Fault System, southern Chile. Geophys. J. Int. 207, 1387–1400.

Hensen, C., Wallmann, K., Schmidt, M., Ranero, C.R., Suess, E., 2004. Fluid expulsion related to mud extrusion off Costa Rica — A window to the subducting slab. Geology 32, 201–204. doi:10.1130/G20119.1

Heredia, N., García-Sansegundo, J., Gallastegui, G., Farias, P., Giacosa, R.E., Giambiagi, L.B., Busquets, P., Colombo, F., Charrier, R., Cuesta, A., Rubio-Ordóñez, A., Ramos, V.A., 2018. Review of the geodynamic evolution of the SW margin of Gondwana preserved in the Central Andes of Argentina and Chile (28 -38 S latitude). J. South Am. Earth Sci. 87, 87–94. doi:10.1016/j.jsames.2017.11.019

Hervé, F., Calderón, M., Fanning, C.M., Pankhurst, R.J., Godoy, E., 2013. Provenance variations in the Late Paleozoic accretionary complex of central Chile as indicated by detrital zircons. Gondwana Res. 23, 1122–1135. doi:10.1016/j.gr.2012.06.016

Hicks, S.P., Rietbrock, A., Haberland, C.A., Ryder, I.M.A., Simons, M., Tassara, A., 2012. The 2010 Mw 8.8 Maule , Chile earthquake : Nucleation and rupture propagation controlled by a subducted topographic high. Geophys. Res. Lett. 39, 1–6. doi:10.1029/2012GL053184

Hicks, S.P., Rietbrock, A., Ryder, I.M.A., Lee, C., Miller, M., 2014. Anatomy of a megathrust: The 2010 M8.8 Maule, Chile earthquake rupture zone imaged using seismic tomography. Earth Planet. Sci. Lett. 405, 142–155. doi:10.1016/j.epsl.2014.08.028

Hickson, C.J., Ferraris, F., Rodriquez, C., Sielfeld, G., Henriquez, R., Gislason, T., Selters, J., Benoit, D., White, P., Southon, J., Ussher, G., Charroy, J., Smith, A., Lovelock, B., Lawless, J., Quinlivan, P., Smith, L., Yehia, R., 2011. The Mariposa Geothermal System , Chile. GRC Trans. 35, 817–826.

Hickson, C.J., Rodríguez, C., Sielfeld, G., Selters, J., Ferraris, F., Henriquez, R., 2010. Mariposa Geothermal System : A Large Geothermal Resource in Central Chile (320MWe inferred). SERNAGEOMIN. https://biblioteca.sernageomin.cl/opac/DataFiles/14127_pp_583_585.pdf (accessed 27.3.20).

Hildreth, W., 2004. Volcanological perspectives on Long Valley, Mammoth Mountain, and Mono Craters: several contiguous but discrete systems. J. Volcanol. Geotherm. Res. 136, 169–198. doi:10.1016/j.jvolgeores.2004.05.019

Hildreth, W., 1981. Gradients in silicic magma chambers: Implications for lithospheric magmatism, Journal of Geophysical Research: Solid Earth. doi:10.1029/JB086iB11p10153

Hildreth, W., Godoy, E., Fierstein, J., Singer, B.S., 2010. Laguna del Maule Volcanic field: eruptive history of a Quaternary basalt-to-rhyolite distributed volcanic field on the Andean range crest in central Chile, Servicio Nacional de Geología y Minería Boletin No. 63. Santiago, Chile.

Hildreth, W., Moorbath, S., 1988. Crustal contributions to arc magmatism in the Andes of central Chile. Contrib. to Mineral. Petrol. 98, 455–489.

Hildreth, W., Singer, B.S., Godoy, E., Munizaga, F., 1998. The Age and Constitution Of Cerro Campanario, a Mafic Stratovolcano In the Andes Of Central Chile. Rev. Geol. Chile 25, 17–28. doi:10.4067/S0716-02081998000100002

Hill, G.J., Bibby, H.M., Ogawa, Y., Wallin, E.L., Bennie, S.L., Caldwell, T.G., Keys, H., Bertrand, E.A., Heise,

W., 2015. Structure of the Tongariro Volcanic system: Insights from magnetotelluric imaging. Earth Planet. Sci. Lett. 432, 115–125. doi:10.1016/j.epsl.2015.10.003

Hill, G.J., Caldwell, T.G., Heise, W., Chertkoff, D.G., Bibby, H.M., Burgess, M.K., Cull, J.P., Cas, R.A.F., 2009. Distribution of melt beneath Mount St Helens and Mount Adams inferred from magnetotelluric data. Nat. Geosci. 2, 785–789. doi:10.1038/ngeo661

Hilton, D.R., Fischer, T.P., Marty, B., 2002. Noble Gases and Volatile Recycling at Subduction Zones. Rev. Mineral. Geochemistry 47, 319–370. doi:10.2138/rmg.2002.47.9

Horton, B.K., Fuentes, F., 2016. Sedimentary record of plate coupling and decoupling during growth of the Andes. Geology 44, 647–650. doi:10.1130/G37918.1

Huang, Y.L., Hwang, R. Der, Jhuang, Y.S., Lin, C.Y., 2017. Rupture features of the 2010 Mw 8.8 Chile earthquake extracted from surface waves. Earth, Planets Sp. 69. doi:10.1186/s40623-017-0624-4

Hübert, J., Whaler, K., Fisseha, S., 2018. The Electrical Structure of the Central Main Ethiopian Rift as Imaged by Magnetotellurics: Implications for Magma Storage and Pathways. J. Geophys. Res. Solid Earth 123, 6019–6032. doi:10.1029/2017JB015160

Hurst, T., Heise, W., Hreinsdottir, S., Hamling, I., 2016. Geophysics of the Taupo Volcanic Zone: A review of recent developments. Geothermics 59, 188–204.

Husen, S., Smith, R.B., Waite, G.P., 2004. Evidence for gas and magmatic sources beneath the Yellowstone volcanic field from seismic tomographic imaging. J. Volcanol. Geotherm. Res. 131, 397–410. doi:10.1016/S0377-0273(03)00416-5

Hyndman, R.D., Yamano, Y., Oleskevich, D.A., 1997. The seismogenic zone of subduction thrust faults. Isl. Arc 6, 244–260.

Introcaso, A., Pacino, M.C., Fraga, H., 1992. Gravity, isostasy and Andean crustal shortening between latitudes 30 and 35'S. Tectonophysics 205, 31–48.

IRIS, 2018. IRIS Interactive earthquake browser: Web interface [WWW Document]. URL https://www.iris.edu/hq/ (accessed 3.5.18).

Iyer, H., 1984. Geophysical Evidence for the Locations , Shapes and Sizes , and Internal Structures of Magma Chambers beneath Regions of Quaternary Volcanism. Philos. Trans. R. Soc. A Math. Phys. Eng. Sci. 310, 473–510.

Jackson, M.D., Blundy, J., Sparks, R.S.J., 2018. Chemical differentiation, cold storage and remobilization of magma in the Earth's crust. Nature 564, 405–409. doi:10.1038/s41586-018-0746-2

Jacques, G., Hoernle, K., Gill, J., 2013. Across-arc geochemical variations in the Southern Volcanic Zone, Chile (34.5–38.0 S): constraints on mantle wedge and slab input compositions. Geochim. Cosmochim. Acta 123, 218–243. doi:10.1016/j.gca.2013.05.016

Jarrard, R.D., 2003. Subduction fluxes of water, carbon dioxide, chlorine, and potassium. Geochemistry, Geophys. Geosystems 4, 1–50. doi:10.1029/2002GC000392

Jellinek, M.A., DePaolo, D.J., 2003. A model for the origin of large silicic magma chambers: precursors of caldera-forming eruptions. Bull. Volcanol. 65, 363–381. doi:10.1007/s00445-003-0277-y

Jiracek, G.R., 1990. Near-surface and topographic distortions in electromagnetic induction. Surv. Geophys. 11, 163–203.

Jiracek, G.R., Gustafson, E.P., Mitchell, P.S., 1983. Magnetotelluric results opposing magma origin of crustal conductors in the Rio Grande Rift. Tectonophysics 94, 299–326.

Jödicke, H., Jording, A., Ferrari, L., Arzate, J., Mezger, K., Rupke, L., 2006. Fluid release from the subducted Cocos plate and partial melting of the crust deduced from magnetotelluric studies in southern Mexico: Implications for the generation of volcanism and subduction dynamics. J. Geophys. Res. 111, 1–22. doi:10.1029/2005JB003739

Jones, A.G., 1999. Imaging the continental upper mantle using electromagnetic methods. Lithos 48, 57–80.

Jones, A.G., 1988. Static shift of magnetotelluric data and its removal in a sedimentary basin environment. Geophysics 53, 967–978.

Jones, A.G., 1983. The problem of current channelling: A critical review. Geophys. Surv. 6, 79–122.

Jones, A.G., Chave, A.D., Egbert, G., Auld, D.O.N., Bahr, K., 1989. A comparison of techniques for magnetotelluric response function estimation. J. Geoph 94, 201–213.

Jordan, T.E., Burns, W.M., Veiga, R., Pangaro, F., Copeland, P., Mpodozis, C., 2001. Extension and basin formation in the southern Andes caused by increased convergence rate. Tectonics 20, 308–424. doi:10.1029/1999TC001181

Jordan, T.E., Isacks, B.L., Allmendinger, R.W., Brewer, J.A., Ramos, V.A., Ando, C.J., 1983. Andean tectonics related to geometry of subducted Nazca plate. Geol. Soc. Am. Bull. 94, 341–361.

Julian, B.R., Pitt, A.M., Foulger, G.R., 1998. Seismic image of a CO2 reservoir beneath a seismically active volcano. Geophys. J. Int. 133, 3–7.

Kalscheuer, T., Juanatey, M.A.G., Meqbel, N., Pedersen, L.B., 2010. Non-linear model error and resolution properties from two-dimensional single and joint inversions of direct current resistivity and radiomagnetotelluric data. Geophys. J. Int. 182, 1174–1188. doi:10.1111/j.1365-246X.2010.04686.x

Kalscheuer, T., Pedersen, L.B., 2007. A non-linear truncated SVD variance and resolution analysis of two-dimensional magnetotelluric models. Geophys. J. Int. 169, 435–447. doi:10.1111/j.1365-246X.2006.03320.x

Kapinos, G., Montahaei, M., Meqbel, N., Brasse, H., 2016. Three-dimensional electrical resistivity image of the South-Central Chilean subduction zone. Tectonophysics 666, 76–89. doi:10.1016/j.tecto.2015.10.016

Karakas, O., Degruyter, W., Bachmann, O., Dufek, J., 2017. Lifetime and size of shallow magma bodies controlled by crustal-scale magmatism. Nat. Geosci. 10, 446–450. doi:10.1038/NGEO2959

Kelbert, A., Egbert, G.D., DeGroot-Hedlin, C., 2012. Crust and upper mantle electrical conductivity beneath the Yellowstone Hotspot Track. Geology 40, 447–450. doi:10.1130/G32655.1

Kelbert, A., Meqbel, N., Egbert, G., Tandon, K., 2014. ModEM: a modular system for inversion of

electromagnetic geophysical data. Comput. Geosci. 66, 40–53. doi:10.1016/j.cageo.2014.01.010

Kendrick, E., Bevis, M., Smalley, R., Brooks, B., Barriga, R., Lauria, E., Fortes, L.P.S., 2003. The Nazca–South America Euler vector and its rate of change. J. South Am. Earth Sci. 16, 125–131. doi:10.1016/S0895-9811(03)00028-2

Kennedy, B.M., Holohan, E.P., Stix, J., Gravley, D.M., Davidson, J.R.J., Cole, J.W., 2018. Magma plumbing beneath collapse caldera volcanic systems. Earth-Science Rev. 177, 404–424. doi:10.1016/j.earscirev.2017.12.002

Keppie, J.D., Ramos, V.A., 1999. Odyssey of terranes in the Iapetus and Rheic oceans during the Paleozoic. Geol. Soc. Am. Spec. Pap. 336, 267–276. doi:10.1130/0-8137-2336-1.267

Keranen, K., Peterson, D.E., Miller, C.A., Garibaldi, N., Tikoff, B., Williams-Jones, G., 2016. Magma-tectonic Interaction at Laguna del Maule, Chile, in: AGU Fall Meeting V53C-3121. San Francisco, CA.

Kerrick, D.M.Y., Connolly, J.A.D., 2001. Metamorphic devolatilization of subducted oceanic metabasalts: implications for seismicity, arc magmatism and volatile recycling. Earth Planet. Sci. Lett. 189, 19–29.

Key, K., 2016. MARE2DEM: a 2-D inversion code for controlled source electromagnetic and magnetotelluric data. Geophys. J. Int. 207, 571–588. doi:10.1093/gji/ggw290

Klügel, A., Longpré, M.A., García-Cañada, L., Stix, J., 2015. Deep intrusions, lateral magma transport and related uplift at ocean island volcanoes. Earth Planet. Sci. Lett. 431, 140–149. doi:10.1016/j.epsl.2015.09.031

Koulakov, I., Kasatkina, E., Shapiro, N.M., Jaupart, C., Vasilevsky, A., El Khrepy, S., Al-Arifi, N., Smirnov, S., 2016. The feeder system of the Toba supervolcano from the slab to the shallow reservoir. Nat. Commun. 7, 12228. doi:10.1038/ncomms12228

Kühn, C., Küster, J., Brasse, H., 2014. Three-dimensional inversion of magnetotelluric data from the Central Andean continental margin. Earth, Planets Sp. 66, 112. doi:10.1186/1880-5981-66-112

Lange, D., Cembrano, J., Rietbrock, A., Haberland, C., Dahm, T., Bataille, K., 2008. First seismic record for intra-arc strike-slip tectonics along the Liquiñe-Ofqui fault zone at the obliquely convergent plate margin of the southern Andes. Tectonophysics 455, 14–24. doi:10.1016/j.tecto.2008.04.014

Larsen, J.C., Mackie, R.L., Manzella, A., Fiordelisi, A., Rieven, S., 1996. Robust smooth magnetotelluric transfer functions. Geophys. J. Int. 124, 801–819. doi:10.1111/j.1365-246X.1996.tb05639.x

Laske, G., Masters, G., Ma, Z., Pasyanos, M.E., 2013. Update on CRUST1.0: A 1-degree Global Model of Earth's Crust, in: EGU2013-2658. Geophys. Res. Abstracts, p. 15.

Lauer, R.M., Saffer, D.M., Harris, R.N., 2017. Links between clay transformation and earthquakes along the Costa Rican subduction margin. Geophys. Res. Lett. 44, 7725–7732. doi:10.1002/2017GL073744

Laumonier, M., Gaillard, F., Muir, D., Blundy, J., Unsworth, M.J., 2017. Giant magmatic water reservoirs at mid-crustal depth inferred from electrical conductivity and the growth of the continental crust. Earth Planet. Sci. Lett. 457, 173–180. doi:10.1016/j.epsl.2016.10.023

Laumonier, M., Gaillard, F., Sifre, D., 2015. The effect of pressure and water concentration on the electrical conductivity of dacitic melts: Implication for magnetotelluric imaging in subduction areas. Chem. Geol. 418, 66–76. doi:10.1016/j.chemgeo.2014.09.019

Lay, T., Kanamori, H., Ammon, C.J., Koper, K.D., Hutko, A.R., Ye, L., Yue, H., Rushing, T.M., 2012. Depth-varying rupture properties of subduction zone megathrust faults. J. Geophys. Res. 117, 1–21. doi:10.1029/2011JB009133

Le Mével, H., Feigl, K.L., Cõrdova, L., DeMets, C., Lundgren, P., 2015. Evolution of unrest at Laguna del Maule volcanic field (Chile) from InSAR and GPS measurements, 2003 to 2014. Geophys. Res. Lett. 42, 6590–6598. doi:10.1002/2015GL064665

Le Mével, H., Gregg, P.M., Feigl, K.L., 2016. Magma injection into a long-lived reservoir to explain geodetically measured uplift: Application to the 2007-2014 unrest episode at Laguna del Maule volcanic field, Chile. J. Geophys. Res. Solid Earth 121, 6092–6108. doi:10.1002/2016JB013066

Lee, B., Unsworth, M.J., Arnason, K., Cordell, D., 2020. Imaging the magmatic system beneath the Krafla geothermal field, Iceland: A new 3-D electrical resistivity model from inversion of magnetotelluric data. Geophys. J. Int. 220, 541–567. doi:10.1093/gji/ggz427

Lee, B.M., Unsworth, M.J., Juliane, H., Richards, J.P., Legault, J.M., 2018. 3D joint inversion of magnetotelluric and airborne tipper data: A case study from the Morrison porphyry Cu–Au–Mo deposit , British. Geophys. Prospect. 66, 397–421. doi:10.1111/1365-2478.12554

Lees, J.M., 2007. Seismic tomography of magmatic systems. J. Volcanol. Geotherm. Res. 167, 37–56. doi:10.1016/j.jvolgeores.2007.06.008

Lezaeta, P., Chave, A.D., Jones, A.G., Evans, R., 2007. Source field effects in the auroral zone: Evidence from the Slave craton (NW Canada). Phys. Earth Planet. Inter. 164, 21–35. doi:10.1016/j.pepi.2007.05.002

Lin, Y.N., Sladen, A., Ortega-culaciati, F., Simons, M., Avouac, J., Fielding, E.J., Brooks, B.A., Bevis, M., Genrich, J., Rietbrock, A., Vigny, C., Smalley, R., Socquet, A., 2013. Coseismic and postseismic slip associated with the 2010 Maule Earthquake, Chile: Characterizing the Arauco Peninsula barrier effect. J. Geophys. Res. 118, 3142–3159. doi:10.1002/jgrb.50207

Lopez-Escobar, L., Cembrano, J., Moreno, H., 1995. Geochemistry and tectonics of the Chilean southern Andes basaltic Quaternary volcanism (37-46°S). Rev. Geol. Chile 22, 219–234. doi:10.5027/andgeoV22n2-a06

Mackie, R., Madden, T., 1993. Three-dimensional magnetotelluric inversion using conjugate gradients. Geophys. J. Int. 215–229.

Mackie, R., Smith, J., Madden, T., 1994. Three-dimensional electromagnetic modeling using finite difference equations: The magnetotelluric example. Radio Sci. 29, 923–935.

Madden, T., Nelson, P., 1964. A Defense of Cagniard's Magnetotelluric Method. Magnetotelluric Methods 89–102.

Madden, T.M., Mackie, R.L., 1989. Three-dimensional magnetotelluric modelling and inversion. Proc. IEEE 77, 318–333. doi:10.1109/5.18628

Madden, T.R., 1964. Spectral, cross-spectral, and bispectral analysis of low frequency electromagnetic data, in: Bleil, D.F. (Ed.), Natural Electromagnetic Phenomena Below 30 Kc/S. Springer US, Boston, MA, pp. 429–450.

Magee, C., Muirhead, J.D., Karvelas, A., Holford, S.P., Jackson, C.A.L., Bastow, I.D., Schofield, N., Stevenson, C.T.E., McLean, C., McCarthy, W., Shtukert, O., 2016. Lateral magma flow in mafic sill complexes. Geosphere 12, 809–841. doi:10.1130/GES01256.1

Magee, C., Stevenson, C.T.E., Ebmeier, S.K., Keir, D., Hammond, J.O.S., Gottsmann, J.H., Whaler, K.A., Schofield, N., Jackson, C.A., Petronis, M.S., Driscoll, B.O., Morgan, J., Cruden, A., Vollgger, S.A., Dering, G., Micklethwaite, S., Jackson, M.D., 2018. Magma plumbing systems: A geophysical perspective. J. Petrol. 0, 1–35. doi:10.1093/petrology/egy064

Maksymowicz, A., Tréhu, A.M., Contreras-reyes, E., Ruiz, S., 2015. Density-depth model of the continental wedge at the maximum slip segment of the Maule Mw 8.8 megathrust earthquake. Earth Planet. Sci. Lett. 409, 265–277. doi:10.1016/j.epsl.2014.11.005

Manea, V.C., Marta, P.G., Manea, M., 2012. Chilean flat slab subduction controlled by overriding plate thickness and trench rollback. Geology 40, 35–38. doi:10.1130/G32543.1

Manga, M., Brodsky, E., 2006. Seismic triggering of eruptions in the far field: Volcanoes and Geysers. Annu. Rev. Earth Planet. Sci. 34, 263–291. doi:10.1146/annurev.earth.34.031405.125125

Mardia, K., 1972. Statistics of Directional Data, Probability and Mathematical Statistics: A Series of Monographs and Textbooks. Academic Press. doi:10.1016/B978-0-12-471150-1.50008-X

Martínez, J.C., Dristas, J.A., Massonne, H.-J., 2012. Palaeozoic accretion of the microcontinent Chilenia, North Patagonian Andes: high-pressure metamorphism and subsequent thermal relaxation. Int. Geol. Rev. 54, 472–490. doi:10.1080/00206814.2011.569411

Marzocchi, W., Casarotti, E., Piersanti, A., 2002. Modeling the stress variations induced by great earthquakes on the largest volcanic eruptions of the 20th century. J. Geophys. Res. Solid Earth 107, ESE 13-1-ESE 13-8. doi:10.1029/2001JB001391

Matsuno, T., Chave, A.D., Jones, A.G., Muller, M.R., Evans, R.L., 2014. Robust magnetotelluric inversion. Geophys. J. Int. 196, 1365–1374. doi:10.1093/gji/ggt484

Maxwell, J.C., 1873. A treatise on electricity and magnetism, Vol I. Cambridge Unviersity Press, Cambridge, UK.

McGary, R., Evans, R., Wannamaker, P.E., 2014. Pathway from subducting slab to surface for melt and fluids beneath Mount Rainier. Nature 511, 338–40. doi:10.1038/nature13493

McNeice, G., Jones, A.G., 2001. Multisite, multifrequency tensor decomposition of magnetotelluric data. Geophysics 66, 158–173.

Meju, M.A., 2009. Regularized extremal bounds analysis (REBA): An approach to quantifying uncertainty in nonlinear geophysical inverse problems. Geophys. Res. Lett. 36, 1–5. doi:10.1029/2008GL036407

Meju, M.A., 2002. Geoelectromagnetic exploration for natural resources: Models, case studies and

challenges. Surv. Geophys. 23, 133–205.

Miensopust, M.P., 2017. Application of 3-D EM Inversion in Practice: Challenges, pitfalls and solution approaches. Surv. Geophys. 38, 869–933. doi:10.1007/s10712-017-9435-1

Miensopust, M.P., Jones, A.G., Hersir, G.P., Vilhjálmsson, A.M., 2014. The Eyjafjallajökull volcanic system, Iceland: Insights from electromagnetic measurements. Geophys. J. Int. 199, 1187–1204. doi:10.1093/gji/ggu322

Miensopust, M.P., Queralt, P., Jones, A.G., Modellers, 3D MT, 2013. Magnetotelluric 3-D inversion—a review of two successful workshops on forward and inversion code testing and comparison. Geophys. J. Int. 193, 1216–1238. doi:10.1093/gji/ggt066

Miller, C.A., Le Mével, H., Currenti, G., Williams-Jones, G., Tikoff, B., 2017a. Microgravity changes at the Laguna del Maule volcanic field: Magma-induced stress changes facilitate mass addition. J. Geophys. Res. Solid Earth 1–18. doi:10.1002/2017JB014048

Miller, C.A., Williams-Jones, G., Fournier, D., Witter, J., 2017b. 3D gravity inversion and thermodynamic modelling reveal properties of shallow silicic magma reservoir beneath Laguna del Maule, Chile. Earth Planet. Sci. Lett. 459, 14–27. doi:10.1016/j.epsl.2016.11.007

Miller, R.L., Kahn, J.S., 1962. Statistical Analysis in the Geological Sciences. John Wiley & Sons, Ltd, New York.

Moorkamp, M., 2017. Integrating Electromagnetic Data with Other Geophysical Observations for Enhanced Imaging of the Earth : A Tutorial and Review. Surv. Geophys. doi:10.1007/s10712-017-9413-7

Moorkamp, M., Jones, A.G., Fishwick, S., 2010. Joint inversion of receiver functions, surface wave dispersion, and magnetotelluric data. J. Geophys. Res. Solid Earth 115, 1–23. doi:10.1029/2009JB006369

Moreno, M., Haberland, C., Oncken, O., Rietbrock, A., Angiboust, S., Heidbach, O., 2014. Locking of the Chile subduction zone controlled by fluid pressure before the 2010 earthquake. Nat. Geosci. 7, 292–296. doi:10.1038/NGEO2102

Moreno, M., Li, S., Melnick, D., Bedford, J., Baez, J., Motagh, M., Metzger, S., Vajedian, S., Sippl, C., Gutknecht, B., Contreras-reyes, E., Deng, Z., Tassara, A., Oncken, O., 2018. Chilean megathrust earthquake recurrence linked to frictional contrast at depth. Nat. Geosci. 11, 285–290. doi:10.1038/s41561-018-0089-5

Moreno, M., Melnick, D., Rosenau, M., Baez, J., Klotz, J., Oncken, O., Tassara, A., Chen, J., Bataille, K., Bevis, M., Socquet, A., Bolte, J., Vigny, C., Brooks, B., Ryder, I., Grund, V., Smalley, B., Carrizo, D., Bartsch, M., Hase, H., 2012. Toward understanding tectonic control on the Mw 8.8 2010 Maule Chile earthquake. Earth Planet. Sci. Lett. 321–322, 152–165. doi:10.1016/j.epsl.2012.01.006

Moscoso, E., Grevemeyer, I., Contreras-reyes, E., Flueh, E.R., Dzierma, Y., Rabbel, W., Thorwart, M., 2011. Revealing the deep structure and rupture plane of the 2010 Maule, Chile earthquake (Mw = 8.8) using wide angle seismic data. Earth Planet. Sci. Lett. 307, 147–155. doi:10.1016/j.epsl.2011.04.025

Mpodozis, C., Ramos, V.A., 1989. The Andes of Chile and Argentina, in: Ericksen, G.E., Cañas Pinochet, M.T., Reinemund, J.A. (Eds.), Geology of the Andes and Its Relation to Hydrocarbon and Mineral Resources. Circum-Pacific Council for Energy and Mineral Resources Earth Science Series, Houston, TX, pp. 59–90. doi:10.1016/j.aqpro.2013.07.003

Muñoz, G., 2014. Exploring for Geothermal Resources with Electromagnetic Methods. Surv. Geophys. 35, 101–122. doi:10.1007/s10712-013-9236-0

Muñoz, M., Fournier, H., Mamani, M., Febrer, J., Borzotta, E., Maidana, A., 1990. A comparative study of results obtained in magnetotelluric deep soundings in Villarrica active volcano zone (Chile) with gravity investigations , distribution of earthquake foci, heat flow empirical relationships, isotopic geochemistry 87Sr / 86Sr and sys. Phys. Earth Planet. Inter. 60, 195–211.

Murphy, B.S., Egbert, G.D., 2019. Synthesizing seemingly contradictory seismic and magnetotelluric observations in the southeastern United States to image physical properties of the lithosphere. Geochemistry, Geophys. Geosystems 20, 2606–2625. doi:10.1029/2019GC008279

Nelson, K.D., Zhao, W., Brown, L.D., Kuo, J., Che, J., Liu, X., Klemperer, S.L., Makovsky, Y., Meissner, R., Mechie, J., Kind, R., Wenzel, F., Ni, J., Nabelek, J., Leshou, C., Tan, H., Wei, W., Jones, A.G., Booker, J., Unsworth, M.J., Kidd, W.S.F., Hauck, M., Alsdorf, D., Ross, A., Cogan, M., Wu, C., Sandvol, E., Edwards, M., 1996. Partially Molten Middle Crust Beneath Southern Tibet: Synthesis of Project INDEPTH Results. Sci. Reports 274, 1684–1688. doi:10.1126/science.274.5293.1684

Nesbitt, B.E., 1993. Electrical resistivities of crustal fluids. J. Geophys. Res. 98, 4301–4310.

Newman, G.A., Alumbaugh, D.L., 2000. Three-dimensional magnetotelluric inversion using non-linear conjugate gradients. Geophys. J. Int. 140, 410–424.

Newman, G.A., Alumbaugh, D.L., 1997. Three-dimensional massively parallel electromagnetic inversion-I . Theory. Geophys. J. Int. 128, 345–354.

Newman, G.A., Wannamaker, P.E., Hohmann, G., 1985. On the detectability of crustal magma chambers using the magnetotelluric method. Geophysics 50, 1136–1143.

Ni, H., Keppler, H., Behrens, H., 2011. Electrical conductivity of hydrous basaltic melts: implications for partial melting in the upper mantle. Contrib. to Mineral. Petrol. 637–650. doi:10.1007/s00410-011-0617-4

Nover, G., 2005. Electrical properties of crustal and mantle rocks - A review of laboratory measurements and their explanation. Surv. Geophys. 26, 593–651. doi:10.1007/s10712-005-1759-6

Ogawa, Y., Ichiki, M., Kanda, W., Mishina, M., Asamori, K., 2014. Three-dimensional magnetotelluric imaging of crustal fluids and seismicity around Naruko volcano, NE Japan. Earth Planets Sp. 66, 1–13.

Okazaki, K., Hirth, G., 2016. Dehydration of lawsonite could directly trigger earthquakes in subducting oceanic crust. Nature 530, 81–84. doi:10.1038/nature16501

Pallares, C., Quidelleur, X., Gillot, P.Y., Kluska, J.M., Tchilinguirian, P., Sarda, P., 2016. The temporal evolution of back-arc magmas from the Auca Mahuida shield volcano (Payenia Volcanic Province, Argentina). J. Volcanol. Geotherm. Res. 323, 19–37. doi:10.1016/j.jvolgeores.2016.04.043

Pardo-Casas, F., Molnar, P., 1987. Relative motion of the Nazca (Farallon) and South American plates since late Cretaceous time. Tectonics 6, 233–248.

Parker, R.L., 2011. New analytic solutions for the 2-D TE mode MT problem. Geophys. J. Int. 186, 980–986. doi:10.1111/j.1365-246X.2011.05091.x

Parker, R.L., 2010. Can a 2-D MT frequency response always be interpreted as a 1-D response? Geophys. J. Int. 181, 269–274. doi:10.1111/j.1365-246X.2010.04512.x

Parker, R.L., 1994. Geophysical Inverse Theory. Princeton University Press, Princeton, NJ.

Parker, R.L., 1980. The inverse problem of electromagnetic induction: existence and construction of solutions based on incomplete data. J. Geophys. Res. Solid Earth 85, 4421–4428.

Parker, R.L., 1977. Understanding inverse theory. Annu. Rev. Earth Planet. Sci. 35–64.

Parker, R.L., Booker, J., 1996. Optimal one-dimensional inversion and bounding of magnetotelluric apparent resistivity and phase measurements. Phys. Earth Planet. Inter. 9201.

Parker, R.L., Whaler, K., 1981. Numerical methods for establishing solutions to the inverse problem of electromagnetic induction. J. Geophys. Res. Solid Earth 86, 9574–9584.

Parmigiani, A., Faroughi, S., Huber, C., Bachmann, O., Su, Y., 2016. Bubble accumulation and its role in the evolution of magma reservoirs in the upper crust. Nature 532, 492–494. doi:10.1038/nature17401

Peacock, S.M., 1990. Fluid processes in subduction zones. Science 248, 329–337.

Pesicek, J.D., Engdahl, E.R., Thurber, C.H., DeShon, H.R., Lange, D., 2012. Mantle subducting slab structure in the region of the 2010 M8.8 Maule earthquake (30-40°S), Chile. Geophys. J. Int. 191, 317–324. doi:10.1111/j.1365-246X.2012.05624.x

Peterson, D.E., Keranen, K., Garibaldi, N., Lara, L., Tikoff, B., Tassara, A., Thurber, C.H., Lanza, F., 2018. Pulsed magmatic inflation and deflation in a silicic system facilitated by trapdoor faulting: Laguna del Maule, Chile, in: AGU Fall Meeting V23C-02. Washington D.C.

Petiau, G., 2000. Second Generation of Lead-lead Chloride Electrodes for Geophysical Applications. Pure Appl. Geophys. 157, 357–382. doi:10.1007/s000240050004

Petrelli, M., El Omari, K., Spina, L., Le Guer, Y., La Spina, G., Perugini, D., 2018. Timescales of water accumulation in magmas and implications for short warning times of explosive eruptions. Nat. Commun. 9. doi:10.1038/s41467-018-02987-6

Piña-Varas, P., Ledo, J., Queralt, P., Marcuello, A., Bellmunt, F., Hidalgo, R., Messeiller, M., 2014. 3-D Magnetotelluric Exploration of Tenerife Geothermal System (Canary Islands, Spain). Surv. Geophys. 35, 1045–1064. doi:10.1007/s10712-014-9280-4

Piña-Varas, P., Ledo, J., Queralt, P., Marcuello, A., Perez, N., 2018. On the detectability of Teide volcano magma chambers (Tenerife, Canary Islands) with magnetotelluric data. Earth, Planets Sp. 70, 1–11. doi:10.1186/s40623-018-0783-y

Plümper, O., John, T., Podladchikov, Y.Y., Vrijmoed, J.C., Scambelluri, M., 2017. Fluid escape from

subduction zones controlled by channel-forming reactive porosity. Nat. Geosci. 10, 150–156. doi:10.1038/NGEO2865

Poli, S., Schmidt, M.W., 1995. H2O transport and release in subduction zones: Experimental constraints on basaltic and andesitic systems. J. Geophys. Res. 100, 299–314.

Pommier, A., 2014. Interpretation of magnetotelluric results using laboratory measurements. Surv. Geophys. 35, 41–84. doi:10.1007/s10712-013-9226-2

Pommier, A., Evans, R.L., 2017. Constraints on fluids in subduction zones from electromagnetic data. Geosphere 13, 1–16. doi:10.1130/GES01473.1

Pommier, A., Le-Trong, E., 2011. "SIGMELTS": A web portal for electrical conductivity calculations. Comput. Geosci. 37, 1450–1459. doi:10.1016/j.cageo.2011.01.002

Portner, D.E., Beck, S.L., Zandt, G., Scire, A., 2017. The nature of subslab slow velocity anomalies beneath South America. Geophys. Res. Lett. 44, 4747–4755. doi:10.1002/2017GL073106

Pous, J., Heise, W., Schnegg, P.A., Muoz, G., Martí, J., Soriano, C., 2002. Magnetotelluric study of the Las Cañadas caldera (Tenerife, Canary Islands): Structural and hydrogeological implications. Earth Planet. Sci. Lett. 204, 249–263. doi:10.1016/S0012-821X(02)00956-1

Price, A.T., 1962. The theory of magnetotelluric methods when the source field is considered. J. Geophys. Res. 67, 1907–1918. doi:10.1029/JZ067i005p01907

Primdahl, F., 1979. The fluxgate magnetometer. J. Phys. E. 12.

Pritchard, M.E., Gregg, P.M., 2016. Geophysical evidence for silicic crustal melt in the continents: Where, what kind, and how much? Elements 12, 121–127. doi:10.2113/gselements.12.2.121

Pritchard, M.E., Jay, J.A., Aron, F., Henderson, S.T., Lara, L.E., 2013. Subsidence at southern Andes volcanoes induced by the 2010 Maule, Chile earthquake. Nat. Geosci. 6, 632–636. doi:10.1038/ngeo1855

Pritchard, M.E., Silva, S.L. De, Michelfelder, G., Zandt, G., Mcnutt, S.R., Gottsmann, J., West, M.E., Blundy, J., Christensen, D.H., Finnegan, N.J., Minaya, E., Sparks, R.S.J., Sunagua, M., Unsworth, M.J., Alvizuri, C., Comeau, M.J., Del Potro, R., Diaz, D., Diez, M., Farrell, A., Henderson, S.T., Jay, J.A., Lopez, T., Legrand, D., Naranjo, J.A., McFarlin, H., Muir, D., Perkins, J.P., Spica, Z., Wilder, A., Ward, K.M., 2018. Synthesis: PLUTONS: Investigating the relationship between pluton growth and volcanism in the Central Andes. Geosphere 14, 954–982. doi:10.1130/GES01578.1

Pritchard, M.E., Simons, M., 2004. An InSAR-based survey of volcanic deformation in the southern Andes. Geophys. Res. Lett. 31, 1–4. doi:10.1029/2004GL020545

Ramos, V.A., 1999. Plate tectonic setting of the Andean Cordillera. Episodes 22, 183–190.

Ramos, V.A., Folguera, A., 2011. Payenia volcanic province in the Southern Andes: An appraisal of an exceptional Quaternary tectonic setting. J. Volcanol. Geotherm. Res. 201, 53–64. doi:10.1016/j.jvolgeores.2010.09.008

Ramos, V.A., Folguera, A., 2009. Andean flat-slab subduction through time. Geol. Soc. London 327, 31–54. doi:10.1144/SP327.3

Ramos, V.A., Kay, S.M., 2006. Overview of the tectonic evolution of the southern Central Andes of Mendoza and Neuquén (35 ° – 39 ° S latitude). Geol. Soc. Am. Spec. Pap. 407, 1–17. doi:10.1130/2006.2407(01).

Ramos, V.A., Litvak, V.D., Folguera, A., Spagnuolo, M., 2014. An Andean tectonic cycle: From crustal thickening to extension in a thin crust (34°-37° SL). Geosci. Front. 5, 351–367. doi:10.1016/j.gsf.2013.12.009

Ranero, C.R., Morgan, J.P., Mcintosh, K., Reichert, C., 2003. Bending-related faulting and mantle serpentinization at the Middle America trench. Nature 425, 367–373.

Ranganayaki, R.P., 1984. An interpretive analysis of magnetotelluric data. Geophysics 49, 1730–1748.

Rawlinson, N., Pozgay, S., Fishwick, S., 2010. Seismic tomography: A window into deep Earth. Phys. Earth Planet. Inter. 178, 101–135. doi:10.1016/j.pepi.2009.10.002

Revil, A., 2013. On charge accumulation in heterogeneous porous rocks under the influence of an external electric field. Geophysics 78, 271–291.

Reyes-Wagner, V., Díaz, D., Cordell, D., Unsworth, M.J., 2017. Regional electrical structure of the Andean subduction zone in central Chile (35° – 36°S) using magnetotellurics. Earth, Planets Sp. 69, 1–9. doi:10.1186/s40623-017-0726-z

Richards, D.R., 1995. Terranes and tectonic evolution of the Andes: a regional synthesis. Unviersity of Arizona. doi:10.16953/deusbed.74839

Rietbrock, A., Ryder, I., Hayes, G., Haberland, C., Comte, D., Roecker, S., Lyon-Caen, H., 2012. Aftershock seismicity of the 2010 Maule Mw=8.8, Chile, earthquake: Correlation between co-seismic slip models and aftershock distribution? Geophys. Rese 39, 2–6. doi:10.1029/2012GL051308

Robertson, K., Thiel, S., Meqbel, N., 2020. Quality over quantity: on workflow and model space exploration of 3D inversion of MT data. Earth, Planets Sp. 72. doi:10.1186/s40623-019-1125-4

Robock, A., 2000. Volcanic eruptions and climate. Rev. Geophys. 38, 191–219.

Rodi, W., Mackie, R.L., 2001. Nonlinear conjugate gradients algorithm for 2-D magnetotelluric inversion. Geophysics 66, 174–187. doi:10.1190/1.1444893

Rojas-Vera, E.A., Folguera, A., Zamora, G., Bottesi, G., Ramos, V.A., 2014. Structure and development of the Andean system between 36 and 39 S. J. Geodyn. 73, 34–52. doi:10.1016/j.jog.2013.09.001

Rojas-Vera, E.A., Sellés, D., Folguera, A., Gímenez, M., Ruíz, F., Orts, D., Zamora Valcarce, G., Martínez, P., Bechis, F., Ramos, V.A., 2014. The origin of the Loncopué Trough in the retroarc of the Southern Central Andes from field, geophysical and geochemical data. Tectonophysics 637, 1–19. doi:10.1016/j.tecto.2014.09.012

Rosas-Carbajal, M., Linde, N., Kalscheuer, T., Vrugt, J.A., 2014. Two-dimensional probabilistic inversion of plane-wave electromagnetic data: Methodology , model constraints and joint inversion with electrical resistivity data. Geophys. J. Int. 196, 1508–1524. doi:10.1093/gji/ggt482.

Rosenberg, C., Handy, M., 2005. Experimental deformation of partially melted granite revisited: implications for the continental crust. J. Metamorph. Geol. 24, 19–28. doi:10.1111/j.1525-

1314.2005.00555.x

Ruegg, J.C., Rudloff, A., Vigny, C., Madariaga, R., Chabalier, J.B. De, Campos, J., 2009. Interseismic strain accumulation measured by GPS in the seismic gap between Constitución and Concepción in Chile. Phys. Earth Planet. Inter. 175, 78–85. doi:10.1016/j.pepi.2008.02.015

Ruiz, S., Madariaga, R., 2018. Historical and recent large megathrust earthquakes in Chile. Tectonophysics 733, 37–56. doi:10.1016/j.tecto.2018.01.015

Saffer, D.M., 2017. Mapping fluids to subduction megathrust locking and slip behavior. Geophys. Res. Lett. 44, 9337–9340. doi:10.1002/2017GL075381

Samrock, F., Grayver, A. V, Eysteinsson, H., Saar, M.O., 2018. Magnetotelluric image of transcrustal magmatic system beneath the Tulu Moye Geothermal Prospect in the Ethiopian Rift. Geophys. Res. Lett. 45, 12847–12855. doi:10.1029/2018GL080333

Samrock, F., Kuvshinov, A., Bakker, J., Jackson, A., Fisseha, S., 2015. 3-D analysis and interpretation of magnetotelluric data from the Aluto-Langano geothermal field, Ethiopia. Geophys. J. Int. 202, 1923–1948. doi:10.1093/gji/ggv270

Scambelluri, M., Pennacchioni, G., Gilio, M., Bestmann, M., Plümper, O., Nestola, F., 2017. Fossil intermediate-depth earthquakes in subducting slabs linked to differential stress release. Nat. Geosci. 10, 960–967. doi:10.1038/s41561-017-0010-7

Schellart, W.P., Rawlinson, N., 2013. Global correlations between maximum magnitudes of subduction zone interface thrust earthquakes and physical parameters of subduction zones. Phys. Earth Planet. Inter. 225, 41–67. doi:10.1016/j.pepi.2013.10.001

Scherwath, M., Contreras-Reyes, E., Flueh, E.R., Grevemeyer, I., Krabbenhoeft, A., Papenberg, C., Petersen, C.J., Weinrebe, R.W., 2009. Deep lithospheric structures along the southern central Chile margin from wide-angle P-wave modelling. Geophys. J. Int. 179, 579–600. doi:10.1111/j.1365-246X.2009.04298.x

Schilling, F.R., Partzsch, G.M., Brasse, H., Schwarz, G., 1997. Partial melting below the magmatic arc in the central Andes deduced from geoelectromagnetic field experiments and laboratory data. Phys. Earth Planet. Inter. 103, 17–31. doi:10.1016/S0031-9201(97)00011-3

Schilling, F.R., Trumbull, R.B., Brasse, H., Haberland, C., Asch, G., Bruhn, D., Mai, K., Haak, V., Giese, P., Muñoz, M., Ramelow, J., Rietbrock, A., Ricaldi, E., Vietor, T., 2006. Partial Melting in the Central Andean Crust: a Review of Geophysical , Petrophysical , and Petrologic Evidence, in: Oncken, O., Chong, G., Franz, G., Giese, P., Götze, H., Ramos, V.A. (Eds.), The Andes. Springer Berlin Heidelberg, pp. 459–474.

Schmandt, B., Jiang, C., Farrell, J., 2019. Seismic perspectives from the western U.S. on magma reservoirs underlying large silicic calderas. J. Volcanol. Geotherm. Res. 384, 158–178. doi:10.1016/j.jvolgeores.2019.07.015

Schmidt, M.W., Poli, S., 1998. Experimentally based water budgets for dehydrating slabs and consequences for arc magma generation. Earth Planet. Sci. Lett. 163, 361–379.

Schnaidt, S., Heinson, G., 2015. Bootstrap resampling as a tool for uncertainty analysis in 2-D

magnetotelluric inversion modelling. Geophys. J. Int. 203, 92–106. doi:10.1093/gji/ggv264

Schöpa, A., Annen, C., 2013. The effects of magma flux variations on the formation and lifetime of large silicic magma chambers. J. Geophys. Res. Solid Earth 118, 926–942. doi:10.1002/jgrb.50127

Schurr, B., Asch, G., Rietbrock, A., Trumbull, R., Haberland, C., 2003. Complex patterns of fluid and melt transport in the central Andean subduction zone revealed by attenuation tomography. Earth Planet. Sci. Lett. 215, 105–119. doi:10.1016/S0012-821X(03)00441-2

Schwarz, G., Krüger, D., 1997. Resistivity cross section through the southern central Andes as inferred from magnetotelluric and geomagnetic deep soundings. J. Geophys. Res. 102, 11957. doi:10.1029/96JB03626

Self, S., 2006. The effects and consequences of very large explosive volcanic eruptions. Philos. Trans. R. Soc. A Math. Phys. Eng. Sci. 364, 2073–2097. doi:10.1098/rsta.2006.1814

Selway, K., Thiel, S., Key, K., 2012. A simple 2-D explanation for negative phases in TE magnetotelluric data. Geophys. J. Int. 188, 945–958. doi:10.1111/j.1365-246X.2011.05312.x

Sentman, D.D., 1996. Schumann resonance spectra in a two-scale-height Earth-ionosphere cavity. J. Geophys. Res. 101, 9479–9487.

Shalivahan, N., Bhattacharya, B.B., 2002. How remote can the far remote reference site for magnetotelluric measurements be? J. Geophys. Res. 107, 1–7. doi:10.1029/2000JB000119

Sherburn, S., Bannister, S., Bibby, H., 2003. Seismic velocity structure of the central Taupo Volcanic Zone, New Zealand, from local earthquake tomography. J. Volcanol. Geotherm. Res. 122, 69–88. doi:10.1016/S0377-0273(02)00470-5

Simpson, F., Bahr, K., 2005. Practical Magnetotellurics. Cambridge Unviersity Press, Cambridge, UK.

Sims, W.E., Bostick, F.X., Smith, H.W., 1971. The estimation of the magnetotelluric impedance tensor elements from measured data. Geophysics 36, 938–942.

Singer, B.S., Andersen, N., Le Mével, H., Feigl, K.L., DeMets, C., Tikoff, B., Thurber, C.H., Jicha, B.R., Cardona, C., Córdova, L., Gil, F., Unsworth, M.J., William-Jones, G., Miller, C.A., Fierstein, J., Hildreth, W., Vazquez, J., 2014. Dynamics of a large, restless, rhyolitic magma system at Laguna del Maule, southern Andes, Chile. GSA Today 4–11. doi:10.1130/GSATG216A.1.

Singer, B.S., Hildreth, W., Vincze, Y., 2000. 40Ar/39Ar evidence for early deglaciation of the central Chilean Andes. Geophys. Res. Lett. 27, 1663–1666.

Singer, B.S., Mével, H. Le, Licciardi, J.M., Córdova, L., Tikoff, B., Garibaldi, N., Andersen, N.L., Diefenbach, A.K., Feigl, K.L., 2018. Geomorphic expression of rapid Holocene silicic magma reservoir growth beneath Laguna del Maule, Chile. Sci. Adv. 4, 1–10.

Singer, B.S., Thompson, R.A., Dungan, M.A., Feeley, T.C., Nelson, S.T., Pickens, J., LL, B., Wulff, A., Davidson, J.P., Metzger, J., 1997. Volcanism and erosion during the past 930 ky at the Tatara–San Pedro complex, Chilean Andes. GSA Bull. 109, 127–142.

Siripunvaraporn, W., 2012. Three-dimensional magnetotelluric inversion: an introductory guide for developers and users. Surv. Geophys. 33, 5–27. doi:10.1007/s10712-011-9122-6

Siripunvaraporn, W., Egbert, G., 2009. WSINV3DMT: vertical magnetic field transfer function inversion and parallel implementation. Phys. Earth Planet. Inter. 173, 317–329. doi:10.1016/j.pepi.2009.01.013

Slezak, K., Jozwiak, W., Nowozynski, K., Orynski, S., Brasse, H., 2018. 3-D studies of MT data in the Central Polish Basin: Influence of inversion parameters , model space and transfer function selectioN. J. Appl. Geophys. 161, 26–36. doi:10.1016/j.jappgeo.2018.11.008

Small, C., Naumann, T., 2001. The global distribution of human population and recent volcanism. Environ. Hazards 3, 93–109.

Smith, J.T., 1996. Conservative modeling of 3-D electromagnetic fields, Part I: Properties and error analysis. Geophysics 61, 1319–1324. doi:10.1190/1.1444055

Sodoudi, F., Yuan, X., Asch, G., Kind, R., 2011. High-resolution image of the geometry and thickness of the subducting Nazca lithosphere beneath northern Chile. J. Geophys. Res. 116, 1–11. doi:10.1029/2010JB007829

Sorey, M.L., McConnell, V.S., Roeloffs, E., 2003. Summary of recent research in Long Valley Caldera, California. J. Volcanol. Geotherm. Res. 127, 165–173. doi:10.1016/S0377-0273(03)00168-9

Soyer, W., Unsworth, M.J., 2006. Deep electrical structure of the northern Cascadia (British Columbia, Canada) subduction zone: Implications for the distribution of fluids. Geology 34, 53–56. doi:10.1130/G21951.1

Sparks, R.S.J., Annen, C., Blundy, J.D., Cashman, K. V, Rust, A.C., Jackson, M.D., 2019. Formation and dynamics of magma reservoirs. Philos. Trans. R. Soc. A Math. Phys. Eng. Sci. 377, 1–30. doi:http://dx.doi.org/10.1098/rsta.2018.0019

Sruoga, P., Elissondo, M., Fierstein, J., García, S., González, R., Rosas, M., 2015. Actividad explosiva postglacial del centro Barrancas, Complejo Volcanico Laguna del Maule (36 05’ S, 70 30’ O). Peligrosidad en Argentina, in: XIV Congreso Geológico Chileno. La Serena, Chile, pp. 49–52.

Stankiewicz, J., Ryberg, T., Haberland, C., Fauzi, N., Natawidjaja, D., 2010. Lake Toba volcano magma chamber imaged by ambient seismic noise tomography. Geophys. Res. Lett. 37, 3–7. doi:10.1029/2010GL044211

Stanley, W.D., Blakely, R.J., 1995. The Geysers-Clear Lake Geothermal Area, California - An updated geophysical perspective of heat sources. Geothermics 24, 187–221.

Stanley, W.D., Tinkler, R.D., 1983. A practical, low-noise coil system for magnetotellurics. United States Geological Survey, Report 83-85, Denver, CO.

Stechern, A., Just, T., Holtz, F., Namur, O., Blume-Oeste, M., 2017. Decoding magma plumbing and geochemical evolution beneath the Lastarria Volcanic Complex (Northern Chile): Evidence for multiple magma storage regions. J. Volcanol. Geotherm. Res. 338, 25–45. doi:10.1016/j.jvolgeores.2017.03.018

Stern, R.J., 2002. Subduction zones. Rev. Geophys. 40, 1012. doi:10.1029/2001RG000108

Sternberg, B.K., Washburne, J.C., Pellerin, L., 1988. Correction for the static shift in magnetotellurics

using transient electromagnetic soundings. Geophysics 53, 1459–1468.

Swift, C.M., 1967. A magnetotelluric investigation of an electrical conductivity anomaly in the southwestern United States. PhD Thesis. Massachussetts Institute of Technology.

Szarka, L., 1987. Geophysical aspects of man-made electromagnetic noise in the earth-A review. Surv. Geophys. 9, 287–318. doi:10.1007/BF01901627

Szarka, L., Menvielle, M., 1997. Analysis of rotational invariants of the magnetotelluric impedance tensor. Geophys. J. Int. 129, 133–142. doi:10.1111/j.1365-246X.1997.tb00942.x

Szymanowski, D., Wotzlaw, J., Ellis, B.S., Bachmann, O., Guillong, M., von Quadt, A., 2017. Protracted near-solidus storage and pre-eruptive rejuvenation of large magma reservoirs. Nat. Geosci. 10, 777–784. doi:10.1038/NGEO3020

Tassara, A., Echaurren, A., 2012. Anatomy of the Andean subduction zone: Three-dimensional density model upgraded and compared against global-scale models. Geophys. J. Int. 189, 161–168. doi:10.1111/j.1365-246X.2012.05397.x

Tassara, A., Götze, H., Schmidt, S., Hackney, R., 2006. Three-dimensional density model of the Nazca plate and the Andean continental margin. J. Geophys. Res. 111, 1–26. doi:10.1029/2005JB003976

Tassara, A., Swain, C., Hackney, R., Kirby, J., 2007. Elastic thickness structure of South America estimated using wavelets and satellite-derived gravity data. Earth Planet. Sci. Lett. 253, 17–36. doi:10.1016/j.epsl.2006.10.008

Telford, W.M., Geldart, L.P., Sheriff, R.E., 1990. Applied Geophysics, 2nd ed. Cambridge Unviersity Press, New York, NY.

Thiel, S., Heinson, G., 2010. Crustal imaging of a mobile belt using magnetotellurics: An example of the Fowler Domain in South Australia. J. Geophys. Res. 115, 1–18. doi:10.1029/2009JB006698

Tikhonov, A., 1950. On determining electrical characteristics of the deep layers of the Earth's crust. Doklady 73, 295–297.

Till, C.B., Pritchard, M.E., Miller, C.A., Brugman, K.K., Ryan-Davis, J., 2018. Super-volcanic investigations. Nat. Geosci. 11, 223–229.

Till, C.B., Vazquez, J.A., Boyce, J.W., 2015. Months between rejuvenation and volcanic eruption at Yellowstone caldera, Wyoming. Geology 43, 695–698. doi:10.1130/G36862.1

Ucok, H., Ershagi, I., Olhoeft, G.R., 1980. Electrical Resistivity of Geothermal Brines. J. Pet. Technol. 32, 717–727. doi:10.2118/7878-PA

Unsworth, M.J., Chira, J., Yupa, R., Antayhua-Vera, Y., Calla-Pilco, D., Baca, B.G., Lee, B.M., Nixon, C., Ramos-Palomino, D., 2018. Magnetotelluric studies of the Andean subduction zone in southern Peru, in: American Geophysical Union 2018 Fall Meeting.

Unsworth, M.J., Rondenay, S., 2013. Mapping the distribution of fluids in the crust and lithospheric mantle utilizing geophysical methods, in: Harlov, D.E., Austrheim, H. (Eds.), Metasomatism and the Chemical Transformation of Rock. Springer Berlin Heidelberg, Berlin, Germany, pp. 535–598. doi:10.1007/978-3-642-28394-9

USGS, 2017. National Water Information System: Web Interface [WWW Document]. URL https://waterdata.usgs.gov/nwis/ (accessed 6.23.17).

van Keken, P.E., Hacker, B.R., Syracuse, E.M., Abers, G.A., 2011. Subduction factory: 4 . Depth-dependent flux of H2O from subducting slabs worldwide. J. Geophys. Res. 116, 1–15. doi:10.1029/2010JB007922

Viljanen, A., 2012. Description of magnetospheric/ionospheric sources, in: Chave, A.D., Jones, A.G. (Eds.), The Magnetotelluric Method. Cambridge Unviersity Press, Cambridge, UK, pp. 96–121.

Viljanen, A., Pirjola, R., Amm, O., 1999. Magnetotelluric source effect due to 3D ionospheric current systems using the complex image method for 1D conductivity structures. Earth Planets Sp. 51, 933–945.

Völker, D., Stipp, M., 2015. Water input and water release from the subducting Nazca Plate along southern Central Chile (33 S - 46 S). Geochemistry, Geophys. Geosystems 16, 1825–1847. doi:10.1002/2015GC005766

Wada, I., Behn, M.D., 2015. Focusing of upward fluid migration beneath volcanic arcs: Effect of mineral grain size variation in the mantle wedge. Geochemistry, Geophys. Geosystems 16, 3905–3923. doi:10.1002/2015GC005950

Wagner, L.S., Beck, S., Zandt, G., 2005. Upper mantle structure in the south central Chilean subduction zone (30° to 36°S). J. Geophys. Res. 110, B01308. doi:10.1029/2004JB003238

Wait, J., 1954. On the relation between telluric currents and the earth's magnetic field. Geophysics 19, 281–289.

Walton, N.R.G., 1989. Electrical Conductivity and Total Dissolved Solids-What is Their Precise Relationship? Desalination 72, 275–292.

Wannamaker, P.E., Caldwell, T.G., Jiracek, G.R., Maris, V., Hill, G.J., Ogawa, Y., Bibby, H.M., Bennie, S.L., Heise, W., 2009. Fluid and deformation regime of an advancing subduction system at Marlborough, New Zealand. Nature 460, 733–736. doi:10.1038/nature08204

Wannamaker, P.E., Evans, R.L., Bedrosian, P.A., Unsworth, M.J., Maris, V., McGary, R.S., 2014. Segmentation of plate coupling, fate of subduction fluids, and modes of arc magmatism in Cascadia, inferred from magnetotelluric resistivity. Geochemistry, Geophys. Geosystems 15, 4230–4253. doi:10.1002/2014GC005509

Wannamaker, P.E., Hohmann, G., Ward, S., 1984. Magnetotelluric responses of three-dimensional bodies in layered earths. Geophysics 49, 1517–1533.

Wannamaker, P.E., Stodt, J.A., Rijo, L., Rijofi, L., 1986. Two-dimensional topographic responses in magnetotellurics modeled using finite elements. Geophysics 51, 2131–2144. doi:10.1190/1.1442065

Waxman, M.H., Smits, L.J.M., 1968. Electrical Conductivities in Oil-Bearing Shaly Sands. Soc. Pet. Eng. J. 8, 107–122.

Weidelt, P., 2005. The relationship between the spectral function and the underlying conductivity

structure in 1-D magnetotellurics. Geophys. J. Int. 161, 566–590. doi:10.1111/j.1365-246X.2005.02625.x

Weidelt, P., 1972. The inverse problem of geomagnetic induction. Zeitschrift für Geophys. 38, 257–289.

Weidelt, P., Kaikkonen, P., 1994. Local 1-D interpretation of magnetotelluric B-polarization impedances. Geophys. J. Int. 117, 733–748. doi:10.1111/j.1365-246X.1994.tb02466.x

Wespestad, C.E., Thurber, C.H., Andersen, N.L., Singer, B.S., Cardona, C., Zeng, X., Bennington, N.L., Keranen, K., Peterson, D.E., Cordell, D., Unsworth, M.J., Miller, C., Williams-Jones, G., 2019. Magma Reservoir Below Laguna del Maule Volcanic Field, Chile, Imaged With Surface-Wave Tomography. J. Geophys. Res. Solid Earth 124, 1–15. doi:10.1029/2018JB016485

Wilson, C.R., Spiegelman, M., Keken, P.E. Van, Hacker, B.R., 2014. Fluid flow in subduction zones: The role of solid rheology and compaction pressure. Earth Planet. Sci. Lett. 401, 261–274. doi:10.1016/j.epsl.2014.05.052

Worzewski, T., Jegen, M., Kopp, H., Brasse, H., Taylor Castillo, W., 2011. Magnetotelluric image of the fluid cycle in the Costa Rican subduction zone. Nat. Geosci. 4, 108–111. doi:10.1038/ngeo1041

Yee, E., Paulson, K. V, 1988. Necessary and Sufficient Conditions for the Existence of a Solution To the One-Dimensional Magnetotelluric Inverse Problem. Geophys. J. 93, 279–293.

Yee, K.S., 1966. Numerical Solution of Initial Boundary Value Problems Involving Maxwell's Equations in Isotropic Media. IEEE Trans. Antennas Propag. 14, 302–307.

Yoshino, T., 2010. Laboratory electrical condcutivity measurement of mantle minerals. Surv. Geophys. 31, 163–206. doi:10.1007/s10712-009-9084-0

Yuan, X., Asch, G., Bataille, K., Bock, G., Bohm, M., Echtler, H., Kind, R., Oncken, O., Wölbern, I., 2006. Deep seismic images of the Southern Andes. Geol. Soc. Am. Spec. Pap. 407, 61–72. doi:10.1130/2006.2407(03).

Yungul, S.H., Hembree, M.R., Greenhouse, J.P., 1973. Telluric anomalies associated with isolated reefs in the Midland Basin, Texas. Geophysics 38, 545–556.

Zellmer, G.F., Annen, C., 2008. An introduction to magma dynamics. Geol. Soc. London 304, 1–13. doi:10.1144/SP304.1

Zhan, Y., Gregg, P.M., Mével, H. Le, Miller, C.A., Cardona, C., 2019. Integrating Reservoir Dynamics, Crustal Stress, and Geophysical Observations of the Laguna del Maule Magmatic System by FEM Models and Data Assimilation. J. Geophys. Res. Solid Earth 124, 1–16. doi:10.1029/2019JB018681

APPENDIX 1: MAGNETOTELLURIC DATA USED IN 3-D INVERSION

The three-dimensional inversions presented in Chapter 5 and Chapter 6 were obtained by inversion of the full impedance tensor data at 71 magnetotelluric stations. Apparent resistivity and phase data from all 71 stations are shown below for all four impedance components (circles and hexagons). The inversion data fit from the preferred model in Chapter 5 is also shown as solid lines. Six of the sites were also used in the two-dimensional inversions shown in Chapter 7 and are duplicated in Appendix 2.

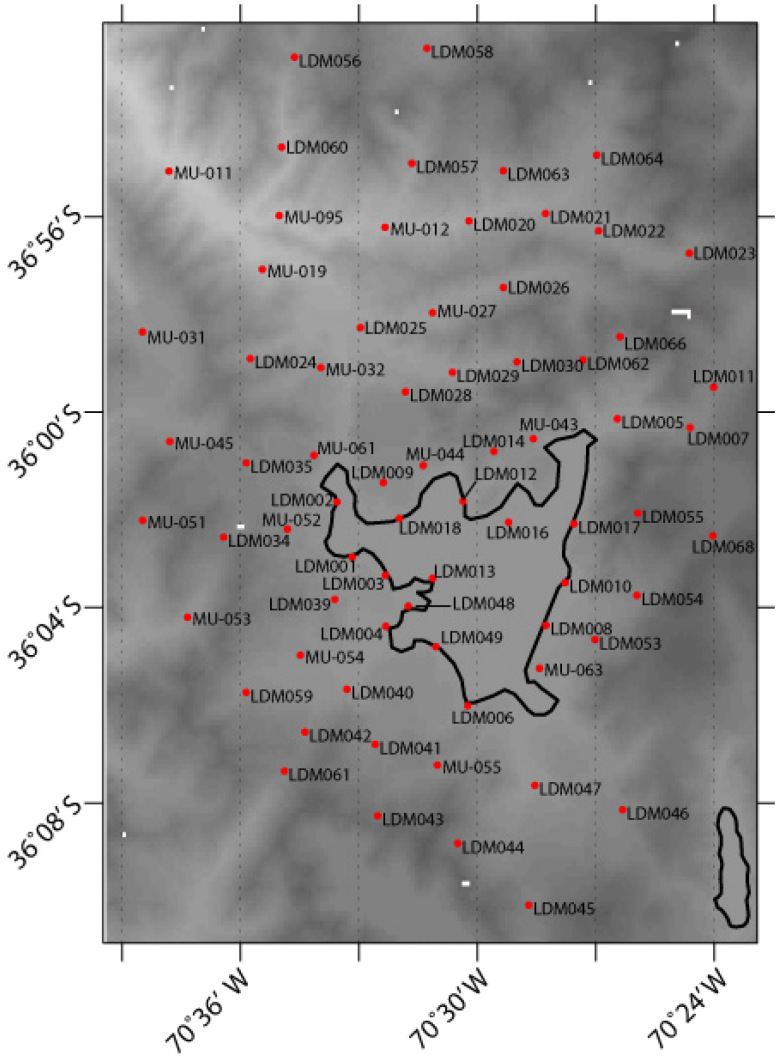

Figure A1.1: A reference map with station locations and labels. The outline of Laguna del Maule is shown for reference.

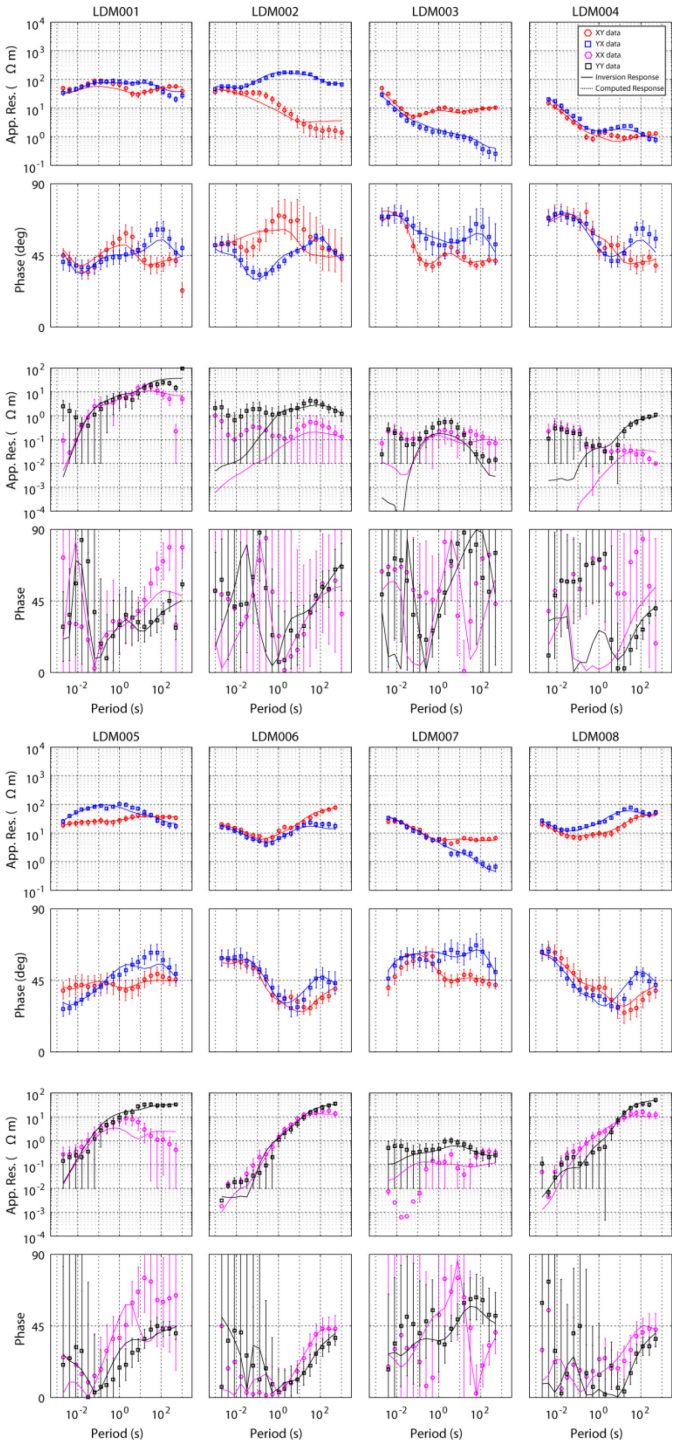

Figure A1.2: Apparent resistivity and phase for all four impedance components for LDM001 through LDM008. Off-diagonal impedance is shown as red (xy) and blue (yx) while diagonal impedances are shown as magenta (xx) and black (yx). The inversion data fit is shown as a solid line.

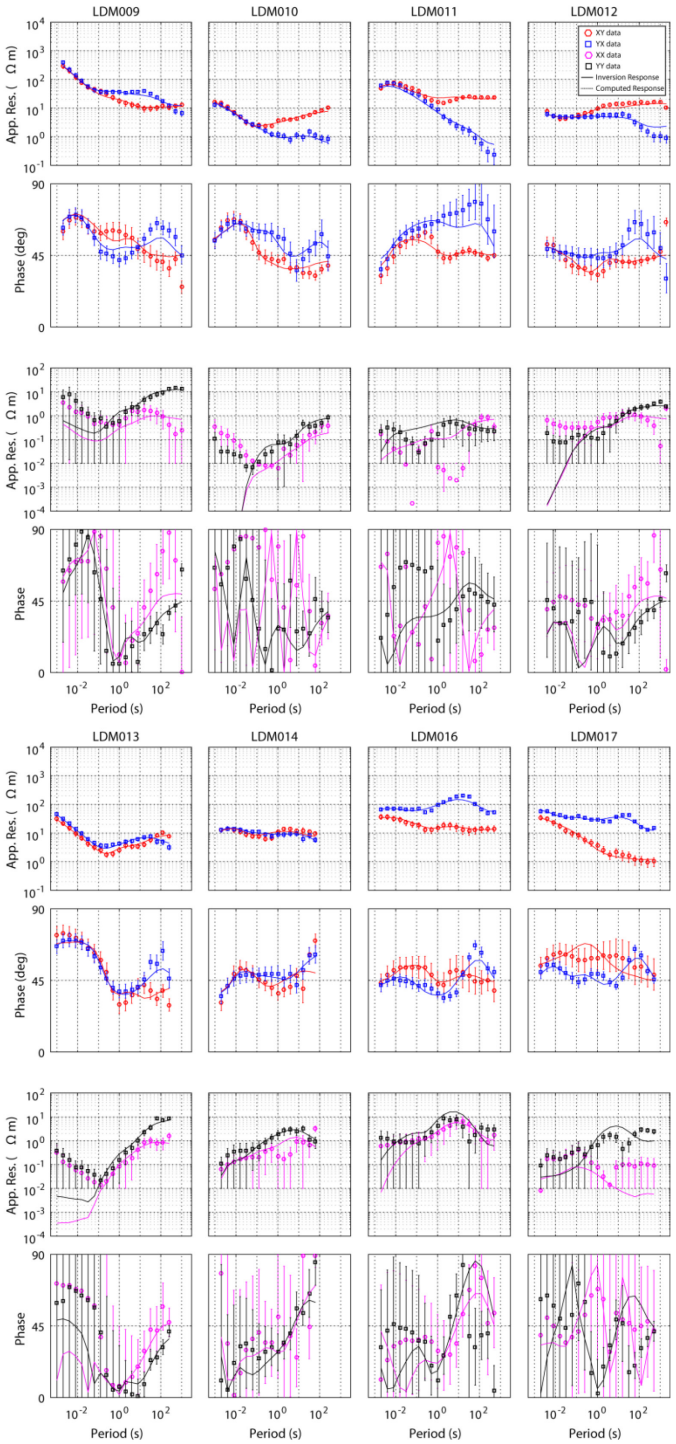

Figure A1.3: Apparent resistivity and phase for all impedance components for LDM009 through LDM017. See Figure A1.2 Caption.

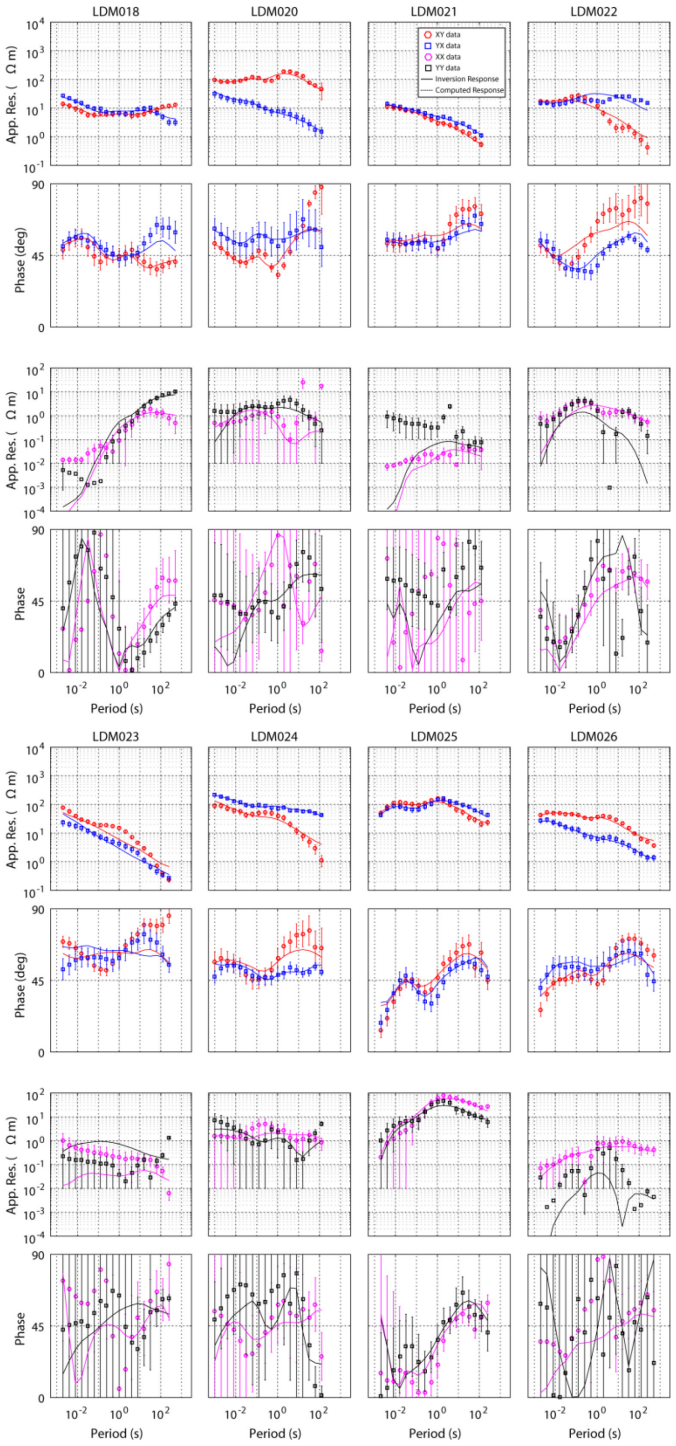

Figure A1.4: Apparent resistivity and phase for all impedance components for LDM018 through LDM026. See Figure A1.2 Caption.

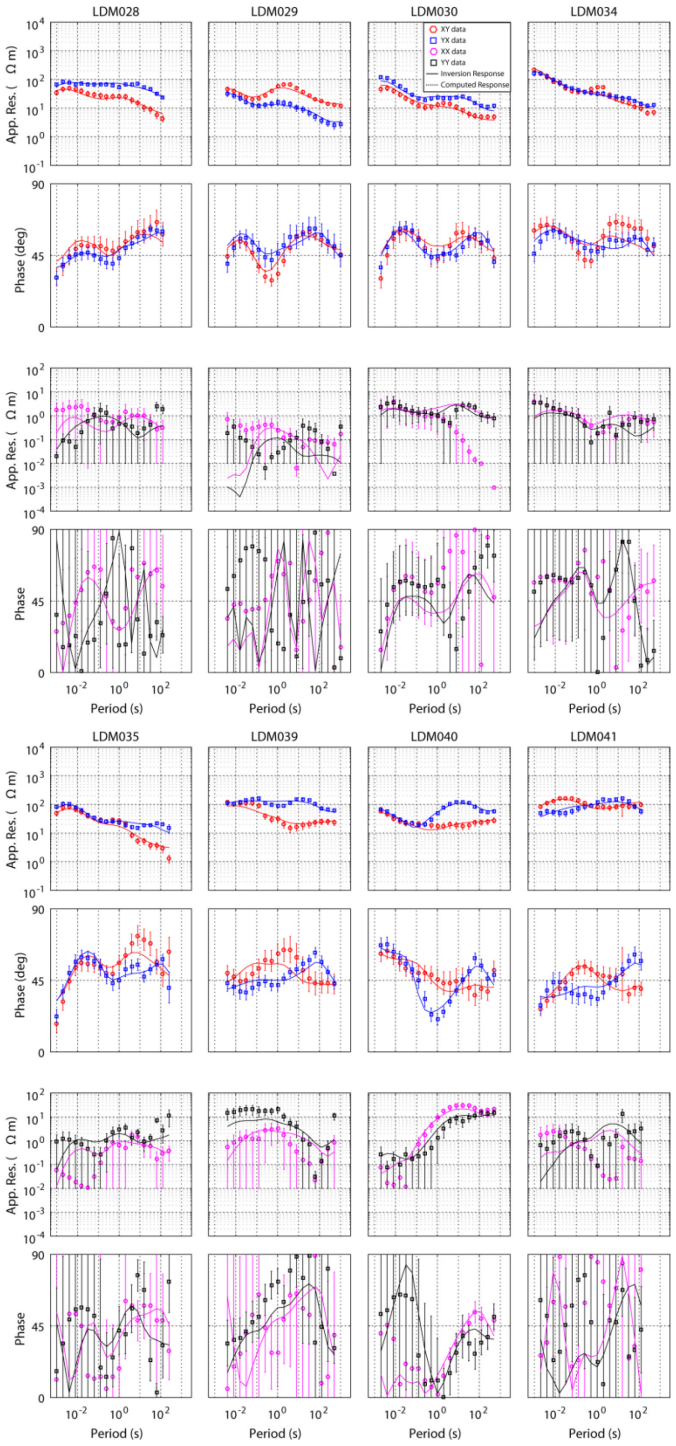

Figure A1.5: Apparent resistivity and phase for all impedance components for LDM028 through LDM041. See Figure A1.2 Caption.

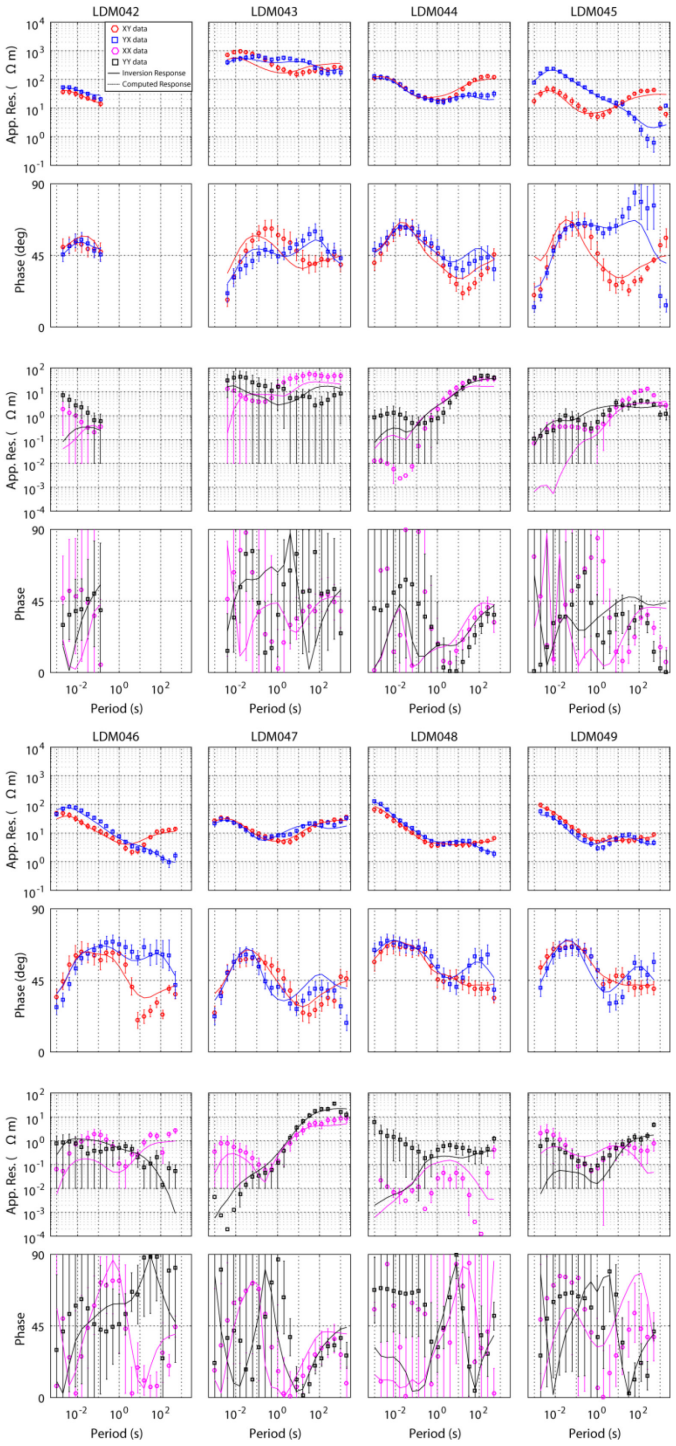

Figure A1.6: Apparent resistivity and phase for all impedance components for LDM042 through LDM049. See Figure A1.2 Caption.

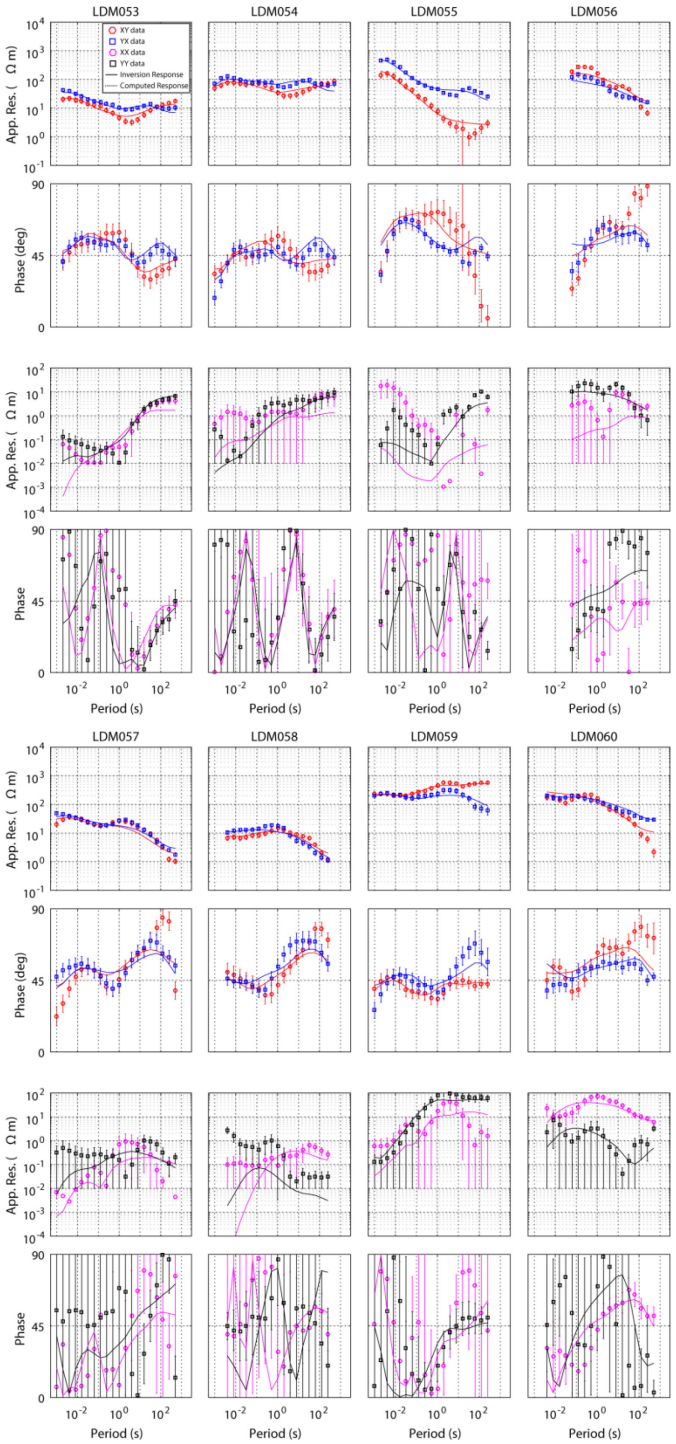

Figure A1.7: Apparent resistivity and phase for all impedance components for LDM053 through LDM060. See Figure A1.2 Caption.

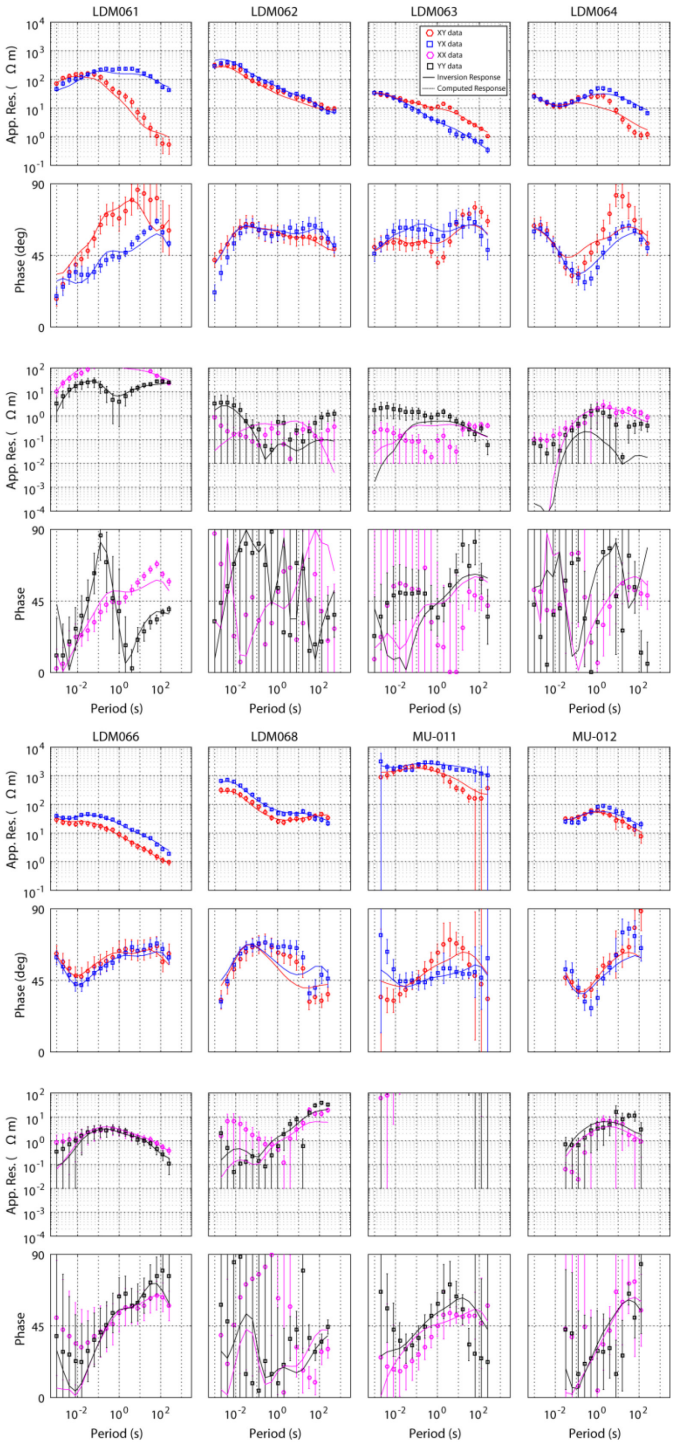

Figure A1.8: Apparent resistivity and phase for all impedance components for LDM061 through LDM068 and MU-011 and MU-012. See Figure A1.2 Caption.

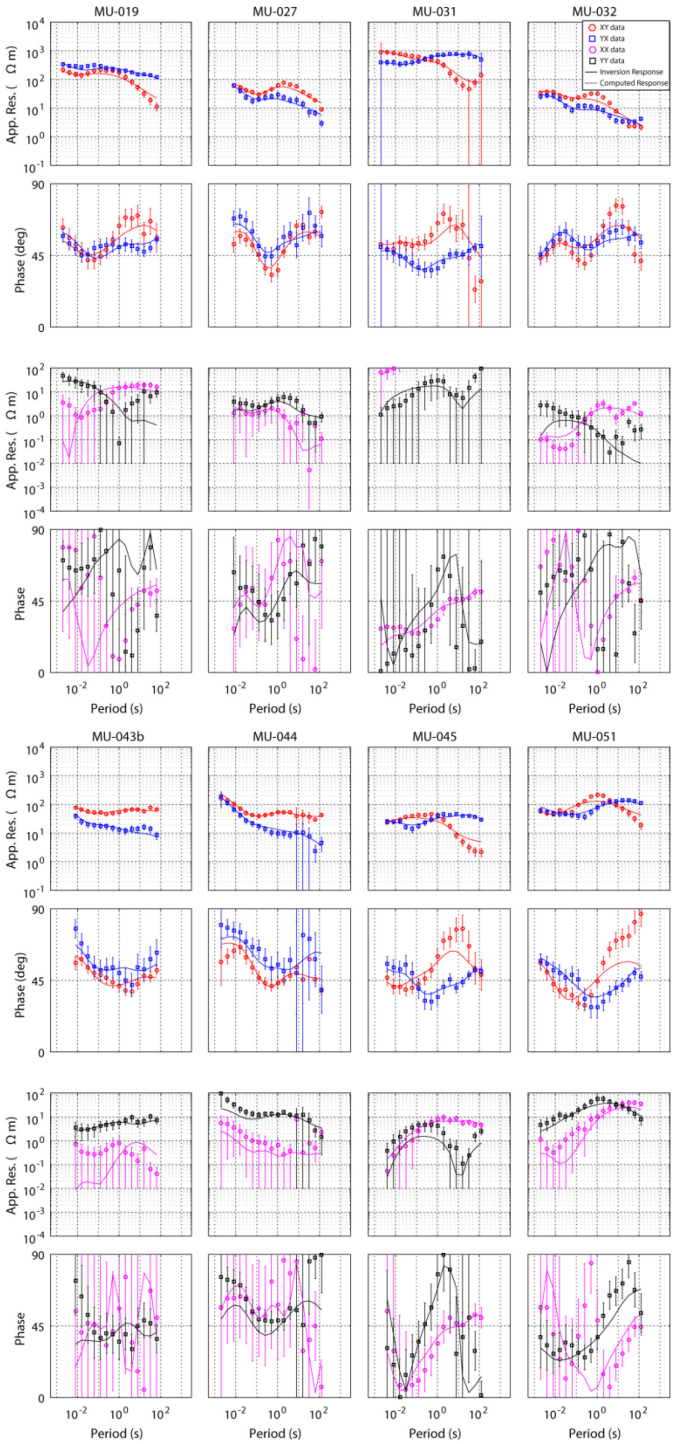

Figure A1.9: Apparent resistivity and phase for all impedance components for MU-019 through MU-051. See Figure A1.2 Caption.

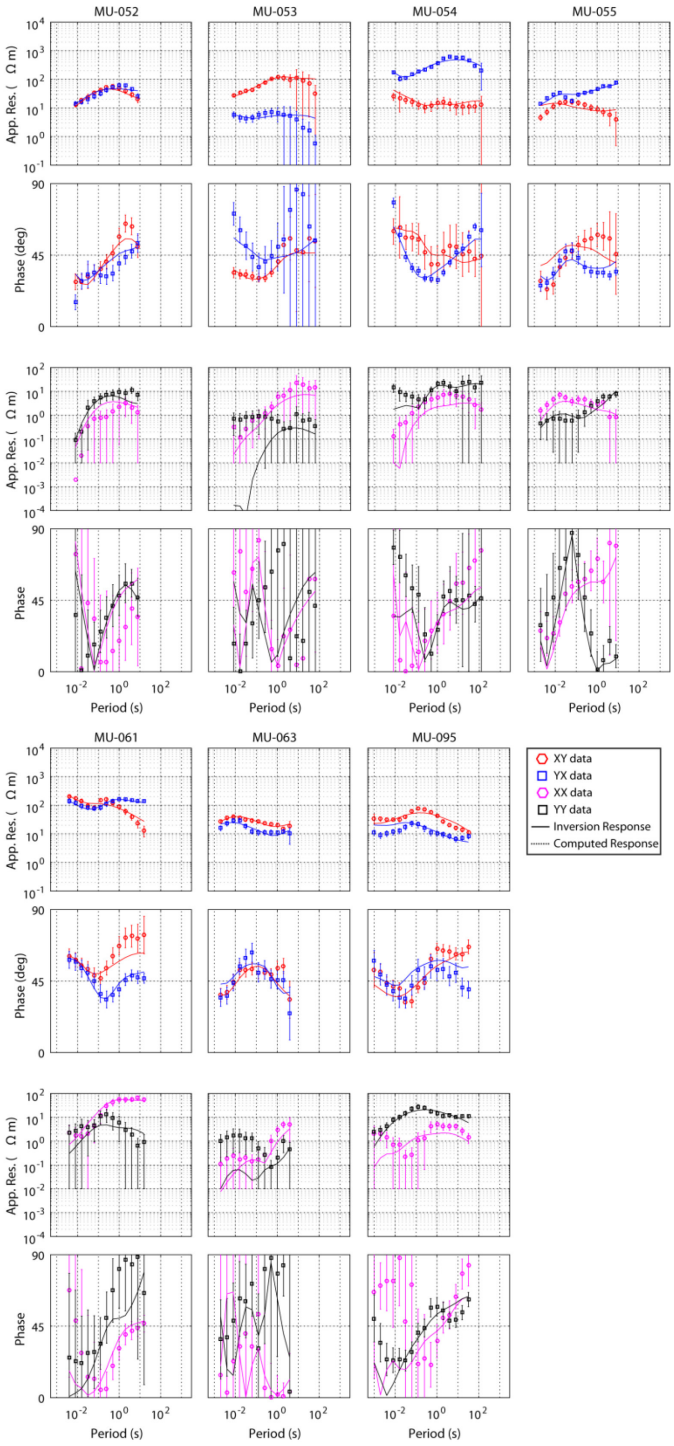

Figure A1.10: Apparent resistivity and phase for all impedance components for MU-052 through MU-095. See Figure A1.2 Caption.

APPENDIX 2: MAGNETOTELLURIC DATA USED IN 2-D INVERSION

The two-dimensional inversions presented in Chapter 7 were obtained by inversion of the off-diagonal impedance tensor data at 38 magnetotelluric stations. Apparent resistivity and phase data from all 38 stations are shown below for both off-diagonal impedance components (red and blue dots). The inversion data fit from the preferred model in Chapter 7 is also shown as solid lines. Six of the sites were also used in the three-dimensional inversions shown in Chapter 5 and 6 and are duplicated in Appendix 1.

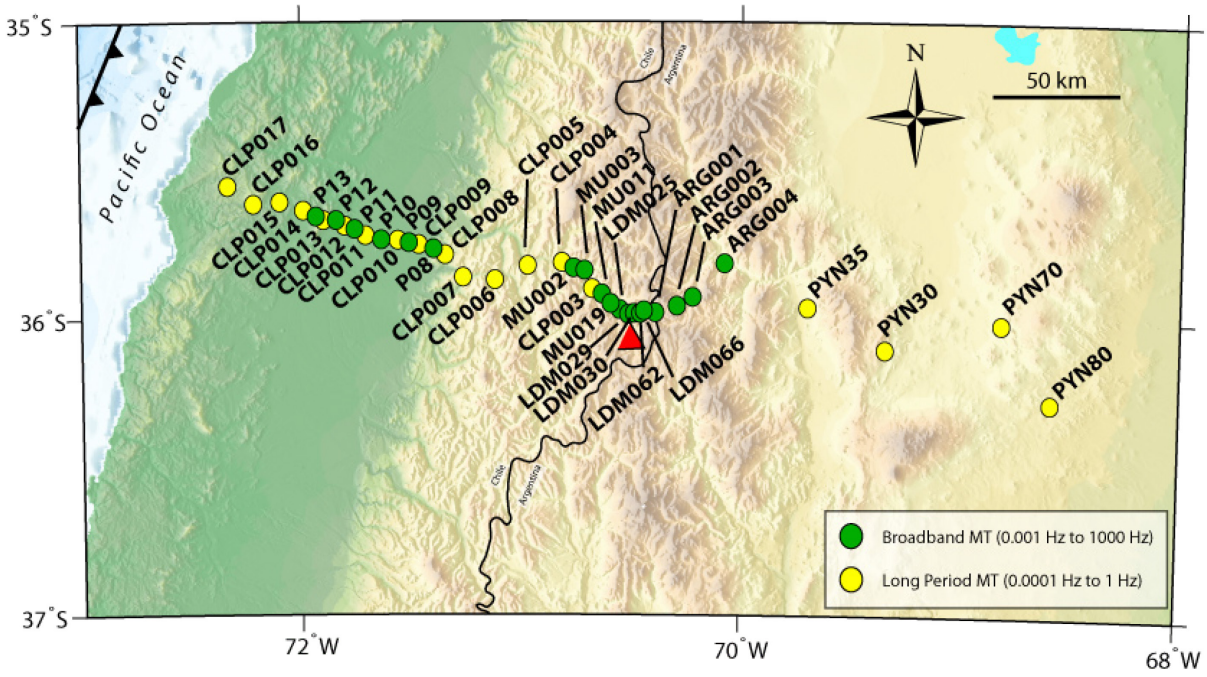

Figure A2.1: Map with site locations and labels. The location of Laguna del Maule is noted with a red triangle.

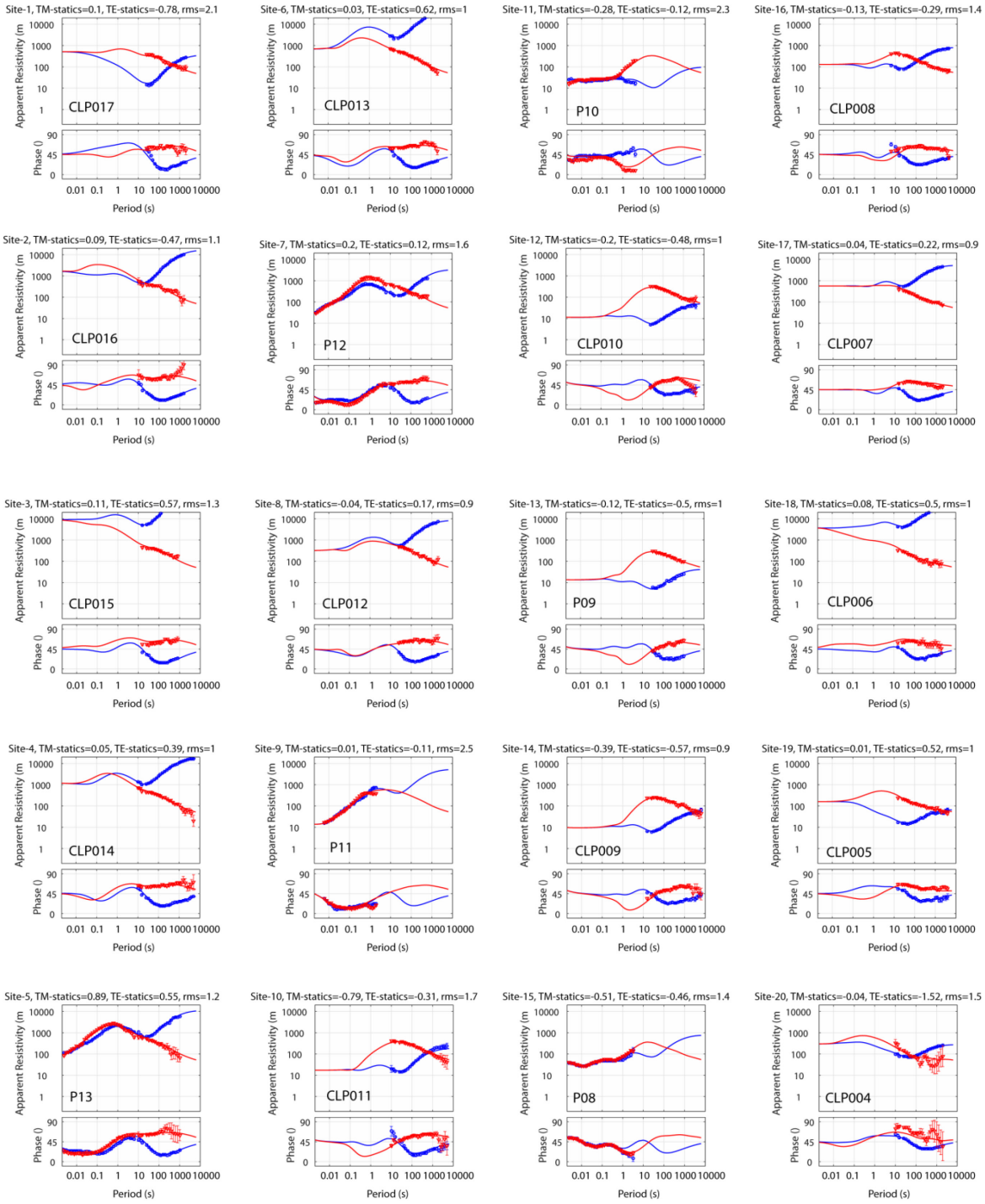

Figure A2.2: Apparent resistivity and phase curves for the 20 magnetotelluric (MT) sites on the western side of the profile. The impedance tensor is rotated 15° E of N such that the TE mode (red dots) has electric fields parallel to geoelectric strike. The TM mode (blue dots) is orthogonal to the TE mode. The inversion data fit for the preferred inversion (shown in Figure 7.15 in the main text) is shown as a solid red line (TE mode) and blue line (TM mode).

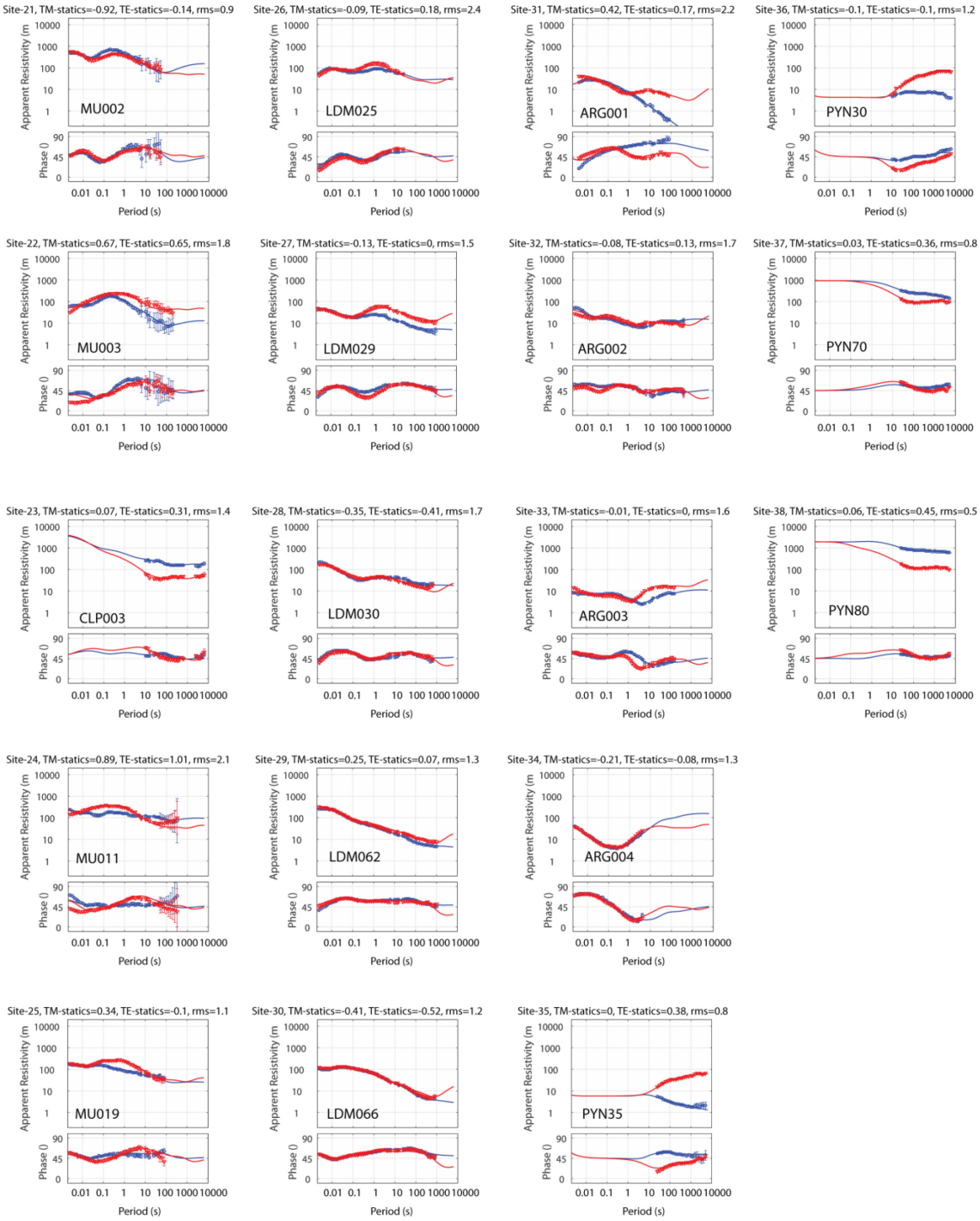

Figure A2.3: Apparent resistivity and phase curves for the 18 magnetotelluric (MT) sites on the eastern side of the profile. See Figure A2.2 caption for details.